How "plasticity" buys time for organisms to evolve *p. 988*

The star formation history of the Universe *pp. 995 & 1031*

Momma spider nurses her young *p. 1052*

Science

$15
30 NOVEMBER 2018
sciencemag.org

AAAS

THE PROTEASOME IN ACTION

Coordinated motion propels substrate into the degradation chamber *p. 1018*

CONTENTS

30 NOVEMBER 2018 • VOLUME 362 • ISSUE 6418

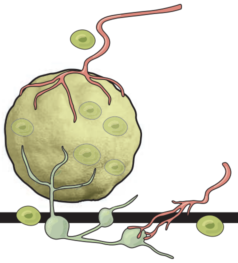

999
The mechanics of metastasis

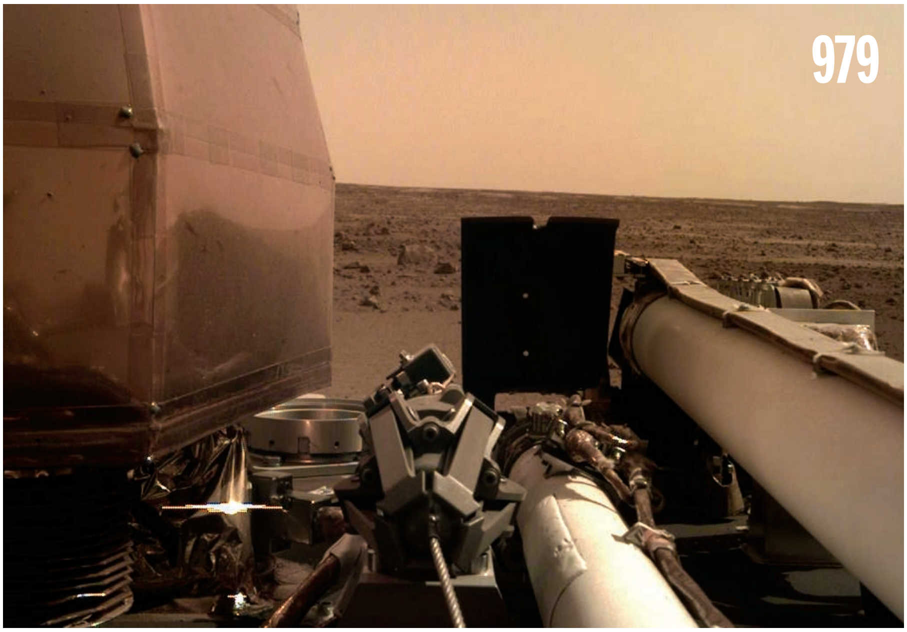

979

Newly arrived lander gets set to deploy instruments on Mars.

NEWS

IN BRIEF

976 News at a glance

IN DEPTH

978 SHOCK GREETS CLAIM OF CRISPR-EDITED BABIES
Apparent germline engineering by Chinese researcher prompts outrage and investigations *By D. Normile*

979 SAFELY SETTLED, INSIGHT GETS READY TO LOOK INSIDE MARS
Lander will deploy seismometer and heat probe to listen for marsquakes and study the planet's interior *By P. Voosen*

980 MIGRANTS AND TRADE SPICED UP CANAANITE METROPOLIS
In Bronze Age tombs, signs of vanilla, 3000 years early, and elaborate medical care *By A. Lawler*

982 CHINA SETS OUT FOR THE FAR SIDE OF THE MOON
Latest mission in ambitious program is a boon for lunar geology and radio astronomy *By D. Normile*

983 EUROPEAN FUNDERS DETAIL THEIR OPEN-ACCESS PLAN
Plan S will allow researchers to publish in hybrid journals that commit to flip to full open access *By T. Rabesandratana*

FEATURES

984 FORGOTTEN NO MORE
A long-overlooked scourge of millions, hepatitis B is in the crosshairs at last
By J. Cohen

988 BUYING TIME
In a fast-changing environment, evolution can be too slow. "Plasticity" can give it a chance to catch up
By E. Pennisi
▸ PODCAST

INSIGHTS

PERSPECTIVES

992 THE LAST OF ASIA CONQUERED BY *HOMO SAPIENS*
Excavation reveals the earliest human colonization of the Tibetan Plateau
By J.-F. Zhang and R. Dennell
▸ REPORT P. 1049

994 NEW DIMENSIONS FOR BRAIN MAPPING
Imaging reveals new features of memory representation in the brain *By Y. Assaf*
▸ REPORT P. 1045

995 CLUES FROM GAMMA RAYS ON THE HISTORY OF STAR BIRTH
The rate of star formation peaked 10 billion years ago *By E. Prandini*
▸ REPORT P. 1031

996 ONE CRYSTAL OUT OF MANY
Fast-moving grain boundaries convert a hanging polycrystalline metal foil into a single crystal
By A. Rollett
▸ RESEARCH ARTICLE P. 1021

998 CULTURE AND CONFORMITY SHAPE FRUITFLY MATING
Potent social learning sustains the inheritance of mating preferences over generations *By A. Whiten*
▸ RESEARCH ARTICLE P. 1025

999 METASTASES GO WITH THE FLOW
Blood flow mechanics influence metastatic efficiency *By J. G. Goetz*

1001 LEON MAX LEDERMAN (1922–2018)
Charismatic particle physics pioneer
By R. Kolb

POLICY FORUM

1002 THE CASE FOR MONITORING LIFE-SPAN INEQUALITY
Focus on variation in age at death, not just average age *By A. A. van Raalte* et al.

BOOKS *ET AL.*

1005 PLAYING WITH PARTICLE PHYSICS
The quantum realm comes to life in a fast-paced new board game
By A. Chuang

1006 THE MYTH OF APOLITICAL SCIENCE
Denouncing state-controlled research, U.S. investigators advanced the American agenda during the Cold War
By A. Wellerstein

LETTERS

1007 PREPARE FOR CASCADIA'S NEXT EARTHQUAKE
By B. A. Leshchinsky et al.

CREDITS (FROM TOP): N. DESAI/*SCIENCE*; NASA/JPL-CALTECH

CONTENTS

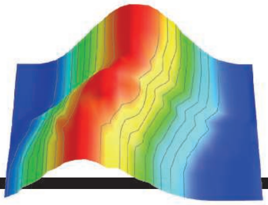

1037

Tracking transitions in VO_2

30 NOVEMBER 2018 • VOLUME 362 • ISSUE 6418

1007 SCAN THE HORIZON FOR UNPRECEDENTED RISKS

By S. Simon et al.

1008 LEGISLATION RESTRICTS RESEARCH IN URUGUAY

By R. Sommaruga et al.

1008 TECHNICAL COMMENT ABSTRACTS

RESEARCH

IN BRIEF

1014 From *Science* and other journals

REVIEW

1017 MICROBIOTA

Colonocyte metabolism shapes the gut microbiota *Y. Litvak* et al.

REVIEW SUMMARY; FOR FULL TEXT: dx.doi.org/10.1126/science.aat9076

RESEARCH ARTICLES

1018 STRUCTURAL BIOLOGY

Substrate-engaged 26S proteasome structures reveal mechanisms for ATP-hydrolysis–driven translocation *A. H. de la Peña* et al.

RESEARCH ARTICLE SUMMARY; FOR FULL TEXT: dx.doi.org/10.1126/science.aav0725

1019 BIOCHEMISTRY

Formyl-methionine as an N-degron of a eukaryotic N-end rule pathway *J.-M. Kim* et al.

RESEARCH ARTICLE SUMMARY; FOR FULL TEXT: dx.doi.org/10.1126/science.aat0174

1020 STRUCTURAL BIOLOGY

An electron transfer path connects subunits of a mycobacterial respiratory supercomplex *H. Gong* et al.

RESEARCH ARTICLE SUMMARY; FOR FULL TEXT: dx.doi.org/10.1126/science.aat8923

1021 METALLURGY

Colossal grain growth yields single-crystal metal foils by contact-free annealing *S. Jin* et al.

▸ PERSPECTIVE P. 996

1025 ANIMAL CULTURE

Cultural flies: Conformist social learning in fruitflies predicts long-lasting mate-choice traditions *E. Danchin* et al.

▸ PERSPECTIVE P. 998; VIDEO

REPORTS

1031 COSMOLOGY

A gamma-ray determination of the Universe's star formation history *The Fermi-LAT Collaboration*

▸ PERSPECTIVE P. 995; PODCAST

1034 DISTANT GALAXIES

The multiple merger assembly of a hyperluminous obscured quasar at redshift 4.6 *T. Díaz-Santos* et al.

1037 SOLID-STATE PHYSICS

Isostructural metal-insulator transition in VO_2 *D. Lee* et al.

1040 SUPERCONDUCTIVITY

Uniaxial pressure control of competing orders in a high-temperature superconductor *H.-H. Kim* et al.

1045 NEUROSCIENCE

Fast track to the neocortex: A memory engram in the posterior parietal cortex *S. Brodt* et al.

▸ PERSPECTIVE P. 994

1049 ARCHAEOLOGY

The earliest human occupation of the high-altitude Tibetan Plateau 40 thousand to 30 thousand years ago *X. L. Zhang* et al.

▸ PERSPECTIVE P. 992

1052 MATERNAL CARE

Prolonged milk provisioning in a jumping spider *Z. Chen* et al.

▸ VIDEO

1055 CANCER

Human tumor genomics and zebrafish modeling identify *SPRED1* loss as a driver of mucosal melanoma *J. Ablain* et al.

1060 CANCER GENOMICS

Single-cell multiomics sequencing and analyses of human colorectal cancer *S. Bian* et al.

1064 IMMUNOLOGY

Pathogen blockade of TAK1 triggers caspase-8–dependent cleavage of gasdermin D and cell death *P. Orning* et al.

DEPARTMENTS

975 EDITORIAL

Define the human right to science

By Jessica M. Wyndham and Margaret Weigers Vitullo

1078 WORKING LIFE

At the end of the road, a new start

By Francis Aguisanda

ON THE COVER

Structures of the actively degrading 26*S* proteasome show consecutive states of the ATPase motor with conserved tyrosine paddles (blue, green, and yellow clusters) arranged in a spiral staircase and pulling a protein substrate (yellow blocks) into a degradation chamber. The original conformational state is transparent, whereas the subsequent state is opaque. The data provide insights into how this member of the AAA+ family couples ATP hydrolysis with conformational changes to produce mechanical work. See page 1018. *Illustration: V. Altounian/*Science*; Structural data: PDB IDs 6EF1 and 6EF3*

Science Staff 974
AAAS News & Notes 1009
New Products 1070
Science Careers 1071

SCIENCE (ISSN 0036-8075) is published weekly on Friday, except last week in December, by the American Association for the Advancement of Science, 1200 New York Avenue, NW, Washington, DC 20005. Periodicals mail postage (publication No. 484460) paid at Washington, DC, and additional mailing offices. Copyright © 2018 by the American Association for the Advancement of Science. The title SCIENCE is a registered trademark of the AAAS. Domestic individual membership, including subscription (12 months): $165 ($74 allocated to subscription). Domestic institutional subscription (51 issues): $1808; Foreign postage extra: Mexico, Caribbean (surface mail) $55; other countries (air assist delivery): $89. First class, airmail, student, and emeritus rates on request. Canadian rates with GST available upon request, GST #125488122. Publications Mail Agreement Number 1069624. **Printed in the U.S.A.**
Change of address: Allow 4 weeks, giving old and new addresses and 8-digit account number. **Postmaster:** Send change of address to AAAS, P.O. Box 96178, Washington, DC 20090–6178. **Single-copy sales:** $15 each plus shipping and handling; bulk rate on request. **Authorization to reproduce** material for internal or personal use under circumstances not falling within the fair use provisions of the Copyright Act is granted by AAAS to libraries and others who use Copyright Clearance Center (CCC) Pay-Per-Use services provided that $35.00 per article is paid directly to CCC, 222 Rosewood Drive, Danvers, MA 01923. The identification code for *Science* is 0036-8075. *Science* is indexed in the *Reader's Guide to Periodical Literature* and in several specialized indexes.

IMAGE: LEE *ET AL.*

Science
AAAS
1200 New York Avenue, NW, Washington, DC 20005
Clarendon House, Clarendon Road, Cambridge, UK CB2 8FH

Editor-in-Chief Jeremy Berg
Executive Editor Monica M. Bradford **News Editor** Tim Appenzeller
Editor, Insights Lisa D. Chong **Editors, Research** Valda Vinson, Jake S. Yeston

Research and Insights

DEPUTY EDITORS Julia Fahrenkamp-Uppenbrink(UK), Stella M. Hurtley(UK), Phillip D. Szuromi, Sacha Vignieri **SR. EDITORIAL FELLOW** Andrew M. Sugden(UK) **SR. EDITORS** Gemma Alderton(UK), Caroline Ash(UK), Pamela J. Hines, Paula A. Kiberstis, Marc S. Lavine(Canada), Steve Mao, Ian S. Osborne(UK), Beverly A. Purnell, L. Bryan Ray, H. Jesse Smith, Jelena Stajic, Peter Stern(UK), Brad Wible, Laura M. Zahn **ASSOCIATE EDITORS** Michael A. Funk, Brent Grocholski, Priscilla N. Kelly, Tage S. Rai, Seth Thomas Scanlon(UK), Keith T. Smith(UK) **ASSOCIATE BOOK REVIEW EDITOR** Valerie B. Thompson **LETTERS EDITOR** Jennifer Sills **LEAD CONTENT PRODUCTION EDITORS** Harry Jach, Lauren Kmec **CONTENT PRODUCTION EDITORS** Amelia Beyna, Jeffrey E. Cook, Amber Esplin, Chris Filiatreau, Cynthia Howe **SR. EDITORIAL COORDINATORS** Carolyn Kyle, Beverly Shields **EDITORIAL COORDINATORS** Aneera Dobbins, Joi S. Granger, Jeffrey Hearn, Lisa Johnson, Maryrose Madrid, Shannon McMahon, Jerry Richardson, Alice Whaley(UK), Anita Wynn **PUBLICATIONS ASSISTANTS** Ope Martins, Nida Masiulis, Dona Mathieu, Ronmel Navas, Hilary Stewart(UK), Alana Warnke, Brian White **EXECUTIVE ASSISTANT** Jessica Slater **ASI DIRECTOR, OPERATIONS** Janet Clements(UK) **ASI SR. OFFICE ADMINISTRATOR** Jessica Waldock(UK)

News

NEWS MANAGING EDITOR John Travis **INTERNATIONAL EDITOR** Martin Enserink **DEPUTY NEWS EDITORS** Elizabeth Culotta, Lila Guterman, David Grimm, Eric Hand, David Malakoff, Leslie Roberts **SR. CORRESPONDENTS** Daniel Clery(UK), Jon Cohen, Jeffrey Mervis, Elizabeth Pennisi **ASSOCIATE EDITORS** Jeffrey Brainard, Catherine Matacic **NEWS WRITERS** Adrian Cho, Jennifer Couzin-Frankel, Jocelyn Kaiser, Kelly Servick, Robert F. Service, Erik Stokstad(Cambridge, UK), Paul Voosen, Meredith Wadman **INTERN** Frankie Schembri **CONTRIBUTING CORRESPONDENTS** Warren Cornwall, Ann Gibbons, Mara Hvistendahl, Sam Kean, Eli Kintisch, Kai Kupferschmidt(Berlin), Andrew Lawler, Mitch Leslie, Eliot Marshall, Virginia Morell, Dennis Normile(Shanghai), Charles Piller, Tania Rabesandratana(London), Emily Underwood, Gretchen Vogel(Berlin), Lizzie Wade(Mexico City) **CAREERS** Donisha Adams, Rachel Bernstein(Editor), Katie Langin **COPY EDITORS** Julia Cole (Senior Copy Editor), Cyra Master (Copy Chief) **ADMINISTRATIVE SUPPORT** Meagan Weiland

Executive Publisher Rush D. Holt
Publisher Bill Moran **Chief Digital Media Officer** Josh Freeman

DIRECTOR, BUSINESS STRATEGY AND PORTFOLIO MANAGEMENT Sarah Whalen **DIRECTOR, PRODUCT AND CUSTOM PUBLISHING** Will Schweitzer **MANAGER, PRODUCT DEVELOPMENT** Hannah Heckner **BUSINESS SYSTEMS AND FINANCIAL ANALYSIS DIRECTOR** Randy Yi **DIRECTOR, BUSINESS OPERATIONS & ANALYST** Eric Knott **ASSOCIATE DIRECTOR, PRODUCT MANAGMENT** Kris Bishop **SENIOR SYSTEMS ANALYST** Nicole Mehmedovich **SENIOR BUSINESS ANALYST** Cory Lipman **MANAGER, BUSINESS OPERATIONS** Jessica Tierney **BUSINESS ANALYSTS** Meron Kebede, Sandy Kim, Jourdan Stewart **FINANCIAL ANALYST** Julian Iriarte **ADVERTISING SYSTEM ADMINISTRATOR** Tina Burks **SALES COORDINATOR** Shirley Young **DIRECTOR, COPYRIGHT, LICENSING, SPECIAL PROJECTS** Emilie David **DIGITAL PRODUCT ASSOCIATE** Michael Hardesty **RIGHTS AND PERMISSIONS ASSOCIATE** Elizabeth Sandler **RIGHTS, CONTRACTS, AND LICENSING ASSOCIATE** Lili Catlett **RIGHTS & PERMISSIONS ASSISTANT** Alexander Lee

DIRECTOR, INSTITUTIONAL LICENSING Iquo Edim **ASSOCIATE DIRECTOR, RESEARCH & DEVELOPMENT** Elisabeth Leonard **SENIOR INSTITUTIONAL LICENSING MANAGER** Ryan Rexroth **INSTITUTIONAL LICENSING MANAGERS** Marco Castellan, Chris Murawski **SENIOR OPERATIONS ANALYST** Lana Guz **MANAGER, AGENT RELATIONS & CUSTOMER SUCCESS** Judy Lillibridge

WEB TECHNOLOGIES TECHNOLOGY DIRECTOR David Levy **PROJECT MANAGER** Dean Robbins **DEVELOPER** Liana Birke

DIGITAL MEDIA DIRECTOR OF ANALYTICS Enrique Gonzales **DIGITAL REPORTING ANALYST** Timothy Frailey **MULTIMEDIA MANAGER** Sarah Crespi **MANAGING WEB PRODUCER** Kara Estelle-Powers **DIGITAL PRODUCER** Jessica Hubbard **VIDEO PRODUCERS** Chris Burns, Meagan Cantwell **SOCIAL MEDIA PRODUCER** Brice Russ

DIGITAL/PRINT STRATEGY MANAGER Jason Hillman **QUALITY TECHNICAL MANAGER** Marcus Spiegler **DIGITAL PRODUCTION MANAGER** Lisa Stanford **ASSISTANT MANAGER DIGITAL/PRINT** Rebecca Doshi **SENIOR CONTENT SPECIALISTS** Steve Forrester, Antoinette Hodal, Lori Murphy **CONTENT SPECIALISTS** Jacob Hedrick, Kimberley Oster

DESIGN DIRECTOR Beth Rakouskas **DESIGN MANAGING EDITOR** Marcy Atarod **SENIOR DESIGNER** Chrystal Smith **DESIGNER** Christina Aycock **GRAPHICS MANAGING EDITOR** Alberto Cuadra **GRAPHICS EDITOR** Nirja Desai **SENIOR SCIENTIFIC ILLUSTRATORS** Valerie Altounian, Chris Bickel **SCIENTIFIC ILLUSTRATOR** Alice Kitterman **INTERACTIVE GRAPHICS EDITOR** Jia You **SENIOR GRAPHICS SPECIALISTS** Holly Bishop, Nathalie Cary **PHOTOGRAPHY MANAGING EDITOR** William Douthitt **PHOTO EDITOR** Emily Petersen **IMAGE RIGHTS AND FINANCIAL MANAGER** Jessica Adams

SENIOR EDITOR, CUSTOM PUBLISHING Sean Sanders: 202-326-6430 **ASSISTANT EDITOR, CUSTOM PUBLISHING** Jackie Oberst: 202-326-6463 **ADVERTISING PRODUCTION OPERATIONS MANAGER** Deborah Tompkins **SR. PRODUCTION SPECIALIST/GRAPHIC DESIGNER** Amy Hardcastle **SR. TRAFFIC ASSOCIATE** Christine Hall **DIRECTOR OF BUSINESS DEVELOPMENT AND ACADEMIC PUBLISHING RELATIONS, ASIA** Xiaoying Chu: +86-131 6136 3212, xchu@aaas.org **COLLABORATION/CUSTOM PUBLICATIONS/JAPAN** Adarsh Sandhu + 81532-81-5142 asandhu@aaas.org **EAST COAST/E. CANADA** Laurie Faraday: 508-747-9395, FAX 617-507-8189 **WEST COAST/W. CANADA** Lynne Stickrod: 415-931-9782, FAX 415-520-6940 **MIDWEST** Jeffrey Dembksi: 847-498-4520 x3005, Steven Loerch: 847-498-4520 x3006 **UK EUROPE/ASIA** Roger Goncalves: TEL/FAX +41 43 243 1358 **JAPAN** Kaoru Sasaki (Tokyo): + 81 (3) 6459 4174 ksasaki@aaas.org

ASSOCIATE DIRECTOR, BUSINESS DEVELOPMENT Justin Sawyers **GLOBAL MARKETING MANAGER** Allison Pritchard **DIGITAL MARKETING ASSOCIATE** Aimee Aponte **MARKETING MANAGER, JOURNALS** Shawana Arnold **MARKETING ASSOCIATES** Mike Romano, Tori Velasquez **SENIOR DESIGNER** Kim Huynh **TRADE SHOW COORDINATOR** Andrew Clamp

GLOBAL SALES DIRECTOR ADVERTISING AND CUSTOM PUBLISHING Tracy Holmes: +44 (0) 1223 326525 **CLASSIFIED** advertise@sciencecareers.org **SALES MANAGER, US, CANADA AND LATIN AMERICA SCIENCE CAREERS** Claudia Paulsen-Young: 202-326-6577, **EUROPE/ROW SALES** Sarah Lelarge **SALES ADMIN ASSISTANT** Kelly Grace +44 (0)1223 326528 **JAPAN** Miyuki Tani(Osaka): +81 (6) 6202 6272 mtani@aaas.org **CHINA/TAIWAN** Xiaoying Chu: +86-131 6136 3212, xchu@aaas.org

AAAS BOARD OF DIRECTORS, CHAIR Susan Hockfield **PRESIDENT** Margaret A. Hamburg **PRESIDENT-ELECT** Steven Chu **TREASURER** Carolyn N. Ainslie **CHIEF EXECUTIVE OFFICER** Rush D. Holt **BOARD** Cynthia M. Beall, May R. Berenbaum, Rosina M. Bierbaum, Kaye Husbands Fealing, Stephen P.A. Fodor, S. James Gates, Jr., Michael S. Gazzaniga, Laura H. Greene, Robert B. Millard, Mercedes Pascual, William D. Provine

SUBSCRIPTION SERVICES For change of address, missing issues, new orders and renewals, and payment questions: 866-434-AAAS (2227) or 202-326-6417, FAX 202-842-1065. Mailing addresses: AAAS, P.O. Box 96178, Washington, DC 20090-6178 or AAAS Member Services, 1200 New York Avenue, NW, Washington, DC 20005

INSTITUTIONAL SITE LICENSES 202-326-6730 **REPRINTS:** Author Inquiries 800-635-7181 **COMMERCIAL INQUIRIES** 803-359-4578 **PERMISSIONS** 202-326-6765, permissions@aaas.org **AAAS Member Central Support** 866-434-2227 www.aaas.org/membercentral.

Science serves as a forum for discussion of important issues related to the advancement of science by publishing material on which a consensus has been reached as well as including the presentation of minority or conflicting points of view. Accordingly, all articles published in *Science*—including editorials, news and comment, and book reviews—are signed and reflect the individual views of the authors and not official points of view adopted by AAAS or the institutions with which the authors are affiliated.

INFORMATION FOR AUTHORS See www.sciencemag.org/authors/science-information-authors

EDITORIAL

Define the human right to science

The adoption of the Universal Declaration of Human Rights (UDHR) by the United Nations (UN) General Assembly will mark its 70th anniversary on 10 December. One right enshrined in the UDHR is the right of everyone to "share in scientific advancement and its benefits." In 1966, this right was incorporated into the International Covenant on Economic, Social and Cultural Rights, a treaty to which 169 countries have voluntarily agreed to be bound. Unlike most other human rights, however, the right to science has never been legally defined and is often ignored in practice by the governments bound to implement it. An essential first step toward giving life to the right to science is for the UN to legally define it.

The UN Educational, Scientific and Cultural Organization began a process for defining the right to science in 2005. Five years later, the American Association for the Advancement of Science (AAAS, the publisher of *Science*) recognized the right as lying at the heart of the organization's mission and began engaging the scientific community, broadly defined, in delineating the right.

The scientific community has contributed three key insights to the ongoing UN process. One is that the right to science is not only a right to benefit from material products of science and technology. It is also a right to benefit from the scientific method and scientific knowledge, whether to empower personal decision-making or to inform evidence-based policy. In addition, access to science needs to be understood as nuanced and multifaceted. People must be able to access scientific information, translated and actionable by a nonspecialist audience. Scientists must have access to the materials necessary to conduct their research, and access to the global scientific community. Essential tools for ensuring access include science education for all, adequate funding, and an information technology infrastructure that serves as a tool of science and a conduit for the diffusion of scientific knowledge. Also, scientific freedom is not absolute but is linked to and must be exercised in a manner consistent with scientific responsibility.

In October 2018, the UN Committee on Economic, Social and Cultural Rights released a list of 29 questions related to defining the right to science. Three of the most important questions were: What should be the relationship between the right to benefit from science and intellectual property rights? How should government obligations under the right differ based on the available national resources? What is scientific knowledge and how should it be differentiated, if at all, from traditional knowledge?

> "...THE RIGHT TO SCIENCE...IS OFTEN IGNORED IN PRACTICE BY THE GOVERNMENTS BOUND TO IMPLEMENT IT."

It is vital that the committee decide which of these and the remaining 26 questions truly need to be answered, which have been sufficiently answered already, and which are beyond the immediate scope of the task. The effort to define the right must not become mired in demands to resolve questions a priori that can only be answered over time. Insights from the scientific and engineering communities provide responses to many of the questions. Civil society must continue to illustrate how the right to science complements existing human rights protections. The scientific community, particularly in the 169 countries bound to implement the right, must demonstrate how the right can be instantiated within their own national contexts. And all interested parties should take the opportunity to contribute their input and insights to the UN process.

The power and potential of the right to science for empowering individuals, strengthening communities, and improving the quality of life can hardly be overstated. It is time for the UN process to reach a responsible and productive end and for the right to science to be put into practice as was intended when it was first recognized by the United Nations in 1948.

–Jessica M. Wyndham and Margaret Weigers Vitullo

Jessica M. Wyndham *is director of the Scientific Responsibility, Human Rights and Law Program at the American Association for the Advancement of Science, Washington, DC, USA. jwyndham@aaas.org*

Margaret Weigers Vitullo *is the deputy director of the American Sociological Association, Washington, DC, USA. mvitullo@asanet.org*

PHOTOS: (FROM TOP) ADAM COHEN; ALAN BRAIN

10.1126/science.aaw1467

Published by AAAS

NEWS

7900 Square kilometers of Brazil's Amazon rainforest destroyed in the 12 months ending in July, up 14% from the previous period and the largest loss in a decade. President-elect Jair Bolsonaro wants to roll back forest protections.

IN BRIEF

Edited by **Jeffrey Brainard**

ENVIRONMENT

Climate impacts worsen, agencies say

Coastal floods, like this one in North Carolina in September, are becoming more common.

In a stark display of the U.S. political tensions surrounding global warming, President Donald Trump's administration is dismissing a major report, written by the government's own experts, which warns that climate change poses a serious and growing threat to the nation's economic and environmental health. More than 300 specialists contributed to the 1600-page report, formally known as Volume II of the *Fourth National Climate Assessment*, released 23 November by federal agencies. It warns that worsening heat waves, coastal flooding, wildfires, and other climate-related impacts are already afflicting the United States and could reduce its economic output by 10% in coming decades. But White House officials downplayed such findings, claiming they are based on outdated climate models and "the most extreme" warming scenario. Despite the report, the administration says it has no plans to alter its efforts to weaken policies aimed at curbing climate change. Meanwhile, the World Meteorological Organization reported on 20 November that atmospheric concentrations of carbon dioxide, a primary warming gas, reached a global average of 405.5 parts per million (ppm) in 2017, up from 403.3 ppm in 2016. Many scientists believe concentrations will need to remain below 450 ppm to avoid catastrophic warming.

Mars rover to study crater

PLANETARY SCIENCE | NASA announced last week it will send its next Mars rover, due for launch in 2020, to Jezero crater, which billions of years ago harbored a lake. The crater still contains a fossilized river delta, the sediments from a river that spilled into the lake, offering a promising place to search for evidence of past life. The rover will gather rock and soil samples for eventual return to Earth by subsequent missions. NASA will consider sending the rover to a second site nearby, called Midway, after its primary mission, but the decision will depend on how the rover performs at Jezero.

Group studies mystery paralysis

PUBLIC HEALTH | The U.S. Centers for Disease Control and Prevention in Atlanta last week formed a task force to study what is causing dozens of cases of sudden paralysis in young children and how best to care for them. Called acute flaccid myelitis (AFM), the sudden loss of strength in arms, legs, or face muscles resembles the paralysis caused by polio. Doctors have had to guess at best treatments; some children have recovered fully, but most have not. More than 116 cases of AFM have been diagnosed in 31 states this year. Similar spikes also occurred in the United States and Europe in 2014 and 2016. Nearly all the children affected had symptoms of a viral infection in the weeks before they lost muscle strength, but tests for specific viruses have been inconclusive. The task force will present its initial findings and recommendations on 6 December.

Conservationists appeal to Iran

INTERNATIONAL AFFAIRS | In a letter last week, some 363 conservationists and scholars from 72 countries rallied to the side of eight Iranian environmentalists imprisoned for months over accusations of using wildlife camera traps to spy on Iran's ballistic missile program. Four of the detainees face a charge that could carry the death penalty. In the letter to Iranian Supreme Leader Ali Khamenei, the authors, including primatologist Jane Goodall, "strongly

PHOTO: JASON MICZEK/REUTERS

condemn” the possibility that “the neutral field of conservation could ever be used to pursue political objectives,” and they declare that they “are convinced our colleagues had no such part.” They call for a “fair and just evaluation of the evidence, access to lawyers of their choice, and a transparent trial.”

Salk settles third gender suit

#METOO | The Salk Institute for Biological Studies in San Diego, California, last week settled the third in a trio of gender discrimination lawsuits filed against it in 2017 by senior female scientists. Salk and Beverly Emerson, 66, now a cancer scientist at the Oregon Health & Science University in Portland, announced the settlement in a joint statement that did not disclose terms. In August, Salk settled out of court with the other two plaintiffs: Vicki Lundblad, 66, a telomere expert, and Katherine Jones, 63, who studies gene transcription. Terms of those agreements were not disclosed, either. Lundblad and Jones have resumed working at Salk.

Taiwan backs nuclear power

ENERGY | Voters in Taiwan have rejected the island’s plan to phase out nuclear power. In a 24 November binding referendum, 59% voted to overturn legislation enacted last year that would shut down Taiwan’s three reactors by 2025. Hundreds of academics had signed a letter earlier this month urging the public to avoid the U-turn; earthquakes and tsunamis make nuclear power unsafe in Taiwan, which lacks a long-term solution for storing waste, they argued. But pro-nuclear advocates called the fears unfounded and said other sources of energy will not provide enough stable electricity for the island. Elsewhere, several voter referenda on nuclear power have gone the other way: In 2017, 58% of voters in Switzerland opted to phase out its reactors, for example.

Trial compares Ebola treatments

INFECTIOUS DISEASE | The Democratic Republic of the Congo last week launched a clinical trial to clarify the worth of three experimental treatments now being given to people infected with the Ebola virus. An outbreak of the virus surfaced 3 months ago in the violence-torn northeastern region of the country and has afflicted more than 400 people to date, half of whom have died. More than 160 infected patients have received at least one of the experimental treatments, but there has been no formal effort to assess their safety or efficacy. (Some 36,000 uninfected people have received an experimental vaccine.) The new study will treat all participants, but will randomly assign people to receive an antiviral drug or one of two different preparations that contain monoclonal antibodies that bind Ebola virus. The trial is taking place at an Ebola treatment center in Beni, a city hardest hit by the outbreak.

Insecticide-treated nets drove an earlier decline in malaria.

PHOTO: MILE 91/BEN LANGDON/ALAMY STOCK PHOTO

INFECTIOUS DISEASE

Malaria cases rise for second year

Malaria cases rose in 2017 for the second year in a row, reaching 219 million cases, the World Health Organization (WHO) in Geneva, Switzerland, said last week. The news is disappointing because cases had steadily declined for several years from a high of 239 million in 2010, largely because of increased use of insecticide-treated bed nets. In 2017, about 70% of the cases were in 10 sub-Saharan African countries and India. Only half of the people at risk in Africa slept under a treated net last year, says WHO’s *World Malaria Report 2018*, and there’s evidence that more mosquitoes have become resistant to the four main classes of insecticides.

Agencies carve up cultured meat

BIOTECHNOLOGY | The U.S. path to market for cell-cultured meat, grown from animal cells in a bioreactor, is becoming clearer. The U.S. Food and Drug Administration (FDA) and the U.S. Department of Agriculture (USDA), which have been vying for jurisdiction over such products, announced 16 November that they will jointly oversee their quality and safety. FDA will monitor the collection, storage, and growth of the cells, while USDA will oversee production and labeling once cells are “harvested.” The agencies concluded that there’s no need for regulation on the topic, though language in a 2019 appropriations bill still under consideration in the U.S. House of Representatives would give primary responsibility to USDA. Still contentious is whether these products can be labeled as “meat”—a designation that some meat producers have argued should be reserved for slaughtered animals.

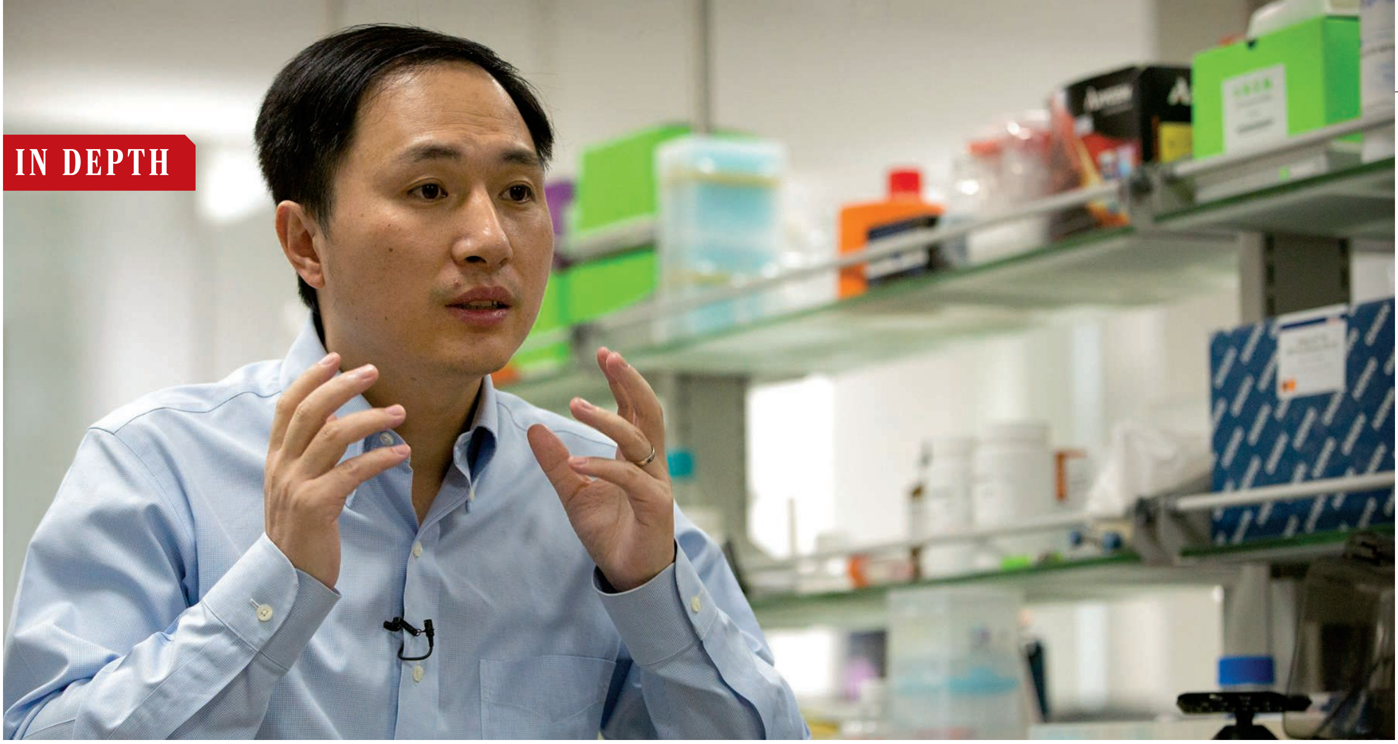

PHOTO: MARK SCHIEFELBEIN/AP IMAGES

BIOETHICS

Shock greets claim of CRISPR-edited babies

Apparent germline engineering by Chinese researcher prompts outrage and investigations

By **Dennis Normile**, *in Hong Kong, China*

The idea that humanity can rewrite its own genetic code long seemed the stuff of a science fiction novel—and a pretty scary one at that. But rapid advances in techniques such as CRISPR have made it possible, at least in principle, to make precise changes to the genome of a human embryo that could help rid families of crippling genetic diseases—or lead to "designer" babies, gene edited to be smarter or more beautiful. A few years ago, at an international summit where scientists, ethicists, and policymakers pondered the consequences of editing human genomes, biologist David Baltimore of the California Institute of Technology in Pasadena declared: "The unthinkable has become conceivable. We're on the cusp of a new era in human history."

Now, that era may have started—suddenly, and in almost surreal fashion. On 26 November, just before Baltimore opened a new summit on genome editing here, a little-known Chinese researcher named He Jiankui announced in an Associated Press (AP) interview and a series of YouTube videos that his team had engineered the DNA of twin baby girls born earlier this month to cripple a key receptor, CCR5, on white blood cells, a modification they may pass on to their descendants. The revelation shocked many scientists—one called the work "monstrous"—because He appears to have skipped the profound ethical debate that participants at the 2015 summit, and many meetings since, agreed should take place before such experiments began. (He did not responds to requests for an interview.)

Fueling the outcry was the fact that He didn't produce any data, let alone a paper, to back up his claim. The biologist was scheduled to speak at the International Summit on Human Genome Editing here this week, but whether he would show up was unclear as *Science* went to press. Meanwhile, the purported justification for He's study—to protect the two girls, named Lulu and Nana, from the AIDS virus, which uses CCR5 to infect cells—was almost immediately dismissed as flawed by HIV experts.

Although He reportedly consulted with bioethicists, condemnation was swift and widespread, even in China, where restrictions on such work are less clear-cut than in other countries. He's academic home, the Southern University of Science and Technology (SUST) in Shenzhen, China, has launched a probe into the research, which it said may "seriously violate academic ethics and academic norms." National authorities have promised investigations as well; the Chinese Society for Cell Biology called the research "a serious violation of the Chinese government's laws and regulations and the consensus of the Chinese scientific community."

Scientists are exploring the use of CRISPR and other gene-editing techniques as treatments for genetic diseases, such as muscular dystrophy and sickle cell anemia. So far, clinical trials have only modified somatic cells—not sperm or eggs, the germ line. But He altered the genome in early stage embryos, creating edits that may be heritable. Many scientists and ethicists don't rule out making such changes to the germ line, but recent reports from the United States's National Academies of Sciences, Engineering, and Medicine and the United Kingdom's Nuffield Council on Bioethics agreed they should only be undertaken under "stringent conditions" and to address a serious unmet medical need.

He's effort had no such justification, critics say. The team worked with embryos created by in vitro fertilization (IVF) with sperm and eggs from seven couples, He said. In each couple the man was infected with HIV, but the woman was not. The small percentage of people who have a natural mutation in the *CCR5* gene are resistant to HIV infection; by disabling the gene in the embryos, He's team aimed to endow children with the same resistance. (Researchers have already used gene-editing techniques to cripple the gene for CCR5 in immune cells from HIV-positive adults and then infused the cells back into the patients, as an experimental treatment.)

Preventing father-to-child transmission of HIV was not the stated purpose of He's work; there is little risk of that, especially with IVF.

He Jiankui says he genetically edited an immune gene in embryos, leading to the birth of healthy twin girls.

He, noting pervasive discrimination against HIV-positive people in China, told AP his goal was instead to protect the babies from possible infection later in life. (An informed consent document for potential study volunteers describes the work as "an AIDS vaccine development project.")

Many HIV scientists say He's goal is a poor reason to subject embryos to the potential risks of CRISPR, which include "off-target" mutations that might lead to cancer. "There are so many ways to adequately, efficiently, and definitively protect yourself against HIV that the thought of editing the genes of an embryo … in my mind is unethical," says Anthony Fauci, who heads the U.S. National Institute of Allergy and Infectious Diseases in Bethesda, Maryland.

He received his Ph.D. at Rice University in Houston, Texas, where he published a paper with his adviser, Michael Deem—who is under investigation by Rice for any role in the human embryo work—about CRISPR's evolution as a bacterial defense mechanism. He later won a generous grant under the Thousand Talents Program to return to China, where he obtained an associate professorship at SUST—although the university says he has been on unpaid leave since February. In various talks, He has described his in vitro work on editing human genetic material.

But Robin Lovell-Badge of The Francis Crick Institute in London, a member of the current summit's organizing committee, says few if any were aware He was trying to implant modified embryos. Where the studies were conducted is unclear; SUST said it wasn't at a university lab. Lovell-Badge says He is not disclosing the hospital involved to protect the family's privacy.

"We believe ethics are on our side of history," He says in one video. Yet some scientists say He has ignored the ethical concerns he and co-authors laid out in a paper this week in *The CRISPR Journal*, in which they wrote: "Performing gene surgery is only permissible when the risks of the procedure are outweighed by a serious medical need."

China has not yet developed guidelines specifically applicable to human gene editing. But bioethicist Qiu Renzong, of the Chinese Academy of Social Sciences in Beijing, told the summit on 27 November that He likely violated health and science ministry regulations prohibiting implanting genetically modified human embryos into human reproductive tracts. The ministry's dilemma, Qiu added, "is that there is no penalty if you violate the regulations." ■

With reporting by Jon Cohen.

PHOTO: NASA/JPL-CALTECH

PLANETARY SCIENCE

Safely settled, InSight gets ready to look inside Mars

Lander will deploy seismometer and heat probe to listen for marsquakes and study the planet's interior

By **Paul Voosen**, *in Pasadena, California*

Ever since Bruce Banerdt saw images of Mars's surface as an intern here at NASA's Jet Propulsion Laboratory (JPL) during the Viking landings of the 1970s, he has wanted to know what lies beneath. Now, his goal is within reach, with this week's arrival of NASA's newest martian robot, the InSight lander, which carries instruments designed to probe the planet's interior. "On some level, I've been planning this for 30 years," says Banerdt, a planetary scientist at JPL and InSight's principal investigator.

On 26 November, the lander's fall from space to the surface made for a tense 6 minutes at JPL's mission control room. But the $814 million lander followed its script to the letter. As it plunged through the atmosphere behind a heat shield, a hush fell over the room during a brief, planned loss of contact. Then came bursts of applause, as communications resumed and the lander relayed signs that it was slowing—first as its parachute deployed and then when its landing thrusters fired. "Thirty meters. Twenty meters," said Christine Szalai, the JPL engineer narrating its descent. "Touchdown confirmed." The ensuing celebrations remained somewhat tempered until confirmation came 6 hours later that the lander had unfurled the solar panels that will power it through its 2-year mission. It was NASA's eighth successful Mars landing in nine tries, and a feat that other space agencies have yet to match, aside from the Soviets with their Mars 3 mission, which failed within a minute of its soft landing in 1971.

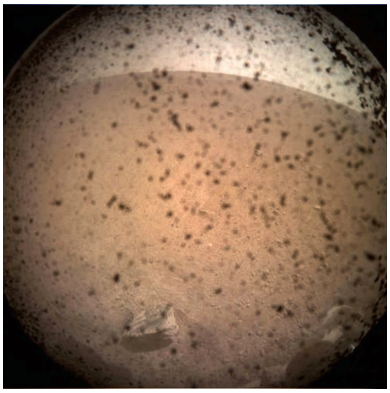

InSight's first view, speckled by dust on a lens cap, showed a mostly featureless plain.

That engineers could even monitor the landing so closely was itself a leap. NASA's Mars orbiters were not set up or positioned to relay live signals from InSight's descent. Instead, the signals were shuttled to Earth in near–real time by Mars Cube One, a pair of briefcase-size spacecraft with experimental radio antennas that rode to Mars along with InSight. During InSight's 6-minute descent, the duo worked flawlessly before coasting past the planet. "We were all pulling for them," says Lori Glaze, NASA's acting director of planetary science in Washington, D.C. "They performed absolutely beautifully."

The spacecraft hit its landing site, a vast lava plain near the equator called Elysium Planitia, close to its bull's-eye, says Tom Hoffman, the project manager at JPL. NASA chose the tropical site for its abundant sunlight and apparent lack of rocks, which could have upset the landing and made it hard to deploy the instruments. InSight's first image, speckled by dust on the lens's transparent cap, showed a rusty plain, featureless aside from a rock near the lander's body. "It does look like a parking lot," Hoffman says. A second photo showed the team may just have been lucky: The terrain is rockier beyond InSight's immediate vicinity.

The lander is designed to reveal the dimensions and composition of the planet's crust, mantle, and core, details that could help scientists understand how planets lose their magnetic fields or develop plate tectonics. It also marks NASA's return to planetary seismology after 4 decades. The two Viking landers both carried seismometers, but one failed and the other was bedeviled by noise.

Over the next couple of weeks, scientists will plan InSight's next two feats: wielding its robotic arm to place its seismometer and heat probe. The arm will first pluck the volleyball-size seismometer from the lander's deck and set it on the ground, with its power provided by a tether; an encircling wind and heat shield, like a bell jar, will follow. The seismometer, developed with French partners, will be placed as far out as possible—

up to the arm's limit of some 1.5 meters—to avoid wind-generated noise channeled into the ground by the lander's legs. Each step will take days to test and confirm. "I liken it to playing that claw game at a carnival, but you're doing it with a really, really valuable prize," says Elizabeth Barrett, a planetary scientist at JPL. "And you're doing it via remote control on another planet."

The heat probe, developed by German partners, will be deployed soon afterward, in January 2019. Over several weeks, thousands of strokes of a tungsten hammer will drive a rod 5 meters into the surface, slipping around small rocks—and hopefully not hitting large ones. The seismometer will listen to the blows to infer the composition of nearby martian crust. At first glance, dust covering one of the lander's feet indicates a sandy surface that could be easier to penetrate, Banerdt says. Once ensconced, the probe will measure how much heat is escaping from the planet, and how quickly—clues to how much heat remains in its interior, and when it was most volcanically active.

Meanwhile, the InSight team will calibrate the seismometer, which is so sensitive that, if placed at JPL, it could detect the churn of Pacific Ocean surf, nearly 40 kilometers away. By March 2019, it is likely to be listening, waiting for a marsquake to strike.

A variety of tricks will allow InSight to use its single seismic station to infer the strength and location of common, small earthquakes. These techniques depend on a sort of circular logic, using models of the planet's interior to understand the interior. But quakes larger than magnitude 5 will set Mars to ringing like a gong. Overlapping surface waves, taking different routes around the planet, will allow InSight to precisely determine the marsquake's strength and location with minimal model reliance. Knowing these details will help investigators interpret other seismic waves from the same quake that pass directly through the planet's deep interior. Such a seismic boon is far from guaranteed—only two or three large marsquakes are likely to occur in the lander's first 2 years.

Banerdt plans to buy two picture frames. One will be filled with InSight's first, speckled image. The second will remain empty until Banerdt gets a squiggly seismogram from that first big quake. "That's going to be the payoff," he says. "That's going to be my legacy." ■

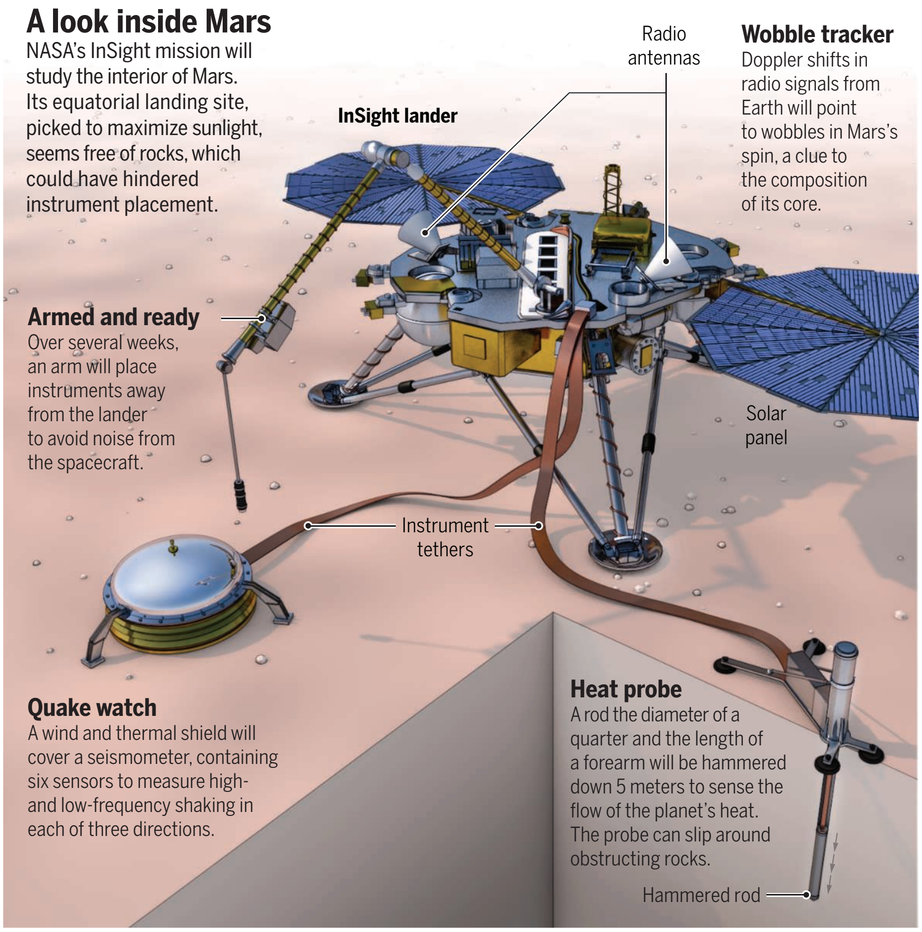

A look inside Mars

NASA's InSight mission will study the interior of Mars. Its equatorial landing site, picked to maximize sunlight, seems free of rocks, which could have hindered instrument placement.

Wobble tracker

Doppler shifts in radio signals from Earth will point to wobbles in Mars's spin, a clue to the composition of its core.

Armed and ready

Over several weeks, an arm will place instruments away from the lander to avoid noise from the spacecraft.

Quake watch

A wind and thermal shield will cover a seismometer, containing six sensors to measure high- and low-frequency shaking in each of three directions.

Heat probe

A rod the diameter of a quarter and the length of a forearm will be hammered down 5 meters to sense the flow of the planet's heat. The probe can slip around obstructing rocks.

GRAPHIC: C. BICKEL AND A. CUADRA/*SCIENCE*

ARCHAEOLOGY

Migrants and trade spiced up Canaanite metropolis

In Bronze Age tombs, signs of vanilla, 3000 years early, and elaborate medical care

By **Andrew Lawler**, *in Denver*

Looming over a strategic spot on Israel's northern coastal plain, the ancient city of Megiddo was often a battleground, befitting its biblical name Armageddon. But in two Bronze Age tombs, archaeologists are finding signs that, nearly 3500 years ago, Megiddo was also a surprisingly cosmopolitan place. It drew immigrants from what is now Armenia, imported exotic spices from tropical climes, and boasted a state-of-the-art health care system—at least for the elite.

At last week's annual meeting of the American Schools of Oriental Research here, Israeli and U.S. researchers laid out the first results from the tombs, which were discovered in 2016 and date from when Megiddo was a major metropolis of the Canaanites, the ancient inhabitants of present-day Israel and Lebanon. The finds add to growing evidence of international trade long before the rise of the Assyrian, Persian, and Roman empires. The people of the Bronze Age Middle East "had much more contact with distant places than we give them credit for," says Eric Cline, an archaeologist at George Washington University in Washington, D.C., and a former member of the project, known as the Megiddo Expedition.

One tomb, dated to about 1600 B.C.E. by radiocarbon and ceramic studies, was a cramped but unusually elaborate vaulted chamber containing nine individuals, including a man between 45 and 60 years old wearing a gold headband, as well as a gold bracelet and other jewelry. Nearby lay a woman aged 25 to 40 with a gold brooch and an elegant silver pin shaped like a duck head. A third skeleton was a child under the age of 10 with similar gold jewelry and two silver rings.

"This seems to be a family grave, given the matching grave goods," says Melissa Cradic, an archaeologist at the University


Jugs held vanilla residues; two men who may have had leprosy were nurtured, not shunned.

PHOTOS: (LEFT TO RIGHT) ADAM PRINS/COURTESY OF THE MEGIDDO EXPEDITION; ROBERT HOMSHER/COURTESY OF THE MEGIDDO EXPEDITION

of California (UC), Berkeley, who led the examination of the tomb. She speculates that the three may represent an elite, if not royal, family that died at about the same time from disease. Analysis of their genetic makeup, which could confirm their family ties, is underway, along with isotopic and other studies that could reveal their diet and health.

The tomb's biggest surprise emerged when three small jugs were tested for residues. Chromatography and mass spectrometry analysis detected chemical components of vanilla. "This was a shock," says Vanessa Linares from Tel Aviv University in Israel, who led the team conducting the work. Botanist Pesach Lubinsky of UC Riverside, a vanilla expert who was not involved in the Megiddo research, says the finding is at odds with current thinking on vanilla's origins. Vanilla is found in tropical orchids on every continent except Antarctica and Australia. Only in Mesoamerica, however, is there evidence of its early domestication, and it was long thought to be unknown in the Old World until the Spanish brought it back from Mexico in the 16th century C.E.

All aromatic vanilla orchids contain a mixture of compounds, including vanilla, 4-hydroxybenzaldehyde, and vanillic acid. The best matches to the residues found in the jugs grow in Mesoamerica, Indonesia, Kenya, and India, Linares says. Ruling out the first two sources because of distance, she speculates that the vanilla may have arrived in Megiddo from Africa, via Egypt, or from India, through trade across the Persian Gulf.

"India is the most likely source," says Cline, who notes the robust trade linking nearby Mesopotamia with India in the Bronze Age. The vanilla may have been traded from southern India through the vestiges of the earlier Indus civilization in the subcontinent's northwest. But Dorian Fuller, an archaeobotanist at University College London, says he "would be cautious in attributing origins, given the lack of much ethnobotanical evidence for the use of native vanilla."

The find, if it proves accurate, would support hints of an early and far-flung spice trade in the ancient Middle East. Peppercorns that likely came from Sri Lanka were stuffed into the nose of Egypt's mummified King Ramses II in 1213 B.C.E., and evidence of cinnamon from Sri Lanka or southern India appears in the Middle East a couple of centuries later.

Investigators also found hints of a grimmer import in a burial pit directly on top of the Megiddo tomb, dating to a century or so later. The pit holds the remains of two men who may have been in their twenties at death. "These were children of misfortune," says Rachel Kalisher, a Brown University archaeologist who examined the remains. Both men's bones were pitted, and one had broken his nose and pinky toes, conditions Kalisher says might be due to leprosy. That disease is thought to have spread from Africa to India by 4000 years ago; trade may then have carried it to the Middle East. Genetic testing is underway to determine whether Kalisher's hunch is correct.

"Their illness left them debilitated, and they needed help to survive," she adds. Both appear to have been carefully tended. Their teeth lacked the wear typical for men of their age, a sign that they may have been fed a special nonabrasive diet designed for weakened jaws. "There was a societal mechanism of health care—they were not ostracized and clearly were given considerable respect," Kalisher adds.

At the end of his life, the more debilitated of the two men underwent a drastic treatment: A physician was called in to cut a window into his skull—a practice called trepanation, often used to treat physical, mental, and spiritual disorders in ancient times. "This was done with fine precision and great expertise," says Kalisher, although the man died within less than a month of the procedure.

Preliminary DNA studies by geneticists Liran Carmel of Hebrew University in Jerusalem and David Reich of Harvard University show the men were brothers. Additional genetic studies may reveal more about their origins and whether they were related to the occupants of the older tomb below.

DNA studies also revealed the far-flung connections of three occupants of another tomb. At the meeting, Carmel said genetic analysis suggests they were recent immigrants from today's Armenia in the Caucasus, some 1300 kilometers to the north. Unlike the vaulted tomb, which lay near Megiddo's palace, this tomb was surrounded by humbler houses and graves. If the results hold up, they hint that long-distance travel was not confined to the elite.

Dozens of ancient DNA samples from the region, including many from Megiddo, are now being analyzed, and may soon shed more light on the genetic makeup of the city's inhabitants, Carmel added.

Glenn Schwartz, an archaeologist at Johns Hopkins University in Baltimore, Maryland, who is not involved with the dig, says the burst of data from Megiddo, rich in genetic and chemical detail, doesn't just provide fresh insight into this important Bronze Age center. The findings also "illustrate the numerous new techniques derived from the natural sciences that archaeologists are now using to identify the source and identity of the humans, animals, plants, and other materials found in the archaeological record." ■

PLANETARY SCIENCE

China sets out for the far side of the moon

Latest mission in ambitious program is a boon for lunar geology and radio astronomy

By **Dennis Normile**, *in Shanghai, China*

China's ambitious program of lunar exploration is about to attempt a spacefaring first: On 8 December it will launch a probe intended to land on the far side of the moon. Besides boasting rights, the Chang'e-4 lander and rover are expected to produce a host of new insights into the moon's composition and history. "Chang'e-4 is an historical mission," says Bernard Foing, director of the European Space Agency's (ESA's) International Lunar Exploration Working Group in Noordwijk, the Netherlands.

Remote observations have shown that the far side of the moon, invisible from Earth, has a much thicker, older crust and is pockmarked by more and deeper craters than the near side, where large dark plains called maria, formed by ancient lava flows, have erased much of the cratering. The big difference "is still a mystery," Foing says, and Chang'e's trip "can give clues."

China started its lunar program 3 decades after the United States and the Soviet Union ended theirs. Chinese geologists eager to study the moon convinced the government to establish the Lunar Exploration Program under the China National Space Administration (CNSA) in 2004. The agency launched Chang'e-1 and Chang'e-2, named after a Chinese moon goddess, in 2007 and 2010, respectively; both produced "a lot of good science," including high-resolution lunar images and new altimetry measurements, says planetary scientist James Head of Brown University.

In 2013, Chang'e-3 became the first craft to land on the moon since the Soviet Union's Luna 24 sample return mission in 1976. The lander and the small rover it carried gathered data on the moon's topography, mineralogy, and elemental abundance. In a first, the rover was equipped with a ground-penetrating radar that profiled buried lava flows and regolith, the broken up rock and dust that makes up the lunar soil.

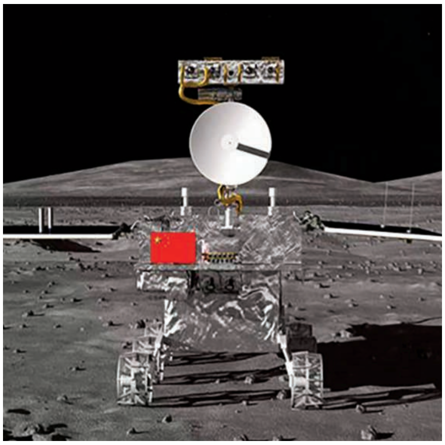

Chang'e-4 will explore a 12-kilometer-deep lunar crater likely formed by a giant asteroid impact.

Chang'e-4 was designed as an identical backup to Chang'e-3, but when that mission proved successful, China's planners became more ambitious. Going to the far side promised "unique and original science" as well as a chance to "develop China's deep space observational capabilities," says Li Chunlai, deputy director-general of the Chinese Academy of Sciences's National Astronomical Observatories of China (NAOC) in Beijing, which advises CNSA on the program's science objectives.

Because the moon will block direct radio contact with the lander and rover, Chang'e-4 will rely on a communications relay satellite, launched in May. Called Queqiao, it's traveling in a loop 65,000 kilometers beyond the moon at Earth-moon Lagrange Point 2, a gravitational balance point. Chang'e-4 itself will land in the Von Kármán crater within the South Pole–Aitken basin. Likely formed by a giant asteroid impact, the basin is roughly 2500 kilometers across and 12 kilometers deep. "It's the moon's largest, deepest, and oldest impact structure," says planetary geoscientist Xiao Long of the China University of Geosciences in Wuhan.

IMAGES: (TOP TO BOTTOM) NASA/GODDARD/ARIZONA STATE UNIVERSITY; CNSA

The moon's far side has a thick, old crust and is pockmarked by many deep craters.

The impact may have brought material from the moon's upper mantle to the surface, a scenario that data from a visible and near-infrared imaging spectrometer might be able to verify. The imaging spectrometer will also explore the geochemical composition of far-side soil, which is likely to differ from the near side because of the same processes that produced the difference in crust thickness.

The rover's ground-penetrating radar—similar to that on Chang'e-3—will provide another look down to about 100 meters beneath the surface, probing the depth of the regolith and looking for subsurface structures. Combining the radar data with surface images from cameras on the lander and rover might advance scientists' understanding of the cratering process.

Going to the far side also opens "a totally new window for radio astronomy," says Ping Jinsong, a NAOC radio astronomer. On Earth, and even in near-Earth space, natural and humanmade interference hampers low-frequency radio observations. The moon blocks this noise. So the mission carries a trio of low-frequency receivers: one on the lander, one—a collaboration with the Netherlands—on Queqiao, and a third on a microsatellite released from Queqiao into a lunar orbit. (Contact with a second microsatellite carrying a fourth receiver has been lost.) The receivers will listen for solar radio bursts, signals from aurorae on other planets, and the faint signals from the primordial clouds of hydrogen gas that coalesced into the universe's first stars (*Science*, 18 May, p. 698).

China's ambitious lunar program will continue with Chang'e-5, a sample return mission, due for launch next year. It will retrieve up to 2 kilograms of soil and rock from the Oceanus Procellarum, a vast lunar mare on the near side untouched by previous landings, and one of the moon's youngest volcanic flows. "It's a great objective and will potentially yield some fantastic science," says Bradley Jolliff, a planetary scientist at Washington University in St. Louis, Missouri, who has urged the United States to launch its own lunar sample return mission.

If China continues its tradition of developing moon missions in pairs, a second sample return mission, Chang'e-6, might follow. Head notes that NASA, ESA, Japan, Russia, and India have all taken a renewed interest in our planet's companion, which holds clues to Earth's own history. "Chang'e-4 and 5 are a major part of this renaissance," Head says, "and in many ways are the current vanguard." ■

PUBLISHING

European funders detail their open-access plan

Plan S will allow researchers to publish in hybrid journals that commit to flip to full open access

By **Tania Rabesandratana**

Plan S, the contentious program that a group of European science funders hopes will end scholarly journals' paywalls, has fleshed out its rules—and softened its tone a bit. In seven pages of implementation guidance released this week, the funders explain how grantees can abide by Plan S. But some critics say the document—which is up for public discussion for 2 months—remains too restrictive.

Debate about Plan S has often been acrimonious since it was unveiled (*Science*, 7 September, p. 957), but both sides were hamstrung by a lack of detail. Robert-Jan Smits, the European Commission's open-access (OA) envoy and one of the creators of Plan S, admitted at a news briefing in London to a "lack of clear communication" about the plan.

Now, the guidance outlines three ways researchers can comply with Plan S, which is backed by national funding agencies of countries including the United Kingdom, France, and Austria, as well as private funders including the Bill & Melinda Gates Foundation. They can publish in an OA journal or platform. They can also publish in a subscription journal, provided they make a final peer-reviewed version or accepted manuscript immediately available in an OA repository. Finally, contrary to earlier indications, grantees can publish in hybrid journals, which charge subscriptions and also offer authors a paid OA option, but only if the journal commits to flip to full OA.

> ***"…feedback from the community has been listened to."***
>
> **Niamh O'Connor**, Association of Learned and Professional Society Publishers

The guidance should quell fears about Plan S's restrictiveness, Smits said. This month, an open letter, now signed by about 1400 researchers, slammed Plan S for its impact on hybrid journals published by scientific societies, saying it would block access to their "valuable and rigorous peer-review system." The guidance now leaves room for hybrid journals, as long as they sign agreements by the end of 2021 pledging to shift to full OA within 3 years.

The architects also addressed criticism of the plan's commitment that funders would pick up the bill for reasonable article-processing charges (APCs), the fees that some journals charge authors to publish OA papers. The letter's authors saw the promise as a needless concession to for-profit OA publications. But John-Arne Røttingen, chief executive of The Research Council of Norway in Oslo, who co-led the group that developed the guidance, denies this: "Plan S is not about one particular business model," he said. "We are neutral and want a plurality of actors," including fee-free OA journals.

"I am glad to see that … feedback from the community has been listened to," says Niamh O'Connor, chair-elect of the Association of Learned and Professional Society Publishers in Watford, U.K. Society publishers will need to find strategies "to adapt and thrive under Plan S," she says. But a spokesperson for AAAS, *Science*'s publisher, says the guidance is only a modest improvement, and Plan S "still jeopardizes" its journals.

Structural biologist Lynn Kamerlin, who co-wrote the open letter, says the guidance still limits researchers' freedom to publish. "It's a step in right direction," she says. Still, funders and publishers should negotiate the specifics, "rather than putting researchers in the crosshairs," adds Kamerlin, who works at Uppsala University in Sweden.

Røttingen said the funders will commission an analysis to find out which disciplines need more OA outlets, and then offer financial incentives to create new journals or flip existing ones to OA. Another study will focus on APCs, which Plan S pledges to standardize and cap.

The guidance document does not say exactly how compliance will be monitored. Røttingen said funding agencies probably won't complete payment of research grants to scientists who don't comply.

The note gives funders some leeway with the implementation timeline. When the rules take effect in 2020, they could apply to existing grants, to newly awarded grants, or "at the very least," to new calls for research proposals. ■

FEATURES

FORGOTTEN NO MORE

A long-overlooked scourge of millions, hepatitis B is in the crosshairs at last

By **Jon Cohen**

In the quest to cure hepatitis B, an infectious disease that afflicts as many as one in four people worldwide, a small laboratory in a lonely nook of the Rocky Mountains of Idaho plays an outsize role. The lab, two nondescript buildings that abut a forest off a dirt road, houses 600 woodchucks, also known as groundhogs. These large rodents are a natural host for a cousin of the hepatitis B virus (HBV), making them a favorite research model for studying the disease. The owner, James Whipple, both traps pregnant females in the wild and breeds woodchucks in the colony. These days, he says, "It's a job keeping up with the demand."

In woodchucks, as in people, the virus is a shape-shifter. It can lie low, tucking itself away in liver cells and giving few signs of its presence. It can establish a chronic infection, churning out new viruses but doing little harm. Or it can rage, triggering liver damage that can develop into HBV-related cirrhosis or cancer, which kills nearly 900,000 people around the world each year. Whipple's woodchucks, which his lab infects with the virus to study its life cycle and assess

PHOTO: ANDREW TOMASINO

Physician Su Wang, who has hepatitis B, is a voice for testing and treatment. None of her family is infected.

Hitting a virus where it lives

In a push to cure hepatitis B, drug developers are targeting nearly every step in the virus's complex life cycle. They are also trying to boost the immune response. But some say it won't be enough to block the virus's entry into the cell (left) or the transcription, assembly, and release of new viruses (right). They believe a curative drug will have to eliminate covalently closed circular DNA (cccDNA), a minichromosome that the virus creates inside an infected cell. The cccDNA can remain latent for years or can adopt a highly active "open" form (inset) that churns out new viruses. (DNA integrated into the host genome produces viral proteins but not new virus.)

Drug functions ● Immune modulation ● Entry inhibitors ● Targeting cccDNA ● RNA interference ● Inhibition of nucleocapsid ● Reverse transcriptase inhibitors ● Inhibitors of HBsAg release

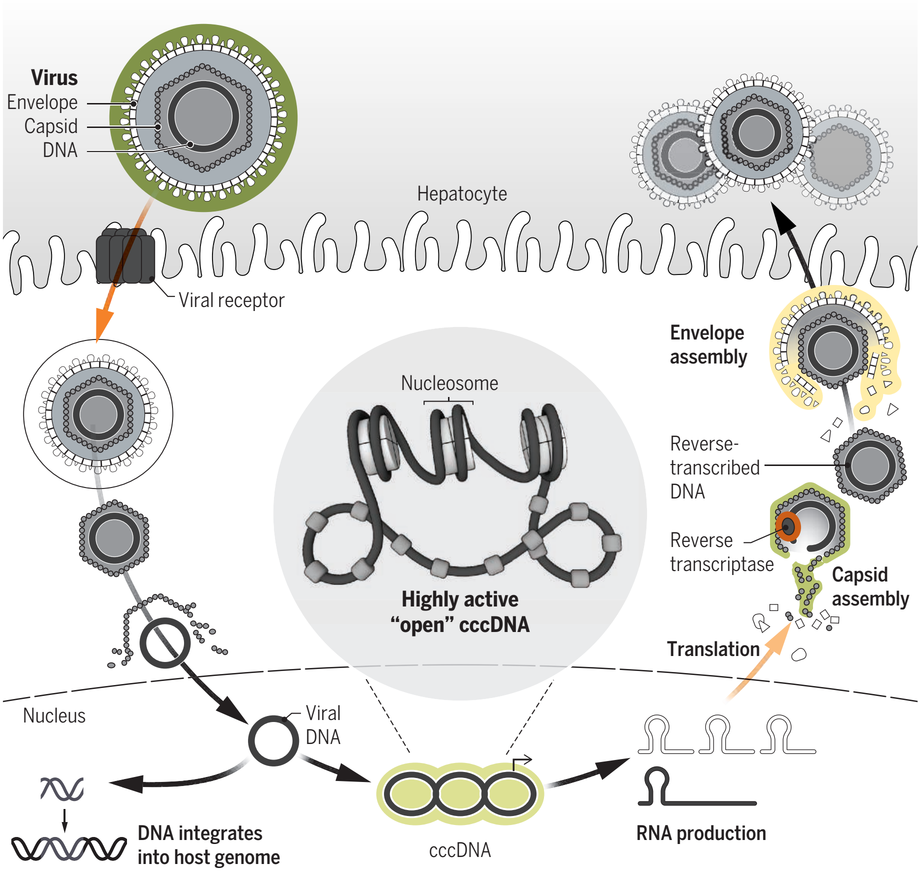

GRAPHIC: V. ALTOUNIAN/SCIENCE

experimental medicines, are also afflicted. On this October morning, a veterinarian is doing an ultrasound on the belly of an animal with a tumor-ridden liver. "That's gnarly," Whipple says as the bulky mass appears on the screen.

HBV can be controlled with drugs and prevented with a vaccine, but the drugs have to be taken for a lifetime and vaccine coverage is spotty, even in many wealthy countries. Now, there's a drive underway to find drugs that can permanently cure the infection, suppressing the virus thoroughly enough to free patients from the burden and expense of daily pills. In all, nearly 50 potential treatments are under development, which either directly attack different steps of the viral life cycle or boost host immunity. It has been a boon for Whipple's business. "There's been a flurry of activity with lots of companies," he says. This year alone, Whipple's lab, Northeastern Wildlife in Harrison, Idaho, has evaluated seven novel treatments.

The push for a cure reflects both need and opportunity. Nearly 300 million people worldwide have chronic infections, although only 10% have been diagnosed, and fewer still receive treatment. Meanwhile, recent insights into the virus's complex life cycle have offered new drug targets, and the advent of remarkable—and extremely profitable—drugs that can cure hepatitis C, caused by an unrelated virus, have raised hopes of a similar victory against HBV. The result was the formation in 2016 of the International Coalition to Eliminate HBV, which includes more than 50 scientists from 21 countries.

Although the coalition has "eliminate" in its name, it has a more modest initial goal. HBV's most insidious feature is a latent form of viral DNA called covalently closed circular DNA (cccDNA), which forms a stealthy minichromosome inside the nucleus of infected cells. Many researchers think HBV infection can't be completely cured without eliminating this stowaway. But no drugs specifically targeting cccDNA are yet in clinical trials, and for now the coalition is trying to catalyze development of "functional" cures. The idea is to knock back the virus, including its cccDNA form, to levels low enough for the immune system to keep the infection in check, allowing people to stop treatment.

Frank Chisari, a pioneering hepatitis immunologist who is a senior adviser to the group and an emeritus professor at Scripps Research in San Diego, California, says cccDNA demands far more attention. "Very little work was done on it until a couple of years ago," says Chisari, who adds, "we know virtually nothing" about how it's created, persists, or decays. That's because basic research on HBV has languished. Unlike, say, cancer and HIV/AIDS, HBV lacks a powerful advocacy group to push for more funding. "I don't understand why hepatitis B is such an orphan," Chisari says. "The magnitude of this disease is enormous."

HBV AMBUSHED Arthur Koo, a structural engineer in Atlanta. After developing double vision that led to a diagnosis of a rare lymphoma, Koo began chemotherapy in early 2015. Routine lab work showed he had no liver abnormalities and no evidence of an HBV infection. By April, scans indicated he was tumor free, his double vision had cleared, and his doctors decided to do a final round of chemo as insurance.

"It was amazing," says his daughter, Joyce Dalrymple. "He was so much better that we were going to take a Disney cruise with all the grandchildren."

On 16 April, when Koo began the last chemo round, tests showed his liver enzymes had become abnormally high, a sign of damage to the organ. His blood also harbored HBV's surface antigen, HBsAg, a protein that signals an active infection. Koo's doctors thought they could treat the virus after he finished chemo. The next day, he felt faint and went to an emergency room. He had an astronomically high viral load and soon was vomiting and battling diarrhea, but it was too late to start HBV drugs. "He was mystified," Dalrymple says. "He had fought all the side effects from the chemo and was prepared for that, but this was shocking."

Koo died 6 days later of fulminant hepatic failure.

Like nearly 2 billion other people, Koo had somehow been infected with HBV and never knew it. HBV is at least 100 times as infectious as HIV, but it moves between people in similar ways: from mother to child (primarily at the time of birth), through sex, and among drug users sharing syringes. Odd clusters of cases have also been linked to day care centers, football teams, butcher shops, a sumo wrestling club, and an acupuncturist—settings where the virus could have spread through seemingly innocuous open wounds. The Western Pacific region, including China and Taiwan, where Koo grew up, accounts for nearly half of the chronically infected population.

Although the HBV vaccine has greatly reduced mother-to-child transmission since it was introduced in 1981, some countries—even wealthy ones such as Canada and several in northern Europe—have been slow to adopt it as a routine childhood immunization because their burden of disease is low. China, which aggressively promotes vaccination, still misses many people in rural areas, says Jake Liang, an HBV researcher at the National Institute of Diabetes and Digestive and Kidney Diseases in Bethesda, Maryland. "They haven't really reached out to the masses," he says, even though up to 15% of the population is infected. Often the vaccine is not used as recommended: The latest global figures show 84% of infants received their three shots, but only 39% of babies got the critical first dose within 24 hours of birth.

Koo was likely infected at birth or early in life. He was among the minority of those infected early who "resolve" the infection, suppressing the virus so well they have no signs of its existence. Other infected children produce huge amounts of virus for years, but they may suffer no apparent harm. That is one of the disease's odd features: HBV itself doesn't kill hepatocytes, the cells that make up the liver. The immune response to the virus does the damage, and many children have relatively tame reactions to it for a few decades, leading to the notion that they "tolerate" the infection.

Most people infected as adults, in contrast, appear to resolve the infection. "There's lots of hand-waving and speculation about why that happens," says Chisari, although it may reflect adults' more mature immune systems.

But most—if not all—of the people who have resolved the infection still harbor cccDNA, and in Koo's case the consequences were fatal. The chemotherapy suppressed his immune system, allowing the cccDNA to reawaken and generate a massive viral onslaught. "Every big cancer center has had at least one of these patients, and they learn from it," says Su Wang, a physician at Saint Barnabas Medical Center in Livingston, New Jersey, who is a friend of the Koo family—and is chronically infected with HBV herself.

Wang is on the executive board of the World Hepatitis Alliance, a London-based nonprofit run by people who are living with, or have cleared, hepatitis B or C infections. This year the alliance launched a program to "find the missing millions" unknowingly infected with these viruses, promoting a "massive scale up" in screening and, ultimately, treatment. One pillar of the campaign is to reduce stigma and discrimination: Wang says people who reveal their status sometimes are dumped by partners or booted from medical school and health care jobs. This is a main reason why she recently decided to start speaking publicly about her own infection.

> ***"Hepatitis B is completely overlooked and the funding is totally out of proportion to the problem and the need."***
>
> **Timothy Block**, Hepatitis B Foundation

Wang only learned her HBV status when she was a university undergraduate. Because she has normal liver enzymes and has consistently maintained low levels of HBsAg and viral DNA, guidelines do not recommend treatment with current HBV drugs. Nor do they recommend treatment for the tolerant group who, despite having high viral loads, have relatively controlled immune responses and no liver damage. But learning about her infection has protected her family. Wang's husband received the vaccine, as did her four children, who were also infused with hepatitis B immunoglobulin (an antibody preparation against the virus). None is infected.

FOR THOSE WHO SHOW SIGNS of liver damage, doctors have been offering the same three first-line drugs for the past 2 decades. Two of them, tenofovir (borrowed from HIV treatment) and entecavir, target the production of viral DNA. Both cripple the reverse transcriptase (RT) enzyme that converts what's known as pregenomic viral RNA—a product of cccDNA—into the DNA of new viruses. The third drug, interferon, is an immune system messenger that by ill-defined mechanisms attacks various parts of the viral life cycle and also boosts the immune response against it. Each of these drugs can reduce a person's viral load to undetectable levels and, in some cases, clear viral antigens from the blood. But none eliminates cccDNA.

A year ago, a small study of HBV patients treated with RT inhibitors for 6 years or longer briefly raised hopes. Three successive liver biopsies found the 43 participants had "profoundly" reduced cccDNA levels after treatment, a group led by hepatologist Ching-Lung Lai of the University of Hong Kong in China wrote last year in the *Journal of Hepatology*. In 21 of them, even the most sensitive tests could not find cccDNA. Yet a follow-up study presented at a liver meeting later in the year found that in 13 of the fully suppressed people who went off their drugs, the virus rebounded within 6 months in all but one of them, leading them to restart treatment.

There's growing hope for a more permanent victory. The Hepatitis B Foundation, a nonprofit based in Doylestown, Pennsylvania, tracks the drug development pipeline; it tallies more than 30 drugs now in human trials—a tripling over the past 10 years. "Hepatitis C was consuming all the hepatitis drug space, and with that cure, we've seen a stampede of interest in hepatitis B," says Timothy Block, a microbiologist who started the foundation after his wife, a nurse, learned she was infected (and promptly lost her job).

The potential treatments move beyond RT inhibition. Almost every known step in HBV's life cycle, from infection to the assembly of new viral particles, is a target for at least one new drug. Others are immune modulators designed to turn up specific beneficial responses or dampen harmful ones. Many researchers suspect that, as with HIV, combining treatments that attack the virus from different angles ultimately has the best chance of success.

The 2012 discovery of the polypeptide receptor that HBV latches onto when it infects a cell was a key advance. It allowed researchers at long last to replicate the entire viral life cycle—including the formation of cccDNA—in laboratory cell cultures. The receptor also gives drug developers a new target. And by engineering the receptor into mice and monkeys, researchers are developing new animal models for HBV that, unlike the woodchuck, are vulnerable to the exact virus that infects humans.

Gilead Sciences of Foster City, California, which makes tenofovir and one of the best-selling hepatitis C cure drugs, has more than 60 scientists aiming to develop a similar weapon against HBV. "It's our larg-

Because woodchucks host a virus similar to hepatitis B, they have become a model for studying the viral life cycle and testing potential treatments.

PHOTO: JON COHEN/SCIENCE

est program in virology by far," says John McHutchison, a gastroenterologist who is the company's chief scientific officer—and keeps a stuffed woodchuck in his office. "If anyone is going to cure hep B, Gilead would like to claim that."

Currently, the firm's lead experimental HBV drug turns on toll-like receptor 8, a protein on certain immune cells that reacts to viral genetic material by boosting production of interferon and other chemical messengers that crank up natural defenses against the virus. As Gilead reported last year at a liver conference, the drug worked well in woodchucks, driving cccDNA down to undetectable levels, and now is in phase II clinical trials. "This may be the next drug that will be licensed for HBV," says Stephan Menne, an immunologist at Georgetown University Medical Center in Washington, D.C., who contributed to the woodchuck study. Other drug developers are pinning their hopes on short interfering RNAs, meant to block the production of RNA from cccDNA, and on compounds designed to inhibit formation of the capsid protein that protects the virus's genetic cargo.

"Lots of pharmaceutical companies are throwing everything against the wall to see what sticks," says Liang, a coalition board member. Chisari worries that immune modulators, a popular strategy, could backfire. If a person has a high percentage of HBV-infected hepatocytes, bolstering the immune response to infected cells could lead to liver failure. "There are a lot of false starts underway, and some might inadvertently do harm," Chisari warns.

LIKE CHISARI, the International Coalition to Eliminate HBV contends that more effort needs to go into targeting the belly of the beast, cccDNA. In September, Gilead signed a $445 million deal with Precision BioSciences of Durham, North Carolina, to codevelop what are known as homing endonucleases—DNA cutting enzymes—designed to snip cccDNA. Gilead scientists have also helped clarify how a particular HBV protein known as X turns on cccDNA to produce more virus, providing a new drug target. "We're in early days," McHutchison says. "The field feels like it's really starting to gain traction and momentum." Other companies hope to use CRISPR, the genome editor, to cripple cccDNA in patients, as it has done in some test tube experiments.

Proving that any treatment significantly depletes cccDNA reservoirs is a tall order. Current clinical trials evaluate how well a drug works by measuring its impact on HBsAg levels and viral load in blood, not on cccDNA. "That is nuts," Chisari says. "They're crossing their fingers and using wishful thinking." Yet monitoring cccDNA directly means subjecting patients to multiple, painful liver biopsies. That could change, if relatively painless and simple fine needle aspirates of the liver can capture enough tissue. Immunologist Mala Maini of University College London has used fine needle aspirates to assess a wide range of immune responses to HBV in the liver, and she's now collaborating with hepatologist Fabien Zoulim of the University of Lyon in France to see whether the technique can work for cccDNA studies.

In contrast to the growing interest in HBV from drug developers, the National Institutes of Health (NIH) spent a mere $44 million on HBV this year—and little of that went to "discovery research," Block says. "Hepatitis B is completely overlooked and the funding is totally out of proportion to the problem and the need," he says. Anthony Fauci, who heads NIH's National Institute of Allergy and Infectious Diseases in Bethesda, agrees and says if the stepped up push for a cure can show some progress, it will drive more funding to research. "All we need is a little bit of success to put more into it," Fauci says.

Eugene Schiff, an 81-year-old liver specialist at the University of Miami in Florida whose father was also a prominent liver clinician, has worked in the field since its birth, and he's bullish about a cure. "A couple of years ago, they said it was impossible to clear cccDNA," says Schiff, who is the co-editor of *Schiff's Diseases of the Liver*, a standard textbook now in its 12th edition. "You never say that with science, and I knew it was BS. Now, people in the field are estimating it will take 5, maybe 10 years to clear cccDNA. And if we can cure the ones who have hepatitis B and continue to vaccinate the ones who don't, we can eradicate the disease." ■

BUYING TIME

In a fast-changing environment, evolution can be too slow. "Plasticity" can give it a chance to catch up

By **Elizabeth Pennisi**, *in Montpellier, France*

When conditions are right, spadefoot toad tadpoles can turn into carnivores like these consuming a metamorphosing relative.

PHOTO: DAVID PFENNIG/UNC

Growing up in South Texas, David Pfennig was fascinated by cannibalistic tadpoles. When summer storms soak the normally dry plains, spadefoot toads emerge from their burrows to lay eggs in short-lived pools. The tadpoles normally dine demurely on algae, tiny crustaceans, and detritus. But even as a boy, Pfennig could tell that the same toads sometimes spawned very different tadpoles. Those tadpoles had bulging jaw muscles and serrated mouthparts. They jostled aggressively in the shrinking puddles. They ate larger crustaceans, such as fairy shrimp—and one another.

Later, when he became a biologist, Pfennig's fascination turned into curiosity. Both kinds of tadpoles had the same parents, and hence the same genes. That they could turn out so differently, presumably because of their environments, didn't square with the gene-centric view he had acquired during his studies in the 1980s. In that view, the genes inherited from parents should dictate every detail of how animals look and behave. "Yet here I was observing these animals that can modify their traits in response to the environment," recalls Pfennig, who now runs a lab at the University of North Carolina in Chapel Hill. "It was sort of mind blowing."

The toads display phenotypic plasticity, the ability to change how they look and act, and how their tissues function, in response to their environment. Other researchers had already documented the tadpole transformations. When algae and tiny prey are abundant, the tadpoles are small-jawed and mild-mannered. But if the pond also contains fairy shrimp, some tadpoles turn into the aggressive carnivores. They take advantage of the atypical food source, grow faster on the extra protein, and have a better chance of making it to adulthood before the water dries up.

Recently, Pfennig and his team have come upon something even more remarkable than that dramatic behavioral plasticity. In one species of spadefoot toad, they found, the carnivorous tadpole stage has become entrenched—there's no need for a dietary trigger. A flexible response to the environment somehow became fixed.

To some, such findings evoke the spirit of the French naturalist Jean-Baptiste Lamarck. Decades before Charles Darwin laid out his evolutionary theory in *On the Origin of Species*, Lamarck and other biologists proposed their own mechanisms for evolutionary change. Among his ideas, Lamarck famously asserted in the early 1800s that organisms can acquire a new trait in their lifetime—longer necks for giraffes reaching for food; webbed feet for water birds—and pass it on to their offspring. Later, biologists cast aside Lamarckism, as the classic view of evolution emerged: that organisms evolve as a result of natural selection acting on random genetic changes.

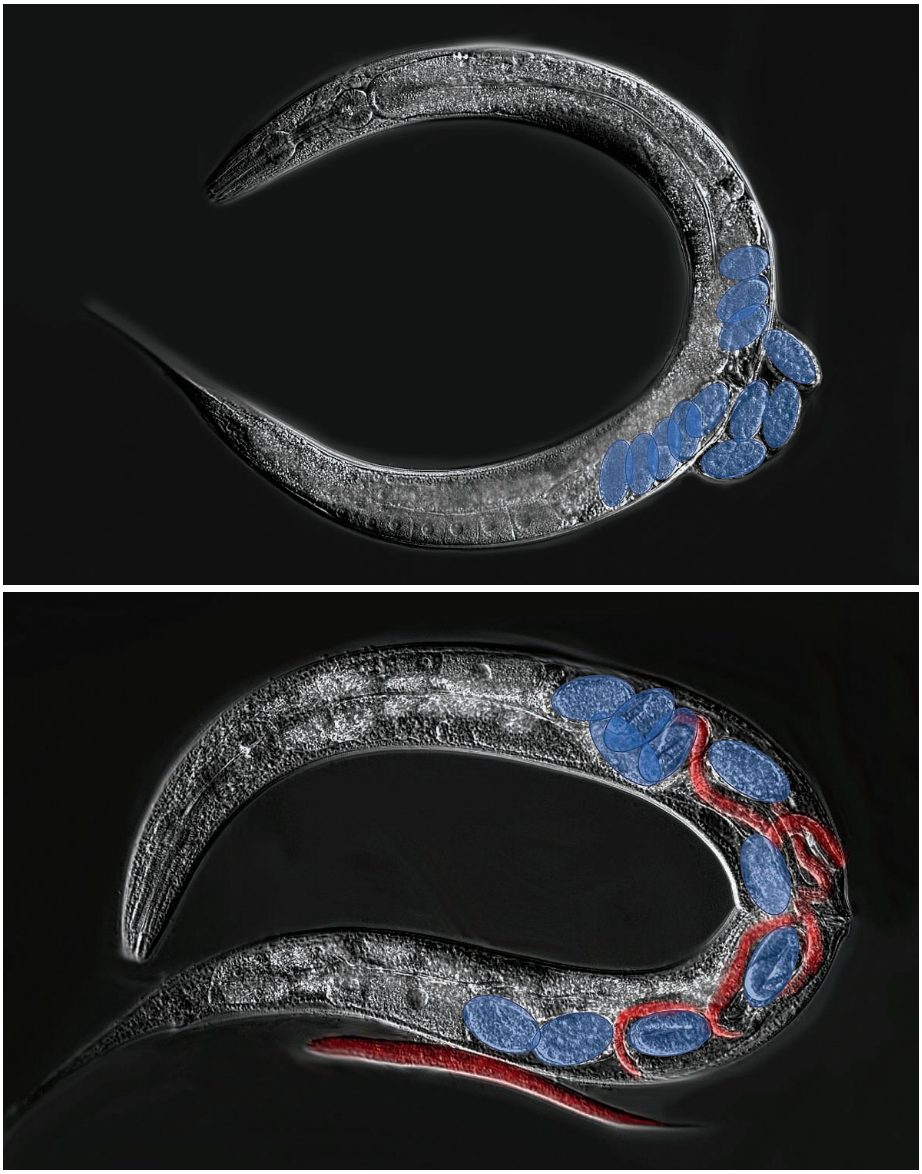
The millimeter-long nematode *Caenorhabditis elegans* normally lays eggs (top), but when food is scarce the eggs (blue) hatch internally and the young (red) consume their mother from within (bottom).

IMAGES: CHRISTIAN BRAENDLE/INSTITUT DE BIOLOGIE VALROSE

Now, however, evolutionary biologists have shown in multiple organisms, including lizards, roundworms, and yeast, that a plastic response can pave the way for permanent adaptations. The new evidence, much of it reported at the Second Joint Congress on Evolutionary Biology here this summer, shows the connection between plasticity and evolution "is a real thing," says Carl Schlichting, an evolutionary biologist at the University of Connecticut in Storrs. "If you look for it, you are going to find it."

On the surface, the findings vindicate Lamarck: Acquired traits can be inherited. But biologists are quick to stress that what these organisms show is not true Lamarckian evolution. Application of Lamarck's idea to modern findings "has led to a lot of confusion and debate," says Cameron Ghalambor, an evolutionary ecologist at Colorado State University in Fort Collins.

As biologists explore the underpinnings of plasticity and how it can lead to permanent change, they've uncovered a process that extends traditional evolutionary mechanisms rather than challenging them. The plasticity those changeable tadpoles display is built into their genetic code. And when an "acquired" trait does become permanent, it is because of mutations that "fixed" the plastic trait—a process biologists call genetic assimilation.

Although some researchers bristle at giving any credence to Lamarckian thinking, “The way plasticity can influence evolution really fits very comfortably in the general framework of how we think evolution works,” Pfennig says.

IN 2003, EVOLUTIONARY BIOLOGIST Mary Jane West-Eberhard of the Smithsonian Tropical Research Institute in Panama City raised eyebrows by suggesting phenotypic plasticity might also set the stage for permanent adjustments. Although her work focused on wasps, she drew on a vast literature about plants, butterflies, and other organisms that changed how they looked or acted. She proposed that, in the face of an environmental challenge, plasticity built into the genome enables at least some members of a species to cope. That would buy time for adaptive mutations to arise and be selected.

Some of those genetic changes would simply increase the proportion of the most flexible individuals. But others might favor a specific trait. “This plasticity-first view solves some of the problems that are inherent if organisms have to wait for a genetic mutation,” explains Renee Duckworth, an evolutionary ecologist at the University of Arizona in Tucson. “That is something that obviously would take a lot of time.”

Pfennig and his lab members think spadefoot toads have followed that evolutionary trajectory. Through decades of fieldwork, his team and others have shown that some species, such as the eastern spadefoot (*Scaphiopus holbrookii*), never naturally develop cannibal tadpoles. Another species, *Spea multiplicata*—the Mexican or desert spadefoot of Pfennig’s childhood—produces a mix of cannibals and omnivores depending on food availability, which may have enabled it to expand its range to shorter-lasting pools. But in populations of the plains spadefoot toad (*Spea bombifrons*) whose tadpoles live in the same ponds with *S. multiplicata*, almost all tadpoles are carnivores.

To see how much plasticity each species can muster in the lab, Pfennig’s graduate student Nicholas Levis recently raised tadpoles on diets with a varying proportion of fairy shrimp. The eastern species, thought to be most representative of the first spadefoot toads to arise in evolution, responded just a little to a 100% shrimp diet, developing a shorter gut—better suited to a carnivorous diet—and mouthparts that were altered but still poorly adapted to catching prey. In short, it had limited phenotypic plasticity.

Desert spadefoot tadpoles responded more strongly to the shrimp-only diet, exhibiting dramatic changes in gut and head shape and behavior. Metabolic genes that help digest protein became more active in these tadpoles, whereas the activity of genes needed to process the fats and starches in a detritus diet declined. But given a diet with little or no shrimp, the tadpoles could reverse all these adaptations.

The plains toads that Levis studied, in contrast, turned out to be confirmed carnivores, he reported at this summer’s evolution meeting and, with Pfennig and lab member Andrew Isdaner, in a paper in the August issue of *Nature Ecology & Evolution*. Some of its tadpoles even hatched as carnivores, without the need of the fairy shrimp diet. And when given a detritus-only diet, the species’s tadpoles had difficulty regaining traits better suited for omnivory. “Some populations seem to have transitioned to all being carnivores, no matter what the situation,” Levis says.

> ***“The way plasticity can influence evolution really fits very comfortably in the general framework of how we think evolution works.”***
>
> **David Pfennig**, University of North Carolina

Pfennig considers this a classic example of what he and others call plasticity-first evolution: Natural selection favored carnivory so strongly in this population of plains toad that this once-inducible phenotype somehow became genetically assimilated. “The idea is that the ancestor has the plastic ability and allows adaptation initially and then fixes it,” Schlichting says. Just why evolution acted to fix the carnivorous traits in this population isn’t clear, Levis says. It could be to avoid competing for the same food as other tadpole species. And Levis told the evolution meeting his group’s unpublished data show that plains toad populations that produce more carnivorous tadpoles do better, a hint there is some advantage to this carnivory.

Ammon Corl, a postdoc with Rasmus Nielsen at the University of California (UC), Berkeley, and his colleagues have traced a similar interplay between plasticity and evolution in the side-blotched lizards of California’s Mojave Desert. He’s even caught a glimpse of the genes responsible. In sandy parts of the Mojave, side-blotched lizards scamper around in shades of tan and brown. But those living on the Mojave’s inky Pisgah lava flow are among the blackest lizards, presumably for camouflage from predators.

In the 1980s, Claudia Luke, then a graduate student at UC Berkeley and now at Sonoma State University in Rohnert Park, California, switched dark and tan lizards between sandy and lava surfaces in the lab and found both varieties can adjust their colors to match their new surroundings in just a few weeks. But she also found the lizards from a sandy environment did not get as dark on lava as the regular lava dwellers, suggesting a genetic difference in the lizards’ ability to change color.

Luke’s observation remained a puzzle for 20 years, until her unpublished thesis was discovered by Corl when he was a graduate student with Barry Sinervo, a behavioral ecologist at UC Santa Cruz. Corl sequenced the genes of the offspring of lizards from on and off the lava to track down genetic differences. He and his colleagues discovered two genes, *PREP* and *PRKAR1A*, that have mutated in the darker lizards. Each influences how much of the dark pigment, melanin, is produced in the skin.

When the lava first cooled 20,000 years ago, the researchers suggest, phenotypic plasticity enabled lizards that wandered onto the newly cooled lava to darken for concealment and survive in the new environment. But these pioneers likely varied in their plasticity, and predators nabbed the lighter ones. That selective pressure favored mutations that increased darkening. “Plastic changes in coloration facilitated initial survival and then genetic adaptations allowed lizards to become even darker,” says Patricia Gibert, an evolutionary biologist at Claude Bernard University in Lyon, France. “This study provides one of the best examples of how plasticity precedes adaptive genetic change,” Ghalambor adds.

SCIENTISTS ARE NOW using fast-breeding organisms to recreate such plasticity-first evolution. In Jonas Warringer’s lab at the University of Gothenburg in Sweden, for example, graduate student Simon Stenberg applies environmental stressors to budding yeast for different lengths of time and tests the organisms for plastic or permanent responses. In one set of experiments, he’s been exposing the yeast to the herbicide paraquat, which causes eukaryotic cells to produce high concentrations of oxygen free radicals that damage DNA and other molecules. To gauge the health of the yeast, he measures its doubling time—how long it takes for a colony to double in size. When Stenberg first applied the toxin, the yeast’s doubling time slowed from the usual 1.5 hours to 5 hours.

The (adjustable) color of lizards

Side-blotched lizards can adjust their skin color to match their environments. After a population moved onto black lava fields long ago, natural selection favored better-camouflaged lizards, and the population eventually developed permanent genetic mutations that enabled them to become even darker (photo).

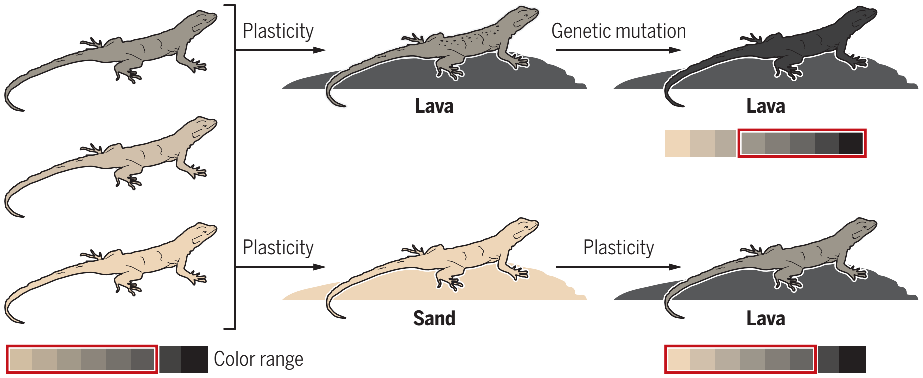

Side-blotched lizards can vary from light to dark to match their environment.

The adjustable coloration makes lizards on different surfaces less visible to predators.

Mutations in lava dwellers (top) allow them to get darker, although they can still adjust their coloring.

CREDITS: (GRAPHIC) N. DESAI/SCIENCE; (PHOTO) AMMON CORL

After as few as four generations, some of the colonies recovered half of their growth rate. Because that's too little time for a genetic adaptation to arise and sweep through a whole colony, Stenberg concluded at least some of the yeast had a form of phenotypic plasticity that allowed them to cope with the excess free radicals. When he stopped applying paraquat and then reapplied it three to 100 generations later, the colonies' growth rates again plummeted after 10 generations. The reduction indicates that the unknown paraquat-resistance mechanism was not yet permanently encoded in the genomes. But after constant exposure to paraquat for 150 generations, the yeast developed a permanent adaptation. They continued to grow even if Stenberg stopped applying the herbicide for 80 generations and then reapplied it.

Since the meeting, Stenberg has found what may be the yeast's coping mechanism: eliminating some or all of the DNA in their mitochondria, the cells' energy-producing organelles. (Mitochondria themselves generate free radicals.) When the yeast were first exposed to herbicide, they temporarily reduced their mitochondrial DNA, a reversible change. After extended exposure, though, the change became lasting as they stopped making mitochondrial genomes altogether. (Yeast are among the few eukaryotic organisms that can survive without these genomes.) "The adaptation had become genetically assimilated," Stenberg says.

SO FAR, STENBERG HASN'T PINNED down the genes responsible for this transition. But other researchers, working with the nematode *Caenorhabditis elegans*, have shown how a single mutation in one wild strain caused a plastic response to starvation to become fixed. In the lab, *C. elegans*—a key model animal for studying development and many other topics—is usually fed *Escherichia coli* bacteria. But in the wild, *C. elegans* lives on microbes in decaying fruit. These wild nematodes and their young live a life of feast and famine: Once the fruit is gone, it could take days to find more.

The worms have a ghoulish way to cope. They stop laying eggs, which instead hatch inside the mother's body, turning it into a lifeline for the developing young as they devour her insides. With enough food to survive, the nematode larvae can then enter a state of suspended animation called the dauer stage until the next windfall of fruit, when they mature and return to egg laying.

In a compost pile outside Paris, biologists have found a *C. elegans* strain in which the plastic response has become permanent. For these worms, matricide is the rule: They don't lay eggs, even when food is plentiful. "All the upstream signals related to food availability are irrelevant," says Christian Braendle, an evolutionary biologist at the French national research agency CNRS and University of Nice Institute of Biology in Valrose, France, who learned of the strain and decided to follow up. The change in strategy must be adaptive—allowing more offspring to survive—because Braendle's team keeps finding other matricidal wild strains.

By crossbreeding the compost pile strain with nonmatricidal worms and analyzing the DNA of offspring, his team has now tracked down the key gene, which codes for an ion channel, a protein in the cell membrane that transmits signals between nerves and muscle cells. In the matricidal strain, a single base change in the gene alters the ion channel. As a result, the worm's vulva muscle fails to respond to food signals that would normally cause it to expel eggs, causing them to hatch internally. "What our research shows is that a single mutation can lead to dramatic effects on life history through loss of ancestral plasticity," Braendle said at the meeting.

To confirm the mutation's effect, his team engineered it into egg-laying worms, which then bore live young. And when they transferred the unmutated gene to the matricidal worms, they reverted to egg-laying, Braendle reported.

"This might be the first description of the genetic mechanism underlying the transition from a historically plastic trait to a fixed trait," Ghalambor says. If Lamarck had come across these matricidal worms, he might have thought a selfless mother had adopted this strategy in a single generation, then passed it on. Braendle's unpublished work shows matricide is actually a plastic response encoded in the genes that, with one more mutation, became permanent.

So 200 years later, biologists are realizing Lamarck wasn't wrong in emphasizing that fast, flexible responses to the environment—what biologists now know as plasticity—can drive lasting change. Although mutations are still important drivers of evolution, responses to the environment "can be the precursors, and the genes are the followers," Gilbert says. "This is a change in the way of thinking." ■

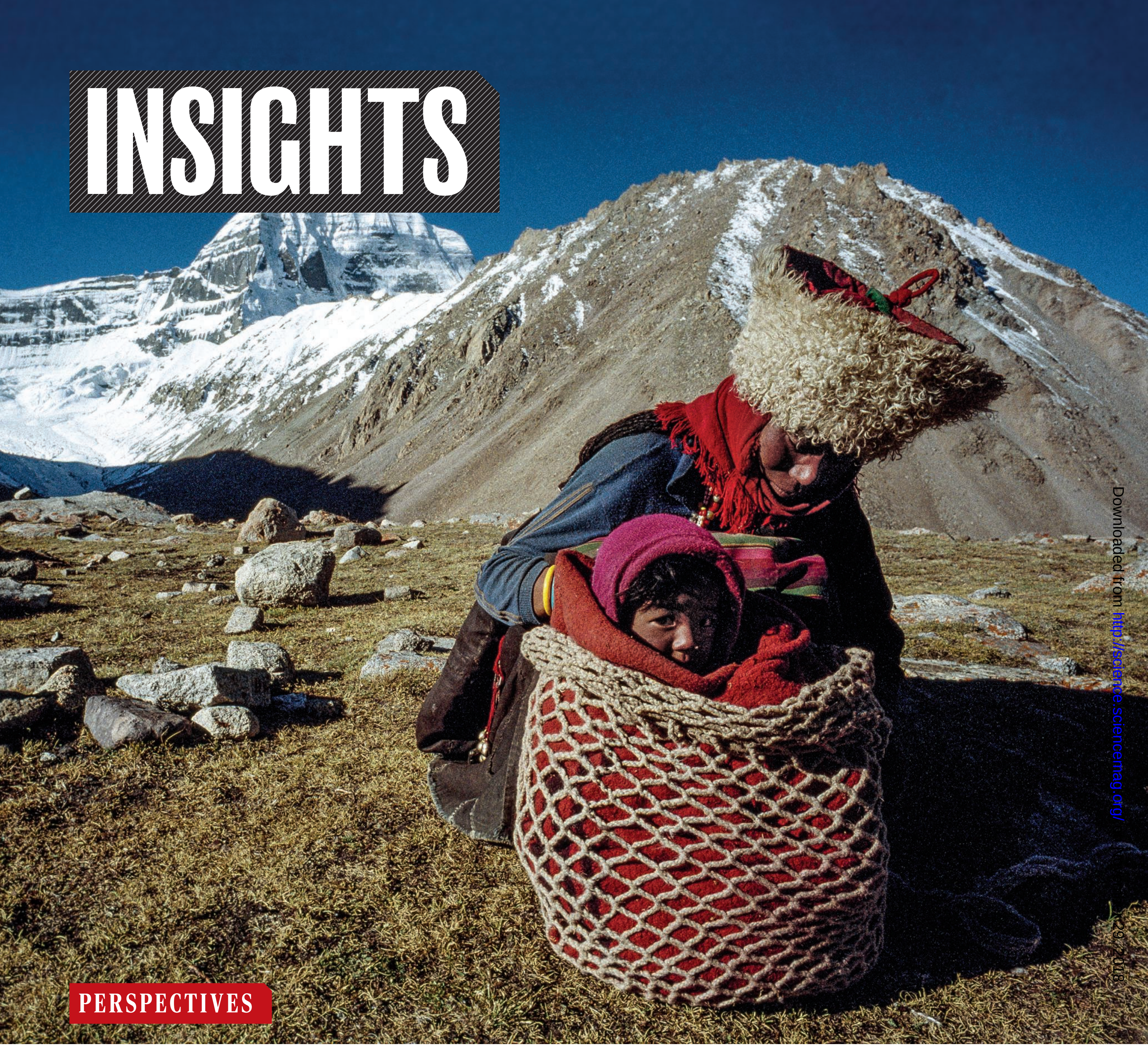

ANTHROPOLOGY

The last of Asia conquered by Homo sapiens

Excavation reveals the earliest human colonization of the Tibetan Plateau

By **Jia-Fu Zhang**[1] *and* **Robin Dennell**[2]

By 30,000 years ago, humans had colonized almost every part of Asia that was not covered by ice sheets and may even have settled on the shores of the Arctic Ocean (*1*). One of the last places in Asia that was colonized was the Tibetan Plateau, one of the most challenging and hostile environments of the Northern Hemisphere (*2*). With an average elevation of about 4000 m above sea level and an average annual temperature close to the freezing point of water, and with only half the concentration of oxygen as at sea level, it is not hard to see why it was such a challenge. Many researchers maintain that it was only colonized in the Holocene (the current epoch, which began approximately 12,000 years ago) with the adoption of agriculture, and the domestication of barley and yak (*3*). Others suggest that it might have been initially colonized at the end of the last ice age after about

PHOTO: LYNN JOHNSON/NATIONAL GEOGRAPHIC IMAGE COLLECTION

A mother and child on a pilgrimage to Mt. Kailash, Tibet. Tibetans may have deep roots in the Old Stone Age.

15,000 years ago, when hunter-foragers began to hunt at higher altitudes during the summer months and gradually learned how to acclimatize to such harsh surroundings (*4*). Some genetic evidence from modern Tibetans suggests that the Plateau might have been colonized 30,000 years ago before the last glacial maximum (*5*), but archaeological evidence for this is lacking. On page 1049 of this issue, Zhang *et al*. (*6*) report that the Tibetan Plateau shows not only the earliest occupation of the "roof of the world" but the earliest record worldwide for humans living at high altitude (see the first photo).

Tibetans watch the excavation of the Nwya Devu site on the Tibetan Plateau.

Zhang *et al*. report the excavation of a site called Nwya Devu, which lies at 4600 m in eastern Tibet (see the second photo). The site is positioned on the edge of a former lake and near a low ridge of black slate that provided an ample high-quality source of flakable stone for making stone tools. Unlike almost all other sites on the Tibetan Plateau that may have paleolithic-looking stone tools, this one is stratified and has almost 2 m of deposits. The site has three strata, of which the lowest is a layer of fine-grained sands denoting gentle deposition. Over 3600 stone artifacts were found, of which 300 are in the lowest layer, and 200 in a middle layer of sands and gravels; the rest were found in the topmost layer of sand and silt. There are no obvious typological, technological, or morphological differences in the assemblages from each layer, and Zhang *et al*. argue that all the artifacts can be regarded as part of the same assemblage. They also argue that the artifacts were primarily associated with the lowest layer but that geological processes such as freeze-thawing and gelifluction moved some of the artifacts upwards through the strata.

Dating is clearly critical here. Because there was not enough material for radiocarbon dating, the layers were dated primarily by optically stimulated luminescence (OSL). This technique measures the time that has lapsed since the dated sediment was last exposed to sunlight. It is now widely used to establish chronologies for human evolution and dispersals during the past 500,000 years on the basis of ubiquitous dating material (quartz and feldspar) within sediments (*7*). The 24 OSL dates are largely internally consistent (*6*). The topmost layer is OSL- and radiocarbon-dated to about 4000 to 13,000 years ago and is largely Holocene in age, and the middle layer dates from 18,000 to 25,000 years ago, indicating deposition during the last glacial maximum when conditions were at their most severe. The oldest dates of 30,000 to 45,000 years ago are from the bottom layer in the deepest part of the stratigraphy and indicate the likely age of the stone tool assemblage. This estimate is consistent with a radiocarbon date on a shell from that layer of 44,000 calibrated years before the present. Paleoenvironmental evidence from the Tibetan Plateau indicates that during this period, the climate was less severe than it is today.

It is obvious from the stone tool assemblage that a primary aim of those who stayed there was to produce long, parallel-sided blades that could be used as knives or scrapers that were most likely hafted onto a bone or wooden handle. Some of these blades were over 20 cm long, which testifies both to the quality of the raw material and the skill of the person flaking it. Because of the proximity of the site to a large source of flakable stone, the site is likely a workshop where tools were made that were then used on hunting expeditions at other locations. For paleolithic hunters, the attractions of the Tibetan Plateau must have been the herds of gazelles, horses, and yaks (and perhaps other herbivores such as woolly rhinoceros); the Plateau was undoubtedly harsh, but it was not barren. The stone tool assemblage is more or less unique in East Asia. The best-known assemblage from this period is that from the site of Shuidonggou locality 1 in Ninxia Province, north China. There, the earliest blades (dated to about 40,000 years ago) were made on a type of flake known as Levallois, followed by assemblages from Shuidonggou locality 2 that have smaller blades (*8*). It should be remembered that the paleolithic record of the vast area of northern China, Tibet, and Mongolia is very poorly known, so it is not surprising that there are no obvious parallels for the Nwya Devu assemblage.

We know from the cave site of Tianyuandong near Beijing that *Homo sapiens* were already in northern China by 40,000 years ago (*9*), so the first Tibetans were also likely *H. sapiens*. An interesting perspective on the colonization of the Tibetan Plateau is that the high-altitude adaptation that may have enabled humans to live at such a location may have come from a now-extinct type of humanity known as Denisovan, named after the cave of Denisova in the Altai Mountains of Siberia where it was first discovered. Denisovans are known only from their ancient DNA preserved in a few fossils. They appear to have been a sister taxon of the better-known Neanderthals. Denisovans may have contributed to adaptation of *H. sapiens* to high-altitude hypoxia (*10*). Denisovans interbred with Neanderthals (*11*), and Neanderthals interbred with *H. sapiens*, and therefore it is very likely that Denisovans interbred with *H. sapiens* as well. In fact, present-day human genetic makeup reflects that varied background, as in modern Melanesian populations, in that about 4 to 6% of our DNA is derived from Denisovans.

Unfortunately, no bone was preserved at Nwya Devu, so there is no direct skeletal evidence of the first Tibetans, nor of the animals that they hunted. Nevertheless, the evidence from Nwya Devu that humans were living at 4600 m above sea level 30,000 to 40,000 years ago provides a graphic example of how successful our species has been as a colonizing animal. ■

REFERENCES AND NOTES

1. C. J. Bae *et al*., *Science* **358**, eaai9067 (2017).
2. L. Barton, *Archaeol. Res. Asia* **5**, 4 (2016).
3. F. H. Chen *et al*., *Science* **347**, 248 (2015).
4. D. B. Madsen, *Archaeol. Res. Asia* **5**, 24 (2016).
5. D. S. Lu *et al*., *Am. J. Hum. Genet*. **99**, 580 (2016).
6. X. L. Zhang *et al*., *Science* **362**, 1049 (2018).
7. R. G. Roberts, Z. Jacobs, *Elements* **14**, 27 (2018).
8. F. Li *et al*., *Sci. China Earth Sci.* **59**, 1540 (2016).
9. M. A. Yang *et al*., *Curr. Biol.* **27**, 3202 (2017).
10. E. Huerta-Sánchez *et al*., *Nature* **512**, 194 (2014).
11. V. Slon *et al*., *Nature* **561**, 113 (2018).

ACKNOWLEDGMENTS

We thank the National Natural Science Foundation of China (grants 41771004 and 41471003) for support.

10.1126/science.aav6863

---

[1]MOE Laboratory for Earth Surface Processes, Department of Geography, College of Urban and Environmental Sciences, Peking University, Beijing, 100871, China. [2]Department of Archaeology, University of Exeter, Exeter, UK. Email: jfzhang@pku.edu.cn; r.w.dennell@exeter.ac.uk

PHOTO: JIA-FU ZHANG

NEUROSCIENCE

New dimensions for brain mapping

Imaging reveals new features of memory representation in the brain

By **Yaniv Assaf**[1,2]

The representation of memory in the brain is one of the unresolved questions in neuroscience. A key feature of learning and memory is the process of neuroplasticity—the ability of the brain to remodel structurally and functionally as a result of cognitive experience. Although the neurobiological basis of this process (that is, synaptic plasticity) is well established, the system level dynamics of neuroplasticity are still unclear. Recently, diffusion-weighted magnetic resonance imaging (DW-MRI), which can be carried out noninvasively in humans, provided a new approach to explore neuroplasticity. One of the parameters extracted from DW-MRI is mean diffusivity (MD) of water molecules, which is a biomarker of tissue microstructure (*1*). By probing changes in MD across the brain, areas of microstructural plasticity can be detected within hours of learning. On page 1045 of this issue, Brodt *et al.* (*2*) used DW-MRI after an object-location memory task and found that brain plasticity occurs in the posterior parietal cortex (PPC) rather than in the hippocampus. Furthermore, they demonstrated that localized DW-MRI changes follow the basic definition of a memory engram (the physical manifestation of memories stored in the brain). These observations go beyond the understanding of memory representation in the brain. Probing MD with DW-MRI appears to provide a detailed and comprehensive monitoring of brain microanatomy, revealing uncharted relations between brain structure and function.

Memory engrams in the brain

A memory circuit occurs in the hippocampal formation between the parahippocampus (PHC), entorhinal cortex (ENT), and perirhinal cortex (PRC). However, DW-MRI revealed that lasting microstructural changes occurred rapidly in the neocortex as a result of learning and memory tasks, suggesting that memory engrams may exist outside the hippocampus.

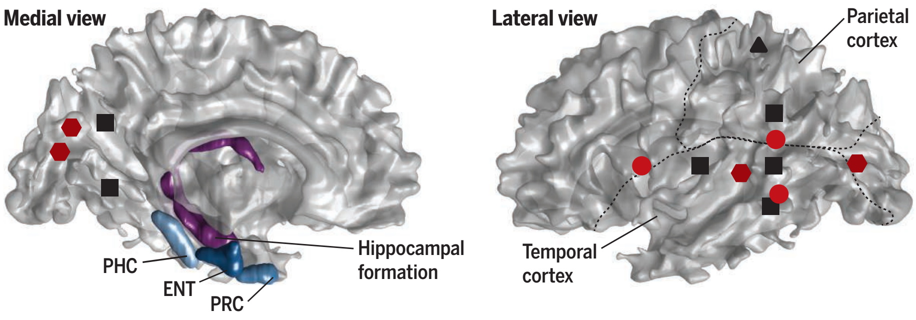

■ Spatial navigation learning ● Phonological learning ▲ Motor sequence learning ⬢ Object location memory

Through the evolution of neuroscience, regardless of the methods used, brain mapping theories to explain how the brain functions have led to the development of two camps: localizationism and globalism. Those two camps differ in their approach regarding how functions are mapped in the brain. Whereas localizationists claim that brain functions are localized in specific anatomic regions, globalists suggest that the brain works as a comprehensive unit. The question of localizationism versus globalism has been a long-standing topic of debate in neuropsychology.

Although evidence for functional localization exists for several cognitive domains, the definition of how memory is mapped in the brain remained elusive. The search for the memory engram has been the aim of many researchers. In 1950, Lashley stated that memory is not stored locally but rather spread throughout the cortex (*3*). Yet, memory disorder studies, such as the studies on patient H.M. who suffered from amnesia after brain surgery to remove the hippocampus, have indicated that the hippocampus is central to memory perception. Using electrophysiology and microscopy, the role of the hippocampus in different types of memory representations became axiomatic. A detailed map of interactions between the different parts of the hippocampus and different phases of memory was created (see the figure). Consequently, the neocortex was considered to imprint memories more slowly than the main memory hippocampal hub. Functional MRI (fMRI), which noninvasively measures brain function by monitoring blood flow and volume changes, followed the path of localizationism and has revolutionized human brain mapping and provided an invaluable noninvasive tool to explore task-specific brain activity. fMRI provides a more detailed and empiric map of brain function than was previously attainable. Such studies supported the concept of the hippocampus as the potential center of the memory engram.

Yet, the study of Brodt *et al.* gives solid experimental proof that a memory engram is present in the PPC, at least with respect to the object-location memory task used (*2*). This suggests that the undisputed role of the hippocampus in learning and memory may be in doubt. Why has this striking observation not been made before? Brodt *et al.* used a different approach to explore the memory engram—characterizing memory-related microstructural plasticity through MD measurements from DW-MRI (*4*, *5*). MD is a nonspecific, but sensitive, marker of tissue microstructure and has been used primarily as an indicator of inflammation and less frequently in conventional brain mapping. Studies in rats have suggested that the neurobiological basis of the rapid microstructural changes that occur after experience-driven neuroplasticity that is measured by MD may be related to astrocyte (a type of glial cell) remodeling (*4*, *5*). Although MD cannot be as specific as advanced microscopy methods, it provides unprecedented high sensitivity to in vivo system-level neuroplasticity in humans.

Recent studies have explored the utility of MD as a rapid and sensitive marker of neuroplasticity in several types of learning: spatial navigation (*5*), motor sequence learning (*6*), phonological language learning (*7*), and object-location memory (*2*). In these studies, the tasks lasted only hours, and, surprisingly, it appears that hippocampal involvement is less compared to other regions. Yet, as noted by Brodt *et al.*, it is not

---

[1] *Department of Neurobiogy, School of Neurobiology, Biochemistry, and Biophysics, George S. Wise Faculty of Life Sciences, Tel Aviv University, Tel Aviv, Israel.* [2] *Sagol School of Neuroscience, Tel Aviv University, Tel Aviv, Israel. Email: assafyan@gmail.com*

GRAPHIC: N. CARY/*SCIENCE*

that the hippocampus is not involved but rather that the changes in the hippocampus are more frequent and diminish rapidly. Indeed, MD measurements in rats undertaking a rapid spatial navigation task revealed that after a few episodes of training, most MD changes are observed in the hippocampus, but additional training, within the time frame of short-term memory, shifts most of the changes to the neocortex (*8*).

The use of MD and memory tasks revealed memory-associated changes in various neocortical regions (which may be newly identified memory engrams). Although these changes were previously shown in rodents (*9*), MD enables the detection of such engrams in humans as well. Moreover, coupled with fMRI, MD measurements from DW-MRI can detect the system-level dynamics of memory formation and storage, indicating that the transfer of memory from the hippocampus to the cortex occurs within minutes, much faster than previously thought. That MD can be used to detect such phenomena underscores its utility: It is a microstructural probe measured on the macroscale.

The ability of MD to detect microstructural imprinting in various neocortical regions exemplifies the localization versus globalization views of brain mapping. Without disproving previous theories and observations, the studies of Brodt *et al.* and others who have used MD postulate that brain mapping is an issue of scales and dimensions. Memory representation can be viewed as a task-specific regional process or as a global feature of the brain that can be segmented into localized domains.

In view of the ability of MD to detect time-dependent, system-level tissue changes, we anticipate that MD will highlight memory processes that have not yet been charted in the human brain. These processes may reveal new features of brain function-structure-cognition relationships that will improve our understanding of the localizationism-globalism symbiosis in brain architecture, network, and hierarchy and enable us to clarify with greater accuracy where memory as well as other cognitive domains are represented in the brain. ■

REFERENCES

1. P. J. Basser *et al*. *J. Magn. Reson. B* **111**, 209 (1996).
2. S. Brodt *et al*. *Science* **362**, 1045 (2018).
3. K. S. Lashley, in *Society of Experimental Biology Symposium No. 4: Physiological Mechanisms of Behavior* (Cambridge Univ. Press, 1950), pp. 454–482.
4. T. Blumenfeld-Katzir *et al*., *PLOS ONE* **6**, e20678 (2011).
5. Y. Sagi *et al*., *Neuron* **73**, 1195 (2012).
6. I. Tavor *et al*., *OHBM* **20**, 2414 (2014).
7. S. Hofstetter *et al*., *Brain Struct. Funct.* **222**, 1231 (2017).
8. S. Hofstetter *et al*., *Neuroimage* **155**, 202 (2017).
9. T. Kitamura *et al*., *Science* **356**, 73 (2017).

10.1126/science.aav7357

COSMOLOGY

Clues from gamma rays on the history of star birth

The rate of star formation peaked 10 billion years ago

By **Elisa Prandini**

The Fermi Gamma-ray Space Telescope, which celebrates its 10th year of operation, measures high-energy γ-ray emission, usually produced when cosmic rays (high-speed electrons or protons) interact with ordinary matter or radiation. Over the past 2 years, the Fermi–Large Area Telescope (LAT) Collaboration has contributed substantially to the birth of "multimessenger" astronomy, a revolutionary approach to study the high-energy Universe that combines the use of four messengers: photons, neutrinos, gravitational waves, and cosmic rays (*1, 2*). On page 1031 of this issue, the collaboration (*3*) reports another milestone of the Fermi-LAT team—consolidating the use of γ rays for measuring the rate of star formation over the history of the Universe.

No main-sequence star—those that fuse hydrogen atoms to form helium atoms in their cores (they constitute ~90% of the stars in the Universe)—can emit high-energy γ rays. How, then, can γ-ray observations provide clues about star formation history? They do so indirectly. While traveling from the emitter toward Earth, each high-energy γ ray has a nonzero probability of interacting with the numerous extragalactic background light (EBL) photons, which is the light emitted by all stars and accreting compact objects along the history of the Universe. The effect is a γ-ray flux suppression that increases

Star formation history

The rate of star formation can be determined by measuring the light from galaxies. The rate can also be determined by measuring the distortion of the high-energy γ-ray flux when interacting with this light. Peak star formation is estimated to have occurred approximately 10 billion years ago.

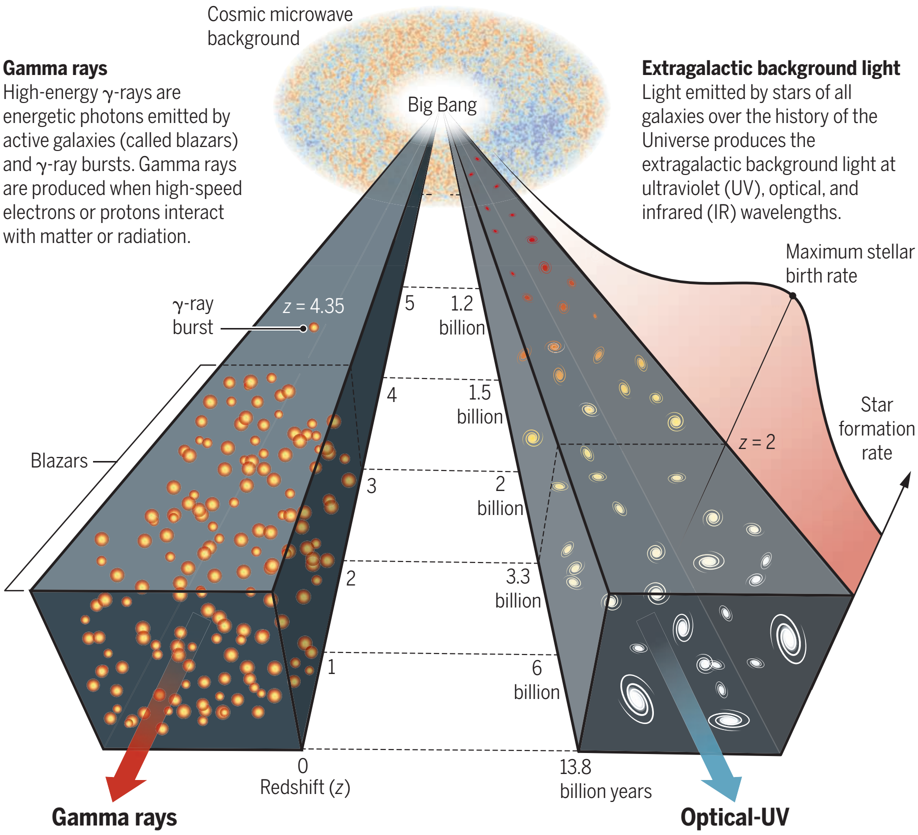

Gamma rays
High-energy γ-rays are energetic photons emitted by active galaxies (called blazars) and γ-ray bursts. Gamma rays are produced when high-speed electrons or protons interact with matter or radiation.

Extragalactic background light
Light emitted by stars of all galaxies over the history of the Universe produces the extragalactic background light at ultraviolet (UV), optical, and infrared (IR) wavelengths.

GRAPHIC: C. BICKEL/SCIENCE

with the distance of the emitter and the photon energy. Gamma-ray absorption can be studied as a function of the redshift (the displacement of spectral lines toward longer wavelengths due to the expansion of the Universe; it is used as a distance tracer) of a large number of emitting sources. This approach allowed the Fermi-LAT team to characterize the EBL in the ultraviolet (UV)-optical band that is commonly measured to estimate the rate of star formation (*4*) and its evolution along the history of the Universe (see the figure). The EBL is the second brightest of the diffuse background radiations permeating the Universe. The brightest is the cosmic microwave background, an echo of the epoch in the early Universe when electrons combined with protons to form neutral atoms.

To make this indirect measurement, the Fermi-LAT team sampled 740 γ-ray emitters, improving on a previous measurement done with fewer emitters (*5*). The most distant source used in the study was a γ-ray burst, a transient phenomenon with intense γ-ray emission detectable even at a redshift larger than 4 (the redshifting of light increases with distance, so the higher the redshift, the further back in time we are seeing; see the figure), when the Universe was less than 1.5 billion years old. All the other sources considered are blazars, the most powerful persistent natural accelerators known.

The Fermi-LAT group reports that, according to the absorption features detected in the γ-ray spectra, the rate of stellar formation in the Universe experienced a maximum ~10 billion years ago (25% of the Universe's history). After this bright peak, the rate of stellar birth started to decrease, and we live now in a Universe much less active in terms of stellar formation. This approach offers an extremely valuable alternative for this key cosmological measurement and is in line with independent results based on large astronomical surveys (*4*).

Remarkably, the Fermi-LAT team has also provided a new constraining limit to the abundance of faint galaxies as far as 12 billion years ago. UV photons from these galaxies are believed to be the main driver of the reionization of neutral hydrogen in the early Universe. Recent analyses of Hubble Deep Fields—images of the ancient Universe constructed from a series of long-lasting observations by the Hubble Space Telescope—give inconclusive and moderately controversial results. The measurement of the Fermi-LAT Collaboration helps to resolve this debate and suggests a turnover in the abundance of early galaxies at large redshifts. However, this result is based almost entirely on the single source located at redshift above 4. Further observations of sources at such large distances will consolidate and improve this first determination.

Estimates of the EBL with γ rays (*6*) have been attempted since the late 1990s by ground-based γ-ray detection instruments. The present generation of ground-based telescopes includes the High Energy Stereoscopic System (H.E.S.S.), the Major Atmospheric Gamma Imaging Cherenkov Telescopes (MAGIC), and the Very Energetic Radiation Imaging Telescope Array System (VERITAS). They observe γ rays at energies higher than those observed by the Fermi-LAT group and are therefore more suited to probe the optical-to-infrared part of the EBL, complementing the Fermi-LAT measurement in the UV-optical band. The γ-ray spectra at different cosmological distances measured from satellite- and ground-based telescopes also offer the opportunity to search for "signatures of physics" beyond the standard model of particle physics. Two effects of interest are the possible oscillation of γ rays into exotic particles called axions (dark matter particle candidates) and a dependence of photon propagation on its energy, an effect called the Lorentz invariance violation (*7, 8*). Both effects would give rise to anomalies in the spectra once corrected for the EBL absorption.

The evidence of such anomalies is a subject of intense debate in the cosmology community (*9, 10*). Major improvements in the field are expected within the first few years of operation of the Cherenkov Telescope Array (CTA). The CTA is a ground-based γ-ray observatory currently in a preconstruction phase. With its extended energy range and excellent sensitivity, the array has the potential of measuring the EBL and the associated cosmological quantities with high precision (*11*). In addition, new space missions, such as the James Webb Space Telescope, aim to measure the optical and infrared light from the deep Universe, providing an independent, more direct estimate of the EBL and its evolution over cosmic time. ■

REFERENCES

1. B. P. Abbott *et al.*, *Astrophys. J. Lett.* **848**, L13 (2017).
2. IceCube Collaboration, *Science* **361**, eaat1378 (2018).
3. The Fermi-LAT Collaboration, *Science* **362**, 1031 (2018).
4. P. Madau, M. Dickinson, *Annu. Rev. Astron. Astrophys.* **52**, 415 (2014).
5. M. Ackermann *et al.*, *Science* **338**, 1190 (2012).
6. F. W. Stecker, O. C. de Jager, M. H. Salamon, *Astrophys. J.* **390**, L49 (1992).
7. A. De Angelis, M. Roncadelli, O. Mansutti, *Phys. Rev. D* **76**, 121301 (2007).
8. G. Amelino-Camelia *et al.*, *Nature* **393**, 763 (1998).
9. D. Horns, M. J. Meyer, *Cosmol. Astropart. Phys.* **2**, 033 (2012).
10. J. Biteau, D. A. Williams, *Astrophys. J.* **812**, 60 (2015).
11. D. Mazin *et al.*, *Astropart. Phys.* **43**, 241 (2013).

10.1126/science.aav7344

Department of Physics and Astronomy, University of Padova, and INFN, Padova, Italy. Email: elisa.prandini@unipd.it

---

METALLURGY

One crystal out of many

Fast-moving grain boundaries convert a hanging polycrystalline metal foil into a single crystal

By **Anthony Rollett**

A large fraction of the "stuff" that surrounds us, whether natural (e.g., rocks) or artificial (e.g., most metals and ceramics), is polycrystalline—assemblies of smaller single crystals. The size and perfection of the crystals govern property optimization. For example, materials made up of nanocrystals can have exceptional strength and damping capability. However, in some cases, single crystals optimize performance. Substantial effort has gone into growing large single crystals of nickel superalloys because at this macroscopic scale, the grain boundaries between crystallites are a source of weakness at the high temperatures used in gas-turbine engines. Converting a sample of conventional polycrystalline material with typical grain sizes of 20 μm into coarse-grained material is not a simple task. The grain boundaries must overcome many physical barriers in order to migrate over distances comparable to the desired grain size. Indeed, it is accepted that thin films rarely will coarsen beyond the thickness of the film itself (*1*). Thus, the study by Jin *et al.* (*2*) on page 1021 of this issue is very surprising because it demonstrates that grain boundaries can be moved in foils of metals such as copper and platinum over distances on the order of centimeters.

> ***"The method relies on annealing an unattached, hanging foil such that the stress is minimized."***

Grain boundaries move or stay put depending on their response to several different types of forces that act on them. One is

Department of Materials Science and Engineering, Carnegie Mellon University, Pittsburgh, PA, USA. Email: rollett@andrew.cmu.edu

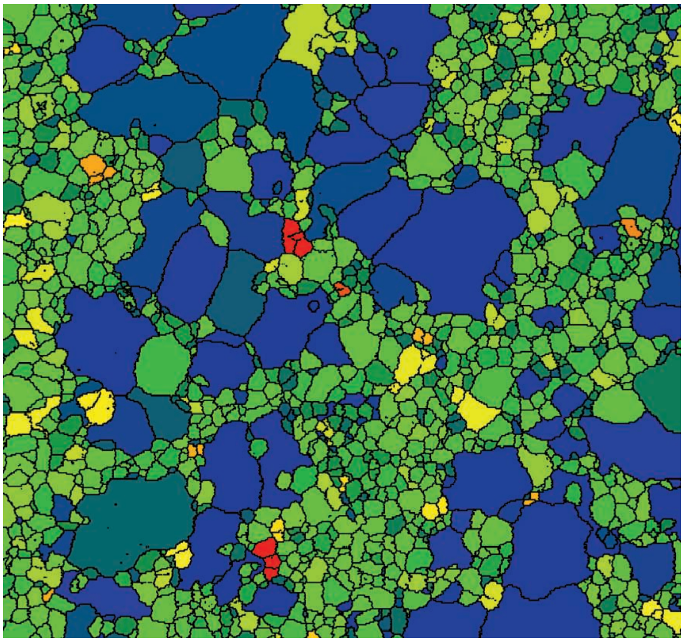

Orientation map obtained with electron backscatter diffraction of a sample of Fe-1%Si undergoing abnormal grain growth, colored according to the average orientation gradient in each grain. The orientation gradients are a consequence of heterogeneously stored dislocations and are therefore a surrogate for stored energy. Grains with low stored energy (blue) have a growth advantage over others.

IMAGE: ANTHONY ROLLETT AND TRICIA BENNETT

the excess free energy associated with the presence of a boundary itself, which is caused by the disorder at the interface, i.e., the absence of regular atomic order enforced by the difference in crystal orientation. Polycrystalline materials generally comprise interfacial networks with threefold junctions of boundaries. The excess free energy leads to a local equilibrium along these triple lines, which, in turn, sets up curvatures. These curvatures cause large grains to expand at the expense of small grains.

Although such a network of boundaries should coarsen indefinitely toward a single crystal, in practice, the driving force is weak enough for micrometer-sized grains to be nullified by solute drag (*3*), pinning by small particles (*4*), or surface grooving (*5*). Small particles pin grain boundaries by locally subtracting area, which is effectively a barrier to a moving boundary and is technologically important in steel used for electrical transformers. Surface grooving, driven by interfacial energy, occurs at the intersection of a grain boundary with a free surface and, once developed, requires moving boundaries to drag along the grooves. Although curvature as a driving force should result in uniform coarsening of the grain structure, the retardation effects described can be heterogeneously distributed, which leads to abnormal (or discontinuous) grain growth; particle pinning is one example of this phenomenon (*6*). No texture development (alignment of grain orientations) is expected theoretically, nor observed in practice.

A completely different circumstance is that where a minority of the grain boundaries in the polycrystal have much higher mobility than all others, in which case grains surrounded by such boundaries will tend to grow abnormally. This situation can occur in subgrain structures, in which low-angle grain boundaries contain dislocations in proportion to the misorientation, and provides a mechanism for the quasinucleation observed at the mesoscale in recrystallization (*7*). It can also occur through complexion transitions where an impurity segregates to grain boundaries, creating a specific atomic structure that possesses high mobility (*8*).

Another important driving force for grain growth is that of the stored energy associated with dislocation content. In the context of annealing after plastic deformation, quasinucleation occurs, and growth is obviously heterogeneous. This behavior is termed primary recrystallization rather than grain growth, and the resulting grain size can be finer than in the undeformed material prior to deformation. In face-centered cubic (fcc) metals such as copper and nickel, very strong biaxial textures can be developed with the family of <100> orientations parallel to both the rolling and normal directions, which are important, for example, in manufacturing long lengths of textured high-temperature superconductors (*9*).

For very low levels of deformation, however, the polycrystal does not appear to be deformed, and no newly undeformed grains appear. Nevertheless, the stored energy can be sufficiently nonuniform to cause certain grains to grow at the expense of others, which then appears as abnormal grain growth (see the image) (*10*). Texture development is theoretically possible from, say, orientation-dependent dislocation storage, but it has not been observed in practice.

Yet another driving force is that of the anisotropy of surface energy. In simple atomic solids such as metals, the minimum surface energy corresponds to the close-packed plane, but such anisotropy exists for essentially all crystalline materials. In thin films that undergo grain growth, the variations in surface energy promote the growth of grains with a low surface energy over all others. Thus, fcc metals have {111} as their close-packed plane with a minimum surface energy that biases the texture toward a common <111> parallel to the film normal, termed a "111 fiber texture."

A more subtle effect is that of elastic anisotropy coupled with elastic strain. Where a thin film is attached to a substrate, any difference in the coefficient of thermal expansion will give rise to an elastic strain in the film. Most materials are strongly anisotropic, which means that the stress in each grain will vary depending on its orientation. Thompson *et al.* (*11*) demonstrated that strongly textured films could be grown in silver, for example, using this effect where the texture is other than that expected from the anisotropy of the surface energy. Again, the texture is also a fiber texture but with a common crystallographic axis (parallel to the direction normal to the film) that differs from that expected on the basis of minimum surface energy.

All of these considerations provide context for explaining why the result of Jin *et al.* in converting centimeter-sized thin films to essentially a single orientation with minimal mosaic spread is so interesting and important. The method relies on annealing an unattached, hanging foil such that the stress is minimized. For the non-noble metals, a hydrogen atmosphere is used to introduce hydrogen atoms to stabilize vacancies that enable atomic motion that promotes grain growth. The orientation is biaxial, i.e., with specific crystal directions aligned both with the foil normal and with the vertical direction. This approach opens up several possibilities for developing new technologies based on the availability of large areas of a single crystal that can be used as a substrate for processes such as growth of graphene or perhaps chiral selection in catalysis of chemical reactions (*12*). ■

REFERENCES

1. K. Barmak *et al*., *Prog. Mater. Sci.* **58**, 987 (2013).
2. S. Jin *et al*., *Science* **362**, 1021 (2018).
3. J. W. Cahn, *Acta Metall.* **10**, 789 (1962).
4. P. A. Manohar, M. Ferry, T. Chandra, *ISIJ Int.* **38**, 913 (1998).
5. W. W. Mullins, *Acta Metall.* **6**, 414 (1958).
6. J. Calvet, C. Renon, *Mem. Sci. Rev. Metall.* **57**, 345 (1960).
7. S. Wang *et al*., *Acta Mater.* **59**, 3872 (2011).
8. P. R. Cantwell *et al*., *Acta Mater.* **62**, 1 (2014).
9. A. Goyal *et al*., *Appl. Supercond.* **4**, 403 (1996).
10. T. A. Bennett, P. N. Kalu, A. D. Rollett, *Microsc. Microanal.* **17**, 362 (2011).
11. J. Greiser, D. Muller, P. Müllner, C. V. Thompson, E. Arzt, *Scripta Mater.* **41**, 709 (1999).
12. C. F. McFadden, P. S. Cremer, A. J. Gellman, *Langmuir* **12**, 2483 (1996).

10.1126/science.aav6733

Virgin female fruitflies' choice of mating partner is strongly biased toward the characteristics of males that a majority of already-mating females prefer, sustaining mate-choice "cultures."

ANIMAL BEHAVIOR

Culture and conformity shape fruitfly mating

Potent social learning sustains the inheritance of mating preferences over generations

By **Andrew Whiten**

Culture pervades every aspect of human lives, its achievements providing a compelling explanation for our species' domination of the planet (*1*). Defined as the matrix of traditions built by previous generations and inherited by social learning, culture was long thought to be uniquely human. In recent decades, however, mounting evidence for culture defined in this way has accumulated for numerous vertebrate species and an expanding diversity of behaviors (*2*). Examples include migratory knowledge in bighorn sheep (*3*); foraging techniques in humpback whales (*4*), great tits (*5*), and bumble bees (*6*); and tool use in apes (*2*). These discoveries suggest that although human culture has developed unprecedented complexities, it evolved from more elementary forms shared with other species. On page 1025 of this issue, Danchin *et al.* (*7*) offer evidence that a species that may surprise many should be added to this growing animal "culture club": the humble fruitfly. They show that the mating preferences of female fruitflies are strongly influenced by the existing preferences they observe in other females, generating traditions that are repeatedly passed on to others and spread in the population. Animal culture may be a much more widespread phenomenon than hitherto acknowledged.

The study of Danchin *et al.* offers further surprises. The most notable concerns conformity—the tendency to copy whatever a majority of one's companions are seen to do, which has long been known to take extreme forms in our own hypercultural species. In a classic human experiment, individuals were invited to judge which of several lines matched the length of a target line (*8*). Although the answer was perceptually obvious, the experimenter arranged that before the subjects voiced their judgment, several stooges placed by the experimenter said it was a different line. Many subjects then conformed in echoing this blatantly false opinion. We humans are prone to conform to many well-established customs, a motivation often interpreted as an adaptive element of our deeply cultural natures (*1*, *9*).

To test for conformity in fruitflies, Danchin *et al.* placed female fruitflies in a hexagonal chamber, encircled by six compartments in each of which they could observe a female fly mating with a male dusted with either pink or green coloring, while the male of the alternative color merely stood by. For some females, all six mating males were pink; for others, all were green. Other females experienced displays with varying proportions of pink versus green males mating, or a neutral experience with equal proportions.

Females were then tested for their mating preferences. As expected, those exposed to the neutral case chose at random, whereas if they had seen mating exclusively with pink males they tended to choose pink, and similarly for those that had seen mating with only green males. Remarkably, however, the relationship between mating preferences witnessed and mating preferences subsequently enacted was far from linear, for as soon as the deviation from equality was as little as 60:40, females echoed that bias in their mate choices as much as if it were 100:0. The intensity of this effect exceeds any in the limited, and debated (*10*), studies reporting such conformist transmission in birds (*6*) and fish (*11*).

Such an exaggerated copying bias has been called "hyperconformity" (*12*). Its occurrence, as earlier demonstrated conceptually and mathematically for humans (*9*), is of considerable importance for cultural evolutionary theory, because it has the potential to maintain traditional preferences across generations (*9*, *12*). In the case of genetically inherited traits, Fisher (*13*) showed that sexual selection, in which females prefer one male characteristic over another, can lead to a runaway evolutionary spiral as the favored male characteristic becomes increasingly common in subsequent generations, along with female preferences for it. Hyperconformity could generate an equivalent runaway cultural effect. If female preferences are selected culturally, along with genetic selection associated with the preferred male characteristic, then genetic and cultural inheritance might interact; this is a question for future research.

To empirically explore the scope for transmission across cultural generations in the fruitflies, Danchin *et al.* used the hexagonal chamber in a different way. This time, a dozen virgin females were placed in the central arena and could observe six males all of the same color, each mating with a female in the surrounding compartments. The first six of the observer females to successfully mate with a male, whether pink or green, then became the "demonstrators" for a further dozen

---

Centre for Social Learning and Cognitive Evolution, School of Psychology and Neuroscience, University of St Andrews, St Andrews KY16 9JP, UK. Email: a.whiten@st-andrews.ac.uk

PHOTO: MICHAEL DURHAM/ MINDEN PICTURES/GETTY IMAGES

virgin females in the central arena. Repeating this process created a "cultural transmission chain" between "cultural generations," which showed that the original color bias was sustained for an average of about eight cultural generations before it faded. This effect exceeded what would be expected if preferences occurred by chance. However, it seems far from the long-term stability that hyperconformity might predict.

The authors suggest that this is because, given copying errors, a population of just six per generation is insufficient for cultural stability. A mathematical model incorporating their findings predicted outcomes in larger populations, which in nature may number in the hundreds. Even with just 30 to 40 individuals, the number of generations the model predicted to display stable preferences rose exponentially into the hundreds and even thousands.

Like all models, these results depend on an array of assumptions and inputs. They await further empirical testing. Experiments directly testing the effect of group sizes greater than 10 on conformity have been rare even for human subjects, and are yet to be explored in animal studies (*6*, *11*). Just one study of primates, focused on transmission of large, group-wide preferences, reported a strong conformity effect (*14*). Danchin *et al.* offer their model in lieu of empirical studies, which are considered impractical with large fruitfly populations. But the short generation time of these tiny flies permits evolution to be traced over scores of generations (*15*). If founder populations similar to but larger than those created for the present study's transmission chains are created and allowed to reproduce, perhaps cultural transmission may be tracked across biological generations, as the population rapidly expands. The potential for examining interactions between the effects of genetic and cultural selection and inheritance in this classic model species is exciting indeed. ■

REFERENCES

1. J. Henrich, *The Secret of Our Success* (Princeton Univ. Press, 2015).
2. A. Whiten *et al.*, *Proc. Natl. Acad. Sci. U.S.A.* **114**, 7775 (2017).
3. B. R. Jesmer *et al.*, *Science* **361**, 1023 (2018).
4. J. Allen *et al.*, *Science* **340**, 485 (2013).
5. L. M. Aplin *et al.*, *Nature* **518**, 538 (2015).
6. S. Alem *et al.*, *PLOS Biol.* **14**, e1002564 (2016).
7. É. Danchin *et al.*, *Science* **362**, 1025 (2018).
8. S. E. Asch, *Psychol. Monogr.* **70**, 1 (1956).
9. R. Boyd, P. J. Richerson, *Culture and the Evolutionary Process* (Univ. of Chicago Press, 1985).
10. E. J. C. van Leeuwen *et al.*, *Anim. Behav.* **110**, e1 (2015).
11. T. W. Pike, K. N. Laland, *Biol. Lett.* **6**, 466 (2010).
12. N. Claidière, A. Whiten, *Psych. Bull.* **138**, 126 (2012).
13. R. A. Fisher, *The Genetical Theory of Natural Selection* (Oxford Univ. Press, 1930).
14. E. van de Waal *et al.*, *Science* **340**, 483 (2013).
15. A. Debelle *et al.*, *J. Evol. Biol.* **29**, 1307 (2016).

10.1126/science.aav5674

CANCER BIOLOGY

Metastases go with the flow

Blood flow mechanics influence metastatic efficiency

By **Jacky G. Goetz**[1,2,3]

To colonize distant organs and thus disseminate throughout the body, cancer cells and associated factors exploit several fluids for transport. Recently, circulating tumor cells (CTCs) were found to survive and exploit the inner biomechanics of the bloodstream to foster tumor metastasis (*1*, *2*). Thus, in addition to using both the blood and lymphatic circulation as a means to travel throughout the body (*3*–*5*), the underlying forces allow CTCs to seed distant metastases. The contribution of fluids, particularly vascular flow mechanics, and physical constraints raises interesting questions about the biology of metastasis.

According to the "seed and soil" theory of metastasis, CTCs survive and establish growing colonies in distant organs within environments that are compatible with their growth. Successful metastatic outgrowth involves several steps, including organ infiltration, immune escape, growth, and survival in supportive niches (*6*). The metastatic potential of tumor cells is also tightly linked to body fluids that favor their journey to distant organs (*1*, *2*). CTCs disseminate early through the lymphatic circulation to spread to tumor-draining lymph nodes, which often correlates with reduced survival. Although removal of these metastatic lymph nodes has shown no benefit on overall survival of patients with, for example, melanoma (*7*), as well as other types of cancer, lymph nodes were recently demonstrated to be intermediate steps for metastases in mice (*3*–*5*). Efficient CTC colonization of distant organs occurs mostly via the blood circulation (*6*) (see the figure).

On their way to blood vessels (intravasation), invading tumor cells encounter mechanical pressures imposed by architectural constraints of tissues. In particular, space constraints induce nuclear squeezing, which challenges the integrity of the nucleus and triggers genomic rearrangements that might foster metastatic potential (*8*). It is likely that such pressure also applies to CTCs during arrest in distant sites, extravasation (exiting vessels), and metastatic outgrowth.

Both individual and rare groups of invasive carcinoma cells enter the tumor-associated vasculature (*9*, *10*). Although it is unclear whether clusters of CTCs can transfer from the lymphatic to the blood circulation (*4*, *5*), a mixture of single and clumps of CTCs disseminate throughout the body before they reach a distant organ (*10*). In the circulation, CTCs face multiple physical constraints that will directly affect successful seeding. Single CTCs need to overcome the mechanical stress imposed by shear forces, likely to induce apoptosis (programmed cell death), before they lodge in a capillary in a distant organ. This mechanical stress can considerably reduce the ability of CTCs to successfully initiate the growth of a metastatic colony. When shed as clumps and traveling as clusters, CTCs are more resistant to shear forces and cytotoxic immune cells (*10*). They are also more likely to become lodged in microvessels in distant organs before seeding metastatic colonies (*10*). Indeed, mechanical constraints imposed by vessel architecture and size contribute to the intravascular arrest of CTCs (*11*), and clusters of CTCs are rapidly trapped in tiny capillaries. Intravital imaging in living mice recently demonstrated that CTC clusters could also form mechanically, as a consequence of the initial arrest of a single CTC (*12*). Nevertheless, some clusters of CTCs avoid lodging and are capable of squeezing through capillary-sized vessels as a group (*13*). Such clusters reduce their hydrodynamic resistance by forming single-file structures that rely on intercellular adhesive interactions. However, whether extravasation from blood vessels of clusters of CTCs is more efficient than single CTCs remains to be demonstrated.

In addition to mechanical trapping imposed by vessel architecture and size, single or clusters of CTCs also rely on blood flow, their adhesive potential, and blood components (such as platelets) to arrest successfully at distant sites (*2*). Indeed, although physical restriction can explain how CTCs become lodged in a capillary bed downstream of the tumor along the anatomical route of the blood circulation, it does not explain the sites of metastasis, which are specific for each cancer type (organotropism). Recent observations demonstrate that both the efficiency and location of CTCs becoming lodged in distant sites correlate with the presence of permissive flow regimes in some vascular regions (*2*). The transit of CTCs in the blood circulation is stopped when their adhesive capacity overcomes the shear forces imposed

---

[1] *INSERM UMR_S1109, Strasbourg, France.* [2] *Université de Strasbourg, Strasbourg, France.* [3] *Fédération de Médecine Translationnelle de Strasbourg (FMTS), Strasbourg, France. Email: jacky.goetz@inserm.fr*

by blood flow. In vivo measurements revealed that CTCs and endothelial cells (which line vessels) rapidly engage adhesion forces that exceed 200 pN, where hemodynamic shear forces (≈100 pN) cannot dislodge them (*2*). Thus, CTCs mostly engage and stabilize adhesions with endothelial cells of vessel walls in regions with low hemodynamic flow. These regions might also favor the sequential formation of intravascular clusters from single CTCs (*12*). An evaluation of a cohort of 100 patients with brain metastasis demonstrated that metastases preferentially develop in anatomical regions with reduced cerebral blood flow dynamics (*2*). In addition to limiting survival of CTCs in transit, shear forces also control the location of their final arrest. Combined with the physical constraints imposed by vessel architecture, shear forces imposed by hemodynamic flow are thus essential factors of hematogenous metastasis.

The influence of fluid mechanics on metastasis

From the onset of tumorigenesis, fluid mechanics in blood and lymph drive tumor growth, invasion, and metastatic potential. Although metastatic tumor cells seed draining lymph nodes, metastases mostly form in distant organs via the circulatory system. Blood flow forces control the arrest and recruitment of myeloid cells and the efficiency of extravasation, which precede metastatic outgrowth.

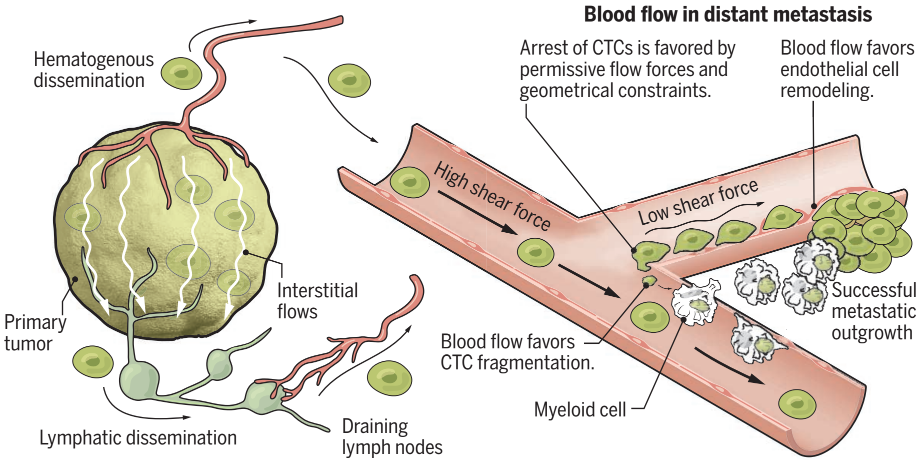

Once lodged in microvessels, CTCs can become fragmented by blood flow, which generates immune-interacting intermediates that promote extravasation and the development of metastases from surviving CTCs (*1*). Intravital imaging of melanoma cell dissemination to the lungs revealed that shear forces caused the formation of microparticles from tumor cells that were lodged in lung capillaries (*1*). These tiny fragments, called cytoplasts, are devoid of nuclear components, are only formed in the presence of shear forces, and are not derived from apoptotic events. Cytoplasts that contain mitochondria adhere to vessel walls and display intravascular migration (crawling along the vascular wall), as has been shown for intact CTCs (*2*), that is favored by hemodynamic flow (*1*). Soon after they are produced, myeloid cells such as neutrophils, conventional and patrolling monocytes, nonalveolar macrophages, and dendritic cells are sequentially recruited and take up (phagocytose) cytoplasts. Phagocyte populations then compete to either stimulate or restrict metastatic outgrowth. Although most of the cytoplast-ingesting myeloid cells are known to facilitate successful metastases, conventional dendritic cells, although sparse and recruited last by the generation of cytoplasts, provide antimetastatic defense. Shear forces are thus essential for CTC fragmentation, yet the flow regimes that induce this phenomenon, if any, remain to be determined. It also remains unclear how flow-mediated fragmentation of a CTC facilitates the extravasation of its corresponding karyoplast (the parental nucleated cell).

Although it is not clear whether blood flow also stimulates CTC transmigration (active migration through the vascular wall) or protects them from immune recognition, endothelial cells respond to shear flow forces by producing cellular protrusions that are capable of engulfing single or clustered CTCs (*2*). This flow-dependent process, called endothelial remodeling, drives subsequent extravasation of arrested CTCs and reestablishes blood perfusion in the capillary. Interestingly, endothelial cells of cerebral microvessels similarly remove blood clots, preventing early embolus formation and reestablishing blood flow in vascular occlusive disorders (*14*).

Multiple challenges remain. For example, further work is needed to address whether hemodynamic shear forces modulate the formation and location of pre-metastatic niches (PMNs). Such niches provide pro-metastatic conditions in tissues that are otherwise hostile to tumor cells and are shaped by tumor-shed factors. Indeed, although several molecular and microenvironmental programs set the basis for metastatic traits and organ-specific tropism of cancer types (*6*), tumor-shed soluble factors and extracellular vesicles disseminate through body fluids and initiate PMN formation (*15*). Fluid-borne tumor-derived factors thus also determine metastatic potential of cancer cells, and it is likely that their target location and extravasation is influenced by fluid mechanics, both in the blood and the lymphatic circulation. The development of animal models, imaging approaches, and biomarkers could help clarify the formation of PMNs in patients. Similarly, how tumor dormancy—in which CTCs are lodged in distant sites but do not grow—is influenced by fluid mechanics (and whether dormancy results from specific PMNs) could be investigated. Organotropism could also be influenced by, in addition to other molecular factors, distinct flow profiles and vessel architecture within and between organs. Myeloid cells detect tumor-derived material, which is either transported or shed by fluid flows. A better understanding of how they compete and are recruited at metastatic or dormancy sites by fluid-borne material could lead to the design of antimetastatic immunotherapy. Similarly, perhaps antiangiogenesis compounds that could reduce flow-mediated pro-metastatic endothelial remodeling should be explored. Blood flow profiles, which can be assessed with contrast-enhanced computed tomography or magnetic resonance imaging, might be used to identify future sites of metastasis and could be used in diagnostics. Further understanding of the molecular mechanisms that underlie flow-mediated endothelial remodeling and subsequent extravasation of CTCs could help to better define interventions for metastasis prevention. ■

REFERENCES AND NOTES

1. M. B. Headley *et al.*, *Nature* **531**, 513 (2016).
2. G. Follain *et al.*, *Dev. Cell.* **45**, 33 (2018).
3. K. Naxerova *et al.*, *Science* **357**, 55 (2017).
4. M. Brown *et al.*, *Science* **359**, 1408 (2018).
5. E. R. Pereira *et al.*, *Science* **359**, 1403 (2018).
6. J. Massagué, A. C. Obenauf, *Nature* **529**, 298 (2016).
7. M. B. Faries *et al.*, *N. Engl. J. Med.* **376**, 2211 (2017).
8. C. M. Denais *et al.*, *Science* **352**, 353 (2016).
9. K. J. Cheung *et al.*, *Proc. Natl. Acad. Sci. U.S.A.* **113**, E854 (2016).
10. N. Aceto *et al.*, *Cell* **158**, 1110 (2014).
11. Y. Kienast *et al.*, *Nat. Med.* **16**, 116 (2010).
12. D. Entenberg *et al.*, *Nat. Methods.* **15**, 73 (2018).
13. S. H. Au *et al.*, *Proc. Natl. Acad. Sci. U.S.A.* **113**, 4947 (2016).
14. J. Grutzendler *et al.*, *Sci. Transl. Med.* **6**, 226ra31 (2014).
15. H. Peinado *et al.*, *Nat. Rev. Cancer.* **17**, 302 (2017).

ACKNOWLEDGMENTS

J.G.G. thanks the Goetz laboratory, F. Winkler, X. Trepat, and H. Peinado for their comments.

10.1126/science.aat9100

GRAPHIC: N. DESAI/*SCIENCE*

PHOTO: WIKIMEDIA COMMONS

RETROSPECTIVE

Leon Max Lederman (1922–2018)

Charismatic particle physics pioneer

By **Rocky Kolb**

Leon Max Lederman passed away quietly on 3 October in Rexburg, Idaho. He was 96 years old. A pioneer in particle physics, Leon shared the 1988 Nobel Prize in Physics. He was an influential public champion for science and science education, a transformational scientific leader, and a role model to generations of scientists young and old.

Leon was born to Russian-Jewish immigrants in New York City on 15 July 1922. Although neither parent had finished school, they instilled in their son a love of learning that he carried with him all his life. Leon's education started at P.S. 92 on Broadway and 95th and ended just a few blocks north of that at Columbia University, where he received a Ph.D. in physics in 1951. In between, he attended New York public schools and earned his undergraduate chemistry degree from the City College of New York in 1943. Columbia University remained his academic home until he left to assume the directorship of Fermi National Accelerator Laboratory (Fermilab) in Batavia, Illinois, in 1979.

Leon often spoke with a combination of pride and humor about his early days at Columbia University. In 1956, Leon and collaborators used Brookhaven's Cosmotron to show the existence of the long-lived neutral kaon, the K_L, distinct from the short-lived neutral kaon, the K_S. This experiment established the weak eigenstates of the neutral kaon that were proposed by physicists Murray Gell-Mann and Abraham Pais in 1955. The next year, Leon's group used the Nevis accelerator to discover nonconservation of parity in muon decay. Remarkably, they conceived of the idea during the half-hour drive from the main campus to Nevis one Friday, constructed the experiment that evening, and collected the data by the end of the weekend, demonstrating clear evidence for the fundamental result.

In 1962, Leon and his colleagues led a team that established the existence of a second-generation neutrino, the muon neutrino. He would share the Nobel Prize in recognition of this work. In addition to the importance of the two-neutrino result in the development of the standard model of particle physics, the experiment pioneered the use of neutrino beams to study weak interactions.

In the 1970s, Leon's interests turned to particles produced at high transverse momentum in high-energy proton-proton collisions. A sequence of ever-higher-energy experiments at Brookhaven, the Intersecting Storage Ring at CERN, and finally at Fermilab culminated in the 1977 discovery of the bottom quark, one of six known quarks. Shortly afterward, Leon became the second director of Fermilab. During his three decades as an experimental particle physicist, he supervised 50 Columbia University Ph.D. candidates and was a mentor to many other young students and postdocs.

Influenced by his mentor, physicist and 1944 Nobel Prize winner Isidor Isaac Rabi, Leon thought big. His 1963 paper, "A truly national laboratory," envisioned a new model for a national accelerator laboratory; the vision was realized in the 1967 founding of the National Accelerator Laboratory (renamed Fermilab). He was also a major proponent and spokesperson for the ill-fated Superconducting Super Collider, a planned 87-km-circumference accelerator that was approved in 1989 and canceled in 1993. He was a founding member of the High-Energy Physics Advisory Panel (to the U.S. Atomic Energy Commission and later to the U.S. Department of Energy) and the International Committee on Future Accelerators.

As director of Fermilab from 1979 to 1989, Leon oversaw the construction of the Tevatron complex, the first superconducting accelerator and the world's most powerful accelerator from 1983 until it was eclipsed by CERN's Large Hadron Collider in 2009. Imagining unification of the inner space of particle physics with the outer space of cosmology, in 1983, Leon started the first astrophysics group at an accelerator laboratory. In addition to scientific leadership, with characteristic charm and humor, Leon transformed Fermilab from a frontier outpost in the cornfields of Illinois into a cosmopolitan center for science and science education.

As a professor at Columbia University, Leon reached many generations of undergraduates in his "physics for poets" class. He transposed his love of teaching to Fermilab, where he instigated Saturday Morning Physics, a weekend class for area high-school students featuring lectures by Leon and other Fermilab scientists. He also started a public education and outreach effort at Fermilab directed toward precollege students. Beyond Fermilab, Leon was a founder of a residential state-sponsored high school for science and mathematics and a Chicago-based teacher academy for math and science. His leadership in education and outreach inspired physicists to communicate with the public. The author of several books for the general public, including *The God Particle,* Leon wrote with the same humor, wit, and charm that drew people to his public lectures. He had no equal in communicating the joys of physics.

One of the great experiences of Fermilab in the 1980s was dining with the Ledermans in their Fermilab farmhouse. Some guests would be from Fermilab and others would be U.S. senators, cabinet members, Department of Energy officials, writers, artists, and poets. After a wonderful dinner prepared by Leon's wife, Ellen, we would retire to the living room, where there always seemed to be a large fire, even in summer. Over cigars and (a lot of) cognac, Leon would regale us with tales of his life in (and out of) physics with humor and wit. He made his discoveries sound easy, but we knew they were built on years of experience.

After stepping down as director of Fermilab, Leon was a professor of physics at the University of Chicago and later at the Illinois Institute for Technology in Chicago. In 2012, Leon retired to rural Idaho. The boy from the Bronx transitioned to hiking, skiing, riding horses, and relaxation. Although removed from his previous life, he remained close to his many friends and admirers. Leon was a great physicist, a visionary leader, a generous mentor, and a charismatic inspiration. The world seems a smaller place without him. ■

Department of Astronomy and Astrophysics, The University of Chicago, Chicago, IL, USA. Email: rocky.kolb@uchicago.edu

10.1126/science.aav9603

POLICY FORUM

DEMOGRAPHY AND INEQUALITY

The case for monitoring life-span inequality

Focus on variation in age at death, not just average age

By **Alyson A. van Raalte**[1], **Isaac Sasson**[2], **Pekka Martikainen**[1,3,4]

Inequality in length of life is the most fundamental of all inequalities; every other type of inequality is conditional upon being alive. As has long been recognized in studies of economic inequality, we can compare populations based on per capita gross national income, but there is a pressing need to further examine how income varies within populations via Gini coefficients and percentile-based metrics. Mortality inequalities should be approached in the same way. Human population health is generally monitored by average mortality levels, typically in terms of life expectancies, which belie substantial variation in length of life. Variation in ages at death, captured by a metric of life-span variation, should be used to supplement measures of average longevity when comparing or monitoring societies and population subgroups (*1*). Although life-span variation has historically been strongly inversely correlated with life expectancy (*2*, *3*), we are beginning to see this relationship reversed, resulting in positive correlation in some countries or subnational populations. Often these changes reflect midlife mortality crises with roots in stratified education and wealth. We discuss these measures and trends and how they can have profound implications for how individuals might plan and live their lives, and for how societies might organize and manage health care, insurance, pensions, and other social policies and programs.

Life expectancy at birth (or simply life expectancy, as we refer to it in the rest of the text) is the most common metric of survival. It is the hypothetical average age at death given age-specific death rates in a given year. Life-span variation, the variability in ages at death around that average, can be measured by using an index of variation or inequality—for instance, the standard deviation, Gini coefficient, or interquartile range. To illustrate, consider age-at-death distributions of non-Hispanic black and non-Hispanic white men in the United States based on 2012–2016 death rates. The life expectancy from this distribution is 72 years for blacks and 77 years for whites [see supplementary materials (SM)]. But the timing of death was variable, skewed below the average in both groups, meaning that deaths were more spread out below the life expectancy than above it. Among blacks, the spread in survival was noticeably wider. Men in the 25th to 75th percentile (the interquartile range) died between 63 and 85 years in the black distribution, whereas those in the white distribution died between 69 and 88 years. Although life expectancy for blacks was only 6% lower than for whites, the age window over which these deaths occurred was 17% larger for blacks.

Some early efforts by the Organization for Economic Co-operation and Development (OECD) to monitor within-group variability included a one-off report that measured life-span variation conditional upon survival to age 10 (*4*). However, although we currently monitor life expectancy at birth in all countries of the world, which captures between-country differences in average mortality, no international organization regularly monitors and compares the within-country variation in age at death. Likewise, many countries evaluate health and social policies by their success in eliminating gaps in life expectancy between race, ethnic, or socioeconomic groups. But few countries monitor the variation in age at death within and across such groups, which ignores an important and substantial part of the inequalities in mortality.

TRENDS IN LIFE-SPAN VARIATION

In high-income countries, life expectancy has doubled over the past century and a half. Life expectancy at birth in 2014 was around 81 years for people living in a country belonging to the OECD (SM). Averting deaths at any age increases life expectancy. But for life-span variation to decrease when life expectancy is increasing, more deaths need to be averted at younger than older ages. This compresses the age-at-death distribution, making ages at death more similar. Whether a death is considered younger or older depends on a threshold age that varies in time and between groups. This age generally sits below the life expectancy, and is specific to the age pattern of mortality (*2*).

In the past, death rates declined faster at younger ages compared to older ages as populations transitioned through different epidemiologic environments (*5*). Gains to life expectancy and concomitant declines in life-span variation resulted from strong reductions in infectious disease, maternal and child mortality, injuries, and more recently, cancers (*6*). Reduced circulatory disease mortality, by contrast, accounted for the bulk of life expectancy gains in the final decades of the 20th century, but its impact on life-span variation trends was moderate. The averted deaths from declining circulatory disease rates occurred at ages above and below the threshold age, which led to either minor increases or decreases in life-span variation depending on the sex, period, and population examined.

As a result of these historical changes, the inverse correlation between life-span variation and life expectancy was so strong that it was reasonable to question how much more information could be gained by looking at life-span variation in addition to life expectancy. Yet, it is becoming increasingly apparent that there are considerable differences between populations with respect to life-span variation at the same levels of life expectancy. For example, a U.S. man retiring at age 67 can expect to live another 16.8 years—almost as long as his British counterpart (17.0 years) (SM). But the American is facing substantially greater variability about that mean with a standard deviation that is 13.8% higher.

Two emerging phenomena, related to age-specific mortality changes below and above the threshold age, may weaken the historical association between life expectancy and life-span variation. One is that some subpopulations are experiencing stalls in reducing mortality at younger ages or even experiencing midlife mortality increase (*7*). The other is that mortality decline is occurring at ever higher ages in many countries (*8*). Further gains in life expectancy in low-mortality countries may increasingly come from disproportionate reductions in old-age mortality. These phenomena acting alone or in concert could result in increases in life-span variation alongside increases in life expectancy; i.e., changing the historically observed correlation from negative to positive.

This is precisely what is being seen at the national level in the United States. From 1980 to 2014, life expectancy increased by about 10% for men and 5% for women

---

[1]Max Planck Institute for Demographic Research, Rostock 18057, Germany. [2]Department of Sociology and Anthropology and the Herczeg Institute on Aging, Tel Aviv University, Tel Aviv 6997801, Israel. [3]Population Research Unit, Faculty of Social Sciences, University of Helsinki, Helsinki 00014, Finland. [4]Department of Public Health Sciences, Stockholm University, SE-106 91 Stockholm, Sweden. Email: vanraalte@demogr.mpg.de

Published by AAAS

Trends in life expectancy and life-span variation for Finnish females, 1971–1975 to 2011–2014

Life expectancy is the average age at death, and life-span variation is the standard deviation, conditional upon survival to age 30, with age-specific death rates frozen at those observed in the given year. See supplementary materials for data and methods, including trends for males (which are qualitatively similar), and robustness checks using alternative measures of life-span variation.

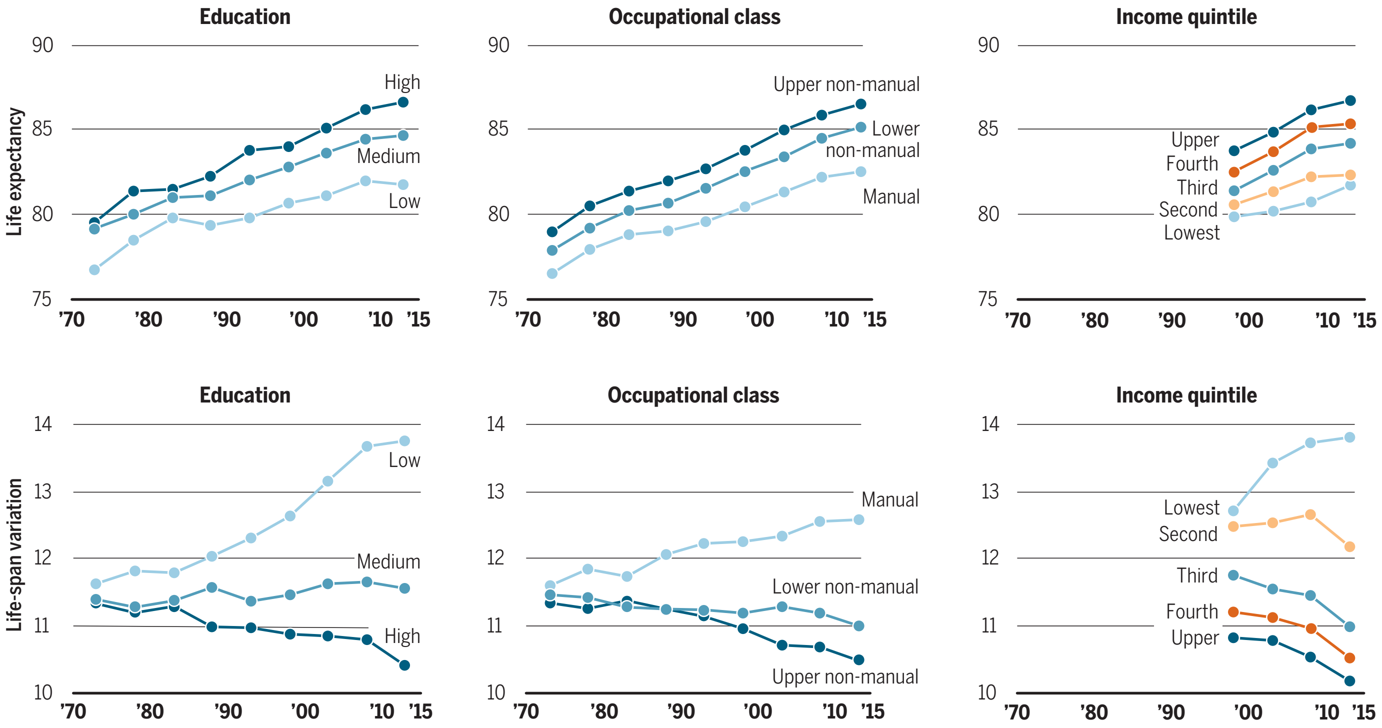

[although both sexes experienced declines from 2014 to 2016 (fig. S1)]. Life-span variation, however, fluctuated sharply over the period, with sustained increases observed in the late 1980s, early 2000s, and the 2010–2016 period (fig. S2). Not coincidentally, these years were marked by mortality episodes that primarily affected young adults—the HIV/AIDS and crack-cocaine epidemics of the 1980s, and more recently, the increase in accidental poisonings, particularly from opioids (SM). Had we been monitoring life-span variation as closely as life expectancy, the U.S. midlife mortality crisis would possibly have been uncovered earlier in an attempt to understand why life-span variation was increasing at the dawn of the 21st century.

Further evidence is observed among subpopulations in Finland, a country with an exceptionally long and good-quality time series of population register data, including socioeconomic status. Over the period 1971 to 2014, we see increasing life expectancy for women (see the figure, top) and men (fig. S3, top) aged 30 and above according to education, occupational class, and income quintile. The increases in life expectancy over time run mostly in parallel with one another, with some divergence because the lower socioeconomic groups experienced slower improvements. A policy implication is that the groups with a lower socioeconomic status are falling behind the upper classes, a lag that may be closed by investing in health and social policies to reduce mortality in the lower socioeconomic groups at all ages.

However, trends in life-span variation (see the figure, bottom; fig. S3, bottom) reveal a more worrisome pattern. The less-advantaged groups were not only dying earlier than advantaged groups, on average, but they faced greater variation in the eventual time of death—a double burden of inequality—which has increased over time. The diverging trends in life-span variation mainly resulted from differences in the pace of early and midlife mortality decline, in particular, slow improvements in early and midlife mortality in the lower socioeconomic groups. The pace of mortality decline at older ages was similar across occupational groups (*9*). A policy implication is that investing in efforts to drive down deaths in midlife—deaths that are typically considered premature and avoidable (e.g., deaths from accidents, violence, or substance abuse)—can reduce life-span variation.

This is not just a Finnish phenomenon. Life-span variation is diverging between social groups wherever it has been examined. In the United States, differentials in life-span variation between those who completed college and those who only completed high school doubled over the 1990–2010 period, mainly because of substantial increases in variability among the high school educated. At the same time, life expectancy differentials by the same two groups widened from 2.2 to 5.7 years (*10*). In Denmark, life-span variation increased among the lowest-income quartile and decreased among the other three quartiles over the 1986–2014 period, although all income groups experienced increases in life expectancy (*11*). It is important to note that in mostof these examples of increasing life-span variation, mortality declined over postretirement ages, even among the lowest socioeconomic groups. The increases in life-span variation among lower socioeconomic groups thus occurred because mortality reduction over preretirement ages was modest or absent.

INDIVIDUAL AND POPULATION IMPACTS

Like life expectancy, life-span variation constitutes a useful summary measure of mortality regimes (i.e., age-specific death rates). We argue that it has two important implications: one at the individual (micro) level and the other at the population (macro) level. Life-span variation reflects both individual uncertainty in the timing of death and heterogeneity in underlying population health.

At the micro level, life-span variation reflects individual discrepancies in the risk

GRAPHIC: J. YOU/SCIENCE

of death. In other words, it measures uncertainty in the timing of death. Economic models have shown that because individuals are inherently risk averse, they would forego additional years of expected life to reduce uncertainty in age at death (*12*). From this perspective, diverging life-span variation between socioeconomic groups means that an overlooked dimension of social inequality in health is increasing—those from more-advantaged groups can more effectively plan their life course, whereas less-advantaged groups face greater and increasing uncertainty about their survival.

For the individual, this can have profound consequences. One's subjective assessments of his or her survival are instrumental when making decisions about lifecycle investment and consumption, including education, training, and retirement (*12*). The Survey of Health, Ageing and Retirement in Europe, as well as its U.S. progenitor the Health and Retirement Study, routinely ask their respondents about their future expectations. These questions probe how long responders expect to live and when they expect to die. Answers to these questions underlie answers to others, such as: Will they work for pay after age 70? How much money will they spend this year? Will they leave an inheritance or help their children financially? Although often framed around financial decisions, these survey questions are attempts to examine responders' expectations about the family sphere (e.g., time spent with family members) and work (e.g., time to retirement), and how these expectations may be influenced by anticipation of one's own mortality.

Individuals are of course mostly unaware of life-span variability statistics, but experience of survival chances of friends and relatives will influence perceptions of survival expectations. For example, because of larger life-span variability, U.S. blacks are more likely than U.S. whites to experience an early death of close relatives (*13*). Studies have shown that these subjective survival expectations predict actual mortality and mirror known socioeconomic disparities in death rates (*1*, *14*). Furthermore, to the extent that mortality regimes (i.e., death rates) become inscribed in individuals' own mortality expectations—by which we mean that excess mortality experienced by certain social groups affects subjective survival assessment and future life course expectations for the members of that group—higher life-span variation also constitutes a form of disadvantage.

At the macro level, life-span variation is an indicator of heterogeneity in underlying population health. Understanding this heterogeneity is crucial for accurate forecasts in insurance and annuity markets, for public provision of medical care, and for creating equitable pension schemes when ages at death vary. Increasing life-span variation among disadvantaged groups implies that the individuals belonging to such groups are living increasingly diverse lives. This increasing heterogeneity mirrors diverging variability in other social realms, including increasing variation in participation in work and family life (*15*). Increasing life-span variation signals uneven age patterns of mortality decline, with faster declines at older rather than at younger ages, or even rising early and midlife mortality. Therefore, monitoring life-span variation may facilitate early detection of adverse mortality developments and warrant social interventions at younger ages.

TOWARD A COMPREHENSIVE MEASUREMENT OF MORTALITY

In our world in which reams of granular data related to health are routinely collected, easy-to-understand summary metrics are needed to set health targets, to evaluate policy outcomes, to uncover emerging threats, and to compare levels and trends in health and mortality across populations. Life expectancy is monitored almost everywhere. But despite growing awareness, life-span variation has not been systematically monitored by any country in the world. We suggest four reasons why this might be the case, and also demonstrate why this does not need to persist. First, given that we already monitor life expectancy, it was unclear to policy-makers whether there was an added benefit to monitoring life-span variation. The examples shown here demonstrate the independence of the two indices. Although life expectancy might still be the best metric for the speed of survival improvements in the population as a whole, life-span variation is its complement, needed to monitor the equality in survival improvement.

Second, as with studies of income inequality, it remains unclear which indicator for measuring life-span variation is the most appropriate. Although there is no gold standard, the high correlation between indices suggests that trends would be broadly similar no matter which index is chosen. Third, officials in statistical offices are not trained to measure life-span variation. Although this is true, all statistical offices produce life tables. Calculating an index of life-span variation is a relatively straightforward procedure from the life table. Fourth, metrics of variability are more difficult to understand than metrics of average levels. But this criticism could equally be leveled at indices of income differentials, yet the widespread adoption of the Gini coefficient by statistical offices suggests that the benefit of monitoring income variation outweighs the disadvantage of a more theoretically complex measure. In our view, this is also true for monitoring mortality.

Many countries and international organizations monitor premature death, but the cut-off age varies across jurisdictions. For instance, Statistics Canada defines premature deaths as those under age 75, the U.S. Centers for Disease Control and Prevention uses age 80 as the cut-off, while the New York City Department of Health uses age 65 (SM). Alternatively, a metric of life-span variation could be easy to understand, be used in various mortality regimes, and be sensitive to deaths that we would normally consider premature, but use mortality over the whole age range to capture this.

Life-span variation might be reduced by decreasing disparities in the social environment, medical care, and how individuals behave and interact within their social sphere. If an average level of health is deemed important enough to regularly monitor and report, we should also regularly summarize the spread around this average. A healthy population is one in which people live for a long time on average—and long lives are enjoyed by everyone. ■

REFERENCES AND NOTES

1. R. D. Edwards, S. Tuljapurkar, *Popul. Dev. Rev.* **31**, 645 (2005).
2. J. W. Vaupel, Z. Zhang, A. A. van Raalte, *BMJ Open*, **1**, e000128 (2011).
3. F. Colchero *et al.*, *Proc. Natl. Acad. Sci. U.S.A.* **113**, E7681 (2016).
4. OECD, *Society at a Glance 2006: OECD Social Indicators*. Organization for Economic Co-operation and Development (2007).
5. J.-M. Robine, *Population* **13**, 173 (2001).
6. B. Seligman, G. Greenberg, S. Tuljapurkar, *Proc. Natl. Acad. Sci. U.S.A.* **113**, 8420 (2016).
7. A. Case, A. Deaton, *Proc. Natl. Acad. Sci. U.S.A.* **112**, 15078 (2015).
8. R. Rau, C. Bohk-Ewald, M. M. Muszyńska, J. W. Vaupel, *Surface Plots of Rates of Mortality Improvement*, in *Visualizing Mortality Dynamics in the Lexis Diagram* (Springer, 2018).
9. A. A. van Raalte, P. Martikainen, M. Myrskylä, *Demography* **51**, 73 (2014).
10. I. Sasson, *Demography* **53**, 269 (2016).
11. H. Brønnum-Hansen, *BMJ Open* **7**, e014489 (2017).
12. R. D. Edwards, *J. Popul. Econ.* **26,** 1485 (2013).
13. D. Umberson *et al.*, *Proc. Natl. Acad. Sci. U.S.A.* **114**, 915 (2017).
14. M. D. Hurd, K. McGarry, *J. Hum. Resour.* **30,** S268 (1995).
15. D. C. Brown *et al.*, *Demography*, **49,** 819 (2012).

ACKNOWLEDGMENTS

We thank J. W. Vaupel, J. P. Mackenbach, and S. Klüsener for helpful comments, and L. M. Junna for help with harmonizing the Finnish mortality data. This analysis was supported by a starting grant from the European Research Council awarded to A.A.vR. (grant no. 716323), grant no. I-2475-119.4/2017 from the German-Israeli Foundation for Scientific Research and Development (GIF) awarded to I.S., and funding to P.M. from the Academy of Finland (grant nos. 1294861 and 1308247).

SUPPLEMENTARY MATERIALS

www.sciencemag.org/content/362/6418/1002/suppl/DC1

10.1126/science aau5811

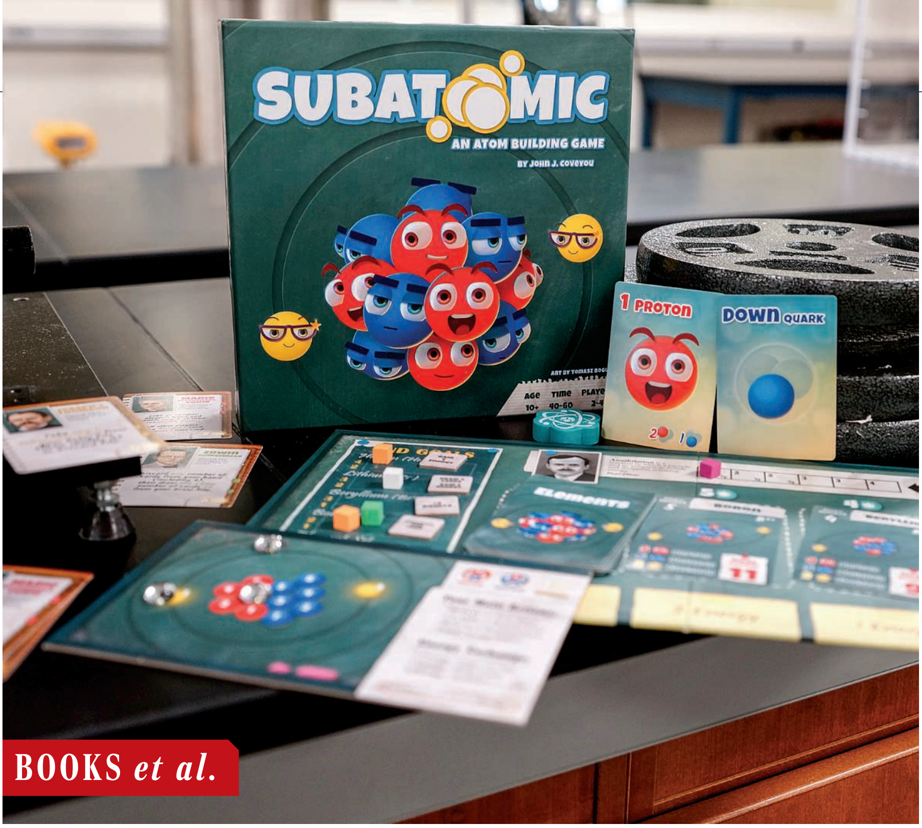

BOOKS *et al.*

PHYSICS

Playing with particle physics

The quantum realm comes to life in a fast-paced new board game

By **Angela Chuang**

The rise in popularity of tabletop board games as a mainstream adult hobby has introduced players to a correspondingly wide breadth of unlikely subjects, from exploding cats to top-secret chili recipes (thankfully not in the same game) (*1*, *2*). Following the notion that no subject is off limits in board gaming, *Subatomic* sets out to add particle physics and chemistry to the milieu.

Despite its modestly sized box and kid-friendly artwork, *Subatomic* is more complex than appearances suggest. It incorporates an impressive array of different game-play mechanisms, not to mention components: 135 cards and 93 wooden, glass, and cardboard pieces. Players compete for the highest score by racing to build various elements from protons, neutrons, and electrons and claiming the corresponding element card.

The points earned match the atomic number of each element. For example, claiming a boron card earns a player 11 points, whereas a helium card only yields a measly 4 points. But, as the heaviest element available, boron requires the most protons and neutrons to build.

Therein lies one of many strategic decisions that a player faces in *Subatomic*: Should I try to build heavier atoms to earn more points or focus on lighter atoms and end the game early by being the first to collect five elements? Only three element cards are available at any one time, which further fosters competitive spirit.

Subatomic
An Atom Building Game
John Coveyou
Genius Games, 2018.

The subatomic particles used to build elements are gained through the game's main deck-building mechanism. Each player begins with a starter deck containing the smallest subatomic components: up quarks, down quarks, and photons. Players can use the right combinations of these cards to purchase proton, neutron, and electron cards. On each turn, a player's hand can be used to purchase more subatomic resource cards, to build an atom, or to create energy, the latter of which is required for various actions.

An accompanying booklet fleshes out the science that is simplified for the purposes of the game.

Careful deck management becomes key for long-term success; every subatomic card that is added will cycle through a player's hand many times because the deck is reshuffled when all of the cards have been played. Players must therefore determine when they have purchased just the right amount of protons, neutrons, and electrons in order to build the elements they desire. Building a well-balanced deck is no easy feat, and this challenge is what will galvanize players to revisit this game again and again.

Appropriately enough, real scientists make an appearance in *Subatomic*. "Scientist" cards can be purchased within the game and added to one's deck, providing powerful special abilities when drawn. Most players will recognize Albert Einstein and Marie Curie, but by including other eminent historical figures, such as Paul Dirac and Maria Goeppert Mayer, the game provides an opportunity for nonscientists to learn about other influential scientists and their contributions.

Dirac, for example, is cleverly featured on the game's main board itself, describing both his pioneering concept of annihilation and the identically named game mechanism. In *Subatomic*, annihilation is an action that allows players to permanently remove two cards from their deck, simulating the collision and resulting disappearance between a particle and its antiparticle. This clever integration of real science and game play is arguably *Subatomic*'s greatest strength.

For those who are unfamiliar with up quarks or only have the foggiest memory of how photons are related to electrons, fear not: An accompanying booklet—"The Science Behind Subatomic"—defines various terms, describes how they are used in the game, and reveals how the underlying concepts affect our lives. Thus, the game achieves pedagogy over pedantry by covering simpler concepts in game play while providing greater detail in a separate, accessible resource.

Overall, *Subatomic* sets a strong standard for future board games co-opting scientific themes, introducing a potentially intimidating topic (atoms and what they are made of) through intuitive game play. In the end, even young players will likely be able to understand that the game boils down to bringing various parts together to make a whole. ■

The reviewer is at the Department of Ecology and Evolutionary Biology, University of Tennessee, Knoxville, TN 37996, USA. Email: angelachuang@utk.edu

REFERENCES

1. *Exploding Kittens* (The Oatmeal, 2015).
2. *The Great Chili Cookoff* (Jolly Roger Games, 2006).

10.1126/science.aav5921

PHOTO: COURTESY OF GENIUS GAMES

HISTORY OF SCIENCE

The myth of apolitical science

Denouncing state-controlled research, U.S. investigators advanced the American agenda during the Cold War

By **Alex Wellerstein**

“Science is apolitical” is a deeply political statement: One only feels the need to assert something like this in times when it is a hard case to make. That science exists within a political environment and participates in political activities should not be controversial. But it is, especially in the current moment, when it would be (politically) convenient to have something in our present world that felt devoid of politics. Audra Wolfe’s provocative new book, *Freedom’s Laboratory*, dives into the fascinating history of why asserting the apolitical nature of science became a political priority during another notably politicized period in America’s past: the Cold War.

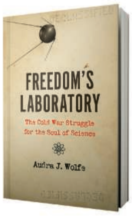

Freedom’s Laboratory
The Cold War Struggle for the Soul of Science
Audra J. Wolfe
Johns Hopkins University Press, 2018.
312 pp.

Wolfe, whose work as a scholar of Cold War science and technology has earned immense respect from other historians of science, approaches this history episodically. The book’s first chapter, for example, goes over the well-trodden ground of the Lysenko affair, in which Mendelian genetics was suppressed in the Soviet Union in the name of a state-sponsored ideological alternative. What makes Wolfe’s account distinct, however, is that her interests are less about what happened in the USSR than about how American scientists mobilized their understanding of what was going on abroad as part of their own propaganda campaigns.

Some scientists resisted making “political” statements, whereas others, such as the Nobel laureate H. J. Muller, thought it was their duty to point out the perversions of science going on behind the Iron Curtain. Such instincts were encouraged by anti-Communist forces in the U.S. government, who saw them as supporting the “American way of life.”

In example after example, Wolfe shows prominent American scientists denouncing the politicization of science while engaging in explicitly political activities. They did not, she repeatedly emphasizes, see any contradiction in this; they believed that the heavy-handed Soviet approach to science was fundamentally antithetical to the pursuit of truth and did not see their own interactions with government funding as being of the same character at all. As Wolfe puts it, “having convinced themselves of the possibility of apolitical science, they saw little reason to turn away funds that might help them achieve their own, supposed enlightened, goals.”

In another chapter, Wolfe describes how the U.S. State Department attempted, without much tangible success, to use “scientific attachés” as a form of cultural diplomacy and intelligence collection. The idea was that American scientists would be stationed abroad, where they would intermingle with scientists in their respective host countries, with the goal of sharing the advantages of the American scientific way of life and observing trends among foreign scientists as a form of intelligence collection. These programs were nearly subverted by the more rabid anti-Communist agencies in the United States, who could not understand why State Department scientists were spending so much time interacting with foreign scientists of dubious character.

In Wolfe’s account, American efforts to mobilize science as a cultural weapon in the Cold War were frequently ineffectual and uncoordinated. The value of science as a form of “soft power” never seems to have been quite as obvious to the U.S. government as its value in building the weapon systems that underwrite “hard power.” And American activities and political life during the Cold War were compromised and constrained in their own ways, leaving potential evangelists for democracy open to charges of hypocrisy or even put under threat by the agents of McCarthyism.

For present-day historians of science, the fact that scientists and their work are intimately intertwined with political forces is neither scandalous nor surprising. Indeed, it is essentially an article of faith that science will be influenced by the context in which it is done, just as it influences that context back again. Science is a social activity and always carries some mark of that, however subtle. As Wolfe notes, even something as seemingly innocuous as secondary science education “teaches students not only facts but also what sorts of facts are worth knowing.”

In her epilogue, Wolfe asks, “Who wins, and who loses, when scientists claim a unique ability to operate free from politics?” Herein lies both the rub and the controversy: In the present day, nearly everything appears to have been politicized. The instinct to say that scientific truth cares not for the whims of political parties is understandable. But is it true?

Wolfe’s history suggests, as good histories of science frequently do, that the answer is a bit more complex than it first appears. Her goal is not to undermine the authority of science; if anything, it is to encourage scientists and their supporters to think more subtly about the ways that they leverage the political uses of claims to apolitical science. ■

10.1126/science.aav4900

The reviewer is at the College of Arts and Letters, Stevens Institute of Technology, Hoboken, NJ 07030, USA. Email: awellers@stevens.edu

Soybeans are the most widely grown and traded oilseeds.

PHOTO: ISTOCK.COM/ZELJKOSANTRAC

PODCAST

The Story of Soy
Christine M. Du Bois
Reaktion Books, 2018. 277 pp.

What do Buddhist missionaries, Henry Ford, and Greenpeace all have in common? As Christine Du Bois reveals in her new book, the answer is the humble soybean. This week on the *Science* podcast, Du Bois discusses soy’s vital role in human history, from its ancient domestication and ascendance as an agricultural staple to its emerging role as a promising biofuel component.

10.1126/science.aav8840

Landslide debris caused destruction after the September earthquake in Hokkaido, Japan.

PHOTO: KYODO/NEWSCOM

Edited by **Jennifer Sills**

Prepare for Cascadia's next earthquake

Landslide debris contributed to extensive damage and the majority of lives lost after Japan's recent 6.7–moment magnitude crustal earthquake, which occurred in the early hours of 6 September in Hokkaido (*1*). Despite these tragic losses, the overall recovery effort was largely successful thanks to Japan's disaster preparedness and investment in combating its frequent earthquakes. Other regions, such as the Cascadia subduction zone in the Pacific Northwest, are at risk of even stronger subduction zone earthquakes but at much longer recurrence intervals [250 to 500 years (*2*–*4*)]. Although northern California, Oregon, Washington, and British Columbia may not be able to invest as much as Japan given the infrequency of seismic activity, thoroughly documenting prehistoric landslides recorded in the topography could be a cost-effective strategy to understand the consequences of previous earthquakes and make targeted preparations for the next Cascadia event.

There are features in the Pacific Northwest landscape that may hint at seismic history, but the scars of massive landslides are now obfuscated by verdant forests (*5*). The impacts of landslides to infrastructure after a Cascadia subduction zone earthquake may have severe effects on post-earthquake recovery, possibly increasing casualties (*6*). Characterizing the scale, distribution, age, and impacts of past landslides is now possible through advances in a technology called lidar (*7*), which enables the creation of high-resolution topographic maps beneath the forest canopy. Scientists and state agencies are leveraging this technology (*8*), along with field-based landslide chronology, to better understand the possible impacts of the next Cascadia subduction zone event on infrastructure critical to postearthquake recovery.

With improved characterization of the style and chronology of past coseismic landslides, we will be able to more reliably assess how and where future landslides might occur and make strategic decisions about preparedness and resilience. However, careful consideration may be required for more refined landslide mapping near private property, as this information can affect zoning, property values, and insurance rates (*9*). We must leverage the experiences of our international counterparts, advances in technology, and collaborative efforts between planners and scientists to successfully prepare for the persisting impacts of landslides well after the earthquake has passed.

Ben A. Leshchinsky[1]*, Adam M. Booth[2], Kira M. Glover-Cutter[3], Curran Mohney[3], Michael J. Olsen[4], Joshua J. Roering[5]

[1]College of Forestry, Oregon State University, Corvallis, OR 97331, USA. [2]Department of Geology, Portland State University, Portland, OR 97207, USA. [3]Oregon Department of Transportation, Salem, OR 97301, USA. [4]School of Civil and Construction Engineering, Oregon State University, Corvallis, OR 97331, USA. [5]Department of Earth Sciences, University of Oregon, Eugene, OR 97403, USA.
*Corresponding author.
Email: ben.leshchinsky@oregonstate.edu

REFERENCES

1. M. Rich, "Deadly earthquake hits Japan, adding to summer of misery," *New York Times* (2018); www.nytimes.com/2018/09/06/world/asia/japan-earthquake-hokkaido-landslide.html.
2. K. Satake *et al.*, *Nature* **379**, 246 (1996).
3. K. Schulz, "The really big one," *The New Yorker* (2015); www.newyorker.com/magazine/2015/07/20/the-really-big-one.
4. B. F. Atwater, E. Hemphill-Haley, "Recurrence intervals for great earthquakes of the past 3,500 years at northeastern Willapa Bay, Washington" (Prof. Pap. No. 1576, U.S. GPO, 1997).
5. J. P. Perkins *et al.*, *Eos* **99**, 10.1029/2018EO103689 (2018).
6. Oregon Seismic Safety Policy Advisory Commission (OSSPAC), "The Oregon resilience plan: Reducing risk and improving recovery for the next Cascadia earthquake and tsunami" (2013); www.oregon.gov/oem/documents/oregon_resilience_plan_final.pdf.
7. A. M. Booth, S. R. LaHusen, A. R. Duvall, D. R. Montgomery, *J. Geophys. Res. Earth Surface* **122**, 456 (2017).
8. W. J. Burns, I. Madin, "Protocol for inventory mapping of landslide deposits from light detection and ranging (LiDAR) imagery" (Oregon Department of Geology and Mineral Industries, Portland, OR, 2009), pp. 1–30.
9. B. McEwen, "Houses in peril, but owners are unaware," *The Oregonian* (2009); www.oregonlive.com/news/index.ssf/2009/01/houses_in_peril_but_owners_una.html.

10.1126/science.aav5615

Scan the horizon for unprecedented risks

In their Policy Forum "Agricultural research, or a new bioweapon system?" (5 October, p. 35), R. G. Reeves *et al.* explore the implications of developing genetically modified viruses that insects deliver to plants. To develop horizontal environmental genetic alteration agents (HEGAAs), a U.S. Defense Advanced Research Projects Agency (DARPA) program promotes laboratories in the field to confer genetic modifications outside the lab. Lab-in-the-field approaches have already been described for gene drives (*1*–*4*), but the multilayered concepts of HEGAAs go far beyond those in time and space. Each layer is characterized by a high degree of complexity and is often novel to regulators and risk assessors. The combination of examining recombinant DNA incorporated into a plant virus, determining the role of the sap-sucking insects that carry it, and documenting the genetic modification that the virus triggers is beyond any risk assessment ever performed in the field of biotechnology.

Even with the option to assess each layer independently, it remains an incalculable task to synthesize these separate results into a reliable overall assessment. Anticipating potential detrimental impacts for HEGAAs in the case of environmental release is paramount. It is remarkable that there has been no public discourse on environmental risks since DARPA published its work plan almost 2 years ago. Given the unprecedented challenges of the HEGAA approach, regulators around the world need to ensure that they are not caught unprepared.

In this regard, HEGAAs serve as a prime example of the pressing need for active horizon scanning in the field of synthetic biology. Such an approach would require three steps to ensure sufficient time for public discourse on applications such as HEGAAs: identification of challenging developments by risk assessment experts, evaluation of wider societal implications, and popularization of the results internationally. We believe that active horizon scanning should be carried out under the umbrella of the United Nations Convention on Biological Diversity.

Samson Simon, Mathias Otto, Margret Engelhard*
Federal Agency for Nature Conservation (BfN) Bonn, Germany.
*Corresponding author.
Email: margret.engelhard@bfn.de

REFERENCES

1. K. M. Esvelt, A. L. Smidler, F. Catteruccia, G. Church, *eLIFE*, 10.7554/eLife.03401.001 (2014).
2. K. M. Esvelt, N. J. Gemmell, *PLOS Biol*. **15**, e2003850 (2017).
3. S. Simon, M. Otto, M. Engelhard, *EMBO Rep*. **19**, e45760 (2018).
4. B. L. Webber, S. Raghu, O. R. Edwards, *Proc. Natl. Acad. Sci. U.S.A*. **112**, 10565 (2015).

10.1126/science.aav7568

Legislation restricts research in Uruguay

Uruguay has shown steady economic growth in the past decade (*1*), which has benefited its citizens but led to environmental degradation such as widespread eutrophication of aquatic ecosystems (*2*, *3*). In 2018, Uruguay's government passed a law that seems to address these issues but applies unreasonable constraints to scientific research.

The law, #19175 decree 115/018 (*4*) and its modification 269/018 (*5*), establishes welcome regulations on the use of aquatic resources and aquaculture, which will be enforced by the National Office of Aquatic Resources (DINARA). However, it also restricts research by requiring scientists to secure a government permit for field activities. Moreover, it forces researchers to withhold publication of results until explicitly authorized by DINARA. These regulations contradict the principle that scientific research is independent of pressures exerted by commissioning parties or by economic, political, and ideological interests.

The Universidad de la República, Uruguay's main national research institution, has filed an appeal for the revocation of decree 115/018 (*6*) and engaged in formal negotiations with the government. We hope that this process will successfully eliminate restrictive regulations. Scientists must make clear to the government that scientific research should progress unimpeded and that results should be accessible to peers and to the public without limitations.

Ruben Sommaruga[1]*, Laura Rodríguez-Graña[2], Danilo Calliari[2,3], Diego Lercari[4], Luis Aubriot[5]
[1]Department of Ecology, University of Innsbruck, Innsbruck, Austria. [2]Centro Universitario Regional del Este, Universidad de la República, Uruguay. [3]Sección Oceanografía y Ecología Marina, Facultad de Ciencias, Universidad de la República, Uruguay. [4]UNDECIMAR, Facultad de Ciencias, Universidad de la República, Uruguay. [5]Sección Limnología, IECA, Facultad de Ciencias, Universidad de la República, Uruguay.
*Corresponding author.
Email: ruben.sommaruga@uibk.ac.at

REFERENCES AND NOTES

1. Trading Economics, Uruguay GDP (https://tradingeconomics.com/uruguay/gdp).
2. F. Vidal *et al*., *Toxins* **9**, 267 (2017).
3. G. Chalar *et al*., *Ecol. Indic*. **11**, 362 (2011).
4. Decreto N° 115/018 (2018); www.impo.com.uy/bases/decretos/115-2018 [in Spanish].
5. Decreto N° 269/018 (2018); www.impo.com.uy/bases/decretos/269-2018 [in Spanish].
6. Track the progress of the Universidad de la República appeal case at www.expe.edu.uy/search.html [in Spanish] by entering the search term 240011-000663-18.

10.1126/science.aav6122

TECHNICAL COMMENT ABSTRACTS

Comment on "Contrasting carbon cycle responses of the tropical continents to the 2015–2016 El Niño"

Frédéric Chevallier

Liu *et al.* (Research Articles, 13 October 2017, eaam5690) inferred carbon flux anomalies in tropical continents with enough confidence to constrain the driving carbon-exchange processes. I show that they underestimated their error budget and that more effort must be invested in the satellite concentration retrievals and in the atmospheric transport models before such precision can be achieved.

Full text: dx.doi.org/10.1126/science.aar5432

Response to Comment on "Contrasting carbon cycle responses of the tropical continents to the 2015–2016 El Niño"

Junjie Liu, Kevin W. Bowman, David Schimel, Nicolas C. Parazoo, Zhe Jiang, Meemong Lee, A. Anthony Bloom, Debra Wunch, Christian Frankenberg, Ying Sun, Christopher W. O'Dell, Kevin R. Gurney, Dimitris Menemenlis, Michelle Gierach, David Crisp, Annmarie Eldering

Chevallier showed a column CO_2 (X_{CO_2}) anomaly of ±0.5 parts per million forced by a uniform net biosphere exchange (NBE) anomaly of 2.5 gigatonnes of carbon over the tropical continents within a year, so he claimed that the inferred NBE uncertainties should be larger than presented in Liu *et al*. We show that a much concentrated NBE anomaly led to much larger X_{CO_2} perturbations.

Full text: dx.doi.org/10.1126/science.aat1211

TECHNICAL COMMENT

CARBON CYCLE

Comment on "Contrasting carbon cycle responses of the tropical continents to the 2015–2016 El Niño"

Frédéric Chevallier*

Liu *et al*. (Research Articles, 13 October 2017) inferred carbon flux anomalies in tropical continents with enough confidence to constrain the driving carbon-exchange processes. I show that they underestimated their error budget and that more effort must be invested in the satellite concentration retrievals and in the atmospheric transport models before such precision can be achieved.

The monitoring of CO_2 concentrations from space addresses a growing demand for improved information about the carbon emissions over the globe and about the absorption of some of these by oceans and terrestrial ecosystems. Several satellites have been specifically designed for that purpose, including the Japanese Greenhouse Gases Observing Satellite (GOSAT) and NASA's second Orbiting Carbon Observatory (OCO-2), respectively launched in 2009 and 2014 (*1*). More spaceborne instruments are being prepared in the United States, Japan, China, and Europe. Given the relatively small space-time variations of CO_2 over the globe and the fact that CO_2 has no chemical sink in the atmosphere, the processing chains that estimate the carbon surface fluxes from these satellite measurements are particularly complex: They have to analyze some subtle details in each measured spectrum in the global context of the atmospheric flow. Various algorithms have been designed by the scientific community and most of them have participated in intercomparison exercises. Results so far have revealed a large uncertainty in the estimated carbon fluxes and in their interannual variability (*2*–*5*). The estimation process still appears to be subjective and is much dependent on technical choices and on expert judgment about the underlying physical and statistical models.

Liu *et al.* (*6*) explain that they have addressed these challenges with GOSAT and OCO-2 measurements to the point that they can confidently quantify the anomalies in the carbon fluxes that occurred in the three tropical subcontinents in 2015 as compared to 2011: They find source differences (i.e., source anomalies) of 0.9 ± 0.22 gigatonnes of carbon (Gt C; estimate ± SD) over tropical America, 0.8 ± 0.29 Gt C over Africa, and 0.8 ± 0.28 Gt C over Asia, for a total of 2.5 ± 0.34 Gt C. The relatively narrow confidence intervals suggest a leap forward in the remote sensing of carbon fluxes and, with additional satellite observations of solar-induced chlorophyll fluorescence, allow the authors to quantify the constituent carbon fluxes of these anomalies.

To illustrate the challenge represented by isolating a tropical continental flux anomaly of a similar amplitude within the global carbon budget, I used an atmospheric transport model (*7*) to simulate the impact of an anomalous source of 2.5 Gt C over the tropical continents together with a compensating source of the same amount in the rest of the world for 2015. To do so, I spread a regular source of 0.27 g C per square meter per day (g C m^{-2} day^{-1}) to the atmosphere over the tropical continents as defined by Liu *et al.*, and a regular sink of 0.01 g C m^{-2} day^{-1} elsewhere. I looked at the impact of this change on the column-averaged CO_2 dry-air mole fraction (X_{CO_2}) satellite retrievals used by Liu *et al.* for 2015, everything else being equal. I then repeated the exercise for an even source of 0.9 Gt C in either tropical America, tropical Africa, or tropical Asia within a fixed tropical carbon budget.

Figure 1 shows the scatter of the resulting change in X_{CO_2}. In all four cases, this change is essentially within ±0.5 parts per million (ppm). The largest values are seen in the case of the three tropical continents aggregated together, but still only 1.5% of the sounding perturbations exceed 0.5 ppm in that case. Consistent with previous studies (*8*, *9*), the figure suggests that subcontinental-scale systematic errors of a few tenths of ppm in the retrievals and in the modeled transport processes may severely distort the estimated tropical carbon flux anomalies. Yet the biases found between the OCO-2 retrievals used by Liu *et al.* and reference validation measurements at 17 surface stations of the worldwide Total Carbon Column Observing Network (*10*) were scattered with a standard deviation as large as 0.8 ppm and a median of 0.6 ppm; some of their patterns correlate with surface brightness, and thus with the target flux signal (*11*). The systematic errors of the GOSAT retrievals are not smaller (*6*). Some of these biases would cancel out when comparing two different years, but only partially because the biases depend on time-varying surface and atmospheric properties. In addition, the reference measurements themselves are tuned against internationally recognized standards at the 0.4-ppm level only (*12*, *13*), whereas only a few measurements support the development of CO_2 transport process models. I therefore argue that the uncertainties stated by Liu *et al.* much underestimate the actual flux error budget. Realistic values would reflect our current difficulty with X_{CO_2} retrievals to reliably discriminate between the anomalies in the three tropical continents and even to isolate some anomaly in the tropical continental budget within the global budget, irrespective of the quality of the satellite instruments themselves.

Monitoring carbon surface fluxes from space is still an emerging technology. An ambitious multimodel approach is needed to distinguish what is robust in current results from what is not. To make better use of existing and of future measurements, more research is needed to make the processing chains robust, in particular through further

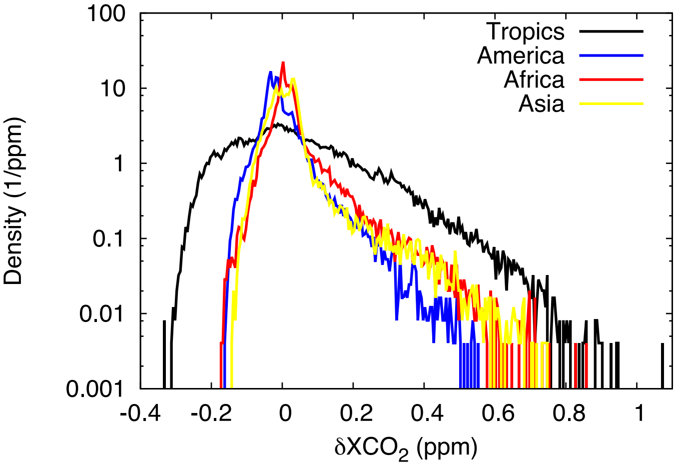

Fig. 1. Density function, in log scale, of the X_{CO_2} perturbations induced by perturbations of the carbon budget of 2.5, 0.9, 0.9, and 0.9 Gt C evenly spread over the tropical continents, over tropical America, over tropical Africa, and over tropical Asia, respectively. Each source is compensated with a sink of the same amplitude outside the tropical continents or in the same latitude band, including the oceans. X_{CO_2} values are simulated at the location of the OCO-2 retrieval used by Liu *et al*. The vertical weighting specific to each retrieval has been applied.

LSCE-IPSL, CEA, CNRS, UVSQ, L'Orme des Merisiers, 91191 Gif-sur-Yvette Cedex, France.
*Corresponding author. Email: frederic.chevallier@lsce.ipsl.fr

development and refinement of the X_{CO_2} reference ground-based network and of measurement programs dedicated to the transport of tracers in the column.

REFERENCES AND NOTES

1. A. Eldering *et al*., *Science* **358**, eaam5745 (2017).
2. F. Chevallier *et al*., *Geophys. Res. Lett.* **41**, 1065–1070 (2014).
3. F. Chevallier *et al*., *Climate Assessment Report for the GHG-CCI Project of ESA's Climate Change Initiative, Version 3* (2016); www.esa-ghg-cci.org/?q=webfm_send/318.
4. S. Houweling *et al*., *J. Geophys. Res. Atmos.* **120**, 5253–5266 (2015).
5. H. Takagi *et al*., *Geophys. Res. Lett.* **41**, 2598–2605 (2014).
6. J. Liu *et al*., *Science* **358**, eaam5690 (2017).
7. R. Locatelli *et al*., *Geosci. Model Dev.* **8**, 129–150 (2015).
8. F. Chevallier, F.-M. Bréon, P. J. Rayner, *J. Geophys. Res.* **112**, D09307 (2007).
9. *18th WMO/IAEA Meeting on Carbon Dioxide, Other Greenhouse Gases and Related Tracers Measurement Techniques (GGMT-2015)*, WMO/GAW report no. 229 (2016); https://library.wmo.int/opac/doc_num.php?explnum_id=3074.
10. D. Wunch *et al*., *Philos. Trans. R. Soc. A* **369**, 2087–2112 (2011).
11. D. Wunch *et al*., *Atmos. Meas. Tech.* **10**, 2209–2238 (2017).
12. D. Wunch *et al*., *Atmos. Meas. Tech.* **3**, 1351–1362 (2010).
13. D. Wunch *et al*., *The Total Carbon Column Observing Network's GGG2014 Data Version* (2015).

ACKNOWLEDGMENTS

Computations were performed using HPC resources of CCRT under allocation A0030102201 made by GENCI (Grand Équipement National de Calcul Intensif). The ACOS OCO-2 data can be obtained from http://co2.jpl.nasa.gov. The data were produced by the ACOS/OCO-2 project at the Jet Propulsion Laboratory, California Institute of Technology. The author was funded by the Copernicus Atmosphere Monitoring Service, implemented by the European Centre for Medium-Range Weather Forecasts (ECMWF) on behalf of the European Commission.

21 November 2017; accepted 4 October 2018
10.1126/science.aar5432

TECHNICAL RESPONSE

CARBON CYCLE

Response to Comment on "Contrasting carbon cycle responses of the tropical continents to the 2015–2016 El Niño"

Junjie Liu[1]*, Kevin W. Bowman[1], David Schimel[1], Nicolas C. Parazoo[1], Zhe Jiang[2], Meemong Lee[1], A. Anthony Bloom[1], Debra Wunch[3], Christian Frankenberg[1,4], Ying Sun[1]†, Christopher W. O'Dell[5], Kevin R. Gurney[6], Dimitris Menemenlis[1], Michelle Gierach[1], David Crisp[1], Annmarie Eldering[1]

Chevallier showed a column CO_2 (X_{CO_2}) anomaly of ±0.5 parts per million forced by a uniform net biosphere exchange (NBE) anomaly of 2.5 gigatonnes of carbon over the tropical continents within a year, so he claimed that the inferred NBE uncertainties should be larger than presented in Liu *et al*. We show that a much concentrated NBE anomaly led to much larger X_{CO_2} perturbations.

Chevallier has asserted that the uncertainties presented in Liu *et al.* (*1*) are too small, sufficiently so that the scientific conclusions are less robust than reported. Chevallier (*2*) showed that uniformly redistributing a net biosphere exchange (NBE) anomaly of 2.5 gigatonnes of carbon (Gt C) (*1*) over the tropical continents throughout a year could result in concentration signals of ±0.5 parts per million (ppm). He then speculated that systematic errors in retrievals and transport models may be similar in magnitude, and therefore argued that the uncertainties should be higher.

However, the uniformly distributed flux anomaly proposed by Chevallier is very different from the actual distribution of the biosphere flux anomaly during the 2015–2016 El Niño event. In fact, the NBE anomaly was highly concentrated in time and space, and so led to much larger column enhancements than Chevallier's simulation. Chevallier simulated a source of 0.27 g C m^{-2} day^{-1} to the atmosphere over the tropical continents, balanced by a regular sink of 0.01 g C m^{-2} day^{-1} elsewhere. However, the actual anomalous CO_2 release over the tropics primarily occurred over small areas that experienced extreme climate conditions [figure 4 of (*1*)] during the period September 2015–March 2016 [figure S1 of (*1*)]. For example, the flux anomaly was more than 2.0 g C m^{-2} day^{-1}, nearly 10 times Chevallier's value, over southwest Kalimantan Island, Indonesia in October and November, when the peak biomass burning occurred.

We carried out an experiment similar to that of Chevallier, using the inferred, spatiotemporally varying real NBE anomaly from the 2015–2016 El Niño as a boundary condition over all three tropical continents. We then sampled the X_{CO_2} perturbations using the sensitivity and locations of OCO-2 observations. Figure 1A shows the mean X_{CO_2} perturbations averaged between September 2015 and March 2016, corresponding to the peak of the 2015–2016 El Niño. Figure 1B shows the percentage of the number of simulated X_{CO_2} perturbations larger than 1.0 ppm at each 4° × 5° grid (the resolution of the transport model), and Fig. 1C is a histogram distribution of X_{CO_2} perturbations.

Figure 1A shows that the X_{CO_2} anomaly was typically much larger than 0.5 ppm during the peak of the 2015–2016 El Niño. About 90% and 70% of samples have enhancements larger than 0.5 ppm and 1.0 ppm, respectively (Fig. 1C), well above the threshold for OCO-2 X_{CO_2} systematic error. More than 60% of the samples at each 4° × 5° grid have perturbations larger than 1.0 ppm (Fig. 1B). This is in stark contrast to Chevallier's claim that "still only 1.5% of the sounding perturbations exceed 0.5 ppm in that case." Aside from using different transport models, the X_{CO_2} differences between the two experiments are due to the spatiotemporal distributions of the flux anomaly: concentrated versus uniformly distributed fluxes.

The perturbed X_{CO_2} signal over each of the three tropical continents arises primarily from flux anomalies in the respective continent [figure S1 of (*1*)]. Consistent with uncertainty quantification (*1*) and fundamental source-receptor relationships (*3*), this analysis supports that our inversion system can discriminate between the anomalies in the three tropical continents, enabling the main conclusion in (*1*) that diverse biogeochemical processes are responsible for the large NBE anomaly over three tropical continents,

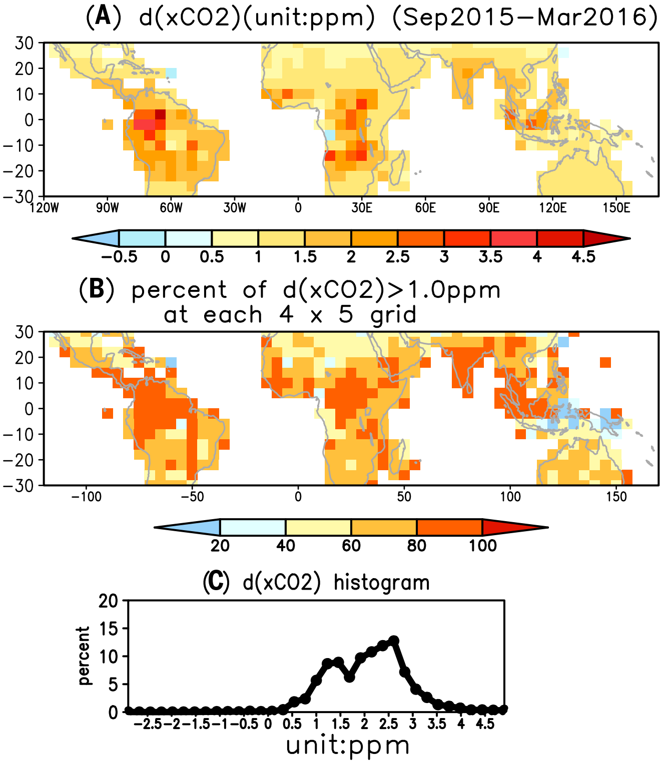

Fig. 1. X_{CO_2} perturbations due to net biosphere flux anomaly during the peak of 2015–2016 El Niño. (**A**) Mean X_{CO_2} perturbations over the period September 2015–March 2016. X_{CO_2} was sampled with OCO-2 sensitivity and locations of OCO-2 observations. (**B**) Percentage of X_{CO_2} perturbations larger than 1 ppm at each 4° × 5° grid. (**C**) Histogram of X_{CO_2} perturbations.

---

[1]Jet Propulsion Laboratory, California Institute of Technology, Pasadena, CA, USA. [2]National Center for Atmospheric Research, Boulder, CO, USA. [3]University of Toronto, Toronto, Ontario, Canada. [4]California Institute of Technology, Pasadena, CA, USA. [5]Colorado State University, Fort Collins, CO, USA. [6]Arizona State University, Tempe, AZ, USA.
***Corresponding author. Email: junjie.liu@jpl.nasa.gov**
†Present address: Soil and Crop Sciences Section, School of Integrative Plant Science, Cornell University, Ithaca, NY, USA.

which was also supported by two additional types of observations: carbon monoxide and solar-induced chlorophyll fluorescence used to constrain biomass burning and plant primary productivity, respectively.

The 2015–2016 El Niño was an extreme climate event, generating intense but localized climate and NBE anomalies (*1*, *4*) that were exploited by the inversion system in (*1*). Systematic errors in X_{CO_2} retrievals are one of the many factors contributing to the overall estimated net biosphere flux uncertainty. Quantification and mitigation of these errors is an active area of research and is likely to lead to improved data products and analyses of subtler phenomena, such as downwind enhancements from megacity fossil fuel emissions. Substantial advances have been demonstrated by the OCO-2 and GOSAT communities, and we expect continued progress toward the capability of quantifying fluxes by the emerging international constellation of satellites with a much higher confidence level than now. We agree with Chevallier that this advancement must remain a priority (*5*).

REFERENCES AND NOTES

1. J. Liu *et al*., *Science* **358**, eaam5690 (2017).
2. F. Chevallier, *Science* **362**, eaar5432 (2018).
3. J. Liu, K. W. Bowman, D. K. Henze, *J. Geophys. Res. Atmospheres* **120**, 5214–5236 (2015).
4. J. C. Jiménez-Muñoz *et al*., *Sci. Rep.* **6**, 33130 (2016).
5. P. J. Sellers, D. S. Schimel, B. Moore III, J. Liu, A. Eldering, *Proc. Natl. Acad. Sci. U.S.A.* **115**, 7860–7868 (2018).

ACKNOWLEDGMENTS

This research was carried out at the Jet Propulsion Laboratory, California Institute of Technology, under a contract with NASA. This work was in part supported by NASA Carbon Monitoring System program grant 14-CMS14-0054 and by NASA Orbiting Carbon Observatory Science team program grants 14-OCO2_14-0007 and 11-OCO211-0024. K.R.G. was supported by NSF CAREER award 0846358.

8 February 2018; accepted 4 October 2018
10.1126/science.aat1211

AAAS and The Lemelson Foundation promote innovators

Program showcases inventors to advance U.S. innovation endeavors, address world challenges

By **Anne Q. Hoy**

Scientist Don McPherson got his start as an inventor melting glass-making ingredients enriched with rare earth elements to create safety eyewear lenses for surgeons. They help surgeons differentiate patient tissues while performing laser procedures and provide protection from laser beam exposure in the operating theater.

In his free time, McPherson was an ultimate Frisbee player. He used the safety eyewear as sunglasses, a practice he picked up from the surgeons who were so enthused with the eyewear's ability to enhance visible colors that they started removing them from the operating room and wearing them outside.

At a Frisbee tournament in Santa Cruz, California, McPherson's friend asked to borrow his sunglasses. Within seconds, his teammate was overcome with amazement: "Dude, I can see the cones," he said, describing a "fluorescent orange" cone and "bright green" grass, colors seen for the first time by someone with red and green color blindness.

In an instant, an invention was born. He was on to something.

The American Association for the Advancement of Science showcases inventors like McPherson, honoring their dedication to solving global challenges and supporting innovations through the AAAS-Lemelson Invention Ambassadors program, founded in 2014 in partnership with The Lemelson Foundation. The program celebrates innovations annually. McPherson and seven others were selected to be 2018–2019 AAAS-Lemelson Invention Ambassadors.

The eight innovators were welcomed to the fifth annual Celebrate Invention event at AAAS headquarters in Washington, D.C., in late July. Each ambassador delivered a presentation describing their inventions, showing how they improve people's lives and tracing the interdisciplinary features of their work.

Rachel Walker, an oncology nurse and assistant professor at the University of Massachusetts, Amherst, College of Nursing, walked through inventions she and an interdisciplinary team have been designing. Included are a portable system to purify water and generate IV fluids onsite in disaster areas; tools to help breast cancer survivors treat residual pain at home; and a mechanism for cancer patients to monitor chemotherapy to ensure that family members avoid exposure when patients administer treatments at home.

Another innovator, Mary Kombolias, a senior chemist at the U.S. Government Publishing Office and a guest researcher at the National Institute of Standards and Technology, explained how she and a group of other scientists brought a cumbersome process from the 1920s into the 21st century. She and fellow researchers developed a novel, non-destructive method of performing fiber analysis of paper. This method has forensic capabilities and also can detect recycled fiber content and determine the relative age of paper.

"The Invention Ambassadors program endeavors to enrich and inspire a fresh and diverse generation of young inventors by expanding global understanding of the realm of invention and innovation," said Shirley Malcom, AAAS senior adviser.

Such innovations have long been powerful contributors to U.S. economic growth. Yet, over the last 45 years such expansion has slowed from a onetime 1.9% annual growth rate to 0.75%, according to a research paper popularly known as "The Lost Einsteins" authored by Stanford University professor Raj Chetty and four other academics and experts associated with Opportunity Insights, an institute dedicated to improving economic opportunities.

"We conclude that increasing exposure to innovation among children who (a) excel in math and science at early ages and (b) are from under-represented groups can have large impacts on aggregate innovation," reported the November 2018 economics paper, previously released as a preliminary draft titled "The Lifecycle of Inventors."

"Indeed, we estimate that if women, minorities, and children from lower-income families were to invent at the same rate as white men from high-income (top-quintile) families, the total number of inventors in the economy would quadruple," the paper stated. "These findings suggest there are many 'lost

Glasses that can open a world of color to those with color vision deficiencies emerged from a nearly accidental discovery by AAAS-Lemelson Invention Ambassador Don McPherson.

PHOTO: ENCHROMA

Einsteins'—individuals who would have had highly impactful inventions had they been exposed to innovation in childhood—especially among women, minorities, and children from low-income families."

Like many innovators, the hint of invention sent McPherson on a years-long information-gathering mission. Some 6 months would pass before he was sufficiently confident to apply for a research grant. In time, the National Eye Institute and the National Cancer Institute would fund McPherson's work with five grants totaling $1.15 million through the National Institutes of Health's Small Business Innovation Research program. McPherson holds 6 patents and has authored 14 scientific research papers.

Progress accelerated in 2010 when he and mathematician Andrew Schmeder cofounded EnChroma, Inc., a Berkeley, California-based company that now uses proprietary lens technology to produce eyeglasses that can help correct color vision deficiencies impacting at least 300 million people across the globe. McPherson is EnChroma's chief science officer, Schmeder is its chief executive officer.

Like many inventors, McPherson's discovery emerged from an early desire—in his case, to become a glass sculptor. It turned out that his visit to Alfred University after graduating from college revealed that it no longer offered a Master of Fine Arts degree in glass making. Instead, a professor advised him to visit the engineering school. McPherson would go on to apply an inventor's curiosity, determination, and persistence to earn a Master of Science and a Ph.D. from the university.

In keeping with the foundational feature of today's inventions, the journey drew from a broad mix of scientific disciplines. At EnChroma, McPherson stopped designing glass lenses and experimented with a range of optical coatings, one used by the aerospace industry. Later, he zeroed in on a military-grade material with the quality of optical glass but none of its heavy density and found "an ideal material."

Mary Kombolias shares her work on a new method of fiber analysis of paper.

The glasses have transformed the lives of children and adults across the world. The moment someone sees colors for the first time prompts powerful emotional responses, McPherson said.

A color-blind marine biologist once reached out to EnChroma seeking a color-vision-correcting scuba mask to allow him to advance his work through underwater research. The marine biologist wrote EnChroma after receiving his scuba goggles, reporting: "My life has changed."

2018 AAAS Fellows approved by the AAAS Council

In October 2018, the Council of the American Association for the Advancement of Science elected 416 members as Fellows of AAAS. These individuals will be recognized for their contributions to science and technology at the Fellows Forum to be held on 16 February 2019 during the AAAS Annual Meeting in Washington, D.C. Presented by section affiliation, they are:

Section on Agriculture, Food, and Renewable Resources

Federica Brandizzi, *Michigan State Univ.*

Robert J. Ferl, *Univ. of Florida*

Elizabeth E. Hood, *Arkansas State Univ.*

Carol A. Ishimaru, *Univ. of Minnesota*

David (Dave) Peter Jackson, *Cold Spring Harbor Laboratory*

Jeffrey B. Jones, *Univ. of Florida*

Bruce A. Kimball, *USDA-ARS/The Greenleaf Group*

Andrew D. B. Leakey, *Univ. of Illinois at Urbana-Champaign*

Jianxin Ma, *Purdue Univ.*

Ray Ming, *Univ. of Illinois at Urbana-Champaign*

Scott Charles Peck, *Univ. of Missouri*

David M. Stelly, *Texas A&M Univ./Texas A&M AgriLife Research*

J. Edward Taylor, *Univ. of California, Davis*

Martin Wiedmann, *Cornell Univ.*

Qijing Zhang, *Iowa State Univ.*

Section on Anthropology

Richard Gutierrez Bribiescas, *Yale Univ.*

Leo Ralph Chavez II, *Univ. of California, Irvine*

Benedikt Hallgrimsson, *Univ. of Calgary (Canada)*

Sang-Hee Lee, *Univ. of California, Riverside*

Torben (Torrey) Charles Rick, *National Museum of Natural History, Smithsonian Institution*

Fred H. Smith, *Illinois State Univ.*

Andrea B. Taylor, *Touro Univ.*

E. Christian Wells, *Univ. of South Florida*

Section on Astronomy

Eric J. Chaisson, *Harvard Univ.*

Jacqueline N. Hewitt, *Massachusetts Institute of Technology*

Michael A. Janssen, *Jet Propulsion Laboratory, California Institute of Technology*

William D. Langer, *Jet Propulsion Laboratory, California Institute of Technology*

Frederic A. Rasio, *Northwestern Univ.*

Massimo Stiavelli, *Space Telescope Science Institute*

Section on Atmospheric and Hydrospheric Science

Ken Owen Buesseler, *Woods Hole Oceanographic Institution*

Michael D. Dettinger, *U.S. Geological Survey*

Manvendra Krishna Dubey, *Los Alamos National Laboratory*

Allen H. Goldstein, *Univ. of California, Berkeley*

Jacqueline M. Grebmeier, *Chesapeake Biological Laboratory, Univ. of Maryland Center for Environmental Science*

Dennis A. Hansell, *Univ. of Miami*

Elisabeth A. Holland, *Univ. of the South Pacific (Fiji)*

Upmanu Lall, *Columbia Univ.*

James A. Yoder, *Woods Hole Oceanographic Institution/Univ. of Rhode Island*

Xubin Zeng, *Univ. of Arizona*

Section on Biological Sciences

Cory Abate-Shen, *Columbia Univ., Vagelos College of Physicians and Surgeons*

Dean C. Adams, *Iowa State Univ.*

Juan D. Alfonzo, *The Ohio State Univ.*

Andreas D. Baxevanis, *National Human Genome Research Institute/NIH*

Paul N. Black, *Univ. of Nebraska-Lincoln*

Holly M. Brown-Borg, *Univ. of North Dakota*

PHOTO: ANDY DELGIUDICE

Christopher G. Burd, *Yale Univ. School of Medicine*
Rebecca D. Burdine, *Princeton Univ.*
Sean M. Burgess, *Univ. of California, Davis*
Craig A. Carlson, *Univ. of California, Santa Barbara*
Prosanta Chakrabarty, *Louisiana State Univ.*
Robert S. Chapkin, *Texas A&M Univ.*
John Chaput, *Univ. of California,Irvine*
Jeffrey D. Cirillo, *Texas A&M Health Science Center*
Lisa M. Coussens, *Oregon Health & Science Univ.*
Thomas L. Crisman, *Univ. of South Florida*
Mary Dasso, *National Institute for Child Health and Human Development/NIH*
Robert J. Denver, *Univ. of Michigan*
Keith M. Derbyshire, *Wadsworth Center, New York State Department of Health*
Douglas Wayne DeSimone, *Univ. of Virginia*
Savithramma P. Dinesh-Kumar, *Univ. of California, Davis*
John M. Drake, *Univ. of Georgia*
Ronald M. Evans, *Salk Institute for Biological Studies/Howard Hughes Medical Institute*
Michael Freitag, *Oregon State Univ.*
Michael A. Gealt, *Central Michigan Univ.*
Wayne W. Grody, *David Geffen School of Medicine at Univ. of California, Los Angeles*
Anne Grove, *Louisiana State Univ.*
James A. Guikema, *Kansas State Univ.*
Kenneth M. Halanych, *Auburn Univ.*
Kathleen B. Hall, *Washington Univ. School of Medicine in St. Louis*
K. David Hambright, *Univ. of Oklahoma*
Kyle Edward Harms, *Louisiana State Univ.*
H. Criss Hartzell, *Emory Univ.*
Jody Hey, *Temple Univ.*
David Scott Hibbett, *Clark Univ.*
Kimberly A. Hughes, *Florida State Univ.*
David Allen Hutchins, *Univ. of Southern California*
Masayori Inouye, *Rutgers-Robert Wood Johnson Medical School*
Bertram L. Jacobs, *Arizona State Univ.*
Fredric J. Janzen, *Iowa State Univ.*
Joseph Jez, *Washington Univ. in St. Louis*
Kristen Marie Johansen, *Iowa State Univ.*
Terrance J. Kavanagh, *Univ. of Washington*
Daniel B. Kearns, *Indiana Univ.*
David M. Kehoe, *Indiana Univ.*
Megerditch (Mike) Kiledjian, *Rutgers, The State Univ. of New Jersey*
George Liang King, *Harvard Medical School*
Carla M. Koehler, *Univ. of California, Los Angeles*
Michael J. Kuhar, *Emory Univ.*
Jay-Terrence Lennon, *Indiana Univ.*
Kim Lewis, *Northeastern Univ.*
Judy Lieberman, *Boston Children's Hospital, Harvard Medical School*
Paul M. Lieberman, *The Wistar Institute*
Jiandie D. Lin, *Univ. of Michigan*
Xiaorong Lin, *Univ. of Georgia*
Iris Lindberg, *Univ. of Maryland, Baltimore*
Hua Lu, *Tulane Univ.*
Micah Luftig, *Duke Univ.*
Julius Lukeš, *Czech Academy of Sciences (Czech Republic)*
David Robert Maddison, *Oregon State Univ.*
William H. McDowell, *Univ. of New Hampshire*
Wladek Minor, *Univ. of Virginia*
Corrie Moreau, *Field Museum of Natural History/ Cornell Univ.*
Frank Edgar Muller-Karger, *Univ. of South Florida*
Karl Joseph Niklas, *Cornell Univ.*
Seiji Ogawa, *Tohoku Fukushi Univ., Kansei Fukushi Research Center*
Neil Osheroff, *Vanderbilt Univ. School of Medicine*
Andrea Page-McCaw, *Vanderbilt Univ.*
Carole A. Parent, *Univ. of Michigan*
John T. Patton, *Indiana Univ.*
Thomas T. Perkins, *JILA/NIST/ Univ. of Colorado Boulder*
Linda Joy Pike, *Washington Univ. School of Medicine in St. Louis*
Joshua B. Plotkin, *Univ. of Pennsylvania*
Eric Post, *Univ. of California, Davis*
Mary V. Relling, *St. Jude Children's Research Hospital*
Jürgen A. Richt, *Kansas State Univ.*
Michael A. Riehle, *Univ. of Arizona*
Pejman Rohani, *Univ. of Georgia*
Noah A. Rosenberg, *Stanford Univ.*
Jean M. Sanger, *SUNY Upstate Medical Univ.*
Samuel Michael Scheiner, *National Science Foundation*
Kevin L. Schey, *Vanderbilt Univ.*
Johannes Schul, *Univ. of Missouri*
Katriona Shea, *Penn State*
Madeline A. Shea, *Univ. of Iowa*
Binghui Shen, *Beckman Research Institute, City of Hope*
Jay Shendure, *Univ. of Washington*
Hal L. Smith, *Arizona State Univ.*
Holger Sondermann, *Cornell Univ.*
Eric V. Stabb, *Univ. of Georgia*
Ramunas Stepanauskas, *Bigelow Laboratory for Ocean Sciences*
Katharine Nash Suding, *Univ. of Colorado Boulder*
Lukas K. Tamm, *Univ. of Virginia*
Allen Taylor, *Tufts Univ.*
Steven M. Theg, *Univ. of California, Davis*
Georgia D. Tomaras, *Duke Univ. Medical Center*
James Frances Anthony Traniello, *Boston Univ.*
Susannah G. Tringe, *U.S. Department of Energy Joint Genome Institute, Lawrence Berkeley National Laboratory*
Maria Vernet, *Scripps Institution of Oceanography, Univ. of California, San Diego*
Charles Walcott, *Cornell Univ.*
Claire E. Walczak, *Indiana Univ.*
Friedbert Weiss, *Scripps Research Institute*
Stephen Halley White, *Univ. of California, Irvine*
Jan A. Witkowski, *Cold Spring Harbor Laboratory*
Floyd L. Wormley Jr., *Univ. of Texas at San Antonio*
Gregory Allan Wray, *Duke Univ.*
Joseph B. Yavitt, *Cornell Univ.*
Malin M. Young, *Pacific Northwest National Laboratory*
Jianming Yu, *Iowa State Univ.*
Jonathan P. Zehr, *Univ. of California, Santa Cruz*
Baohong Zhang, *East Carolina Univ.*
Dong-Er Zhang, *Univ. of California, San Diego*

Section on Chemistry

Thomas E. Albrecht-Schmitt, *Florida State Univ.*
Matthew John Allen, *Wayne State Univ.*
Kara L. Bren, *Univ. of Rochester*
Phillip Franklin Britt, *Oak Ridge National Laboratory*
Donna A. Chen, *Univ. of South Carolina*
Peng Chen, *Cornell Univ.*
Zhan Chen, *Univ. of Michigan*
Wonhwa Cho, *Univ. of Illinois at Chicago*
Robert E. Continetti, *Univ. of California, San Diego.*
Marcetta Y. Darensbourg, *Texas A&M Univ.*
Olafs Daugulis, *Univ. of Houston*
Xiangfeng Duan, *Univ. of California, Los Angeles*
Fillmore Freeman, *Univ. of California, Irvine*
Teresa Fryberger, *National Academies of Science, Engineering, and Medicine (Retired)*
Neil K. Garg, *Univ. of California, Los Angeles*
David S. Gottfried, *Georgia Institute of Technology*
John H. Griffin, *Numerate, Inc.*
Robert (Barney) Grubbs, *Stony Brook Univ.*
Marina G. Guenza, *Univ. of Oregon*
Wayne Charles Guida, *Univ. of South Florida*
P. Shiv Halasyamani, *Univ. of Houston*
Trevor W. Hayton, *Univ. of California, Santa Barbara*
Stefan W. Hell, *Max Planck Institute for Biophysical Chemistry/Max Planck Institute for Medical Research (Germany)*
William H. Hersh, *Queens College of the City Univ. of New York*
Stephan Irle, *Oak Ridge National Laboratory*
Jeffrey Scott Johnson, *Univ. of North Carolina at Chapel Hill*
Dimitris Katsoulis, *The Dow Chemical Company*
Sung-Hou Kim, *Univ. of California, Berkeley*
Aravinda (Arvind) M. Kini, *U.S. Department of Energy (Retired)*
Carlito B. Lebrilla, *Univ. of California, Davis*
Zhiqun Lin, *Georgia Institute of Technology*
Todd B. Marder, *Universität Würzburg (Germany)*
Heather D. Maynard, *Univ. of California, Los Angeles*
Shelley D. Minteer, *Univ. of Utah*
Bruce A. Moyer, *Oak Ridge National Laboratory*
Luciano Mueller, *Bristol-Myers Squibb*
Janet Elizabeth Nelson, *Univ. of Idaho*

Paula J. Olsiewski, *Alfred P. Sloan Foundation*
Thalappil Pradeep, *Indian Instiute of Technology Madras (India)*
Glenn D. Prestwich, *Univ. of Utah, College of Pharmacy*
Ursula Roethlisberger, *École Polytechnique Fédérale de Lausanne, Institute of Chemical Sciences and Engineering (Switzerland)*
Stewart W. Schneller, *Auburn Univ.*
Ram Seshadri, *Univ. of California, Santa Barbara*
Page O. Stoutland, *Nuclear Threat Initiative*
Mas Subramanian, *Oregon State Univ.*
John T. Vaughey, *Argonne National Laboratory*
Javier Vela, *Iowa State Univ.*

Section on Dentistry and Oral Health Sciences

Robert C. Angerer, *National Institute of Dental and Craniofacial Research/NIH*
Hyun (Michel) Koo, *Univ. of Pennsylvania*
Susan T. Reisine, *Univ. of Connecticut School of Dental Medicine*
Candan Tamerler, *Univ. of Kansas*
Richard W. Valachovic, *American Dental Education Association*

Section on Education

Jeffrey Bennett, *Big Kid Science*
Beth A. Cunningham, *American Association of Physics Teachers*
Ali Eskandarian, *The George Washington Univ.*
Tuajuanda C. Jordan, *St. Mary's College of Maryland*
Tamara S. Ledley, *STEM Education Consultant, Earth and Climate Science*
Nancy Pearson Moreno, *Baylor College of Medicine*
Jeffrey M. Osborn, *The College of New Jersey*
Nancy Pelaez, *Purdue Univ.*
Eliza Jane Reilly, *National Center for Science and Civic Engagement*
Kathrin Friederike Stanger-Hall, *Univ. of Georgia*
Linette M. Watkins, *James Madison Univ.*

Section on Engineering

Narayana R. Aluru, *Univ. of Illinois at Urbana-Champaign*
Guillermo A. Ameer, *Northwestern Univ.*
Craig H. Benson, *Univ. of Virginia*
Shekhar Bhansali, *Florida International Univ.*
Karen J. L. Burg, *Univ. of Georgia*
Jian Cao, *Northwestern Univ.*
Krishnendu Chakrabarty, *Duke Univ.*
Chau-Chyun Chen, *Texas Tech Univ.*
Long-Qing Chen, *Penn State*
Chang-Beom Eom, *Univ. of Wisconsin-Madison*
Ali Erdemir, *Argonne National Laboratory*
Venkat Ganesan, *Univ. of Texas at Austin*
Keith William Hipel, *Univ. of Waterloo (Canada)*
M. Saif Islam, *Univ. of California, Davis*
Pramod P. Khargonekar, *Univ. of California, Irvine*
Joseph A. King Jr., *U.S. Department of Energy-ARPA-E*
Ratnesh Kumar, *Iowa State Univ.*
Satish Kumar, *Georgia Institute of Technology, School of Materials Science and Engineering*
Jinsong Leng, *Harbin Institute of Technology (China)*
John H. Lienhard V, *Massachusetts Institute of Technology*
Jingyu Lin, *Texas Tech Univ.*
Gregory V. Lowry, *Carnegie Mellon Univ.*
Dimitrios Maroudas, *Univ. of Massachusetts Amherst*
Louis A. Martin-Vega, *North Carolina State Univ.*
Amit Misra, *Univ. of Michigan*
Aydogan Ozcan, *Univ. of California, Los Angeles*
Matteo Pasquali, *Rice Univ.*
Athina P. Petropulu, *Rutgers, The State Univ. of New Jersey*
Kristala L. J. Prather, *Massachusetts Institute of Technology*
K. T. Ramesh, *Johns Hopkins Univ.*
Liangfang Zhang, *Univ. of California, San Diego*

Section on General Interest in Science and Engineering

Carol Lynn Alpert, *Museum of Science, Boston*
Karl Leif Bates, *Duke Univ.*
Ann K. Finkbeiner, *Freelance Writer*
Tee Lamont Guidotti, *The George Washington Univ. Hospital*
Sue Nichols, *Michigan State Univ.*
John Archie Pollock, *Duquesne Univ.*
David J. Skorton, *The Smithsonian Institution*
David S. Torain II, *Montgomery College*
Karen McNulty Walsh, *Brookhaven National Laboratory*

Section on Geology and Geography

Richard W. Battarbee, *Univ. College London (UK)*
Ann F. Budd, *Univ. of Iowa*
Andrew M. Davis, *Univ. of Chicago*
Malcolm S. Field, *U.S. Environmental Protection Agency*
Karl W. Flessa, *Univ. of Arizona*
Sarah Elizabeth Gergel, *Univ. of British Columbia (Canada)*
Ethan L. Grossman, *Texas A&M Univ.*
Susumu Honjo, *Woods Hole Oceanographic Institution*
David R. Janecky, *Los Alamos National Laboratory (Retired)*
Richard A. Kerr, *AAAS/Science (Retired)*
Bruce P. Luyendyk, *Univ. of California, Santa Barbara*
James G. Ogg, *Purdue Univ./Chengdu Univ. of Technology (China)*
Frederick J. Swanson, *USDA Forest Service Pacific Northwest Research Station*
Kenneth R. Young, *Univ. of Texas at Austin*

Section on History and Philosophy of Science

Helen E. Longino, *Stanford Univ.*
Jürgen Renn, *Max Planck Institute for the History of Science (Germany)*
James Francis Woodward, *Univ. of Pittsburgh*

Section on Industrial Science and Technology

Robert W. Boyd, *Univ. of Ottawa (Canada)/Univ. of Rochester*
Federico Faggin, *Federico and Elvia Faggin Foundation*
Avetik P. Harutyunyan, *Honda Research Institute, USA*
Allan J. Jacobson, *Univ. of Houston*
Gerd Leuchs, *Max Planck Institute for the Science of Light (Germany)*
David L. Morse, *Corning Incorporated*
William D. Phillips, *National Institute for Standards and Technology*
Esther S. Takeuchi, *Stony Brook Univ./Brookhaven National Laboratory*

Section on Information, Computing, and Communication

Ronald J. Brachman, *Jacobs Technion-Cornell Institute at Cornell Tech*
David J. Farber, *Keio Univ. (Japan)*
Peter Arthur Fox, *Rensselaer Polytechnic Institute*
William D. Gropp, *Univ. of Illinois at Urbana-Champaign*
Rajesh K. Gupta, *Univ. of California, San Diego*
Gregory D. Hager, *Johns Hopkins Univ.*
Vasanth G. Honavar, *Penn State*
Huan Liu, *Arizona State Univ.*
Stefano Lonardi, *Univ. of California, Riverside*
Patricia Morreale, *Kean Univ.*
Lynne E. Parker, *Univ. of Tennessee, Knoxville*
C. Raymond Perrault, *SRI International*
Pavel A Pevzner, *Univ. of California, San Diego*
Vir V. Phoha, *Syracuse Univ.*
Lawrence Rauchwerger, *Texas A&M Univ.*
Amit P. Sheth, *Wright State Univ.*
Steven Skiena, *Stony Brook Univ.*
Peter Stone, *Univ. of Texas at Austin*
Jie Wu, *Temple Univ.*
Katherine A. Yelick, *Univ. of California, Berkeley/Lawrence Berkeley National Laboratory*

Section on Linguistics and Language Sciences

Dragomir R. Radev, *Yale Univ.*
Thomas Wasow, *Stanford Univ.*

Section on Mathematics

Eric M. Friedlander, *Univ. of Southern California*

Ilse C. F. Ipsen, *North Carolina State Univ.*

George Em Karniadakis, *Brown Univ.*

C. T. Kelley, *North Carolina State Univ.*

David E. Keyes, *King Abdullah Univ. of Science and Technology (Saudi Arabia)*

Yi Li, *John Jay College of Criminal Justice, CUNY*

Section on Medical Sciences

Samuel Achilefu, *Washington Univ. School of Medicine in St. Louis*

Victor R. Ambros, *Univ. of Massachusetts Medical School*

Richard Axel, *Columbia Univ.*

Norbert W. Bischofberger, *Gilead Sciences, Inc.*

Guojun Bu, *Mayo Clinic*

Henry Joseph Donahue, *Virginia Commonwealth Univ.*

Stephen J. Elledge, *Harvard Medical School/Brigham and Women's Hospital*

Eric R. Fearon, *Univ. of Michigan*

Victoria J. Fraser, *Washington Univ. School of Medicine in St. Louis*

Jeffrey E. Gershenwald, *The Univ. of Texas MD Anderson Cancer Center*

Thomas W. Glover, *Univ. of Michigan*

Jacqueline Tauber Hecht, *Univ. of Texas Health Science Center at Houston*

Patrick Hwu, *The Univ. of Texas MD Anderson Cancer Center*

Thomas J. Inzana, *Long Island Univ., College of Veterinary Medicine*

Alec J. Jeffreys, *Univ. of Leicester (UK)*

Philip H. Kass, *Univ. of California, Davis*

John F. Kearney, *Univ. of Alabama at Birmingham*

Kevin E. Kip, *Univ. of South Florida*

Steven D. Leach, *Dartmouth College/Dartmouth-Hitchcock*

Mark E. Lowe, *Washington Univ. School of Medicine in St. Louis*

Wayne D. Newhauser, *Louisiana State Univ./Mary Bird Perkins Cancer Center*

Paul Nurse, *The Francis Crick Institute (UK)*

Isaac Ness Pessah, *Univ. of California, Davis*

Alvin Carter Powers, *Vanderbilt Univ. /Vanderbilt Univ. Medical Center*

Donald G. Puro, *Univ. of Michigan*

Lawrence I. Rothblum, *Univ. of Oklahoma Health Sciences Center*

Sharon Irene Smith Rounds, *Brown Univ.*

Deborah C. Rubin, *Washington Univ. School of Medicine in St. Louis*

Liangyou Rui, *Univ. of Michigan*

Warren Ston Sandberg, *Vanderbilt Univ. Medical Center*

L. David Sibley, *Washington Univ. School of Medicine in St. Louis*

Gary Arthur Silverman, *Washington Univ. School of Medicine in St. Louis*

Lilianna Solnica-Krezel, *Washington Univ. School of Medicine in St. Louis*

William J. Steinbach, *Duke Univ. Medical Center*

Vincent W. Yang, *Stony Brook Univ.*

Section on Neuroscience

Roger L. Albin, *Univ. of Michigan*

Jonathan Brewer Cohen, *Harvard Medical School*

John C. Crabbe, *Oregon Health & Science Univ./U.S. Department of Veterans Affairs*

Ruth Anne Eatock, *Univ. of Chicago*

David C. Gadsby, *The Rockefeller Univ.*

Katheleen Gardiner, *Univ. of Colorado School of Medicine*

Robert Gereau, *Washington Univ. School of Medicine in St. Louis*

David D. Ginty, *Harvard Univ./Howard Hughes Medical Institute*

Margaret E. Gnegy, *Michigan Medicine*

Andrea G. Hohmann, *Indiana Univ.*

Robin Howard Lovell-Badge, *The Francis Crick Institute (UK)*

Pedro Ricardo Lowenstein, *Michigan Medicine*

Donata Oertel, *Univ. of Wisconsin-Madison, School of Medicine and Public Health*

Michael Andrew Rogawski, *Univ. of California, Davis*

Hee-Sup Shin, *Institute for Basic Science (Republic of Korea)*

Judith Richmond Walters, *National Institute of Neurological Disorders and Stroke/NIH*

Section on Pharmaceutical Sciences

William Steven Dalton, *M2Gen*

Kathryn Elaine Meier, *Washington State Univ.*

John L. Nitiss, *Univ. of Illinois at Chicago*

Natalia Y. Tretyakova, *Univ. of Minnesota*

Section on Physics

Charles H. Ahn, *Yale Univ.*

Farhat N. Beg, *Univ. of California, San Diego*

Nora Berrah, *Univ. of Connecticut*

Girsh Blumberg, *Rutgers, The State Univ. of New Jersey*

Joel N. Butler, *Fermi National Accelerator Laboratory*

Shi-Jie Chen, *Univ. of Missouri*

Wai-Yim Ching, *Univ. of Missouri-Kansas City*

Timothy Edward Chupp, *Univ. of Michigan*

Jodi A. Cooley, *Southern Methodist Univ.*

Thomas E. Cravens, *Univ. of Kansas*

Zachary Fisk, *Univ. of California, Irvine*

James K. Freericks, *Georgetown Univ.*

Adam Leibovich, *Univ. of Pittsburgh*

Jeremy Levy, *Univ. of Pittsburgh*

Adriana Moreo, *Univ. of Tennessee, Knoxville*

David Howard Reitze, *California Institute of Technology/Univ. of Florida*

Gregory W. Swift, *Los Alamos National Laboratory*

Scott Thomas, *Rutgers, The State Univ. of New Jersey*

Remco G. T. Zegers, *Michigan State Univ.*

Section on Psychology

Jennifer Crocker, *The Ohio State Univ.*

Eric Eich, *Univ. of British Columbia (Canada)*

Russell H. Fazio, *The Ohio State Univ.*

William E. Haley, *Univ. of South Florida*

Steven C. Hayes, *Univ. of Nevada, Reno*

Daphne McDonell Maurer, *McMaster Univ. (Canada)*

Brian A. Nosek, *Univ. of Virginia/Center for Open Science*

Robert M. Nosofsky, *Indiana Univ.*

K. Daniel O'Leary, *Stony Brook Univ.*

Ellen Peters, *The Ohio State Univ.*

Toru Shimizu, *Univ. of South Florida*

Peter M. Todd, *Indiana Univ.*

Elaine F. Walker, *Emory Univ.*

Elke U. Weber, *Princeton Univ.*

Section on Social, Economic, and Political Sciences

Carter Tribley Butts, *Univ. of California, Irvine*

John B. Casterline, *The Ohio State Univ.*

Kathleen M. Heide, *Univ. of South Florida*

Monica Kirkpatrick Johnson, *Washington State Univ.*

J. Michael McGinnis, *National Academy of Medicine*

Willard L. Rodgers, *Univ. of Michigan*

Dani Rodrik, *Harvard Univ.*

Elaine Wethington, *Cornell Univ.*

Oran R. Young, *Univ. of California, Santa Barbara*

Section on Societal Impacts of Science and Engineering

Diana Hicks, *Georgia Institute of Technology*

Jennifer Kuzma, *North Carolina State Univ.*

Jennifer Poulakidas, *Association of Public and Land-grant Universities*

Susan Sauer Sloan, *The National Academies of Sciences, Engineering and Medicine*

Amy K. Wolfe, *Oak Ridge National Laboratory*

Section on Statistics

A. John Bailer, *Miami Univ.*

Song Xi Chen, *Peking Univ. (China)*

Dianne M. Finkelstein, *Massachusetts General Hospital/Harvard T. H. Chan School of Public Health*

Edward L. Ionides, *Univ. of Michigan*

David A. Marker, *Westat*

Sharon-Lise Teresa Normand, *Harvard Medical School*

Giovanni Parmigiani, *Dana-Farber Cancer Institute*

RESEARCH

Structure of a mycobacterial respiratory machine

Gong et al., *p. 1020*

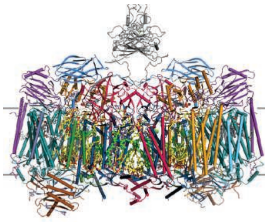

IN *SCIENCE* JOURNALS

Edited by **Stella Hurtley**

ANIMAL CULTURE

Trendsetting flies

Though once believed to be confined to humans, culture has now been demonstrated in many different animal species, from whales to parrots. Most such animals have high levels of cognition, but the basics of transmission and copying could easily occur in less cognitively advanced species. Danchin *et al*. show that mating culture can be passed on in *Drosophila* and model the process by which this occurs (see the Perspective by Whiten). Their results suggest that culture and copying may be much more widespread across the animal kingdom than previously believed. —SNV

Science, this issue p. 1025; see also p. 998

Fruitflies learn behaviors by copying one another.

ARCHAEOLOGY

Paleolithic occupation of Tibet

Human colonization of the high-altitude Tibetan Plateau has generally been thought to have been confined to the past few thousand years of the Holocene. Zhang *et al*. report an investigation of the Nwya Devu archaeological site in central Tibet, 4600 meters above sea level, with Paleolithic occupation dates of ~40 thousand to 30 thousand years ago (see the Perspective by Zhang and Dennell). The site has yielded a range of stone tools, indicating the adaptive ability of early modern humans to the harsh environment of the "roof of the world." The findings also suggest that people from Tibet and Siberia may have interacted at this time. —AMS

Science, this issue p. 1049; see also p. 992

MICROBIOLOGY

A β-barrel trigger for autophagy

Autophagy can help to clear pathogen infections. Chaudhary *et al*. showed that outer membrane proteins with a β-barrel tertiary structure from Gram-negative bacteria or mitochondria were recognized by specific receptors on macrophages and epithelial cells. Adding outer membrane proteins to mouse macrophages induced autophagy and enabled the mice to successfully rid themselves of *Salmonella* Typhimurium infection. Thus, the immune responses activated by outer membrane proteins may contribute to pathogen clearance or autoimmune diseases. —WW

Sci. Signal. **11**, eaat7493 (2018).

METALLURGY

Turning many into one

Single-crystal metal foils are valuable for their surface properties that allow for synthesis of materials like graphene. Jin *et al*. present a strategy for creating colossal single-crystal metal foils called "contact-free annealing" (see the Perspective by Rollett). The method relies on hanging and heating commercially available, inexpensive, cold-rolled metal foils. Almost as if by magic, the polycrystalline grains rotate and anneal into a large single-crystal sheet with a specific crystal orientation. The strategy allows for the creation of much larger and much cheaper single-crystal metal foils. —BG

Science, this issue p. 1021; see also p. 996

SUPERCONDUCTIVITY

Squeezing into the third dimension

Cuprate superconductors are known to harbor charge order in part of their phase diagram. Curiously, the order has a two-dimensional (2D) character at zero magnetic field, whereas a 3D order appears at high fields. Kim *et al*. now show that in a yttrium-based cuprate, a 3D

CREDITS: (TOP TO BOTTOM) GONG *ET AL.*; DANCHIN *ET AL.*

charge order can be induced even at zero magnetic field. The authors compressed the material along one direction and measured a large inelastic x-ray scattering signal that was consistent with the formation of a 3D order. The measurements suggest that the induced order is associated with an optical lattice mode in the material. —JS

Science, this issue p. 1040

CELL BIOLOGY

A stem cell–integrated microneedle patch

More than 600,000 people in the United States suffer a heart attack each year. Stem cell therapy has been used to improve treatment options for survivors, but so far, cardiac stem cell retention rates have been low. To better integrate the stem cells into viable heart tissue, Tang *et al*. created a microneedle patch. Its biocompatible needles penetrate the skin and serve as communication channels between the patch and the heart, getting nutrients to the heart while delivering stem cells to the injured area. When tested in rats and pigs after acute heart attack, the patch boosted the development of heart tissue, reduced scar size, and increased cardiac functions. —PJB

Sci. Adv. 10.1126/sciadv.aat9365 (2018)

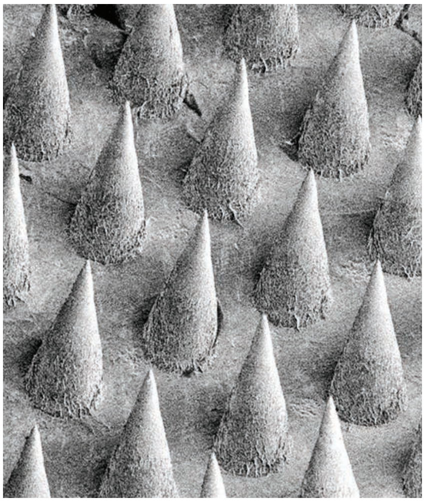

Cardiac stem cells growing on a microneedle array

DISTANT GALAXIES

Mergers drive a powerful dusty quasar

Massive galaxies in the early Universe host supermassive black holes at their centers. When material falls toward the black hole, it releases energy and is observed as a quasar. Astronomers found a population of powerful distant quasars that are obscured by dust, but it has been unclear how they are formed. Díaz-Santos *et al*. observed the dust-obscured quasar WISE J224607.56−052634.9 at submillimeter wavelengths, finding three small companion galaxies connected to the quasar by bridges of gas and dust. They inferred that galaxy mergers can provide both the raw material to power a quasar and large quantities of dust to obscure it. —KTS

Science, this issue p. 1034

CANCER

Hunting and fishing for cancer genes

Mucosal melanoma is a rare, but deadly, form of melanoma that occurs in sun-protected tissues. Little is known about the genetic alterations that drive the growth of these tumors. Ablain *et al*. sequenced mucosal melanomas from 43 patients and found that a substantial fraction showed inactivation or loss of *SPRED1*, a gene that encodes a negative regulator of RAS–MAPK (mitogen-activated protein kinase) signaling. Using a platform called MAZERATI (Modeling Approach in Zebrafish for Rapid Tumor Initiation), they discovered that *SPRED1* loss may help explain the poor response of melanoma patients to drugs that inhibit the KIT tyrosine kinase. The results suggest that a combination of KIT inhibitors and drugs that inhibit MAPK signaling may be more effective. —PAK

Science, this issue p. 1055

IN OTHER JOURNALS

Edited by **Caroline Ash** *and* **Jesse Smith**

Aquilegia coerulea is found widely around the Northern Hemisphere.

PLANT GENOMICS

Columbine's puzzling chromosome

The columbine genus *Aquilegia* is found across the Northern Hemisphere and arose through two adaptive radiations, giving rise to 70 extant species. Filiault *et al.* deep sequenced *Aquilegia coerulea* to create a reference genome and compared it to 10 other sequenced *Aquilegia* spp. from Europe, Asia, and North America. Although the genomes generally exhibited low genetic diversity within species, consistent with previous studies, chromosome 4 showed an overall greater diversity, a higher number of older genetic variants, and different phylogenetic relationships among the species. The differences in chromosome 4 relative to the rest of the genome may be due to hybridization among species and a differential reduction in selection after *Aquilegia* diversified for this chromosome. —LMZ

eLife **7**, e36426 (2018).

BIOTECHNOLOGY

Precision genome engineering

Genome editing through CRISPR-Cas systems has the potential to correct genetic mutations that occur in diseased cells, such as cancer cells. However, the ability to selectively activate CRISPR-Cas systems in diseased cells is important to ensure that gene editing only occurs where it is wanted. Zhu *et al*. developed a system whereby gene editing could be activated by a magnetic field, thus allowing spatial control. The use of

PHOTOS: (LEFT TO RIGHT) TANG *ET AL*., *SCIENCE ADVANCES*, 10.1126/SCIADV.AAT9365 (2018); ISTOCK.COM/MICHAELJUST

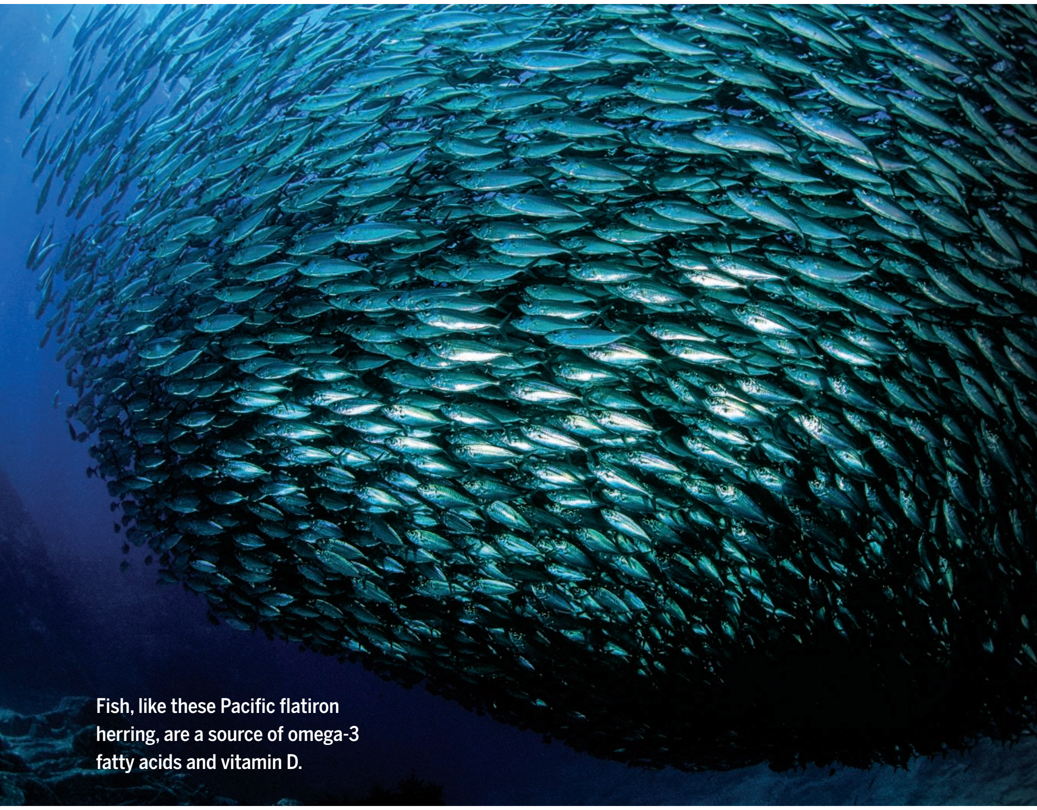

Fish, like these Pacific flatiron herring, are a source of omega-3 fatty acids and vitamin D.

DISEASE PREVENTION

Some fishy supplements?

More than half of the adult population in the United States consumes dietary supplements in the hope of staving off common, life-threatening diseases. Omega-3 fatty acids (fish oil) and vitamin D are especially popular because animal studies and small observational studies hinted that they prevent heart disease and cancer. Manson *et al*. tested these supplements in a randomized placebo-controlled trial of 26,000 people 50 years of age and older. At a median follow-up time of 5 years, there was no evidence that the supplements provided health benefits; the incidences of cancer and cardiovascular disease in the supplement group were similar to those in the placebo group. —PAK

New Engl. J. Med. 10.1056/NEJMoa1809944, 10.1056/NEJMoa1811403 (2018).

nanomagnets in their system also improved transduction into target cells in tumor-bearing mouse models. This approach could potentially allow the translation of CRISPR-Cas systems into therapeutic agents. —GKA

Nat. Biomed. Eng. 10.1038/s41551-018-0318-7 (2018).

PLATELETS

Transfusions for preterm babies

Platelets are immune cell fragments that act like molecular band-aids to control bleeding and help blood to clot. Premature babies can have abnormally low platelet numbers (thrombocytopenia) in the days after birth and are often given platelet transfusions to help prevent infections. Curley *et al*. studied >600 babies in a randomized clinical trial to determine just how low platelets have to get to warrant intervention. Only those infants with severely low platelet levels (<25,000 per cubic millimeter; normal is around 150,000) benefited from transfusion. By contrast, thrombocytopenic babies with somewhat higher platelet counts (<50,000 per cubic millimeter) that received more transfusions had poorer outcomes and an increased rate of death. These surprising findings suggest that not all babies with low platelet counts should receive a prophylactic transfusion, which should lead to safer management of premature babies. —PNK

N. Engl. J. Med. 10.1056/NEJMoa1807320 (2018).

LINGUISTICS

The linguistic expression of senses

In Western cultures, it has been argued that vision and hearing are the senses that are most easily expressed in language. One theory holds that this ease of expression for some senses over others is due to universal features of perception. To test whether there is a universal hierarchy of senses, Majid *et al*. examined how sensory stimuli are linguistically coded across 20 unrelated languages. They found little evidence for a hierarchy of senses, suggesting that although vision and hearing may be the senses most accessible to English speakers, this may not be true in other cultures. These data have implications for understanding the relative influences of culture and language on perceptual experience. —TSR

Proc. Natl. Acad. Sci. U.S.A. **115**, 11369 (2018).

CLIMATE CHANGE

Energy, rain, and the future

The intensification of precipitation over land owing to rising atmospheric temperature is expected to increase in the 21st century, but there are still many details about why and how much that need to be better understood. Richardson *et al*. used a suite of climate models to analyze the atmospheric energy budget and its effects on the fast (due to atmospheric components like carbon dioxide and sulfate) and slow (due to surface temperature changes) drivers of precipitation change. They discuss likely future changes over land and sea and the causes of the past and projected trends and find that the increase may become clearly observable by around 2050. —HJS

J. Clim. **31**, 9641 (2018).

GEOPHYSICS

Dropping ferric iron into a low spin

Iron located in lower-mantle bridgmanites undergoes a spin transition that could alter the seismic properties deep in Earth. Liu *et al*. found that ferric iron undergoes a spin transition in one of the cation sites of mantle bridgmanite at mid-mantle pressures. The completion of this now-well-constrained spin-transition pressure range roughly lines up with the point at which the relative viscosity of the lower mantle decreases while not having much impact on the seismic wave properties. These new data help us understand the dynamics and interpret the seismic picture of Earth's inaccessible mantle. —BG

Nat. Comm. **9**, 1284 (2018).

PHOTO: STEVE BLOOM IMAGES/ALAMY STOCK PHOTO

ALSO IN *SCIENCE* JOURNALS

Edited by **Stella Hurtley**

MICROBIOTA

Metabolic regulation of microbiota

The gut microbiota affects human health, but we are only just beginning to develop a mechanistic understanding of some of the host-microbe interactions involved. Litvak *et al*. review how host colon epithelial cells mediate the symbiosis. Healthy colonocytes maintain anaerobic conditions in the gut lumen because their metabolism ensures rapid oxygen consumption. Such conditions select for obligate anaerobic organisms. These tend to be those that consume dietary fiber and produce short-chain fatty acids beneficial to the host. If there is a shift in colonocyte metabolism—because of disease, diet, or other damage—the epithelium becomes oxygenated. The presence of oxygen allows expansion of facultative aerobic organisms. Microbes in genera that include pathogens are often oxygen-tolerant, and dysbiosis can be the result. —CA

Science, this issue p. 1017

STRUCTURAL BIOLOGY

Molecular-motor coordination

The proteasome is a cytosolic molecular machine that recognizes and degrades unneeded or damaged proteins that have been tagged with ubiquitin. A heterohexameric adenosine triphosphatase motor pulls the substrate into the proteolytic chamber, while at the same time, a protein located at the entrance of this motor removes the ubiquitin. De la Peña *et al*. trapped the substrate inside the motor by inhibiting removal of ubiquitin. This allowed them to determine cryo–electron microscopy structures in the presence of substrate and adenosine triphosphate (ATP). The findings distinguish three sequential conformational states that show how ATP binding, hydrolysis, and phosphate release are coordinated between the six subunits of the motor to cause the conformational changes that translocate the substrate through the proteasome. —VV

Science, this issue p. 1018

BIOCHEMISTRY

Another N-end rule to add

Proteins that emerge from a ribosome bear the N-terminal methionine (Met) residue. In bacteria, Met is formylated before translation starts, whereas in eukaryotes, most nascent proteins seemed to start with unmodified Met. Working in yeast, Kim *et al*. found that the N-terminal formylation of eukaryotic proteins is detectable even under normal conditions and is greatly increased upon specific stresses, which cause some Fmt1 formyltransferase to be retained in the cytoplasm. The retention of this normally mitochondrial protein was found to require the Gcn2 kinase. In addition, the Psh1 ubiquitin ligase was shown to target N-terminally formylated eukaryotic proteins for proteasome-dependent degradation by the so-called fMet/N-end rule pathway. —SMH

Science, this issue p. 1019

STRUCTURAL BIOLOGY

An electron bridge in place of a ferry

Respiratory complexes are massive, membrane-embedded scaffolds that position redox cofactors so as to permit electron transfer coupled to the movement of protons across a membrane. Gong *et al*. used cryo–electron microscopy to determine a structure of a stable assembly of mycobacterial complex III-IV, in which a complex III dimer is sandwiched between two complex IV monomers. A potential direct electron transfer path stretches from the quinone oxidizing centers in complex III to the oxygen reduction centers in complex IV. A loosely associated superoxide dismutase may play a role in detoxifying superoxide produced from uncoupled oxygen reduction. —MAF

Science, this issue p. 1020

SOLID-STATE PHYSICS

Separating structure and electrons in VO_2

Above 341 kelvin—not far from room temperature— bulk vanadium dioxide (VO_2) is a metal. But as soon as the material is cooled below 341 kelvin, VO_2 turns into an insulator and, at the same time, changes its crystal structure from rutile to monoclinic. Lee *et al*. studied the peculiar behavior of a heterostructure consisting of a layer of VO_2 placed underneath a layer of the same material that has a bit less oxygen. In the VO_2 layer, the structural transition occurred at a higher temperature than the metal-insulator transition. In between those two temperatures, VO_2 was a metal with a monoclinic structure—a combination that does not occur in the absence of the adjoining oxygen-poor layer. —JS

Science, this issue p. 1037

COSMOLOGY

Gamma rays reveal the Universe's history

How many stars have formed in the Universe, and when did they do so? These fundamental questions are difficult to answer because there are systematic uncertainties in converting the light we observe into the total mass of stars in galaxies. The Fermi-LAT Collaboration addressed these questions by exploiting the way that gamma rays from distant blazars propagate through intergalactic space, which depends on the total amount of light emitted by all galaxies. The collaboration found that star formation peaked about 3 billion years after the Big Bang (see the Perspective by Prandini). Although this is similar to previous estimates from optical and infrared observations, the results provide valuable confirmation because they should be affected by different systematic effects. —KTS

Science, this issue p. 1031; see also p. 995

NEUROSCIENCE

Memories reach the cortex rapidly

How fast do learning-induced anatomical changes occur in the brain? The traditional view postulates that neocortical memory representations reflect reinstatement processes initiated by the hippocampus and that a genuine physical trace develops only through reactivation over extended periods. Brodt *et al*. combined functional magnetic resonance imaging (MRI) with diffusion-weighted MRI during an associative declarative learning task to examine experience-dependent structural brain plasticity in human subjects (see the Perspective by Assaf). This plasticity was rapidly induced after learning, persisted for more than 12 hours, drove behavior, and was localized in areas displaying memory-related functional brain activity. These plastic changes in the posterior parietal cortex, and their fast temporal dynamics, challenge traditional views of systems memory consolidation. —PRS

Science, this issue p. 1045; see also p. 994

CANCER GENOMICS

scTrio-seq identifies colon cancer lineages

To better design treatments for cancer, it is important to understand the heterogeneity

Published by AAAS

in tumors and how this contributes to metastasis. To examine this process, Bian *et al*. used a single-cell triple omics sequencing (scTrio-seq) technique to examine the mutations, transcriptome, and methylome within colorectal cancer tumors and metastases from 10 individual patients. The analysis provided insights into tumor evolution, linked DNA methylation to genetic lineages, and showed that DNA methylation levels are consistent within lineages but can differ substantially among clones. —LMZ

Science, this issue p. 1060

IMMUNOLOGY

Caspase-8 is a player in pyroptosis

The activation of certain pattern-recognition receptors by pathogen-associated molecular patterns results in the formation of inflammasome complexes. Inflammasome complexes can initiate both the maturation of inflammatory cytokines and pyroptotic cell death via the caspase-mediated cleavage of gasdermin D (GSDMD). As of now, the only known regulators of GSDMD in macrophages are caspase-1 and caspase-11. Orning *et al*. report an additional pathway controlling GSDMD processing. YopJ, an effector molecule produced by *Yersinia* (the causative agent of plague), inhibits TAK1–IκB kinase signaling. This, in turn, results in caspase-8–directed cleavage of GSDMD, pyroptosis, and the release of interleukin 1β (IL-1β) and IL-18. Thus, in the arms race between host and pathogen, the host recognizes signaling disturbances as pathogenic and counters with inflammation and cell death. —STS

Science, this issue p. 1064

CANCER BIOLOGY

Fluid mechanics influence metastasis

To reach distant organs, circulating tumor cells that are shed from primary tumors must withstand considerable shear forces in the lymph and blood. In a Perspective, Goetz discusses the influence of flow mechanics on tumor cell distribution to distant sites and the formation of metastases. Understanding this process more clearly may help identify targets to prevent metastatic outgrowth, the main cause of death in cancer patients. —GKA

Science, this issue p. 999

SURGICAL ADHESIONS

Getting adhesions unstuck

Peritoneal adhesions are ectopic fibrotic tissues induced by surgical perturbations that result in postoperative morbidities such as small bowel obstruction. The cellular origin of adhesions remains unclear. Now, Tsai *et al*. show that mesothelial cells overlying organs and the abdominal wall give rise to adhesions after surgery in mice. The injured mesothelium up-regulated mesothelial-specific genes known to be highly expressed during fetal development. Targeting adhesions with antibodies against the mesothelial marker mesothelin eliminated adhesions that had formed after surgery. Injured mesothelium responded to hypoxia, and this was mediated by the hypoxia-inducible factor 1 alpha (HIF1α) pathway. Blocking HIF1α with small-molecule inhibitors prevented adhesion formation in mice after surgery. —OMS

Sci. Transl. Med. **10**, eaan6735 (2018).

CANCER IMMUNOLOGY

Immunoediting of polychromatic tumors

As tumors grow, they evolve genetically. The resulting genetic heterogeneity contributes to the emergence of variants that may ultimately display increased resistance to immune effector mechanisms and enhanced metastatic potential. Milo *et al*. used multicolor barcoding of a mouse lymphoma line to determine whether increased immune selection pressure by the host accelerates the emergence of dominant clones. When barcoded male lymphoma cells were given to male and female recipients, clonal dominance emerged more rapidly in female recipients because more neoantigens were available to elicit a host T cell response. Checkpoint blockade with anti–PD-1 (programmed cell death protein 1) promoted a similar contraction of intratumor diversity. These findings provide fresh insights into the immunoediting mechanisms by which active antitumor immunity directs the in vivo selection of less immunogenic tumor variants. —IRW

Sci. Immunol. **3**, eaat1435 (2018).

MATERNAL CARE

Spider nursery

Mammals produce milk to feed their offspring, and maternal care often continues well after the young can forage for themselves. Though other cases of milk-like secretions have been found, this combination of ongoing maternal care has largely been considered a uniquely mammalian trait. Chen *et al*. describe an ant-mimicking jumping spider that secretes a nutritious milk-like substance on which its young offspring are entirely dependent. The spider also continues to care for the spiderlings as they mature and become independent. Thus, this type of maternal care may be more widespread than has been assumed. —SNV

Science, this issue p. 1052

REVIEW SUMMARY

MICROBIOTA

Colonocyte metabolism shapes the gut microbiota

Yael Litvak, Mariana X. Byndloss, Andreas J. Bäumler*

BACKGROUND: An imbalance in the colonic microbiota might underlie many human diseases, but the mechanisms that balance our microbial self during homeostasis have long remained elusive. Understanding how our immune system maintains homeostasis is of particular interest in the colon, because this organ harbors the largest microbial community in our body. Recent advances in high-throughput sequencing link an imbalance in this microbial community (dysbiosis) to many chronic human illnesses. Yet it is a daunting task to define what constitutes a balanced microbial community in the colon, because the resident microbiota is highly diverse, differs between individuals, and shifts with changes in the diet. In turn, not knowing what features characterize a balanced colonic microbiota has hampered progress in specifying immune functions or cell types required for maintaining homeostasis in the colon.

ADVANCES: Clues about immune functions important for balancing the microbiota have emerged by viewing coevolution of microbial communities with their hosts from an ecological perspective, which suggests that our immune system evolved to maintain homeostasis by shaping the microbiota to be beneficial. The central role of colonic epithelial cells (colonocytes) in maintaining homeostasis by shaping the colonic microbiota to provide benefit is now beginning to be appreciated. Recent insights suggest that, similar to macrophages, differentiated colonocytes can polarize metabolically into distinct effector phenotypes. During gut homeostasis, the metabolism of surface colonocytes is directed toward oxidative phosphorylation and oxidation of fatty acids, resulting in high epithelial oxygen consumption. The consequent epithelial hypoxia helps to maintain a microbial community dominated by obligate anaerobic bacteria, which provide benefit by converting fiber into fermentation products that are absorbed by the host. Conditions that shift the metabolism of colonocytes away from lipid oxidation cause an increase in the amount of oxygen emanating from the mucosal surface, thereby driving a shift in the microbial community from obligate to facultative anaerobes, a hallmark of dysbiosis in the colon. Thus, the metabolism of colonocytes functions as a control switch of the gut microbiota, mediating a shift between homeostatic and dysbiotic communities. Subversion of colonocyte cell metabolism by enteric pathogens is a recently uncovered virulence strategy that enables these intruders to escape niche protection conferred by the gut microbiota.

ON OUR WEBSITE

Read the full article at http://dx.doi.org/10.1126/science.aat9076

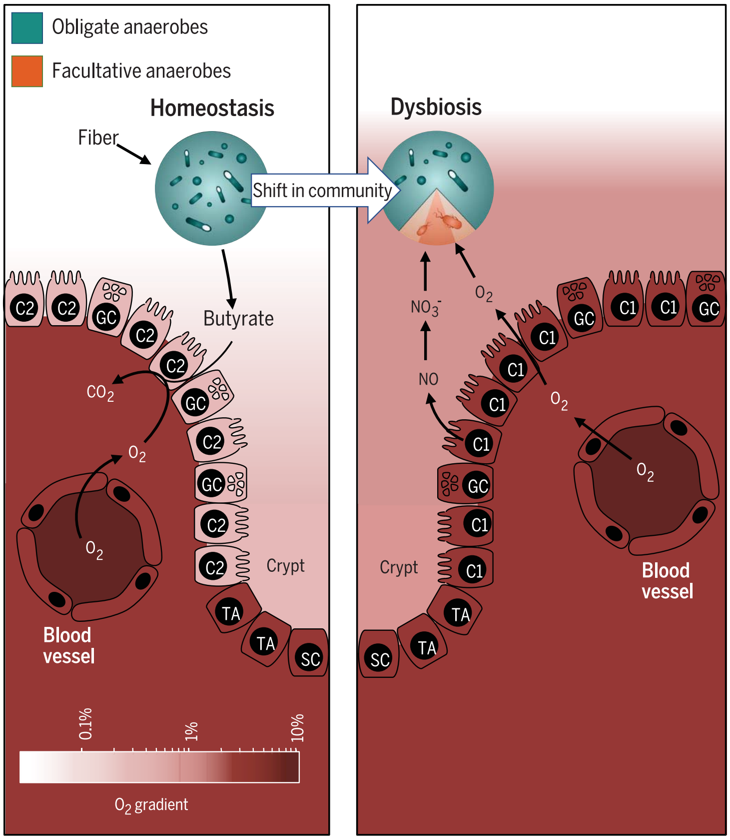

Epithelial metabolism shapes the colonic microbiota. Left: During gut homeostasis, obligate anaerobic bacteria convert fiber into fermentation products (butyrate) to maintain the epithelium in a metabolic state characterized by high oxygen consumption. This metabolic polarization of differentiated colonocytes (C2) maintains epithelial hypoxia (<1% oxygen) to limit the amount of oxygen (O_2) diffusing into the gut lumen. Right: A metabolic reorientation of terminally differentiated colonocytes toward low oxygen consumption (C1) increases the concentration of respiratory electron acceptors (O_2 and NO_3^-) emanating from the epithelial surface, thereby causing a shift in the microbial community from obligate to facultative anaerobic bacteria. The color scale at the bottom indicates O_2 levels. SC, stem cell; TA, undifferentiated transit-amplifying cell; C2, terminally differentiated C2-skewed colonocyte; C1, terminally differentiated C1-skewed colonocyte; GC, goblet cell; NO, nitric oxide.

OUTLOOK: The concept that colonocyte metabolism is a common driver of dysbiosis in the large bowel has ramifications for the design of intervention strategies. Because our immune system already has a way to balance the colonic microbiota by maintaining an epithelial surface that is metabolically polarized toward oxidative phosphorylation, harnessing this host control mechanism for therapeutic means could provide an alternative to targeting the microbes themselves for remediation of dysbiosis. Metabolic reprogramming of colonocytes to restore epithelial hypoxia represents a promising new therapeutic approach for rebalancing the colonic microbiota in a broad spectrum of human diseases. ■

Department of Medical Microbiology and Immunology, School of Medicine, University of California, Davis, CA 95616, USA.
***Corresponding author. Email: ajbaumler@ucdavis.edu**
Cite this article as Y. Litvak *et al.*, *Science* 362, eaat9076 (2018). DOI: 10.1126/science.aat9076

Litvak *et al.*, *Science* **362**, 1017 (2018) 30 November 2018 **1 of 1**

REVIEW

MICROBIOTA

Colonocyte metabolism shapes the gut microbiota

Yael Litvak, Mariana X. Byndloss*, Andreas J. Bäumler†

An imbalance in the colonic microbiota might underlie many human diseases, but the mechanisms that maintain homeostasis remain elusive. Recent insights suggest that colonocyte metabolism functions as a control switch, mediating a shift between homeostatic and dysbiotic communities. During homeostasis, colonocyte metabolism is directed toward oxidative phosphorylation, resulting in high epithelial oxygen consumption. The consequent epithelial hypoxia helps to maintain a microbial community dominated by obligate anaerobic bacteria, which provide benefit by converting fiber into fermentation products absorbed by the host. Conditions that alter the metabolism of the colonic epithelium increase epithelial oxygenation, thereby driving an expansion of facultative anaerobic bacteria, a hallmark of dysbiosis in the colon. Enteric pathogens subvert colonocyte metabolism to escape niche protection conferred by the gut microbiota. The reverse strategy, a metabolic reprogramming to restore colonocyte hypoxia, represents a promising new therapeutic approach for rebalancing the colonic microbiota in a broad spectrum of human diseases.

One major task of our immune system is to defend against microbial pathogens, such as bacteria, viruses, parasites, or fungi, by recognizing these intruders and removing them from the body. The emerging field of microbiota research has raised awareness that our immune system might also act to balance microbial communities inhabiting our skin and mucosal surfaces (the microbiota). Although we know in some detail the immune functions that control microbial pathogens, we know little about the host cell types and mechanisms involved in balancing our microbial self. Understanding how our immune system maintains homeostasis is of particular importance in the colon because it harbors the largest microbial community in our body. Recent advances in high-throughput sequencing link an imbalance in this microbial community (dysbiosis) to many chronic human illnesses, including colorectal cancer, obesity, diabetes, arthritis, asthma, cardiovascular disease, and neurological disorders [reviewed in (*1*)]. Yet it is a daunting task to define what a balanced microbial community in the colon represents, because the resident microbiota is highly diverse (*2*), differs between individuals (*3*), and shifts with changes in the diet (*4*). In turn, not knowing what features characterize a balanced colonic microbiota has hampered progress in specifying the immune functions or cell types required for maintaining homeostasis in the colon.

Homeostasis: Pulling diffuse concepts into focus

Clues about immune functions important for balancing the microbiota have emerged by viewing coevolution of microbial communities with their hosts from an ecological perspective, which suggests that the immune system maintains homeostasis by shaping the microbiota to be beneficial (*5*). Applying this concept to the colonic microbiota puts the spotlight on the benefit provided by this microbial community, which is to aid in the digestion of nutrients that cannot be processed by host enzymes. Specifically, complex dietary carbohydrates (fiber) are broken down by the colonic microbiota into fermentation products that are absorbed by the host (*6*) and contribute to host nutrition (*7*), immune development (*8*–*11*), and niche protection against enteric pathogens (*12*). Bacterial diversity in the colon is beneficial because it increases the probability of including species that can break down any complex carbohydrate into fermentation products (*13*). Members of the classes Clostridia (phylum Firmicutes) and Bacteroidia (phylum Bacteroidetes), which dominate the community of obligate anaerobic bacteria in the adult colon, provide benefit because they encode a broad spectrum of enzymes for hydrolyzing different complex carbohydrates (*14*). In contrast, facultative anaerobic bacteria, such as members of the phylum Proteobacteria, do not specialize in consuming fiber and might even interfere with host nutrition by metabolizing fermentation products to carbon dioxide when oxygen is present (*15*, *16*). Thus, viewing host control over microbes from an ecological perspective predicts that our immune system maintains homeostasis by shaping the colonic microbiota to be diverse and dominated by obligate anaerobic bacteria, thereby ensuring that this microbial community provides benefit by generating fermentation products from fiber (*17*).

Studies of host control mechanisms that shape the colonic microbiota to be beneficial suggest that colonic epithelial cells (colonocytes) play a central role in this process (*12*), which is somewhat surprising because immune functions are typically associated with cells of the hematopoietic lineage. The colonic epithelium is continually renewed by colonic stem cells located at the base of intestinal glands, termed the crypts of Lieberkühn. Asymmetric cell division of colonic stem cells generates transit-amplifying cells, an early intermediate cell type involved in tissue regeneration that divides a finite number of times until terminally differentiating into various epithelial cell types, including colonocytes, enteroendocrine cells, and goblet cells (*18*). The dividing cells located at the base of crypts obtain energy through anaerobic glycolysis, which is characterized by conversion of glucose into lactate even in the presence of oxygen (*19*), a process known as the Warburg metabolism (*20*). Epithelial differentiation requires PPAR-γ (peroxisome proliferator-activated receptor–γ) (*21*), a nuclear receptor primarily synthesized in differentiated cells of the colonic epithelium of rodents and humans (*22*). PPAR-γ activates fatty acid metabolism, resulting in mitochondrial β-oxidation of long-chain and short-chain fatty acids and oxygen consumption through oxidative phosphorylation (*23*–*25*). This energy metabolism of mature colonocytes is characterized by high oxygen consumption, resulting in an oxygen partial pressure of less than 7.6 mmHg (<1% oxygen), a condition known as epithelial hypoxia (*26*). Because oxygen freely diffuses across biological membranes, epithelial hypoxia limits the amount of oxygen emanating from the mucosal surface, which helps to maintain anaerobiosis in the intestinal lumen (Fig. 1A) (*27*). In turn, anaerobiosis ensures that the colonic microbiota is dominated by obligate anaerobic bacteria, which provide benefit to the host by converting fiber into fermentation products (*17*). Through this mechanism, the colonic epithelium shapes the microbiota to be beneficial, thereby maintaining gut homeostasis.

Colonocyte metabolism drives gut dysbiosis

The above considerations suggest that the colonic epithelium might contribute to immune functions that maintain homeostasis by shaping the microbiota to be beneficial (*5*). Therefore, an imbalance in the microbial community could be caused by an underlying defect in epithelial immune functions that maintain homeostasis in the colon (*17*). Dysbiosis in the colon is commonly associated with an increased abundance of facultative anaerobic bacteria (*28*, *29*), which is observed in individuals undergoing antibiotic therapy (*30*), consuming a high-fat Western-style diet (*31*, *32*), or suffering from inflammatory bowel disease (*33*), colorectal cancer (*34*), irritable

---

Department of Medical Microbiology and Immunology, School of Medicine, University of California, Davis, CA 95616, USA.
*Present address: Department of Pathology, Microbiology and Immunology, Vanderbilt University Medical Center, Nashville, TN 37232, USA.
†Corresponding author. Email: ajbaumler@ucdavis.edu

bowel syndrome (35, 36), or necrotizing enterocolitis (37). Because only facultative anaerobic bacteria can respire oxygen, it has been proposed that a shift in the microbial community from obligate to facultative anaerobic bacteria might be associated with a disruption in anaerobiosis, a concept known as the "oxygen hypothesis" (38). We now know that the population of facultative anaerobic bacteria expands in the colon during dysbiosis because a disruption of epithelial hypoxia increases the amount of oxygen emanating from the colonic epithelium (39). Thus, the shift in the colonic microbiota composition from obligate to facultative anaerobic bacteria, associated with many chronic human illnesses, might have a common underpinning in colonocyte dysfunction (27).

Early insights into mechanisms that disrupt gut homeostasis were obtained by studying the effect of antibiotic treatment (40), which alters epithelial metabolism by depleting microbes that produce fermentation products, including the short-chain fatty acids butyrate, propionate, and acetate (12). Short-chain fatty acids are absorbed in the colon, where they bind to G protein–coupled receptors to maintain the regulatory T cell pool in the murine mucosa, thereby inhibiting intestinal inflammation (8–11). Butyrate activates PPAR-γ signaling in human epithelial cells (41) to drive the metabolism of surface colonocytes toward mitochondrial β-oxidation of fatty acids (23–25), which is important for maintaining epithelial hypoxia (12). Thus, antibiotic-mediated depletion of short-chain fatty acids silences epithelial PPAR-γ signaling (12) and lowers the number of regulatory T cells in mouse models (8, 11). As a result, antibiotic treatment increases the inflammatory tone of the colonic mucosa (42). The concomitant elevation of inflammatory signals shifts the metabolism of terminally differentiated surface colonocytes toward anaerobic glycolysis, a metabolism characterized by low oxygen consumption, high glucose consumption, and high lactate release (12, 43). This metabolic reprogramming results in a loss of epithelial hypoxia (40). In turn, increased epithelial oxygenation elevates the amount of oxygen emanating from the mucosal surface, thereby driving an expansion of facultative anaerobic bacteria by aerobic respiration (Fig. 1B) (12, 44).

Metabolic polarization of colonocytes

The picture emerging from these studies is that in a healthy gut, butyrate-activated PPAR-γ signaling increases oxygen consumption in terminally differentiated colonocytes by polarizing their intracellular metabolism toward mitochondrial β-oxidation of fatty acids. However, proinflammatory signals can change the colonocyte phenotype by reorienting their metabolism toward anaerobic glycolysis, thereby lowering oxygen consumption, which ultimately leads to a shift in the microbial community from obligate to facultative anaerobic bacteria (17). These two opposing colonocyte phenotypes are strikingly similar to the alternatively activated (M2) and classically activated (M1) polarization states of macrophages, which also require a reversible metabolic reprogramming. Although the M1-M2 dichotomy is an oversimplification, macrophages in vivo regularly mimic M1 or M2 polarization states, which continues to make this nomenclature useful (45). During M2 polarization, interleukin (IL)–4 and IL-13 induce STAT6 signaling to activate PPAR-γ, which drives the energy metabolism of macrophages toward mitochondrial β-oxidation of fatty acids and oxidative phosphorylation (Fig. 2A) (46). In contrast, M1 macrophages emerge when proinflammatory signals, such as gamma interferon (IFN-γ) or lipopolysaccharide (LPS), polarize the macrophage metabolism toward anaerobic glycolysis, thereby increasing glucose consumption and lactate release (Fig. 2B) (45). One metabolic signature of M1 macrophages is the conversion of L-arginine and oxygen into nitric oxide and L-citrulline by inducible nitric oxide synthase (iNOS). Similarly, metabolic polarization of colonocytes toward anaerobic glycolysis is accompanied by elevated iNOS synthesis and increased nitric oxide production (12). In the intestinal lumen, nitric oxide is converted into nitrate, which can be used by many facultative anaerobic bacteria as an electron acceptor for anaerobic respiration (47). In turn, colonocyte-derived nitrate contributes to a dysbiotic expansion of facultative anaerobic Proteobacteria, such as *Escherichia coli*, in the colon of antibiotic-treated mice (12, 42, 44). Together, these findings indicate that the different metabolic states adopted by colonocytes during gut homeostasis or dysbiosis closely resemble the metabolic programming of M2 or M1 macrophages.

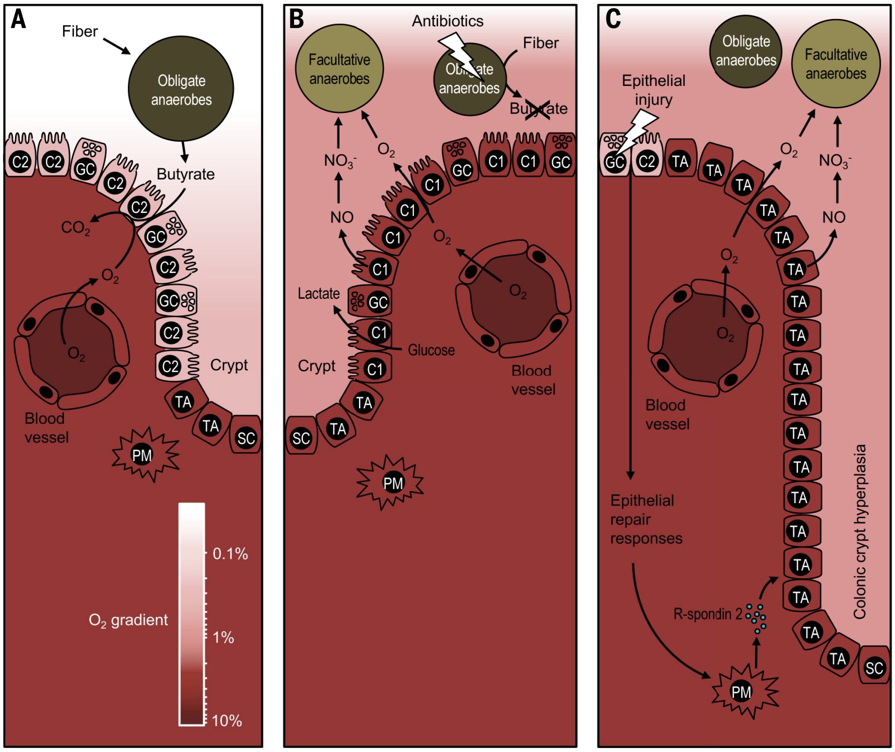

Fig. 1. Epithelial metabolism shapes the colonic microbiota. (**A**) During gut homeostasis, obligate anaerobic bacteria convert fiber into fermentation products, such as butyrate, to maintain differentiated colonocytes in a C2-skewed metabolic state. The metabolism of C2-skewed colonocytes is characterized by high oxygen consumption, which maintains epithelial hypoxia (<1% oxygen) to limit the amount of oxygen diffusing into the gut lumen. The color scale at the bottom indicates oxygen (O_2) levels, which are between 3% and 10% in normoxic tissue (85). (**B**) Disruption of the gut microbiota by antibiotic treatment depletes microbe-derived fermentation products, causing a metabolic reorientation of terminally differentiated colonocytes toward a C1-skewed metabolism, which is characterized by high lactate release, low oxygen consumption, and elevated synthesis of iNOS, an enzyme that generates nitric oxide (NO). Conversion of nitric oxide into nitrate (NO_3^-) in the gut lumen together with oxygen (O_2) emanating from C1-skewed colonocytes provide electron acceptors that drive an expansion of facultative anaerobic bacteria. (**C**) Epithelial injury activates epithelial repair responses, including a release of R-spondin 2 to stimulate cell division of undifferentiated transit-amplifying cells. Excessive cell division of undifferentiated transit-amplifying cells leads to colonic crypt hyperplasia and an increased epithelial oxygenation. Nitrate and oxygen emanating from the mucosal surface during colonic crypt hyperplasia drive an expansion of facultative anaerobic bacteria. PM, pericryptal myofibroblast; SC, stem cell; TA, undifferentiated transit-amplifying cell; C2, terminally differentiated C2-skewed colonocyte; C1, terminally differentiated C1-skewed colonocyte; GC, goblet cell.

To better conceptualize how the host shapes its colonic microbiota, it seems useful to expand the concept that metabolic features of even nonhematopoietic host cells are deeply associated with immune functions. By analogy with macrophage polarization, microbiota-derived signals, such as short-chain fatty acids, induce a homeostatic (C2) activation state in colonocytes to maintain anaerobiosis (Fig. 2C), which in turn ensures that obligate anaerobic bacteria dominate the microbial community, thereby completing the circuit and guaranteeing microbial conversion of fiber into fermentation products (Fig. 1A). Conversely, dysbiosis ensues when the colonic epithelium loses its homeostatic C2 state. For example, a metabolic reprogramming of terminally differentiated colonocytes toward an inflammation-associated (C1) activation state (Fig. 2D) (*12*, *43*) elevates the luminal availability of host-derived respiratory electron acceptors, thereby fueling a dysbiotic expansion of facultative anaerobic Enterobacteriaceae, a family within the phylum Proteobacteria (*12*). Thus, maintenance of a microbiota composition characteristic of a healthy gut is intimately linked to a homeostatic C2-skewed metabolism of differentiated surface colonocytes in the colon.

Colonocyte metabolism in ulcerative colitis

A homeostatic C2-skewed colonic epithelial surface can also be lost during excessive epithelial repair, which is observed during ulcerative colitis, an inflammatory bowel disease affecting the colon. To repair epithelial injury, pericryptal myofibroblasts secrete the mitogen R-spondin 2, which triggers division of colonic stem cells and undifferentiated transit-amplifying cells near the base of the crypts (*48*). Excessive epithelial repair drives an accumulation of dividing transit-amplifying cells, thereby causing crypt elongation. This histopathological change is known as colonic crypt hyperplasia (*48*), which is a common feature of ulcerative colitis. This hyperplasia gives rise to a reduction in the number of terminally differentiated epithelial cells, such as goblet cells, and a concomitant thinning of the mucus layer in patients with ulcerative colitis (*49*, *50*). Because PPAR-γ is primarily synthesized in terminally differentiated epithelial cells (*22*), the accumulation of undifferentiated transit-amplifying cells is expected to lower epithelial PPAR-γ synthesis during colonic crypt hyperplasia, thereby reducing mitochondrial β-oxidation of fatty acids in the colonic epithelium. Consistent with this prediction, colonic epithelial cells from ulcerative colitis patients exhibit lower epithelial PPAR-γ synthesis (*51*) and reduced mitochondrial β-oxidation of butyrate to carbon dioxide (*52*). Low epithelial PPAR-γ synthesis resulting from the accumulation of transit-amplifying cells might also contribute to the development of a "leaky gut"; diminished epithelial PPAR-γ signaling increases colonic permeability in a rat colitis model (*53*), presumably because PPAR-γ up-regulates tight junction molecules in epithelial cells (Fig. 2C) (*54*). The metabolism of transit-amplifying cells is characterized by low oxygen consumption (*19*), so an accumulation of these cells increases epithelial oxygenation (*55*). Another by-product of colitis is the generation of nitrate in the gut lumen (*56*), which depends on synthesis of the host enzyme iNOS (*47*). The increased luminal availability of oxygen and nitrate allows populations of facultative anaerobic Enterobacteriaceae, such as *E. coli*, to expand in mouse models of ulcerative colitis (Fig. 1C) (*47*, *57*). Thus, the hypothesis that dysanaerobiosis is a driver of dysbiosis during ulcerative colitis (*38*, *58*) can be explained mechanistically in animal models by the loss of a C2-skewed epithelial surface during colonic crypt hyperplasia.

The observation that ulcerative colitis can respond to antibiotic treatment suggests that dysbiosis exacerbates intestinal inflammation (*59*), although the underlying mechanism is not fully resolved. However, disruption of the gut microbiota with broad-spectrum antibiotics is itself associated with dysbiosis (*60*), indicating that a rational manipulation of the gut microbiota by targeting only potentially harmful microbes could provide greater benefit. Consistent with this idea, intestinal inflammation can be moderated by selectively inhibiting an expansion of facultative anaerobic Enterobacteriaceae through precision editing of the gut microbiota in mouse

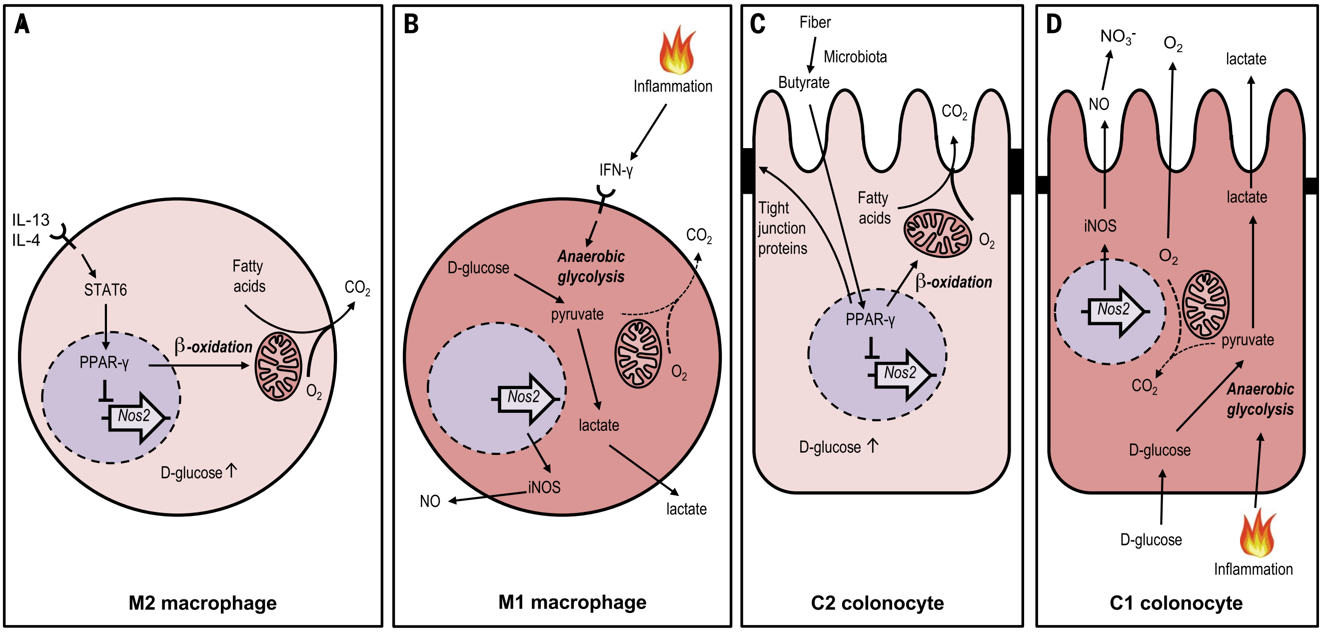

Fig. 2. Extending the M1/M2 paradigm to colonocytes. (**A** and **B**) Cytokine signaling can polarize macrophage metabolism and function, a process that is reversible. (A) IL-4 and IL-13 stimulate polarization into alternatively activated M2 macrophages by inducing STAT6 signaling to drive a PPAR-γ–dependent activation of mitochondrial β-oxidation and concomitant repression of the *Nos2* gene. (B) Proinflammatory signals, such as IFN-γ, stimulate polarization into classically activated M1 macrophages by shifting the host cell metabolism toward anaerobic glycolysis. (**C**) The microbiota converts fiber into fermentation products, such as butyrate, which stimulates a metabolic polarization into homeostatically activated C2 colonocytes by inducing a PPAR-γ–dependent activation of mitochondrial β-oxidation, thereby lowering epithelial oxygenation. (**D**) Proinflammatory signals stimulate a metabolic polarization into C1 colonocytes by shifting the host cell metabolism toward anaerobic glycolysis, thereby increasing epithelial oxygenation, which results in oxygen (O_2) emanating from the epithelial surface. Lactate produced during anaerobic glycolysis is released into the gut lumen, whereas nitric oxide (NO) produced by iNOS is converted to nitrate (NO_3^-).

models of ulcerative colitis (61). This approach is based on selective inhibition of molybdenum cofactor–dependent microbial respiratory pathways that are operational only during episodes of inflammation (61), thus providing a proof of concept that rational chemical modulation of specific enzymatic activities in complex microbial communities could be developed as an intervention strategy (62).

Because the host maintains homeostasis using a C2-skewed colonocyte metabolism, harnessing this epithelial control mechanism for therapeutic purposes could be an alternative strategy for rebalancing the microbiota. Specifically, a PPAR-γ–mediated differentiation of transit-amplifying cells into colonocytes would be expected to restore a C2-type epithelial surface, thereby remediating dysbiosis and reducing inflammation. Consistent with this idea, treatment with PPAR-γ agonists reduces crypt hyperplasia by inhibiting excessive division of transit-amplifying cells (63). Furthermore, topical treatment of the epithelial surface with the PPAR-γ agonist 5-aminosalicylic acid is a first-line therapy for bringing mild to moderate cases of ulcerative colitis into remission (64–67) and is associated with lowering the abundance of Proteobacteria in the colonic microbiota (68). These data support the hypothesis that rebalancing the gut microbiota by reinstating a homeostatic C2 state of the colonic surface (12) represents a feasible therapeutic approach for restoring homeostasis (68).

Pathogens manipulate colonocyte metabolism for growth

Some intracellular bacterial pathogens can alter macrophage polarization to obtain nutrients from host cells to support microbial growth and long-term persistence in host tissue (69). One example is *Brucella abortus*, a pathogen that persists in M2-polarized macrophages of the murine liver and spleen. PPAR-γ–activated β-oxidation of fatty acids leads to a high availability of glucose (Fig. 2A), a carbon source that fuels pathogen growth within alternatively activated macrophages (70). Similar to an exploitation of macrophage polarization, recent findings suggest that bacterial pathogens can also manipulate colonocyte metabolism to favor their luminal growth during competition with the gut microbiota.

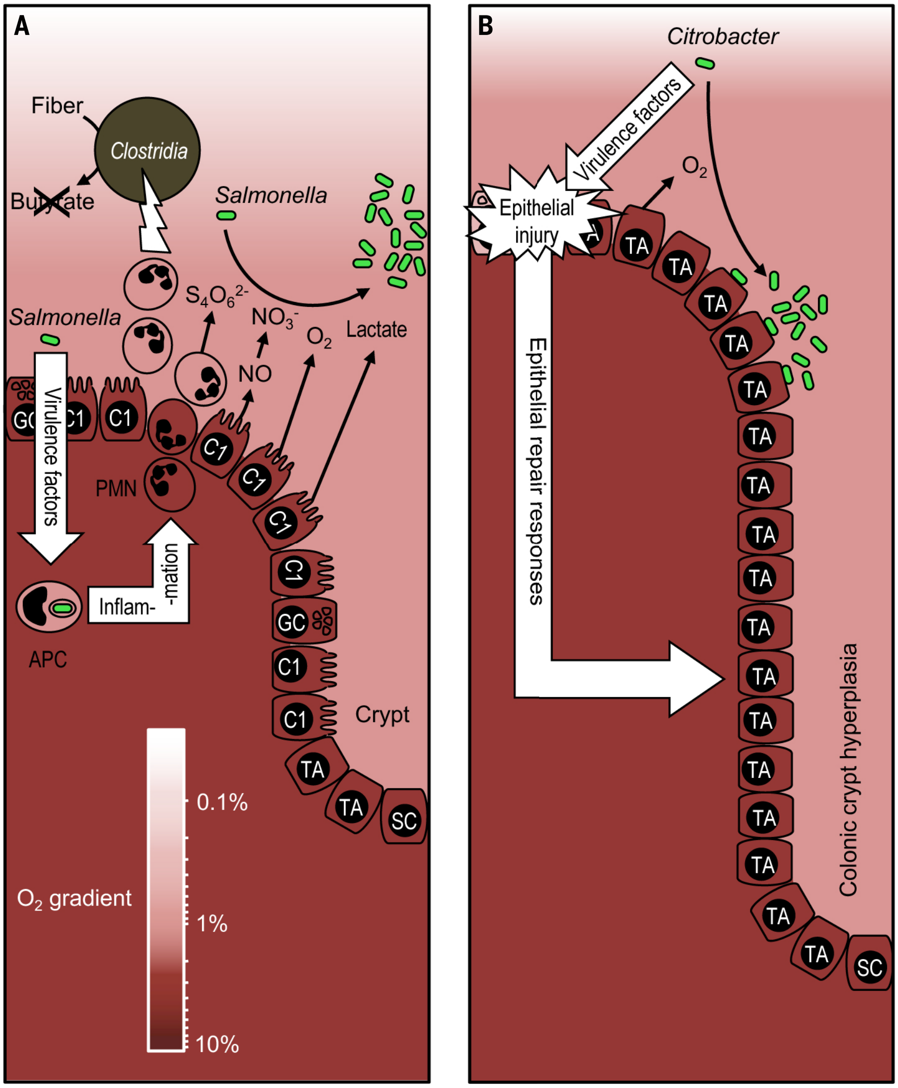

Fig. 3. Enteric pathogens overcome niche protection by manipulating colonocyte metabolism. (**A**) *S. enterica* (*Salmonella*) uses its virulence factors to trigger neutrophil transepithelial migration, which leads to a depletion of *Clostridia*, thereby lowering the luminal concentration of short-chain fatty acids such as butyrate. The consequent metabolic reprogramming of the epithelium increases the luminal bioavailability of oxygen (O_2) and lactate. The inflammatory response generates additional electron acceptors, including tetrathionate ($S_4O_6^{2-}$) and nitrate (NO_3^-). These host-derived resources drive an expansion of the facultative anaerobic pathogen. (**B**) Virulence factors of *C. rodentium* (*Citrobacter*) cause epithelial injury, thereby triggering epithelial repair responses leading to colonic crypt hyperplasia. The resulting increase in epithelial oxygenation drives a *C. rodentium* expansion by aerobic respiration. APC, antigen-presenting cell; PMN, neutrophil; other abbreviations as in Fig. 1.

An important function of a C2-skewed colonic surface is to limit the luminal availability of host-derived respiratory electron acceptors, which confers niche protection against facultative anaerobic enteric pathogens (60). The enteric pathogen *Salmonella enterica* (family Enterobacteriaceae) overcomes such niche protection by using its virulence factors to trigger severe acute intestinal inflammation (71). Neutrophils migrating into the intestinal lumen during gut inflammation deplete *Clostridia* spp. (72, 73). This has the effect of decreasing the concentration of short-chain fatty acids, which steers the metabolism of terminally differentiated colonocytes toward an inflammation-associated C1 activation state and increased epithelial oxygenation (43, 74). The respiratory burst of phagocytes migrating into the intestinal lumen during *S. enterica*–induced colitis generates additional electron acceptors for anaerobic respiration, including nitrate (75, 76) and tetrathionate (77) (Fig. 3A). *S. enterica* uses a combination of aerobic and anaerobic respiration to expand in the lumen of the inflamed gut (74). Respiration provides *S. enterica* a growth advantage over obligate anaerobic bacteria because it enables the pathogen to consume microbiota-derived fermentation products, such as succinate (16), butyrate (15), ethanolamine (78), or 1,2-propanediol (79). Interestingly, the high lactate release characteristic of a C1-skewed epithelial surface (Fig. 1B) also provides *S. enterica* with a host-derived carbon source to support its respiratory growth (43) (Fig. 3A). Thus, *S. enterica* uses its virulence factors to direct the epithelial surface toward a C1 activation state, which provides the pathogen with both a host-derived electron acceptor (i.e., oxygen) and a host-derived carbon source (i.e., lactate) and thus allows it to outcompete obligate anaerobic bacteria in the gut lumen (43, 74).

Citrobacter rodentium (family Enterobacteriaceae) is an enteric pathogen of mice that uses virulence mechanisms similar to those employed by human attaching-and-effacing pathogens, such as enteropathogenic *E. coli* (EPEC) or enterohemorrhagic *E. coli* (EHEC) (80). *C. rodentium* uses its virulence factors to intimately attach to the colonic surface, which enables the pathogen to compete with the gut microbiota (81, 82). Epithelial injury caused by *C. rodentium* virulence factors triggers excessive epithelial repair, leading to colonic crypt hyperplasia and accumulation of undifferentiated transit-amplifying cells at the mucosal surface (Fig. 1C) (80). The resulting loss of a C2-skewed epithelium increases the amount of oxygen emanating from the mucosal surface and drives growth of *C. rodentium* through aerobic respiration (55) (Fig. 3B). Respiration supports growth of *C. rodentium* on microbiota-derived fermentation products, such as formate, which enables the pathogen to compete with the gut microbiota (55).

These results indicate that both *S. enterica* and *C. rodentium* use their virulence factors to ablate a homeostatic C2-skewed colonic surface, albeit through different mechanisms. However, in each case the pathogen alters colonocyte metabolism to obtain critical resources from host cells to allow it to compete against the resident gut microbiota. Thus, subversion of colonocyte cell metabolism by enteric pathogens is emerging as a novel strategy to overcome niche protection conferred by the gut microbiota.

Future directions

The finding that colonocytes play a central role in sculpting the gut microbiota points to changes in colonocyte metabolism as a common driver of dysbiosis in the large bowel (17). We argue that metabolic polarization of colonocytes functions as a control switch for the gut microbiota, mediating the shift between balanced and dysbiotic communities. There is compelling evidence that loss of C2-skewed colonocytes contributes to dysbiosis in antibiotic-treated mice (12), chemically induced colitis (47, 57), or infection with enteric pathogens (43, 55, 74). Decreased colonic PPAR-γ synthesis has been observed in rhesus macaques chronically infected with simian immunodeficiency virus (83), which suggests that a change in colonocyte metabolism might also underpin the expansion of Proteobacteria observed in HIV-infected subjects (84). However, additional work is needed to investigate whether changes in the microbial community from obligate to facultative anaerobic bacteria observed in patients with colorectal cancer (34) or irritable bowel syndrome (35, 36), or in individuals consuming a high-fat Western-style diet (31, 32), are caused by an underlying loss of C2-skewed colonocytes. The view that our immune system balances the colonic microbiota by maintaining a C2-skewed epithelial surface suggests that harnessing this host control mechanism for therapeutic means could provide an alternative to targeting the microbes themselves for remediating dysbiosis, and may lead to new therapeutic strategies for rebalancing the colonic microbiota in a broad spectrum of human diseases.

REFERENCES AND NOTES

1. P. D. Cani, Gut microbiota—at the intersection of everything? *Nat. Rev. Gastroenterol. Hepatol.* **14**, 321–322 (2017). doi: 10.1038/nrgastro.2017.54; pmid: 28442782
2. P. B. Eckburg *et al*., Diversity of the human intestinal microbial flora. *Science* **308**, 1635–1638 (2005). doi: 10.1126/science.1110591; pmid: 15831718
3. J. Tap *et al*., Towards the human intestinal microbiota phylogenetic core. *Environ. Microbiol.* **11**, 2574–2584 (2009). doi: 10.1111/j.1462-2920.2009.01982.x; pmid: 19601958
4. P. J. Turnbaugh *et al*., The effect of diet on the human gut microbiome: A metagenomic analysis in humanized gnotobiotic mice. *Sci. Transl. Med.* **1**, 6ra14 (2009). doi: 10.1126/scitranslmed.3000322; pmid: 20368178
5. K. R. Foster, J. Schluter, K. Z. Coyte, S. Rakoff-Nahoum, The evolution of the host microbiome as an ecosystem on a leash. *Nature* **548**, 43–51 (2017). doi: 10.1038/nature23292; pmid: 28770836
6. G. den Besten *et al*., The role of short-chain fatty acids in the interplay between diet, gut microbiota, and host energy metabolism. *J. Lipid Res.* **54**, 2325–2340 (2013). doi: 10.1194/jlr.R036012; pmid: 23821742
7. O. C. Velázquez, H. M. Lederer, J. L. Rombeau, Butyrate and the colonocyte. Production, absorption, metabolism, and therapeutic implications. *Adv. Exp. Med. Biol.* **427**, 123–134 (1997). pmid: 9361838
8. K. Atarashi *et al*., Induction of colonic regulatory T cells by indigenous Clostridium species. *Science* **331**, 337–341 (2011). doi: 10.1126/science.1198469; pmid: 21205640
9. N. Arpaia *et al*., Metabolites produced by commensal bacteria promote peripheral regulatory T-cell generation. *Nature* **504**, 451–455 (2013). doi: 10.1038/nature12726; pmid: 24226773
10. Y. Furusawa *et al*., Commensal microbe-derived butyrate induces the differentiation of colonic regulatory T cells. *Nature* **504**, 446–450 (2013). doi: 10.1038/nature12721; pmid: 24226770
11. P. M. Smith *et al*., The microbial metabolites, short-chain fatty acids, regulate colonic T_{reg} cell homeostasis. *Science* **341**, 569–573 (2013). doi: 10.1126/science.1241165; pmid: 23828891
12. M. X. Byndloss *et al*., Microbiota-activated PPAR-γ signaling inhibits dysbiotic Enterobacteriaceae expansion. *Science* **357**, 570–575 (2017). doi: 10.1126/science.aam9949; pmid: 28798125
13. N. T. Porter, E. C. Martens, The Critical Roles of Polysaccharides in Gut Microbial Ecology and Physiology. *Annu. Rev. Microbiol.* **71**, 349–369 (2017). doi: 10.1146/annurev-micro-102215-095316; pmid: 28657886
14. A. El Kaoutari, F. Armougom, J. I. Gordon, D. Raoult, B. Henrissat, The abundance and variety of carbohydrate-active enzymes in the human gut microbiota. *Nat. Rev. Microbiol.* **11**, 497–504 (2013). doi: 10.1038/nrmicro3050; pmid: 23748339
15. D. N. Bronner *et al*., Genetic Ablation of Butyrate Utilization Attenuates Gastrointestinal Salmonella Disease. *Cell Host Microbe* **23**, 266–273.e4 (2018). doi: 10.1016/j.chom.2018.01.004; pmid: 29447698
16. L. Spiga *et al*., An Oxidative Central Metabolism Enables Salmonella to Utilize Microbiota-Derived Succinate. *Cell Host Microbe* **22**, 291–301.e6 (2017). doi: 10.1016/j.chom.2017.07.018; pmid: 28844888
17. M. X. Byndloss, A. J. Bäumler, The germ-organ theory of non-communicable diseases. *Nat. Rev. Microbiol.* **16**, 103–110 (2018). doi: 10.1038/nrmicro.2017.158; pmid: 29307890
18. N. Barker, M. van de Wetering, H. Clevers, The intestinal stem cell. *Genes Dev.* **22**, 1856–1864 (2008). doi: 10.1101/gad.1674008; pmid: 18628392
19. Y. Y. Fan *et al*., A bioassay to measure energy metabolism in mouse colonic crypts, organoids, and sorted stem cells. *Am. J. Physiol. Gastrointest. Liver Physiol.* **309**, G1–G9 (2015). doi: 10.1152/ajpgi.00052.2015; pmid: 25977509
20. O. Warburg, F. Wind, E. Negelein, The Metabolism of Tumors in the Body. *J. Gen. Physiol.* **8**, 519–530 (1927). doi: 10.1085/jgp.8.6.519; pmid: 19872213
21. Z. Tylichová *et al*., Activation of autophagy and PPARγ protect colon cancer cells against apoptosis induced by interactive effects of butyrate and DHA in a cell type-dependent manner: The role of cell differentiation. *J. Nutr. Biochem.* **39**, 145–155 (2017). doi: 10.1016/j.jnutbio.2016.09.006; pmid: 27840291
22. M. Lefebvre *et al*., Peroxisome proliferator-activated receptor γ is induced during differentiation of colon epithelium cells. *J. Endocrinol.* **162**, 331–340 (1999). doi: 10.1677/joe.0.1620331; pmid: 10467224
23. K. Duszka, M. Oresic, C. Le May, J. König, W. Wahli, PPARγ Modulates Long Chain Fatty Acid Processing in the Intestinal Epithelium. *Int. J. Mol. Sci.* **18**, 2559 (2017). doi: 10.3390/ijms18122559; pmid: 29182565
24. D. R. Donohoe *et al*., The microbiome and butyrate regulate energy metabolism and autophagy in the mammalian colon. *Cell Metab.* **13**, 517–526 (2011). doi: 10.1016/j.cmet.2011.02.018; pmid: 21531334
25. W. E. Roediger, Role of anaerobic bacteria in the metabolic welfare of the colonic mucosa in man. *Gut* **21**, 793–798 (1980). doi: 10.1136/gut.21.9.793; pmid: 7429343
26. G. T. Furuta *et al*., Hypoxia-inducible factor 1-dependent induction of intestinal trefoil factor protects barrier function during hypoxia. *J. Exp. Med.* **193**, 1027–1034 (2001). doi: 10.1084/jem.193.9.1027; pmid: 11342587
27. Y. Litvak, M. X. Byndloss, R. M. Tsolis, A. J. Bäumler, Dysbiotic Proteobacteria expansion: A microbial signature of epithelial dysfunction. *Curr. Opin. Microbiol.* **39**, 1–6 (2017). doi: 10.1016/j.mib.2017.07.003; pmid: 28783509
28. N. R. Shin, T. W. Whon, J. W. Bae, Proteobacteria: Microbial signature of dysbiosis in gut microbiota. *Trends Biotechnol.* **33**, 496–503 (2015). doi: 10.1016/j.tibtech.2015.06.011; pmid: 26210164
29. G. Rizzatti, L. R. Lopetuso, G. Gibiino, C. Binda, A. Gasbarrini, Proteobacteria: A Common Factor in Human Diseases. *BioMed Res. Int.* **2017**, 9351507 (2017). doi: 10.1155/2017/9351507; pmid: 29230419
30. E. J. Vollaard, H. A. Clasener, A. J. Janssen, Co-trimoxazole impairs colonization resistance in healthy volunteers. *J. Antimicrob. Chemother.* **30**, 685–691 (1992). doi: 10.1093/jac/30.5.685; pmid: 1493984
31. S. Devkota *et al*., Dietary-fat-induced taurocholic acid promotes pathobiont expansion and colitis in $Il10^{-/-}$ mice. *Nature* **487**, 104–108 (2012). doi: 10.1038/nature11225; pmid: 22722865
32. M. Martinez-Medina *et al*., Western diet induces dysbiosis with increased E coli in CEABAC10 mice, alters host barrier function favouring AIEC colonisation. *Gut* **63**, 116–124 (2014). doi: 10.1136/gutjnl-2012-304119; pmid: 23598352
33. X. C. Morgan *et al*., Dysfunction of the intestinal microbiome in inflammatory bowel disease and treatment. *Genome Biol.* **13**, R79 (2012). doi: 10.1186/gb-2012-13-9-r79; pmid: 23013615
34. J. C. Arthur *et al*., Intestinal inflammation targets cancer-inducing activity of the microbiota. *Science* **338**, 120–123 (2012). doi: 10.1126/science.1224820; pmid: 22903521
35. I. M. Carroll, T. Ringel-Kulka, J. P. Siddle, Y. Ringel, Alterations in composition and diversity of the intestinal microbiota in patients with diarrhea-predominant irritable bowel syndrome. *Neurogastroenterol. Motil.* **24**, 521–530 (2012). doi: 10.1111/j.1365-2982.2012.01891.x; pmid: 22339879
36. L. Krogius-Kurikka *et al*., Microbial community analysis reveals high level phylogenetic alterations in the overall gastrointestinal microbiota of diarrhoea-predominant irritable bowel syndrome sufferers. *BMC Gastroenterol.* **9**, 95 (2009). doi: 10.1186/1471-230X-9-95; pmid: 20015409
37. E. Normann, A. Fahlén, L. Engstrand, H. E. Lilja, Intestinal microbial profiles in extremely preterm infants with and without necrotizing enterocolitis. *Acta Paediatr.* **102**, 129–136 (2013). doi: 10.1111/apa.12059; pmid: 23082780
38. L. Rigottier-Gois, Dysbiosis in inflammatory bowel diseases: The oxygen hypothesis. *ISME J.* **7**, 1256–1261 (2013). doi: 10.1038/ismej.2013.80; pmid: 23677008
39. F. Rivera-Chávez, C. A. Lopez, A. J. Bäumler, Oxygen as a driver of gut dysbiosis. *Free Radic. Biol. Med.* **105**, 93–101 (2017). doi: 10.1016/j.freeradbiomed.2016.09.022; pmid: 27677568
40. C. J. Kelly *et al*., Crosstalk between Microbiota-Derived Short-Chain Fatty Acids and Intestinal Epithelial HIF Augments Tissue Barrier Function. *Cell Host Microbe* **17**, 662–671 (2015). doi: 10.1016/j.chom.2015.03.005; pmid: 25865369
41. S. Alex *et al*., Short-chain fatty acids stimulate angiopoietin-like 4 synthesis in human colon adenocarcinoma cells by activating peroxisome proliferator-activated receptor γ. *Mol. Cell. Biol.* **33**, 1303–1316 (2013). doi: 10.1128/MCB.00858-12; pmid: 23339868
42. A. M. Spees *et al*., Streptomycin-induced inflammation enhances Escherichia coli gut colonization through nitrate respiration. *mBio* **4**, e00430-13 (2013). doi: 10.1128/mBio.00430-13; pmid: 23820397
43. C. C. Gillis *et al*., Dysbiosis-Associated Change in Host Metabolism Generates Lactate to Support Salmonella Growth. *Cell Host Microbe* **23**, 54–64.e6 (2018). doi: 10.1016/j.chom.2017.11.006; pmid: 29276172

44. A. T. Reese *et al*., Antibiotic-induced changes in the microbiota disrupt redox dynamics in the gut. *eLife* **7**, e35987 (2018). doi: 10.7554/eLife.35987; pmid: 29916366
45. X. Geeraerts, E. Bolli, S. M. Fendt, J. A. Van Ginderachter, Macrophage Metabolism As Therapeutic Target for Cancer, Atherosclerosis, and Obesity. *Front. Immunol.* **8**, 289 (2017). doi: 10.3389/fimmu.2017.00289; pmid: 28360914
46. I. F. Charo, Macrophage polarization and insulin resistance: PPARγ in control. *Cell Metab.* **6**, 96–98 (2007). doi: 10.1016/j.cmet.2007.07.006; pmid: 17681144
47. S. E. Winter *et al*., Host-derived nitrate boosts growth of E. coli in the inflamed gut. *Science* **339**, 708–711 (2013). doi: 10.1126/science.1232467; pmid: 23393266
48. O. Papapietro *et al*., R-spondin 2 signalling mediates susceptibility to fatal infectious diarrhoea. *Nat. Commun.* **4**, 1898 (2013). doi: 10.1038/ncomms2816; pmid: 23695692
49. V. Strugala, P. W. Dettmar, J. P. Pearson, Thickness and continuity of the adherent colonic mucus barrier in active and quiescent ulcerative colitis and Crohn's disease. *Int. J. Clin. Pract.* **62**, 762–769 (2008). doi: 10.1111/j.1742-1241.2007.01665.x; pmid: 18194279
50. D. A. McCormick, L. W. Horton, A. S. Mee, Mucin depletion in inflammatory bowel disease. *J. Clin. Pathol.* **43**, 143–146 (1990). doi: 10.1136/jcp.43.2.143; pmid: 2318990
51. L. Dubuquoy *et al*., Impaired expression of peroxisome proliferator-activated receptor γ in ulcerative colitis. *Gastroenterology* **124**, 1265–1276 (2003). doi: 10.1016/S0016-5085(03)00271-3; pmid: 12730867
52. W. E. Roediger, The colonic epithelium in ulcerative colitis: An energy-deficiency disease? *Lancet* **ii**, 712–715 (1980). doi: 10.1016/S0140-6736(80)91934-0; pmid: 6106826
53. A. Ponferrada *et al*., The role of PPARγ on restoration of colonic homeostasis after experimental stress-induced inflammation and dysfunction. *Gastroenterology* **132**, 1791–1803 (2007). doi: 10.1053/j.gastro.2007.02.032; pmid: 17484875
54. N. Ogasawara *et al*., PPARγ agonists upregulate the barrier function of tight junctions via a PKC pathway in human nasal epithelial cells. *Pharmacol. Res.* **61**, 489–498 (2010). doi: 10.1016/j.phrs.2010.03.002; pmid: 20227502
55. C. A. Lopez *et al*., Virulence factors enhance Citrobacter rodentium expansion through aerobic respiration. *Science* **353**, 1249–1253 (2016). doi: 10.1126/science.aag3042; pmid: 27634526
56. S. P. Dudhgaonkar, S. K. Tandan, D. Kumar, V. Raviprakash, M. Kataria, Influence of simultaneous inhibition of cyclooxygenase-2 and inducible nitric oxide synthase in experimental colitis in rats. *Inflammopharmacology* **15**, 188–195 (2007). doi: 10.1007/s10787-007-1603-3; pmid: 17943250
57. E. R. Hughes *et al*., Microbial Respiration and Formate Oxidation as Metabolic Signatures of Inflammation-Associated Dysbiosis. *Cell Host Microbe* **21**, 208–219 (2017). doi: 10.1016/j.chom.2017.01.005; pmid: 28182951
58. M. A. Henson, P. Phalak, Microbiota dysbiosis in inflammatory bowel diseases: In silico investigation of the oxygen hypothesis. *BMC Syst. Biol.* **11**, 145 (2017). doi: 10.1186/s12918-017-0522-1; pmid: 29282051
59. K. J. Khan *et al*., Antibiotic therapy in inflammatory bowel disease: A systematic review and meta-analysis. *Am. J. Gastroenterol.* **106**, 661–673 (2011). doi: 10.1038/ajg.2011.72; pmid: 21407187
60. E. E. Olsan *et al*., Colonization resistance: The deconvolution of a complex trait. *J. Biol. Chem.* **292**, 8577–8581 (2017). doi: 10.1074/jbc.R116.752295; pmid: 28389556
61. W. Zhu *et al*., Precision editing of the gut microbiota ameliorates colitis. *Nature* **553**, 208–211 (2018). doi: 10.1038/nature25172; pmid: 29323293
62. V. M. Rekdal, E. P. Balskus, Gut Microbiota: Rational Manipulation of Gut Bacterial Metalloenzymes Provides Insights into Dysbiosis and Inflammation. *Biochemistry* **57**, 2291–2293 (2018). doi: 10.1021/acs.biochem.8b00340; pmid: 29633827
63. C. Rousseaux *et al*., The 5-aminosalicylic acid antineoplastic effect in the intestine is mediated by PPARγ. *Carcinogenesis* **34**, 2580–2586 (2013). doi: 10.1093/carcin/bgt245; pmid: 23843037
64. R. N. Brogden, E. M. Sorkin, Mesalazine. A review of its pharmacodynamic and pharmacokinetic properties, and therapeutic potential in chronic inflammatory bowel disease. *Drugs* **38**, 500–523 (1989). doi: 10.2165/00003495-198938040-00003; pmid: 2684592
65. S. M. Greenfield, N. A. Punchard, J. P. Teare, R. P. Thompson, The mode of action of the aminosalicylates in inflammatory bowel disease. *Aliment. Pharmacol. Ther.* **7**, 369–383 (1993). doi: 10.1111/j.1365-2036.1993.tb00110.x; pmid: 8105984
66. S. Y. Zhou *et al*., Intestinal metabolism and transport of 5-aminosalicylate. *Drug Metab. Dispos.* **27**, 479–485 (1999). pmid: 10101143
67. C. Rousseaux *et al*., Intestinal antiinflammatory effect of 5-aminosalicylic acid is dependent on peroxisome proliferator-activated receptor-γ. *J. Exp. Med.* **201**, 1205–1215 (2005). doi: 10.1084/jem.20041948; pmid: 15824083
68. J. Xu *et al*., 5-Aminosalicylic Acid Alters the Gut Bacterial Microbiota in Patients With Ulcerative Colitis. *Front. Microbiol.* **9**, 1274 (2018). doi: 10.3389/fmicb.2018.01274; pmid: 29951050
69. E. Muraille, O. Leo, M. Moser, TH1/TH2 paradigm extended: Macrophage polarization as an unappreciated pathogen-driven escape mechanism? *Front. Immunol.* **5**, 603 (2014). doi: 10.3389/fimmu.2014.00603; pmid: 25505468
70. M. N. Xavier *et al*., PPARγ-mediated increase in glucose availability sustains chronic Brucella abortus infection in alternatively activated macrophages. *Cell Host Microbe* **14**, 159–170 (2013). doi: 10.1016/j.chom.2013.07.009; pmid: 23954155
71. B. Stecher *et al*., Salmonella enterica serovar typhimurium exploits inflammation to compete with the intestinal microbiota. *PLOS Biol.* **5**, e244 (2007). doi: 10.1371/journal.pbio.0050244; pmid: 17760501
72. I. Sekirov *et al*., Salmonella SPI-1-mediated neutrophil recruitment during enteric colitis is associated with reduction and alteration in intestinal microbiota. *Gut Microbes* **1**, 30–41 (2010). doi: 10.4161/gmic.1.1.10950; pmid: 21327114
73. N. Gill *et al*., Neutrophil elastase alters the murine gut microbiota resulting in enhanced Salmonella colonization. *PLOS ONE* **7**, e49646 (2012). doi: 10.1371/journal.pone.0049646; pmid: 23155475
74. F. Rivera-Chávez *et al*., Depletion of Butyrate-Producing Clostridia from the Gut Microbiota Drives an Aerobic Luminal Expansion of Salmonella. *Cell Host Microbe* **19**, 443–454 (2016). doi: 10.1016/j.chom.2016.03.004; pmid: 27078066
75. C. A. Lopez *et al*., Phage-mediated acquisition of a type III secreted effector protein boosts growth of salmonella by nitrate respiration. *mBio* **3**, e00143-12 (2012). doi: 10.1128/mBio.00143-12; pmid: 22691391
76. C. A. Lopez, F. Rivera-Chávez, M. X. Byndloss, A. J. Bäumler, The Periplasmic Nitrate Reductase NapABC Supports Luminal Growth of Salmonella enterica Serovar Typhimurium during Colitis. *Infect. Immun.* **83**, 3470–3478 (2015). doi: 10.1128/IAI.00351-15; pmid: 26099579
77. S. E. Winter *et al*., Gut inflammation provides a respiratory electron acceptor for Salmonella. *Nature* **467**, 426–429 (2010). doi: 10.1038/nature09415; pmid: 20864996
78. P. Thiennimitr *et al*., Intestinal inflammation allows Salmonella to use ethanolamine to compete with the microbiota. *Proc. Natl. Acad. Sci. U.S.A.* **108**, 17480–17485 (2011). doi: 10.1073/pnas.1107857108; pmid: 21969563
79. F. Faber *et al*., Respiration of Microbiota-Derived 1,2-propanediol Drives Salmonella Expansion during Colitis. *PLOS Pathog.* **13**, e1006129 (2017). doi: 10.1371/journal.ppat.1006129; pmid: 28056091
80. J. W. Collins *et al*., Citrobacter rodentium: Infection, inflammation and the microbiota. *Nat. Rev. Microbiol.* **12**, 612–623 (2014). doi: 10.1038/nrmicro3315; pmid: 25088150
81. N. Kamada *et al*., Regulated virulence controls the ability of a pathogen to compete with the gut microbiota. *Science* **336**, 1325–1329 (2012). doi: 10.1126/science.1222195; pmid: 22582016
82. C. Lupp *et al*., Host-mediated inflammation disrupts the intestinal microbiota and promotes the overgrowth of Enterobacteriaceae. *Cell Host Microbe* **2**, 204 (2007). doi: 10.1016/j.chom.2007.08.002; pmid: 18030708
83. V. Kumar *et al*., miR-130a and miR-212 Disrupt the Intestinal Epithelial Barrier through Modulation of PPARγ and Occludin Expression in Chronic Simian Immunodeficiency Virus-Infected Rhesus Macaques. *J. Immunol.* **200**, 2677–2689 (2018). doi: 10.4049/jimmunol.1701148; pmid: 29514950
84. E. A. Mutlu *et al*., A compositional look at the human gastrointestinal microbiome and immune activation parameters in HIV infected subjects. *PLOS Pathog.* **10**, e1003829 (2014). doi: 10.1371/journal.ppat.1003829; pmid: 24586144
85. A. Carreau, B. El Hafny-Rahbi, A. Matejuk, C. Grillon, C. Kieda, Why is the partial oxygen pressure of human tissues a crucial parameter? Small molecules and hypoxia. *J. Cell. Mol. Med.* **15**, 1239–1253 (2011). doi: 10.1111/j.1582-4934.2011.01258.x; pmid: 21251211

ACKNOWLEDGMENTS

Funding: Work in A.J.B.'s laboratory is supported by USDA award 2014-09901 and Public Health Service Grants AI044170, AI096528, AI112445, and AI112949. **Author contributions:** Y.L., M.X.B., and A.J.B. contributed to the writing of the article. A.J.B. generated the figures. **Competing interests:** M.X.B. and A.J.B. filed invention report number 0577501-16-0038 at iEdison.gov for a treatment to prevent post-antibiotic expansion of Enterobacteriaceae.

10.1126/science.aat9076

RESEARCH ARTICLE SUMMARY

STRUCTURAL BIOLOGY

Substrate-engaged 26*S* proteasome structures reveal mechanisms for ATP-hydrolysis–driven translocation

Andres H. de la Peña*, Ellen A. Goodall*, Stephanie N. Gates*, Gabriel C. Lander†, Andreas Martin†

INTRODUCTION: As the major protease in eukaryotic cells and the final component of the ubiquitin-proteasome system, the 26*S* proteasome is responsible for protein homeostasis and the regulation of numerous vital processes. Misfolded, damaged, or obsolete regulatory proteins are marked for degradation by the attachment of polyubiquitin chains, which bind to ubiquitin receptors of the proteasome. A heterohexameric ring of AAA+ (ATPases associated with diverse cellular activities) subunits then uses conserved pore loops to engage, mechanically unfold, and translocate protein substrates into a proteolytic core for cleavage while the deubiquitinase Rpn11 removes substrate-attached ubiquitin chains.

RATIONALE: Despite numerous structural and functional studies, the mechanisms by which adenosine triphosphate (ATP) hydrolysis drives the conformational changes responsible for protein degradation remained elusive. Structures of related homohexameric AAA+ motors, in which bound substrates were stabilized with ATP analogs or hydrolysis-eliminating mutations, revealed snapshots of ATPase subunits in different nucleotide states and spiral-staircase arrangements of pore loops around the substrate. These structures gave rise to "hand-over-hand" translocation models by inferring how individual subunits may progress through various substrate-binding conformations. However, the coordination of ATP-hydrolysis steps and their mechanochemical coupling to propelling substrate were unknown.

RESULTS: We present the cryo–electron microscopy (cryo-EM) structures of the actively ATP-hydrolyzing, substrate-engaged 26*S* proteasome with four distinct motor conformations. Stalling substrate translocation at a defined position by inhibiting deubiquitination led to trapped states in which the substrate-attached ubiquitin remains functionally bound to the Rpn11 deubiquitinase, and the scissile isopeptide bond of ubiquitin is aligned with the substrate-translocation trajectory through the AAA+ motor. Our structures suggest a ubiquitin capture mechanism, in which mechanical pulling on the substrate by the AAA+ motor delivers ubiquitin modifications directly into the Rpn11 catalytic groove and accelerates isopeptide cleavage for efficient, cotranslocational deubiquitination.

These structures also show how the substrate polypeptide traverses from the Rpn11 deubiquitinase, through the AAA+ motor, and into the core peptidase. The proteasomal motor thereby adopts staircase arrangements with five substrate-engaged subunits and one disengaged subunit. Four of the substrate-engaged subunits are ATP bound, whereas the subunit at the bottom of the staircase and the disengaged subunit are bound to adenosine diphosphate (ADP).

ON OUR WEBSITE

Read the full article at http://dx.doi.org/10.1126/science.aav0725

CONCLUSION: Of the four distinct motor states we observed, three apparently represent sequential stages of ATP binding, hydrolysis, and substrate translocation and hence reveal the coordination of individual steps in the ATPase cycle and their mechanochemical coupling with translocation. ATP hydrolysis occurs in the fourth substrate-engaged subunit from the top, concomitantly with exchange of ADP for ATP in the disengaged subunit. The subsequent transition, which is likely triggered by phosphate release from the fourth, posthydrolysis subunit of the staircase, then involves major conformational changes of the entire ATPase hexamer. The bottom ADP-bound subunit is displaced and the previously disengaged subunit binds the substrate at the top of the staircase, while the four engaged subunits move downward as a rigid body and translocate substrate toward the peptidase. Our likely consecutive proteasome conformations, together with previously determined substrate-free structures, suggest a sequential progression of ATPase subunits through the ATP-hydrolysis cycle. We hypothesize that, in general, hexameric AAA+ translocases function by this sequential mechanism. ■

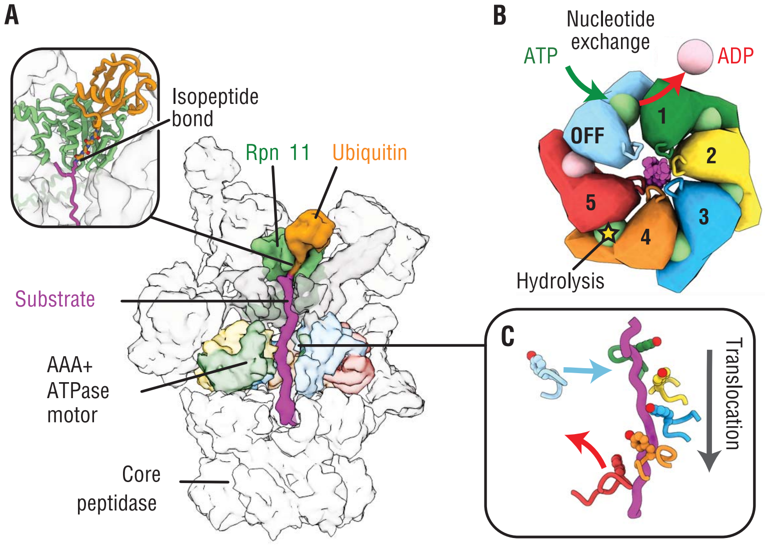

Cryo-EM structures of the substrate-engaged 26*S* proteasome. (**A**) Substrate path through the proteasome, with ubiquitin bound to Rpn11 (left inset) and the substrate polypeptide traversing through the AAA+ motor into the core peptidase. (**B**) Schematic showing coordinated ATP hydrolysis and nucleotide exchange observed between consecutive motor states. (**C**) Substrate translocation is driven by changes in the spiral-staircase arrangement of pore loops, as indicated by arrows.

The list of author affiliations is available in the full article online.
*These authors contributed equally to this work.
†Corresponding author. Email: glander@scripps.edu (G.C.L.); a.martin@berkeley.edu (A.M.)
Cite this article as A. H. de la Peña *et al.*, *Science* **362**, eaav0725 (2018). DOI: 10.1126/science.aav0725

de la Peña *et al.*, *Science* **362**, 1018 (2018) 30 November 2018 **1 of 1**

RESEARCH ARTICLE

STRUCTURAL BIOLOGY

Substrate-engaged 26*S* proteasome structures reveal mechanisms for ATP-hydrolysis–driven translocation

Andres H. de la Peña[1]*, Ellen A. Goodall[2,3]*, Stephanie N. Gates[2,3,4]*, Gabriel C. Lander[1]†, Andreas Martin[2,3,4]†

The 26*S* proteasome is the primary eukaryotic degradation machine and thus is critically involved in numerous cellular processes. The heterohexameric adenosine triphosphatase (ATPase) motor of the proteasome unfolds and translocates targeted protein substrates into the open gate of a proteolytic core while a proteasomal deubiquitinase concomitantly removes substrate-attached ubiquitin chains. However, the mechanisms by which ATP hydrolysis drives the conformational changes responsible for these processes have remained elusive. Here we present the cryo–electron microscopy structures of four distinct conformational states of the actively ATP-hydrolyzing, substrate-engaged 26*S* proteasome. These structures reveal how mechanical substrate translocation accelerates deubiquitination and how ATP-binding, -hydrolysis, and phosphate-release events are coordinated within the AAA+ (ATPases associated with diverse cellular activities) motor to induce conformational changes and propel the substrate through the central pore.

The 26*S* proteasome, the final component of the ubiquitin-proteasome system, is central to general proteostasis and the regulation of essential processes in eukaryotic cells (*1*). Proteins are targeted for proteasomal degradation through the covalent attachment of polyubiquitin chains to lysine residues (*2*). To safeguard against indiscriminate degradation, the proteolytic active sites of the proteasome are sequestered within the barrel-shaped 20*S* core particle (CP). Access to these active sites is controlled by the 19*S* regulatory particle (RP), which binds to one or both ends of the CP, recruits ubiquitinated proteins, and catalyzes their deubiquitination, unfolding, and translocation through a central pore into the proteolytic chamber of the CP for degradation (*3*). The RP can be further subdivided into the base and lid subcomplexes. The nine-subunit lid subcomplex fulfills important scaffolding functions and contains the Zn^{2+}-dependent deubiquitinase Rpn11, which is positioned above the central pore of the proteasome to remove ubiquitin chains from substrates before degradation (*4*–*8*). The base subcomplex consists of 10 subunits, including three ubiquitin receptors and six distinct AAA+ ATPases (ATPases associated with diverse cellular activities), Rpt1 to Rpt6 (*3*, *9*). These ATPases (adenosine triphosphatases) form a heterohexameric ring (in the order Rpt1, Rpt2, Rpt6, Rpt3, Rpt4, and Rpt5) that is the molecular motor of the proteasome (*10*). Each Rpt consists of a N-terminal helix, an oligonucleotide binding (OB)–fold domain, and a C-terminal AAA+ motor domain. In the heterohexamer, the N-terminal helices of neighboring Rpt pairs form a coiled coil, and the six OB-fold domains assemble into a rigid N-ring above the AAA+ motor ring (*6*, *8*). After ubiquitin-mediated substrate recruitment, the ATPase motor engages a flexible initiation region of the substrate for subsequent mechanical translocation and unfolding (*11*). To facilitate substrate transfer to the CP, the ATPase hexamer also triggers opening of the CP access gate by docking conserved C-terminal tails of Rpt subunits into pockets at the surface of the CP α ring (*12*–*14*).

Like other AAA+ ATPases, the Rpt subunits contain a highly conserved nucleotide binding pocket that couples ATP binding and hydrolysis with conformational changes to produce mechanical work (*15*, *16*). This pocket is largely formed by the signature Walker-A and Walker-B motifs, responsible for nucleotide binding and hydrolysis, respectively, and an arginine finger provided by the clockwise-neighboring ATPase subunit that coordinates the γ phosphate of ATP during hydrolysis and enables subunit communication (*17*). Conserved pore-1 loops protrude from each ATPase subunit into the central channel, where they sterically interact with the substrate polypeptide and transduce nucleotide-dependent conformational changes into directional translocation (*18*–*21*).

The common functional architecture of ring-shaped hexameric helicases and AAA+ translocases gave rise to a “hand-over-hand” model for substrate translocation (*22*–*24*), which is supported by numerous cryo–electron microscopy (cryo-EM) structures of substrate-bound homohexameric AAA+ motors (*25*–*30*). These prior structures were trapped using hydrolysis-inactivating Walker-B mutations, nonhydrolyzable ATP analogs, or analogs that are slowly hydrolyzed, to reveal series of subunits in the hexamer that resemble the ATP-bound, adenosine diphosphate (ADP)–bound, and nucleotide-free states. Generally, five nucleotide-bound subunits contact the substrate polypeptide in a spiral-staircase arrangement of pore loops, whereas one subunit remains disengaged and nucleotide-free. The hand-over-hand model stems from inferences regarding how individual subunits may progress through the various nucleotide states and substrate-binding conformations around the ring. The heterohexameric proteasomal AAA+ motor adopts distinct spiral-staircase arrangements with individual Rpts in different vertical positions (*6*, *31*–*35*) and thus promises more detailed insights into the progression of states during the ATP-hydrolysis and substrate-translocation cycles. However, high-resolution structural studies of the proteasome during active substrate translocation have so far been unsuccessful.

In the absence of substrate, the ATP-hydrolyzing proteasome primarily adopts the s1 state (*6*, *36*) in which the ATPase domains of Rpt1 to Rpt6 form a spiral staircase that is not coaxially aligned with the CP and Rpn11 is positioned offset from the central pore of the motor. A low-resolution structure of the proteasome trapped with a stalled protein in the central pore revealed that upon substrate engagement the RP transitions from the s1 state to a processing conformation, which is characterized by a more planar ATPase ring, a rotated lid subcomplex, and a coaxial alignment of Rpn11, the Rpt hexamer, and the CP (*31*). However, the limited resolution and strong heterogeneity of the ATPases within these stalled proteasome complexes prevented the visualization of substrate and the identification of distinct motor states.

States that share structural similarities with the substrate-processing conformation are also observed for the substrate-free proteasome as a small subpopulation in the presence of ATP (s2 state) and upon ATPase inhibition using either ATP analogs or Walker-B mutations in individual Rpt subunits (s3, s4, s5, and s6 states and the unnamed state seen in ADP-AlF_x) (*14*, *33*–*35*). Cryo-EM reconstructions of these states revealed distinct spiral-staircase arrangements and nucleotide occupancies of Rpt subunits, but the lack of ATP hydrolysis and the absence of substrate limited the conclusions that could be drawn regarding the mechanisms for ATP-hydrolysis–coupled translocation.

---

[1]Department of Integrative Structural and Computational Biology, The Scripps Research Institute, 10550 N. Torrey Pines Road, La Jolla, CA 92037, USA. [2]Department of Molecular and Cell Biology, University of California, Berkeley, CA 94720, USA. [3]California Institute for Quantitative Biosciences, University of California at Berkeley, Berkeley, CA 94720, USA. [4]Howard Hughes Medical Institute, University of California at Berkeley, Berkeley, CA 94720, USA.
*These authors contributed equally to this work.
†Corresponding author. Email: glander@scripps.edu (G.C.L.); a.martin@berkeley.edu (A.M.)

We explored the mechanistic details of ATP-hydrolysis–driven substrate translocation by determining the structure of the substrate-engaged 26*S* proteasome in the presence of ATP. Unlike previous studies that used ATPase inhibition to trap substrate-bound states of other AAA+ motors, we stalled substrate translocation in the actively hydrolyzing motor of the proteasome by inhibiting Rpn11-mediated deubiquitination. We describe four cryo-EM structures, depicting four distinct motor states with the unambiguous assignment of substrate polypeptide traversing the RP from the lysine-attached ubiquitin at the Rpn11 active site, through the Rpt hexamer, to the gate of the CP. Three of these states appear to represent sequential stages of ATP binding, hydrolysis, and substrate translocation and hence reveal the coordination of individual steps in the ATPase cycle of the AAA+ hexamer and their mechanochemical coupling with translocation.

Four substrate-bound 26*S* proteasome structures

To stall translocation at a defined substrate position, we inactivated the Rpn11 deubiquitinase of *Saccharomyces cerevisiae* 26*S* proteasomes by incubation with the inhibitor ortho-phenanthroline (4) and added a globular substrate with a single polyubiquitinated lysine flanking an unstructured C-terminal initiation region. Proteasomes engaged the flexible initiation region and translocated the substrate until the attached ubiquitin chain reached the inhibited Rpn11, preventing further translocation and trapping the substrate in the central pore, which is indicated by a complete inhibition of degradation (fig. S1A). Stalling substrate translocation in the proteasome does not also stall the AAA+ motor, as we observed a rate of ATP hydrolysis that was even slightly elevated compared with that of freely translocating proteasomes (fig. S1B). We posit that this stalled state resembles the scenario when the proteasome encounters thermodynamically stable substrate domains that require repeated pulling by the ATPase to be unfolded (31, 37).

After incubation with substrate, proteasomes were vitrified for cryo-EM single-particle analysis, which produced reconstructions of the 26*S* proteasome in six distinct conformational states. In the initial 3D classification, roughly 42% of particles were observed to be substrate free, adopting an s1-like state (fig. S2A and table S1), whereas the rest of the particles were sorted into reconstructions that showed ubiquitin density adjacent to Rpn11 and adopted non–s1-like conformations (fig. S2A). Further focused classification of the ATPase motor resulted in four s4-like reconstructions and one reconstruction that resembled the s2 state but lacked density for substrate within the central channel of the AAA+ motor. In contrast, the four s4-like reconstructions (ranging from ~4.2 to ~4.7 Å in overall resolution) showed clearly visible substrate density threaded through the center of the RP (Fig. 1, figs. S2 and S3A, and table S1).

Proteasome interactions with the translocating substrate

The stalled proteasome states not only revealed the detailed path of the substrate polypeptide from the RP to the CP but also resolved the structure of ubiquitin-bound Rpn11 in the context of the 26*S* holoenzyme (Fig. 1A and movie S1). The most proximal, substrate-attached ubiquitin moiety of the polyubiquitin chain is positioned in the catalytic groove of Rpn11, whose ubiquitin-interacting Insert-1 region adopts the same active β-hairpin conformation previously observed in the crystal structure of the isolated ubiquitin-bound Rpn11-Rpn8 dimer (Fig. 1B and fig. S3B). Although the catalytic Zn^{2+} ion is not visible in the Rpn11 active site, likely due to the treatment with ortho-phenanthroline, the conformations of ubiquitin and Rpn11 match the active, Zn^{2+}-containing structure (Fig. S3B), with the addition of an intact isopeptide bond to the substrate lysine.

Upstream (N-terminal) of the ubiquitin-modified lysine, only two amino acids of the substrate were resolved. The orientation of these residues delineates a path near the N-terminal helix of Rpt2 by which substrates may approach the central pore of the proteasome (Fig. 1A), yet to what extent this path outside the N-ring is fixed or substrate dependent remains unclear. Downstream (C-terminal) of the ubiquitinated lysine, the substrate is confined to the narrow central channel of the Rpt hexamer (Fig. 1A and fig. S3, C and D). An axial view of the RP reveals that the Rpn11 catalytic groove is aligned with the trajectory of substrate translocation through this channel, which follows a straight line from the isopeptide bond into the AAA+ motor (fig. S3D). This alignment explains how vectorial tugging by the motor can pull ubiquitin directly into the cup-shaped Rpn11 binding site and thus accelerate cotranslocational deubiquitination (38). The active β-hairpin conformation of Rpn11's Insert-1

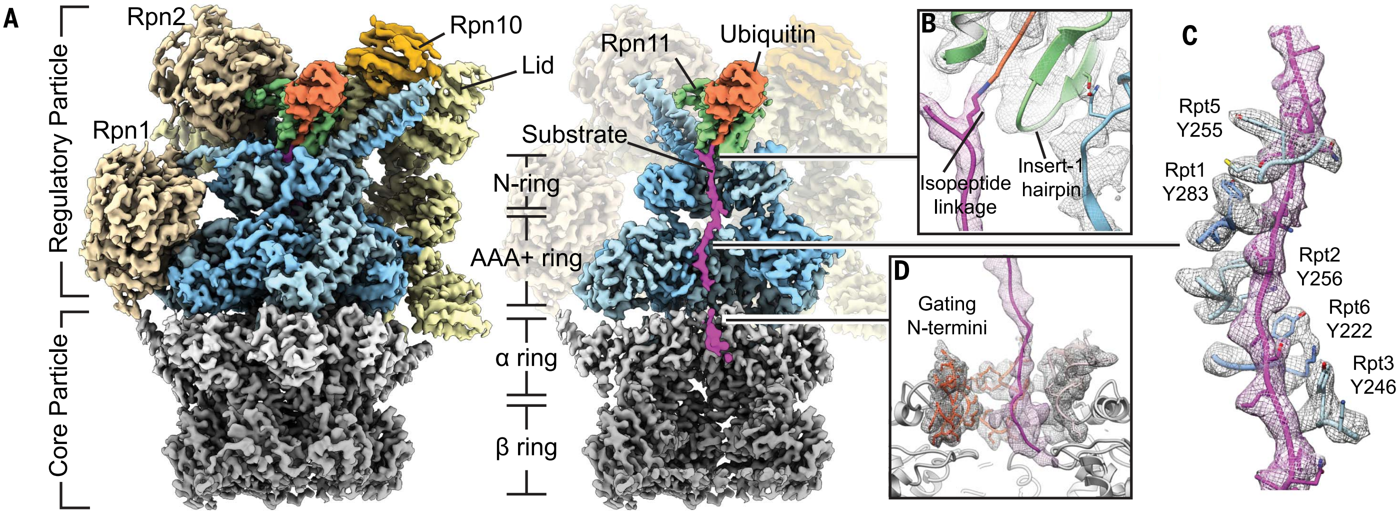

Fig. 1. High-resolution structure of the substrate-engaged 26*S* proteasome. (**A**) Exterior (left) and cutaway (right) views of the substrate-engaged proteasome cryo-EM reconstruction. The substrate (magenta) is shown extending from the ubiquitin moiety (orange), through the central pore formed by the N-ring and the AAA+ motor (blue), into the gate of the 20*S* core particle (gray). (**B**) The isopeptide bond between the substrate lysine and the C terminus of the ubiquitin moiety is bound in the catalytic groove of Rpn11 (green), with the Insert-1 region in its active, β-hairpin state that is stabilized by a contact to the N-terminal helix of Rpt5 (blue). (**C**) The substrate polypeptide is encircled by a spiral staircase of pore-1 loop tyrosines (Y) projecting from the Rpt subunits. (**D**) Substrate enters the open gate of the core particle. The gating N termini of α subunits 2, 3, and 4 (red) extend toward the AAA+ motor, forming a hydrophobic collar in conjunction with the N termini of the other four α subunits (pink).

region appears to be stabilized through additional contacts with Rpt5 at the base of the Rpt4-Rpt5 coiled coil (Fig. 1B). Our structures suggest that the translocation stall originates from ubiquitin becoming trapped as it is pulled into the catalytic groove of inactive Rpn11, rather than sterically clashing with the narrow entrance of the N-ring. Despite having the ATPase ring in distinct hydrolysis states (see below), all four proteasome structures show ubiquitin functionally bound to Rpn11, indicating that deubiquitination indeed occurs cotranslocationally, after the regulatory particle has switched to an engaged conformation and while the substrate is threaded into the pore. This observation is consistent with a mechanism in which the regulatory particle does not adopt a specific conformation for deubiquitination but cleaves off ubiquitin modifications as they approach Rpn11 during processive substrate translocation.

Because of the defined stall at the single ubiquitin chain, we were able to reliably model the C-terminally inserted substrate and assign a specific sequence to the polypeptide density within the AAA+ motor (Fig. 1C). The pore-1 loop Tyr and neighboring Lys residue of individual Rpt subunits form a spiral staircase that tightly encircles the substrate, consistent with a translocation mechanism that involves steric interactions with amino acid side chains of the polypeptide (Fig. 1C). As in many other AAA+ motors, the pore-2 loops (a second loop that protrudes from each ATPase subunit into the pore) are arranged in a second staircase that lies in close proximity to the substrate below the pore-1 loop spiral (fig. S3E). In contrast to the pore-1 loops, the pore-2 loops do not contain bulky residues and may contribute to translocation through interactions of their backbones with the substrate (fig. S3E), as suggested by defects previously observed for pore-2 loop mutations (*20*).

After traversing the AAA+ motor, the substrate enters the gate of the CP (Fig. 1D). Our four cryo-EM structures reveal two gating conformations with distinct RP-CP interactions and

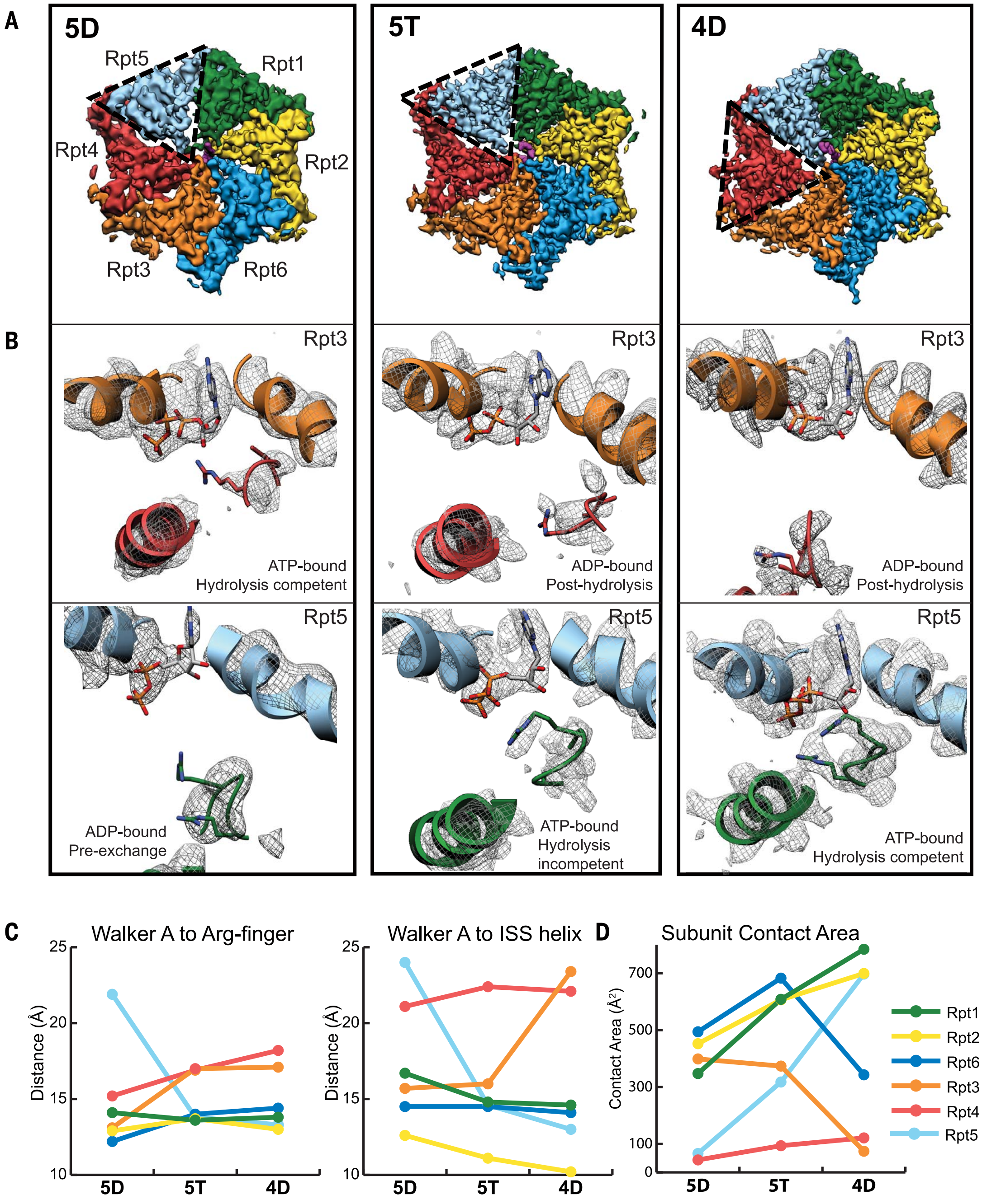

Fig. 2. Nucleotide-pocket analysis of three sequential substrate-engaged AAA+ motor conformations. (**A**) Top view of AAA+ motor density maps for three sequential states, with the substrate-disengaged Rpt subunits indicated by a dashed triangle. Substrate density (magenta) is shown in the central pore formed by Rpt1 (green), Rpt2 (yellow), Rpt6 (blue), Rpt3 (orange), Rpt4 (red), and Rpt5 (light blue). (**B**) Close-up views of the Rpt3 nucleotide-binding pocket, showing the neighboring Rpt4 providing the Arg finger (top row) and the Rpt5 binding pocket with the Arg finger from the neighboring Rpt1 (bottom row). Individual states, left to right, are arranged in the order of motor progression. (**C**) Measurements of nucleotide-pocket openness colored by nucleotide-bound Rpt subunit. Shown are the distances between the α carbon of Walker-A Thr and the α carbon of the neighboring subunit's Arg finger (left) or the centroid of α-helix 10 flanking the ISS motif (right). (**D**) Contact area between the large AAA+ domains of neighboring Rpt subunits.

arrangements for the N termini of CP α subunits (fig. S4). In all structures, the C termini of HbYX (hydrophobic–Tyr–any amino acid)–motif containing Rpt subunits (Rpt2, Rpt3, and Rpt5) occupy the intersubunit pockets of the CP α ring, whereas the pockets for the C termini of Rpt1 and Rpt6 vary in occupancy (fig. S4A). Two of the structures show all Rpt tails except for Rpt4 docked into the intersubunit pockets and, consequently, a completely open gate, similar to previously described states in substrate-free proteasomes (*14*, *35*) (fig. S4, B to D). In this open conformation, the gating N termini of α subunits 2, 3, and 4 become directed toward the base subcomplex and interact with the N termini of the other four α subunits through a conserved Tyr residue (fig. S4E). This results in the formation of a hydrophobic collar directly beneath the exit from the AAA+ motor (fig. S4E). The other two structures, which exhibit lower levels of Rpt1- and Rpt6-tail occupancies in the respective α-ring pockets, reveal a partially open gate (fig. S4, C and D). This observation supports a recently proposed model in which cooperative gate opening is driven by the tail insertion of Rpt1 and Rpt6, after the three HbYX-containing tails are docked (*14*, *35*).

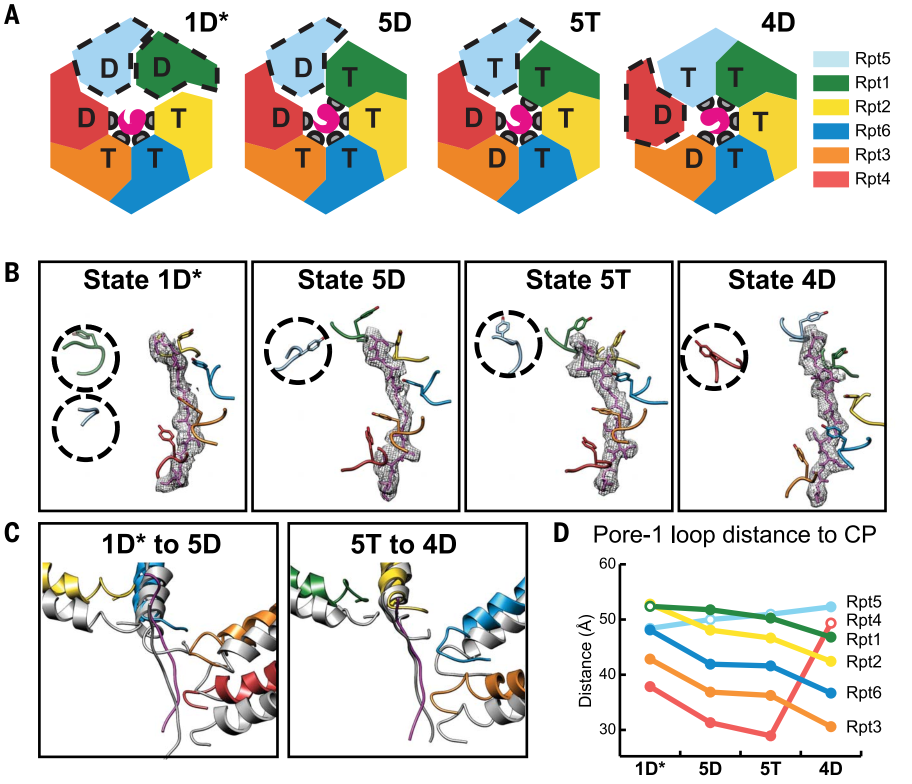

Fig. 3. Pore-1 loop tyrosines define three distinct spiral-staircase conformations of the AAA+ motor. (**A**) Summary of nucleotide states and staircase arrangement in the 1D*, 5D, 5T, and 4D states. Coloring of the motor subunits—Rpt1 (green), Rpt2 (yellow), Rpt6 (blue), Rpt3 (orange), Rpt4 (red), and Rpt5 (light blue)—is consistent throughout the figure. Pore-1 loop contacts (gray) with substrate (magenta) are not present in the disengaged subunits (dashed outline). (**B**) Pore-1 loop Tyr staircases for each of the substrate-bound states. Substrate polypeptide (mesh) is encircled by four or five engaged pore-1 loops in each state. Disengaged pore-1 loops are indicated by dashed circles. (**C**) Vertical movement of substrate-engaged pore-1 loops is observed during motor transition from the 1D* to 5D and 5T to 4D states. The lower state (5D and 4D, respectively) is shown in gray. (**D**) Plot of distances between the α carbon of the pore-1 loop tyrosines to the plane of the core particle's gate. Filled circles represent substrate-engaged pore loops; open circles indicate disengaged pore loops.

Distinct nucleotide states give rise to four ATPase conformations

Our four substrate-engaged proteasome structures show distinct motor conformations with nucleotide density present in all six ATP-binding pockets and one or two subunits that do not interact with substrate (Fig. 2A and fig. S5A). To reliably assign nucleotide identities and thereby establish the progression of the ATP-hydrolysis cycle within the actively hydrolyzing Rpt hexamer, we assessed not only the occupying nucleotide densities but also the geometries of the ATPase sites, the structural stability of allosteric motifs, and the intersubunit contact areas (Fig. 2 and table S2). ATP-bound, hydrolysis-competent subunits form a closed pocket with an increased intersubunit contact area characterized by a direct interaction between the γ phosphate of ATP and the well-resolved Arg fingers of the clockwise neighboring subunit (Fig. 2, B to D, and fig. S5, B to F). In contrast, ADP-bound subunits are more open with a decreased intersubunit contact area and Arg fingers that are more flexible, as indicated by lower resolvability (Fig. 2, B to D, and fig. S5, B to F). Subunits that are ATP bound but not yet hydrolysis competent and subunits where ATP hydrolysis has just occurred show similar, intermediate Arg-finger distances (Fig. 2, B and C). To distinguish between these pre- and posthydrolysis states, we assessed the pocket openness by measuring the intersubunit contact area or the distance between the conserved Walker-A motif Thr and the helix preceding the intersubunit signaling (ISS) motif of the neighboring subunit (Fig. 2, C and D, and fig. S5, B to E) (*26*, *33*). Our analyses revealed a continuum of nucleotide states within the Rpt hexamers, ranging from ATP-bound partially open pockets with semi-engaged Arg fingers (hydrolysis incompetent) to ATP-bound closed pockets with fully engaged Arg fingers (hydrolysis competent), ADP-bound closed pockets with disengaged Arg fingers (posthydrolysis), and ADP-bound open pockets with disengaged Arg fingers (pre–nucleotide exchange) (Fig. 2B). Individual Rpt subunits show a progression through discrete nucleotide states around the hexameric ring (Fig. 3A), indicating that each reconstruction reflects a distinct snapshot of the proteasomal AAA+ motor during the ATPase cycle and that Rpts likely progress sequentially through this cycle. Our structures allow us to correlate the distinct vertical registers and nucleotide states of Rpt subunits and analyze the coupling of individual ATPase steps with each other and with the mechanical translocation of substrate.

Sequential motor states reveal the mechanism for ATP-hydrolysis–driven substrate translocation

The current hand-over-hand translocation model for hexameric AAA+ ATPases is based on observations of the subunits encircling and interacting with substrate in a staircase-like organization, with the exception of the sixth subunit (often referred to as the "seam subunit") that is displaced from the substrate and positioned between the lowest and highest subunits of the staircase (*25*–*30*). Consistent with this previously observed configuration, we see that in all substrate-engaged proteasome states the Rpt subunits interact with the substrate through their pore-1 loops in a spiral-staircase arrangement, with the pore-2 loops forming a similar staircase underneath (figs. S6, A and B). A characteristic seam is observed along the interface between the highest substrate-engaged subunit of the staircase and the neighboring substrate-disengaged subunit (Figs. 2A and 3, A and B, and fig. S5A). We name our four proteasome states based on the identity and the nucleotide state of this substrate-disengaged "seam" subunit: Rpt1-ADP, Rpt5-ADP, Rpt5-ATP, and Rpt4-ADP are named as 1D*, 5D, 5T, and 4D, respectively (Fig. 3A).

In these four conformations, three different Rpt subunits occupy the uppermost substrate-bound position of the staircase. In 1D*, Rpt2 is in the top substrate-bound position with the seam subunit Rpt1 displaced from the substrate (Fig. 3B). Unexpectedly, Rpt5 is also disengaged in this conformation, indicating that 1D* may represent an off-pathway ATPase configuration (see discussion below).

On the basis of their nucleotide occupancies and spiral-staircase arrangements, we posit that the remaining three conformations—5D, 5T, and 4D—represent consecutive states whose transitions include a nucleotide exchange, a hydrolysis event, and a translocation step (Fig. 3 and movie S2). In 5D and 5T, the vertical staircase register is shifted by one subunit in the counterclockwise direction compared with 1D*, such that Rpt1 assumes the uppermost substrate-bound position, whereas the other subunits move downward and only Rpt5 is substrate disengaged (Fig. 3C). During the 5D-to-5T transition, the staircase arrangement of Rpt subunits remains largely the same (fig. S6D), but the density for the Rpt5-bound nucleotide changes concomitantly with a substantial closure of the binding pocket that brings the Arg fingers of Rpt1 into close proximity (Fig. 2B), which is consistent with an exchange of ADP for ATP. This exchange and the resulting shift of Rpt5 toward the central pore likely primes this subunit by allosterically positioning the pore loops for substrate engagement in the subsequent 4D state (Fig. 3B). Nucleotide exchange in the disengaged Rpt thus appears prerequisite for substrate binding at the top of the spiral staircase, which agrees with the highest substrate-contacting subunit always being bound to ATP (Fig. 3A). Notably, concurrent with ATP binding to Rpt5, Rpt3 hydrolyzes ATP during the 5D-to-5T transition, as indicated by correlative changes in the Rpt3-bound nucleotide density and the disengagement of the neighboring Arg finger (Fig. 2, B and C). Neither the nucleotide exchange nor the hydrolysis event cause substantial conformational changes in the Rpt hexamer, but they represent the trigger for the most pronounced rearrangement of the mechanochemical cycle in the subsequent transition to 4D.

During this 5T-to-4D transition, we observe an opening of the Rpt3 nucleotide-binding pocket and a disruption of the intersubunit interactions with the neighboring Rpt4 (Fig. 2, B and D). Rpt4 separates from Rpt3, disengages from substrate, and moves from the bottom of the staircase out and upward, which is likely driven by the topologically closed ring architecture of the Rpt hexamer. At the same time, the ATP-bound Rpt5 at the top of the staircase moves to a more central position and binds substrate (Fig. 3B), whereas the substrate-engaged subunits Rpt1, Rpt2, Rpt6, and Rpt3 move as a rigid body downward by one register and translocate the substrate toward the CP gate (Fig. 3, C and D, and movie S2).

Even though we do not detect concrete nucleotide-density changes between the 5T and 4D conformations, we can postulate based on the preceding ATP-hydrolysis event in Rpt3 and the subsequent opening of its pocket that phosphate release from Rpt3 is responsible for the disruption of intersubunit interactions with Rpt4 and the consequent conformational changes of the entire ATPase ring. This model is consistent with our observations that the penultimate subunit in the staircase exhibits a completely or partially closed pocket in all proteasome conformations, whereas the lowest substrate-engaged subunit is always ADP bound with an open pocket (Figs. 3A; and 2, C and D; and fig. S5, B to E). Furthermore, it agrees with previous single-molecule data on the homohexameric ClpX ATPase, suggesting that phosphate release represents the force-generating step of the ATPase cycle (39). Similar to the coordinated nucleotide-exchange and ATP-hydrolysis steps in the previous 5D-to-5T transition, the disruption of the Rpt3-Rpt4 interface through potential phosphate release, the substrate-engagement by Rpt5, and the movement of a four-subunit rigid body for substrate translocation appear to be interdependent and tightly coupled during the 5T-to-4D transition.

For the ATP-hydrolysis and substrate-translocation cycles, our findings suggest that a particular subunit binds ATP and engages substrate at the uppermost position, hydrolyzes ATP when at the penultimate position of the staircase, releases phosphate as it moves to the bottom of the ring, and disengages from substrate in the next step (Fig. 4A). AAA+ motor movements and substrate translocation would thus be powered by sequential ATP hydrolysis and phosphate release as each Rpt transitions to the bottom of the staircase. Our observation of four substrate-engaged subunits moving as a rigid body to translocate substrate in response to ATP hydrolysis and phosphate release is consistent with previous biochemical studies of the ClpX ATPase, which indicated that several subunits interact synergistically with substrate, allowing even a pore-1 loop–deficient subunit to drive translocation (40, 41). The rigid-body movement of four Rpts vertically advances the engaged pore-1 loop Tyr residues by ~6 Å (Fig. 3C and D), suggesting a fundamental step size of two amino acids per hydrolyzed ATP for proteasomal substrate translocation.

We do not observe a vertical movement of substrate due to the defined stall of translocation upon Rpn11 inhibition, and all of our proteasome conformations show largely the same stretch of polypeptide in the central channel. Nevertheless, the substrate responds to staircase rearrangements with lateral movements in the ATPase channel, shifting toward the engaged pore-1 loops and away from the disengaged subunits (fig. S6A). The substrate backbone follows the spiral-staircase arrangement of pore loops rather than traversing the motor in a straight vertical path, and its lateral position in the channel rotates counterclockwise around the hexamer as the Rpts progress through the various nucleotide states (fig. S6A).

Additional states of the proteasomal ATPase cycle

Whereas 5D, 5T, and 4D each contain four ATP-bound and two ADP-bound subunits, 1D* shows three ATP-bound and three ADP-bound subunits (Fig. 3A). We interpret this conformation as an alternate, potentially off-pathway version of a 1D state. A comparison of the Rpt subunit organization in 1D* with those in the 5D, 5T, and 4D states, as well as other proteasome and AAA+ motor structures (figs. S7, A and B), suggests that Rpt5 has prematurely released from substrate at the bottom of the spiral after opening of the Rpt4 nucleotide-binding pocket, and hence both Rpt5 and Rpt1 are disengaged (Fig. 3B and fig. S7A). The Rpt5 pore-1 loop is divergent from the other Rpts, containing a conserved Met rather than a Lys (42), which could result in weaker substrate interactions, especially when translocation is stalled, and thus contribute to the premature disengagement in the 1D* state. Conversely, the 1D* state might be explained by failed nucleotide exchange in Rpt1 at the top of the spiral, which would prevent substrate engagement and the consequent rearrangement of the staircase to the 5D state. Notably, the previously described s3 conformation of the substrate-free proteasome shows the expected staircase arrangement of 1D, with Rpt5 remaining in the lowest position of the staircase (fig. S7B) (33).

Our three distinct spiral-staircase states offer a view of the discrete events leading to a complete step of hydrolysis-driven substrate translocation, yet the current hand-over-hand model requires that every Rpt subunit cycles through all the states. Previous biochemical studies have indicated that ATP hydrolysis in almost all Rpt subunits contribute to substrate engagement and translocation (20, 43, 44). Therefore, the proteasome conformations described here likely represent only a subset of states that may be complemented by the corresponding 4T, 3D, 3T, 6D, 6T, 2D, and 2T states, as well as an additional 1T state between 1D and 5D (Fig. 4, B to D, and fig. S7), to complete the ATP-hydrolysis and substrate-translocation cycles of the proteasome.

Indeed, several additional staircases have been previously observed for the proteasome, albeit in the absence of substrate and induced by non-hydrolyzable ATP analogs, which hampered robust conclusions about mechanochemical coupling or the ATPase cycle. Their overall similarity to our Rpt staircase arrangements is sufficient to designate specific spiral-staircase states. Some of these states (e.g., the ADP-AlF$_x$–bound and s2 states) were regarded as unlikely processing conformations of the AAA+ motor, as they were associated with a partially open CP gate (14, 33, 34). However, two of our engaged states similarly contain only partially open gates yet clearly show substrate being threaded through the central channel to the CP gate (fig. S4). This indicates that a fully open gate is not required for every step of substrate translocation, but its openness may vary depending on the state of the Rpt staircase and corresponding allosteric subtleties in Rpt-tail interactions with the CP. More predictive criteria for a processing motor state are the coaxial alignment of the AAA+ motor with CP, the rotation of the lid subcomplex, and the presence of rigid bodies formed between the large AAA subdomain of one subunit and the small AAA subdomain of its neighbor in all but the substrate-disengaged Rpts. On the basis of these criteria and their staircase orientation, the s2 and recently described s5 states (*14*) would represent 3D or 3T states, and the ADP-AlF$_x$–bound proteasome conformation (*34*) resembles a putative 2D* or 2T* state, with two substrate-disengaged subunits similar to 1D* (Fig. 4, B and C). The s4 and S$_{D2}$ states, which had previously been proposed as potential processing states (*33*, *35*), show overall staircase similarities with our substrate-engaged 4D and 5D states, respectively, even though some of their Rpts are distorted as a likely consequence of inhibited ATP hydrolysis and the absence of substrate (fig. S7, C and D).

Our substrate-engaged proteasome states provide a structural context for previously described ATP analog–bound conformations, enabling us to approximate all possible Rpt staircases, except for the 6D and 6T states, and thus support the model of a sequential hand-over-hand mechanism wherein each Rpt transitions through the ATP-hydrolysis and substrate-translocation cycles (Fig. 4D). Why the proteasome in the presence of substrate preferentially adopts only the 1D*, 5D, 5T, and 4D states remains unclear; however, the likely consecutive 5D, 5T, and 4D states are sufficient to provide us with a complete picture of subunit transitions during the ATPase cycle and substrate translocation.

Outlook

We elucidated structures of the substrate-engaged 26*S* proteasome that answer many of the outstanding questions regarding proteasomal degradation and the general mechanism by which AAA+ translocases process their substrates. Inhibiting deubiquitination by Rpn11 led to a trapped state in which the substrate-attached ubiquitin remains functionally bound in the Rpn11 catalytic groove and the scissile isopeptide bond is linearly aligned with the translocation trajectory through the AAA+ motor (Fig. 1). We conclude that during normal degradation, ubiquitin modifications are pulled directly into the Rpn11 catalytic groove. This ubiquitin-capture mechanism explains how Rpn11 functions as a gatekeeper to efficiently remove all ubiquitin modifications from a substrate during processive translocation, as well as how deubiquitination can be accelerated by mechanical pulling of the AAA+ motor on the substrate polypeptide (*38*).

We resolved three apparently sequential states of the Rpt heterohexamer, which provide a model for the intersubunit coordination during nucleotide exchange, ATP hydrolysis, and phosphate release within the AAA+ motor, as well as how these events are mechanochemically coupled to substrate translocation. Consistent with other substrate-bound AAA+ ATPase structures, the proteasome motor adopts staircase arrangements that encircle the unfolded polypeptide substrate, with one subunit disengaged (*25*–*29*, *45*). Four of the substrate-engaged subunits are ATP bound, whereas the subunit at the bottom of the staircase and the disengaged subunit are bound to ADP. Our structures suggest that nucleotide exchange primes the disengaged subunit for substrate binding at the top of the staircase and that this exchange occurs concomitantly with ATP hydrolysis in the fourth substrate-engaged subunit from the top. Both steps of the ATPase cycle are associated with only subtle allosteric rearrangements, whereas the entire ATPase hexamer undergoes major conformational changes during the subsequent transition that appears to be linked to phosphate release from the posthydrolysis, fourth subunit of the staircase. These rearrangements include the displacement of the bottom ADP-bound subunit, substrate binding of the previously disengaged subunit at the top of the staircase, and the downward movement of the remaining four substrate-engaged subunits as a rigid body. It appears that all of these processes must happen in a coordinated fashion for substrate translocation to occur.

The likely consecutive ATPase states that we observe, together with equivalent staircase arrangements in previous substrate-free proteasome

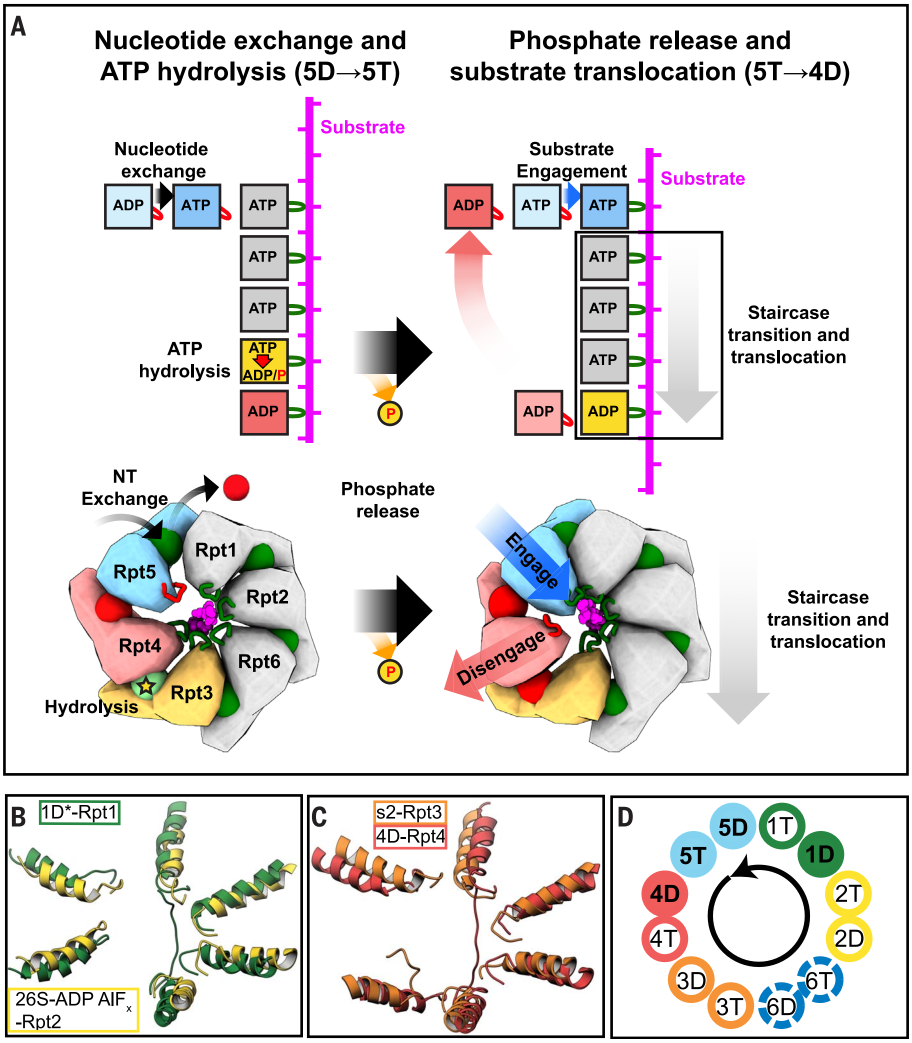

Fig. 4. Coordinated ATP-hydrolysis and substrate-translocation cycles of the proteasome. (**A**) Model for the coordination of ATP-hydrolysis steps and their coupling to substrate translocation. Nucleotide exchange and ATP hydrolysis occur simultaneously in the substrate-disengaged (blue) and penultimate subunit (orange) of the staircase, respectively, with no major conformational changes of the motor. Subsequent phosphate release from the penultimate subunit leads to the displacement of the bottom subunit (red), substrate-engagement by the top subunit (blue), and downward movement of a four-subunit rigid body (boxed) to translocate substrate. (**B**) Spiral staircases of 1D* (dark green) and the 26*S*-ADP-AlF$_x$ [yellow; PDB:5wvk (*35*)], rotated to overlay the disengaged subunits (1D*-Rpt1 and 26*S*-ADP-AlF$_x$-Rpt2) and aligned by the pore-1 loop helices. (**C**) Spiral staircases of the s2 state [orange; PDB: (*33*)] and the 4D state, rotated to overlay the disengaged subunits (s2-Rpt3 and 4D-Rpt4) and aligned by the pore-1 loop helices. (**D**) Schematic of the possible progression of proteasome states, colored by the disengaged subunit, with our observed staircase states indicated by filled circles, staircases from substrate-free proteasome states indicated by open circles, and potential additional states represented by dashed circles.

structures, suggest a sequential progression of individual Rpt subunits through the ATPase cycle, rather than a burst mechanism, where several subunits hydrolyze in rapid succession before nucleotide exchange, as proposed for the ClpX motor on the basis of single-molecule measurements (46, 47). Given the structural and functional similarities between the proteasomal Rpt hexamer and other AAA+ motors, we hypothesize that this sequential ATP-hydrolysis and substrate-translocation mechanism applies to hexameric AAA+ translocases in general. It is reminiscent of a six-subunit conveyor belt, in which a four-subunit rigid body grips the substrate and moves downward as the bottommost subunit disengages and the topmost subunit reengages substrate (Fig. 4A). The coordinated gripping by pore loops of four subunits, which are stabilized by ATP-bound, closed interfaces, likely enables higher pulling forces and reduced slippage, consistent with previous biochemical studies of the ClpX motor (40, 41). Similar conveyor-belt mechanisms have been proposed previously for AAA+ protein translocases as well as DNA and RNA helicases (22, 23, 26–29, 45), yet our structures clarify the precise movement of ATPase subunits and their coordination with individual steps of the ATP-hydrolysis cycle.

Materials and methods

Sample preparation

Purification of proteasome holoenzyme

26*S* proteasomes were purified from strain YYS40 [*MAT*a *leu2-3,112 trp1-1 can1-100 ura3-1ade2-1 his3-11,15 RPN11::RPN11-3XFLAG (HIS3)*] (48) as previously described (49). Briefly, frozen yeast paste from saturated cultures was lysed in a Spex SamplePrep 6875 Freezer/Mill, and cell powder was resuspended in 60 mM HEPES, pH 7.6, 20 mM NaCl, 20 mM KCl, 8 mM $MgCl_2$, 2.5% glycerol, 0.2% NP-40, and ATP regeneration mix (5 mM ATP, 0.03 mg/ml creatine kinase, 16 mM creatine phosphate). Proteasomes were batch-bound to anti-FLAG M2 Affinity Gel (Millipore Sigma), washed with Wash Buffer (60 mM HEPES, pH 7.6, 20 mM NaCl, 20 mM KCl, 8 mM $MgCl_2$, 2.5% glycerol, 5 mM ATP), eluted with 3XFLAG peptide, and further separated by size-exclusion chromatography using a Superose 6 Increase column in 60 mM HEPES, pH 7.6, 20 mM NaCl, 20 mM KCl, 10 mM $MgCl_2$, 2.5% glycerol, and 1 mM ATP.

Preparation of ubiquitinated model substrate

A model substrate consisting of an N-terminal Cys, lysine-less titin-I27^{V15P}, a single-lysine-containing sequence derived from an N-terminal fragment of *Sphaerechinus granularis* cyclinB (residues 22 to 42, with Lys-to-Ala substitutions), a Rsp5 recognition motif (PPPY), and 6X His-tag, was purified after expression in *Escherichia coli* BL21-Star by standard methods. Briefly, In Terrific Broth, protein expression was induced with IPTG at OD_{600} = 1.2 to 1.5 for 5 hours at 30°C. Cells were harvested by centrifugation, resuspended in chilled lysis buffer (60 mM HEPES, pH 7.6 100 mM NaCl, 100 mM KCl, 15 mM imidazole) and lysed by sonication. Following clarification by centrifugation at 20,000 × g, the protein was purified using Ni-NTA affinity chromatography. The substrate was fluorescently labeled using 5-fluoroscein maleimide at pH 7.2 for 3 hours at room temperature and quenched with DTT. Free dye was separated from the substrate by size-exclusion chromatography with a Superdex 200 column (GE Healthcare), buffer exchanging the substrate into 60 mM HEPES, pH 7.6, 20 mM NaCl, 20 mM KCl, 10 mM $MgCl_2$, 2.5% glycerol.

The substrate at final substrate concentration of 50 μM was modified with long, K63-linked ubiquitin chains using 5 μM *Mus musculus* Uba1, 5 μM *S. cerevisiae* Ubc1, 20 μM *S. cerevisiae* Rsp5ΔWW (20, 50), and 2 mM *S. cerevisiae* ubiquitin, in 60 mM HEPES, pH 7.6, 20 mM NaCl, 20 mM KCl, 10 mM $MgCl_2$, 2.5% glycerol, and 15 mM ATP for 3 hours at 25°C, followed by incubation overnight at 4°C.

ATPase assay

Proteasome ATPase activity was monitored using a spectrophotometric assay that couples regeneration of hydrolyzed ATP to the oxidation of NADH (51). Reactions contained a final concentration of 150 nM 26*S* proteasome that had been preincubated with ortho-phenanthroline and ATPase mix for 5 min on ice or mock treated before bringing the sample to 25°C and adding FAM-labeled ubiquitinated substrate to a final concentration of 3 μM and ortho-phenanthroline to a final concentration of 3 mM. Absorbance at 340 nm was measured for 10 min with 12-s intervals in a 384-well plate (Corning) using a Biotek Synergy Neo2 plate reader. Reactions were done in 60 mM HEPES, pH 7.6, 20 mM NaCl, 20 mM KCl, 10 mM $MgCl_2$, 2.5% glycerol 1 mM TCEP, and 1 X ATPase mix (5 mM ATP, 3 U ml^{-1} pyruvate kinase, 3 U ml^{-1} lactate dehydrogenase, 1 mM NADH, and 7.5 mM phosphoenol pyruvate).

Gel-based and fluorescence anisotropy–based monitoring of proteasome degradation

200 nM proteasome was pre-incubated with 3mM ortho-phenanthroline as described in the ATPase assay. Upon the addition of substrate, fluorescence anisotropy of the substrate-attached FAM dye was measured with a 5-s interval in a 384-well plate (Corning) using a Biotek Synergy Neo2 plate reader. 10 min after the addition of ubiquitinated substrate, samples were quenched by the addition of 2% SDS and separated on a 4 to 20% gradient Tris-Glycine SDS-PAGE gel (BioRad). Fluorescence at 530nm from the FAM-labeled substrate was measured using a BioRad ChemiDoc MP imager.

Grid preparation for cryo–electron microscopy

26*S* proteasomes were diluted to a concentration of 20 μM in a solution containing 20 mM HEPES, pH 7.6, 25 mM NaCl, 25 mM KCl, 10 mM $MgCl_2$, 1 mM TCEP, 0.05% NP-40, an ATP regeneration mix (5 mM ATP, 0.03 mg/ml creatine kinase, 16 mM creatine phosphate), and 6 mM ortho-phenanthroline. This solution was mixed with an equal volume of 50 μM ubiquitinated model substrate. Three microliters of the holoenzyme-substrate solution were immediately applied to R2/2 400-mesh grids (Quantifoil) that had been plasma treated for 20 s using a glow discharger (Electron Microscopy Sciences) operated under atmospheric gases. The grids were manually blotted to near dryness with Whatman no. 1 filter paper inside a cold room (4°C) and gravity plunged into liquid ethane using a home-built system.

Data collection and image processing

Cryo-EM data were acquired using the Leginon software for automated data acquisition (52) and a Titan Krios (Thermo Fisher) equipped with a K2 Summit (Gatan) direct electron detector in counting mode (table S1). Movies were collected by navigating to the center of a hole and sequentially image shifting to 10 targets situated at the periphery of the 2-μm hole (fig. S2F). To maximize the number of targets per hole, a nanoprobe beam of 597 nm in diameter was utilized. This resulted in a total acquisition of 11,656 movies at an approximate rate of 2200 movies per day. Movies were recorded at a nominal magnification of 29000x (1.03-Å magnified pixel size) and composed of 25 frames (250 ms per frame, ~50 $e^-/Å^2$ per movie). Movie collection was guided by real-time assessment of image and vitrified sample quality using the Appion image-processing software (53). Frame alignment and dose weighting were performed in real-time using UCSF Motioncor2 (54). CTF estimation on aligned, unweighted, micrographs was performed with Gctf (55).

All data postprocessing steps were conducted in RELION 2.1 (56, 57). Holoenzyme particles were picked using s1 proteasome templates generated from 2D class averages obtained from a prior cryo-EM experiment. This resulted in 579,361 particle picks that were extracted (660 pixels × 660 pixels) and downsampled (110 pixels × 110 pixels) for reference-free 2D classification. 298,997 particles, belonging to the 2D classes demonstrating features characteristic of secondary structural elements, were subjected to 3D refinement and subsequent 3D classification (k = 10). A 3D template of an s1 proteasome was utilized to guide the initial 3D refinement and 3D classification, which ensured that s4-like or substrate-bound reconstructions did not arise from template bias. 238,828 particles corresponding to 3D classes without artefactual features were chosen for further data processing. To minimize the detrimental effects of the holoenzyme's pseudo-symmetry (C2) on resolution, the raw holoenzyme particles were C2 symmetry expanded, 3D refined, and a python script was used to determine the x and y coordinates corresponding to the center of the ATPase within the regulatory particles (RP). In this way, the RPs at each end of every core particle were re-extracted to serve as individual asymmetric units without down-sampling. A round of reference-free 2D classification enabled us to remove the ends of core particles that lacked a regulatory particle. This combined expansion and classification approach netted 380,011 distinct RP-containing particles.

We performed 3D classification on the RP dataset and isolated 242,980 particles whose parent 3D class exhibited a globular ubiquitin-shaped density in the periphery of the Rpn11 active site. Further classification aimed to identify substrate in the central pore of the proteasome. To accomplish this, a soft mask encompassing the AAA+ motor was used to exclude the rest of the proteasome for 3D classification and 3D refinement. This resulted in four distinct AAA+ motor reconstructions containing density attributed to substrate in the central pore with nominal resolutions ranging from 3.9 to 4.7 Å (fig. S2). To further increase map quality outside the AAA+ motor, the global maps corresponding to each AAA+ motor were subdivided into 12 regions for focused 3D refinement, and a composite map consisting of all 12 focused 3D refinements was then generated for each reconstruction to facilitate atomic model building (fig. S2E).

Atomic model building

All atomic models were built using the s4 proteasome model [PDB ID: 5MPC (*33*)] as a template. The initial template's subunits were individually rigid body fit into each of the four EM reconstructions (1D*, 5D, 5T, and 4D) with Chimera "Fit in Map" (*58*). The docked templates were then subjected to one cycle of morphing and simulated annealing in PHENIX, followed by a total of 10 real-space refinement macrocycles utilizing atomic displacement parameters, secondary structure restraints (xsdssp), local grid searches, and global minimization (*59*). After automated PHENIX refinement, manual real-space refinement was performed in Coot (*60*). Residue side chains without attributable density were truncated at the α-carbon, ions were removed, and atoms corresponding to the β-ring, N-ring, and RP lid were removed in the 1D*, 5D, and 5T models due to redundancy and to accelerate refinement. For the 4D state, a similar approach was followed, but atoms corresponding to the N-ring were not removed to facilitate template-based (PDB ID: 5U4P) (*38*) modeling of ubiquitin at the Rpn11 active site. Isopeptide bond-length restraints were manually created and implemented during PHENIX refinement (*59*). Multiple rounds of real-space refinement in PHENIX (five macro cycles, no morphing, no simulated annealing) and Coot were performed to address geometric and steric discrepancies identified by the RCSB PDB validation server and MolProbity (*59*–*61*). To ensure atomic models were not overfit by simulated annealing, morphing, and real space refinement, map-model FSCs were calculated with PHENIX (fig. S2H).

All images were generated using UCSF Chimera (*58*) and ChimeraX (*62*).

REFERENCES AND NOTES

1. G. A. Collins, A. L. Goldberg, The Logic of the 26S Proteasome. *Cell* **169**, 792–806 (2017). doi: 10.1016/j.cell.2017.04.023; pmid: 28525752
2. D. Komander, M. Rape, The ubiquitin code. *Annu. Rev. Biochem.* **81**, 203–229 (2012). doi: 10.1146/annurev-biochem-060310-170328; pmid: 22524316
3. J. A. M. Bard *et al*., Structure and Function of the 26S Proteasome. *Annu. Rev. Biochem.* **87**, 697–724 (2018). doi: 10.1146/annurev-biochem-062917-011931; pmid: 29652515
4. T. Yao, R. E. Cohen, A cryptic protease couples deubiquitination and degradation by the proteasome. *Nature* **419**, 403–407 (2002). doi: 10.1038/nature01071; pmid: 12353037
5. R. Verma *et al*., Role of Rpn11 metalloprotease in deubiquitination and degradation by the 26S proteasome. *Science* **298**, 611–615 (2002). doi: 10.1126/science.1075898; pmid: 12183636
6. G. C. Lander *et al*., Complete subunit architecture of the proteasome regulatory particle. *Nature* **482**, 186–191 (2012). doi: 10.1038/nature10774; pmid: 22237024
7. M. H. Glickman *et al*., A subcomplex of the proteasome regulatory particle required for ubiquitin-conjugate degradation and related to the COP9-signalosome and eIF3. *Cell* **94**, 615–623 (1998). doi: 10.1016/S0092-8674(00)81603-7; pmid: 9741626
8. K. Lasker *et al*., Molecular architecture of the 26S proteasome holocomplex determined by an integrative approach. *Proc. Natl. Acad. Sci. U.S.A.* **109**, 1380–1387 (2012). doi: 10.1073/pnas.1120559109; pmid: 22307589
9. M. H. Glickman, D. M. Rubin, V. A. Fried, D. Finley, The regulatory particle of the Saccharomyces cerevisiae proteasome. *Mol. Cell. Biol.* **18**, 3149–3162 (1998). doi: 10.1128/MCB.18.6.3149; pmid: 9584156
10. R. J. Tomko Jr., M. Funakoshi, K. Schneider, J. Wang, M. Hochstrasser, Heterohexameric ring arrangement of the eukaryotic proteasomal ATPases: Implications for proteasome structure and assembly. *Mol. Cell* **38**, 393–403 (2010). doi: 10.1016/j.molcel.2010.02.035; pmid: 20471945
11. T. Inobe, S. Fishbain, S. Prakash, A. Matouschek, Defining the geometry of the two-component proteasome degron. *Nat. Chem. Biol.* **7**, 161–167 (2011). doi: 10.1038/nchembio.521; pmid: 21278740
12. D. M. Smith *et al*., Docking of the proteasomal ATPases' carboxyl termini in the 20S proteasome's alpha ring opens the gate for substrate entry. *Mol. Cell* **27**, 731–744 (2007). doi: 10.1016/j.molcel.2007.06.033; pmid: 17803938
13. S. Chen *et al*., Structural basis for dynamic regulation of the human 26S proteasome. *Proc. Natl. Acad. Sci. U.S.A.* **113**, 12991–12996 (2016). doi: 10.1073/pnas.1614614113; pmid: 27791164
14. M. R. Eisele *et al*., Expanded Coverage of the 26S Proteasome Conformational Landscape Reveals Mechanisms of Peptidase Gating. *Cell Reports* **24**, 1301–1315.e5 (2018). doi: 10.1016/j.celrep.2018.07.004; pmid: 30067984
15. J. P. Erzberger, J. M. Berger, Evolutionary relationships and structural mechanisms of AAA+ proteins. *Annu. Rev. Biophys. Biomol. Struct.* **35**, 93–114 (2006). doi: 10.1146/annurev.biophys.35.040405.101933; pmid: 16689629
16. P. I. Hanson, S. W. Whiteheart, AAA+ proteins: Have engine, will work. *Nat. Rev. Mol. Cell Biol.* **6**, 519–529 (2005). doi: 10.1038/nrm1684; pmid: 16072036
17. P. Wendler, S. Ciniawsky, M. Kock, S. Kube, Structure and function of the AAA+ nucleotide binding pocket. *Biochim. Biophys. Acta* **1823**, 2–14 (2012). doi: 10.1016/j.bbamcr.2011.06.014; pmid: 21839118
18. J. Hinnerwisch, W. A. Fenton, K. J. Furtak, G. W. Farr, A. L. Horwich, Loops in the central channel of ClpA chaperone mediate protein binding, unfolding, and translocation. *Cell* **121**, 1029–1041 (2005). doi: 10.1016/j.cell.2005.04.012; pmid: 15989953
19. A. Martin, T. A. Baker, R. T. Sauer, Pore loops of the AAA+ ClpX machine grip substrates to drive translocation and unfolding. *Nat. Struct. Mol. Biol.* **15**, 1147–1151 (2008). doi: 10.1038/nsmb.1503; pmid: 18931677
20. R. Beckwith, E. Estrin, E. J. Worden, A. Martin, Reconstitution of the 26S proteasome reveals functional asymmetries in its AAA+ unfoldase. *Nat. Struct. Mol. Biol.* **20**, 1164–1172 (2013). doi: 10.1038/nsmb.2659; pmid: 24013205
21. J. Erales, M. A. Hoyt, F. Troll, P. Coffino, Functional asymmetries of proteasome translocase pore. *J. Biol. Chem.* **287**, 18535–18543 (2012). doi: 10.1074/jbc.M112.357327; pmid: 22493437
22. N. D. Thomsen, J. M. Berger, Running in reverse: The structural basis for translocation polarity in hexameric helicases. *Cell* **139**, 523–534 (2009). doi: 10.1016/j.cell.2009.08.043; pmid: 19879839
23. E. J. Enemark, L. Joshua-Tor, Mechanism of DNA translocation in a replicative hexameric helicase. *Nature* **442**, 270–275 (2006). doi: 10.1038/nature04943; pmid: 16855583
24. A. Martin, T. A. Baker, R. T. Sauer, Rebuilt AAA + motors reveal operating principles for ATP-fuelled machines. *Nature* **437**, 1115–1120 (2005). doi: 10.1038/nature04031; pmid: 16237435
25. S. N. Gates *et al*., Ratchet-like polypeptide translocation mechanism of the AAA+ disaggregase Hsp104. *Science* **357**, 273–279 (2017). doi: 10.1126/science.aan1052; pmid: 28619716
26. C. Puchades *et al*., Structure of the mitochondrial inner membrane AAA+ protease YME1 gives insight into substrate processing. *Science* **358**, eaao0464 (2017). doi: 10.1126/science.aao0464; pmid: 29097521
27. N. Monroe, H. Han, P. S. Shen, W. I. Sundquist, C. P. Hill, Structural basis of protein translocation by the Vps4-Vta1 AAA ATPase. *eLife* **6**, e24487 (2017). doi: 10.7554/eLife.24487; pmid: 28379137
28. Z. A. Ripstein, R. Huang, R. Augustyniak, L. E. Kay, J. L. Rubinstein, Structure of a AAA+ unfoldase in the process of unfolding substrate. *eLife* **6**, e25754 (2017). doi: 10.7554/eLife.25754; pmid: 28390173
29. C. Deville *et al*., Structural pathway of regulated substrate transfer and threading through an Hsp100 disaggregase. *Sci. Adv.* **3**, e1701726 (2017). doi: 10.1126/sciadv.1701726; pmid: 28798962
30. C. Alfieri, L. Chang, D. Barford, Mechanism for remodelling of the cell cycle checkpoint protein MAD2 by the ATPase TRIP13. *Nature* **559**, 274–278 (2018). doi: 10.1038/s41586-018-0281-1; pmid: 29973720
31. M. E. Matyskiela, G. C. Lander, A. Martin, Conformational switching of the 26S proteasome enables substrate degradation. *Nat. Struct. Mol. Biol.* **20**, 781–788 (2013). doi: 10.1038/nsmb.2616; pmid: 23770819
32. P. Śledź *et al*., Structure of the 26S proteasome with ATP-γS bound provides insights into the mechanism of nucleotide-dependent substrate translocation. *Proc. Natl. Acad. Sci. U.S.A.* **110**, 7264–7269 (2013). doi: 10.1073/pnas.1305782110; pmid: 23589842
33. M. Wehmer *et al*., Structural insights into the functional cycle of the ATPase module of the 26S proteasome. *Proc. Natl. Acad. Sci. U.S.A.* **114**, 1305–1310 (2017). doi: 10.1073/pnas.1621129114; pmid: 28115689
34. Z. Ding *et al*., High-resolution cryo-EM structure of the proteasome in complex with ADP-AlFx. *Cell Res.* **27**, 373–385 (2017). doi: 10.1038/cr.2017.12; pmid: 28106073
35. Y. Zhu *et al*., Structural mechanism for nucleotide-driven remodeling of the AAA-ATPase unfoldase in the activated human 26S proteasome. *Nat. Commun.* **9**, 1360 (2018). doi: 10.1038/s41467-018-03785-w; pmid: 29636472
36. F. Beck *et al*., Near-atomic resolution structural model of the yeast 26S proteasome. *Proc. Natl. Acad. Sci. U.S.A.* **109**, 14870–14875 (2012). doi: 10.1073/pnas.1213333109; pmid: 22927375
37. A. Henderson, J. Erales, M. A. Hoyt, P. Coffino, Dependence of proteasome processing rate on substrate unfolding. *J. Biol. Chem.* **286**, 17495–17502 (2011). doi: 10.1074/jbc.M110.212027; pmid: 21454622
38. E. J. Worden, K. C. Dong, A. Martin, An AAA Motor-Driven Mechanical Switch in Rpn11 Controls Deubiquitination at the 26S Proteasome. *Mol. Cell* **67**, 799–811.e8 (2017). doi: 10.1016/j.molcel.2017.07.023; pmid: 28844860
39. M. Sen *et al*., The ClpXP protease unfolds substrates using a constant rate of pulling but different gears. *Cell* **155**, 636–646 (2013). doi: 10.1016/j.cell.2013.09.022; pmid: 24243020
40. O. Iosefson, A. R. Nager, T. A. Baker, R. T. Sauer, Coordinated gripping of substrate by subunits of a AAA+ proteolytic machine. *Nat. Chem. Biol.* **11**, 201–206 (2015). doi: 10.1038/nchembio.1732; pmid: 25599533
41. O. Iosefson, A. O. Olivares, T. A. Baker, R. T. Sauer, Dissection of Axial-Pore Loop Function during Unfolding and Translocation by a AAA+ Proteolytic Machine. *Cell Rep.* **12**, 1032–1041 (2015). doi: 10.1016/j.celrep.2015.07.007; pmid: 26235618
42. F. Zhang *et al*., Structural insights into the regulatory particle of the proteasome from Methanocaldococcus jannaschii. *Mol. Cell* **34**, 473–484 (2009). doi: 10.1016/j.molcel.2009.04.021; pmid: 19481527
43. D. M. Rubin, M. H. Glickman, C. N. Larsen, S. Dhruvakumar, D. Finley, Active site mutants in the six regulatory particle

ATPases reveal multiple roles for ATP in the proteasome. *EMBO J.* **17**, 4909–4919 (1998). doi: 10.1093/emboj/17.17.4909; pmid: 9724628
44. Y. C. Kim, X. Li, D. Thompson, G. N. Demartino, ATP-binding by proteasomal ATPases regulates cellular assembly and substrate-induced functions of the 26S proteasome. *J. Biol. Chem.* **288**, 3334–3345 (2013). doi: 10.1074/jbc.M112.424788
45. H. Han, N. Monroe, W. I. Sundquist, P. S. Shen, C. P. Hill, The AAA ATPase Vps4 binds ESCRT-III substrates through a repeating array of dipeptide-binding pockets. *eLife* **6**, e31324 (2017). doi: 10.7554/eLife.31324; pmid: 29165244
46. R. A. Maillard *et al.*, ClpX(P) generates mechanical force to unfold and translocate its protein substrates. *Cell* **145**, 459–469 (2011). doi: 10.1016/j.cell.2011.04.010; pmid: 21529717
47. P. Rodriguez-Aliaga, L. Ramirez, F. Kim, C. Bustamante, A. Martin, Substrate-translocating loops regulate mechanochemical coupling and power production in AAA+ protease ClpXP. *Nat. Struct. Mol. Biol.* **23**, 974–981 (2016). doi: 10.1038/nsmb.3298; pmid: 27669037
48. T. Sone, Y. Saeki, A. Toh-e, H. Yokosawa, Sem1p is a novel subunit of the 26 S proteasome from Saccharomyces cerevisiae. *J. Biol. Chem.* **279**, 28807–28816 (2004). doi: 10.1074/jbc.M403165200; pmid: 15117943
49. D. S. Leggett, M. H. Glickman, D. Finley, Purification of proteasomes, proteasome subcomplexes, and proteasome-associated proteins from budding yeast. *Methods Mol. Biol.* **301**, 57–70 (2005). pmid: 15917626
50. H. C. Kim, J. M. Huibregtse, Polyubiquitination by HECT E3s and the determinants of chain type specificity. *Mol. Cell. Biol.* **29**, 3307–3318 (2009). doi: 10.1128/MCB.00240-09; pmid: 19364824
51. J. G. Nørby, Coupled assay of Na+,K+-ATPase activity. *Methods Enzymol.* **156**, 116–119 (1988). doi: 10.1016/0076-6879(88)56014-7; pmid: 2835597
52. B. Carragher *et al.*, Leginon: An automated system for acquisition of images from vitreous ice specimens. *J. Struct. Biol.* **132**, 33–45 (2000). doi: 10.1006/jsbi.2000.4314; pmid: 11121305
53. G. C. Lander *et al.*, Appion: An integrated, database-driven pipeline to facilitate EM image processing. *J. Struct. Biol.* **166**, 95–102 (2009). doi: 10.1016/j.jsb.2009.01.002; pmid: 19263523
54. S. Q. Zheng *et al.*, MotionCor2: Anisotropic correction of beam-induced motion for improved cryo-electron microscopy. *Nat. Methods* **14**, 331–332 (2017). doi: 10.1038/nmeth.4193; pmid: 28250466
55. K. Zhang, Gctf: Real-time CTF determination and correction. *J. Struct. Biol.* **193**, 1–12 (2016). doi: 10.1016/j.jsb.2015.11.003; pmid: 26592709
56. S. H. Scheres, S. Chen, Prevention of overfitting in cryo-EM structure determination. *Nat. Methods* **9**, 853–854 (2012). doi: 10.1038/nmeth.2115; pmid: 22842542
57. D. Kimanius, B. O. Forsberg, S. H. Scheres, E. Lindahl, Accelerated cryo-EM structure determination with parallelisation using GPUs in RELION-2. *eLife* **5**, e18722 (2016). doi: 10.7554/eLife.18722; pmid: 27845625
58. E. F. Pettersen *et al.*, UCSF Chimera—a visualization system for exploratory research and analysis. *J. Comput. Chem.* **25**, 1605–1612 (2004). doi: 10.1002/jcc.20084; pmid: 15264254
59. P. V. Afonine *et al.*, Towards automated crystallographic structure refinement with phenix.refine. *Acta Crystallogr. D Biol. Crystallogr.* **68**, 352–367 (2012). doi: 10.1107/S0907444912001308; pmid: 22505256
60. P. Emsley, B. Lohkamp, W. G. Scott, K. Cowtan, Features and development of Coot. *Acta Crystallogr. D Biol. Crystallogr.* **66**, 486–501 (2010). doi: 10.1107/S0907444910007493; pmid: 20383002
61. V. B. Chen *et al.*, MolProbity: All-atom structure validation for macromolecular crystallography. *Acta Crystallogr. D Biol. Crystallogr.* **66**, 12–21 (2010). doi: 10.1107/S0907444909042073; pmid: 20057044
62. T. D. Goddard *et al.*, UCSF ChimeraX: Meeting modern challenges in visualization and analysis. *Protein Sci.* **27**, 14–25 (2018). doi: 10.1002/pro.3235; pmid: 28710774

ACKNOWLEDGMENTS

We thank B. M. Gardner, J. A. M. Bard, A. L. Yokom, and C. Puchades for comments and critical evaluation of the manuscript; all members of the Martin and Lander laboratories for discussions, suggestions, and support; and R. J. Beckwith for cloning the model substrate. All cryo-EM data were collected at The Scripps Research Institute (TSRI) electron microscopy facility. We thank B. Anderson for microscope support and J. C. Ducom at TSRI's High Performance Computing facility for computational support. **Funding:** A.H.P. is a fellow of the American Cancer Society (132279-PF-18-189-01-DMC). S.N.G. is a Howard Hughes Medical Institute Fellow of the Damon Runyon Cancer Research Foundation (DRG-2342-18). G.C.L. is supported as a Pew Scholar in the Biomedical Sciences by the Pew Charitable Trusts. A.M. is an investigator of the Howard Hughes Medical Institute. This work was funded by the National Institutes of Health (DP2EB020402 to G.C.L. and R01-GM094497 to A.M.) and the Howard Hughes Medical Institute (A.M.). Computational analyses of EM data were performed using shared instrumentation at SR funded by NIH S10OD021634. **Author contributions:** A.H.P., E.A.G., and S.N.G. designed experiments and performed data analysis. A.H.P. performed cryo-EM sample preparation, data collection, and data processing. E.A.G. expressed and purified constructs and performed biochemical experiments. G.C.L and A.M. designed and supervised the study. All authors wrote the manuscript. **Competing interests:** The authors declare no competing interests. **Data and materials availability:** Structural data are available in the Electron Microscopy Databank and the RCSB Protein Databank (EMDB IDs 9042, 9043, 9044, and 9045 and PDB IDs 6EF0, 6EF1, 6EF2, and 6EF3 for the proteasome states 1D*, 5D, 5T, and 4D, respectively). All other data are available in the main text or the supplementary materials.

SUPPLEMENTARY MATERIALS

www.sciencemag.org/content/362/6418/eaav0725/suppl/DC1
Figs. S1 to S7
Tables S1 to S2
Reference (*63*)
Movies S1 and S2

10 August 2018; accepted 4 October 2018
Published online 30 October 2018
10.1126/science.aav0725

RESEARCH ARTICLE SUMMARY

BIOCHEMISTRY

Formyl-methionine as an N-degron of a eukaryotic N-end rule pathway

Jeong-Mok Kim, Ok-Hee Seok, Shinyeong Ju, Ji-Eun Heo, Jeonghun Yeom, Da-Som Kim, Joo-Yeon Yoo, Alexander Varshavsky, Cheolju Lee*, Cheol-Sang Hwang*

INTRODUCTION: In both bacteria and eukaryotic mitochondria and chloroplasts, the ribosomal synthesis of proteins is initiated with the N-terminal (Nt) formyl-methionine (fMet) residue. Nt-fMet is produced pretranslationally by formyltransferases, which use 10-formyltetrahydrofolate as a cosubstrate. By contrast, proteins synthesized by cytosolic ribosomes of eukaryotes were always presumed to bear unformylated N-terminal Met (Nt-Met). The unformylated Nt-Met residue of eukaryotic proteins is often cotranslationally Nt-acetylated, a modification that creates specific degradation signals, Ac/N-degrons, which are targeted by the Ac/N-end rule pathway. The N-end rule pathways are a set of proteolytic systems whose unifying feature is their ability to recognize proteins containing N-degrons, thereby causing the degradation of these proteins by the proteasome or autophagy in eukaryotes and by the proteasome-like ClpAP protease in bacteria. The main determinant of an N-degron is a destabilizing Nt-residue of a protein. Studies over the past three decades have shown that all 20 amino acids of the genetic code can act, in cognate sequence contexts, as destabilizing Nt-residues. The previously known eukaryotic N-end rule pathways are the Arg/N-end rule pathway, the Ac/N-end rule pathway, and the Pro/N-end rule pathway. Regulated degradation of proteins and their natural fragments by the N-end rule pathways has been shown to mediate a broad range of biological processes.

RATIONALE: The chemical similarity of the formyl and acetyl groups and their identical locations in, respectively, Nt-formylated and Nt-acetylated proteins led us to suggest, and later to show, that the Nt-fMet residues of nascent bacterial proteins can act as bacterial N-degrons, termed fMet/N-degrons. Here we wished to determine whether Nt-formylated proteins might also form in the cytosol of a eukaryote such as the yeast *Saccharomyces cerevisiae* and to determine the metabolic fates of Nt-formylated proteins if they could be produced outside mitochondria. Our approaches included molecular genetic techniques, mass spectrometric analyses of proteins' N termini, and affinity-purified antibodies that selectively recognized Nt-formylated reporter proteins.

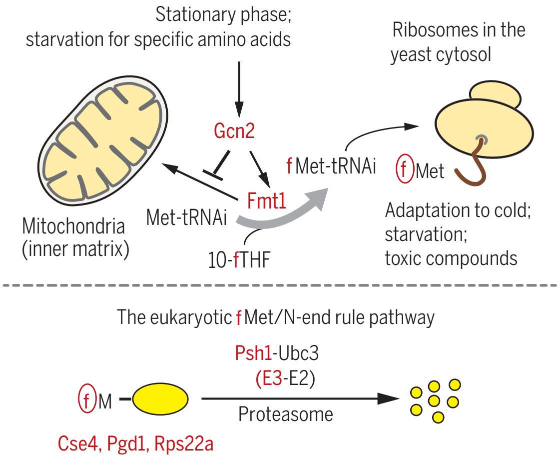

The eukaryotic fMet/N-end rule pathway. (Top) Under undernutrition conditions, the Gcn2 kinase augments the cytosolic localization of the Fmt1 formyltransferase, and possibly also its enzymatic activity. Consequently, Fmt1 up-regulates the cytosolic fMet–tRNAi (initiator transfer RNA), and thereby increases the levels of cytosolic Nt-formylated proteins, which are required for the adaptation of cells to specific stressors. (Bottom) The Psh1 E3 ubiquitin ligase targets the N-terminal fMet-residues of eukaryotic cytosolic proteins, such as Cse4, Pgd1, and Rps22a, for the polyubiquitylation-mediated, proteasome-dependent degradation.

RESULTS: We discovered that the yeast formyltransferase Fmt1, which is imported from the cytosol into the mitochondria inner matrix, can generate Nt-formylated proteins in the cytosol, because the translocation of Fmt1 into mitochondria is not as efficacious, even under unstressful conditions, as had previously been assumed. We also found that Nt-formylated proteins are greatly upregulated in stationary phase or upon starvation for specific amino acids. The massive increase of Nt-formylated proteins strictly requires the Gcn2 kinase, which phosphorylates Fmt1 and mediates its retention in the cytosol. Notably, the ability of Gcn2 to retain a large fraction of Fmt1 in the cytosol of nutritionally stressed cells is confined to Fmt1, inasmuch as the Gcn2 kinase does not have such an effect, under the same conditions, on other examined nuclear DNA–encoded mitochondrial matrix proteins. The Gcn2-Fmt1 protein localization circuit is a previously unknown signal transduction pathway. A down-regulation of cytosolic Nt-formylation was found to increase the sensitivity of cells to undernutrition stresses, to a prolonged cold stress, and to a toxic compound. We also discovered that the Nt-fMet residues of Nt-formylated cytosolic proteins act as eukaryotic fMet/N-degrons and identified the Psh1 E3 ubiquitin ligase as the recognition component (fMet/N-recognin) of the previously unknown eukaryotic fMet/N-end rule pathway, which destroys Nt-formylated proteins.

ON OUR WEBSITE

Read the full article at http://dx.doi.org/10.1126/science.aat0174

CONCLUSION: The Nt-formylation of proteins, a long-known pretranslational protein modification, is mediated by formyltransferases. Nt-formylation was thought to be confined to bacteria and bacteria-descended eukaryotic organelles but was found here to also occur at the start of translation by the cytosolic ribosomes of a eukaryote. The levels of Nt-formylated eukaryotic proteins are greatly increased upon specific stresses, including undernutrition, and appear to be important for adaptation to these stresses. We also discovered that Nt-formylated cytosolic proteins are selectively destroyed by the eukaryotic fMet/N-end rule pathway, mediated by the Psh1 E3 ubiquitin ligase. This previously unknown proteolytic system is likely to be universal among eukaryotes, given strongly conserved mechanisms that mediate Nt-formylation and degron recognition. ■

The list of author affiliations is available in the full article online.

*Corresponding author. Email: cshwang@postech.ac.kr (C.-S.H.); clee270@kist.re.kr (C.L.)

Cite this article as J.-M. Kim *et al.*, *Science* **362**, eaat0174 (2018). DOI: 10.1126/science.aat0174

RESEARCH ARTICLE

BIOCHEMISTRY

Formyl-methionine as an N-degron of a eukaryotic N-end rule pathway

Jeong-Mok Kim[1], Ok-Hee Seok[1], Shinyeong Ju[2,3], Ji-Eun Heo[1], Jeonghun Yeom[2,4], Da-Som Kim[1], Joo-Yeon Yoo[1], Alexander Varshavsky[5], Cheolju Lee[2,4,6]*, Cheol-Sang Hwang[1]*

In bacteria, nascent proteins bear the pretranslationally generated N-terminal (Nt) formyl-methionine (fMet) residue. Nt-fMet of bacterial proteins is a degradation signal, termed fMet/N-degron. By contrast, proteins synthesized by cytosolic ribosomes of eukaryotes were presumed to bear unformylated Nt-Met. Here we found that the yeast formyltransferase Fmt1, although imported into mitochondria, could also produce Nt-formylated proteins in the cytosol. Nt-formylated proteins were strongly up-regulated in stationary phase or upon starvation for specific amino acids. This up-regulation strictly required the Gcn2 kinase, which phosphorylates Fmt1 and mediates its retention in the cytosol. We also found that the Nt-fMet residues of Nt-formylated proteins act as fMet/N-degrons and identified the Psh1 ubiquitin ligase as the recognition component of the eukaryotic fMet/N-end rule pathway, which destroys Nt-formylated proteins.

Nascent proteins bear the N-terminal (Nt) methionine residue, encoded by the AUG initiation codon. In bacteria and in eukaryotic mitochondria and chloroplasts, virtually all nascent proteins bear the N-terminal formyl-methionine (Nt-fMet), which is generated pretranslationally. Formyltransferases (FMTs) use 10-formyltetrahydrofolate as a cosubstrate to N^{α}-terminally formylate the Met moiety of initiator Met-tRNAs. Consequently, nascent bacterial proteins bear Nt-fMet (*1*–*7*). By contrast, proteins synthesized by the cytosolic ribosomes of eukaryotes bear the unformylated Nt-Met residue. This Nt-Met is often N^{α}-terminally acetylated by Nt-acetylases (*8*). We have previously shown that the cotranslational Nt-acetylation of eukaryotic proteins creates specific degradation signals, termed Ac/N-degrons, that are targeted by a distinct N-end rule pathway, termed the Ac/N-end rule pathway (fig. S1F) (*9*–*13*).

The N-end rule pathways are a set of proteolytic systems whose unifying feature is their ability to recognize proteins containing degradation signals called N-degrons, thereby causing the degradation of these proteins by the proteasome or autophagy in eukaryotes and by the proteasome-like ClpAP protease in bacteria (fig. S1) (*9*–*26*). The main determinant of an N-degron is a destabilizing Nt-residue of a protein. Initially, most N-degrons are pro–N-degrons. They are converted to active N-degrons either constitutively (e.g., during the emergence of a protein from a ribosome) or conditionally, via regulated steps. Among the routes to N-degrons are site-specific cleavages of proteins by proteases such as, for example, caspases or calpains, and/or enzymatic Nt-acetylation, Nt-deamidation, Nt-arginylation, or Nt-leucylation of specific proteins at the α-amino groups of their Nt-residues (*10*, *22*). Studies over the past three decades have shown that all 20 amino acids of the genetic code can act, in cognate sequence contexts, as destabilizing Nt-residues (fig. S1). Consequently, many proteins in a cell are conditionally short-lived N-end rule substrates, either as full-length proteins or as protease-generated natural protein fragments. Recognition components of N-end rule pathways, called N-recognins, are either E3 ubiquitin (Ub) ligases or other proteins that can target N-degrons (*10*, *22*).

Regulated degradation of proteins and/or their fragments by the N-end rule pathways mediates a multitude of processes, including the sensing of oxygen, nitric oxide, and heme; the control of subunit stoichiometries in protein complexes; the elimination of misfolded proteins and also of proteins retrotranslocated to the cytosol from other compartments; the regulation of apoptosis and repression of neurodegeneration; the regulation of DNA repair, transcription, replication, and chromosome cohesion and segregation; the regulation of chaperones, G proteins, cytoskeletal proteins, autophagy, gluconeogenesis, peptide import, meiosis, circadian rhythms, fat metabolism, cell migration, immunity, cardiovascular development, spermatogenesis, and neurogenesis; and the regulation of leaf development, senescence, and many other processes in plants [(*10*, *18*–*20*, *22*) and references therein].

Eukaryotes have been known to contain three N-end rule pathways. One of them is the Ac/N-end rule pathway (fig. S1F) (*9*–*13*). At least 60 and 80% of nascent proteins in, respectively, the yeast *Saccharomyces cerevisiae* and human cells are cotranslationally and irreversibly Nt-acetylated by ribosome-associated Nt-acetylases (*8*). Many Nt-acetylated proteins contain Ac/N-degrons, whose regulation includes their reversible steric shielding in cognate protein complexes (*11*–*13*, *27*).

Another N-end rule pathway is the Arg/N-end rule pathway. It targets unacetylated Nt-residues (fig. S1G) (*10*, *14*, *15*, *28*). N-terminal Arg, Lys, His, Leu, Phe, Tyr, Trp, Ile, and Met (if Met is followed by a bulky hydrophobic residue) are directly recognized by N-recognins (*12*, *29*, *30*). By contrast, N-terminal Asn, Gln, Glu, and Asp (as well as Cys, under some conditions) are destabilizing owing to enzymatic deamidation of Nt-Asn and Nt-Gln and Nt-arginylation of Nt-Asp and Nt-Glu (*25*, *26*, *31*).

The third eukaryotic N-end rule pathway, termed the Pro/N-end rule pathway, targets proteins that bear the Nt-Pro residue or a Pro at position two, in addition to adjoining and required sequence motifs (fig. S1E) (*20*). Physiological substrates of the Pro/N-end rule pathway include gluconeogenic enzymes, which are long-lived in cells deprived of glucose but are selectively destroyed upon return to glucose-replete conditions (*20*).

N-terminally formylated proteins in eukaryotic cytosol

In bacteria, the formyl group of Nt-fMet is cotranslationally removed from most (though not all) nascent proteins by the ribosome-associated peptide-deformylase (PDF) (*2*, *3*, *5*). Some fungal and animal genomes, such as those of *S. cerevisiae* and the nematode *Caenorhabditis elegans*, do not encode proteins that are sequelogous [similar in sequence (*32*)] to PDFs (*6*). By contrast, the FMTs, which produce fMet-tRNAi from Met-tRNAi are encoded by all examined eukaryotic genomes, in addition to being universal among bacteria. Mitochondrial FMTs, specified by nuclear DNA, are imported from the cytosol to the inner matrix of mitochondria. Consequently, eight proteins that are encoded by the *S. cerevisiae* mitochondrial DNA, are pretranslationally Nt-formylated at the start of their synthesis in the matrix and retain the formyl group of their Nt-fMet, in agreement with the (inferred) absence of PDF in yeast (*6*).

Nt-acetylation of eukaryotic proteins creates Ac/N-degrons (fig. S1F) (*9*–*13*). The chemical similarity of the formyl and acetyl groups and their identical locations in, respectively, Nt-formylated and Nt-acetylated proteins led us to suggest (*9*), and later to show (*7*), that the fMet

---

[1] Department of Life Sciences, Pohang University of Science and Technology, Pohang, Gyeongbuk 37673, Republic of Korea. [2] Center for Theragnosis, Korea Institute of Science and Technology, Seoul 02792, Republic of Korea. [3] Department of Life Science and Research Institute for Natural Sciences, Hanyang University, Seoul 04763, Republic of Korea. [4] Division of Bio-Medical Science & Technology, KIST School, Korea University of Science and Technology, Seoul 02792, Republic of Korea. [5] Division of Biology and Biological Engineering, California Institute of Technology, Pasadena, CA 91125, USA. [6] Department of Converging Science and Technology, KHU-KIST, Kyung Hee University, Seoul 02447, Republic of Korea.
*Corresponding author. Email: cshwang@postech.ac.kr (C.-S.H.); clee270@kist.re.kr (C.L.)

residues at the N termini of nascent bacterial proteins can act as bacterial N-degrons, termed fMet/N-degrons (fig. S1C).

Given this function of Nt-fMet in bacteria (*7*), and also because a eukaryotic FMT enzyme, before its import into mitochondria, is transiently cytosolic, we began this study by expressing *Escherichia coli* FMT (*Ec*FMT) in yeast. Such an expression was previously shown to convert up to 70% of yeast Met-tRNAi to fMet-tRNAi and to inhibit growth, suggesting that Nt-formylated proteins might be generated in the yeast cytosol (*4*). Our initial aim was to address this possibility directly and to determine the metabolic fate of Nt-formylated proteins if they could be produced outside mitochondria.

*Ec*FMT or vector alone were expressed in yeast from the P_{GAL1} promoter. Wild-type *Ec*FMT (but not its inactive *Ec*FMT^{R43L} mutant; R43L, Arg^{43}→Leu) retarded yeast growth (fig. S2B). These assays involved stable-isotope labeling by amino acids in cell culture (SILAC), an enrichment for Nt-peptides, and capillary liquid chromatography–tandem mass spectrometry (cLC-MS/MS) (fig. S2A). We found that ~11% of nuclear DNA–encoded proteins that yielded Nt-peptides analyzable by cLC-MS/MS were Nt-formylated in yeast cells that expressed *Ec*FMT. Forty-two Nt-formylated peptides were detected by cLC-MS/MS, out of 467 distinct Nt-peptides, which were derived from 357 detected proteins (fig. S2, A, C, and E, and table S1).

An unexpected result of these analyses was the outcome of controls: In yeast lacking *Ec*FMT, ~3% of nuclear DNA–encoded nonmitochondrial proteins contained Nt-fMet (figs. S2, A, C, and D, and S3; and table S1). Thus, notably, proteins containing Nt-fMet were synthesized in the yeast cytosol under normal conditions as well. Additional and independent evidence for this conclusion is described below.

Nt-formylated proteins in wild-type (lacking *Ec*FMT) yeast that were identified by cLC-MS/MS were Act1 (actin), Bos1 (a SNAP receptor), Bud27 (a bud site selector), Rps28a and Rps28b (ribosomal proteins), Leu2 (3-isopropyl malate dehydrogenase), Sup45 (a peptide chain release factor), Dyn2 (a dynein light chain), Uso1 (a vesicle transporter), and Vps52 (a vacuolar sorting–associated protein) (figs. S2D and S3). We also detected mitochondrial DNA–encoded Cox3, which is produced by mitochondrial ribosomes and thus would be expected to bear Nt-fMet, in contrast to nuclear DNA–encoded proteins (figs. S2D and S3G) (*6*).

A parsimonious explanation of these results is that Nt-formylation of nonmitochondrial proteins in wild-type (lacking *Ec*FMT) yeast is caused by low but notable cytosolic levels of the nuclear DNA–encoded *S. cerevisiae* Fmt1 (*Sc*Fmt1) formyltransferase. In this interpretation, the translocation of *Sc*Fmt1 from the cytosol (in which *Sc*Fmt1 is produced) into the mitochondrial matrix (in which *Sc*Fmt1 normally resides) is not as efficient, even under unstressful conditions, as had previously been assumed. Consequently, enough *Sc*Fmt1 would be present in the cytosol to cause the formation of cytosolic fMet-tRNAi and the pretranslational Nt-formylation of cytosolic proteins (fig. S2D and tables S1 and S2). This explanation was found to be correct—the levels of an Nt-formylated Nt-fMet reporter became negligible in *fmt1Δ* yeast (Fig. 1, B and D; see below for details).

Given the pretranslational synthesis of fMet-tRNA, one would expect, a priori, a uniform "partitioning" of the Nt-fMet residues among all or most proteins of a cell's proteome. We do not understand why the actual mass spectrometry (MS)–based results (figs. S2, D and E, and S3; and tables S1 and S2) are different from this expectation, that is, why only some proteins were detected as (partially) Nt-formylated ones. Plausible explanations include an incomplete cLC-MS/MS–mediated coverage of the proteome, different rates of degradation of specific Nt-formylated proteins, and/or that the efficiency of translation initiation with fMet-tRNAi is not the same for all proteins synthesized in the cytosol.

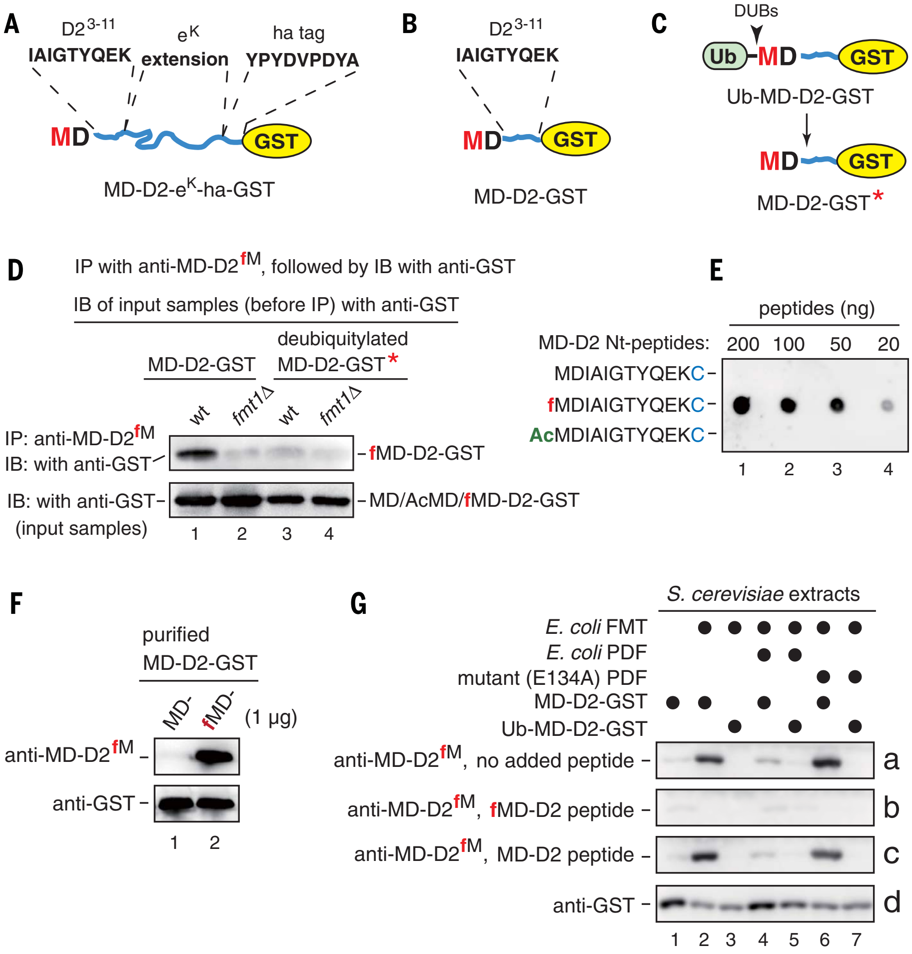

Fig. 1. Antibody specific for a set of N-terminally formylated reporters. (**A**) MD-D2-e^{K}-ha-GST and some of its amino acid sequences. (**B**) MD-D2-GST, same fusion as in (A) but lacking the e^{K}-ha segment. (**C**) Same fusion as in (B) but including the Nt-Ub moiety. (**D**) fMD-D2-GST is produced in wild-type yeast. Lane 1, upper panel: MD-D2-GST was expressed in wild-type (*FMT1*) *S. cerevisiae* and was immunoprecipitated (IP) from yeast extracts with anti–MD-D2^{fM} antibody (which selectively recognized Nt-formylated fMD-D2-GST), followed by SDS-PAGE and immunoblotting (IB) with anti-GST. Lane 2: Same as lane 1 but with *fmt1Δ* yeast. Lane 3: Same as lane 1 but with Ub-MD-D2-GST. Lane 4: Same as lane 3 but with *fmt1Δ* yeast. Lower panel, inputs: Immunoblotting with anti-GST. The red asterisk in (C) and (D) indicates a version of the MD-D2-GST fusion that was produced through deubiquitylation of Ub-MD-D2-GST. (**E**) Dot immunoblotting with anti–MD-D2^{fM} antibody versus decreasing amounts of the unmodified MDIAIGTYQEKC peptide and either its Nt-formylated or its Nt-acetylated counterparts. (**F**) Purified unformylated MD-D2-GST (lane 1) and Nt-formylated fMD-D2-GST (lane 2) were subjected to SDS-PAGE and immunoblotting with either anti–MD-D2^{fM} (upper panel) or anti-GST (lower panel). (**G**) Pretranslational Nt-formylation of MD-D2-GST. The upper three panels show immunoblots, using anti–MD-D2^{fM}, of SDS-PAGE-fractionated extracts from *S. cerevisiae* that expressed (or did not express) specific proteins indicated above the panels (see the main text). Immunoblots a, b, and c with anti–MD-D2^{fM} were performed in the absence or presence of the indicated peptides. Immunoblot d is the same as immunoblot a but with anti-GST.

Antibody to N-terminally formylated protein reporters

The 33-kDa reporter, denoted as MD-D2-e^{K}-ha-GST, was identical to our previously characterized reporter MD-D2-e^{K}-ha-Ura3, save for the glutathione transferase (GST) moiety, used alternately with Ura3 (*7*). The reporter comprised the Nt-sequence MDIAIGTYQEK [denoted as MD-D2 (*7*)], followed by a 44-residue sequence e^{K} [extension (e) containing lysine (K)], by the ha epitope (YPYDVPDYA), by the AFLGQ linker (*9*), and by either GST or Ura3 (Figs. 1A and 2B). The e^{K} segment is often used in reporters because it is unstructured (disordered) while lacking degrons in *E. coli* and yeast (*10*). MD-D2-GST was identical to MD-D2-e^{K}-ha-GST save for the absence of the e^{K}-ha segment (Fig. 1B). (Single-letter abbreviations for amino acid residues are as follows: A, Ala; C, Cys; D, Asp; E, Glu; F, Phe; G, Gly; H, His; I, Ile; K, Lys; L, Leu; M, Met; N, Asn; P, Pro; Q, Gln; R, Arg; S, Ser; T, Thr; V, Val; W, Trp; and Y, Tyr.)

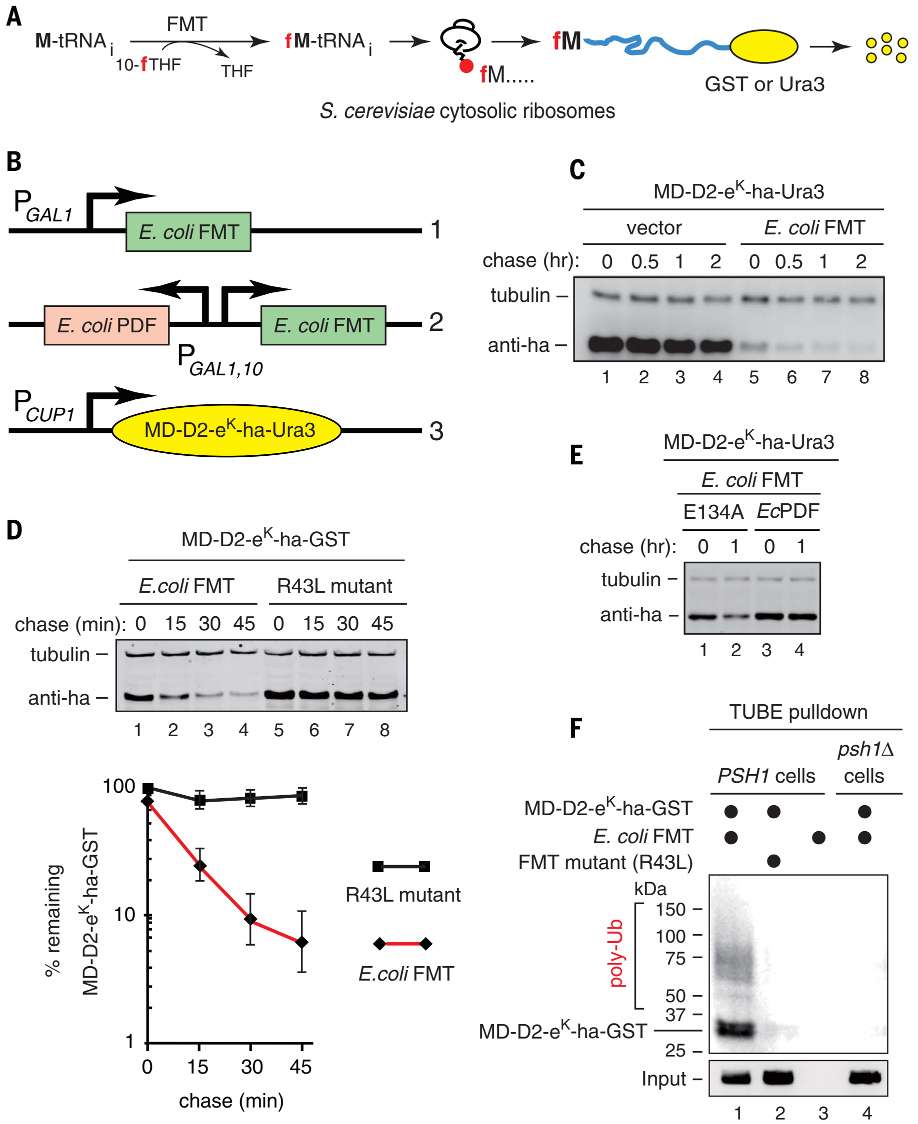

Fig. 2. Selective in vivo degradation of Nt-formylated proteins. (**A**) A diagram of the fMet-mediated cytosolic synthesis and degradation of a GST-based or Ura3-based Nt-formylation reporter (relevant to Figs. 2, B to F, and 3A, and to figs. S4, E to I). tRNAi, initiator transfer RNA. (**B**) Diagrams for the expression of *Ec*FMT, *Ec*PDF, or MD-D2-e^{K}-ha-Ura3. 1) A high-copy plasmid expressing *Ec*FMT in *S. cerevisiae* from the P$_{GAL1}$ promoter, 2) a high-copy plasmid expressing *Ec*FMT and *Ec*PDF from the bidirectional P$_{GAL1,10}$ promoter, and 3) a low-copy plasmid expressing MD-D2-e^{K}-ha-Ura3 (or MD-D2-e^{K}-ha-GST) from the P$_{CUP1}$ promoter. (**C**) CHX-chases with MD-D2-e^{K}-ha-Ura3 in *naa20Δ ubr1Δ S. cerevisiae* (see the main text) that expressed either vector alone (lanes 1 to 4) or *Ec*FMT (lanes 5 to 8). Immunoblotting was performed with anti-ha. (**D**) Same as in (C) but with MD-D2-e^{K}-ha-GST and cells that expressed either *Ec*FMT (lanes 1 to 4) or its inactive *Ec*FMT^{R43L} mutant (lanes 5 to 8). The graph shows quantification of data (three independent pairs of CHX-chases), with mean ± standard error. (**E**) CHX-chases, using anti-ha, with MD-D2-e^{K}-ha-Ura3 in *naa20Δ ubr1Δ S. cerevisiae* that expressed wild-type *Ec*FMT and also expressed either wild-type *Ec*PDF (lanes 3 and 4) or its inactive *Ec*PDF^{E134A} mutant (lanes 1 and 2). (**F**) TUBE-pulldowns with *S. cerevisiae* expressing (or not expressing) either MD-D2-e^{K}-ha-GST or *Ec*FMT or its *Ec*FMT^{R43L} mutant, with anti-GST immunoblotting, after TUBE-pulldowns. The lower panel shows inputs and immunoblotting with anti-GST.

Cycloheximide (CHX)–chases with MD-D2-e^{K}-ha-Ura3 or MD-D2-e^{K}-ha-GST showed that these reporters were short-lived in wild-type *S. cerevisiae* but were nearly completely stable in double-mutant *naa20Δ ubr1Δ* cells that lacked both the NatB (Naa20) Nt-acetylase and the Arg/N-end rule pathway (owing to the absence of Ubr1) (fig. S4, A and B). The *naa20Δ* mutation abrogated the otherwise expected Nt-acetylation, by NatB, of MD-D2-e^{K}-ha–based reporters and thereby precluded their degradation by the Ac/N-end rule pathway (*8*–*13*). Given the stability of MD-D2-e^{K}-ha–based reporters in *naa20Δ ubr1Δ* cells (fig. S4, A and B), most degradation assays were performed in this genetic background.

To detect Nt-fMet by a method independent of mass spectrometry, the synthetic Nt-formylated peptide fMDIAIGTYQEK (the fMD-D2 moiety; Fig. 1, A and B) was used to produce an affinity-purified rabbit antibody, termed anti–MD-D2^{fM}, which recognized the above Nt-formylated peptide and also fMD-D2-GST but did not recognize their unformylated or Nt-acetylated counterparts (Fig. 1E). Nt-formylated and unformylated MD-D2-GST were produced in *E. coli* that were either incubated or not incubated with actinonin, an inhibitor of PDF-mediated deformylation (*5*). The presence of Nt-fMet or unformylated Nt-Met in MD-D2-GST was verified using both MS and anti–MD-D2^{fM} antibody (Fig. 1F and fig. S5).

SDS–polyacrylamide gel electrophoresis (SDS-PAGE) and immunoblotting with anti–MD-D2^{fM} detected Nt-formylated fMD-D2-GST in extracts from *Ec*FMT-expressing yeast (Fig. 1, B and G). More sensitive immunoprecipitation-immunoblotting assays could also detect fMD-D2-GST in extracts from yeast that lacked *Ec*FMT (Fig. 1D). The specificity of anti–MD-D2^{fM} (Fig. 1, E and F) was also confirmed by observing the quenching of immunoblotting signal by the Nt-formylated fMD-D2 peptide but not by its unformylated counterpart (Fig. 1G).

In cells expressing MD-D2-GST, the Nt-fMet residue of fMD-D2-GST was generated pre-translationally (see introduction) (Fig. 1B). By contrast, MD-D2-GST was generated cotranslationally from Ub-MD-D2-GST (bearing the Nt-Ub moiety) upon the cleavage-mediated removal of Nt-Ub by deubiquitylases (Fig. 1C) (*10*). Whereas directly expressed MD-D2-GST could be readily detected (using anti–MD-D2^{fM}) as the Nt-formylated fMD-D2-GST species, no Nt-fMet was detected in MD-D2-GST* that resulted from deubiquitylation of Ub-MD-D2-GST (the asterisk of MD-D2-GST* denotes its distinct origin) (Fig. 1, C and G). Besides confirming the specificity of anti–MD-D2$^{\mathrm{fM}}$, these results indicated the pretranslational (at the level of fMet-tRNAi) origin of the Nt-fMet moiety of fMD-D2-GST. In addition, coexpression of *Ec*FMT and *E. coli* PDF (*Ec*PDF) (but not of its inactive mutant) in yeast strongly down-regulated the Nt-formylated fMD-D2-GST (Fig. 1G), in agreement with the (inferred) absence of PDF in *S. cerevisiae* (*6*).

Selective degradation of Nt-formylated proteins

The expression of *Ec*FMT in yeast resulted in rapid degradation of the otherwise long-lived MD-D2-e$^{\mathrm{K}}$-ha-Ura3 and MD-D2-e$^{\mathrm{K}}$-ha-GST (Fig. 2, A to D, and fig. S4, E to I). By contrast, no discernible degradation of MD-D2-e$^{\mathrm{K}}$-ha-Ura3 or MD-D2-e$^{\mathrm{K}}$-ha-GST occurred upon expression of the inactive *Ec*FMT$^{\mathrm{R43L}}$ mutant or vector alone (Fig. 2, C and D, and fig. S4, E, F, and H). The *Ec*FMT-induced degradation of MD-D2-e$^{\mathrm{K}}$-ha-GST and MD-D2-e$^{\mathrm{K}}$-ha-Ura3 in yeast was nearly abolished by coexpression of the *Ec*PDF but not of its inactive *Ec*PDF$^{\mathrm{E134A}}$ mutant (Fig. 2, B and E, and fig. S4G).

Increasing the levels of *Ec*FMT, using the incrementally stronger yeast promoters P$_{ADH1}$, P$_{TEF1}$, and P$_{TDH3}$, progressively destabilized MD-D2-e$^{\mathrm{K}}$-ha-GST, in part by decreasing its prechase (time-zero) levels (fig. S4H). By contrast, the expression of inactive *Ec*FMT$^{\mathrm{R43L}}$ had no effect (fig. S4H). *Ec*FMT did not discernibly alter the rate of protein synthesis in *S. cerevisiae*, in comparison to expression of inactive *Ec*FMT$^{\mathrm{R43L}}$ (fig. S6, A and B).

Tandem Ub-binding entity (TUBE)–pulldowns showed that MD-D2-e$^{\mathrm{K}}$-ha-GST was polyubiquitylated in yeast upon expression of *Ec*FMT (but not of inactive *Ec*FMT$^{\mathrm{R43L}}$), suggesting that the degradation of Nt-formylated fMD-D2-e$^{\mathrm{K}}$-ha-GST was Ub-dependent (Fig. 2F). Assays with MG132, a proteasome inhibitor, indicated that the degradation of fMD-D2-e$^{\mathrm{K}}$-ha-GST was also proteasome-dependent (fig. S4I). Importantly, the use of anti–MD-D2$^{\mathrm{fM}}$ showed that the *Ec*FMT-induced degradation of MD-D2-e$^{\mathrm{K}}$-ha–based fusions involved, selectively, their Nt-formylated subsets (fig. S4I).

Together, these results (Figs. 1 and 2, and figs. S2 and S4) indicated that the *Ec*FMT-mediated production of fMet-tRNAi in the yeast cytosol causes the synthesis of Nt-formylated proteins, which are rapidly degraded. This degradation required the Nt-fMet residue of an Nt-formylated protein because the protein could be stabilized by coexpression of the active (but not inactive) *Ec*PDF (Fig. 2E and fig. S4G).

We conclude that the Nt-fMet residues of proteins in a eukaryotic cell could act as specific degradation signals, termed fMet/N-degrons. The bulk of these results were obtained with *S. cerevisiae* that ectopically expressed *Ec*FMT. Crucially, however, a minor, but discernible, fraction of nuclear DNA–encoded nonmitochondrial yeast proteins contained Nt-fMet even in *S. cerevisiae* that did not express *Ec*FMT (figs. S2D and S3, and tables S1 and S2).

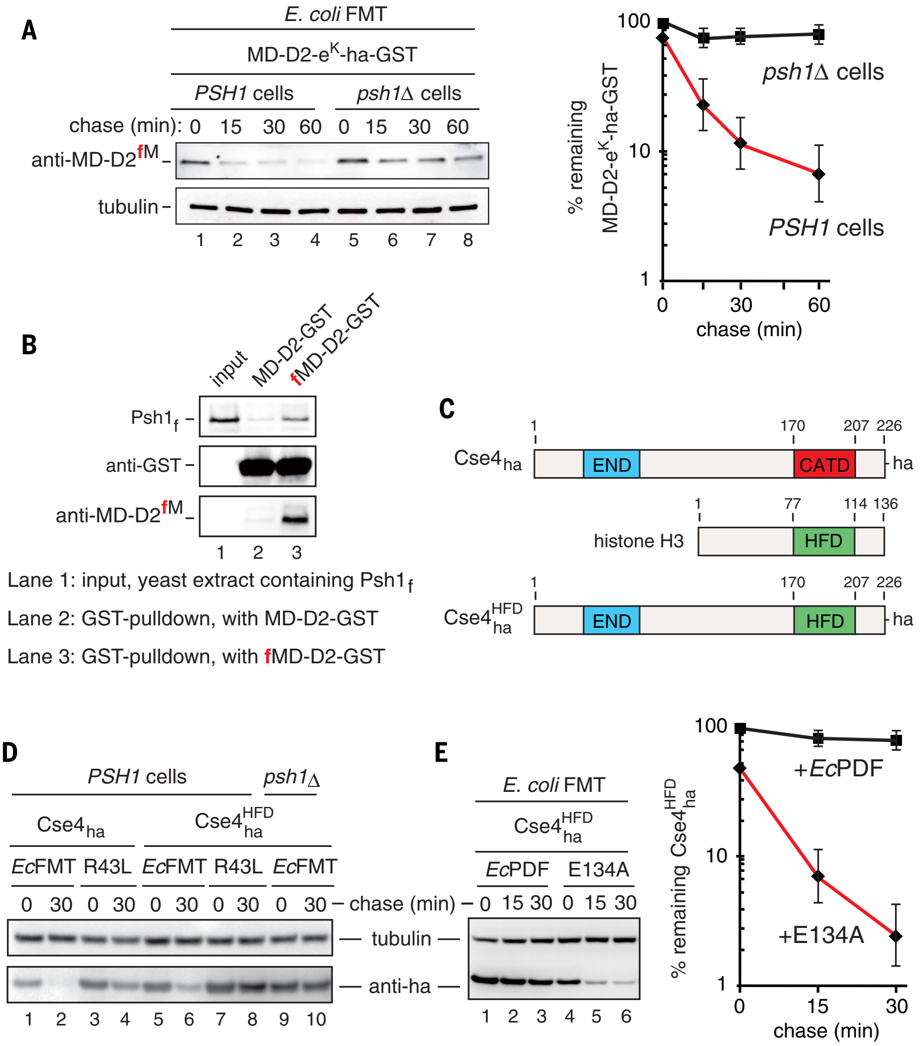

Fig. 3. The Psh1 E3 Ub ligase as an fMet/N-recognin. (**A**) CHX-chases with MD-D2-e$^{\mathrm{K}}$-ha-GST in *naa20Δ ubr1Δ S. cerevisiae* (see the main text) that expressed *Ec*FMT and either contained (lanes 1 to 4) or lacked (lanes 5 to 8) the Psh1 E3. Immunoblotting with anti–fMD-D2$^{\mathrm{fM}}$. The graph shows quantification of data (three independent pairs of CHX-chases), with mean ± standard error. (**B**) GST-pulldowns with purified Nt-formylated fMD-D2-GST versus unformylated MD-D2-GST and extracts of *S. cerevisiae* that expressed Psh1$_{\mathrm{f}}$ (see materials and methods). Detection with anti-flag (specific for Psh1$_{\mathrm{f}}$), anti-GST, and anti–fMD-D2$^{\mathrm{fM}}$ (specific for Nt-formylated fMD-D2-GST). Lanes 1 to 3 are described in (B). Note specific binding of Psh1$_{\mathrm{f}}$ to fMD-D2-GST. (**C**) Wild-type ha-tagged Cse4$_{\mathrm{ha}}$, histone H3, and "hybrid" Cse4$_{\mathrm{ha}}^{\mathrm{HFD}}$ (see the main text). (**D**) CHX-chases with Cse4$_{\mathrm{ha}}$ (lanes 1 to 4) and Cse4$_{\mathrm{ha}}^{\mathrm{HFD}}$ (lanes 5 to 10) in *S. cerevisiae* expressing *Ec*FMT or its *Ec*FMT$^{\mathrm{R43L}}$ mutant. Lanes 9 and 10 are the same as lanes 5 and 6 but in *psh1Δ* yeast. Immunoblotting was performed with anti-ha. (**E**) CHX-chases of Cse4$_{\mathrm{ha}}^{\mathrm{HFD}}$ in *Ec*FMT-expressing *S. cerevisiae* that also expressed *Ec*PDF (lanes 1 to 3) or its inactive *Ec*PDF$^{\mathrm{E134A}}$ mutant (lanes 4 to 6). The graph shows quantification of data (three independent pairs of CHX-chases), with mean ± standard error.

Degradation of Nt-formylated proteins requires the Psh1 E3 ubiquitin ligase

Given these results, we screened a collection of single-mutant *S. cerevisiae* strains that lacked specific E3 Ub ligases and expressed both *Ec*FMT and MD-D2-e$^{\mathrm{K}}$-ha-GST. (*Ec*FMT was used to augment the synthesis of Nt-formylated proteins.) Extracts from 78 mutant strains were fractionated by SDS-PAGE and immunoblotted with anti-ha, anti–MD-D2$^{\mathrm{fM}}$, and anti-tubulin (fig. S7). Anti-ha detected all species of MD-D2-e$^{\mathrm{K}}$-ha-GST, whereas anti–MD-D2$^{\mathrm{fM}}$ selectively detected fMD-D2-e$^{\mathrm{K}}$-ha-GST. The Nt-formylated fMD-D2-e$^{\mathrm{K}}$-ha-GST (relative to total MD-D2-e$^{\mathrm{K}}$-ha-GST) was strongly increased in the *psh1Δ* mutant, implying the in vivo stabilization of fMD-D2-e$^{\mathrm{K}}$-ha-GST in the absence of Psh1 (fig. S7A, lane 10).

Nt-formylated fMD-D2-e$^{\mathrm{K}}$-ha-GST was also increased in three other E3 mutants (figs. S7A, lane 13; S7D, lane 9; and S7F, lane 11). However, those increases were much less than the one in *psh1Δ* cells and were also accompanied by higher levels of total MD-D2-e^K-ha-GST, in contrast to the strong and selective increase of fMD-D2-e^K-ha-GST in *psh1*Δ cells (fig. S7A, lane 10). In agreement with this screen (fig. S7), the degradation of fMD-D2-e^K-ha-GST required the Psh1 E3 (Fig. 3A). In addition, the polyubiquitylation of MD-D2-e^K-ha-GST was nearly abolished in *psh1*Δ yeast, despite the presence of *Ec*FMT (Fig. 2F, lane 4).

The levels of mRNA encoding MD-D2-e^K-ha-GST were approximately equal in *PSH1* versus *psh1*Δ yeast (fig. S8A). Furthermore, C-terminally flag-tagged Psh1 (Psh1$_f$) interacted with the Nt-formylated fMD-D2-GST but not with its unformylated counterpart, indicating that physical binding by the Psh1 E3 required the Nt-formyl group of fMD-D2-GST (Fig. 3B).

We conclude that Psh1 is an N-recognin, termed the fMet/N-recognin, of a eukaryotic N-end rule pathway, termed the fMet/N-end rule pathway (fig. S1B). Psh1 is a 406-residue RING-type E3 Ub ligase that acts together with the Ubc8 or Ubc3 E2 enzymes (*33*–*36*). In *Ec*FMT-expressing yeast, the degradation of fMD-D2-e^K-ha-GST was comparably efficacious in *UBC8* and *ubc8*Δ cells (fig. S8C). By contrast, fMD-D2-e^K-ha-GST was stabilized in a temperature-sensitive Ubc3 (Ubc3^{ts}) mutant at nonpermissive temperature, indicating that the Psh1 fMet/N-recognin mediates the fMet/N-end rule pathway largely together with the Ubc3 E2 (figs. S1B and S8B).

Nt-formylation of the Cse4 histone accelerates its Psh1-mediated degradation

Until now, the sole known physiological substrate of Psh1 was Cse4 (called CENP-A in mammals), the centromere-specific histone H3 variant whose degradation is both Psh1-dependent and proteasome-dependent (*33*–*37*). Using the same approach that yielded anti–MD-D2^{fM}, we produced an antibody, termed anti-Cse4^{fM}, that selectively recognized the Nt-formylated fMet-Cse4 (fig. S4, C and D). C-terminally ha-tagged Cse4 (Cse4$_{ha}$) was strongly destabilized, in a Psh1-dependent manner, in wild-type yeast that expressed *Ec*FMT (but not its inactive *Ec*FMT^{R43L} mutant) (Fig. 3, C and D, and fig. S8H).

Recognition of Cse4 by Psh1 involves the CENP-A targeting domain (CATD) of Cse4 (Fig. 3C) (*34*, *35*). To address the targeting of Cse4 through its Nt-fMet residue versus the CATD, we replaced CATD with the loop 1–α2 helix of the histone fold domain (HFD) of the main histone H3 (*34*), yielding a chimeric Cse4$^{HFD}_{ha}$ protein. In the absence of *Ec*FMT, Cse4$^{HFD}_{ha}$ was longer-lived than Cse4$_{ha}$, but both Cse4$^{HFD}_{ha}$ and Cse4$_{ha}$ were strongly destabilized in yeast that expressed the active (but not inactive) *Ec*FMT (Fig. 3, C and D, and fig. S8E). Immunoblotting with anti-Cse4^{fM} confirmed the Nt-formylation of Cse4$^{HFD}_{ha}$ in the presence of *Ec*FMT (fig. S4D). In agreement with these results, Cse4$^{HFD}_{ha}$, which was short-lived in *Ec*FMT-expressing wild-type yeast, was stabilized either by coexpression of the *Ec*PDF or by ablation of the yeast Psh1 E3 (Fig. 3, D and E, and fig. S8E). Cse4$^{HFD}_{ha}$ was also stabilized in yeast Ubc3^{ts} cells (but not in *ubc8*Δ cells) at nonpermissive temperature, again indicating that Ubc3 is the main E2 of the Psh1-mediated fMet/N-end rule pathway (fig. S8, E and F).

Psh1-mediated targeting of fMet/N-degrons in proteins other than Cse4

Thus far, 42 yeast proteins have been identified, by cLC-MS/MS, as those that are partially Nt-formylated in *Ec*FMT-expressing *S. cerevisiae* (fig. S2E). We asked whether some of these proteins were metabolically unstable, and, if so, whether the bulk of their degradation required both Nt-formylation and the Psh1 Ub ligase.

Forty-one proteins (all except Leu2) (fig. S2E) were C-terminally ha tagged and analyzed by CHX-chases in *PSH1* and *psh1*Δ yeast cells that expressed *Ec*FMT. Anti-ha cannot distinguish between Nt-formylated and unformylated versions of these proteins. Observing the degradation of a protein that was dependent on both the Psh1 E3 and *Ec*FMT would indicate that a large fraction of the protein's molecules contained Nt-fMet. Out of 41 proteins examined, these assays identified two proteins, Pgd1 and Rps22a, whose degradation required both Psh1 and *Ec*FMT (fig. S6, C to H), similarly to the Cse4 histone (Fig. 3, C to E, and fig. S8, E to H).

Pgd1 is a subunit of the Mediator complex that functions together with RNA polymerase II (*38*). Degradation of Pgd1 required both *Ec*FMT and the Psh1 E3 and could be counteracted by coexpression of the *Ec*PDF (but not of its inactive mutant) (fig. S6D). Similar results were obtained with the ribosomal protein Rps22a (fig. S6H). The other 39 proteins, which were also partially Nt-formylated in *Ec*FMT-expressing yeast (fig. S2E), yielded negative results (an example, with Hxk1, is shown in fig. S6I).

Thus, although Nt-formylated versions of the above proteins in *Ec*FMT-expressing yeast could be detected by cLC-MS/MS (fig. S2E), the relative levels of Nt-formylated proteins, vis-à-vis their unformylated counterparts, would be too low for observing degradation of Nt-formylated species using anti-ha, which did not distinguish between Nt-formylated and unformylated versions of these proteins. Another, not mutually exclusive explanation would be the conditionality of fMet/N-degrons in these endogenous (not overexpressed) proteins, owing to a rapid posttranslational shielding (sequestration) of their fMet/N-degrons. The shielding would occur through an intramolecular protein folding and/or through formation of oligomeric protein complexes. This mechanism of conditionality has been demonstrated for Ac/N-degrons in proteins whose degradation by the Ac/N-end rule pathway could be halted in the presence of their natural protein ligands (*11*).

Psh1-mediated destruction of Nt-formylated proteins counteracts their toxicity

Slow growth of *Ec*FMT-expressing *S. cerevisiae* could be rescued by expression of *Ec*PDF but not of its inactive mutant (*4*). Because the levels of Nt-formylated proteins are increased in *Ec*FMT-expressing yeast (Fig. 1G; fig. S2, C to E; and table S1), and because the Psh1 Ub ligase mediates the degradation of Nt-formylated proteins (Fig. 3, A, B, and D; and figs. S6, C, E, and F, and S8, E, G, and H), an ablation of Psh1 would be expected to make cells hypersensitive to Nt-formylated proteins. In agreement with this prediction, the growth defect of *Ec*FMT-expressing yeast was notably higher in *psh1*Δ cells, either on plates or in liquid cultures (fig. S9). Deformylation of Nt-formylated proteins, through a coexpression of *Ec*PDF (but not of its inactive mutant), nearly abolished the growth-rate difference between *PSH1* and *psh1*Δ cells that expressed *Ec*FMT (fig. S9B).

These (fig. S9) and other results (see below) implied an increase in steady-state levels of Nt-formylated proteins both in *psh1*Δ cells and in stationary-phase wild-type cells. We performed additional SILAC-based cLC-MS/MS surveys (as described above and in fig. S2), but this time without ectopic *Ec*FMT, and with stationary-phase wild-type cells versus stationary-phase *psh1*Δ cells. This set of MS/MS analyses, with cells not expressing *Ec*FMT, identified 21 Nt-formylated proteins in wild-type yeast and 26 Nt-formylated proteins in *psh1*Δ yeast, with both cultures in stationary phase (table S2).

Up-regulation of Nt-formylated proteins upon starvation for specific amino acids

Similarly to the effect of expressing *Ec*FMT in *S. cerevisiae*, an expression, also in yeast, of *Sc*Fmt1$^{\Delta 1-26}$, a derivative of the yeast *Sc*Fmt1 that lacked its mitochondrial presequence, increased the levels of Nt-formylated fMD-D2-GST (fig. S8D). The levels of Nt-formylated fMD-D2-GST were further increased when yeast cultures expressing *Sc*Fmt1$^{\Delta 1-26}$ reached the stationary phase, despite the presence of the fMet/N-end rule pathway in these cells (Fig. 4A and fig. S1B).

A strong increase of Nt-formylated fMD-D2-GST was also observed with wild-type stationary-phase yeast, that is, with cells that expressed neither *Ec*FMT nor the presequence-lacking *Sc*Fmt1$^{\Delta 1-26}$ (Fig. 4B). By contrast, no Nt-formylated fMD-D2-GST was present in *fmt1*Δ yeast under any growth conditions (Figs. 1D and 4B). These results were an independent confirmation of the cLC-MS/MS findings that the endogenous wild-type *Sc*Fmt1, though normally imported into mitochondria, also mediated the synthesis of Nt-formylated cytosolic proteins (fig. S2D and tables S1 and S2).

We wished to identify other stresses, more specific than stationary phase, that could up-regulate Nt-formylated proteins. To facilitate the detection of Nt-formylated fMD-D2-GST by anti–MD-D2^{fM}, wild-type *Sc*Fmt1 was moderately overexpressed from a low-copy plasmid and the constitutive P$_{TDH3}$ promoter in *psh1*Δ *S. cerevisiae*, which lacked the fMet/N-end rule pathway and could not degrade Nt-formylated proteins.

Nt-formylated fMD-D2-GST was greatly up-regulated when yeast cells (auxotrophic for His, Lys, Leu, and Trp) were transferred, for

24 hours, to synthetic media lacking His or Lys (Fig. 4E). By contrast, starvation for Leu alone or Trp alone did not produce a similar effect (Fig. 4E). Furthermore, decreases of His in the medium could incrementally up-regulate Nt-formylated fMD-D2-GST, in contrast to similar decreases of Trp, which did not alter the (initially low) level of fMD-D2-GST (Fig. 4, F and G). Nt-formylated fMD-D2-GST was up-regulated upon starvation for His (in yeast that expressed either wild-type *Sc*Fmt1 or the cytosol-localized *Sc*Fmt1$^{\Delta 1–26}$) even in *PSH1* cells, which contained the fMet/N-end rule pathway and could degrade Nt-formylated proteins (Fig. 4, H and I).

Up-regulation of Nt-formylated fMD-D2-GST in stationary-phase cells or upon starvation for His was completely abolished in *gcn2*Δ cells, which lacked Gcn2, a stress-activated multifunctional protein kinase (Fig. 4, J and K). Even the much stronger increase, at stationary phase, of Nt-formylated fMD-D2-GST in *psh1*Δ

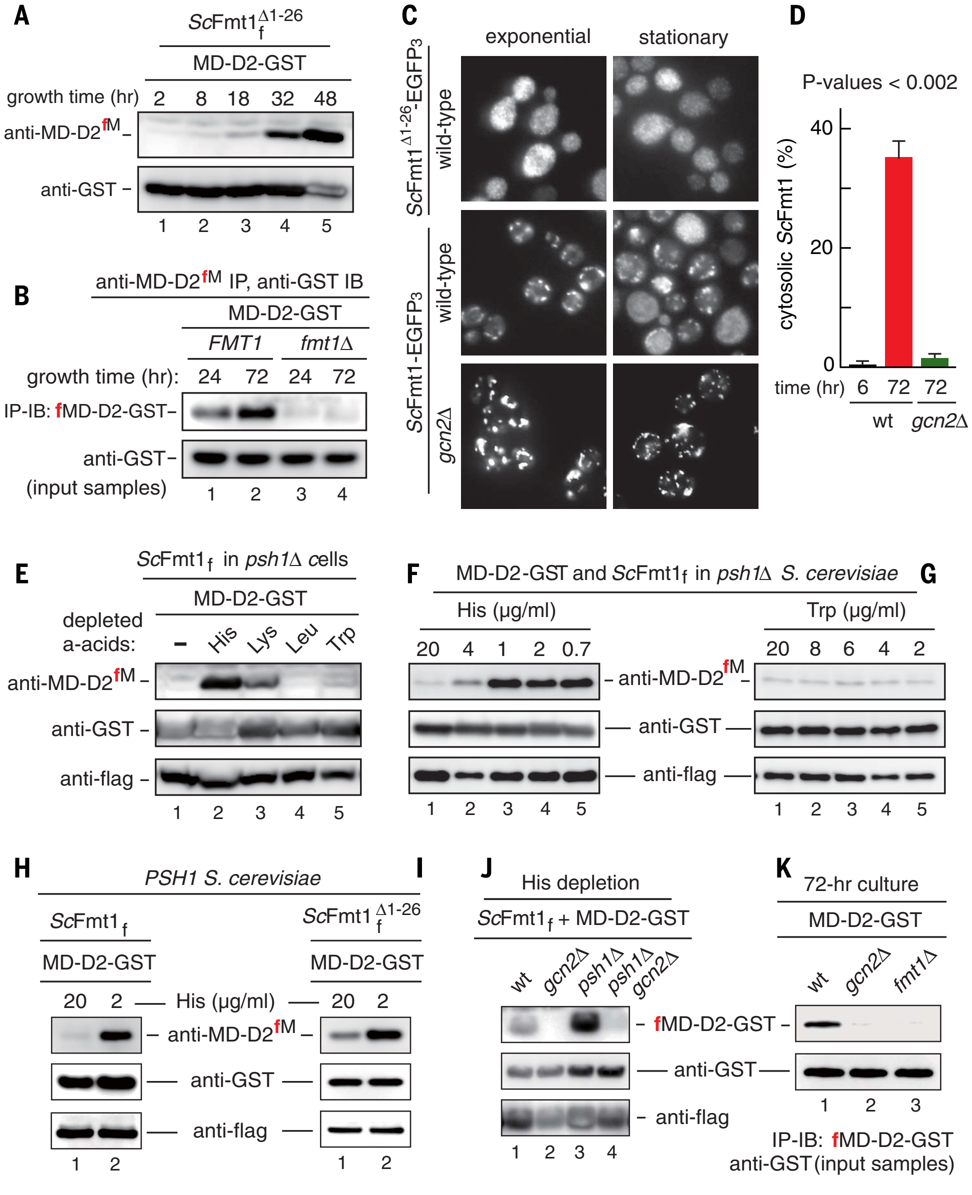

Fig. 4. Up-regulation of Nt-formylated proteins and cytosolic localization of mitochondrial formyltransferase upon starvation in yeast. (**A**) *S. cerevisiae* expressing MD-D2-GST and the mitochondrial presequence–lacking *Sc*Fmt1$_f^{\Delta 1–26}$ were grown in SC medium until stationary phase (48 hours), followed by SDS-PAGE of cell extracts and detection of Nt-formylated fMD-D2-GST by immunoblotting with anti–MD-D2^{fM}. The lower panel shows immunoblotting with anti-GST. (**B**) *FMT1* (lanes 1 and 2) and *Sc*Fmt1-lacking *fmt1*Δ *S. cerevisiae* (lanes 3 and 4) expressing MD-D2-GST were grown in SC medium from 24 to 72 hours (reaching stationary phase), followed by immunoprecipitation of cell extracts with anti–MD-D2^{fM}, SDS-PAGE of immunoprecipitates, and immunoblotting with anti-GST (upper panel). The lower panel shows immunoblotting with anti-GST, but of total (input) samples. (**C**) Representative images of fluorescent wild-type cells expressing, respectively, the presequence-lacking *Sc*Fmt1$^{\Delta 1–26}$-EGFP$_3$ fusion (two upper squares) and wild-type *Sc*Fmt1-EGFP$_3$ (two middle squares). The two bottom squares show *gcn2*Δ cells expressing wild-type *Sc*Fmt1-EGFP$_3$. The left and right squares show, respectively, cells in exponential growth and in stationary phase. Note the increased cytosolic localization of *Sc*Fmt1-EGFP$_3$ in wild-type cells in stationary phase (middle-right square) but not in stationary-phase *gcn2*Δ cells (bottom-right square). (**D**) Relative amounts of the cytosolically localized *Sc*Fmt1-EGFP$_3$ in wild-type cells during exponential growth (6-hour growth) and in stationary-phase (72-hour growth) wild-type versus *gcn2*Δ cells. The data are shown as means ± standard deviations for ~300 cells in each of three independent experiments. *P* values of less than 0.002 were calculated using a two-tailed Student's *t* test. (**E**) Stationary (48 hour; A_{600} of ~3.5) cultures of *psh1*Δ *S. cerevisiae* (auxotrophic for His, Lys, Leu, and Trp) expressing MD-D2-GST and the wild-type flag-tagged *Sc*Fmt1$_f$ in SC medium were incubated for another 24 hours in fresh SC that either contained His, Lys, Leu, and Trp (lane 1) or lacked either His, Lys, Leu, or Trp (lanes 2 to 5, respectively). SDS-PAGE of cell extracts was followed by immunoblotting with anti–MD-D2^{fM}, anti-GST, and anti-flag. a-acids, amino acids. (**F**) Twenty-four–hour cultures (A_{600} of ~3.0) of *psh1*Δ *S. cerevisiae* (auxotrophic for His, Lys, Leu, and Trp) expressing MD-D2-GST and wild-type *Sc*Fmt1$_f$ were diluted to A_{600} of ~0.1 and thereafter were grown for 48 hours in SC that contained either the standard (20 μg/ml) concentration of His (lane 1) or decreasing concentrations of His, as indicated in lanes 2 to 5, followed by immunoblotting as described in (E). (**G**) Same as in (F) but with Trp instead of His. (**H** and **I**) Twenty-four–hour cultures (A_{600} of ~3.0) of *PSH1 S. cerevisiae* expressing MD-D2-GST and either wild-type *Sc*Fmt1$_f$ (H) or *Sc*Fmt1$_f^{\Delta 1-26}$ (I) were diluted to A_{600} of ~0.1 and thereafter were grown for 48 hours in SC containing His at either 20 or 2 μg/ml, followed by SDS-PAGE of cell extracts and immunoblotting with anti–MD-D2^{fM}, anti-GST, and anti-flag. (**J**) *S. cerevisiae* (A_{600} of ~3.5), of the indicated genotypes, expressing MD-D2-GST and wild-type *Sc*Fmt1$_f$, were incubated for another 24 hours in the absence of added His, followed by analyses described in (E). (**K**) Wild-type, *gcn2*Δ, and *fmt1*Δ *S. cerevisiae* expressing MD-D2-GST were grown in SC to stationary phase (for 72 hours) and were analyzed by immunoblotting, as in (B).

cells (which could not destroy Nt-formylated proteins) was completely abolished in double-mutant *gcn2Δ psh1Δ* cells that lacked both Psh1 and Gcn2 (Fig. 4J).

Further analyses of the Gcn2 effect (Fig. 4, J and K) used Phos-tag, a phosphate-binding compound that can be linked to polyacrylamide and thereby selectively "gel shift" phosphorylated proteins, relative to their unphosphorylated (or less phosphorylated) counterparts. Phosphorylation of *Sc*Fmt1$_{\text{myc}}$ (*Sc*Fmt1 bearing a C-terminal myc tag) was substantially increased upon starvation for His in wild-type cells but did not increase in *gcn2Δ* cells (fig. S10B). Thus, large increases of Nt-formylation in the yeast cytosol upon specific starvation stresses involved the Gcn2-mediated phosphorylation of *Sc*Fmt1, a modification that may also regulate the enzymatic activity of *Sc*Fmt1 and/or its cytosolic localization, as described below.

Starvation increases the Gcn2-dependent cytosolic localization of *Sc*Fmt1

Localization of *Sc*Fmt1 was analyzed using cells expressing, from a low-copy plasmid and the native P$_{FMT1}$ promoter, either "wild-type" *Sc*Fmt1-EGFP$_3$ (bearing three C-terminal EGFP moieties) or *Sc*Fmt1$^{\Delta 1-26}$-EGFP$_3$ (lacking the mitochondrial presequence). The *Sc*Fmt1-EGFP$_3$ fusion was functionally active and was able to rescue the impaired growth of *fmt1Δ* W303 *S. cerevisiae* on 2% glycerol–containing nonfermentable respiratory medium (fig. S10A). As would be expected, in exponentially growing cells [absorbance at 600 nm (A$_{600}$) < 0.8)], the bulk (> 97%) of *Sc*Fmt1-EGFP$_3$ was present in mitochondria, whereas the presequence-lacking *Sc*Fmt1$^{\Delta 1-26}$-EGFP$_3$ was distributed throughout the cytosol

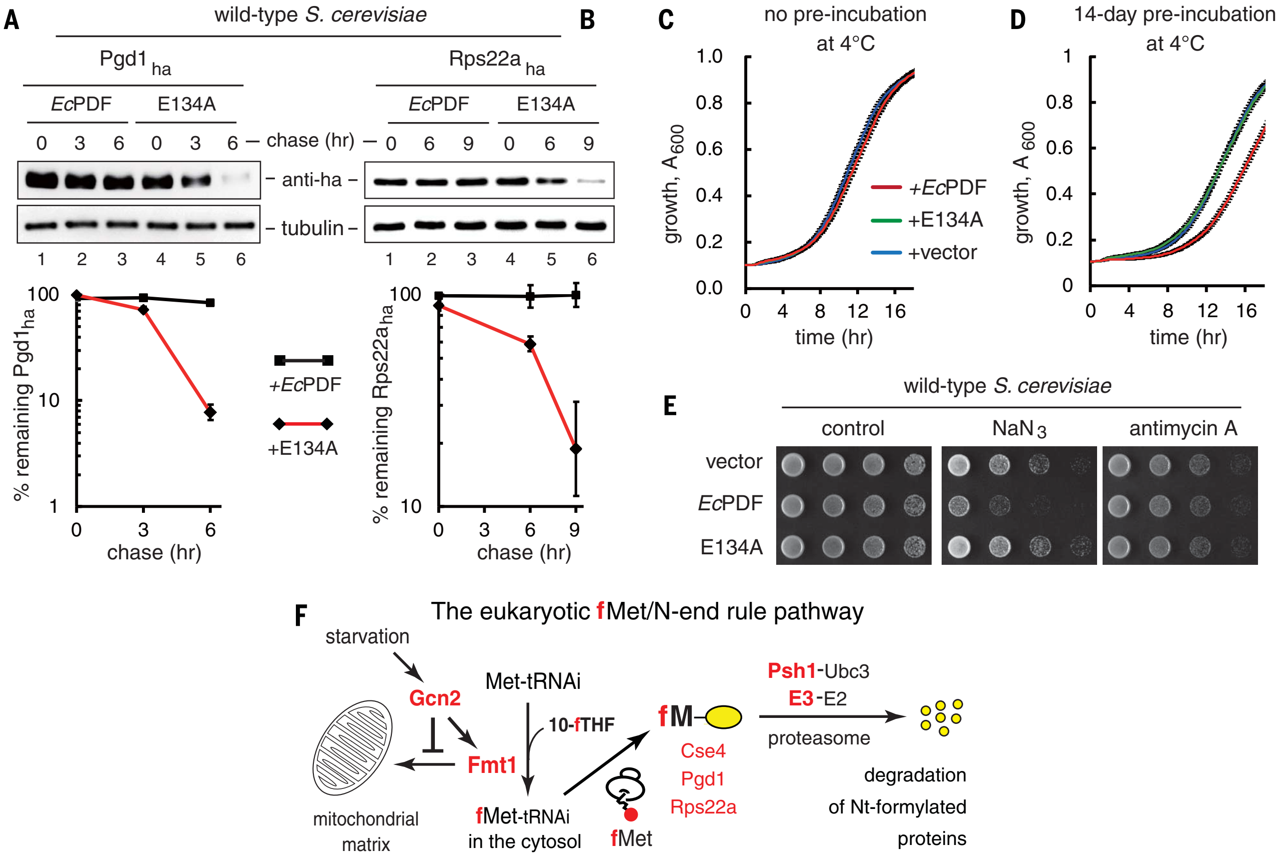

Fig. 5. Toxicity of deformylase is augmented by low temperature and azide. (**A**) CHX-chases for 0, 3, and 6 hours with C-terminally ha-tagged Pgd1$_{\text{ha}}$ and 48-hour culture (stationary phase) of wild-type *S. cerevisiae* that expressed either *Ec*PDF or its catalytically inactive *Ec*PDF$^{\text{E134A}}$ mutant. Before these assays in liquid cultures, cells were kept as streaked-out cultures on plates for ~14 days at 4°C (see the main text). The graphs show quantification of data (three independent pairs of CHX-chases), with mean ± standard error. (**B**) Same as in (A), but CHX-chases were for 0, 6, and 9 hours with Rps22a$_{\text{ha}}$. (**C**) Growth (A$_{600}$) of wild-type yeast in SC medium, measured in 96-well microplates using orbital shaker and Epoch 2 microplate spectrophotometer. *S. cerevisiae* expressed either vector alone or *Ec*PDF or its inactive *Ec*PDF$^{\text{E134A}}$ mutant and were not preincubated at 4°C. Note indistinguishable rates of growth, irrespective of expression of *Ec*PDF. (**D**) Same as in (C) but yeast were kept as streaked-out cultures on plates for 14 days at 4°C [see (A) and the main text] before growth assays in liquid culture. Note a discernibly slower growth, with preincubation at 4°C, of cells that expressed *Ec*PDF (but not its inactive *Ec*PDF$^{\text{E134A}}$ mutant). In (C) and (D), each point on the curve also shows ± standard error of A$_{600}$ values (at 10-min intervals), with measurements carried out independently six times. (**E**) Wild-type *S. cerevisiae* that expressed either vector alone or *Ec*PDF or its inactive *Ec*PDF$^{\text{E134A}}$ mutant were serially diluted (fivefold) and spotted on galactose-containing minimal medium (SGal) plates with or without either 20 μM NaN$_3$ or 20 nM antimycin A. The plates were incubated at 30°C for 3 days. As in (A) to (D), yeast cells were kept for ~14 days at 4°C before 16-hour liquid-culture growth and spot assays. (**F**) A partial summary of main results. Upon specific nutritional stresses (including stationary phase), the *Sc*Fmt1 formyltransferase is substantially retained in the cytosol, an alteration that strictly requires the Gcn2 kinase, which phosphorylates *Sc*Fmt1 and might also increase its enzymatic activity. The effect of Gcn2 on the cytosolic retention of *Sc*Fmt1 appears to be confined to *Sc*Fmt1, that is, it does not extend to other nuclear DNA–encoded mitochondrial matrix proteins. The increased cytosolic localization of *Sc*Fmt1 increases production of cytosolic fMet-tRNAi, and thereby up-regulates cytosolic Nt-formylated proteins. The latter are targeted for degradation by the Psh1 Ub ligase, the fMet/N-recognin of the proteasome-mediated fMet/N-end rule pathway.

(Fig. 4C and fig. S10C). However, in stationary-phase cells, ~35% of wild-type *Sc*Fmt1-EGFP$_3$ became localized in the cytosol, instead of mitochondria, whereas the largely cytosolic localization of the *Sc*Fmt1$^{\Delta 1-26}$-EGFP$_3$ remained unchanged (Fig. 4, C and D, and fig. S10C).

In contrast to *Sc*Fmt1, other examined mitochondrial matrix proteins, such as Sod2, Ifm1, or Cit1, which are also translocated into the matrix from the cytosol, continued to be efficiently (>90%) imported into mitochondria even in stationary phase (fig. S11). Most tellingly, and in agreement with the above Gcn2-*Sc*Fmt1 results, the partitioning of ~35% of *Sc*Fmt1 into the cytosol in stationary-phase cells was nearly completely abrogated in *gcn2*Δ cells (Fig. 4C and fig. S10C).

Toxicity of deformylation is augmented by low temperature and azide

What might be a biological role(s) of cytosolic Nt-formylated proteins that are produced in wild-type *S. cerevisiae* and are destroyed by the fMet/N-end rule pathway? To address this question, we asked whether ectopic expression of *Ec*PDF, and the resulting deformylation of Nt-formylated proteins, might increase the sensitivity of cells to specific stressors. (Wild-type *S. cerevisiae* lacks a deformylase.) As described above, the ectopic Nt-formylation of yeast proteins, through expression of *Ec*FMT, caused degradation of these proteins by the Psh1-mediated fMet/N-end rule pathway, including degradation of the endogenous (nonreporter) proteins Pgd1 and Rps22a (fig. S6, C to H).

The same degradation assays but with wild-type yeast (i.e., with cells that lacked ectopic *Ec*FMT and contained solely the endogenous *Sc*Fmt1) showed that the endogenous Pgd1 and Rps22a proteins became short-lived in stationary phase, a setting that strongly augments Nt-formylation (Fig. 5, A and B). The stationary-phase degradation of Pgd1 and Rps22a required Nt-formylation of these proteins because this degradation could be abolished by ectopically expressed *Ec*PDF but not by its catalytically inactive mutant *Ec*PDF$^{\mathrm{E134A}}$ (Fig. 5, A and B).

Furthermore, the Nt-formylation-dependent degradation of Pgd1 and Rps22a (Fig. 5, A and B) was observed only if yeast were preincubated, as streaked-out cultures on plates, for ~14 days at 4°C before inoculating cells into synthetic complete (SC) liquid medium for stationary-phase degradation assays at 30°C. A shorter, 7-day preincubation of yeast at 4°C did not suffice for the degradation of Pgd1 and Rps22a to take place. In agreement with these (technically robust) findings, ectopic expression of *Ec*PDF, but not of its inactive mutant, reproducibly prolonged the lag period (before exponential growth) of wild-type yeast in SC liquid medium. This effect only took place if cell growth was measured with yeast that had been preincubated at 4°C for 14 days (as described above) before their transfers to liquid cultures for growth assays (Fig. 5D). By contrast, no *Ec*PDF-mediated growth retardation was observed with cells that had not been preincubated at 4°C or were preincubated at 4°C for only 7 days (Fig. 5C and fig. S12A).

Furthermore, the expression of *Ec*PDF (but not of its inactive mutant) in cold-primed yeast (preincubated on plates at 4°C for 14 days) rendered cell growth on a galactose-containing minimal solid medium markedly hypersensitive to Na-azide, which inhibits cytochrome c oxidase, adenosine triphosphate (ATP) synthesis, and plasma membrane permeability. The same *Ec*PDF expression, under the same conditions, did not affect cell growth in the presence of other respiratory-chain inhibitors, such as antimycin A, oligomycin, or cyanide (Fig. 5E and fig. S12B). In addition, *Ec*PDF did not discernibly affect the growth of mitochondrial respiratory chain mutants *cox5a*Δ, *coq5*Δ, and *atp11*Δ (fig. S12C).

Together, these findings made it unlikely that the observed toxicity of ectopic cytosolic *Ec*PDF (its inactive mutant was nontoxic) stemmed from deformylation of the eight Nt-formylated mitochondrial matrix proteins that are encoded by mitochondrial DNA in the matrix (see introduction). The robust and reproducible dependence of the toxicity of deformylation by *Ec*PDF on a sufficiently long (~14 days) preexposure of cells to 4°C suggests that natural Nt-formylation of cytosolic eukaryotic proteins may be functionally important and potentially beneficial under conditions of specific undernutrition and/or low temperatures. Future studies will analyze this temperature effect. In nontropical climes, ecological niches of *S. cerevisiae* would sometimes expose yeast to temperatures near 0°C. Because it is likely (but remains to be verified) that Nt-formylation of cytosolic proteins is universal among eukaryotes, it would also be interesting to explore Nt-formylation in hibernating animals, whose body temperatures can become low in winter.

Our findings indicate that the observed retention of the (normally mitochondrial) *Sc*Fmt1 formyltransferase in the cytosol of stationary-phase and other starving cells is the cause of massive increases of Nt-formylated proteins. As described above, the retention of *Sc*Fmt1 in the cytosol strictly requires the Gcn2 kinase (Fig. 4, C and D, and fig. S10C). This effect of Gcn2 is apparently specific for *Sc*Fmt1, because other examined nuclear DNA–encoded mitochondrial-matrix proteins were imported into mitochondria of stationary-phase cells, despite the presence of Gcn2 (fig. S11). The observed up-regulation of Nt-formylated proteins under the above conditions may contribute, in ways that remain to be understood, to adaptations of cells to specific undernutrition stresses.

The eukaryotic fMet/N-end rule pathway

We discovered that the Nt-formylation of proteins, a long-known pretranslational protein modification previously thought to be confined to bacteria and bacteria-descended eukaryotic organelles, can also occur at the start of translation by the cytosolic ribosomes of a eukaryote such as *S. cerevisiae* (Fig. 5F). The Nt-formylation of cytosolic proteins was strongly up-regulated upon specific starvation stresses, including stationary phase or depletion of some amino acids, such as His or Lys (Fig. 4). Intriguingly, down-regulation of cytosolic Nt-formylation (through ectopic expression of deformylase) increased sensitivity of cells to specific undernutrition stresses, and/or to a prolonged cold (4°C) stress, and to Na-azide (Fig. 5 and fig. S12).

We also discovered that Nt-formylated cytosolic proteins are targeted by the Psh1 E3 Ub ligase (together with the Ubc3 E2 enzyme), which acts as the recognition component of the previously unknown eukaryotic fMet/N-end rule pathway that destroys Nt-formylated proteins (Fig. 5F). In agreement with these results, we also showed that the Psh1 fMet/N-recognin physically binds to the formyl group of the Nt-fMet residue (Fig. 3B). Nt-formylation of yeast cytosolic proteins is caused by the endogenous *Sc*Fmt1, whose translocation from the cytosol to the inner matrix of mitochondria is not as efficient, even under normal conditions, as had previously been assumed, and was strongly impaired in stationary phase (Fig. 4, C and D, and figs. S10C and S11).

We also discovered that the up-regulation of Nt-formylated cytosolic proteins in starving cells strictly requires Gcn2, a stress-activated protein kinase (Fig. 4, J and K). Gcn2 mediated the stress-induced increase of Nt-formylated proteins by controlling the cytosolic localization of the *Sc*Fmt1 enzyme and by being essential for *Sc*Fmt1 phosphorylation (Fig. 4, C and D, and fig. S10, B and C). The latter result suggests that Gcn2 may also regulate the enzymatic activity of *Sc*Fmt1.

Notably, the ability of Gcn2 to retain a large fraction of *Sc*Fmt1 in the cytosol of nutritionally stressed cells is apparently confined to *Sc*Fmt1, inasmuch as Gcn2 does not have such an effect, under the same conditions, on other examined nuclear DNA–encoded mitochondrial matrix proteins (Figs. 4C and 5F, and figs. S10C and S11). The regulation of *Sc*Fmt1 by Gcn2 is a specific protein localization circuit.

Nt-formylation and Nt-acetylation, two mutually exclusive Nt-modifications of proteins, generate, respectively, fMet/N-degrons and Ac/N-degrons (fig. S1, B and F). fMet/N-degrons are recognized by the Psh1 fMet/N-recognin, a component of the fMet/N-end rule pathway (fig. S1B). The pretranslational Nt-formylation of Met-tRNAi, by an FMT enzyme such as *Sc*Fmt1, requires 10-formyltetrahydrofolate as a cosubstrate, whereas the cotranslational Nt-acetylation of proteins by Nt-acetylases requires the acetyl coenzyme A (Ac-CoA) cosubstrate (Fig. 2A and fig. S1, B and F).

What might be an adaptive (fitness-increasing) value of the Gcn2 kinase–dependent up-regulation of Nt-formylated proteins? One possibility is that specific physiological perturbations, such as some nutritional and/or low-temperature stresses (see above), may retain adequate levels of intracellular 10-formyltetrahydrofolate (required for

Nt-formylation) while not retaining adequate levels of Ac-CoA (required for Nt-acetylation). Under such conditions, an increased Nt-formylation of newly made proteins (through a cytosolic retention of formyltransferase) would maintain, owing to the fMet/N-end rule pathway, degradation-based protein quality control. As shown previously, in the absence of stress, this control is mediated, in part, by the Ac/N-end rule pathway (*9*–*13*). In the resulting model, the fMet/N-end rule pathway and the Ac/N-end rule pathway are functionally complementary, in that the former may assist the latter under metabolic conditions that favor Nt-formylation over Nt-acetylation. The fMet/N-end rule pathway (fig. S1, A and B) is the fourth eukaryotic N-end rule pathway that was discovered over the past three decades. The three previously identified N-end rule pathways are universal among eukaryotes (fig. S1, E to G) (*9*–*15*, *20*). The fMet/N-end rule pathway (Fig. 5F and fig. S1B) is likely to be universal as well, given strongly conserved mechanisms that mediate Nt-formylation and degron recognition.

Materials and methods summary

Yeast strains, plasmids, genetic techniques, and degradation assays

Standard techniques were used for construction of plasmids and strains. Protein degradation assays were performed largely as described (*9*, *11*). Tables S3 to S5 list *S. cerevisiae* strains, plasmids, and PCR primers. See supplementary materials and methods for details.

Mass spectrometric analyses

SILAC and cLC-MS/MS were carried out as described in the supplementary materials and methods.

Production of antibodies specific for two Nt-formylated proteins

Nt-formylated peptides and its unformylated counterparts were synthesized by Abfrontier or AbClon (Seoul, Republic of Korea). Production and purification of anti–MD-D2^{fM} and anti-Cse4^{fM} antibodies (Fig. 1, D to G, and fig. S4, C and D) are described in the supplementary materials and methods.

GST-pulldown assays with Psh1

Nt-formylated fMD-D2-GST and its unformylated MD-D2-GST counterpart were produced using *E. coli* in either the presence or absence of actinonin, a deformylase inhibitor. GST-pulldowns with yeast extracts containing C-terminally flag-tagged *S. cerevisiae* Psh1 (Psh1$_f$) used purified Nt-formylated fMD-D2-GST versus unformylated MD-D2-GST and were carried out as described in the supplementary materials and methods.

REFERENCES AND NOTES

1. B. S. Laursen, H. P. Sørensen, K. K. Mortensen, H. U. Sperling-Petersen, Initiation of protein synthesis in bacteria. *Microbiol. Mol. Biol. Rev.* **69**, 101–123 (2005). doi: 10.1128/MMBR.69.1.101-123.2005; pmid: 15755955
2. D. Mazel, S. Pochet, P. Marlière, Genetic characterization of polypeptide deformylase, a distinctive enzyme of eubacterial translation. *EMBO J.* **13**, 914–923 (1994). doi: 10.1002/j.1460-2075.1994.tb06335.x; pmid: 8112305
3. G. Kramer, D. Boehringer, N. Ban, B. Bukau, The ribosome as a platform for co-translational processing, folding and targeting of newly synthesized proteins. *Nat. Struct. Mol. Biol.* **16**, 589–597 (2009). doi: 10.1038/nsmb.1614; pmid: 19491936
4. V. Ramesh, C. Köhrer, U. L. RajBhandary, Expression of *Escherichia coli* methionyl-tRNA formyltransferase in *Saccharomyces cerevisiae* leads to formylation of the cytoplasmic initiator tRNA and possibly to initiation of protein synthesis with formylmethionine. *Mol. Cell. Biol.* **22**, 5434–5442 (2002). doi: 10.1128/MCB.22.15.5434-5442.2002; pmid: 12101237
5. R. Bingel-Erlenmeyer *et al.*, A peptide deformylase-ribosome complex reveals mechanism of nascent chain processing. *Nature* **452**, 108–111 (2008). doi: 10.1038/nature06683; pmid: 18288106
6. C. Giglione, S. Fieulaine, T. Meinnel, N-terminal protein modifications: Bringing back into play the ribosome. *Biochimie* **114**, 134–146 (2015). doi: 10.1016/j.biochi.2014.11.008; pmid: 25450248
7. K. I. Piatkov, T. T. M. H. Vu, C.-S. Hwang, A. Varshavsky, Formyl-methionine as a degradation signal at the N-termini of bacterial proteins. *Microb. Cell* **2**, 376–393 (2015). doi: 10.15698/mic2015.10.231; pmid: 26866044
8. H. Aksnes, A. Drazic, M. Marie, T. Arnesen, First things first: Vital protein marks by N-terminal acetyltransferases. *Trends Biochem. Sci.* **41**, 746–760 (2016). doi: 10.1016/j.tibs.2016.07.005; pmid: 27498224
9. C. S. Hwang, A. Shemorry, A. Varshavsky, N-terminal acetylation of cellular proteins creates specific degradation signals. *Science* **327**, 973–977 (2010). doi: 10.1126/science.1183147; pmid: 20110468
10. A. Varshavsky, The N-end rule pathway and regulation by proteolysis. *Protein Sci.* **20**, 1298–1345 (2011). doi: 10.1002/pro.666; pmid: 21633985
11. A. Shemorry, C. S. Hwang, A. Varshavsky, Control of protein quality and stoichiometries by N-terminal acetylation and the N-end rule pathway. *Mol. Cell* **50**, 540–551 (2013). doi: 10.1016/j.molcel.2013.03.018; pmid: 23603116
12. H. K. Kim *et al.*, The N-terminal methionine of cellular proteins as a degradation signal. *Cell* **156**, 158–169 (2014). doi: 10.1016/j.cell.2013.11.031; pmid: 24361105
13. S. E. Park *et al.*, Control of mammalian G protein signaling by N-terminal acetylation and the N-end rule pathway. *Science* **347**, 1249–1252 (2015). doi: 10.1126/science.aaa3844; pmid: 25766235
14. A. Bachmair, D. Finley, A. Varshavsky, In vivo half-life of a protein is a function of its amino-terminal residue. *Science* **234**, 179–186 (1986). doi: 10.1126/science.3018930; pmid: 3018930
15. T. Tasaki, S. M. Sriram, K. S. Park, Y. T. Kwon, The N-end rule pathway. *Annu. Rev. Biochem.* **81**, 261–289 (2012). doi: 10.1146/annurev-biochem-051710-093308; pmid: 22524314
16. D. Finley, H. D. Ulrich, T. Sommer, P. Kaiser, The ubiquitin-proteasome system of *Saccharomyces cerevisiae*. *Genetics* **192**, 319–360 (2012). doi: 10.1534/genetics.112.140467; pmid: 23028185
17. R. Schmidt, R. Zahn, B. Bukau, A. Mogk, ClpS is the recognition component for *Escherichia coli* substrates of the N-end rule degradation pathway. *Mol. Microbiol.* **72**, 506–517 (2009). doi: 10.1111/j.1365-2958.2009.06666.x; pmid: 19317833
18. D. J. Gibbs, J. Bacardit, A. Bachmair, M. J. Holdsworth, The eukaryotic N-end rule pathway: Conserved mechanisms and diverse functions. *Trends Cell Biol.* **24**, 603–611 (2014). doi: 10.1016/j.tcb.2014.05.001; pmid: 24874449
19. N. Dissmeyer, S. Rivas, E. Graciet, Life and death of proteins after protease cleavage: Protein degradation by the N-end rule pathway. *New Phytol.* **218**, 929–935 (2018). doi: 10.1111/nph.14619; pmid: 28581033
20. S. J. Chen, X. Wu, B. Wadas, J.-H. Oh, A. Varshavsky, An N-end rule pathway that recognizes proline and destroys gluconeogenic enzymes. *Science* **355**, eaal3655 (2017). doi: 10.1126/science.aal3655; pmid: 28126757
21. I. Rivera-Rivera, G. Román-Hernández, R. T. Sauer, T. A. Baker, Remodeling of a delivery complex allows ClpS-mediated degradation of N-degron substrates. *Proc. Natl. Acad. Sci. U.S.A.* **111**, E3853–E3859 (2014). doi: 10.1073/pnas.1414933111; pmid: 25187555
22. S. M. Shim *et al.*, The endoplasmic reticulum-residing chaperone BiP is short-lived and metabolized through N-terminal arginylation. *Sci. Signal.* **11**, eaan0630 (2018). doi: 10.1126/scisignal.aan0630; pmid: 29295953
23. J. H. Oh, J. Y. Hyun, A. Varshavsky, Control of Hsp90 chaperone and its clients by N-terminal acetylation and the N-end rule pathway. *Proc. Natl. Acad. Sci. U.S.A.* **114**, E4370–E4379 (2017). doi: 10.1073/pnas.1705898114; pmid: 28515311
24. K. I. Piatkov, C. S. Brower, A. Varshavsky, The N-end rule pathway counteracts cell death by destroying proapoptotic protein fragments. *Proc. Natl. Acad. Sci. U.S.A.* **109**, E1839–E1847 (2012). doi: 10.1073/pnas.1207786109; pmid: 22670058
25. B. Wadas, K. I. Piatkov, C. S. Brower, A. Varshavsky, Analyzing N-terminal arginylation through the use of peptide arrays and degradation assays. *J. Biol. Chem.* **291**, 20976–20992 (2016). doi: 10.1074/jbc.M116.747956; pmid: 27510035
26. R.-G. Hu *et al.*, The N-end rule pathway as a nitric oxide sensor controlling the levels of multiple regulators. *Nature* **437**, 981–986 (2005). doi: 10.1038/nature04027; pmid: 16222293
27. D. C. Scott, J. K. Monda, E. J. Bennett, J. W. Harper, B. A. Schulman, N-terminal acetylation acts as an avidity enhancer within an interconnected multiprotein complex. *Science* **334**, 674–678 (2011). doi: 10.1126/science.1209307; pmid: 21940857
28. C.-S. Hwang, A. Shemorry, D. Auerbach, A. Varshavsky, The N-end rule pathway is mediated by a complex of the RING-type Ubr1 and HECT-type Ufd4 ubiquitin ligases. *Nat. Cell Biol.* **12**, 1177–1185 (2010). doi: 10.1038/ncb2121; pmid: 21076411
29. W. S. Choi *et al.*, Structural basis for the recognition of N-end rule substrates by the UBR box of ubiquitin ligases. *Nat. Struct. Mol. Biol.* **17**, 1175–1181 (2010). doi: 10.1038/nsmb.1907; pmid: 20835240
30. E. Matta-Camacho, G. Kozlov, F. F. Li, K. Gehring, Structural basis of substrate recognition and specificity in the N-end rule pathway. *Nat. Struct. Mol. Biol.* **17**, 1182–1187 (2010). doi: 10.1038/nsmb.1894; pmid: 20835242
31. M. K. Kim, S. J. Oh, B. G. Lee, H. K. Song, Structural basis for dual specificity of yeast N-terminal amidase in the N-end rule pathway. *Proc. Natl. Acad. Sci. U.S.A.* **113**, 12438–12443 (2016). doi: 10.1073/pnas.1612620113; pmid: 27791147
32. A. Varshavsky, 'Spalog' and 'sequelog': Neutral terms for spatial and sequence similarity. *Curr. Biol.* **14**, R181–R183 (2004). doi: 10.1016/j.cub.2004.02.014; pmid: 15028230
33. G. Hewawasam *et al.*, Psh1 is an E3 ubiquitin ligase that targets the centromeric histone variant Cse4. *Mol. Cell* **40**, 444–454 (2010). doi: 10.1016/j.molcel.2010.10.014; pmid: 21070970
34. P. Ranjitkar *et al.*, An E3 ubiquitin ligase prevents ectopic localization of the centromeric histone H3 variant via the centromere targeting domain. *Mol. Cell* **40**, 455–464 (2010). doi: 10.1016/j.molcel.2010.09.025; pmid: 21070971
35. W. C. Au *et al.*, A novel role of the N terminus of budding yeast histone H3 variant Cse4 in ubiquitin-mediated proteolysis. *Genetics* **194**, 513–518 (2013). doi: 10.1534/genetics.113.149898; pmid: 23525333
36. M. B. Metzger, J. L. Scales, M. F. Dunklebarger, A. M. Weissman, The ubiquitin ligase (E3) Psh1p is required for proper segregation of both centromeric and two-micron plasmids in *Saccharomyces cerevisiae*. *G3 (Bethesda)* **7**, 3731–3743 (2017). pmid: 28928274
37. H. Cheng, X. Bao, X. Gan, S. Luo, H. Rao, Multiple E3s promote the degradation of histone H3 variant Cse4. *Sci. Rep.* **7**, 8565 (2017). doi: 10.1038/s41598-017-08923-w; pmid: 28819127
38. P. J. Robinson *et al.*, Structure of a complete mediator-RNA polymerase II pre-initiation complex. *Cell* **166**, 1411–1422.e16 (2016). doi: 10.1016/j.cell.2016.08.050; pmid: 27610567

ACKNOWLEDGMENTS

We thank W.-K. Huh (Seoul National University, Seoul, Republic of Korea) for yeast deletion library mutants, S. Biggins (Hutchinson Cancer Center, Seattle, WA, USA) for pSB1535 and pSB1541, and R. Sauer (MIT, Cambridge, MA, USA) for AG110A(DE) *E. coli*. We also thank the present and former members of the Hwang laboratory for their assistance and advice. **Funding:** This work was supported by grants from the Samsung Science & Technology Foundation (SSTF-BA1401-17) and the BK21 plus program (C.-S.H.), by NRF grants of the Korean Government (MSIP) [NRF-2017M3A9F9030559 (C.L.) and NRF-2017R1A5A1015366 (J.-Y.Y.)], and by NIH grants R01GM031530 and R01DK039520 (A.V.). **Author contributions:** C.-S.H., J.-M.K., J.-Y.Y., C.L., A.V., and other coauthors designed the research. J.-M.K., O.-H.S., S.J., J.-E.H., J.Y., D.-S.K., and C.-S.H. performed the research, and all coauthors analyzed data. C.-S.H., J.-M.K., C.L., and A.V. wrote the paper. **Competing interests:** All coauthors declare no competing interests. **Data and materials availability:** All mass spectrometric data of this study are available in the PRIDE database (accession number: PXD010780). All (other) data needed to evaluate the conclusions in the paper are present in the paper or in the supplementary materials.

SUPPLEMENTARY MATERIALS

www.sciencemag.org/content/362/6418/eaat0174/suppl/DC1
Materials and Methods
Figs. S1 to S12
Tables S1 to S5
References (*39*–*48*)

16 January 2018; resubmitted 24 August 2018
Accepted 24 October 2018
Published online 8 November 2018
10.1126/science.aat0174

RESEARCH ARTICLE SUMMARY

STRUCTURAL BIOLOGY

An electron transfer path connects subunits of a mycobacterial respiratory supercomplex

Hongri Gong*, Jun Li*, Ao Xu*, Yanting Tang, Wenxin Ji, Ruogu Gao, Shuhui Wang, Lu Yu, Changlin Tian, Jingwen Li, Hsin-Yung Yen, Sin Man Lam, Guanghou Shui, Xiuna Yang, Yuna Sun, Xuemei Li, Minze Jia, Cheng Yang, Biao Jiang, Zhiyong Lou, Carol V. Robinson, Luet-Lok Wong, Luke W. Guddat, Fei Sun†, Quan Wang†, Zihe Rao†

INTRODUCTION: Cellular respiration is a core feature in the metabolism of many organisms that allows for the generation of a proton gradient across a membrane. During respiration, electrons are transferred from electron donors to oxygen through an electron transport chain. The energy created allows protons to be pumped across a membrane (cellular or mitochondrial). In electron transport chains, quinones and cytochrome *c* are two of the electron carriers that shuttle electrons to and from large macromolecular structures that are embedded in the membrane. The components that allow respiratory chains to function in the mitochondria are well characterized, but the situation is less clear and more varied in prokaryotic systems. A soluble cytochrome *c* pathway for electron transfer similar to that in mitochondria is commonly found in Gram-negative bacteria. Gram-positive bacteria such as *Mycobacteria* are devoid of a soluble cytochrome *c* but instead possess cytochrome *c* proteins that are anchored onto the membrane or have a fused cytochrome *c* domain to mediate electron transfer between two of the major complexes, which are referred to as CIII and CIV.

Structures of eukaryotic respiratory supercomplexes have been reported, but cytochrome *c* is not visible in any of these structures. Thus, a complete pathway for electron flow has not yet been visualized. CIII–CIV supercomplexes have been isolated from *Mycobacterium smegmatis*, *Corynebacterium glutamicum*, and *Mycobacterium tuberculosis* and shown to couple quinol oxidation to oxygen reduction without an external electron shuttle, suggesting that the flow of electrons is internalized in this type of complex. The determination of the structure of this complex reveals a path for electron transfer between the subunits of these supercomplexes.

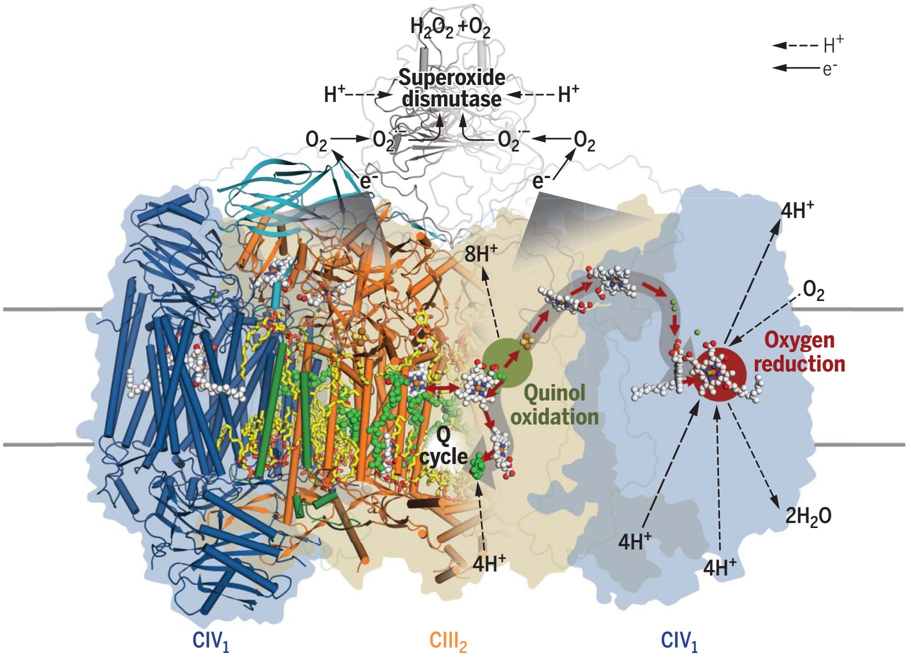

Structure of mycobacterial respiratory supercomplex $CIII_2CIV_2SOD_2$. Overall architecture of the *bcc-aa*$_3$–type respiratory CIII–CIV supercomplex from *M. smegmatis*. The cryo-EM map of the supercomplex shows a linear twofold dimerized form of CIV_1–$CIII_2$–CIV_1.

RATIONALE: The structural information provided here is required to understand the molecular details of electron transport in *Mycobacteria*. We have selected the supercomplex CIII–CIV from *M. smegmatis* because it is highly similar to the CIII–CIV complex from the human pathogen *M. tuberculosis*. This complex was amenable to expression and purification and analysis by means of cryo–electron microscopy (cryo-EM).

ON OUR WEBSITE

Read the full article at http://dx.doi.org/10.1126/science.aat8923

RESULTS: We have determined a cryo-EM structure of a respiratory supercomplex isolated from *M. smegmatis*. The structure allows the complete visualization of 20 subunits that associate to form the complex. Central to the supercomplex is a CIII dimer that is flanked on either side by individual CIV subunits. Fused *c*-type cytochrome domains bridge and mediate electron transfer from CIII to CIV. The structure also reveals three previously unidentified associated subunits that contribute to the stability of the supercomplex and the presence of superoxide dismutase (SOD), which may be responsible for the detoxification of superoxide formed by CIII.

CONCLUSION: This study of a respiratory supercomplex in *Mycobacteria* reveals cofactors positioned at distances that permit electron tunneling, enabling direct intrasupercomplex electron transfer from menaquinol to oxygen without the need for a separate cytochrome *c* electron shuttle. The presence of a bound SOD to the respiratory supercomplex suggests a mechanism of mycobacterial resistance against exogenous and endogenous oxidative stress in macrophages and host immune responses. The structure of the quinone binding sites provides a framework for rational structure-based *M. tuberculosis* drug discovery. A binding site can be proposed for the candidate antimycobacterial drug Q203, which acts by inhibiting the activity of this supercomplex. ■

---

*These authors contributed equally to this work.

Cite this article as H. Gong *et al.*, *Science* **362**, eaat8923 (2018). DOI: 10.1126/science.aat8923

†Corresponding author. Email: raozh@tsinghua.edu.cn (Z.R.); wangq@ibp.ac.cn (Q.W.); feisun@ibp.ac.cn (F.S.)

Gong *et al.*, *Science* **362**, 1020 (2018) 30 November 2018 **1 of 1**

RESEARCH ARTICLE

STRUCTURAL BIOLOGY

An electron transfer path connects subunits of a mycobacterial respiratory supercomplex

Hongri Gong[1]*, Jun Li[2,3]*, Ao Xu[1,4]*, Yanting Tang[1], Wenxin Ji[4,5], Ruogu Gao[4,5], Shuhui Wang[2,3], Lu Yu[6], Changlin Tian[6,7], Jingwen Li[8], Hsin-Yung Yen[8,9], Sin Man Lam[10], Guanghou Shui[10], Xiuna Yang[2,3], Yuna Sun[4], Xuemei Li[4], Minze Jia[4], Cheng Yang[1], Biao Jiang[2], Zhiyong Lou[11], Carol V. Robinson[8], Luet-Lok Wong[12], Luke W. Guddat[13], Fei Sun[4,5]†, Quan Wang[4]†, Zihe Rao[1,2,3,4,11]†

We report a 3.5-angstrom-resolution cryo–electron microscopy structure of a respiratory supercomplex isolated from *Mycobacterium smegmatis.* It comprises a complex III dimer flanked on either side by individual complex IV subunits. Complex III and IV associate so that electrons can be transferred from quinol in complex III to the oxygen reduction center in complex IV by way of a bridging cytochrome subunit. We observed a superoxide dismutase-like subunit at the periplasmic face, which may be responsible for detoxification of superoxide formed by complex III. The structure reveals features of an established drug target and provides a foundation for the development of treatments for human tuberculosis.

In cellular respiration, chemical energy is extracted by coupling the oxidation of an energy source (such as sugars, fatty acids, or amino acids) and the reduction of an electron acceptor (such as oxygen, sulfur, nitrate, or sulfate) to synthesize adenosine triphosphate (ATP), which powers cellular reactions. In aerobic organisms, electrons are transferred from electron donors to oxygen, the terminal acceptor, through the electron transport chain (ETC) to pump protons across a membrane (cellular or mitochondrial). This creates a transmembrane proton gradient [proton motive force (PMF)] that drives ATP synthesis (*1*). In ETCs, quinones and cytochromes are two types of electron carriers that shuttle electrons to and from large macromolecular structures embedded in the membrane. In the mitochondrial respiratory chain, four membrane oxidoreductases are involved in electron transfer: complex I [reduced form of oxidized nicotinamide adenine dinucleotide (NADH):ubiquinone oxidoreductase] (CI), complex II (succinate:ubiquinone oxidoreductase) (CII), complex III (bc_1-type ubiquinol:cytochrome *c* oxidoreductase) (CIII), and complex IV (aa_3-type cytochrome *c* oxidase) (CIV). CIII oxidizes ubiquinol to ubiquinone and passes the electrons to soluble cytochrome *c*, which then shuttles them to CIV, where oxygen is reduced to water (Fig. 1A). The transmembrane PMF is generated by proton pumping in CI, CIII, and CIV.

The situation is more complicated in prokaryotic respiratory chains (Fig. 1A) (*2*). A soluble cytochrome *c* pathway similar to that in mitochondria is common in Gram-negative bacteria. Variations include a membrane-anchored cytochrome *c* mediating electron transfer from CIII to CIV (*3*) and a caa_3-type CIV with a fused cytochrome *c* domain (*4*). Gram-positive bacteria usually possess cytochrome *c* proteins that are anchored onto the membrane (*5*), or a fused cytochrome *c* domain (*bcc*-type CIII or caa_3-type CIV) to mediate electron transfer between CIII and CIV (*6*, *7*). *Mycobacteria* and other *Actinobacteria* such as *Corynebacterium glutamicum* are inherently devoid of a soluble cytochrome *c* in their genomes (*8*) but contain a *bcc*-type CIII with a di-heme cytochrome *c* domain fused to CIII (*9*, *10*). Variations are also observed within CIII and CIV. Alternative complex IIIs (ACIIIs), structurally unrelated to bc_1-type CIII, mediate quinol oxidation (*11*). Quinol oxidases couple quinol oxidation to oxygen reduction without the need for cytochrome *c* (*12*). Alternative oxidases (Aoxs) catalyze quinol oxidation/oxygen reduction without proton pumping (*13*).

Despite variation with ETCs, homologs or analogs of CI through to CIV are the most common components of respiratory chains in aerobic organisms. Structures of both prokaryotic and eukaryotic CI (*14*–*16*), CII (*17*, *18*), CIII (*19*–*21*), and CIV (*22*–*24*) have been determined, elucidating the flow of electrons within these individual complexes. Structural information for the mitochondrial respirasome $CI_1CIII_2CIV_1$ and preliminary electron microscopic study of a $CIII_2CIV_2$ supercomplex from yeast have been reported (*25*, *26*). However, cytochrome *c* is not visible in any of these structures. Thus, a complete pathway for electron flow is yet to be fully elucidated. Understanding the precise details of the structural assembly for a CIII–CIV supercomplex will greatly assist in this endeavor (*27*, *28*). It has been reported recently that respiratory supercomplexes in situ have a conserved core of CI and a dimer of CIII, but otherwise, their stoichiometry and structure vary (*29*). Up to two copies of monomeric CIV were found associated with the CI_1CIII_2 assembly in bovine heart and the yeast *Yarrowia lipolytica*, but their positions varied (*30*). The conserved features of supercomplex assemblies such as CI_1CIII_2 and $CIII_2CIV_2$ suggest that these types of associations have important roles in respiratory electron transfer.

The *bcc*-type CIII from *Actinobacteria* has a di-heme *c* subunit (*7*). It has been suggested that one cytochrome *c* domain is the donor for the aa_3-type CIV, and the other is the acceptor for the CIII Rieske Fe-S protein (*31*). In support of this concept of intrasupercomplex electron transfer, CIII–CIV supercomplexes have been isolated from *Mycobacterium smegmatis*, *C. glutamicum*, and *Mycobacterium tuberculosis* and shown to couple quinol oxidation to oxygen reduction without an external electron shuttle (*9*, *10*, *32*). Therefore, structural data for the *bcc*-aa_3–type CIII–CIV supercomplex (SC III–IV) can provide answers as to how CIII and CIV are coupled and how electrons are transferred from CIII to CIV.

Purification and characterization of SC III–IV

To isolate the SC III–IV in a functional form, we engineered the genome of *M. smegmatis* to incorporate a 10× His tag at the C terminus of the QcrB subunit of CIII and extracted and purified the CIII–CIV complex by means of nickel–nitrilotriacetic acid (Ni-NTA) affinity chromatography and gel filtration. Gel filtration and blue native polyacrylamide gel electrophoresis (BN-PAGE) showed a single peak and a single band, suggesting a highly ordered supramolecular assembly (fig. S1, A and B). SDS-PAGE and mass spectrometry confirmed the presence of all the

---

[1]State Key Laboratory of Medicinal Chemical Biology and College of Life Science, Nankai University, Tianjin 300353, China. [2]Shanghai Institute for Advanced Immunochemical Studies, ShanghaiTech University, Shanghai, 201210, China. [3]CAS Center for Excellence in Molecular Cell Science, Shanghai Institute of Biochemistry and Cell Biology, Chinese Academy of Sciences (CAS), 320 Yueyang Road, Shanghai 200031, China. [4]National Laboratory of Biomacromolecules, CAS Center for Excellence in Biomacromolecules, Institute of Biophysics, CAS, Beijing 100101, China. [5]University of Chinese Academy of Sciences, Beijing, China. [6]High Magnetic Field Laboratory, CAS, Hefei 230031, China. [7]Hefei National Laboratory of Physical Sciences at Microscale and School of Life Sciences, University of Science and Technology of China, Hefei 230027, China. [8]Department of Chemistry, University of Oxford, Physical and Theoretical Chemistry Laboratory, South Parks Rd, Oxford, OX1 3QZ, UK. [9]OMass Technologies, Begbroke Science Park, Woodstock Rd, Yarnton, Kidlington OX5 1PF, UK. [10]State Key Laboratory of Molecular Developmental Biology, Institute of Genetics and Developmental Biology, CAS, Beijing 100101, China. [11]Laboratory of Structural Biology, Tsinghua University, Beijing 100084, China. [12]Department of Chemistry, University of Oxford, Inorganic Chemistry Laboratory, South Parks Road, Oxford OX1 3QR, UK. [13]School of Chemistry and Molecular Biosciences, The University of Queensland, Brisbane, 4072 Queensland, Australia.

*These authors contributed equally to this work.

†Corresponding author. Email: raozh@tsinghua.edu.cn (Z.R.); wangq@ibp.ac.cn (Q.W.); feisun@ibp.ac.cn (F.S.)

known components of CIII and CIV as well as several previously unknown components (fig. S1D and table S1). Native Orbitrap mass spectrometry gave a molecular weight of 873.4 kDa ± 10.4 Da for the complex (fig. S1E). Both the electronic absorption spectrum and the electron paramagnetic resonance (EPR) spectrum showed peaks expected from the various hemes, copper centers, and [2Fe-2S] prosthetic groups in CIII and CIV (fig. S1K). Because the *bcc*:aa_3 preparations from *M. smegmatis* are active with the more soluble menadiol (2-methyl-1,4-naphthoquinol) as substrate ([33](#)), the quinol:oxygen oxidoreductase activity of SC III–IV was assayed by measuring the rate of O_2 consumption in the presence of

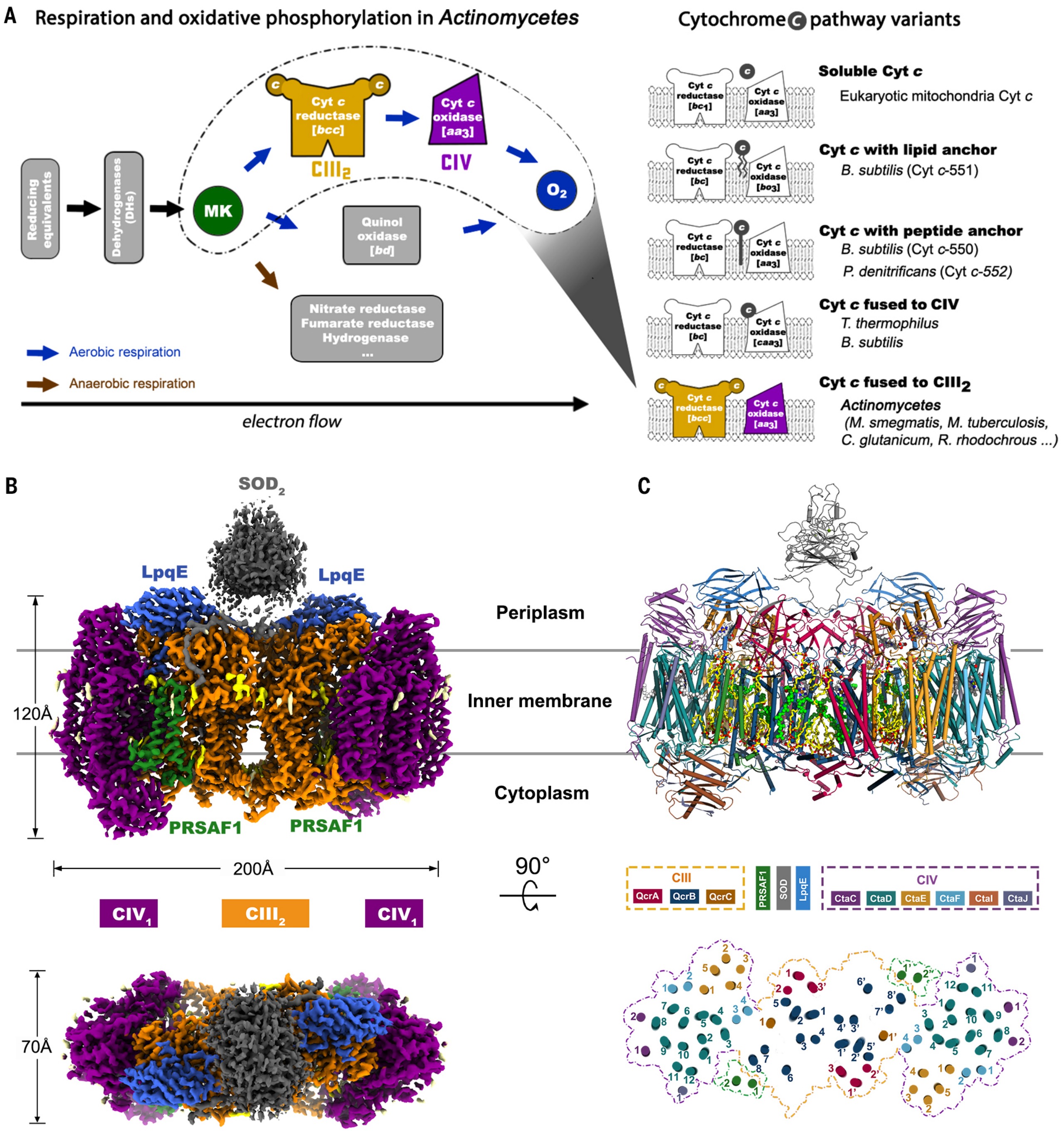

Fig. 1. Respiration in *Actinomycetes* and overall architecture of the mycobacterial respiratory machine $CIII_2CIV_2SOD_2$. (**A**) The respiratory electron transfer chain in *Actinomycetes* (left) and the five major prokaryotic cytochrome *c* pathway variants with the organization schemes in representative organisms (right). The *M. smegmatis* cytochrome *c* pathway has its cytochrome *c* fused with complex III, forming a *bcc*-type complex III that interacts with the aa_3-type complex IV to assemble into a CIII–CIV supercomplex. MK, menaquinone/menaquinol. (**B**) Overall architecture of the *bcc*-aa_3–type respiratory CIII–CIV supercomplex from *M. smegmatis*. The cryo-EM map of the supercomplex shows a linear twofold dimerized form of CIV_1–$CIII_2$–CIV_1 with dimensions 200 Å by 70 Å by 120 Å. CIII is colored in orange, CIV is in magenta and the association factors, PRSAF1 is in green, LpqE is in blue, and SOD is in gray. (**C**) Cartoon representation of the side view of the supercomplex (top) and a cross-sectional view (bottom). The MK is presented as bright green–colored solid spheres, and the phospholipids are shown as yellow sticks. In the cross-sectional view (bottom), the boundaries of CIII, CIV, and the association factor PRSAF1 are depicted with dashed lines in color (orange for CIII, magenta for CIV, and green for PRSAF1).

menadiol. SC III–IV oxidized menadiol and reduced O_2 with an apparent catalytic rate constant (k_{cat}) of 2.80 ± 0.05 s^{-1} for O_2 consumption or 11.20 ± 0.20 e^{-} s^{-1} and a Michaelis constant (K_m) of 120.70 ± 3.72 μM for menadiol (fig. S2, A to C). The k_{cat} value is comparable to the 65 e^{-} s^{-1} reported for this complex, with 2,3-dimethyl-1,4-naphthoquinol ($DMNQH_2$) as the electron donor (*9*); the difference is likely due to $DMNQH_2$ being more reducing and a closer structural analog of the natural substrate menaquinol (MKH_2) than menadiol. The data confirm that the purified sample is a functioning supercomplex containing CIII and CIV and capable of directly coupling quinol oxidation to oxygen reduction.

Overall architecture of SC III–IV

The structure of SC III–IV was determined by means of cryo–electron microscopy (cryo-EM) to an overall resolution of 3.5 Å (Fig. 1B; table S2; fig. S3, A to G; and movie S1). The dimensions of the supercomplex are 200 Å by 70 Å by 120 Å, with a linear dimeric CIV_1–$CIII_2$–CIV_1 arrangement in which individual CIVs flank the central CIII dimer on either side (Fig. 1, B and C, and Movie 1). This C_2 symmetrized linear architecture is completely different from those previously reported for respiratory supercomplexes (fig. S4). CIII is composed of canonical three subunits as a homodimer (Fig. 2A and fig. S5A). In addition to the four known subunits of *M. smegmatis* CIV, two subunits were observed that match two of the newly identified proteins, CtaI and CtaJ (Fig. 2B and fig. S3H), showing a similar topology and binding schema to those of subunit Va and IV in mitochondrial CIV (fig. S5J).

There is extra density within the interface between CIII and CIV as well as at the top of the CIII dimer (Fig. 1B). The density within the interface could be modeled by two proteins, LpqE and PRSAF1 (prokaryotic respiratory supercomplex association factor 1) (Fig. 1C and Movie 1). LpqE was found to be a N-terminal triacylated lipoprotein, with a *N*-acylated-*S*-diacylated modification of Cys24 within the lipobox (–^{21}L*xx*^{24}C–) sequence (*34*). On the periplasmic side, the density on top of the CIII dimer consisted of a peptide fragment linked with a region of bulk density that could be visualized in a low-pass filtered map. The peptide fragment was modeled with residues Cys^{21}–Pro^{45} of the N-terminal sequence of superoxide dismutase (SOD) SodC of *M. smegmatis*. The EM map indicated side chain modifications, including triacylation at Cys^{21} that was part of a lipobox (–^{18}L*xx*^{21}C–) sequence and possible glycosylation sites (fig. S3H). Native mass spectrometry further identified that SodC is a component of SC III–IV (fig. S1F). The stoichiometry of SodC was confirmed as a dimer through the collisional dissociation of the SodC complex. Extensive glycosylation and copper-binding of SodC was observed in the mass spectrum (fig. S1F). The bulk density was therefore fitted with a dimer of SodC (Fig. 1, B and C, and fig. S3F). SC III–IV possesses SOD activity, with a specific activity of 132.56 ± 12.57 IU/mg-SOD, assuming 100% occupancy (fig. S2E). SodC association with SC III–IV was also confirmed through isolation of the supercomplex by means of Ni-affinity chromatography when a His-tag was introduced only to the C terminus of SodC and not any of the CIII and CIV subunits. The SodC-tagged form of the complex showed a higher specific activity of 957.36 ± 23.34 IU/mg-SOD but still lower than the 1000 to 6000 IU/mg-SOD that is typically observed with soluble SOD enzymes. It also indicates an ~14% $(SodC)_2$ occupancy in the purified QcrB-tagged SC III–IV particles for cryo-EM study. Thus, it appears that there might be some dissociation of SodC from

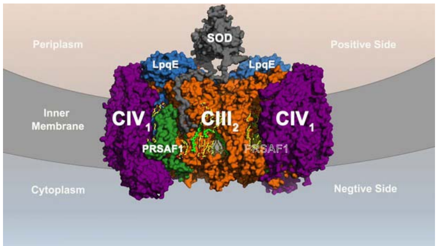

Movie 1. The overall architecture of the supercomplex. Cartoon representation of the supercomplex. The menaquinone/menaquinol (MK) is presented as bright green–colored solid spheres, and the phospholipids are shown as yellow sticks.

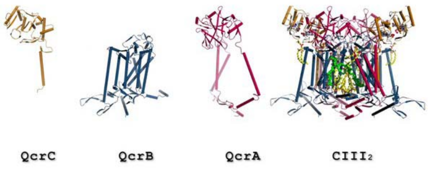

Movie 2. The composition and structure of CIII dimer. Cartoon representation of complex III. The menaquinone/menaquinol (MK) is presented as bright green–colored solid spheres, and the phospholipids are shown as yellow sticks.

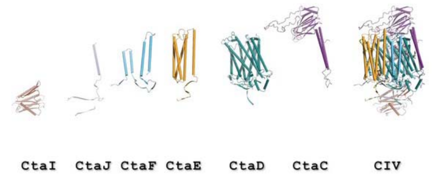

Movie 3. The composition and structure of CIV. Cartoon representation of complex IV. The phospholipids are shown as yellow sticks.

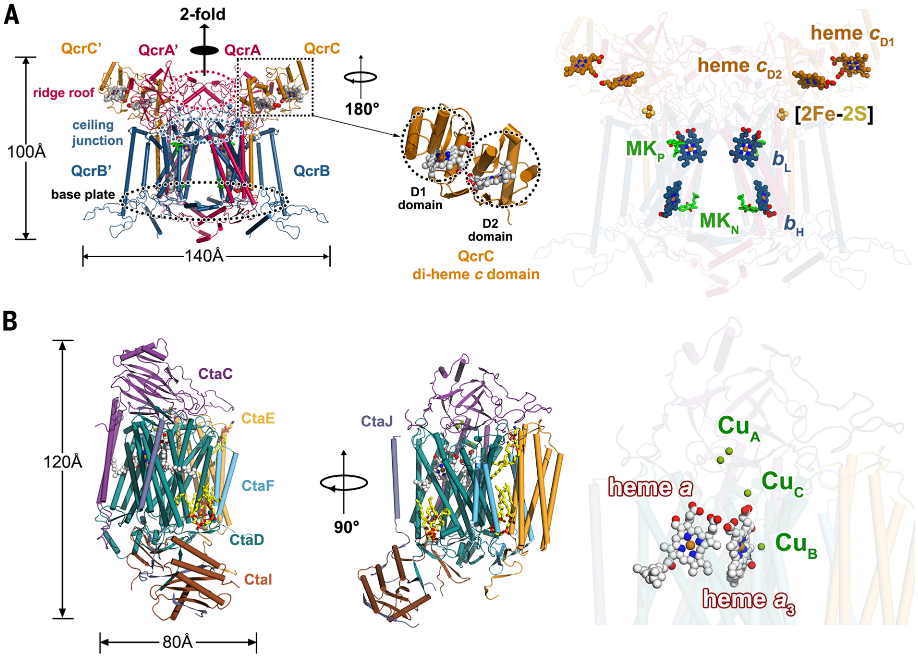

Fig. 2. Structure of $CIII_2$ and CIV from *M. smegmatis*. (**A**) Overall structure of the CIII dimer (left) and the spatial location (right) of prosthetic groups. QcrA, QcrB, and QcrC are colored pink, blue, and gold, respectively. The twofold symmetry of the dimer is depicted by the black axis. The zoom-in view shows the heme *c* binding domains (D1 and D2) of QcrC. The heme groups (b_H, b_L, c_{D1}, and c_{D2}) and [2Fe-2S] clusters are shown as spheres, and menaquinone/menaquinol (MK) are shown as sticks. The regions of ridge roof, ceiling junction, and base plate of CIII dimer are marked with dashed ellipses. (**B**) Overall structure of CIV (left) and the spatial location (right) of prosthetic groups. CtaC, CtaD, CtaE, CtaF, CtaI, and CtaJ are colored in magenta, dark green, yellowish brown, cyan, brown, and violet, respectively. Prosthetic groups are shown as spheres.

SC III–IV during detergent solubilization. It is also possible that the SOD occupancy is growth-regulated because an up-regulation of *sodC* (the gene encoding the SOD here) in response to phagocytosis by human macrophages has been reported (*35*). Further work on the role of SOD in association with SC III–IV is in progress.

All the prosthetic groups predicted from the canonical CIII and CIV subunits were clearly resolved and found to be coordinated with conserved canonical residues (figs. S3J and S8). Menaquinone (MK) molecules were observed at the quinone binding sites in CIII (fig. S7, A and B). The calculated molar ratio between iron atoms and copper atoms in the final model is 1.6, which is in excellent agreement with the value of 1.5 determined with atomic absorption spectroscopy (AAS) (fig. S1C). SodC from *M. tuberculosis* does not contain zinc (*36*), and AAS analysis showed that zinc was absent from SC III–IV (fig. S1C). In total, we were able to build 34 phospholipids (fig. S3I) and 10 MK molecules (fig. S7) in SC III–IV. The total molecular mass of the model, including the new identified subunits, is ~760 kDa, which is lower than the 873.4 kDa ± 10.4 Da determined with native Orbitrap mass spectrometry (fig. S1E). This difference may be accountable on the basis of contributions from the detergents and lipids and the possibility of the presence of additional unidentified subunits.

Structure of CIII and CIV in the supercomplex

The cryo-EM map clearly shows QcrA, QcrB, and QcrC of CIII in a dimeric form with all their prosthetic groups visualized (Fig. 2A; fig. S3, H and J; and Movie 2). QcrA has a "U"-shaped structure within its N-terminal domain, whereas the equivalent subunit in *bc*$_1$-type CIII has only one transmembrane helix (TMH) (equivalent to $_{\text{QcrA}}$TMH3) (Fig. 2A and fig. S5A). The region linking the two arms is located near the cytoplasmic side. The C-terminal domain of $_{\text{QcrA}}$TMH3 is on the periplasmic side and holds the [2Fe-2S] cluster. QcrA here also has a roof-like structure on the periplasmic side that is involved in the dimerization of CIII (Fig. 2A), whereas the *bc*$_1$-type CIIIs do not have this feature. The heme b_H and heme b_L cofactors are bound within four TMHs in QcrB (Fig. 2A). The N-terminal periplasmic portion of QcrC can be divided into two heme-containing cytochrome *c* domains, D1 and D2 (equivalent to the c_1 domain in *bc*$_1$ complex) (Fig. 2A and fig. S5N). These two domains are in close contact with and face each other in an antiparallel orientation. The D2 domain interacts extensively with QcrA and QcrB, whereas the additional D1 domain protrudes out of the core of CIII and is involved in direct intrasupercomplex electron transfer. Overall, although the *bcc*-type CIII in the supercomplex shares a similar dimeric association as that of the bacterial *bc*$_1$-type CIII and mitochondrial CIII, the structural details are markedly different (fig. S5B).

CIV in SC III–IV belongs to the type A heme-copper oxidase (HCO) family (Fig. 2B and Movie 3) (*37*). The central cavity of the barrel-like arrangement of the 12 TMHs in the CtaD subunit holds heme *a*, heme a_3, and Cu$_B$. The C-terminal hydrophilic β barrel domain of CtaC holds the two Cu$_A$ ions. The four protons required for oxygen reduction by heme a_3:Cu$_B$ in CIVs are transferred to the catalytic center through two pathways, denoted D and K (*38*). Because of the limited resolution, water molecules are not observed in our model. However, structure comparison revealed that the D and K pathways are conserved in SC III–IV (fig. S5, K and L).

Interaction between CIII and CIV and the contribution of association subunits and lipids

The linear form of SC III–IV arises from the dimerization of CIII, which is mediated by contacts between subunits QcrA and QcrB (Fig. 2A and fig. S6, A to D). There are extensive contacts

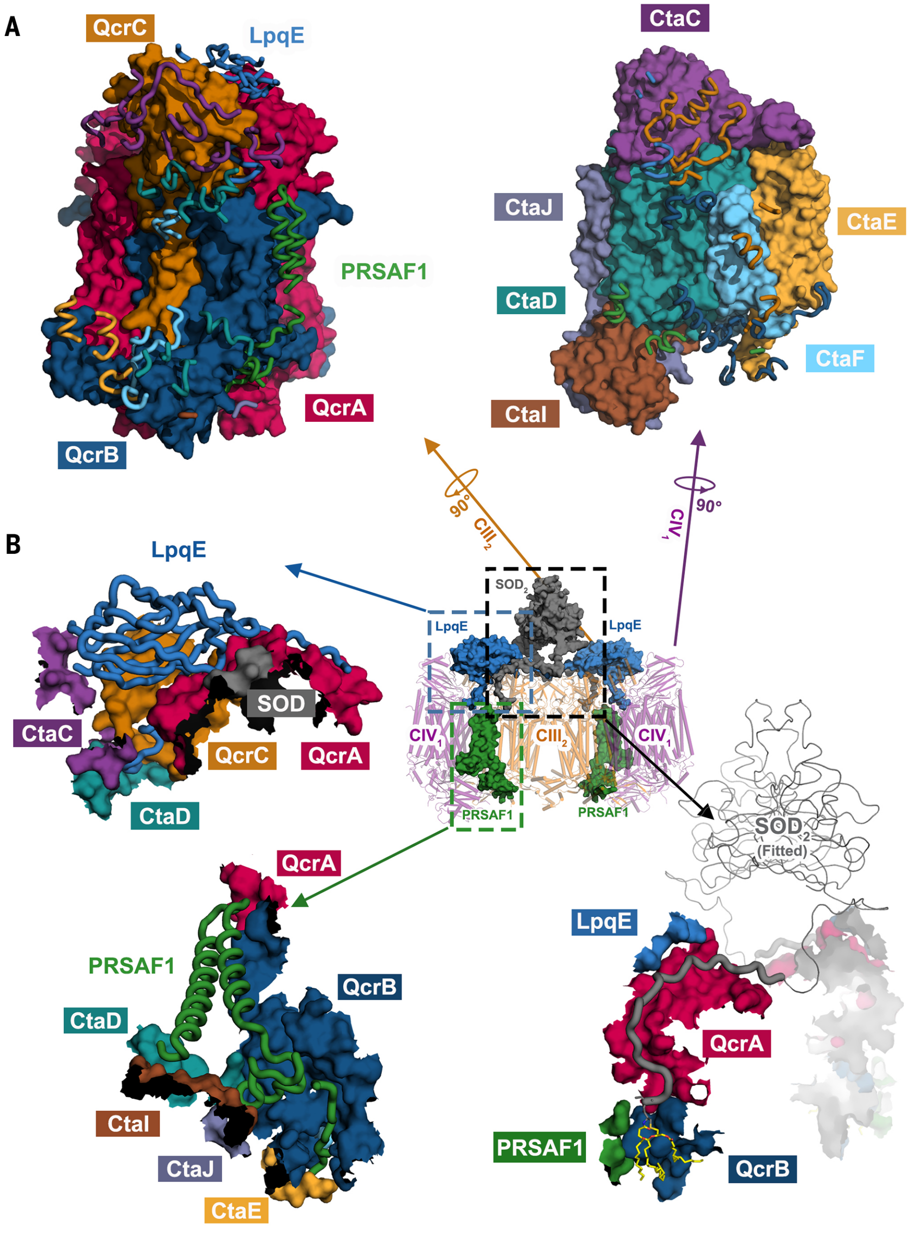

Fig. 3. Interaction between CIII and CIV and roles of association subunits. (**A**) A section profile of the interaction interface between CIII and CIV. The left and right images show the surface of CIII and CIV and the bound structural segments from CIV and CIII subunits and the association subunits, LpqE and PRSAF1. (**B**) Interactions between the association subunits (PRSAF1, LpqE, and SOD) and the subunits of CIII and CIV. The corresponding subunits of CIII and CIV are shown in surface representation and colored as indicated. The association subunits are shown in ribbon and colored as indicated. The catalytic domain of SOD was fitted in map and shown as a dimer (SOD$_2$). The lipid modification of SOD is shown in yellow sticks (detail provided in Fig. 4E).

between CIII and CIV on both the cytoplasmic and periplasmic sides of the membrane (Fig. 3). Of the three association subunits LpqE, PRSAF1, and SOD in SC III–IV, both LpqE and PRSAF1 form numerous contacts with CIII and CIV, suggesting an important role for both in supercomplex stability (Fig. 3B and fig. S6, E to G). SOD uses its lipid-modified N-terminal fragment to associate with CIII (Fig. 4E) and forms a dimer on the periplasmic side of the CIII dimer. There are no direct interactions between the main body of the SOD dimer and CIII or CIV. This might allow a flexible orientation for this subunit, which could be important for efficient clearance of reactive oxygen species (ROS) generated by side reactions when electrons are transferred from CIII to CIV.

Phospholipids, especially cardiolipin (CL), are known to contribute to both the assembly and stability of respiratory complexes and supercomplexes (*39*). In the structure of SC III–IV, phospholipids are identified in the transmembrane space of CIII and CIV and the interface between CIII and CIV (Fig. 4). Of particular note are the four CL molecules in the large groove between CIII and CIV (Fig. 4D); the 16 fatty acid chains fill most of the space in the groove and may play an important role in stabilizing the supercomplex. The N-terminal–modified lipid tails of the lipoproteins SOD and LpqE mediate intersubunit hydrophobic interactions and contribute to the stability of the supercomplex (Fig. 4, E and F). These lipid modifications described here are similar to those observed in a recently described structure of alternative complex III (*11*).

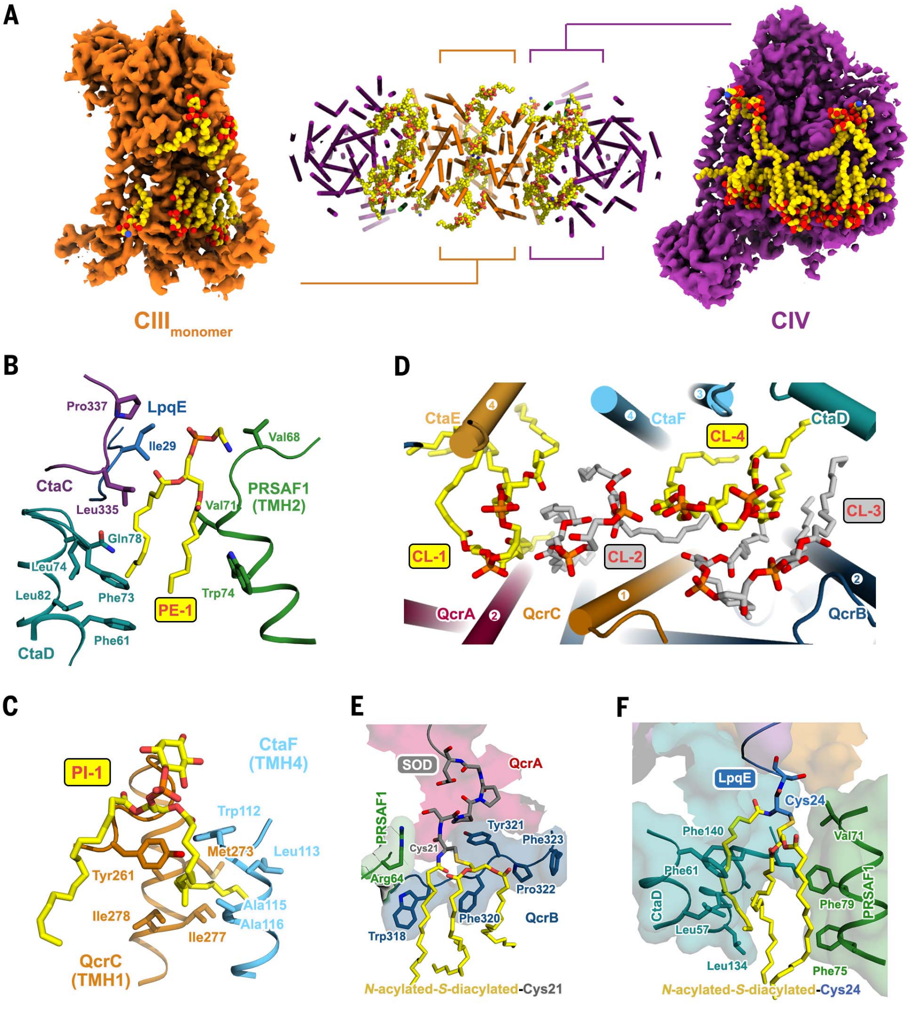

Fig. 4. Important roles of phospholipids in the stability and assembly of the supercomplex. (**A**) The distribution of phospholipids in the membrane region (middle, view from periplasmic side) at the junction between the CIII monomers (left) and the interfaces between CIII and CIV (right). (**B**) A polyethylene (PE) molecule mediates the interaction between PRSAF1 (TMH2) and CIV (CtaC and CtaD). (**C**) A polyimide (PI) molecule binds to the interface between $_{\text{QcrC}}$TMH1 and $_{\text{CtaF}}$TMH4. (**D**) Four CL molecules are bound in the groove between the TM regions of CIII and CIV. (**E**) The N-terminal lipid modification of SOD at Cys21 binds to QcrB via hydrophobic interactions. (**F**) The N-terminal lipid modification of LpqE at Cys24 mediates the interactions between CtaD and PRSAF1.

Quinone and quinone binding pockets

Quinone binding sites of respiratory complexes are of great interest because they are part of the Q-cycle hypothesis. They have varied sequences and specificities between species and are often the sites for inhibitor binding and thus are important for drug discovery. We have identified the two quinone binding sites (Q_P and Q_N) in SC III–IV (Fig. 5). The quinol oxidation site (Q_P site) responsible for MKH_2 oxidation is near heme b_L, whereas the quinone reduction site (Q_N site) responsible for MK reduction is close to heme b_H.

The Q_P site near heme b_L is at the center of an inverted triangle structure and surrounded by helices (Fig. 5A). Residues at this site are not conserved compared with the bc_1 complex (Fig. 5C). The typical "PEWY" motif in the bc_1 complex is replaced by "PDFY" (Fig. 5C). One MK molecule is identified at this site with its naphthoquinone ring surrounded mainly by hydrophobic residues. The edge-to-edge distance from MK to heme b_L is 16 Å. Thus, we speculate that the endogenous electron donor MKH_2 would bind closer to heme b_L to facilitate electron transfer, and what we observe here might be a representation of the oxidized product as it leaves the Q_P site. Furthermore, there are no observed hydrogen bonds to the carbonyl groups of MK (Fig. 5A). It is known that proton abstraction from MKH_2 is coupled to electron donation to CIII. Thus, hydrogen bonds are needed between the binding residues and the hydroxyl group of MKH_2 to help deprotonate the substrate. Hence, MKH_2 should bind deeper inside the pocket, close to polar residues such as $_{\text{QcrB}}\text{Tyr}^{159}$, $_{\text{QcrB}}\text{Thr}^{308}$, and $_{\text{QcrB}}\text{Asp}^{309}$ (Fig. 5A). Structural superposition with the inhibitor-bound bc_1 complex (*40*) shows that the MK at the Q_P site binds deeper into the pocket in the bc_1 complex than in this SC III–IV complex.

By contrast, the head group of MK at the Q_N site is bound in a similar fashion to ubiquinone in the structures of bc_1 complexes (Fig. 5B). As found for the Q_P site, these residues are not conserved compared with the bc_1 complexes from bacteria to eukaryotes (Fig. 5C). In particular, the carbonyl groups of ubiquinone are coordinated by the conserved His and Asp amongst bc_1 complexes; these residues are substituted by $_{\text{QcrB}}\text{Trp}^{231}$ and $_{\text{QcrB}}\text{Ser}^{261}$ in the *bcc*-type CIII of *M. smegmatis*. The carbonyl groups of MK in SC III–IV interact with the side chains of $_{\text{QcrB}}\text{Tyr}^{48}$ and $_{\text{QcrB}}\text{Ser}^{261}$ that may supply protons for MK reduction. The MK head group is ideally placed for electron transfer, being within 5 Å of the A-edge of heme b_H.

Besides finding quinone molecules at the Q sites, we also observed map signals for another three possible MK/MKH_2 molecules in the supercomplex (fig. S7, C to E). However, further experiments are needed to clarify the identity and function of these molecules.

The new family of candidate antimycobacterials, the imidazo[1,2-a]pyridines (IP) represented by Q203, operate by competing with MK for binding at the Q_P site of CIII of *M. tuberculosis* (41). Sequence alignments indicate a high similarity between the Q_P sites of CIIIs from *M. tuberculosis* and *M. smegmatis* (Fig. 5C), thus suggesting that Q203 would also have a similar binding mechanism and a similar effect on the activity of *M. smegmatis* CIII. Indeed, recent studies of the antimycobacterial activity of Q203 on *M. tuberculosis* and *M. smegmatis* demonstrated that Q203 targets the *bcc* complex in both with similar affinity (42). We investigated the in vitro inhibition of *M. smegmatis* SC III–IV by Q203 by means of the menadiol/oxygen oxidoreductase activity assay and compared the effect with a hybrid supercomplex of *M. tuberculosis bcc*-CIII and *M. smegmatis* aa_3-CIV. Q203 showed inhibition of menadiol-induced oxygen consumption, with median inhibitory concentration (IC_{50}) values of 0.84 ± 0.22 μM and 0.61 ± 0.16 μM for SC III–IV and the hybrid supercomplex, respectively (fig. S2D).

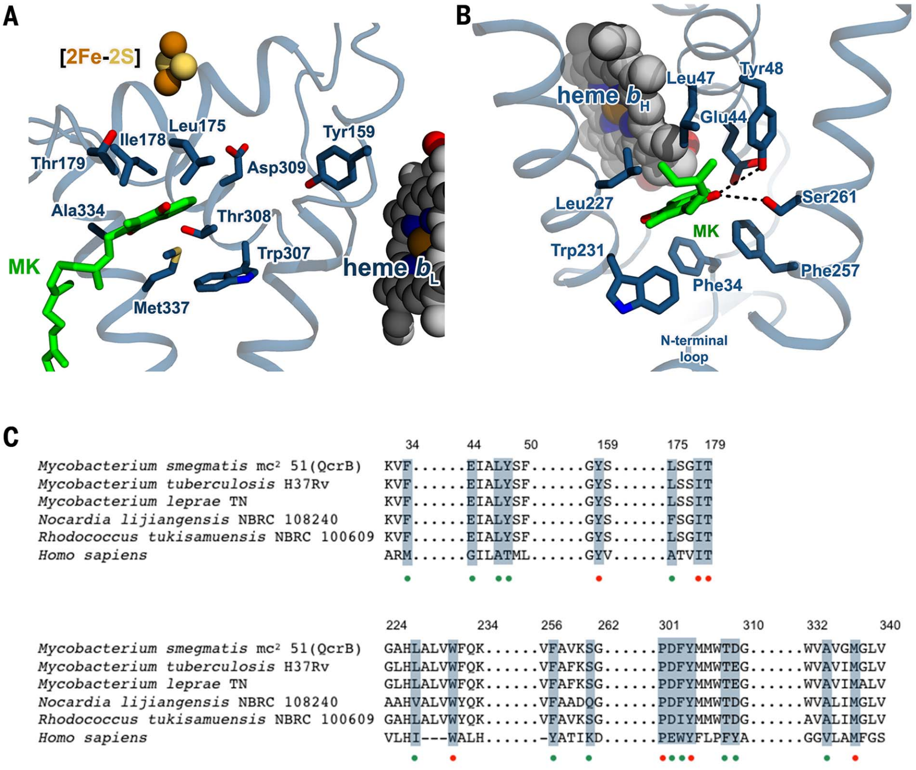

Fig. 5. Structures of the MK/MKH_2 binding sites in *M. smegmatis* CIII. (**A**) The Q_P binding site. (**B**) The Q_N binding site. The residues potentially involved in the binding of MK/MKH_2 are shown with side chains in a stick representation. The MK molecules are colored in green. The heme and [2Fe-2S] groups are shown in spheres and labeled accordingly. (**C**) Sequence alignment for the Q_P site and Q_N site in QcrB with other *Actinobacteria* and *Homo sapiens* ETC systems. The red and green dots indicate whether *H. sapiens* shares a common conservative site with *Actinobacteria* (red) or not (green).

Prosthetic groups and implication for direct electron transfer

The prosthetic groups of CIII (heme b_H/b_L, [2Fe-2S] clusters, and heme c_{D1}/c_{D2}) and CIV (Cu_A, Cu_B, and heme a/a_3) are clearly identified from the cryo-EM map (Fig. 2, A and B, and fig. S3J). The redox centers in CIII and CIV are within distances that allow long-range electron transfer (Fig. 6A). Both heme b_L and heme b_H are found in $QcrB_{CIII}$ (figs. S3J and S8A). The edge-to-edge distance between the two heme groups is 12 Å, allowing rapid inter-heme electron transfer. The shortest distance from b_L to MK at the Q_P site and from b_H to MK at the Q_N site are 16 and 5 Å, respectively (Fig. 6A). Previous studies have proposed that CIIIs from different species adopt a dimeric architecture and form an H-shaped electron transfer system that distributes electrons between four quinone oxidation-reduction sites within the CIII dimer (43). Consistent with this hypothesis, upon dimerization of *M. smegmatis* CIII, the two b_L heme groups from the CIII monomers are 14 Å apart (Fig. 6A), allowing electron tunneling between the two hemes.

The heme c_{D1}-containing D1 domain of $QcrC_{CIII}$ protrudes into the periplasm and interacts with the Cu_A-containing periplasmic domain of $CtaC_{CIV}$ (Fig. 6A). The edge-to-edge distance from heme c_{D1} to the Cu_A center is 12 Å. At the interface between these two domains is a gating residue ${}_{CtaC}Trp^{138}$ on the Cu_A binding loop. The distance between ${}_{CtaC}Trp^{138}$ and the Cu_A center and that between ${}_{CtaC}Trp^{138}$ and heme c_{D1} are approximately equal. It has been proposed, on the basis of mutagenesis studies, that the corresponding Trp^{121} (44) of *Paracoccus denitrificans* CIV is the electron entry site from cytochrome *c*. CIVs from *Bos taurus* also possesses a tryptophan residue at the equivalent location (45). Thus, the heme c_{D1}-containing D1 domain of $QcrC_{CIII}$ here interacts with CIV on a similar electron entry site as in other respiratory complexes.

Within CIV, the heme *a* group is just below the Cu_A center, and the heme a_3 group is beside heme *a* (Fig. 6A). Cu_B is coordinated to three conserved His residues. The space between the iron of heme a_3 and Cu_B is the catalytic center for reduction of oxygen. In proximity to propionate groups of heme a_3, a Cu_C ion was modeled according to the cryo-EM map (fig. S3J). In other reported CIV structures, the equivalent density at this site is occupied by a water molecule (46) or a Mg^{2+} ion (47). However, we did not detect magnesium in our AAS analysis (fig. S1C). The edge-to-edge distance between Cu_C and the Cu_A center and that between Cu_C and heme a_3 are 12 and 9 Å, respectively.

From the positions of the prosthetic groups in *M. smegmatis* SC $CIII_2CIV_2SOD_2$ and the redox center separations, it is possible to trace an uninterrupted pathway for the flow of electrons within the supercomplex starting from the electron donor at the Q_P site in CIII to the final site of oxygen reduction in CIV (Fig. 6B). MKH_2 from the Q-pool binds at the Q_P site near heme b_L and transfers one electron to the [2Fe-2S] cluster and the other to heme b_L, which passes the electron via heme b_H to a MK bound at the Q_N site, generating the highly reactive intermediate menasemiquinone (MK•). The reduced [2Fe-2S] cluster is within electron tunneling distance to transfer an electron to heme c_{D2}, which rapidly passes the electron to heme c_{D1}. A second MKH_2 then binds at the Q_P site and repeats the process. The MK• at the Q_N site is fully reduced to MKH_2 and released to the Q-pool. This completes the Q cycle. An electron path between CIIIs in the dimer is also possible through tunneling between the adjacent b_L heme groups, albeit with low efficiency (43). The reduced [2Fe-2S] cluster again transfers the other electron to heme c_{D2}/c_{D1}. Once heme c_{D1} is reduced, two Cu_A ions of $CtaC_{CIV}$ accept the electron through contacts forged with the D1 domain of $QcrC_{CIII}$. At this point, an electron is transferred from CIII to CIV. Within CIV, the electron is transferred through heme *a* (or possibly the Cu_C center) and finally reaches the terminal heme a_3:Cu_B reaction center for oxygen reduction. As a consequence of the electron transfer, protons are translocated to the periplasm, forming a transmembrane PMF. Throughout the entire pathway from the Q_P site to the terminal oxygen reduction center, electrons tunnel between prosthetic groups that are all buried inside this integral complex.

Quinone reduction at the Q_N site to complete the Q cycle can be bypassed or "short-circuited" if both electrons from MKH_2 oxidation at the Q_P site are transferred to the [2Fe-2S] cluster and then to CIV for oxygen reduction. Hence, competent energy transduction requires that electron transfer from the Q_P site has to be bifurcated between reduction of the [2Fe-2S] cluster and heme b_L. In essence, the pathway for transferring electrons from the [2Fe-2S] cluster eventually to CIV has to be sufficiently slow for electron transfer to the Q_N site for quinone reduction to occur. In the bc_1 complex, the [2Fe-2S] cluster domain cycles between "*b*" and "c_1" states. In the *b*-state, the [2Fe-2S] cluster is close to the Q_P site to accept an electron from quinol oxidation but too far away (26 Å) (fig. S5E) to transfer an electron to the c_1 heme at an appreciable rate. The cluster domain undergoes a "head displacement" conformation change to the c_1-state, in which the [2Fe-2S] cluster moves to within 11 Å of the c_1 heme to facilitate electron transfer. This head displacement or "gating" step occurs with a rate constant of 6×10^4 s^{-1} (48).

We cannot rule out the possibility that SC III–IV could adopt a different conformation and cycle between states similar to the *b* and c_1 states of bc_1 complexes. However, the dimer of QcrA is held firmly in place by the periplasmic roof-like structure and further surrounded by QcrB and QcrC, which might limit the space for the potential conformational change (fig. S5D). Structural superposition shows that the position of the [2Fe-2S] in QcrA is similar to that of bc_1-type CIII in the *b* state—rapid cluster reduction by MKH_2 can occur. The [2Fe-2S] cluster is at a distance of 16 Å from heme c_{D2}. We used this distance, the reported midpoint potentials of the prosthetic groups (10), and a reorganization energy (λ) of 0.7 eV to calculate a rate constant of electron transfer of 5.6×10^2 s^{-1} from [2Fe-2S] to heme c_{D2} (49). This is much slower than the head displacement gating step in bc_1 complexes (6×10^4 s^{-1}). We conclude that short-circuiting in SC III–IV is likely to be rate-limited by slow electron transfer between the [2Fe-2S] cluster and heme *c* made possible by positioning of the chain of redox centers, rather than by conformational changes as found in bc_1 complexes.

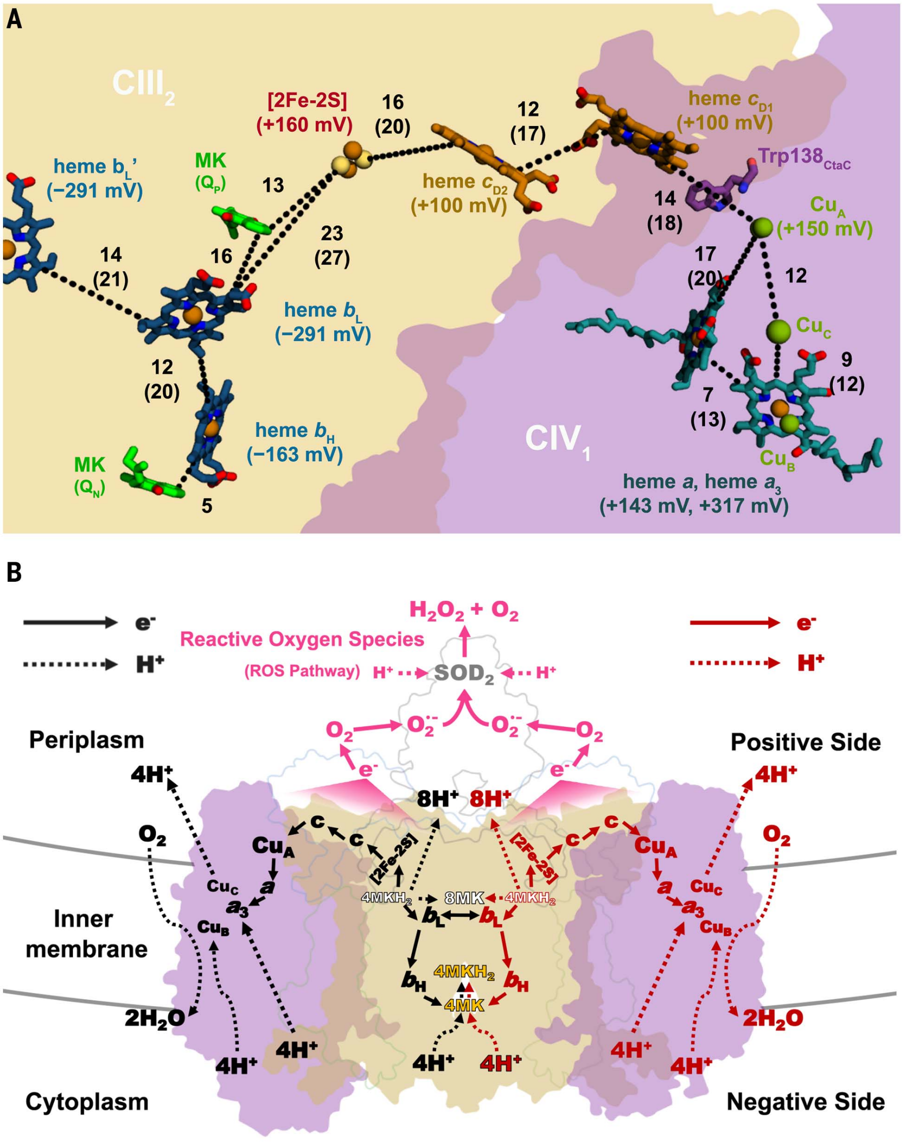

$$8MKH_2 + 4MK + 2O_2 + 24H^+_N \xrightarrow{CIV_1-CIII_2-CIV_1} 4MKH_2 + 8MK + 4H_2O + 24H^+_P$$

Fig. 6. The complete electron transfer pathway in the *bcc-aa₃*–type respiratory CIII/CIV supercomplex. (**A**) The prosthetic groups in the supercomplex are shown in sticks or spheres and labeled accordingly, with the corresponding midpoint potentials shown in parentheses. These values are based on the measurement of that of the *bcc-aa₃*–type supercomplex from *C. glutamicum* (10). The edge-to-edge distances between adjacent prosthetic groups are shown in black dashed lines, with the numbers in the parentheses representing the center-to-center distances. (**B**) A schematic diagram showing the entire electron transfer pathway from CIII to CIV and the relevant proton translocations in CIII and CIV. The potential role of associated SOD for the clearance of ROS is also proposed.

Role of SOD association

In aerobic organisms, the respiratory ETC not only generates the energy needed to fuel biological functions but is also a major source of intracellular ROS that can cause damage to cellular structures and components (50). Complex III is one of the major sites of ROS production (51). Although ROS are emerging as important elements in the bacterial response to lethal stress (52), it is well documented that they can disturb respiratory activity through oxidative damage of ETC complexes, which are in turn protected by the ROS scavengers SOD and catalase (53–55). Up-regulation of *M. tuberculosis sodC* (the gene encoding the SOD here) in response to phagocytosis by human macrophages has been observed (35). This mycobacterial Cu, Zn SOD SodC was identified as a membrane-bound enzyme and proposed to protect specific membrane-associated targets from oxy-radical damage, thus facilitating mycobacterial intracellular growth (35). A null *sodC* mutant of *M. tuberculosis* was shown to be readily killed by externally generated superoxide and by activated macrophages producing oxidative bursts (56). In this work, we found that catalytically active SodC is an integral part of a respiratory supercomplex $CIII_2CIV_2SOD_2$. SodC could serve to scavenge ROS generated locally or by other ETC complexes as well as ROS released by the immune response of the host. Its recruitment has the potential to make this critical respiratory machinery a robust system even under the high oxidative stress inside macrophages. Immunoblotting of *Caenorhabditis elegans* respiratory supercomplexes separated by means of BN-PAGE showed that mitochondrial SOD-2 (mtSOD-2) is associated with the respirasome CI–$CIII_2$–CIV, suggesting that the mtSOD might also provide similar local protection against ROS damage (57).

Conclusions

The cryo-EM structure of a CIII–CIV respiratory supercomplex from *M. smegmatis* has revealed a complete intracomplex electron transfer pathway from quinol oxidation in CIII to oxygen reduction in CIV, a new mechanism for bifurcating electron transfer to ensure completion of the Q cycle for energy transduction, and the association of a SOD that can provide protection against oxidative damage by ROS. The structure of the quinone binding sites also provides a framework for structure-based antimycobacterial drug discovery.

Materials and methods

Bacterial strain

A *M. tuberculosis*–like highly hydrogen peroxide-resistant *M. smegmatis* mutant strain, mc^2 51 (58), was used in this study. The draft genome sequence data can be obtained through the GenBank accession no. JAJD00000000.1. The code for the 10× His tag was introduced at the C terminus of the QcrB or SodC genome loci through homologous recombination. This modification allowed the metal affinity purification step. The presence of the histidine tag was confirmed by PCR and Western blot.

M. smegmatis culture and membrane isolation

Culturing of the cells and membrane isolation were performed as described in previously published protocols, with some modifications (9, 32). The cells were grown in LB media supplemented with hygromycin (50 μg/mL), carbenicillin (20 μg/mL) and Tween 80 (1 mL/L), at 37°C with shaking to maintain oxygenation. A total of 10× 1 L bacteria solutions were cultured until the OD_{600} reached ~1.5 and then harvested by centrifugation for 30 min at 4,000 rpm. The obtained bacteria were resuspended in buffer A (20 mM MOPS, pH 7.4, 100 mM NaCl, 1 mM EDTA, 1 mM PMSF). Cell lysis was achieved by three passes through a high pressure cell disrupter at 4°C and 1200 bar. The lysate was centrifuged at 14,000 rpm for 10 min to remove cell debris and non-lysed cells. The resulting supernatant was centrifuged at 36,900 rpm for 1 hour in a Ti45 rotor (Beckman). The membrane pellets were harvested and stored at –80°C.

Supercomplex purification

Membranes were thawed and homogenized in buffer A. Respiratory supercomplexes were extracted from the membrane by 1% (w/v) digitonin for three hours with slow stirring at 4°C. Insoluble materials were removed by centrifugation at 18,000 rpm for 30 min at 4°C. The supernatant was loaded onto a Ni-NTA column followed by gravity feeding three column volumes of buffer A through the resin. The resin was further washed by buffer B (20 mM MOPS, pH 7.4, 100 mM NaCl, 1 mM EDTA, 0.1% (w/v) digitonin, 50 mM imidazole). The protein was eluted with buffer C (20 mM MOPS, pH 7.4, 100 mM NaCl, 1 mM EDTA, 0.1% (v/w) digitonin, 500 mM imidazole). Eluted protein was concentrated using a 100-kDa cut-off centrifugal concentrator (Millipore) and this sample was then loaded onto a Superose 6 (10/300 GL, GE Healthcare) column equilibrated in a buffer containing 20 mM MOPS, pH 7.4, 100 mM NaCl, 1 mM EDTA and 0.1% (v/w) digitonin. The peak fractions (elution volume between 12.25 mL and 13 mL) were pooled and concentrated to 5.5 mg mL^{-1} by using a 100-kDa cutoff centrifugal concentrator.

Characterization of the respiratory supercomplex $CIII_2CIV_2SOD_2$

The supercomplex was characterized by optical spectroscopy, mass spectrometry (MS) and 3,3′-diaminobenzidine (DAB) staining. To identify the heme groups, selected fractions were analyzed by recording spectra from 250 to 700 nm before and after reduction with dithionite according to previously described methods (9, 32). To detect the protein components, the concentrated supercomplex sample was subjected to MS analysis at the National Center for Protein Science (Shanghai, China). The protein sample was analyzed by BN-PAGE and then a separate strip of the gel was stained with DAB (59–61).

Pyridine hemochrome assay

For denaturing redox difference spectra samples were taken up in 20% (v/v) pyridine, 0.1 M NaOH. Redox difference spectra were recorded in the range 500–620 nm using potassium ferricyanide for oxidation and sodium dithionite for reduction. Potassium ferricyanide (250 μM) was added to the sample and the spectrum of this oxidized form was recorded. Sodium dithionite (5 mM) was then added to this sample, the solution was mixed well and the spectrum was scanned repeatedly until it remained unchanged, giving the spectrum of the reduced form. The heme *a*, *b*, and *c* contents were determined from the reduced-minus-oxidized difference spectrum using the following extinction coefficients $\Delta\varepsilon_{587\text{–}620} = 21.7\ \text{mM}^{-1}\cdot\text{cm}^{-1}$, $\Delta\varepsilon_{557\text{–}540} = 23.98\ \text{mM}^{-1}\cdot\text{cm}^{-1}$, $\Delta\varepsilon_{550\text{–}535} = 23.97\ \text{mM}^{-1}\cdot\text{cm}^{-1}$.

Native mass spectrometry of supercomplex

Purified supercomplex was buffer exchanged into 200 mM ammonium acetate buffer pH 7.5 containing DDM at 2 times critical micelle concentration. The sample was immediately introduced into a modified Q-Exactive mass spectrometer (Thermo) and ions were transferred into the Higher-energy collisional dissociation (HCD) cell following a gentle voltage gradient (injection flatapole, inter-flatapole lens, bent flatapole, transfer multipole: 7.9, 6.94, 5.9, 4 V respectively). The capillary voltage was maintained at 1.2 to 1.4 eV at temperature of 200°C. The optimized acceleration voltage for intact supercomplex is 150 V and 100-120 V in the source and HCD cell, respectively. SodC subunits were dissociated from the complex with high acceleration voltage (250 to 300 V) in the source and the collisional dissociation of dimeric SodC was performed with the voltage ramp from 0-150 V in HCD cells. Backing pressure was maintained at ~1.20×10^{-9} mbar and data was analyzed using Xcalibur 2.2 SP1.48.

Independent lipidomics analysis 1

Co-purified lipids from supercomplex were extracted by chloroform/methanol (2:1, v/v) and lyophilized and re-dissolved in 60% acetonitrile (ACN). For LC-MS/MS analysis, the extracted lipids were loaded into a 5-μl sample loop using an autosampler by a full-loop method with an overfill factor of 1.4, and then transferred to a 1-μl injection loop using a loading pump at a flow rate of 5 μl/min with 70% solution A and 30% solution B. The lipids in the injection loop were injected onto a C18 column (Acclaim PepMap 100, C18, 75 μm × 15 cm, Thermo Fisher Scientific) using a nanopump at a flow rate of 300 nl/min, 30% solution B. The lipids were separated on the C18 column at 40°C by a gradient starting from 30% solution B. After 10 min, solution B was ramped to 65% over 1 min, then 80% over 6 min, before being held at 80% for 10 min, then ramped to 99% over 6 min and held for 7 min. [Solution A: (ACN: H2O (60:40), 10 mM ammonium formate, 0.1% formic acid] and solution B [IPA: ACN (90:10), 10 mM ammonium formate, 0,1% formic acid]. The column eluent was delivered via a dynamic nanospray source to a hybrid LTQ Orbitrap mass spectrometer (Thermo Scientific). Typical MS conditions were: spray voltage (1.8 kV) and capillary temperature (175°C). The LTQ-Orbitrap XL was operated in negative ion mode and in data-dependent acquisition with one MS scan followed by five MS/MS scans. Survey full-scan MS spectra were acquired in the orbitrap (m/z 350 to 2000) with a resolution of 60,000. Collision-induced dissociation (CID) fragmentation in the linear ion trap was performed for the five most intense ions at an automatic gain control target of 30,000 and a normalized collision energy of 38% at an activation of $q = 0.25$ and an activation time of 30 ms.

Independent lipidomics analysis 2

Homogenized membranes and protein crystals were extracted with 800 μL of chloroform:methanol:water (1:1:0.1) in glass vials. After shaking the samples vigorously at 1500 rpm for 30 min at 4°C, 350 μL of water was added to break the phases. Samples were centrifuged and the lower organic phase was transferred to new glass vials. The remaining membrane and/or protein pellets were re-extracted with 400 μL of chloroform. The combined extracts were dried using a SpeedVac (Genevac, UK). Samples were stored at –80°C until mass spectrometric analysis.

Liquid chromatography-mass spectrometric (LCMS) analyses were carried out on an Exion UPLC coupled with a SciexQTRAP 6500 Plus mass spectrometer. Analysis of phospholipids and free mycolic acids were carried out using normal-phase LCMS as described previously (62, 63). Levels of MK species were quantified using a reverse-phase LCMS method (64).

Quinone reduction

Menadiol was prepared as previously described, with minor modifications (65). To prepare reduced menadiol, 3.4 mg 2-methyl-1,4-naphthoquinone (Sigma M5625) was dissolved in 1 mL N_2-saturated anhydrous cyclohexane to yield a 20 mM solution. The solution was mixed with 5 mL N_2-saturated 1 M sodium dithionite solution (in H_2O) and shaken vigorously. After phase separation, the organic phase containing the reduced menadiol was removed and transferred to a 15 mL centrifuge tube (all steps performed under a stream of N_2). The cyclohexane was evaporated under an N_2 stream, while the sample was kept at 40°C in a water bath. Subsequently, the reduced quinol was dissolved in N_2-saturated, acidified ethanol (ethanol with 10 mM HCl), aliquoted, flash frozen in liquid nitrogen, and stored at −20°C.

Oxygen consumption assay

Since the *bcc*:aa_3 preparations from *M. smegmatis* are active with menadiol (2-methyl-1,4-naphthoquinol) as substrate and electron donor, which has better solubility in water than MKH_2 (*33*), the supercomplex was routinely characterized by its menadiol:O_2 oxidoreductase activity. Rates of oxygen consumption were determined using a Clark-type oxygen electrode (Hansatech) in a magnetically stirred chamber at 25°C in 20 mM MOPS pH 7.4, 100 mM NaCl, 0.005% LMNG, 5 mM DTT, following a method previously described, with minor modifications (*33*). The rate of menadiol autoxidation was measured in parallel as a reference and subtracted from the supercomplex-dependent rate.

Enzyme kinetics of supercomplex $CIII_2CIV_2SOD_2$

The Michaelis-Menten curves were obtained by measuring the initial supercomplex-dependent oxygen consumption rates as a function of menadiol concentration. The initial rate data were fitted to the Michealis-Menten equation using a nonlinear fitting program (GraphPad Prism 6.0).

In vitro inhibition of the supercomplex activity by Q203

The supercomplexes were preincubated for 10 min with inhibitors, menadiol was added as electron donor to a final concentration of 200 μM and the oxygen respiration was measured for 3 min. Data were normalized relative to solvent (Ethanol) control for full activity and to a sample with 160 μM Antimycin A for complete inhibition.The supercomplex-dependent initial rates were used to generate an inhibition curve and determine the IC_{50} value.

Determination of SOD activity in the supercomplex

The SOD activity was measured using a SOD Assay Kit-WST (19160; Sigma-Aldrich) following the kit instruction. Since the absorption maximum of WST-1 formazan is 450 nm and it is proportional to the amount of superoxide anion, the SOD activity (inhibition rate %) as an inhibition activity can be quantified by measuring the decrease in the color development at 450 nm. The SOD activity of the complex purifications and a reference SOD sample with a known specifice activity in IU/mg (international unit per milligram) from bovine erythrocytes (Catalog number S5395; Sigma) were both determined in this assay. Based on the linear relationship between 1/(inhibition rate) and 1/(enzyme activity), the IC_{50} (50% inhibition activity) of the complex and bovine SOD can be determined. By comparing the IC_{50} of each, the specific SOD activity of the complex purification was determined and normalized into international unit per milligram. To be noted, the IU here refers to the MF unit (the McCord-Fridovich unit) which is determined by measuring the reduction of cytochrome *c* by the xanthine oxidase/hypoxanthine system at 550 nm and is the international unit for SOD activity (EC 1.15.1.1) measurement (*66*). To avoid the potential interference from the cytochrome *c* domains of QcrC subunite, the McCord–Fridovich test was not used here.

EPR spectroscopy

Low temperature EPR spectra were recorded on a Bruker X-band (9.4 GHz) EMX plus 10/12 spectrometer equipped with an Oxford Instrument EPR 910 liquid Helium continuous-flow cryostat. A cylindrical resonator (ER4119hs TE011) was used for data collection. 100 μL of supercomplex solution at 10 μM was transferred to an EPR tube (Wilmad 707-SQ-250M Quartz EPR sample tube) and rapidly frozen in liquid nitrogen before inserting into the resonator. For the reduced sample, sodium dithionite (100mM) was added and mixed with the supercomplex to give them the spectrum of the reduced form. Specific parameters for EPR experiments were summarized here: temperature 10 K, microwave power 2.0 mW, microwave frequency 9.39 GHz, modulation amplitude 0.9 mT, modulation frequency 100 kHz, time constant 163.84 ms, and scan rate 3.125 mT/s. Multiple scans were accumulated to obtain a good S/N ratio.

Cryo–electron microscopy analysis

Uranyl acetate (1% w/v) was used for negative staining. 5 μL of the supercomplex sample at concentration of 0.05 mg mL^{-1} was applied to glow discharged copper grids supported by a thin layer of carbon film (Zhongjingkeyi Technology Co. Ltd) for one minute and stored at room temperature. Images were taken on an FEI Tecnai Spirit microscope operating at 120 kV. This data allowed initial model building.

Aliquots (4 μL) of freshly purified supercomplex at a concentration of 0.5 mg mL^{-1} were applied to glow-discharged holey carbon grids (Quantifoil Au R1.2/1.3). The glow discharge followed the standard recipes of H_2 and O_2 mixture in Gatan Solarus 950 for 1 min. Grids were blotted for 2.5 s and flash-frozen in liquid ethane cooled by liquid nitrogen using an FEI Mark IV Vitrobot operated at 8°C and 100% humidity. Images were taken using an FEI Titan Krios electron microscope operating at 300 kV with a Gatan K2 Summit detector at a nominal magnification of 18,000×. Images were recorded in super-resolution mode and binned to a pixel size of 1.35 Å. Automated single-particle data acquisition was performed with SerialEM (*67*). Defocus values varied from 1.3 to 2.7 μm. 32 frames per stack were collected with a total exposure time of 11.4 s. The dose rate was set to ~8 e^-/pixel/s and the total dose was ~50 e^-/Å^2.

Image processing

We first generated a low-resolution reconstruction of the supercomplex from 53 micrographs of the negative-stained sample. Particle picking was performed with the EMAN2 (*68*) subroutine e2boxer.py in an interactive boxing mode, yielding 25,287 particles. Reference-free classification was performed with e2refine2d.py, generating 36 good classes from a total of 80 classes. The reconstruction model was generated by the good classes using e2initialmodel.py, which served as an initial model for the subsequent cryo-EM image processing.

For cryo-EM image processing, a total of 7,600 good micrographs were manually selected from 8200 original micrographs. All processing steps were performed using Relion 1.4 or Relion 2.0 (*69*–*72*). A diagram of the procedures for data processing is presented in fig. S3C. At the whole-image level motion-corrected stacks were produced and binned 2 fold by MotionCorr (*73*) to produce motion-corrected stacks. Further motion correction and dose weighting was performed by MotionCorr2 (*74*) to average the output stacks. The contrast transfer function parameters of each image were estimated using Gctf (*75*). A total of ~1,294,000 particles were automatically picked using Gautomatch (www.mrc-lmb.cam.ac.uk/kzhang/Gautomatch). The particles were extracted using a 336^2 pixel box and sorted by two rounds of reference-free 2D classification, resulting in ~844,000 particles selected from good 2D classes. These were subjected to 3D classification with the initial model that was low-pass filtered to 60 Å. The 3D classification was performed several times with different K values resulting in ~400,000 particles of good quality. The relative orientation of the QcrC subunit was variable, producing 3D classes with two different states. After 3D classification, the sets of particles within class-I and class-II were re-extracted and re-centered using a 292^2 pixel box and subjected to the final refinement, respectively. The resolution of class-I particles was then corrected using the "high-resolution noise substitution" method (*76*) and estimated as 3.9 Å according to the gold-standard FSC (Fourier shell correlation) 0.143 criterion. The pixel size was also calibrated to 1.30 Å/pixel provided by the Center for Biological Imaging (CBI), Institute of Biophysics, Chinese Academy of Science. Then the resolution of the class-II particles was estimated to be 4.9 Å. Another 3D classification with class-I particles was performed by applying C_2 symmetry, resulting in ~202,000 particles with good symmetry. The particles with C_2 symmetry were further refined to yield a final reconstruction with the resolution of 3.5 Å according to the gold-standard FSC 0.143 criterion. Prior to visualization, all density maps were corrected for the modulation transfer function (MTF) of the detector, and then sharpened by applying a negative B-factor (*77*) that was estimated using automated procedures. Local resolution variations were estimated using ResMap (*78*). The orientation distribution of the particles used in the final reconstruction was calculated using RELION 2.0.

Model building and refinement

All the subunits were initially built as poly-alanine chains, except for the residues that coordinate the prosthetic groups. Then residue assignment was performed, which was guided largely by secondary structure analysis carried out using PSIPRED (*79*) and Phyre2 (*80*).

It is noteworthy that the sequence of PRSAF1 in the model has an extra 16 amino acids before the N terminus of WP_003893930.1 but it is consistent with the revised complete ORF in the genome of *M. smegmatis* str. MC^2 51 (genome locus tag AD56_RS0106885 added with the immediately preceding 64 bp). Model building was performed using Coot 0.8 (*81*) and further refined using the real space method in Phenix (*82*), except for the SOD catalytic domain (47Ala-236Gly) which was homology modeled (*83*) based on the structure of Sodc from *M. tuberculosis* (PDB Code: 1PZS) (*36*) and fitted into the map with the aid of the "Fit in Map" feature of Chimera (*84*). The completeness of the final resulting model was summarized in table S3.

For the phospholipids, the results of three independent mass spectrometry analyses confirmed that the majority variants of lipids in the purified sample are PE, PI and CL (fig. S1, L and N). No PC or other branching phospholipids was detected. Since most of the phospholipids are localized through the neighboring pipetides and are located in the transmembrane space which falls in the 3.2to 3.5 Å high local resolution range, the CL moleculars were readily identified based on the four alkyl groups and the PI and PE molecules were distinguishable through the significent difference in their "head" group size. A CL molecular was also distinguishable from two PI or PE moleculars through the differnet distances between the two phosphatidic acid moieties. Finially, all the identified and assigned lipid backbones were modeled according to the EM potential map with necessary truncations and the results are summarized and illustrated against the context of the covering map in fig. S3I.

All the figures were created using PyMOL (*85*) or UCSF Chimera (*84*).

REFERENCES AND NOTES

1. P. Mitchell, Coupling of phosphorylation to electron and hydrogen transfer by a chemi-osmotic type of mechanism. *Nature* **191**, 144–148 (1961). doi: 10.1038/191144a0; pmid: 13771349
2. A. M. Melo, M. Teixeira, Supramolecular organization of bacterial aerobic respiratory chains: From cells and back. *Biochim. Biophys. Acta* **1857**, 190–197 (2016). doi: 10.1016/j.bbabio.2015.11.001; pmid: 26546715
3. E. A. Berry, B. L. Trumpower, Isolation of ubiquinol oxidase from *Paracoccus denitrificans* and resolution into cytochrome bc1 and cytochrome c-aa3 complexes. *J. Biol. Chem.* **260**, 2458–2467 (1985). pmid: 2982819
4. J. A. Fee, M. G. Choc, K. L. Findling, R. Lorence, T. Yoshida, Properties of a copper-containing cytochrome c1aa3 complex: A terminal oxidase of the extreme thermophile *Thermus thermophilus* HB8. *Proc. Natl. Acad. Sci. U.S.A.* **77**, 147–151 (1980). doi: 10.1073/pnas.77.1.147; pmid: 6244539
5. J. Bengtsson, C. Rivolta, L. Hederstedt, D. Karamata, *Bacillus subtilis* contains two small c-type cytochromes with homologous heme domains but different types of membrane anchors. *J. Biol. Chem.* **274**, 26179–26184 (1999). doi: 10.1074/jbc.274.37.26179; pmid: 10473570
6. M. Saraste *et al.*, The *Bacillus subtilis* cytochrome-c oxidase. Variations on a conserved protein theme. *Eur. J. Biochem.* **195**, 517–525 (1991). doi: 10.1111/j.1432-1033.1991.tb15732.x; pmid: 1847686
7. N. Sone *et al.*, A novel hydrophobic diheme c-type cytochrome. Purification from Corynebacterium glutamicum and analysis of the QcrCBA operon encoding three subunit proteins of a putative cytochrome reductase complex. *Biochim. Biophys. Acta* **1503**, 279–290 (2001). doi: 10.1016/S0005-2728(00)00205-X; pmid: 11115640
8. S. T. Cole *et al.*, Deciphering the biology of *Mycobacterium tuberculosis* from the complete genome sequence. *Nature* **393**, 537–544 (1998). doi: 10.1038/31159; pmid: 9634230
9. J. A. Megehee, J. P. Hosler, M. D. Lundrigan, Evidence for a cytochrome bcc-aa3 interaction in the respiratory chain of *Mycobacterium smegmatis*. *Microbiology* **152**, 823–829 (2006). doi: 10.1099/mic.0.28723-0; pmid: 16514162
10. W. C. Kao *et al.*, The obligate respiratory supercomplex from Actinobacteria. *Biochim. Biophys. Acta* **1857**, 1705–1714 (2016). doi: 10.1016/j.bbabio.2016.07.009; pmid: 27472998
11. C. Sun *et al.*, Structure of the alternative complex III in a supercomplex with cytochrome oxidase. *Nature* **557**, 123–126 (2018). doi: 10.1038/s41586-018-0061-y; pmid: 29695868
12. A. Puustinen, M. Finel, T. Haltia, R. B. Gennis, M. Wikström, Properties of the two terminal oxidases of *Escherichia coli*. *Biochemistry* **30**, 3936–3942 (1991). doi: 10.1021/bi00230a019; pmid: 1850294
13. A. L. Moore, M. S. Albury, Further insights into the structure of the alternative oxidase: From plants to parasites. *Biochem. Soc. Trans.* **36**, 1022–1026 (2008). doi: 10.1042/BST0361022; pmid: 18793182
14. R. Baradaran, J. M. Berrisford, G. S. Minhas, L. A. Sazanov, Crystal structure of the entire respiratory complex I. *Nature* **494**, 443–448 (2013). doi: 10.1038/nature11871; pmid: 23417064
15. K. R. Vinothkumar, J. Zhu, J. Hirst, Architecture of mammalian respiratory complex I. *Nature* **515**, 80–84 (2014). doi: 10.1038/nature13686; pmid: 25209663
16. J. Zhu, K. R. Vinothkumar, J. Hirst, Structure of mammalian respiratory complex I. *Nature* **536**, 354–358 (2016). doi: 10.1038/nature19095; pmid: 27509854
17. V. Yankovskaya *et al.*, Architecture of succinate dehydrogenase and reactive oxygen species generation. *Science* **299**, 700–704 (2003). doi: 10.1126/science.1079605; pmid: 12560550
18. F. Sun *et al.*, Crystal structure of mitochondrial respiratory membrane protein complex II. *Cell* **121**, 1043–1057 (2005). doi: 10.1016/j.cell.2005.05.025; pmid: 15989954
19. D. Xia *et al.*, Crystal structure of the cytochrome bc1 complex from bovine heart mitochondria. *Science* **277**, 60–66 (1997). doi: 10.1126/science.277.5322.60; pmid: 9204897
20. S. Iwata *et al.*, Complete structure of the 11-subunit bovine mitochondrial cytochrome bc1 complex. *Science* **281**, 64–71 (1998). doi: 10.1126/science.281.5373.64; pmid: 9651245
21. Z. Zhang *et al.*, Electron transfer by domain movement in cytochrome bc1. *Nature* **392**, 677–684 (1998). doi: 10.1038/33612; pmid: 9565029
22. S. Iwata, C. Ostermeier, B. Ludwig, H. Michel, Structure at 2.8 A resolution of cytochrome c oxidase from *Paracoccus denitrificans*. *Nature* **376**, 660–669 (1995). doi: 10.1038/376660a0; pmid: 7651515
23. T. Tsukihara *et al.*, The whole structure of the 13-subunit oxidized cytochrome c oxidase at 2.8 A. *Science* **272**, 1136–1144 (1996). doi: 10.1126/science.272.5265.1136; pmid: 8638158
24. S. Yoshikawa *et al.*, Redox-coupled crystal structural changes in bovine heart cytochrome c oxidase. *Science* **280**, 1723–1729 (1998). doi: 10.1126/science.280.5370.1723; pmid: 9624044
25. J. A. Letts, K. Fiedorczuk, L. A. Sazanov, The architecture of respiratory supercomplexes. *Nature* **537**, 644–648 (2016). doi: 10.1038/nature19774; pmid: 27654913
26. E. Mileykovskaya *et al.*, Arrangement of the respiratory chain complexes in *Saccharomyces cerevisiae* supercomplex III2IV2 revealed by single particle cryo-electron microscopy. *J. Biol. Chem.* **287**, 23095–23103 (2012). doi: 10.1074/jbc.M112.367888; pmid: 22573332
27. J. A. Letts, L. A. Sazanov, Clarifying the supercomplex: The higher-order organization of the mitochondrial electron transport chain. *Nat. Struct. Mol. Biol.* **24**, 800–808 (2017). doi: 10.1038/nsmb.3460; pmid: 28981073
28. D. Milenkovic, J. N. Blaza, N. G. Larsson, J. Hirst, The enigma of the respiratory chain supercomplex. *Cell Metab.* **25**, 765–776 (2017). doi: 10.1016/j.cmet.2017.03.009; pmid: 28380371
29. J. D. Chavez *et al.*, Chemical crosslinking mass spectrometry analysis of protein conformations and supercomplexes in heart tissue. *Cell Syst.* **6**, 136–141.e5 (2018). doi: 10.1016/j.cels.2017.10.017; pmid: 29199018
30. K. M. Davies, T. B. Blum, W. Kühlbrandt, Conserved in situ arrangement of complex I and III$_2$ in mitochondrial respiratory chain supercomplexes of mammals, yeast, and plants. *Proc. Natl. Acad. Sci. U.S.A.* **115**, 3024–3029 (2018). doi: 10.1073/pnas.1720702115; pmid: 29519876
31. A. Niebisch, M. Bott, Molecular analysis of the cytochrome bc1-aa3 branch of the *Corynebacterium glutamicum* respiratory chain containing an unusual diheme cytochrome c1. *Arch. Microbiol.* **175**, 282–294 (2001). doi: 10.1007/s002030100262; pmid: 11382224
32. M. S. Kim *et al.*, Isolation and characterization of a hybrid respiratory supercomplex consisting of *Mycobacterium tuberculosis* cytochrome bcc and *Mycobacterium smegmatis* cytochrome aa3. *J. Biol. Chem.* **290**, 14350–14360 (2015). doi: 10.1074/jbc.M114.624312; pmid: 25861988
33. E. Lemma, H. Schägger, A. Kröger, The menaquinol oxidase of *Bacillus subtilis* W23. *Arch. Microbiol.* **159**, 574–578 (1993). doi: 10.1007/BF00249037; pmid: 8394685
34. M. M. Babu *et al.*, A database of bacterial lipoproteins (DOLOP) with functional assignments to predicted lipoproteins. *J. Bacteriol.* **188**, 2761–2773 (2006). doi: 10.1128/JB.188.8.2761-2773.2006; pmid: 16585737
35. M. D'orazio *et al.*, Lipid modification of the Cu,Zn superoxide dismutase from *Mycobacterium tuberculosis*. *Biochem. J.* **359**, 17–22 (2001). doi: 10.1042/bj3590017; pmid: 11563965
36. L. Spagnolo *et al.*, Unique features of the sodC-encoded superoxide dismutase from *Mycobacterium tuberculosis*, a fully functional copper-containing enzyme lacking zinc in the active site. *J. Biol. Chem.* **279**, 33447–33455 (2004). doi: 10.1074/jbc.M404699200; pmid: 15155722
37. F. L. Sousa *et al.*, The superfamily of heme-copper oxygen reductases: Types and evolutionary considerations. *Biochim. Biophys. Acta* **1817**, 629–637 (2012). doi: 10.1016/j.bbabio.2011.09.020; pmid: 22001780
38. M. Svensson-Ek *et al.*, The X-ray crystal structures of wild-type and EQ(I-286) mutant cytochrome c oxidases from Rhodobacter sphaeroides. *J. Mol. Biol.* **321**, 329–339 (2002). doi: 10.1016/S0022-2836(02)00619-8; pmid: 12144789
39. A. Magalon, R. Arias-Cartin, A. Walburger, Supramolecular organization in prokaryotic respiratory systems. *Adv. Microb. Physiol.* **61**, 217–266 (2012). doi: 10.1016/B978-0-12-394423-8.00006-8; pmid: 23046955
40. D. Birth, W. C. Kao, C. Hunte, Structural analysis of atovaquone-inhibited cytochrome bc1 complex reveals the molecular basis of antimalarial drug action. *Nat. Commun.* **5**, 4029 (2014). doi: 10.1038/ncomms5029; pmid: 24893593
41. K. Pethe *et al.*, Discovery of Q203, a potent clinical candidate for the treatment of tuberculosis. *Nat. Med.* **19**, 1157–1160 (2013). doi: 10.1038/nm.3262; pmid: 23913123
42. P. Lu *et al.*, The anti-mycobacterial activity of the cytochrome bcc inhibitor Q203 can be enhanced by small-molecule inhibition of cytochrome bd. *Sci. Rep.* **8**, 2625 (2018). doi: 10.1038/s41598-018-20989-8; pmid: 29422632
43. M. Swierczek *et al.*, An electronic bus bar lies in the core of cytochrome bc1. *Science* **329**, 451–454 (2010). doi: 10.1126/science.1190899; pmid: 20651150
44. H. Witt, F. Malatesta, F. Nicoletti, M. Brunori, B. Ludwig, Tryptophan 121 of subunit II is the electron entry site to cytochrome-c oxidase in *Paracoccus denitrificans*. Involvement of a hydrophobic patch in the docking reaction. *J. Biol. Chem.* **273**, 5132–5136 (1998). doi: 10.1074/jbc.273.9.5132; pmid: 9478966
45. S. Shimada *et al.*, Complex structure of cytochrome c-cytochrome c oxidase reveals a novel protein-protein interaction mode. *EMBO J.* **36**, 291–300 (2017). doi: 10.15252/embj.201695021; pmid: 27979921
46. T. Soulimane *et al.*, Structure and mechanism of the aberrant ba$_3$-cytochrome c oxidase from thermus thermophilus. *EMBO J.* **19**, 1766–1776 (2000). doi: 10.1093/emboj/19.8.1766; pmid: 10775261
47. C. Ostermeier, A. Harrenga, U. Ermler, H. Michel, Structure at 2.7 A resolution of the Paracoccus denitrificans two-subunit cytochrome c oxidase complexed with an antibody FV fragment. *Proc. Natl. Acad. Sci. U.S.A.* **94**, 10547–10553 (1997). doi: 10.1073/pnas.94.20.10547; pmid: 9380672

48. F. Millett, B. Durham, Chapter 5 Use of ruthenium photooxidation techniques to study electron transfer in the cytochrome bc1 complex. *Methods Enzymol.* **456**, 95–109 (2009). doi: 10.1016/S0076-6879(08)04405-4; pmid: 19348884
49. C. C. Moser, J. M. Keske, K. Warncke, R. S. Farid, P. L. Dutton, Nature of biological electron transfer. *Nature* **355**, 796–802 (1992). doi: 10.1038/355796a0; pmid: 1311417
50. S. Bhattacharya, *Reactive Oxygen Species and Cellular Defense System* (Springer, 2015), pp. 17-29.
51. J. F. Turrens, A. Boveris, Generation of superoxide anion by the NADH dehydrogenase of bovine heart mitochondria. *Biochem. J.* **191**, 421–427 (1980). doi: 10.1042/bj1910421; pmid: 6263247
52. X. Zhao, K. Drlica, Reactive oxygen species and the bacterial response to lethal stress. *Curr. Opin. Microbiol.* **21**, 1–6 (2014). doi: 10.1016/j.mib.2014.06.008; pmid: 25078317
53. G. Petrosillo, F. M. Ruggiero, N. Di Venosa, G. Paradies, Decreased complex III activity in mitochondria isolated from rat heart subjected to ischemia and reperfusion: Role of reactive oxygen species and cardiolipin. *FASEB J.* **17**, 714–716 (2003). doi: 10.1096/fj.02-0729fje; pmid: 12586737
54. G. Paradies, G. Petrosillo, M. Pistolese, F. M. Ruggiero, The effect of reactive oxygen species generated from the mitochondrial electron transport chain on the cytochrome c oxidase activity and on the cardiolipin content in bovine heart submitochondrial particles. *FEBS Lett.* **466**, 323–326 (2000). doi: 10.1016/S0014-5793(00)01082-6; pmid: 10682852
55. G. Paradies, G. Petrosillo, V. Paradies, F. M. Ruggiero, Oxidative stress, mitochondrial bioenergetics, and cardiolipin in aging. *Free Radic. Biol. Med.* **48**, 1286–1295 (2010). doi: 10.1016/j.freeradbiomed.2010.02.020; pmid: 20176101
56. D. L. Piddington *et al*., Cu,Zn superoxide dismutase of *Mycobacterium tuberculosis* contributes to survival in activated macrophages that are generating an oxidative burst. *Infect. Immun.* **69**, 4980–4987 (2001). doi: 10.1128/IAI.69.8.4980-4987.2001; pmid: 11447176
57. W. Suthammarak, B. H. Somerlot, E. Opheim, M. Sedensky, P. G. Morgan, Novel interactions between mitochondrial superoxide dismutases and the electron transport chain. *Aging Cell* **12**, 1132–1140 (2013). doi: 10.1111/acel.12144; pmid: 23895727
58. X. Li, F. Liu, Y. Hu, K. Mi, Draft genome sequence of mc^{2}51, a highly hydrogen peroxide-resistant *Mycobacterium smegmatis* mutant strain. *Genome Announc.* **2**, e00092-14 (2014). doi: 10.1128/genomeA.00092-14; pmid: 24558240
59. I. Wittig, H. P. Braun, H. Schägger, Blue native PAGE. *Nat. Protoc.* **1**, 418–428 (2006). doi: 10.1038/nprot.2006.62; pmid: 17406264
60. I. Wittig, H. Schägger, Features and applications of blue-native and clear-native electrophoresis. *Proteomics* **8**, 3974–3990 (2008). doi: 10.1002/pmic.200800017; pmid: 18763698
61. L. Y. J. García Montes de Oca *et al*., The composition of the Bacillus subtilis aerobic respiratory chain supercomplexes. *J. Bioenerg. Biomembr.* **44**, 473–486 (2012). doi: 10.1007/s10863-012-9454-z; pmid: 22790590
62. S. M. Lam *et al*., Extensive characterization of human tear fluid collected using different techniques unravels the presence of novel lipid amphiphiles. *J. Lipid Res.* **55**, 289–298 (2014). doi: 10.1194/jlr.M044826; pmid: 24287120
63. G. Shui *et al*., Mycolic acids as diagnostic markers for tuberculosis case detection in humans and drug efficacy in mice. *EMBO Mol. Med.* **4**, 27–37 (2012). doi: 10.1002/emmm.201100185; pmid: 22147526
64. L. Lim *et al*., Lanosterol induces mitochondrial uncoupling and protects dopaminergic neurons from cell death in a model for Parkinson's disease. *Cell Death Differ.* **19**, 416–427 (2012). doi: 10.1038/cdd.2011.105; pmid: 21818119
65. S. Graf *et al*., Rapid electron transfer within the III-IV supercomplex in Corynebacterium glutamicum. *Sci. Rep.* **6**, 34098 (2016). doi: 10.1038/srep34098; pmid: 27682138
66. J. M. McCord, I. Fridovich, Superoxide dismutase. An enzymic function for erythrocuprein (hemocuprein). *J. Biol. Chem.* **244**, 6049–6055 (1969). pmid: 5389100
67. D. N. Mastronarde, Automated electron microscope tomography using robust prediction of specimen movements. *J. Struct. Biol.* **152**, 36–51 (2005). doi: 10.1016/j.jsb.2005.07.007; pmid: 16182563
68. G. Tang *et al*., EMAN2: An extensible image processing suite for electron microscopy. *J. Struct. Biol.* **157**, 38–46 (2007). doi: 10.1016/j.jsb.2006.05.009; pmid: 16859925
69. S. H. Scheres, Semi-automated selection of cryo-EM particles in RELION-1.3. *J. Struct. Biol.* **189**, 114–122 (2015). doi: 10.1016/j.jsb.2014.11.010; pmid: 25486611
70. S. H. Scheres, A Bayesian view on cryo-EM structure determination. *J. Mol. Biol.* **415**, 406–418 (2012). doi: 10.1016/j.jmb.2011.11.010; pmid: 22100448
71. S. H. Scheres, RELION: Implementation of a Bayesian approach to cryo-EM structure determination. *J. Struct. Biol.* **180**, 519–530 (2012). doi: 10.1016/j.jsb.2012.09.006; pmid: 23000701
72. D. Kimanius, B. O. Forsberg, S. H. Scheres, E. Lindahl, Accelerated cryo-EM structure determination with parallelisation using GPUs in RELION-2. *eLife* **5**, e18722 (2016). doi: 10.7554/eLife.18722; pmid: 27845625
73. X. Li *et al*., Electron counting and beam-induced motion correction enable near-atomic-resolution single-particle cryo-EM. *Nat. Methods* **10**, 584–590 (2013). doi: 10.1038/nmeth.2472; pmid: 23644547
74. S. Q. Zheng *et al*., MotionCor2: Anisotropic correction of beam-induced motion for improved cryo-electron microscopy. *Nat. Methods* **14**, 331–332 (2017). doi: 10.1038/nmeth.4193; pmid: 28250466
75. K. Zhang, Gctf: Real-time CTF determination and correction. *J. Struct. Biol.* **193**, 1–12 (2016). doi: 10.1016/j.jsb.2015.11.003; pmid: 26592709
76. S. Chen *et al*., High-resolution noise substitution to measure overfitting and validate resolution in 3D structure determination by single particle electron cryomicroscopy. *Ultramicroscopy* **135**, 24–35 (2013). doi: 10.1016/j.ultramic.2013.06.004; pmid: 23872039
77. P. B. Rosenthal, R. Henderson, Optimal determination of particle orientation, absolute hand, and contrast loss in single-particle electron cryomicroscopy. *J. Mol. Biol.* **333**, 721–745 (2003). doi: 10.1016/j.jmb.2003.07.013; pmid: 14568533
78. A. Kucukelbir, F. J. Sigworth, H. D. Tagare, Quantifying the local resolution of cryo-EM density maps. *Nat. Methods* **11**, 63–65 (2014). doi: 10.1038/nmeth.2727; pmid: 24213166
79. L. J. McGuffin, K. Bryson, D. T. Jones, The PSIPRED protein structure prediction server. *Bioinformatics* **16**, 404–405 (2000). doi: 10.1093/bioinformatics/16.4.404; pmid: 10869041
80. L. A. Kelley, S. Mezulis, C. M. Yates, M. N. Wass, M. J. Sternberg, The Phyre2 web portal for protein modeling, prediction and analysis. *Nat. Protoc.* **10**, 845–858 (2015). doi: 10.1038/nprot.2015.053; pmid: 25950237
81. P. Emsley, B. Lohkamp, W. G. Scott, K. Cowtan, Features and development of Coot. *Acta Crystallogr. D Biol. Crystallogr.* **66**, 486–501 (2010). doi: 10.1107/S0907444910007493; pmid: 20383002
82. P. D. Adams *et al*., PHENIX: A comprehensive Python-based system for macromolecular structure solution. *Acta Crystallogr. D Biol. Crystallogr.* **66**, 213–221 (2010). doi: 10.1107/S0907444909052925; pmid: 20124702
83. J. Yang *et al*., The I-TASSER Suite: Protein structure and function prediction. *Nat. Methods* **12**, 7–8 (2015). doi: 10.1038/nmeth.3213; pmid: 25549265
84. E. F. Pettersen *et al*., UCSF Chimera—A visualization system for exploratory research and analysis. *J. Comput. Chem.* **25**, 1605–1612 (2004). doi: 10.1002/jcc.20084; pmid: 15264254
85. W. L. Delano, The PyMOL Molecular Graphics System (DeLano Scientific, 2002).

ACKNOWLEDGMENTS

We thank J. Zhang, Y. Zhang, and L. Wang from C.-C. Wang's Research Group (National Laboratory of Biomacromolecules, Institute of Biophysics, CAS) for their technical support on Clark-type oxygen electrode and oxygen consumption assay and K. Mi (CAS Key Laboratory of Pathogenic Microbiology and Immunology, Institute of Microbiology, CAS) for sharing the strain *M. smegmatis* mc^2 51. We are also grateful to B. Zhu, X. Huang, and G. Ji from Center for Biological Imaging (CBI), Institute of Biophysics, CAS, and staff members from National Center for Protein Science Shanghai (NCPSS) for their technical support on cryo-EM and C. Peng from the Mass Spectrometry System of NCPSS for his technical support. We also thank T. Niu from the HPC-Service Station in CBI and X. Jian and X. Meng from TianHe-1(A) at the National Supercomputer Center in Tianjin for computational support. **Funding:** This work was supported by grants from the National Key Research and Development Program of China (grant 2017YFC0840300), the Strategic Priority Research Program of the Chinese Academy of Sciences (grant XDB08020200), the State Key Development Program for Basic Research of the Ministry of Science and Technology of China (973 Project Grants 2014CB542800 and 2014CBA02003 to Z.R. and 2014CB910700 to F.S.), and the National Natural Science Foundation of China (Grant Nos. 813300237 and 81520108019). **Author contributions:** Z.R. conceived, initiated, and coordinated the project. H.G., Ju.L., and S.W. purified the *M. smegmatis* SC III-IV supercomplex; H.G., Y.T., and Ju.L. characterized the spectroscopic features of the samples; Ji.L., H.-Y.Y., C.V.R., S.M.L., and G.S. preformed mass spectrometry analysis and identified the contents of the complex; Y.T. and Q.W. set up the biochemical assays and measured the menadiol: O_2 oxidoreductase activity of the complex; H.G. measured the SOD activity of the complex; L.Y. and C.T. performed the EPR experiments and data analysis; A.X. and Q.W. collected and processed cryo-EM data; Q.W. reconstructed the 3.5 Å resolution map and supervised cryo-EM structure determination; Q.W., A.X., R.G., and W.J. built and refined the structure model; Ju.L., Q.W., F.S., H.G., A.X., X.Y., Y.S., X.L., M.J., C.T., C.Y., B.J., Z.L., L.W.G., L.-L.W., and Z.R. analyzed the structure and discussed the results; and the manuscript was written by F.S., Q.W., Ju.L., W.J., A.X., H.G., R.G., Z.L., L.W.G., L.-L.W., and Z.R. **Competing interests:** The authors declare no competing interests. L.W. is a founder and consultant of Oxford Biotrans, UK. C.V.R. is a founding director and consultant of OMass Technologies, UK. **Data and materials availability:** All data are available in the manuscript or the supplementary materials. The accesion no. for the 3D cryo-EM density map reported in this paper is EMD-9610. The PDB accession no. for the coordinates of the CIII-CIV complex is 6ADQ.

SUPPLEMENTARY MATERIALS

www.sciencemag.org/content/362/6418/eaat8923/suppl/DC1
Figs. S1 to S8
Tables S1 to S4
References (*86*–*94*)
Movie S1

16 April 2018; accepted 10 October 2018
Published online 25 October 2018
10.1126/science.aat8923

RESEARCH ARTICLE

METALLURGY

Colossal grain growth yields single-crystal metal foils by contact-free annealing

Sunghwan Jin[1], Ming Huang[1,2], Youngwoo Kwon[1], Leining Zhang[1,2], Bao-Wen Li[1], Sangjun Oh[3], Jichen Dong[1], Da Luo[1], Mandakini Biswal[1], Benjamin V. Cunning[1], Pavel V. Bakharev[1], Inyong Moon[4], Won Jong Yoo[4], Dulce C. Camacho-Mojica[1], Yong-Jin Kim[1], Sun Hwa Lee[1], Bin Wang[1], Won Kyung Seong[1], Manav Saxena[1], Feng Ding[1,2], Hyung-Joon Shin[1,2]*, Rodney S. Ruoff[1,2,3,5]*

Single-crystal metals have distinctive properties owing to the absence of grain boundaries and strong anisotropy. Commercial single-crystal metals are usually synthesized by bulk crystal growth or by deposition of thin films onto substrates, and they are expensive and small. We prepared extremely large single-crystal metal foils by "contact-free annealing" from commercial polycrystalline foils. The colossal grain growth (up to 32 square centimeters) is achieved by minimizing contact stresses, resulting in a preferred in-plane and out-of-plane crystal orientation, and is driven by surface energy minimization during the rotation of the crystal lattice followed by "consumption" of neighboring grains. Industrial-scale production of single-crystal metal foils is possible as a result of this discovery.

Polycrystalline metals have numerous grain boundaries (GBs) that affect their electrical and mechanical properties, whereas single-crystal metals have no GBs and show different properties. For example, single-crystal Cu has a lower electrical resistivity than polycrystalline Cu owing to the elimination of electron scattering at GBs (*1*, *2*), and single-crystal superalloys have a high resistance to creep (*3*), which can be driven by the sliding of GBs. The growth of graphene on catalytic single-crystal metal substrates by chemical vapor deposition has attracted great attention because certain planes have a small lattice mismatch with graphene [Cu(111): ~3 to 4%; Ni(111): ~1%; Co(0001): ~2%] (*4*, *5*) and can be used as substrates for the heteroepitaxial growth of single-crystal graphene without GBs (*6*–*10*). The epitaxial growth of large-scale hexagonal boron nitride, diamond, and tetrahedrally bonded BN that have a small lattice mismatch with a single-crystal metal has also increased interest in and demand for large-area single-crystal metal substrates.

The traditional methods for synthesizing single-crystal metals are by bulk crystal growth (the Czochralski or Bridgman methods). Single-crystal thin metal films can also be deposited on top of single-crystal inorganic substrates (*8*, *11*–*14*). These methods lead to small and expensive single-crystal metals. An alternative strategy is to eliminate GBs in polycrystalline solids by grain growth during annealing. Grain growth produces single-crystal alloy metal sheets but only for the Cu-Al-Mn alloy (*15*, *16*). Annealing of polycrystalline Cu foils yields Cu(111)-oriented foils (*9*, *10*), but the mechanism for this transformation is unclear. We prepared Cu(111), Ni(111), Co(0001), Pt(111), and Pd(111) single-crystal foils with a large grain size up to 32 cm^2 with "contact-free annealing" (CFA). CFA has advantages as it does not require single-crystal seeds or templates that limit the maximum crystal size, and commercial polycrystalline metal foils are readily converted into single crystals. We heat the foils near their melting temperatures and typically under a hydrogen atmosphere and find an unusual conversion from the polycrystalline grains to a specific orientation in both the in-plane and normal directions. This specific orientation likely arises by crystal lattice rotation accompanied by the removal of stacking faults, resulting in a lowered surface energy.

Single-crystal metal foils produced by contact-free annealing

Grooves typically develop along the GBs on the surface of metals during annealing as a result of equilibrium between the energy of the free surface and the GBs; such "thermal grooves" can be observed with the naked eye when the size of individual grains reaches the cm scale (*17*–*19*). We annealed commercial polycrystalline Cu foils near their melting points with CFA (*20*) (Fig. 1, A and B). Thermal grooves are typically not present on the surface of the annealed Cu foil after CFA (Fig. 1C), reflecting an absence of GBs in the entire foil (about 2 cm by 8 cm in size).

We studied the crystallographic orientations of the annealed Cu foils by x-ray diffraction (XRD) and electron backscatter diffraction (EBSD). We found Bragg reflections from the (111) and (222) crystal planes (Fig. 1D). The inverse pole figure (IPF) color maps from EBSD show only the (111) plane of Cu (blue color, Fig. 1E), consistent with the XRD data. The entire region also has the same crystallographic orientation in the in-plane direction (<112>, the rolling direction), as shown in the pole figures of the (001) poles (Fig. 1F). We found a very small misorientation (below 1°) in all kernel average misorientation (KAM) maps, which measure the local average misorientation between a measured point and its neighbors (*21*) (Fig. 1G). Our measurements show that the Cu foil was converted to a {111}<112> single crystal over an area of 2 cm by 8 cm. By contrast, the grains in thin metal films have a maximum size of a few millimeters (*22*–*29*), by abnormal grain growth. CFA reproducibly yields (111) single-crystal foils up to 32 cm^2 (fig. S1). This colossal grain growth markedly improves the size of single-crystal foils.

The close-packed {111} crystallographic plane of Cu has the lowest surface energy of all the planes, as is well known for the face-centered cubic (fcc) structure (*30*–*32*). If surface energy is the major driving force for grain growth in polycrystalline fcc metals, they should spontaneously transform into grains with a {111} surface because of surface energy minimization (*22*–*24*). However, this may not be the case if other energy terms such as strain energy caused by thermal stress are large compared to the surface energy (*24*). We found that suspending the metal foil eliminates or at least minimizes deformation from thermal stress that arises as a result of interfacial contact (*20*) (figs. S2 to S4). This allowed us to reproducibly obtain single-grain Ni foils with a {111} normal and Co foils with a {0001} normal over large areas with the same strategy as for Cu (*20*) (figs. S5 to S7).

We used resistive heating to convert polycrystalline Pt to a single crystal (Fig. 2A) because of the high melting temperature (2041 K). We first attached the Pt foil to two electrodes to pass current, and the Pt foil deformed in the middle from thermal expansion during annealing. This resulted in GBs near, and in, this deformed region (Fig. 2, B to D). To avoid this outcome, we attached the bottom electrode to a movable stage whose position was manually adjusted to keep the foil "flat" during expansion and contraction. We achieved a large-area single-crystal Pt foil region with a {111} surface, although the regions near the water-cooled electrode attachment did not convert (Fig. 2, E to I). As long as mechanical deformation is minimized during annealing (fig. S8), we expect this method to work for other foils [it did for Pd (*20*) (fig. S9)].

Colossal growth of grains with a {111}<112> orientation

We investigated the microstructural and texture evolution of Cu foils by varying annealing time

---

[1] Center for Multidimensional Carbon Materials (CMCM), Institute for Basic Science (IBS), Ulsan 44919, Republic of Korea. [2] School of Materials Science and Engineering, Ulsan National Institute of Science and Technology (UNIST), Ulsan 44919, Republic of Korea. [3] Department of Chemistry, Ulsan National Institute of Science and Technology (UNIST), Ulsan 44919, Republic of Korea. [4] SKKU Advanced Institute of Nano-Technology (SAINT), Sungkyunkwan University, Suwon, Gyeonggi-do 16419, Republic of Korea. [5] School of Energy and Chemical Engineering, Ulsan National Institute of Science and Technology (UNIST), Ulsan 44919, Republic of Korea.
***Corresponding author. Email: shinhj@unist.ac.kr (H.-J.S.); ruofflab@gmail.com or rsruoff@ibs.re.kr (R.S.R.)**

(at 1323 K) in order to understand the colossal grain growth. We analyzed the texture of each Cu foil using the orientation distribution function (ODF) from the EBSD data (Fig. 3A). The as-received Cu foil showed mostly elongated grains along the rolling direction, and strong {112}<111> and {110}<112> texture (Fig. 3B), as expected for a cold-rolled Cu foil (*33*). The elongated grains recrystallized to larger polygonal grains after 1 hour of annealing. In addition, small grains with a {111}<112> texture ({111}<112> grains) started to appear among the {112} and {110} grains (Fig. 3C). We found that not all {111} grains grew to cm scale. Only a limited number of {111} grains located near the edge of the foils grew abnormally, likely as a result of the energy stored near the foil edge resulting from cutting or handling. Our observations strongly suggest that the stored energy at the edges of the foil accelerates the selective growth of the {111} grain(s). These abnormal {111} grains grow extremely fast (~70 μm/s) by consuming the surrounding grains (*20*) (figs. S10 to S12). This result is similar to abnormal grain growth driven by the critical strain annealing process, which promotes the growth of a limited number of grains (*34*). After 2 hours, we observed two cm-scale grains, separated by numerous μm-scale grains with various orientations. Both of these large grains had a {111}<112> texture (Fig. 3D). After we annealed the same Cu foil for an additional 5.5 hours, GBs (excluding the polygranular regions at the edges) were not found by the naked eye. We did, however, find a subgrain boundary with scanning elecron microscopy (SEM) at the marked region between the two large {111}<112> grains in Fig. 3D (Fig. 3E). This region showed a strong {111}<112> texture, and there was no clear contrast difference across the subgrain boundary in the IPF map (Fig. 3F), which showed only a small misorientation, below 1°, across the subgrain boundary (Fig. 3G). Unlike typical abnormal grain growth, the extremely fast growth of particular {111} grain(s) allows further growth up to cm scale. In addition, those grains (or nuclei) that can grow rapidly, which are limited in number throughout the sample, have an identical <112> in-plane orientation, and they form single-crystal foil over a large area when they grow larger and coalesce.

Origin of the {111}<112> orientation in single-crystal fcc metal foils

Most of the fcc (111) foils that we studied (which had initial {112}<111> texture) showed identical orientations of both their in-plane and normal directions ({111}<112>) (Fig. 4A). Although the preferential growth of grains with a <111> normal direction in fcc metals by surface energy minimization has been reported (*22*–*24*), growth of preferred in-plane orientation in fcc metals has been harder to achieve. We studied various factors that we thought could affect the colossal grain growth of {111}<112>: initial textures, misorientation angles, thickness, and purity of the metal foil. We found that the initial textures of foils are critical to obtain single-crystal {111}<112> foils. If the strongest texture in the initial foil is not {112}<111>, a different final orientation is obtained such as {111} fiber and {100}<001> (*20*) (tables S1 and S2 and figs. S13 to S18).

We also considered the possibility that the dominant {112}<111> orientation of our cold-rolled metal foils was responsible for the final {111}<112> orientation after CFA. To test whether {111}<112> arises from {112}<111>, we performed CFA on sub-mm-scale {112}<111> grains. We found these sub-mm–scale {112}<111> grains in the polygranular region of the annealed Cu foil that was in contact with the ceramic holder during CFA. We cut this region to obtain only {112}<111> grains at the edge of the Cu foil sample, and further annealed the foil in the suspended sample configuration at 1323 K for 12 hours. We found that {112}<111> grains converted to {111}<112> grains after CFA without substantial change of microstructure (Fig. 4B). Thus, {111}<112> grains originate from {112}<111> grains.

A contact-free foil is very likely a stress-free foil, and thus the driving force for the continuous rotation required for the transformation from a {112}<111> grain to a {111}<112> grain was not immediately apparent. We know that annealing near the melting point activates many vacancies in the bulk, and the concentration of these vacancies is further increased by the introduction of hydrogen into the metal. Our density functional theory (DFT) calculations show that the formation energy of a single vacancy in bulk Cu is 1.64 eV, but it is 1.20 and 0.72 eV when the vacancy is passivated by either one or two H atoms, respectively (*20*) (fig. S22). This large reduction in the vacancy-formation energy

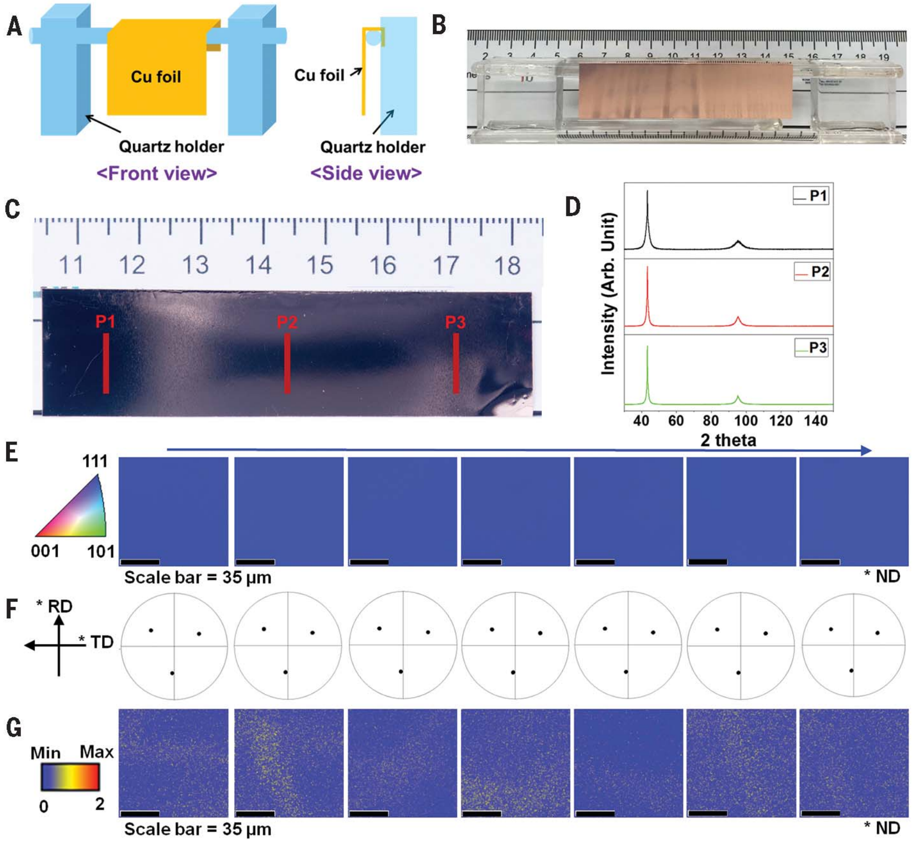

Fig. 1. A single-crystal Cu(111) foil produced by CFA. (**A**) Schematic of the quartz holder from which the Cu foil is suspended. (**B**) Photograph of the configuration shown schematically in (A). (**C**) Photograph of the annealed single-crystal Cu foil (the larger numbered lines on the ruler in the photographs denote centimeters). (**D**) The XRD 2θ scans of the three regions in the annealed single-crystal Cu foil indicated by P1 to P3 in (C) by using Cu-Kα radiation (45 kV and 200 mA). The peaks at 43.3 and 95.1 are assigned to Bragg reflections from the (111) and (222) crystallographic planes. (**E**) EBSD IPF maps in the normal direction. (**F**) (001) pole figures. (**G**) KAM maps (first nearest-neighbor kernel) of the single-crystal Cu foil at various points along the section from P1 to P3 (the distance between adjacent EBSD measurement points was more than 5 mm). (ND, normal direction; RD, rolling direction; TD, transverse direction).

must result in a substantial increase in the bulk vacancy concentration. Our experiments and simulations show the importance of hydrogen for grain growth, because vacancies in the bulk are critical for grain rotation and when H atoms diffuse in these metals they strongly stabilize vacancies. As an exceptional case, Pt foil samples showed cm-scale grain growth during CFA both with, but also without, hydrogen. Because Pt has a much higher vacancy concentration than other metals at the annealing temperature used, we found that the Pt foil has a large-scale grain without hydrogen (*20*) (table S3 and figs. S19 to S21). We performed molecular dynamics (MD) simulations on a model grain possessing a {112} surface with ~4.5% vacancies in the bulk to further understand the relationship between the vacancies and the grain rotation. We found that, after the simulation, the entire grain rotated 2.02° toward the {111} direction, which resulted in the removal of one step on the surface and a {7 7 13} surface. We introduced additional vacancies (~5.0%) to this rotated structure, and after relaxation, a further 7.42° rotation toward the {111} direction was observed, resulting in the removal of two additional surface steps and a {7 7 10} surface (Fig. 4C). A larger-scale model also showed a similar result (*20*) (fig. S23).

Our MD simulations indicate that, with vacancies, the rotation of the {112} grain may occur in a stress-free environment. The mechanism that we observed has several steps (Fig. 4D): (i) Vacancies first aggregate to form an intrinsic (111) stacking fault (SF) accompanied by Frank partial dislocations (FPDs). (ii) The climbing of the FPD occurs by absorbing more vacancies, resulting in SF growth (fig. S24), which eventually spans the entire thickness of the grain and leads to the disappearance of the FPDs on the surface. (iii) The interaction between the SF and the surface causes a Shockley partial dislocation (SPD) at one side of the SF. This SPD then glides from the surface into the bulk, resulting in continuous shrinkage of the SF area accompanied by rotation of the crystal lattice toward the {111} direction. The gliding of the SPD is key in forming the {111} surface. Because the gliding of the SPD along the SF results in both the removal of SFs and the formation of a perfect crystal lattice (lower energy state), motion of the SPD is irreversible once SPD initiates from the surface. The gliding of the SPD can initiate in two directions from the surface (Fig. 4E). Initiation in one direction causes the surface step height to increase, whereas initiation

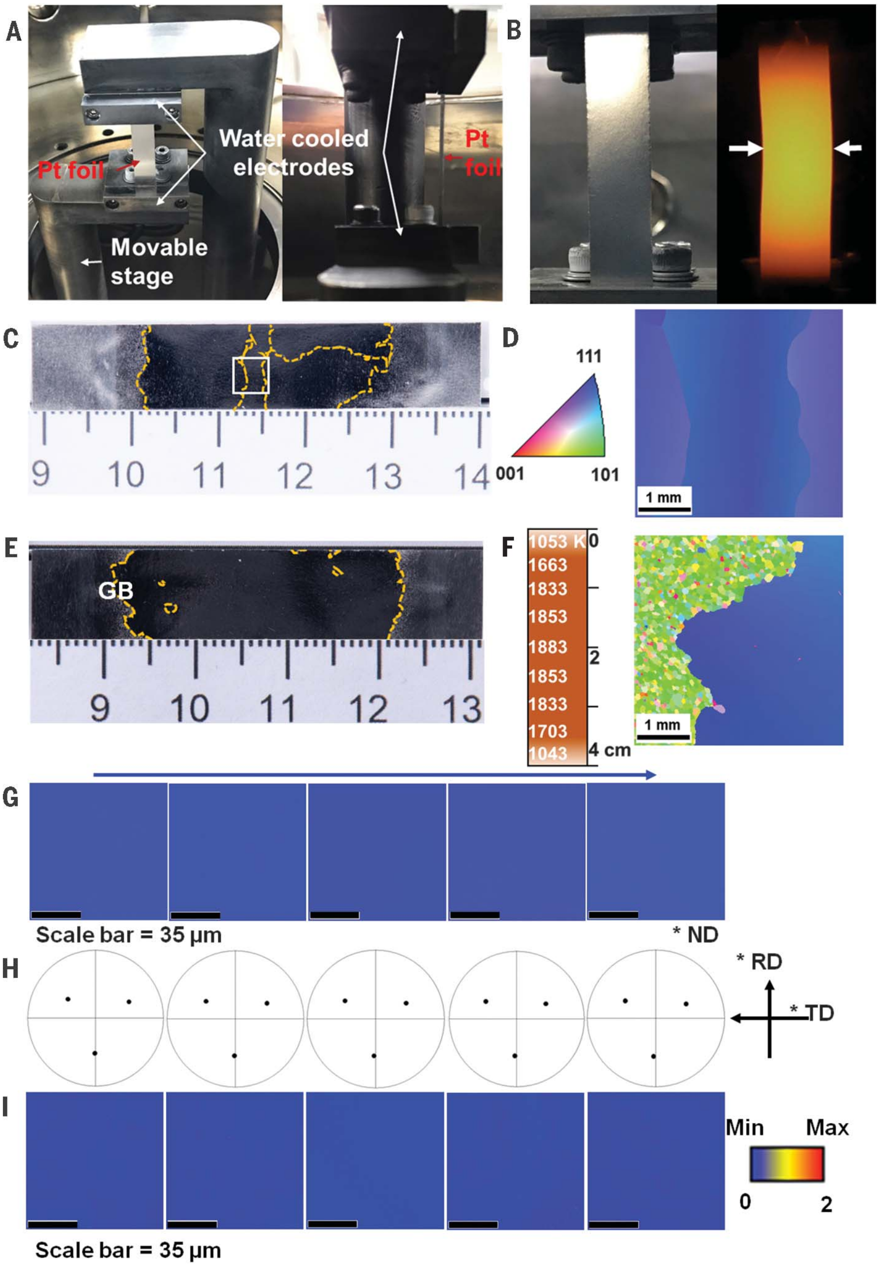

Fig. 2. A single-crystal Pt(111) foil region produced by CFA. (**A**) Photograph of water-cooled electrodes with a Pt foil for resistive heating (left: front view; right: side view). Different from CFA with a ceramic holder, we fixed the foil to two water-cooled electrodes. (**B**) Photograph of a Pt foil before heating (left), and then during heating (right) but without stage movement; white arrows indicate bending of the foil. (**C**) Photograph of the same annealed Pt foil [yellow dashed lines correspond to GBs between large single-grain and polygranular regions or between large grains that have orientations close to (111)]. (**D**) EBSD IPF map of the white square region in (C). (**E**) Photograph of a single-crystal Pt foil (about 3 cm^2 in the single-crystal region; yellow dashed lines indicate GBs between the single-grain and polygranular regions) after annealing with appropriate movement of one electrode (stage) to minimize the thermal stress during annealing and cooling. (**F**) Temperature distribution in a Pt foil during annealing (left), and EBSD IPF map of the region marked "GB" in (E). (**G**) EBSD IPF maps, (**H**) (001) pole figures, and (**I**) KAM maps (first nearest-neighbor kernel) of the single-crystal Pt foil at various points along its length in the large single-grain region (the distance between each EBSD measurement point was more than 5 mm). All these foils were annealed at 1883 K for 12 hours (ND, normal direction; RD, rolling direction; TD, transverse direction).

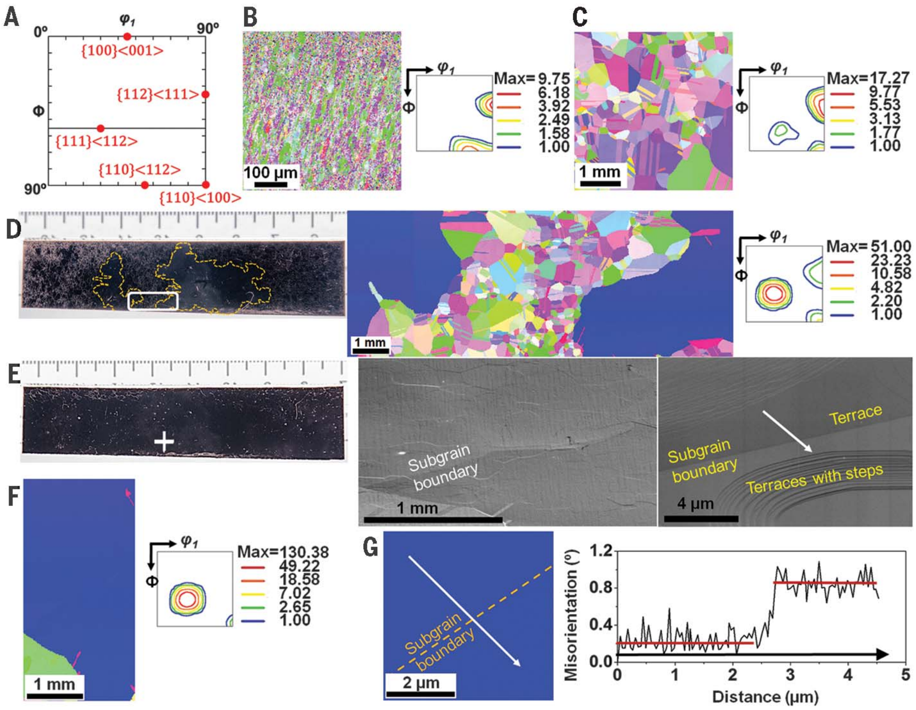

Fig. 3. Texture evolution and grain growth for the large-area single-crystal Cu. (**A**) ODF section with $\varphi_2 = 45°$, indicating the position of the major components of the texture in fcc metals. (**B** and **C**) IPF (left) and ODF (right) maps (Φ, $\varphi_1 = 0 \sim 90°$, $\varphi_2 = 45°$) of (B) an as-received Cu foil and (C) a Cu foil annealed at 1323 K for 1 hour. (**D**) A Cu foil annealed at 1323 K for 2 hours: photograph (left, yellow dashed lines correspond to GBs between large single-grain and polygranular regions), and IPF (middle) and ODF (right) maps of the region marked with a white rectangle in the photograph. (**E**) The same Cu foil as in (D) after annealing for an additional 5.5 hours at 1323 K: photograph (left), and SEM (middle) and its higher-magnification SEM (right) images of the region marked with a white cross in the photograph. (**F**) IPF (left) and ODF (right) maps at the same region as in the lower-magnification SEM in (E). (**G**) IPF (left) maps at the same region as in the higher-magnification SEM in (E) and the misorientation profile along the white arrow in this higher-magnification SEM image and the corresponding IPF map. All SEM images are tilted by 70° because a sample tilt of 70° is required for EBSD observation.

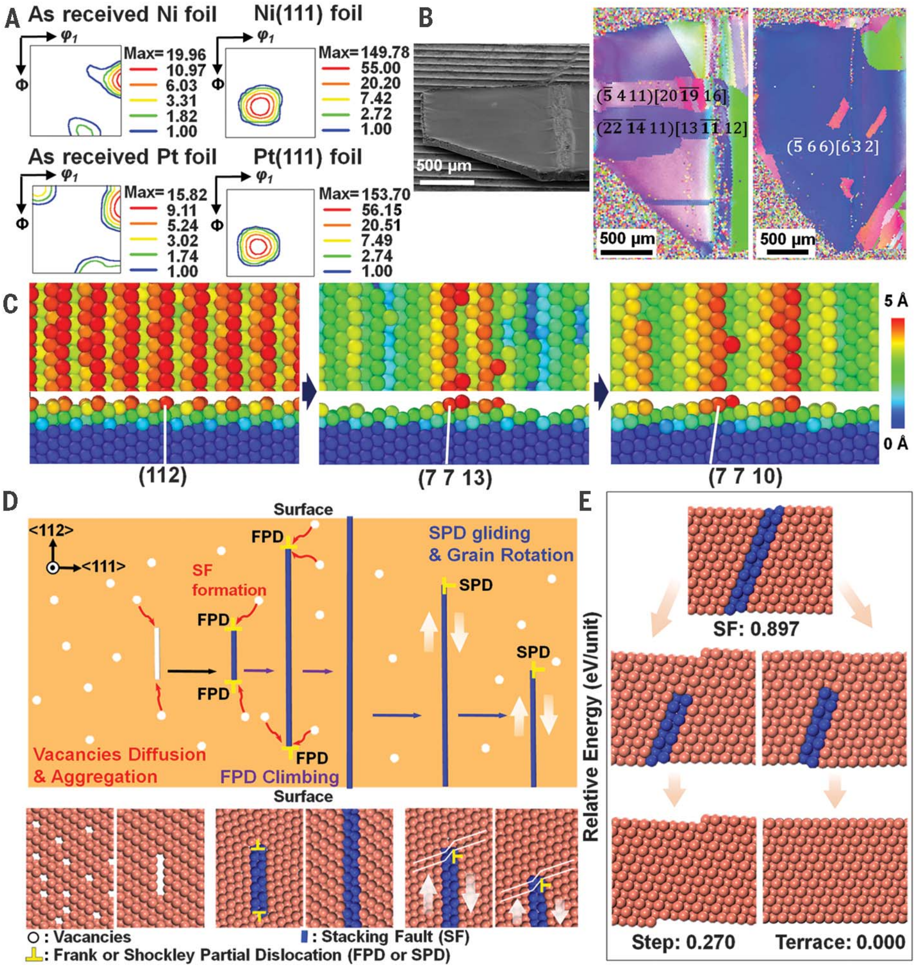

Fig. 4. Transformation from the {112}<111> to the {111}<112> orientation for the single-crystal fcc foils. (**A**) ODF section with $\varphi_2 = 45°$ of as-received Ni and Pt foils, and Ni(111) and Pt(111) foils (Φ, $\varphi_1 = 0 \sim 90°$). (**B**) SEM image of the isolated {112}<111> grain region (left), and IPF maps of this region before (middle) and after (right) CFA. (**C**) Cu grain model viewed in the surface normal (top) and <110> direction (bottom) surface: initial {112} grain (left), annealing at 1000 K for 10 ns with 4.5% vacancies (middle), and further annealing under the same condition with 5.0% vacancies (right). The color profile on the right represents the relative height of the surface. The slab contains 3604 atoms with dimensions of 5.01 nm by 2.04 nm by 4.40 nm. (**D**) Schematics of grain rotation during the removal of SF by dislocation glide (top) and its corresponding MD model (bottom). (**E**) Relative energy of Cu unit cell with 198 atoms.

in the other direction results in the removal of the surface step and a flat surface. DFT energy calculations of these states demonstrate that the gliding of the SPD that results in the flat surface is more energetically favorable, and this causes rotation toward the {111} orientation. Accordingly, during annealing, the grain surface both flattens and rotates, eventually resulting in a {111} surface.

These observations show that the grain rotation occurs along the "surface energy minimization pathway" of Cu from {112} to {111} (fig. S25) during the migration and elimination of SFs in the {112} grain(s), which are the major component ({112}<111>) in cold-rolled fcc metal foils. But our experimental results show that the {110} grain(s), which is the second major component ({110}<112>) in cold-rolled fcc foils, does not rotate during the annealing (fig. S26). The {110} orientation is located at a saddle point in the calculated surface energy map (fig. S25); therefore, the driving force for initiating the rotation is zero. The observed rotation from {112} to {111} is the rotation along the <110> axis, which corresponds to the rotation from the {112}<111> orientation to the {111}<112> orientation. Once the new {111}<112> grain(s) is nucleated by grain rotation, it grows rapidly in the highly textured matrix to minimize the surface energy. This is accelerated by the locally stored energy at the edges. Eventually this transformation forms the large {111}<112> grain(s) over the entire foil.

Potential applications of single-crystal metal foils

These single-crystal metal foils should find many uses in surface science, fundamental catalysis research, and a variety of other applications. For example, using a single-crystal metal foil as a high-quality catalyst, we demonstrated the heteroepitaxial growth of single-crystal monolayer and multilayer graphene islands on a pure Cu(111) foil and a Cu/Ni(111) foil, respectively (*20*) (figs. S27 to S29). In addition, we measured a 7% reduction in the room-temperature resistivity of Cu(111) foils compared to the as-received Cu foils (table S4 and figs. S30 and S31). In another example, we obtained single-orientation surfaces [different from (111)] by "simply" cutting polycrystalline foils and then annealing them (fig. S32).

Contact-free annealing enables preparation of single-crystal metal foils with specific in-plane and out-of-plane crystallographic orientations. The orientation originates from the rotation of the dominant texture component of the as-received foils, likely through dislocation gliding as a result of removal of the stacking faults in the presence of large amounts of vacancies. Our results suggest the possibility of achieving very large single-crystal metal foils from polycrystalline foils for many other metals, in addition to the scaled manufacture of at least Cu, Ni, Co, Pt, and Pd foils, by a process such as CFA.

REFERENCES AND NOTES

1. Y. C. Cho *et al*., *Cryst. Growth Des.* **10**, 2780–2784 (2010).
2. M. Ajmal *et al*., *CrystEngComm* **14**, 1463–1467 (2012).
3. F. I. Versnyder, M. E. Shank, *Mater. Sci. Eng.* **6**, 213–247 (1970).
4. X. Mi, V. Meunier, N. Koratkar, Y. F. Shi, *Phys. Rev. B* **85**, 155436 (2012).
5. C. M. Seah, S. P. Chai, A. R. Mohamed, *Carbon* **70**, 1–21 (2014).
6. Y. Ogawa *et al*., *J. Phys. Chem. Lett.* **3**, 219–226 (2012).
7. A. Varykhalov, O. Rader, *Phys. Rev. B* **80**, 035437 (2009).
8. T. Iwasaki *et al*., *Nano Lett.* **11**, 79–84 (2011).
9. V. L. Nguyen *et al*., *Adv. Mater.* **27**, 1376–1382 (2015).
10. L. Brown *et al*., *Nano Lett.* **14**, 5706–5711 (2014).
11. B. S. Hu *et al*., *Carbon* **50**, 57–65 (2012).
12. K. M. Reddy, A. D. Gledhill, C. H. Chen, J. M. Drexler, N. P. Padture, *Appl. Phys. Lett.* **98**, 113117 (2011).
13. C. M. Orofeo *et al*., *Carbon* **50**, 2189–2196 (2012).
14. D. L. Miller, M. W. Keller, J. M. Shaw, A. N. Chiaramonti, R. R. Keller, *J. Appl. Phys.* **112**, 064317 (2012).
15. T. Omori *et al*., *Science* **341**, 1500–1502 (2013).
16. T. Kusama *et al*., *Nat. Commun.* **8**, 354 (2017).
17. W. W. Mullins, *J. Appl. Phys.* **28**, 333–339 (1957).
18. W. W. Mullins, *Acta Metall. Mater.* **6**, 414–427 (1958).
19. H. J. Frost, C. V. Thompson, D. T. Walton, *Acta Metall. Mater.* **38**, 1455–1462 (1990).
20. Materials, methods, and additional data are available as supplementary materials.
21. S. I. Wright, M. M. Nowell, D. P. Field, *Microsc. Microanal.* **17**, 316–329 (2011).
22. R. Carel, C. V. Thompson, H. J. Frost, *Acta Mater.* **44**, 2479–2494 (1996).
23. C. C. Wong, H. I. Smith, C. V. Thompson, *Appl. Phys. Lett.* **48**, 335–337 (1986).
24. C. V. Thompson, R. Carel, *J. Mech. Phys. Solids* **44**, 657–673 (1996).
25. M. Seita, C. M. Pecnik, S. Frank, R. Spolenak, *Acta Mater.* **58**, 6513–6525 (2010).
26. D. S. Lee *et al*., *Jpn. J. Appl. Phys.* **40**, L1–L3 (2001).
27. J. Greiser, P. Mullner, E. Arzt, *Acta Mater.* **49**, 1041–1050 (2001).
28. A. Gangulee, F. M. Dheurle, *Thin Solid Films* **12**, 399–402 (1972).
29. J. Greiser, D. Muller, P. Mullner, C. V. Thompson, E. Arzt, *Scr. Mater.* **41**, 709–714 (1999).
30. G. C. Kallinteris, N. I. Papanicolaou, G. A. Evangelakis, D. A. Papaconstantopoulos, *Phys. Rev. B* **55**, 2150–2156 (1997).
31. L. Vitos, A. V. Ruban, H. L. Skriver, J. Kollar, *Surf. Sci.* **411**, 186–202 (1998).
32. Q. Jiang, H. M. Lu, M. Zhao, *J. Phys. Condens. Matter* **16**, 521–530 (2004).
33. S. Suwas, R. K. Ray, *Crystallographic Texture of Materials*. Engineering materials and processes (Springer, London, 2014).
34. C. P. Blankenship Jr., W. T. Carter Jr., A. E. Murut, M. F. Henry, *Scr. Metall. Mater.* **31**, 647–652 (1994).

ACKNOWLEDGMENTS

We thank P. Thrower for comments on manuscript preparation. **Funding:** This work was supported by IBS-R019-D1. **Author contributions:** R.S.R. and S.J. conceived the experiments. S.J., Y.K., and S.O. performed the annealing and polishing of the metal foils and their characterizations. R.S.R. supervised the project. H.-J.S. provided critical insight about the texture of metal foils and their influence. B.-W.L. and M.H. performed graphene growth experiments. B.-W.L., M.H., and B.W. performed graphene transfer and characterization. M.H. and M.B. performed POM characterization of graphene. S.J. and D.L. performed atomic force microscopy analysis. F.D. provided the model about the rotation of grains. L.Z., J.D., and F.D. performed DFT and MD simulations. I.M. and W.J.Y measured the resistivity of the metal foils. P.V.B. and S.J. performed the residual gas analysis experiment. B.V.C. and D.C.C.-M. provided comments on the manuscript. M.S. provided the blueprint of the quartz holder. S.H.L. performed DSC measurements. W.K.S. prepared the customized equipment for fast annealing. S.J., R.S.R., H.-J.S., and Y.-J.K. wrote the manuscript. All coauthors revised and commented on the manuscript. **Competing interests:** A patent was filed and has been issued (KR 10-1878465B), and a PCT application has been published (WO 2018/012864 A1) by the Institute for Basic Science (IBS) and Ulsan National Institute of Science and Technology (UNIST), along with their researchers (R.S.R. and S.J.). **Data and materials availability:** All data are available in the main text or the supplementary materials.

SUPPLEMENTARY MATERIALS

www.sciencemag.org/content/362/6418/1021/suppl/DC1
Materials and Methods
Supplementary Text
Figs. S1 to S32
Tables S1 to S4
References (*35*–*71*)

11 July 2017; resubmitted 24 August 2018
Accepted 8 October 2018
Published online 18 October 2018
10.1126/science.aao3373

ANIMAL CULTURE

Cultural flies: Conformist social learning in fruitflies predicts long-lasting mate-choice traditions

Etienne Danchin[1]*†, Sabine Nöbel[1,2]*, Arnaud Pocheville[3]*, Anne-Cecile Dagaeff[1], Léa Demay[1], Mathilde Alphand[1], Sarah Ranty-Roby[1], Lara van Renssen[1,4], Magdalena Monier[1], Eva Gazagne[5], Mélanie Allain[1,6], Guillaume Isabel[6]

Despite theoretical justification for the evolution of animal culture, empirical evidence for it beyond mammals and birds remains scant, and we still know little about the process of cultural inheritance. In this study, we propose a mechanism-driven definition of animal culture and test it in the fruitfly. We found that fruitflies have five cognitive capacities that enable them to transmit mating preferences culturally across generations, potentially fostering persistent traditions (the main marker of culture) in mating preference. A transmission chain experiment validates a model of the emergence of local traditions, indicating that such social transmission may lead initially neutral traits to become adaptive, hence strongly selecting for copying and conformity. Although this situation was suggested decades ago, it previously had little empirical support.

Researchers increasingly acknowledge that cultural traditions exist in nonhuman animals, including chimpanzees (*1*), orangutans (*2*), cetaceans (*3*), meerkats (*4*), and birds (*5*). However, thus far, examples have been limited to higher vertebrates. Exploration of this question in other taxa requires a transferable definition of culture. The typical criterion of culture is generally that transferred traits must be socially acquired and spread to others repeatedly (*6*).

Here, we propose a definition focusing on the properties of social learning. Integrating with previous studies, we define animal culture as phenotypic variation that is inherited through a form of social learning (i.e., learning from others) (criterion 1) (*1*, *5*–*9*). Cultural inheritance will occur if social learning occurs across age classes (minimally, from older to younger individuals) (criterion 2) (*9*, *10*), is maintained over the long term to be copied (criterion 3) (*11*), produces trait-based copying (criterion 4) (*12*), and incorporates repair or reinforcement mechanisms (*13*) [e.g., conformity (*5*, *14*, *15*) or information digitalization (*16*)] (criterion 5). Lastly, to connect this mechanistic definition with classical definitions focusing on the sole existence of behavioral variation across populations, we tested whether the observed cognitive properties can generate local traditions spanning over generations (the most notable marker of culture) (*13*, *17*). Cultural inheritance then makes cultural variation subject to selection and evolution.

We tested this multicriterion definition in fruitflies, which are known to have the capacity to socially learn sexual preferences from the observation of copulating conspecifics (*18*–*20*).

To test criterion 1 of social learning, we used the "speed-learning" design (Fig. 1) (*20*), testing whether, after watching a single demonstrator female choosing between two males of contrasting phenotypes, an observer female shows a bias for the male of the phenotype she saw being chosen during the demonstration. This two-step protocol involves a demonstration in a tube device (fig. S1) during which an observer female separated by a glass partition can watch a demonstrator female freely choosing between one green and one pink male, immediately followed by a mate-choice test during which the observer female chooses to copulate with one of two new males, one of each color. The partition was transparent glass (informed females) or opaque white paper (uninformed control females).

The social learning index quantifying the learned bias toward the male of the color preferred during demonstrations (see S1.4 in the supplementary materials) differed between informed and uninformed replicates [generalized linear mixed model (GLMM), Wald χ^2 test; $n = 127$; $\chi^2_1 = 5.115$; $P = 0.024$] (Fig. 1B). Uninformed observer females chose in a way that did not differ from random (binomial test; $n = 63$; $P = 1$). Informed females mated preferentially with new males of the color they saw being chosen during the demonstration (binomial test; $n = 64$; $P = 0.002$) (Fig. 1B) whatever the color chosen during the demonstration (GLMM, Wald χ^2 test; $n = 127$; $\chi^2_1 = 0.0112$; $P = 0.916$). Thus, observer females learned to prefer the male of the color that was favored during demonstrations, exhibiting social learning and fulfilling criterion 1.

To satisfy criterion 2 of transmission across age classes, socially learned traits must be transmitted vertically or simply from older to younger individuals (*9*, *10*). We replicated in tubes the horizontal informed treatment of criterion 1 (in which both females were 3 days old) as a positive horizontal control and compared it with an across-age-class treatment in which demonstrator females were 11 days older (i.e., of an age similar to that of the flies' parents) (Fig. 2).

Both treatments were biased in favor of the male of the color that copulated during demonstrations (binomial tests; $n = 65$, $P = 0.025$, and $n = 63$, $P = 0.011$ for horizontal and across-age-class treatments, respectively) (Fig. 2). We found no difference between horizontal and across-age-class trials (GLMM, Wald χ^2 test; $n = 128$; $\chi^2_1 = 0.0555$; $P = 0.814$), showing that social transmission was equally efficient in the two contexts and thus fulfilling criterion 2.

To satisfy culture criterion 3, that of durability, learned preferences must be maintained

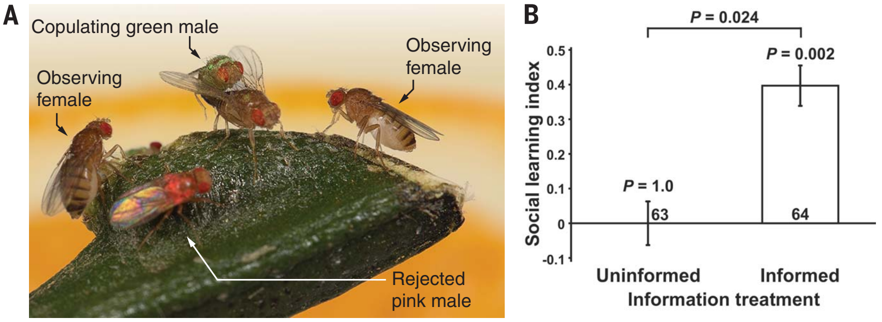

Fig. 1. Criterion 1 of social learning. (**A**) A situation of mate-copying in which two females watch a copulating green male while a pink male is rejected. (**B**) Social learning index of informed versus uninformed observer females. Positive social learning indices reveal preference for the male color chosen during demonstrations, whereas zero reveals random choice. *P* values above bars, binomial tests of departure from random choice; error bars, SEM.

ILLUSTRATION (TOP): D. DUNEAU

---

[1] Laboratoire Évolution and Diversité Biologique (EDB UMR 5174), Université de Toulouse, CNRS, IRD, 118 route de Narbonne, Bat 4R1, F-31062 Toulouse cedex 9, France. [2] Université Toulouse 1 Capitole and Institute for Advanced Study in Toulouse (IAST), Toulouse, France. [3] Department of Philosophy and Charles Perkins Centre, University of Sydney, Sydney, NSW 2006, Australia. [4] Groningen Institute for Evolutionary Life Sciences (GELIFES), University of Groningen, 9747 AG Groningen, Netherlands. [5] Behavioural Biology Unit, Department of Biology, Ecology and Evolution, University of Liège, 4020 Liège, Belgium. [6] Centre de Recherches sur la Cognition Animale, Centre de Biologie Intégrative, Université de Toulouse, CNRS, UPS, 118 route de Narbonne, F-31062 Toulouse cedex 9, France.
*These authors contributed equally to this work.
†Corresponding author. Email: etienne.danchin@univ-tlse3.fr

(*11*). Multiple spaced training (a series of training phases separated by resting periods) (*21*) in invertebrates and vertebrates leads to a stable form of long-lasting memory (*22*). We transposed this long-term memory protocol in *Drosophila* (*23*) to our visual social learning. After watching five conditioning demonstrations spaced by 15- to 30-min resting periods, observer females were tested for social long-term memory 24 hours later.

Informed spaced-trained flies displayed unusually high mate-copying after 24 hours (binomial test; $n = 62$; $P < 0.0001$) (Fig. 3A), but the uninformed ones did not (binomial test; $n = 65$; $P = 0.457$) (Fig. 3A). To confirm that this social long-term memory depends on de novo protein synthesis, a third group of spaced-trained flies fed an inhibitor of protein synthesis (cycloheximide) was tested in parallel. The cycloheximide treatment disrupted social long-term memory [$n = 65$, $P = 0.804$ (binomial test); $n = 192$, $\chi_1^2 = 15.6934$, $P = 0.0004$ (GLMM for the three treatment groups tested after 24 hours, Wald χ^2 test)] (Fig. 3A). Furthermore, cycloheximide-treated observer females tested shortly after a single demonstration did not differ from the horizontal control for criterion 2 [GLMM for informed cycloheximide-treated females versus non–cycloheximide-treated females of the horizontal control (Fig. 2); $n = 131$; $\chi_1^2 = 0.016$; $P = 0.898$ (Fig. 3B)] and showed significant mate-copying (binomial test; $n = 66$; $P = 0.036$) (Fig. 3B). Thus, the cycloheximide treatment did not impair mate-copying (*21*, *23*). In a complementary experiment, we found that the high average learning index 24 hours after a spaced training (0.55, corresponding to a mate-copying index of 0.78) was produced by both spaced training and the 24-hour delay (see fig. S2). Thus, flies built de novo protein synthesis–dependent durable memory, meeting criterion 3.

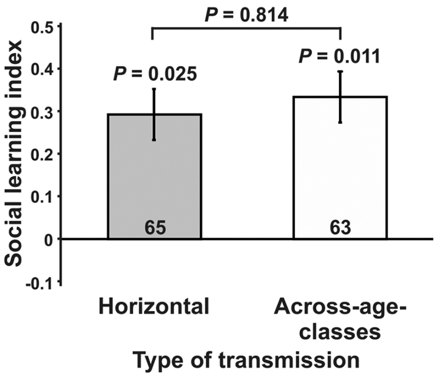

Fig. 2. Criterion 2 of across-age-class transmission. Social learning indices of 3-day-old observer females learning from 3-day-old (horizontal) or 14-day-old (across-age-class) demonstrator females. *P* values above bars, binomial tests of departure from random choice; error bars, SEM.

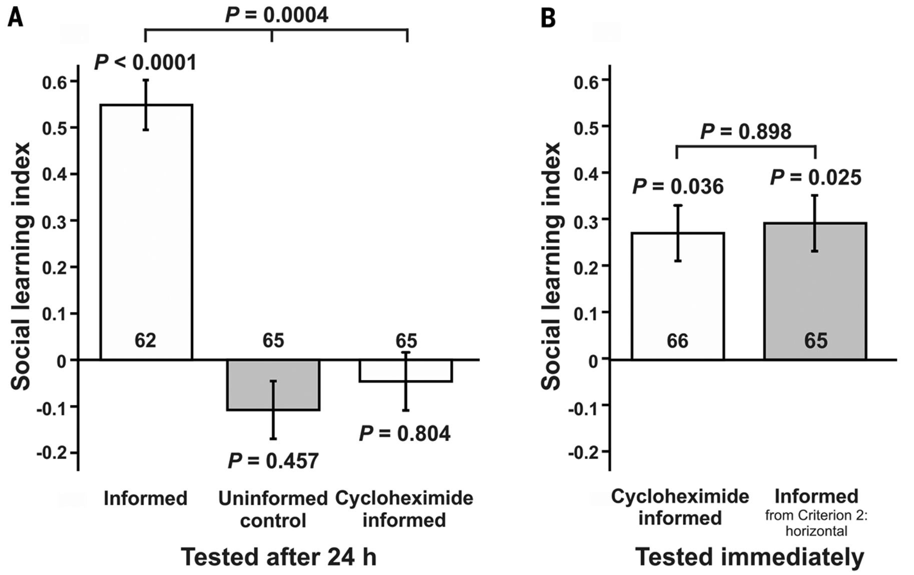

Fig. 3. Criterion 3 of durable social learning. (**A**) Long-term memory in mate-copying 24 hours after demonstrations. (**B**) Cycloheximide-treated females within the usual protocol of a single live demonstration immediately followed by the mate-choice test showed mate-copying similar to that of the non-cycloheximide–treated females of the horizontal-transmission group in Fig. 2. *P* values above bars, binomial tests of departure from random choice; error bars, SEM.

Criterion 4 states that copying must be trait based (*11*, *12*). In all the experiments described above [and most previous experiments (*18*, *20*, *24*, *25*)], mate-choice tests used new green and pink males, suggesting that observer females learned to prefer any male of the same color. However, observer females may have confounded test males with demonstration males of the same color. To test whether females learned to prefer males of a given color, we used very different looking mutant males during mate-choice tests to rule out the possibility that observer females confounded test males with demonstrator males. Demonstrations involved a wild-type demonstrator female freely choosing between one green and one pink wild-type male, whereas males (green and pink) used in mate-choice tests were either both wild type (controls) or both curly-winged or white-eyed mutants (two experimental treatments). In a previous study, we showed that flies exhibit mate-copying with wild-type and curly-winged males instead of color variants, demonstrating that the flies do distinguish these genetic variants (*26*).

In all three treatments, during the mate-choice test observer females preferred males of the same color as the one chosen during demonstrations, with similar social learning indices (GLMM, genotype effect; $n = 152$; $\chi_2^2 = 0.714$; $P = 0.70$) (Fig. 4), despite their contrasting and distinguishable (*26*) genotypes relative to those of demonstrator males. Females performed trait-based copying, therefore meeting criterion 4.

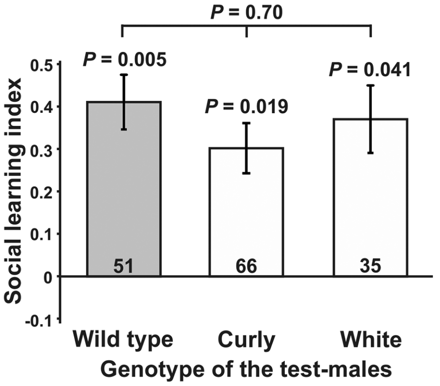

Fig. 4. Criterion 4 of trait-based copying. Social learning indices according to the genotype of the males used during mate-choice tests. Demonstrations involved a wild-type demonstrator female freely choosing between one green and one pink wild-type male. We previously showed that females clearly distinguish wild-type from curly-winged genetic variants (*26*). *P* values above bars, binomial tests of departure from random choice; error bars, SEM.

Criterion 5 concerns the existence of a repair mechanism such as a conformist bias (an exaggerated tendency to copy the majority) (*5*, *14*, *27*, *28*). To test this, we used a new device we called "the hexagon" (fig. S1B). By introducing already-copulating pairs along with a

Fig. 5. Criterion 5 of conformist mate-copying. The nine demonstration treatments with various proportions of demonstrator females copulating with the pink males (*x* axis). Level of majority, proportion of the most commonly chosen male color during demonstrations; error bars, SEM; *P* values above or below bars, binomial tests of departure from random. The four treatments with a majority of pink (P) demonstrations differed from controls ($n = 348$; $P < 0.0004$). So did the four treatments with a majority of green (G) demonstrations ($n = 333$; $P = 0.042$), and these two blocks differed from each other ($n = 513$; $P = < 0.0001$).

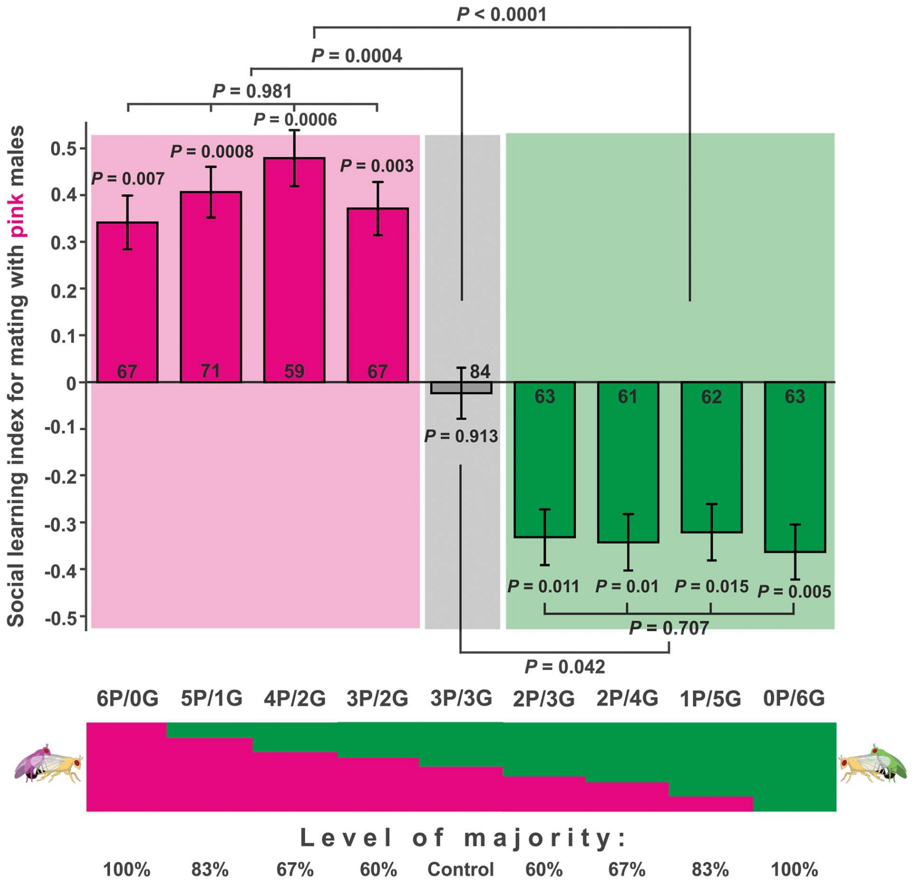

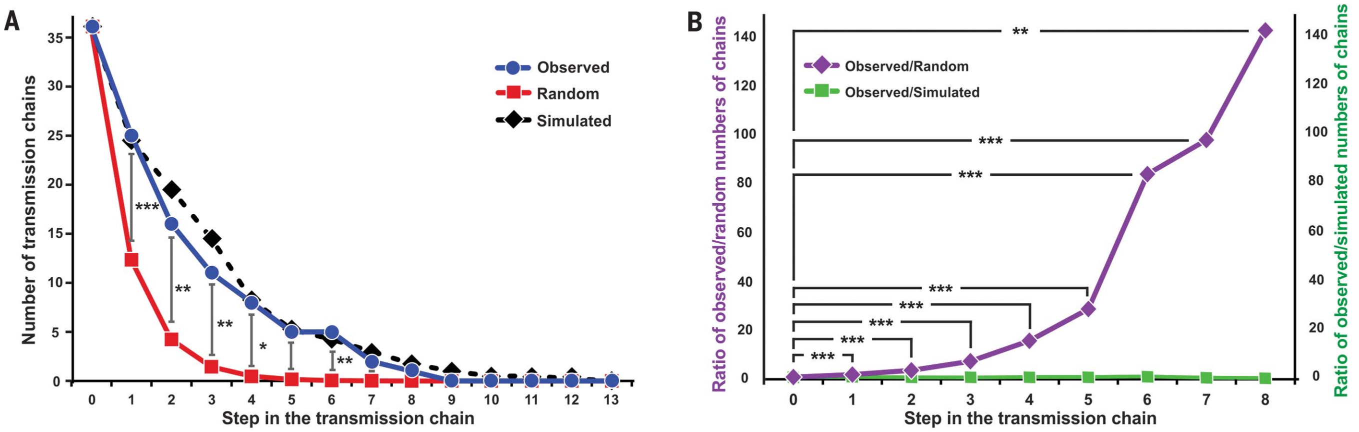

Fig. 6. Transmission chain in which observer females of one step became demonstrators for the next step. (**A**) Number of the 36 chains that kept the initial preference for the indicated number of steps. Both experimental and simulation data involved only six observer females, which explains the relatively short persistence of the population preference (arrow in Fig. 7B). For each step, asterisks indicate the significance of the pairwise binomial test between the observed number of chains reaching that step (blue) and the number expected under random choice (red). Simulated data (black) were obtained under conditions mimicking experimental chains (see S1.5 and S1.6). Asterisks indicate the significance of the binomial test between the observed and expected numbers of chains reaching the step in view of the number that reached the previous step. (**B**) Ratio of the observed number of chains reaching the indicated step to either the number predicted under random choice (purple) or the number produced by simulations (green). Asterisks indicate the significance of the binomial test between the observed number of chains reaching that step and the number predicted by chance from the initial number of 36 chains under the null hypothesis that females choose randomly (i.e., binomial test against a probability of 0.3438^x, where x is the step number) (see S1.5 and table S2). *$P < 0.05$; **P value < 0.01; ***$P < 0.001$. More information is provided in S1.5 and table S2.

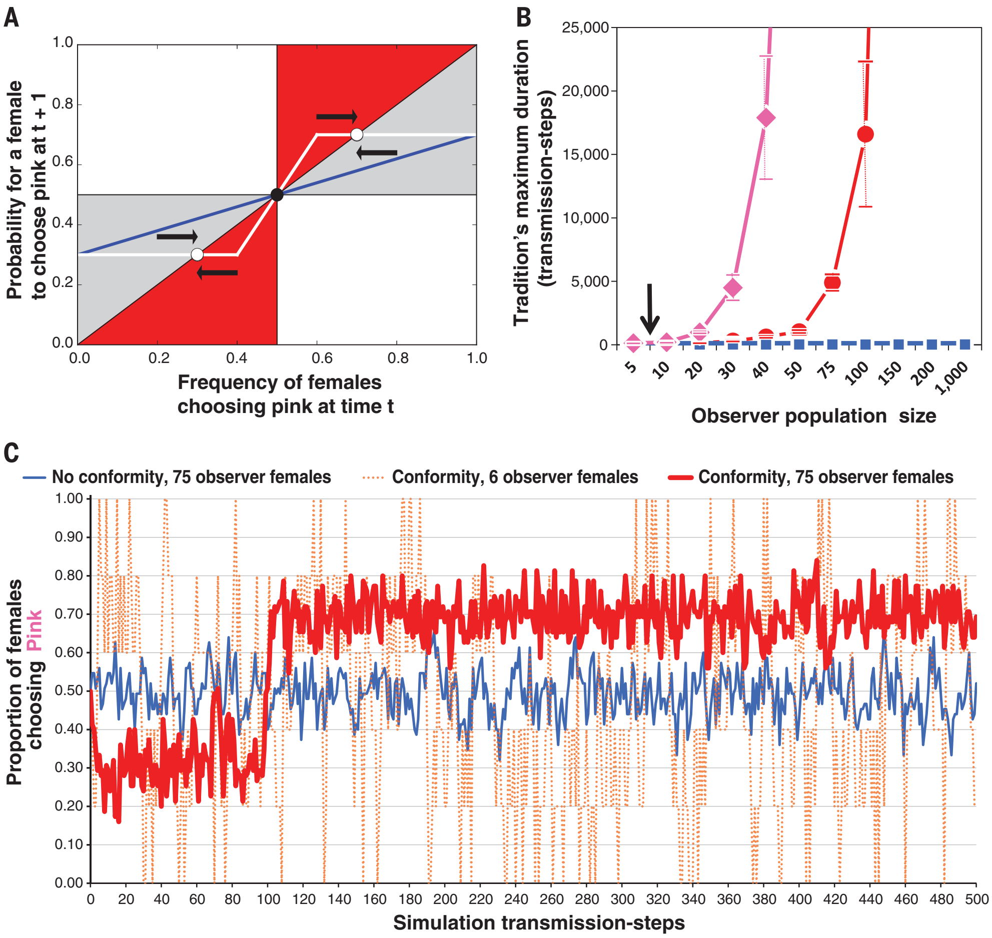

Fig. 7. A model of local tradition emergence in *D. melanogaster*. (**A**) Areas of the set of possible population mating preference response functions to demonstrations. Red areas, areas where observer females copy at a higher rate than the majority (i.e., exaggerate the choice of the majority), driving the population toward a preference for one color (white dots); gray areas, areas where observer females copy at a lower rate than the majority, driving the population toward the stable equilibrium of no preference (black dot); white areas, zones of anticonformity (a bias for males of the most commonly nonpreferred phenotype); blue line, without conformity; white line, the conformity function documented in Fig. 5. (**B**) Effect of observer female number and mate-copying index on mean maximum population preference durations during five simulations of 100,000 transmission steps. Blue, simulations without conformity, as in the blue line of (A); red, simulations with conformity, as in the white line of (A), and with the mate-copying index set at 0.68 (i.e., the average in all experiments but long-term memory); pink, same simulations but with a mate-copying index of 0.78, as observed in long-term memory; vertical bars, SDs (most are too small to be visible); arrow, situation of the transmission chain performed in this study (Fig. 6). With transmission steps occurring every 24 hours (Fig. 3), the maximum tradition durations reported with conformity would correspond to thousands of *Drosophila* generations. (**C**) Simulated dynamics over 500 transmission steps. Blue, dynamics without conformity [as in the blue line of (A)] with 75 observer females; red, dynamics with conformity with 75 observer females; orange, simulations with conformity and only six observer females, leading to frequent population preference shifts (this mimics the parameter of the transmission chain of Fig. 6). More results are shown in S1.6 and figs. S4 to S6.

male of the other color in each peripheral compartment of the hexagon, we manipulated the proportion of demonstrator females copulating with green or pink males (x axis of Fig. 5). We set up four situations with a majority of females copulating with pink males and four with a majority copulating with green males (100, 83, 67, and 60%), as well as one control in which three females copulated with green males and three with pink males.

As expected, control observer females did not build any mating preference (gray in Fig. 5), and replicates in which all six demonstrator females copulated with the same male color revealed strong mate-copying as in the above-described experiments. More surprisingly, as long as one male phenotype was chosen more often than the other (range, 100 to 60%), observer females learned to prefer males of the most commonly chosen phenotype (every color bar in Fig. 5 significantly differed from zero). We found no significant difference among the four treatments with a majority for one color [for the proportion of females copulating with pink as a class factor or a continuous effect, n = 264 and P = 0.981 or 0.813, respectively (Fig. 5, pink block); for green, n = 249 and P = 0.707 or 0.920, respectively], indicating that social learning did not decline as the proportion of the most commonly chosen male decreased down to only 60%. Thus, mate-copying followed a step function, with females learning equally well to prefer the most commonly chosen male color whatever the level of majority (Fig. 5), revealing strong conformity in mate-copying and fulfilling criterion 5.

Fisher (*29*) speculated that by mating with their preferred males, females produce offspring that may inherit both the male trait and the mating preference in association, triggering the Fisher runaway process (*29*). In a theoretical population with A and B male phenotypes and in which more females mate with A males, females choosing B males will have sons of the nonpreferred phenotype and daughters that will learn to prefer A males (as we show here). This will strongly diminish the fitness of nonconformist females (here choosing B males), thus favoring conformist females (here choosing A males). Consequently, as soon as even the slightest detectable mating preference emerges within a population, conformist females are favored, as they transmit the most attractive trait to their male descendants while potentially culturally transmitting the preference for that same male trait to their daughters and/or to younger females.

Animal culture is classically studied through the existence of local traditions (*1*–*4*, *10*). To study the capacity of the observed mate-copying in the fruitfly to generate persistent population preferences (i.e., traditions), we performed 36 transmission chains in hexagons in which the six observer females of one step were used as the six freely choosing demonstrators of the following step. A chain started with a demonstration where all six females chose the same male color and ended when the preference for the initially induced population preference became ≤50%. In this experiment, because the population had only six observer females, the frequency of shifts from a majority of females (four or more) choosing one color at one step to a majority of females choosing the other was high (0.2936) (S1.5 and table S2). Nonetheless, experimental chains lasted much longer than predicted by chance, as revealed by Fig. 6A, in which the blue curve (representing observed behavior) is significantly higher than the red curve (representing behavior predicted by chance alone). These significant differences at each step accumulated so that the observed number of chains that reached the eighth step was 142 times as high as the number predicted by chance (Fig. 6B; more details are in S1.5). Thus, because of the effect of mate-copying, transmission chains lasted far longer than expected on the basis of chance alone.

The transmission chain experiment indicates that the social learning capacities in *Drosophila melanogaster* have the potential of stabilizing a preference for an arbitrary male phenotype at the scale of a population. However, for practical reasons, we cannot perform experiments under different conditions—for instance, under such conditions as large populations. Thus, to explore theoretically the effects of key parameters documented in testing criteria 1 to 5, we built a dynamical model of culture recapitulating our results. This model simulated a sequence of transmission steps in which observer females of one step became the demonstrators of the following step, as in our transmission chain experiment.

In infinitely large populations, the model is deterministic. A graphical analysis shows that nonconformist observer females (gray areas in Fig. 7A) always adopt an attenuated preference at each transmission step, leading initial preference for one male phenotype to fade away toward the black dot of Fig. 7A and generating dynamics as in the blue curve of Fig. 7C. Contrastingly, conformist learning [usually modeled with response functions entirely within the red areas of Fig. 7A, e.g., as in (*27*)] reinforces any initial preference, making population preference persistent. In *Drosophila*, however, parts of the response function (white line of Fig. 7A) are outside of this red area, making it difficult to extrapolate results from previous models.

In finite populations, the model is stochastic and cultural drift occurs, much as genetic drift occurs in finite populations. In small populations, odds that 50% or more of the flies make a copying "error" just by chance can be high, each time leading to a cultural shift in the population mating preference (Fig. 7C and figs. S4 to S6) and thus forbidding the establishment of a local tradition. For instance, with a mate-copying index of 0.68 (our observed average) (see S1.6) and six observer females, the probability that at each step at least half of the females choose the incorrect color by chance is 0.2936 (calculation in S1.5). This probability drops rapidly with increasing population size down to <0.001 and <0.0001 with 80 and 114 observer females, respectively (see S1.5). With a mate-copying index of 0.78 (as observed in long-term memory), odds that 50% or more observer flies make a copying error by chance are 0.139 for six flies and drop below 0.001 and 0.0001 with only 32 and 48 observer females, respectively. Thus, the bigger the population and the higher the mate-copying index, the less frequently cultural shifts will occur and the longer the local population preference will persist, making it a cultural tradition.

To study this phenomenon, we built an individual-based model using the fruitfly response function (as in the white line of Fig. 7A). Simulations under the conditions of our transmission chain experiment (six observer flies, the initial preference at 100%, and ending when the initial preference drops to 50% or below) provided distributions of chain durations that closely matched the observed ones (black curve of Fig. 6A), which validates our model. In view of this validation, we then used this model to explore the effect of sets of parameters that would make transmission chain experiments infeasible for the capacity of the documented social learning function to produce persistent population preferences and thus cultural traditions. The form of conformity observed in *Drosophila* elicited long-lasting local preference (red line, Fig. 7C) corresponding to the stable equilibria of the infinite population model, with tradition stability strongly depending on both the population size and the mate-copying index [Fig. 7B and figs. S4 to S6; see also (*30*)]. For instance, these traditions potentially lasted for more than 100,000 transmission steps with 150 observer flies and a mate-copying index of 0.68 (red curve in Fig. 7B). The same result was obtained with only 50 observer females with a mate-copying index of 0.78 (the value observed with long-term memory) (pink curve in Fig. 7B). These population sizes are well below those observed in nature (S1.6). With one step representing 1 day (as suggested in Fig. 3), this would mean that traditions would theoretically last for thousands of fruitfly generations (see SI.5).

Culture used to be considered to be limited to humans. However, the range of species showing patterns of local variation in behavior akin to traditions now includes several mammals and birds (*1*–*4*). In this study, we found that fruitfly females express strong social learning (criterion 1) across age classes (criterion 2) that is memorized for sufficient time to be copied (criterion 3) and is trait-based (criterion 4) and conformist (criterion 5). With a model parameterized with the properties documented in our experiments, we found that these social learning properties can foster persistent local traditions in mating preference in populations of sizes common in nature. We have shown that population mate preference is maintained in transmission chains for longer than expected on the basis of chance in a way that closely matches our model predictions. Our lab experiments thus can be seen as a proof of concept in the lab that *D. melanogaster* has all the cognitive capacities and dispositions to transmit female mating preferences culturally across generations in ways that can elicit potentially long-lasting traditions of preferring an arbitrary male phenotype. This suggests that the taxonomical range of culture may be much broader than ever before envisioned.

Our simulations also show that as predicted by theoretical consideration (*15*, *27*, *31*), a major characteristic for tradition emergence and maintenance is the existence of a correcting, or repair, mechanism such as trait-based conformity (*5*, *14*, *27*, *28*, *32*), as we empirically and theoretically document here. Conformity alone, however, does not necessarily result in culture and cultural inheritance (*28*). The fulfillment of a battery of other criteria is also necessary to generate persistent population preferences, eventually leading to cultural traditions. Although we adopted a demanding definition of culture jointly addressing all criteria discussed in the literature, the first explicit test of all these conditions simultaneously involves a nonsocial insect species. Cultural inheritance may thus have been a substantial part of evolutionary processes for extended periods of time.

Our study trait, mate choice, has considerable evolutionary implications, as strong local traditions in mating preference can amplify local sexual selection while hampering gene flow among populations with different traditions, favoring premating reproductive isolation and potentially speciation (*33*). In this mate-choice context, the Fisher runaway process can lead initially neutral male traits (such as those in our experiments) to quit neutrality as soon as chance generates some detectable statistical preference for one male phenotype. This starts a snowball effect favoring conformist females, a situation that was modeled decades ago (*29*, *33*–*36*) but that still had little empirical evidence. The tradition then becomes part of the niche to which newcomers have to adapt by copying it (in German, *Gruppenzwang*, or "peer pressure"). Such strong selection for conformity in effect provides a general evolutionary explanation for mate-copying (*18*, *37*) and speed learning (*20*) because it is essential for females to quickly grasp the local tradition before mating. More generally, our study shows one major way by which culture can affect evolution as it changes the selective social context of every individual.

REFERENCES AND NOTES

1. A. Whiten, *Proc. Natl. Acad. Sci. U.S.A.* **114**, 7790–7797 (2017).
2. C. P. van Schaik *et al.*, *Science* **299**, 102–105 (2003).
3. H. Whitehead, *Proc. Natl. Acad. Sci. U.S.A.* **114**, 7814–7821 (2017).
4. A. Thornton, J. Samson, T. Clutton-Brock, *Proc. R. Soc. London Ser. B* **277**, 3623–3629 (2010).
5. L. M. Aplin *et al.*, *Nature* **518**, 538–541 (2015).
6. A. Mesoudi, *Proc. Natl. Acad. Sci. U.S.A.* **114**, 7853–7860 (2017).
7. E. Danchin, L. A. Giraldeau, T. J. Valone, R. H. Wagner, *Science* **305**, 487–491 (2004).
8. É. Danchin *et al.*, *Nat. Rev. Genet.* **12**, 475–486 (2011).
9. É. Danchin, R. H. Wagner, *Oikos* **119**, 210–218 (2010).
10. E. Avital, E. Jablonka, *Animal Traditions: Behavioural Inheritance in Evolution* (Cambridge Univ., 2000).
11. R. Brooks, *Trends Ecol. Evol.* **13**, 45–46 (1998).
12. R. I. Bowers, S. S. Place, P. M. Todd, L. Penke, J. B. Asendorpf, *Behav. Ecol.* **23**, 112–124 (2012).
13. R. Boyd, P. J. Richerson, *Philos. Trans. R. Soc. London Ser. B* **364**, 3281–3288 (2009).

14. J. Henrich, R. Boyd, *Evol. Hum. Behav.* **19**, 215–241 (1998).
15. A. Kandler, K. N. Laland, *J. Theor. Biol.* **332**, 191–202 (2013).
16. H. P. Yockey, *Information Theory, Evolution, and the Origin of Life* (Cambridge Univ., 2005).
17. A. Whiten *et al.*, *Nature* **399**, 682–685 (1999).
18. F. Mery *et al.*, *Curr. Biol.* **19**, 730–734 (2009).
19. A. Loyau, S. Blanchet, P. Van Laere, J. Clobert, E. Danchin, *Sci. Rep.* **2**, 768 (2012).
20. A.-C. Dagaeff *et al.*, *Anim. Behav.* **121**, 163–174 (2016).
21. T. Tully, T. Preat, S. C. Boynton, M. Del Vecchio, *Cell* **79**, 35–47 (1994).
22. P. Smolen, Y. Zhang, J. H. Byrne, *Nat. Rev. Neurosci.* **17**, 77–88 (2016).
23. P. Y. Plaçais *et al.*, *Nat. Neurosci.* **15**, 592–599 (2012).
24. A. Loyau, J. H. Cornuau, J. Clobert, E. Danchin, *PLOS ONE* **7**, e51293 (2012).
25. M. Germain, S. Blanchet, A. Loyau, É. Danchin, *Behav. Processes* **125**, 76–84 (2016).
26. S. Nöbel, E. Danchin, G. Isabel, *Behav. Ecol.* **29**, 1150–1156 (2018).
27. C. Efferson, R. Lalive, P. J. Richerson, R. McElreath, M. Lubell, *Evol. Hum. Behav.* **29**, 56–64 (2008).
28. E. J. C. van Leeuwen, R. L. Kendal, C. Tennie, D. B. M. Haun, *Anim. Behav.* **110**, e1–e4 (2015).
29. R. A. Fisher, *The Genetical Theory of Natural Selection* (Clarendon Press, 1930).
30. A. Mesoudi, *Evol. Biol.* **43**, 481–497 (2015).
31. N. Creanza, O. Kolodny, M. W. Feldman, *Proc. Natl. Acad. Sci. U.S.A.* **114**, 7782–7789 (2017).
32. L. M. Aplin, B. C. Sheldon, R. McElreath, *Proc. Natl. Acad. Sci. U.S.A.* **114**, 7830–7837 (2017).
33. R. Lande, *Proc. Natl. Acad. Sci. U.S.A.* **78**, 3721–3725 (1981).
34. K. N. Laland, *Theor. Popul. Biol.* **45**, 1–15 (1994).
35. M. Andersson, *Sexual Selection* (Monographs in Behavior and Ecology, Princeton Univ., 1994).
36. R. F. Lachlan, M. R. Servedio, *Evolution* **58**, 2049–2063 (2004).
37. L. Rendell *et al.*, *Science* **328**, 208–213 (2010).
38. E. Danchin *et al.*, Dryad (2018); doi:10.5061/dryad.683870h.

ACKNOWLEDGMENTS

We thank F. Mery, A. Mesoudi, B. Pujol, L. Chittka, and K. Witte for comments on previous versions of this paper. M. Montevil and P. Bourrat helped in designing and coding the simulation model. A. Loyau participated in the idea of the hexagon. N. Parthuisot helped in fly food production and A. Dussutour in providing equipment. L. Polizzi from the LCAR-IRSAMC physics lab in Toulouse built the prototype of the hexagon. Support from the ANR–Labex IAST is gratefully acknowledged. **Funding:** This work was supported by the Agence Nationale pour la Recherche in the form of the projects entitled Laboratoire d'Excellence (LABEX) TULIP (ANR-10-LABX-41), the Toulouse Initiative of Excellence IDEX UNITI (ANR11-IDEX-0002-02) transversality grant, and the MoleCulture (ANR-18-CE37-0015) to G.I. and E.D. A.P. was supported by the Judith and David Coffey Life Lab, Charles Perkins Centre, The University of Sydney, and a grant from the Templeton World Charity Foundation (TWCF0242). The opinions expressed in this publication are those of the authors and do not necessarily reflect the views of the Templeton World Charity Foundation. The work of E.D., S.N., A.-C.D., L.D., M.Alp., E.G., M.All., L.v.R., M.M., and S.R.-R. was also part of the Soc-H^2 ANR project grant (ANR-13-BSV7-0007-01) to E.D. S.N.'s salary was provided by Soc-H^2 and a Prestige European Marie Curie grant (PRESTIGE-2014-1-0005). G.I. was a CNRS Excellence Chair fellow. **Author contributions:** E.D. and G.I. designed and supervised the study. A.-C.D. proposed and tested the speed-learning design, crafted the hexagon, performed preliminary experiments, and co-supervised E.G. in testing trait-based copying and conformity. S.N. collected most of the data, alone or with the help of L.D., M.Alp., S.R.-R., L.v.R., M.All., and M.M., and performed statistical analyses with E.D. A.P. designed and wrote the theoretical model and helped E.D. in performing simulations. E.D. ran simulations and wrote the paper with the help of S.N., G.I., and A.P. **Competing interests:** The authors declare no competing interests. **Data and materials availability:** Data, materials, associated protocols, and technical details, as well as the simulation code, are available to researchers desiring to replicate or expand studies of *Drosophila* mate-copying. Data and the R code for simulations can be downloaded at Dryad (*38*). The hexagon device can be purchased from Toulouse Tech Transfer and Paul Sabatier University.

SUPPLEMENTARY MATERIALS

www.sciencemag.org/content/362/6418/1025/suppl/DC1
Materials and Methods
Figs. S1 to S11
Tables S1 and S2
References (*39*–*41*)

23 February 2018; accepted 23 October 2018
10.1126/science.aat1590

REPORT

COSMOLOGY

A gamma-ray determination of the Universe's star formation history

The Fermi-LAT Collaboration*†

The light emitted by all galaxies over the history of the Universe produces the extragalactic background light (EBL) at ultraviolet, optical, and infrared wavelengths. The EBL is a source of opacity for gamma rays via photon-photon interactions, leaving an imprint in the spectra of distant gamma-ray sources. We measured this attenuation using 739 active galaxies and one gamma-ray burst detected by the Fermi Large Area Telescope. This allowed us to reconstruct the evolution of the EBL and determine the star formation history of the Universe over 90% of cosmic time. Our star formation history is consistent with independent measurements from galaxy surveys, peaking at redshift *z* ~ 2. Upper limits of the EBL at the epoch of reionization suggest a turnover in the abundance of faint galaxies at *z* ~ 6.

Stars produce the bulk of the optical light in the Universe and synthesize most of the elements found in galaxies. The cosmic star formation history (SFH)—that is, the stellar birth rate as a function of the Universe's age—summarizes the history of stellar formation since the Big Bang (*1*). The rate of star formation is commonly estimated by measuring direct emission of light from massive short-lived stars, typically in the ultraviolet (UV), and/or by detecting the reprocessed radiation from dusty star-forming regions in the infrared (IR). The conversion from the UV light emitted by a minority of stars to the stellar mass formed per year relies on assumptions about the mass distribution of the newly formed stellar population (the initial mass function), the element enrichment history of the interstellar medium, and obscuration by dust. Such estimates of the SFH rely on the detection of many individual galaxies in deep surveys (*2*–*4*). Because not even the most powerful telescope can detect all the galaxies in a representative field, one of the largest sources of uncertainty in the SFH is estimating the amount of light from undetected galaxies, and thereby estimating the star formation associated with those galaxies. This difficulty becomes particularly relevant within the first billion years after the Big Bang when a large population of faint, still undetected, galaxies existed (*5*). These galaxies are expected to have driven the reionization of the Universe: the period when energetic UV photons from young stars escaped into intergalactic space and ionized the neutral hydrogen of the intergalactic medium. Similarly, recent (i.e., within 1 billion years from the present age) star formation measured using space-borne UV observatories is based on surveys extending over small solid angles (*6*) and is therefore subject to density fluctuations in the large-scale structure, an effect known as cosmic variance.

Observational estimates of the SFH are sufficiently uncertain that measurements with multiple independent methodologies are desirable. Starlight that escapes galaxies is almost never destroyed and becomes part of the extragalactic background light (EBL), the total light accumulated by all sources over the lifetime of the Universe (*7*–*9*). Accurate measurements of this diffuse all-sky background at UV to IR wavelengths, and particularly its buildup over time, have only just become possible (*10*).

We present an alternative approach to measuring the SFH, based on the attenuation that the EBL produces in the γ-ray spectra of distant sources. Gamma rays with sufficient energy can annihilate when they collide with EBL photons and produce electron-positron pairs (i.e., the reaction $\gamma\gamma \rightarrow e^+e^-$), effectively being absorbed as a result of the interaction (*11*). Above a given threshold energy, the attenuation experienced by every γ-ray source at a similar distance depends on the number density of the EBL target photons integrated along the line of sight; observations of γ-ray sources at different distances (as measured by the sources' redshifts) can be used to measure the density of EBL photons at different cosmic times.

We analyzed γ-ray photons detected by the Large Area Telescope (LAT) instrument onboard the Fermi Gamma-ray Space Telescope over 9 years of operations. Our sample of suitable objects for this analysis consists of 739 blazars—galaxies hosting a supermassive black hole with a relativistic jet pointed at a small angle to the line of sight. The distances of these blazars correspond to lookback times of 0.2 to 11.6 billion years according to the standard cosmological model (*12*). We performed a likelihood analysis to find the EBL attenuation experienced by all blazars while

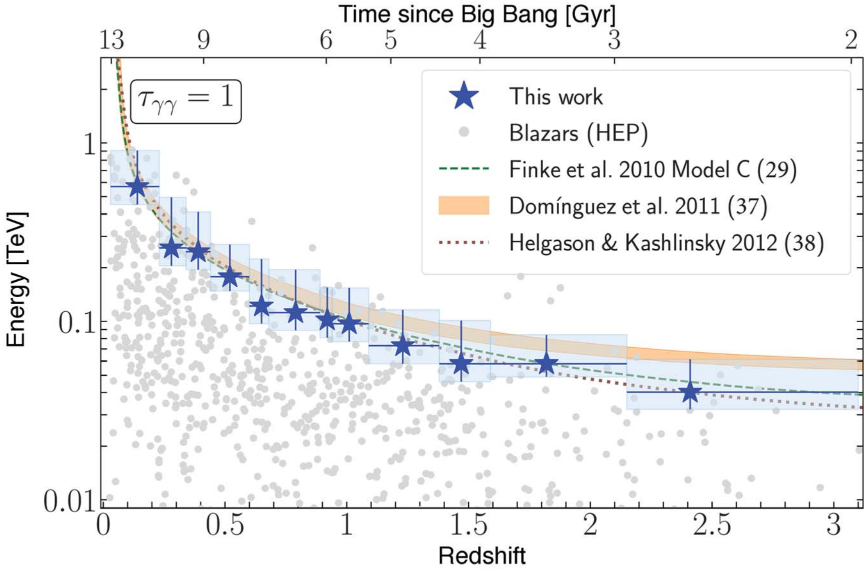

Fig. 1. The cosmic γ-ray horizon. Measurement of the cosmic γ-ray horizon ($\tau_{\gamma\gamma}$ = 1, i.e., the point after which the Universe becomes opaque to γ rays) as a function of redshift (blue stars). Horizontal and vertical blue lines represent the redshift bin size and the uncertainty on the energy, respectively. Also shown are predictions from three different EBL models (*29*, *37*, *38*) for comparison. The gray points show the highest-energy photon (HEP) detected from each blazar considered in this work. Gyr, billions of years.

---

*Fermi-LAT Collaboration authors and affiliations are listed in the supplementary materials.
†Email: majello@g.clemson.edu; helgason@hi.is; vpaliya@g.clemson.edu; justin.finke@nrl.navy.mil; abhishd@g.clemson.edu; alberto@gae.ucm.es

simultaneously optimizing the spectral parameters independently for each blazar (*13*). This can be accomplished individually for each source by defining a region of interest that comprises all γ rays detected within 15° of the source position and creating a sky model that includes all sources of γ rays in the field. The parameters of the sky model are then optimized by a maximum likelihood method. For every blazar, the fitting is performed below an energy at which the EBL attenuation is negligible and thus yields a measurement of the intrinsic (i.e., unabsorbed) blazar spectrum. The intrinsic spectra are described using simple empirical functions (*14*) and extrapolated to higher energy, where the γ rays are expected to be attenuated by the EBL.

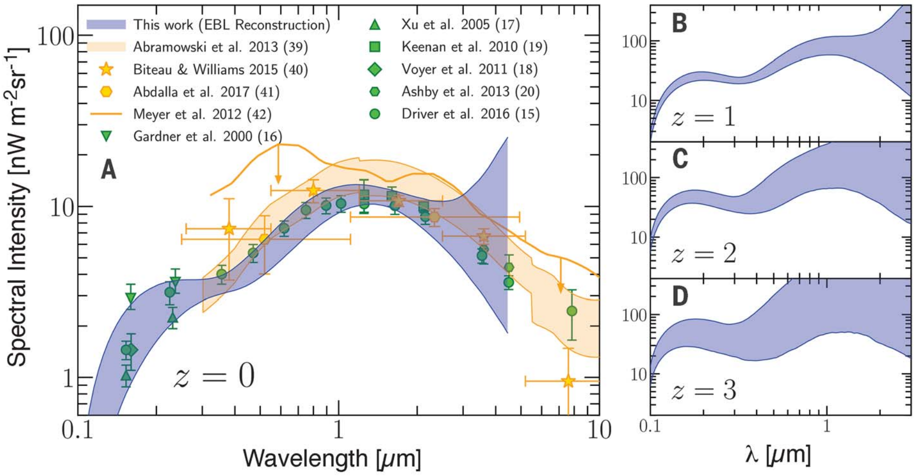

Fig. 2. The spectral intensity of the EBL at redshifts 0, 1, 2, and 3. (**A**) Today's Universe ($z = 0$). The blue area shows the 1σ confidence regions based on the reconstructed cosmic emissivity (*14*). Data from other γ ray–based measurements are shown with orange symbols (*39*–*42*); integrated galaxy counts are displayed with green symbols (*15*–*20*). Horizontal yellow lines represent the wavelength range; vertical yellow and green lines represent the uncertainty on the intensity of the EBL. The downward-pointing arrows show upper limits on the intensity of the EBL from (*42*). (**B** to **D**) At higher redshifts ($z = 1$, 2, and 3, respectively), the EBL is shown in physical coordinates. Figure S8 includes a more complete set of measurements from the literature.

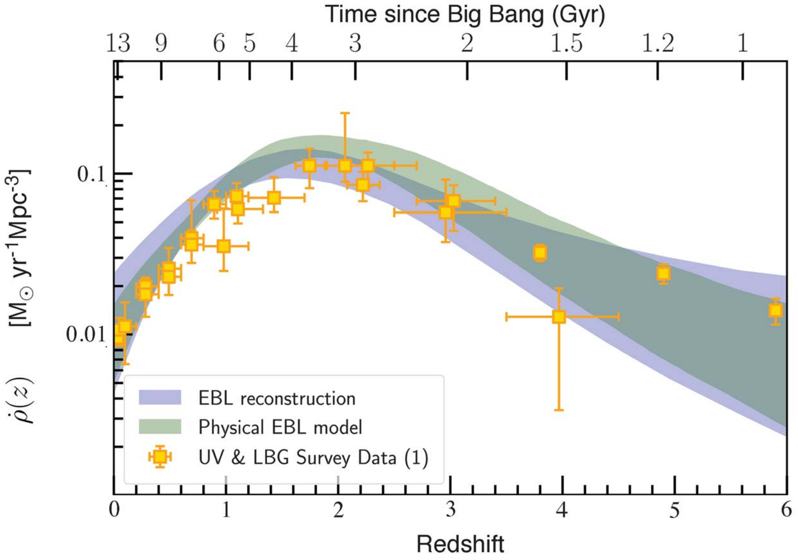

Fig. 3. Cosmic star formation history as constrained from optical depth data. The shaded regions correspond to the 1σ confidence regions on the star formation rate density as a function of redshift, $\dot\rho(z)$, obtained from two independent methods, based on a physical EBL model (green) and an empirical EBL reconstruction [blue; see (*14*)]. The data points show the star formation history derived from UV surveys at low z and deep Lyman-break galaxy surveys at high z [see (*1*) and references therein]. Horizontal and vertical yellow lines represent the redshift bin size and the uncertainty on the cosmic star formation history. Figure S11 includes a more complete set of data from different tracers of the star formation rate.

Potential EBL absorption is added to the fitted spectra as follows:

$$\left(\frac{\mathrm{d}N}{\mathrm{d}E}\right)_{\mathrm{obs}} = \left(\frac{\mathrm{d}N}{\mathrm{d}E}\right)_{\mathrm{int}} \exp[-b\cdot\tau_{\gamma\gamma}(E,z)] \qquad (1)$$

where $(\mathrm{d}N/\mathrm{d}E)_{\mathrm{obs}}$ and $(\mathrm{d}N/\mathrm{d}E)_{\mathrm{int}}$ are the observed and intrinsic blazar spectra, respectively; $\tau_{\gamma\gamma}(E, z)$ is the EBL optical depth as estimated from models (at a given energy E and redshift z); and b is a free parameter. The data from all blazars are combined to yield the best-fitting value of b for each model. A value of $b = 0$ implies that no EBL attenuation is present in the spectra of blazars, whereas $b \approx 1$ implies an attenuation compatible with the model prediction. Twelve of the most recent models that predict the EBL attenuation up to a redshift of $z = 3.1$ have been tested in this work. We detect the attenuation due to the EBL in the spectra of blazars at ≳16 standard deviations (σ) for all models tested (see table S2).

Our analysis leads to detections of the EBL attenuation across the entire $0.03 < z < 3.1$ redshift range of the blazars. From this, we identify the redshift at which, for a given energy, the Universe becomes opaque to γ rays, known as the cosmic γ-ray horizon (Fig. 1). With the optical depths measured in six energy bins (10 to 1000 GeV) across 12 redshift bins (*14*), we are able to reconstruct the intensity of the EBL at different epochs (Fig. 2). We model the cosmic emissivity (luminosity density) of sources as several simple spectral components at UV, optical, and near-IR (NIR) wavelengths. These components are allowed to vary in amplitude and evolve with redshift independently of each other to reproduce, through a Markov chain Monte Carlo (MCMC) analysis, the optical depth data. The emissivities as a function of wavelength and redshift allow us to reconstruct the history of the EBL over ~90% of cosmic time.

At $z = 0$, the energy spectrum of the EBL is close to the one inferred by resolving individual galaxies in deep fields (*15*). At all other epochs, Fermi LAT is most sensitive to the UV-optical component of the EBL and is only able to constrain the NIR component at more recent times (see Fig. 2). The intensity of the UV background in the local Universe remains uncertain, with independent studies reporting differing values (*16*–*18*). Our determination of $2.56^{+0.92(2.23)}_{-0.87(1.49)}$ nW m^{-2} sr^{-1} [1σ (2σ)] at 0.2 μm favors an intermediate UV intensity in agreement with (*18*). In the NIR, our measurement of $11.6^{+1.3(2.6)}_{-1.4(3.1)}$ nW m^{-2} sr^{-1} [1σ (2σ)] at 1.4 μm is consistent with integrated galaxy counts (*19*, *20*), leaving little room for additional components, contrary to some suggestions (*21*, *22*). This notably includes contributions from stars that have been stripped from galaxies, as the technique presented here is sensitive to all photons (*23*, *24*).

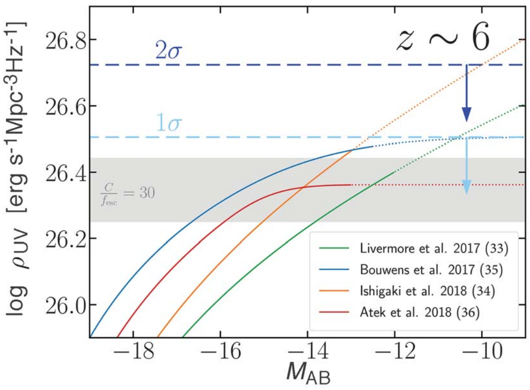

Fig. 4. Upper limits on the UV luminosity density of galaxies at *z* ~ 6. The 1σ and 2σ limits are shown as dashed horizontal lines, light blue and dark blue, respectively. The solid curves show the *z* ~ 6 UV emissivity from (*33*–*36*) of the Hubble Frontier Fields (HFF) program as a function of the lower integration limit of the UV luminosity function. The dotted lines correspond to extrapolations beyond the limiting magnitude of the HFF analyses. The data from (*35*) are those derived using the GLAFIC magnification model. The lines of (*34*) and (*36*) have been shifted up by 0.15 dex to account for evolution of their combined sample (*z* ~ 6 to 7) to *z* ~ 6. The gray area corresponds to the luminosity required to keep the Universe ionized at *z* = 6 assuming C/f_{esc} = 30, where *C* is the clumping factor of ionized hydrogen and f_{esc} is the mean escape fraction of ionizing photons (*14*).

At any epoch, the EBL is composed of the emission of all stars (*25*) that existed up to that point in time and can therefore be used to infer properties related to the evolution of galaxy populations. We focus on the cosmic SFH, which we determine using two independent methods. First, we use the reconstructed UV emissivity across cosmic time to derive the SFH from established relations between the UV luminosity and the star formation rate (*26*), taking into account the mean dust extinction within galaxies (*10*, *27*, *28*). The second approach uses a physical EBL model (*29*) to calculate the optical depth due to the EBL directly from the SFH. The SFH is then optimized using a MCMC to reproduce the Fermi-LAT optical depth data (*14*). The two approaches yield consistent results for the SFH, which is well constrained out to a redshift of $z \approx 5$—that is, to the epoch 1.5 billion years after the Big Bang (Fig. 3).

Because optical depth increases with the distance traveled by the γ rays, we obtain the tightest constraints in the redshift range $0.5 < z < 1.5$, beyond which our sensitivity decreases because of the smaller number of observed blazars. To improve the constraint of the SFH beyond $z = 3$, we have complemented the blazar sample with a γ-ray burst (GRB 080916C) at $z = 4.35$ (*30*). This allows us to place upper limits on the SFH at $z \gtrsim 5$, because photons generated at redshifts higher than the $z = 4.35$ limit of our sample remain in the EBL, become redshifted, and start to interact with the γ rays from the blazars and the γ-ray burst used here at $z \leq 4.35$.

At $z \gtrsim 6$, the far-UV background (photon energy > 13.6 eV) is responsible for the reionization of the neutral hydrogen in the Universe, but the nature of ionizing sources has not been conclusively identified. One possibility is that ultra-faint galaxies existing in large numbers can provide the required ionizing photons (*31*, *32*). In this case, the galaxy UV luminosity function must be steep at the faint end. Recent measurements of the luminosity function in the deepest Hubble fields remain inconclusive at the faintest levels (absolute AB magnitude $M_{AB} \gtrsim -15$), with some suggesting a continued steep faint-end slope (*33*, *34*) and others claiming a turnover (*35*, *36*). Our upper limits at $z = 5$ to 6 on the UV emissivity $\rho_{UV} < 3.2\ (5.3) \times 10^{26}$ erg s^{-1} Mpc^{-3} Hz^{-1} [1σ (2σ)] (Fig. 4) suggest a turnover of the luminosity function at $M_{AB} \sim -14$, in agreement with previous claims (*35*, *36*). This still provides abundant photons to drive the reionization.

REFERENCES AND NOTES

1. P. Madau, M. Dickinson, *Annu. Rev. Astron. Astrophys.* **52**, 415–486 (2014).
2. N. A. Grogin *et al.*, *Astrophys. J. Suppl. Ser.* **197**, 35 (2011).
3. G. D. Illingworth *et al.*, *Astrophys. J. Suppl. Ser.* **209**, 6 (2013).
4. J. M. Lotz *et al.*, *Astrophys. J.* **837**, 97 (2017).
5. R. J. McLure *et al.*, *Mon. Not. R. Astron. Soc.* **432**, 2696–2716 (2013).
6. D. Schiminovich *et al.*, *Astrophys. J.* **619**, L47–L50 (2005).
7. M. G. Hauser, E. Dwek, *Annu. Rev. Astron. Astrophys.* **39**, 249–307 (2001).
8. A. Kashlinsky, *Phys. Rep.* **409**, 361–438 (2005).
9. E. Dwek, F. Krennrich, *Astropart. Phys.* **43**, 112–133 (2013).
10. S. K. Andrews *et al.*, *Mon. Not. R. Astron. Soc.* **470**, 1342–1359 (2017).
11. A I. Nikishov, *Sov. Phys. JETP* **14**, 393 (1962).
12. We adopted the following values for the Hubble constant and cosmological parameters: H_0 = 70 km s^{-1} Mpc^{-1}, Ω_M = 0.3, and Ω_Λ = 0.7.
13. M. Ackermann *et al.*, *Science* **338**, 1190–1192 (2012).
14. See supplementary materials.
15. S. P. Driver *et al.*, *Astrophys. J.* **827**, 108 (2016).
16. J. P. Gardner, T. M. Brown, H. C. Ferguson, *Astrophys. J.* **542**, L79–L82 (2000).
17. C. K. Xu *et al.*, *Astrophys. J.* **619**, L11–L14 (2005).
18. E. N. Voyer, J. P. Gardner, H. I. Teplitz, B. D. Siana, D. F. de Mello, *Astrophys. J.* **736**, 80 (2011).
19. R. C. Keenan, A. J. Barger, L. L. Cowie, W.-H. Wang, *Astrophys. J.* **723**, 40–46 (2010).
20. M. L. N. Ashby *et al.*, *Astrophys. J. Suppl. Ser.* **209**, 22 (2013).
21. R. A. Bernstein, *Astrophys. J.* **666**, 663–673 (2007).
22. S. Matsuura *et al.*, *Astrophys. J.* **839**, 7 (2017).
23. M. Zemcov *et al.*, *Science* **346**, 732–735 (2014).
24. C. Burke, M. Hilton, C. Collins, *Mon. Not. R. Astron. Soc.* **449**, 2353–2367 (2015).
25. The contribution of active galactic nuclei is small in comparison (*14*).
26. R. C. Kennicutt Jr., *Annu. Rev. Astron. Astrophys.* **36**, 189–231 (1998).
27. R. J. Bouwens *et al.*, *Astrophys. J.* **754**, 83 (2012).
28. D. Burgarella *et al.*, *Astron. Astrophys.* **554**, A70 (2013).
29. J. D. Finke, S. Razzaque, C. D. Dermer, *Astrophys. J.* **712**, 238–249 (2010).
30. Fermi LAT and Fermi GBM Collaborations, *Science* **323**, 1688–1693 (2009).
31. S. L. Finkelstein *et al.*, *Astrophys. J.* **810**, 71 (2015).
32. B. E. Robertson, R. S. Ellis, S. R. Furlanetto, J. S. Dunlop, *Astrophys. J.* **802**, L19 (2015).
33. R. C. Livermore, S. L. Finkelstein, J. M. Lotz, *Astrophys. J.* **835**, 113 (2017).
34. M. Ishigaki *et al.*, *Astrophys. J.* **854**, 73 (2018).
35. R. J. Bouwens, P. A. Oesch, G. D. Illingworth, R. S. Ellis, M. Stefanon, *Astrophys. J.* **843**, 129 (2017).
36. H. Atek, J. Richard, J.-P. Kneib, D. Schaerer, arXiv:1803.09747 (26 March 2018).
37. A. Domínguez *et al.*, *Mon. Not. R. Astron. Soc.* **410**, 2556–2578 (2011).
38. K. Helgason, A. Kashlinsky, *Astrophys. J.* **758**, L13 (2012).
39. A. Abramowski *et al.*, *Astron. Astrophys.* **550**, A4 (2013).
40. J. Biteau, D. A. Williams, *Astrophys. J.* **812**, 60 (2015).
41. H. Abdalla *et al.*, *Astron. Astrophys.* **606**, A59 (2017).
42. M. Meyer, M. Raue, D. Mazin, D. Horns, *Astron. Astrophys.* **542**, A59 (2012).

ACKNOWLEDGMENTS

Funding: Supported by NSF and NASA through grants AST-1715256, NNX16AR72G, and 80NSSC17K0506 (M.Aj., V.P., and A.De.); Icelandic Research Fund grant 173728-051 (K.H.); the Chief of Naval Research and a grant of computer time from the Department of Defense High Performance Computing Modernization Program at the Naval Research Laboratory (J.F.); the Juan de la Cierva program from the Spanish MEC (A.Do.); Wallenberg Academy (J.C.); and Italian Ministry of Education, University and Research (MIUR) contract FIRB-2012-RBFR12PM1F (M.R.). The Fermi-LAT Collaboration acknowledges generous ongoing support from a number of agencies and institutes that have supported both the development and the operation of the LAT as well as scientific data analysis. These include NASA and the U.S. Department of Energy (DOE); the Commissariat à l'Energie Atomique and the Centre National de la Recherche Scientifique/Institut National de Physique Nucléaire et de Physique des Particules (France); the Agenzia Spaziale Italiana and the Istituto Nazionale di Fisica Nucleare (Italy); the Ministry of Education, Culture, Sports, Science and Technology (MEXT), High Energy Accelerator Research Organization (KEK), and Japan Aerospace Exploration Agency (JAXA) (Japan); and the K. A. Wallenberg Foundation, the Swedish Research Council, and the Swedish National Space Board (Sweden). Additional support for science analysis during the operations phase came from the Istituto Nazionale di Astrofisica, Italy, and the Centre National d'Études Spatiales, France. This work was performed in part under DOE contract DE-AC02-76SF00515. **Author contributions:** M.Aj. designed the project and wrote most of the paper; V.P. performed the analysis of the γ-ray data; K.H. derived the constrains on the EBL and the star formation history and wrote all the corresponding text; J.F. derived the results of the stellar population method and wrote the corresponding text; A.De. tested all the EBL models; A.Do. provided all the EBL-related data reported in the figures and wrote the corresponding text; and all co-authors have read, provided comments on, and approved the manuscript. **Competing interests:** All co-authors declare that there are no competing interests. **Data and materials**

availability: The data used to derive the results presented in this paper are provided in tabular form in the supplementary materials. The Fermi-LAT data and software needed for analysis are available from the Fermi Science Support Center, http://fermi.gsfc.nasa.gov/ssc. The reconstructed optical depth templates, EBL, and SFH are also available at https://figshare.com/s/14f943002230d69a4afd. The tool to produce physical models of blazars' SEDs is available at www.isdc.unige.ch/sedtool.

SUPPLEMENTARY MATERIALS

www.sciencemag.org/content/362/6418/1031/suppl/DC1
Authors and Affiliations
Materials and Methods
Figs. S1 to S12
Tables S1 to S5
Data S1
References (*43*–*115*)

6 April 2018; accepted 11 October 2018
10.1126/science.aat8123

DISTANT GALAXIES

The multiple merger assembly of a hyperluminous obscured quasar at redshift 4.6

T. Díaz-Santos[1]*, R. J. Assef[1], A. W. Blain[2], M. Aravena[1], D. Stern[3], C.-W. Tsai[4], P. Eisenhardt[3], J. Wu[5], H. D. Jun[6], K. Dibert[7], H. Inami[8], G. Lansbury[9], F. Leclercq[8]

Galaxy mergers and gas accretion from the cosmic web drove the growth of galaxies and their central black holes at early epochs. We report spectroscopic imaging of a multiple merger event in the most luminous known galaxy, WISE J224607.56−052634.9 (W2246−0526), a dust-obscured quasar at redshift 4.6, 1.3 billion years after the Big Bang. Far-infrared dust continuum observations show three galaxy companions around W2246−0526 with disturbed morphologies, connected by streams of dust likely produced by the dynamical interaction. The detection of tidal dusty bridges shows that W2246−0526 is accreting its neighbors, suggesting that merger activity may be a dominant mechanism through which the most luminous galaxies simultaneously obscure and feed their central supermassive black holes.

Structure formation in the early Universe proceeded through the hierarchical assembly of dark matter haloes and the galaxies they host, with the densest structures collapsing first (*1*). During the periods of most intense accretion and growth, galaxies and their central supermassive black holes (SMBHs) are expected to be obscured by interstellar gas and dust (*2*). The obscuring material absorbs the ultraviolet and optical light from stars and the active galactic nucleus (AGN) powered by the SMBH and re-emits it in the infrared (*2*).

The Wide-field Infrared Survey Explorer (WISE) (*3*) space telescope studied the formation and evolution of galaxies in the high-redshift Universe. A population of hyperluminous obscured quasars were found at redshifts $\gtrsim 2$, with bolometric luminosities $L_{\mathrm{bol}} \gtrsim 10^{13}\,L_{\odot}$ (*4*, *5*), where L_{bol} is the luminosity integrated across the entire electromagnetic spectrum, and $L_{\odot}$ is the luminosity of the Sun. Known as hot, dust-obscured galaxies (hot DOGs), these systems are mainly powered by accretion onto their central SMBHs, which may be radiating close to the limit allowed by their own gravity (*6*). The dominant mechanism supplying the material necessary to sustain such high luminosities remains unknown. Rapid growth of galaxies and SMBHs can be accomplished via galaxy mergers, which would effectively funnel low angular momentum gas into the central AGN (*7*, *8*). If hot DOGs form in overdense environments, merger-driven instabilities could deliver large amounts of gas and dust to the galaxy. However, there is only indirect, statistical evidence that this is the case. Combined observations of 10 hot DOGs at 850 μm reveal more than twice as many sources within 1.5 arc min as in random fields (*9*), and shallow near-infrared (NIR) images show that the number density of red sources within 1 arc min of hot DOGs is, on average, higher than that of field galaxies (*10*). In submillimeter observations of 10 hot DOGs, the cumulative number counts of companion sources also support dense environments around hot DOGs (*11*). However, the morphological evidence for dynamical interactions in individual systems remains elusive, and observations obtained with the Hubble Space Telescope (HST) of a sample of hot DOGs at redshift $z \sim 2$ have yielded ambiguous results (*12*, *13*).

With $L_{\mathrm{bol}} = 3.5 \times 10^{14}\,L_{\odot}$ (*14*, *15*), the hot DOG WISE J224607.56−052634.9 (hereafter W2246−0526) is the most luminous galaxy known. Previous observations with the Atacama Large Millimeter/Sub-millimeter Array (ALMA) of the ionized carbon ([C II]) emission line at 158 μm (*16*) have shown W2246−0526 is located at a redshift of 4.601, which is equivalent to ~1.3 billion years after the Big Bang, assuming standard cosmological parameters (*15*). The line profile shows a uniform, large-velocity dispersion, with a full-width at half-maximum (FWHM) of ~500 to 600 km s^{-1} across the whole galaxy where emission is detected (~2.5 kpc) (*16*). This suggests a highly turbulent interstellar medium (ISM), likely resulting from the energy and momentum injected by the central SMBH into the surrounding gas.

The [C II] observations had also shown two nearby companion galaxies to W2246−0526 (*16*). We detected a third companion in a blind search for emission line sources in the data cube, which we confirmed via its Lyman-α emission line in an optical spectrum obtained with the Keck telescope (*15*). The star-formation rates (SFRs) of the companions based on their [C II] luminosities are at least 7 to 27 solar mass ($M_{\odot}$) year^{-1} (*15*). Other recent studies have also identified companion galaxies close to unobscured high-redshift quasars. ALMA [C II] observations of luminous quasars at $z \sim 4.8$ and >6 (*17*, *18*) show that a large fraction of them are accompanied by actively star-forming galaxies at projected distances <100 kpc and within radial velocities $\lesssim$600 km s^{-1}. However, there were no direct morphological signatures that show dynamical interaction between the companion galaxies and central source.

We present deep ALMA observations of the dust continuum emission at rest frame 212 μm in W2246−0526 at an angular resolution of ~0.5 arc sec, which is equivalent to ~3.3 kpc at that distance (*15*). The dust continuum map shown in Fig. 1 reveals bridges of material connecting the central galaxy to the companions, which we denote C1, C2, and C3. The detection of dust indicates that the gas associated with these structures has been already enriched with elements heavier than hydrogen or helium and is thus not primordial. C2 has a stream of dust extending like a tidal tail all the way to W2246−0526, over at least 35 kpc. One of the densest regions in this structure, denoted K1 and located ~1.5 arc sec northwest of C2 (Fig. 1), has a counterpart identified in rest-frame near ultraviolet (UV) emission (Fig. 2). The UV image was obtained with the HST by using the NIR F160W filter and was previously analyzed in (*16*). The detection of the UV counterpart suggests that at least a fraction of the dust in the tidal tail could be heated through in situ star formation (*15*). Low-surface-brightness dust emission south of C3 is coincident with strong UV emission seen in the HST image as well (denoted U1) (Fig. 2), although this source could be at a different redshift because it is not detected in [C II] line emission. Two more sources with unknown redshifts (U2 and U3) are also identified 6 arc sec to the northwest and 8.5 arc sec to the southwest of W2246−0526, respectively, in the HST image.

The detection of streams of dust emission on such large physical scales suggests that W2246−0526 is in the process of accreting its neighbors—or at least stripping a large fraction of their gas—and provides evidence that (i) merger activity is taking place and (ii) the entire system may be undergoing a morphological transformation. Gas and dust accretion triggered by galaxy mergers can provide strong, yet probably intermittent, influx of material toward the nuclei of high-redshift

---

[1]Núcleo de Astronomía, Facultad de Ingeniería y Ciencias, Universidad Diego Portales, Ejército Libertador 441, Santiago, 8320000, Chile. [2]Department of Physics and Astronomy, University of Leicester, University Road, Leicester LE1 7RH, UK. [3]Jet Propulsion Laboratory, California Institute of Technology, 4800 Oak Grove Drive, Pasadena, CA 91109, USA. [4]Department of Physics and Astronomy, University of California, Los Angeles, Los Angeles, CA 90095, USA. [5]National Astronomical Observatories, Chinese Academy of Sciences, 20A Datun Road, Chaoyang District, Beijing 100012, China. [6]School of Physics, Korea Institute for Advanced Study, 85 Hoegiro, Dongdaemun-gu, Seoul 02455, Korea. [7]Department of Physics, Massachusetts Institute of Technology, 77 Massachusetts Avenue, Cambridge, MA 02139, USA. [8]Université Lyon, Université Lyon1, École Normale Supérieure de Lyon, Centre National de la Recherche Scientifique, Centre de Recherche Astrophysique de Lyon UMR5574, 69230 Saint-Genis-Laval, France. [9]Institute of Astronomy, University of Cambridge, Madingley Road, Cambridge CB3 0HA, UK.
*Corresponding author. Email: tanio.diaz@mail.udp.cl

hyperluminous galaxies, simultaneously feeding and obscuring their SMBHs.

We performed additional observations with the Karl G. Jansky Very Large Array (VLA) of the $J = 2 \rightarrow 1$ transition line of carbon monoxide (CO) in W2246–0526, where J is the rotational quantum number (*15*). The luminosity of low-J transitions of the CO molecule is regularly used as a proxy for the cold molecular gas content of galaxies. In Fig. 3, we compare the CO(2→1) line map with contours of the 212 μm dust continuum. The CO(2→1) emission is marginally resolved (the beam FWHM is 2.47 by 2.01 arc sec, which is equivalent to ~16 by 13 kpc), with tentative low-surface-brightness regions extending toward the companion C3 and in the direction of the tidal tail. The FWHM of the CO line in the central beam is ~600 km s^{-1}, which is similar to that of the [C II] line (fig. S3) (*16*), suggesting that the cold molecular gas phase of the ISM traced by CO in W2246–0526 is also very turbulent and probably affected by the strong feedback from the AGN on scales of at least a few kiloparsecs.

The dust mass in W2246–0526 alone (within the central 1 arc sec ~ 7 kpc) is in the range of 5.6×10^8 to 17×10^8 $M_\odot$ (assuming a dust temperature of 100 to 50 K) (*15*). This is similar to the total dust mass content of dusty ultraluminous infrared galaxies (ULIRGs) in the nearby Universe, which span a range between ~10^8 and 10^9 $M_\odot$ (although W2246–0526 is 100 times more luminous) (*19*). The rest of the system—including the companion galaxies C1, C2, and C3 and the extended emission—contains at least as much dust as W2246–0526 alone (table S1). The three companions contribute ~25% of the dust mass outside W2246–0526 and ~13% of the entire merger system. U2 and U3 are not included in this calculation because they may not be part of the system. The tidal tail contains almost as much dust as the sum of that of all three companion galaxies. Assuming that the dust and gas are well mixed and a standard gas-to-dust ratio (δ_{GDR}) that is typical of local, solar-metallicity galaxies (*20*), $\delta_{\mathrm{GDR}} = 100$, W2246–0526 harbors a total gas mass (M_{gas}) reservoir of ~0.6×10^{11} to 1.7×10^{11} $M_\odot$, with the entire system containing M_{gas} ~ 1.2×10^{11} to 3.6×10^{11} $M_\odot$. The total molecular gas mass estimated from the CO(2→1) line is $1.5\ (\pm\ 0.8) \times 10^{11}$ $M_\odot$ (*15*), which is in agreement with the estimate from the dust.

On the basis of the [C II] kinematics, we calculated the dynamical mass (M_{dyn}) of W2246–0526 to be ~$0.8\ (\pm\ 0.4) \times 10^{11}$ $M_\odot$, which is within a factor of ~2 of the baryonic mass of the galaxy (*15*), which is similar to observations of some compact galaxies at z ~ 2 (*21*). The dynamical mass favors the lower bound of the dust-based gas estimate (*15*), which is as expected if most of the dust within the central core of W2246–0526 (within a few kiloparsecs) is being heated to temperatures >100 K because of its closer proximity to the central AGN.

The M_{gas} and stellar mass ($M_\star$) in the W2246–0526 merger system imply a baryonic gas fraction f_{gas} ~ 0.3 to 0.6 [where $f_{\mathrm{gas}} = M_{\mathrm{gas}}/(M_\star + M_{\mathrm{gas}})$], which is lower than the value expected for most galaxies at similar redshifts (*22*). The SFR within the central ~4 arc sec is estimated to be ~560 $M_\odot$ year^{-1}, with a factor of two uncertainty (*15*). This translates into a specific SFR (SSFR; the star formation rate divided by the stellar mass) of ~2.2 billion year^{-1}, which is equivalent to a mass doubling-time of ~450 million years, both with an uncertainty of a factor of three. The derived SSFR is only slightly lower than that of main-sequence galaxies at redshifts of 3.5 to 5 (*22*, *23*). However, the gas depletion time scale is only ~125 million to 700 million years (*15*), which is between main-sequence and starburst galaxies at approximately the same redshift (*22*). The free-fall time of the gas in the system is ~100 million to 170 million years (*15*), which is at least an order of magnitude larger than the active period of hyperluminous quasars (*24*) and suggests that the hot DOG phase is shorter than the dynamical time scale of the merger. On the basis of the M_{gas} of the tidal tail and companion galaxies, the average accretion rate of gas toward the center of W2246–0526 could be as high as dM_{gas}/dt ~ 550 to 900 $M_\odot$ year^{-1} (*15*), which is similar to the estimated SFR of the underlying galaxy.

Fig. 1. ALMA 212 μm dust continuum emission map of the W2246–0526 merger system. The color bar shows the flux density on a logarithmic scale in units of millijansky (1 mJy = 10^{-26} erg s^{-1} cm^{-2} Hz^{-1}). North is up, and east is to the left. The angular resolution (beam size FWHM) of the observations is 0.54 by 0.46 arc sec, or ~3.6 by 3.1 kpc at the redshift of W2246–0526, and it is shown by the ellipse at the bottom left corner. The offsets in the right ascension and declination axes are given in arc seconds relative to the center of W2246–0526, whose coordinates are: 22 hours 46 min 07.55 s, −05° 26′ 35.0″. The relative velocities of three companion galaxies (labeled as C1, C2, and C3) and the redshift of W2246–0526 are measured via the [C II] emission line (*16*) and suggest that W2246–0526 and its companions are gravitationally bound. A stream of dusty material resembling a tidal tail connects W2246–0526 with C2, and bridges join the central galaxy with C1 and C3. Three sources with unknown redshifts and the knot ~ 1.5 arc sec northwest of C2 are labeled as U1, U2, U3, and K1, respectively. Solid contours represent levels of [2.5, 3, 4, 6, 9, 15, 30, 50] × σ, where σ is the measured root mean square (RMS) of the background. Dotted contours indicate [−2.5, −3] × σ negative flux. An equivalent map with lower-significance contours is shown in fig. S2.

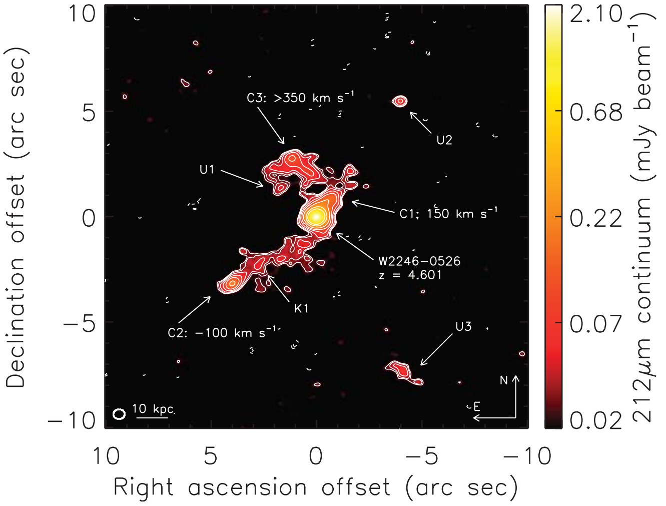

Fig. 2. Rest-frame near UV (~2860 Å) continuum image of W2246–0526 with overlaid contours of the 212 μm dust-continuum map. The color bar shows the near-UV flux density on a logarithmic scale. The emission at the top left corner is from a low-redshift foreground galaxy. The companion galaxies C1, C2, and C3 are detected in both the dust continuum and near-UV emission, as are the sources with unknown redshifts (U1, U2, and U3) and the tidal tail knot (K1).

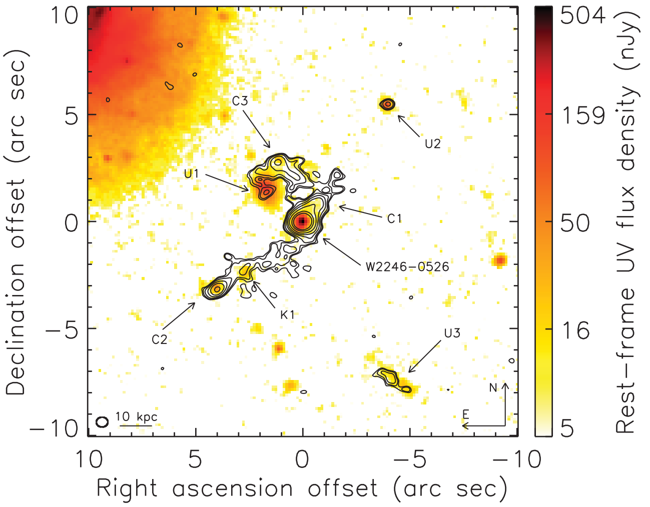

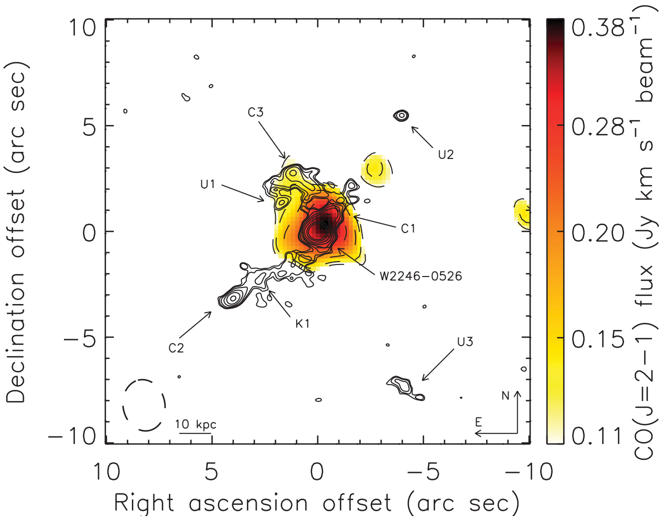

Fig. 3. CO(2→1) emission line map of W2246–0526 with overlaid contours of the 212 μm dust-continuum map. The color bar shows the line flux per beam on a logarithmic scale. The angular resolution (beam size FWHM) of the observations is 2.47 by 2.01 arc sec, or ~16 by 13 kpc at the redshift of W2246–0526, and it is illustrated by the dashed ellipse. The dashed contours represent CO levels of [2.5, 3, 4, 6, 9] × σ, where σ is the measured RMS of the background. The CO(2→1) emission is only marginally resolved, slightly extending toward the companion C3, northeast of W2246–0526, and southeast in the direction of the tidal tail.

We interpret these results as showing that merger-driven accretion of neighbor galaxies can be a catalytic mechanism that simultaneously (i) obscures the central SMBH in W2246–0526 under large columns of dust and gas and (ii) provides the intermittent, large-scale influx of material needed to generate its extreme luminosity and maintain star formation in the host galaxy, which would otherwise quickly deplete its gas reservoir. The energetic AGN feedback resulting from this accretion is likely responsible for maintaining the turbulence of the gas at the center of W2246–0526. Slow, nearly isotropic ISM outflows on scales of a few kiloparsecs can coexist with the accretion of material stripped from in-falling galaxies at larger scales (even if the companions themselves may only fly by), which can be funneled efficiently into the central AGN through collimated, filamentary structures (*25*–*27*). If W2246–0526 is representative of the hot DOG population, our results suggest that hyperluminous obscured quasars may be interacting systems, the result of ongoing merger-driven peaks of SMBH accretion and massive galaxy assembly in the early Universe.

REFERENCES AND NOTES

1. A. V. Kravtsov, S. Borgani, *Annu. Rev. Astron. Astrophys.* **50**, 353–409 (2012).
2. D. B. Sanders, I. F. Mirabel, *Annu. Rev. Astron. Astrophys.* **34**, 749–792 (1996).
3. E. L. Wright *et al.*, *Astron. J.* **140**, 1868–1881 (2010).
4. J. Wu *et al.*, *Astrophys. J.* **756**, 96 (2012).
5. P. Eisenhardt *et al.*, *Astrophys. J.* **755**, 173 (2012).
6. J. Wu *et al.*, *Astrophys. J.* **852**, 96 (2017).
7. D. B. Sanders *et al.*, *Astrophys. J.* **325**, 74 (1988).
8. P. F. Hopkins, L. Hernquist, T. J. Cox, D. Kereš, *Astrophys. J. Suppl. Ser.* **175**, 356–389 (2008).
9. S. F. Jones *et al.*, *Mon. Not. R. Astron. Soc.* **443**, 146–157 (2014).
10. R. J. Assef *et al.*, *Astrophys. J.* **804**, 27 (2015).
11. L. Fan, S. F. Jones, Y. Han, K. K. Knudsen, *Publ. Astron. Soc. Pac.* **129**, 124101 (2017).
12. D. Farrah *et al.*, *Astrophys. J.* **844**, 106 (2017).
13. L. Fan *et al.*, *Astrophys. J.* **822**, 32 (2016).
14. C.-W. Tsai *et al.*, *Astrophys. J.* **805**, 90 (2015).
15. Materials and methods are available as supplementary materials.
16. T. Diaz-Santos *et al.*, *Astrophys. J.* **816**, 6 (2016).
17. B. Trakhtenbrot *et al.*, *Astrophys. J.* **836**, 8 (2017).
18. R. Decarli *et al.*, *Nature* **545**, 457–461 (2017).
19. E. da Cunha *et al.*, *Astron. Astrophys.* **523**, A78 (2010).
20. B. T. Draine *et al.*, *Astrophys. J.* **663**, 866–894 (2007).
21. P. van Dokkum *et al.*, *Astrophys. J.* **813**, 23 (2015).
22. N. Scoville *et al.*, *Astrophys. J.* **837**, 150 (2017).
23. C. Schreiber *et al.*, *Astron. Astrophys.* **575**, A74 (2015).
24. R. Trainor, C. C. Steidel, *Astrophys. J.* **775**, L3 (2013).
25. M. Gaspari, M. Ruszkowski, S. P. Oh, *Mon. Not. R. Astron. Soc.* **432**, 3401–3422 (2013).
26. H. R. Russell *et al.*, *Mon. Not. R. Astron. Soc.* **458**, 3134–3149 (2016).
27. H. R. Russell *et al.*, *Mon. Not. R. Astron. Soc.* **472**, 4024–4037 (2017).

ACKNOWLEDGMENTS

We thank A. Stanford and M. Baloković for helping to obtain optical spectra for W2246–0526 on November 2010 and October 2013, respectively. We thank J. González López for helpful suggestions regarding the cleaning algorithms of CASA. ALMA is a partnership of the European Southern Observatory (ESO) (representing its member states), NSF (United States), and the National Institute of Natural Sciences (Japan), together with the National Research Council (Canada) and National Science Council and Academia Sinica's Institute of Astronomy and Astrophysics (Taiwan), in cooperation with the Republic of Chile. The Joint ALMA Observatory is operated by ESO, Associated Universities Inc. (AUI)/National Radio Astronomy Observatory (NRAO) and National Astronomical Observatory of Japan. The NRAO is a facility of NSF operated under cooperative agreement by AUI. This work is also based in part on archival observations from the Spitzer Space Telescope, the Herschel Space Observatory, WISE, as well as from the NASA/European Space agency HST. Some of the data were obtained at the W. M. Keck Observatory, which is operated as a scientific partnership among the California Institute of Technology, the University of California, and NASA. The Observatory was made possible by the generous financial support of the W. M. Keck Foundation. **Funding:** T.D.-S. acknowledges support from ALMA-CONYCIT project 31130005 and Fondo Nacional de Desarrollo Científico y Tecnológico (FONDECYT) project 1151239. R.J.A. acknowledges support from FONDECYT 1151408. The work of C-W.T., J.W., P.E., and D.S. was carried out at the Jet Propulsion Laboratory, California Institute of Technology, under a contract with NASA, and supported by grant ADAP13-0092. M.A. acknowledges partial support from FONDECYT through grant 1140099. J.W. acknowledges support from the Ministry of Science and Technology of China through grant 2016YFA0400702 and National Natural Science Foundation of China 11673029. This research was supported by the Basic Science Research Program through the National Research Foundation of Korea (NRF) funded by the Ministry of Education (NRF-2017R1A6A3A04005158). **Author contributions:** T.D.-S. lead the overall project. R.J.A. and A.W.B. contributed to the interpretation of the results. M.A. helped with processing the ALMA and VLA data. D.S. led the spectroscopic identification campaign of hot DOGs. C.-W.T., P.E., and J.W. contributed to the discussion of the results. K.D., H.I, G.L., and F.L. were part of the team that acquired the optical spectra of W2246–0526. **Competing interests:** The authors declare that there are no competing interests. **Data and materials availability:** The ALMA observations are available at http://almascience.nrao.edu/aq under project 2015.1.00883.S (principal investigator, T.D.-S.). The VLA observations can be retrieved from https://science.nrao.edu/facilities/vla/archive/index under project 15B-192 (principal investigator, R.J.A.). The Spitzer data can be retrieved from the Spitzer Heritage Archive (SHA) at http://sha.ipac.caltech.edu/applications/Spitzer/SHA under project 70162 (principal investigator, P.E.). The Herschel data are available at the Herschel Science Archive (HSA) http://archives.esac.esa.int/hsa/whsa under project OT1_peisenha_1 (principal investigator, P.E.). The WISE data can be accessed at http://wise2.ipac.caltech.edu/docs/release/allwise with documentation at http://wise2.ipac.caltech.edu/docs/release/allwise/expsup. The HST data are available at https://archive.stsci.edu/hst/search.php under project 12930 (principal investigator, C. Bridge). The Keck data are available in the Keck Observatory Archive at https://koa.ipac.caltech.edu by searching with the observation dates (*15*).

SUPPLEMENTARY MATERIALS

www.sciencemag.org/content/362/6418/1034/suppl/DC1
Materials and Methods
Figs. S1 to S4
Table S1
References (*28*–*57*)

9 November 2017; accepted 26 October 2018
Published online 15 November 2018
10.1126/science.aap7605

SOLID-STATE PHYSICS

Isostructural metal-insulator transition in VO_2

D. Lee[1], B. Chung[2], Y. Shi[3], G.-Y. Kim[4]*, N. Campbell[5], F. Xue[3], K. Song[4], S.-Y. Choi[4]*, J. P. Podkaminer[1], T. H. Kim[1], P. J. Ryan[6,7], J.-W. Kim[6], T. R. Paudel[8], J.-H. Kang[1], J. W. Spinuzzi[9], D. A. Tenne[9], E. Y. Tsymbal[8], M. S. Rzchowski[5], L. Q. Chen[3], J. Lee[2]†, C. B. Eom[1]†

The metal-insulator transition in correlated materials is usually coupled to a symmetry-lowering structural phase transition. This coupling not only complicates the understanding of the basic mechanism of this phenomenon but also limits the speed and endurance of prospective electronic devices. We demonstrate an isostructural, purely electronically driven metal-insulator transition in epitaxial heterostructures of an archetypal correlated material, vanadium dioxide. A combination of thin-film synthesis, structural and electrical characterizations, and theoretical modeling reveals that an interface interaction suppresses the electronic correlations without changing the crystal structure in this otherwise correlated insulator. This interaction stabilizes a nonequilibrium metallic phase and leads to an isostructural metal-insulator transition. This discovery will provide insights into phase transitions of correlated materials and may aid the design of device functionalities.

Understanding metal-insulator transitions in strongly correlated materials is one of the major challenges in condensed matter physics (*1*–*5*), with implications for both fundamental science and technology (*6*, *7*). Correlated materials exhibit strong coupling between charge, spin, and lattice degrees of freedom, so that the metal-insulator transition is almost always accompanied by an associated structural phase transition. This coexistence obscures the underlying physics, making it difficult to disentangle the different intrinsic interactions controlling the metal-insulator transition. Furthermore, the structural transition generally limits the ultimate switching speed (*8*, *9*) and endurance (*6*, *10*) of ultrafast electronic devices (*6*, *7*, *11*) based on the metal-insulator transition in these correlated materials. Achieving an isostructural metal-insulator transition is thus of great interest.

As a model system for this study, we chose the archetypal correlated material vanadium dioxide (VO_2) (*12*–*27*). VO_2 is metallic at high temperatures and becomes insulating near room temperature (341 K in bulk) (*12*); the metal-insulator transition is accompanied by a structural phase transition from the high-temperature rutile structure to the low-temperature monoclinic structure via the formation of V-V dimers along the *c* axis. There has been extensive debate over whether the primary mechanism of the metal-insulator transition in VO_2 is an electron-lattice interaction (Peierls transition) (*13*) or an electron-electron interaction (Mott transition) (*14*), and it is now accepted that both Peierls and Mott physics are important (*15*, *16*). In particular, recent ultrafast photoexcitation experiments (*21*, *22*) have revealed the presence of a nonequilibrium metallic monoclinic state in addition to the known bulk equilibrium phases (i.e., insulating monoclinic and metallic rutile phases). This metallic transition in photoexcited monoclinic VO_2 could originate from the dynamically screened Coulomb interaction (*22*), assisted by an electronically one-dimensional characteristic of V-V dimers (*27*), and suggests a route for an isostructural metal-insulator transition: If the metallic monoclinic phase could be stabilized, rather than just being transient, we could achieve an isostructural metallic transition in insulating monoclinic VO_2.

To this end, we considered a nanoscale bilayer consisting of two VO_2 layers with different transition temperatures (T_1 and T_2 in Fig. 1A). In this bilayer, a rutile/monoclinic heterostructure can occur at intermediate temperatures between T_1 and T_2, in which interval the desired metallic monoclinic phase might be stabilized (e.g., via a collective carrier delocalization) (*19*). To experimentally realize such a bilayer, we needed to achieve control over the transition temperature in a VO_2 layer; to do that, we used an intrinsic point defect (i.e., oxygen vacancy) (*28*) and the resulting electron doping. Introducing a minute amount of oxygen vacancies can lower the transition temperature of VO_2 without compromising the sharp metal-insulator transition (*29*). By changing the oxygen partial pressure during film growth (figs. S1 to S4) (*30*), we prepared an artificial bilayer (Fig. 1B, inset), fully coherent on TiO_2 (001) substrate, consisting of slightly oxygen-deficient $VO_{2-\delta}$ and stoichiometric VO_2 layers. The individual 8-nm-thick $VO_{2-\delta}$ and VO_2 layers have transition temperatures of T_1 ~ 279 K and T_2 ~ 287 K, respectively (Fig. 1A).

To visualize the oxygen vacancy profile in the bilayer, we carried out atomic-scale imaging using scanning transmission electron microscopy (STEM) (*30*). In STEM, the low-angle annular dark field (LAADF) image is very sensitive to the strain fields from oxygen vacancies (*28*), whereas the high-angle annular dark field (HAADF) image is dominated by the (high-Z) cation sites (Fig. 1B). The HAADF image shows little intensity change across the $VO_{2-\delta}/VO_2$ interface (denoted by the white dashed line). In contrast, the LAADF image displays a noticeable, abrupt intensity change across the $VO_{2-\delta}/VO_2$ interface, emphasizing the oxygen deficiency in the $VO_{2-\delta}$ layer. Our results show

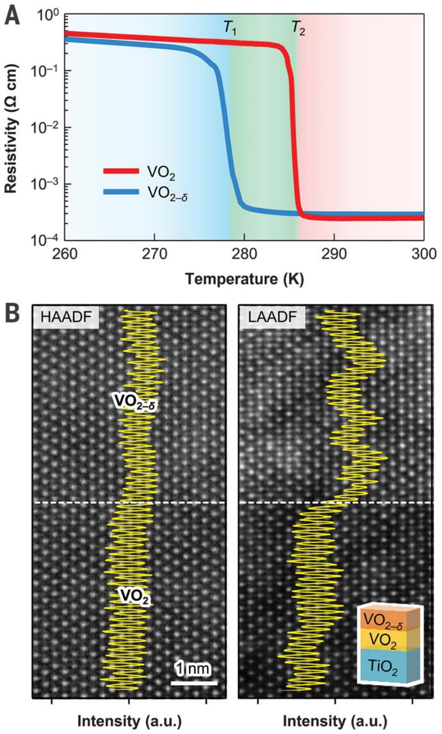

Fig. 1. Design of an artificial $VO_{2-\delta}/VO_2$ bilayer. (**A**) Electrical resistivity measured as a function of temperature of 8-nm-thick epitaxial VO_2 and $VO_{2-\delta}$ single-layer films on (001) TiO_2 substrates. The oxygen vacancy concentration δ is roughly estimated as δ ~ 0.01 (fig. S3). (**B**) HAADF- and LAADF-STEM images of the $VO_{2-\delta}/VO_2$ bilayer (inset) projected along [100]. Yellow lines show the average line profile of the HAADF (left) and LAADF (right) image intensities. White dashed lines represent a nominal interface between VO_2 and $VO_{2-\delta}$.

---

[1]Department of Materials Science and Engineering, University of Wisconsin, Madison, WI 53706, USA. [2]School of Advanced Materials Science and Engineering, Sungkyunkwan University, Suwon 16419, Korea. [3]Department of Materials Science and Engineering, Pennsylvania State University, University Park, PA 16802, USA. [4]Department of Materials Modeling and Characterization, Korea Institute of Materials Science, Changwon 642-831, Korea. [5]Department of Physics, University of Wisconsin, Madison, WI 53706, USA. [6]Advanced Photon Source, Argonne National Laboratory, Argonne, IL 60439, USA. [7]School of Physical Sciences, Dublin City University, Dublin 9, Ireland. [8]Department of Physics and Astronomy and Nebraska Center for Materials and Nanoscience, University of Nebraska, Lincoln, NE 68588, USA. [9]Department of Physics, Boise State University, Boise, ID 83725, USA.
*Present address: Department of Materials and Science, POSTECH, Pohang 37673, Korea.
†Corresponding author. Email: eom@engr.wisc.edu (C.B.E.); jclee@skku.edu (J.L.)

that introducing a small amount of oxygen vacancies, rather than extrinsic dopants, creates a chemically sharp interface with a sub–1-nm width (fig. S5) and leads to a quasi-homogeneous, single-crystalline character of the bilayer. Electron energy loss spectroscopy (EELS) measurements (fig. S6) independently quantified the oxygen vacancy difference between the layers. Considering this nanoengineered oxygen vacancy profile, we expect two distinct transition temperatures in the top $VO_{2-\delta}$ and bottom VO_2 layers.

Using Raman spectroscopy (*30*), we monitored the structural phase transition in the $VO_{2-\delta}$/VO_2 bilayer (Fig. 2, A and B). With decreasing temperature, several noticeable Raman peaks (e.g., ω_1, ω_2, and ω_3 peaks in Fig. 2A) arise suddenly from the monoclinic distortions during the structural transition (*31*, *32*). Our quantitative analysis (Fig. 2B) clearly shows the two-step structural phase transition in the $VO_{2-\delta}$/VO_2 bilayer, contrary to the single-step transition in a VO_2 single layer. Using temperature-dependent x-ray diffraction measurements (Fig. 2, C to E) (*30*) and phase-field simulations (fig. S14), we confirmed the two-step structural phase transition in the bilayer. This two-step structural phase transition can be explained by two separate structural transitions: at T ~ 279 K for the top $VO_{2-\delta}$ layer, and at T ~ 287 K for the bottom VO_2 layer. At intermediate temperatures between T ~ 279 K and 287 K (Fig. 2, B and E, green), the top $VO_{2-\delta}$ and bottom VO_2 layers have rutile and monoclinic structures, respectively, which together form the desired rutile/monoclinic heterostructure (Fig. 2B, inset).

We explored the electronic phase transition in the $VO_{2-\delta}$/VO_2 bilayer by measuring the electrical resistivity (Fig. 3A) and carrier concentration (fig. S7). In stark contrast to the two-step structural transition, our bilayer showed a single-step, collective metal-insulator transition at T ~ 279 K. The electronic phase transition of the bilayer looked nearly identical to that of a $VO_{2-\delta}$ single layer (Fig. 3A, black dashed line), which means that in the $VO_{2-\delta}$/VO_2 bilayer, the electronic phase (i.e., metallic or insulating) of the VO_2 layer collectively follows that of the $VO_{2-\delta}$ layer. Notably, when an ultrathin (~2 nm) TiO_2 layer was inserted between $VO_{2-\delta}$ and VO_2, the $VO_{2-\delta}$/TiO_2/VO_2 system exhibited a two-step metal-insulator transition (fig. S8). This confirms the intrinsic effect of the rutile/monoclinic interface on the observed single-step, collective metal-insulator transition in the $VO_{2-\delta}$/VO_2 bilayer.

Taken together, our observations of the two-step structural and single-step electronic phase transitions unambiguously confirm the emergence of a stable metallic monoclinic phase in the $VO_{2-\delta}$/VO_2 bilayer. With the decrease in temperature, the bottom VO_2 layer exhibited the rutile-to-monoclinic structural transition at T ~ 287 K (Fig. 3B), but the global metallicity of the whole bilayer remained unchanged (Fig. 3A and fig. S7). This is consistent with the explanation that, when interfaced with the metallic rutile $VO_{2-\delta}$ layer, the bottom VO_2 layer becomes a stable metallic monoclinic phase. This interface-induced bulk carrier delocalization (*19*) plays a decisive role in the single-step metal-insulator transition. Figure 3C shows little change in the peak positions of ω_2 and ω_3, attributed to the ionic motion of V-V dimers (*23*, *32*), during the metal-insulator transition at ~279 K. This directly illustrates the isostructural metal-insulator transition without any crystalline structure change at ~279 K in the bottom stoichiometric VO_2 layer.

To further understand the emergence of isostructural metal-insulator transition, we carried out theoretical modeling of the rutile/monoclinic heterostructure. First, we performed non–spin-polarized density functional theory (DFT) calculations (*30*) with Hubbard U correction for properly predicting the insulating monoclinic ground state in bulk VO_2 (*33*). The calculated density of states of the heterostructure (Fig. 4A) manifested the metallic nature in the monoclinic region (Fig. 4B and fig. S10), consistent with our experimental observation (Fig. 3). Inside the monoclinic region, the electronic structure was strongly modified, resulting in noticeable band gap narrowing. This was largely driven by hole doping of the monoclinic region (fig. S12), stemming from the different work functions of the rutile and monoclinic phases (*34*). Such a hole doping reduces electronic correlations, causing a complete collapse of the band gap in monoclinic VO_2 (*22*). Simultaneously, from the DFT results, we infer that the rutile/monoclinic heterostructure has a very small interfacial energy (*30*), which may also play a role in stabilizing the metallic monoclinic phase.

To explore the effects of electronic correlations and interfacial energy, we used a generalized Landau thermodynamic approach implemented

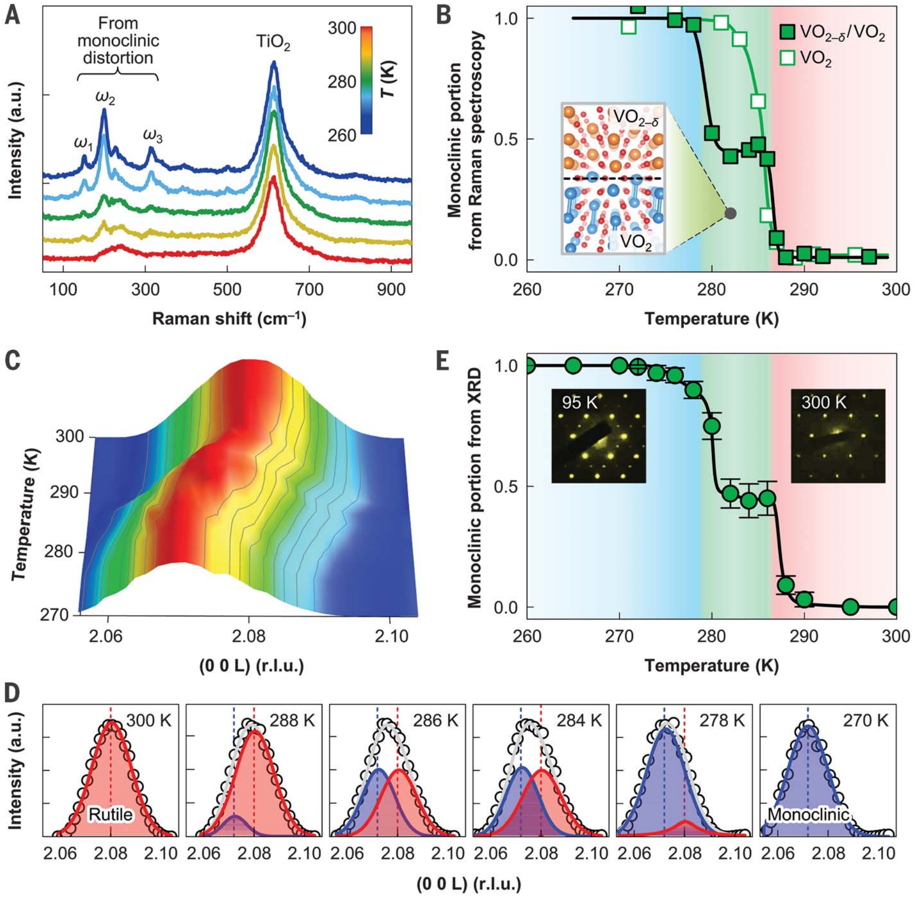

Fig. 2. Structural phase transition in the $VO_{2-\delta}$/VO_2 bilayer. (**A**) Raman spectra of $VO_{2-\delta}$ (8 nm)/VO_2 (8 nm) bilayer at various temperatures. Raman peaks from the monoclinic distortion are denoted ω_1, ω_2, and ω_3; a.u., arbitrary units. (**B**) Relative monoclinic portion as a function of temperature, estimated from monoclinic Raman intensity in (A). Inset: Schematic of atomic structure of $VO_{2-\delta}$/VO_2 bilayer at intermediate temperatures. (**C**) X-ray diffraction (XRD) (00L) scans of $VO_{2-\delta}$/VO_2 bilayer, measured upon cooling. (**D**) Representative XRD peaks at several temperatures. Red and blue vertical dashed lines indicate the XRD peak positions for rutile (L ~ 2.080) and monoclinic (L ~ 2.072) phases, respectively. We fit the measured XRD data (open circles) with a sum (gray curve) of two Gaussian curves with the peaks at L ~ 2.080 (red curve) and L ~ 2.072 (blue curve). (**E**) Relative monoclinic portion as a function of temperature, estimated from XRD peak analysis in (D). Error bars denote SD of the fitted peak area. Insets show the measured electron diffraction patterns of the bilayer at low and high temperatures.

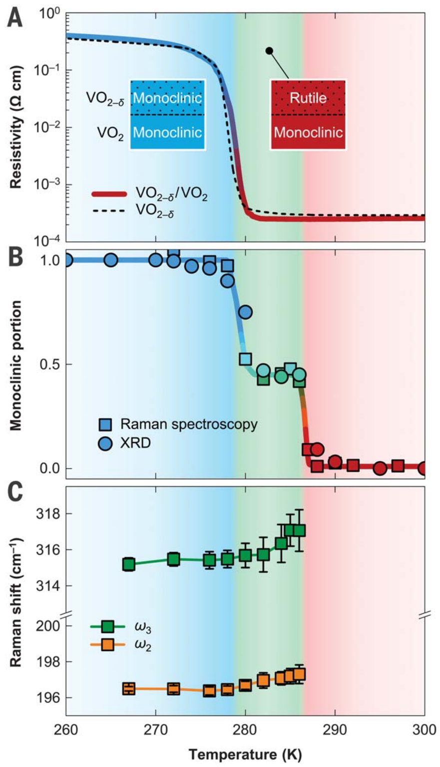

Fig. 3. Isostructural metal-insulator transition in the VO$_{2-\delta}$/VO$_2$ bilayer. (**A**) Electrical resistivity versus temperature of VO$_{2-\delta}$ (8 nm)/VO$_2$ (8 nm) bilayer (solid line) and 8-nm-thick VO$_{2-\delta}$ single layer (black dashed line), measured upon cooling. Metallic and insulating phases are represented by red and blue colors, respectively. (**B**) Monoclinic portion (from Fig. 2, B and E) as a function of temperature. (**C**) Temperature dependence of monoclinic Raman shift (i.e., ω_2 and ω_3 in Fig. 2A). Error bars denote SD of the fitted Raman peak position. We fit the measured Raman peak with a Gaussian curve.

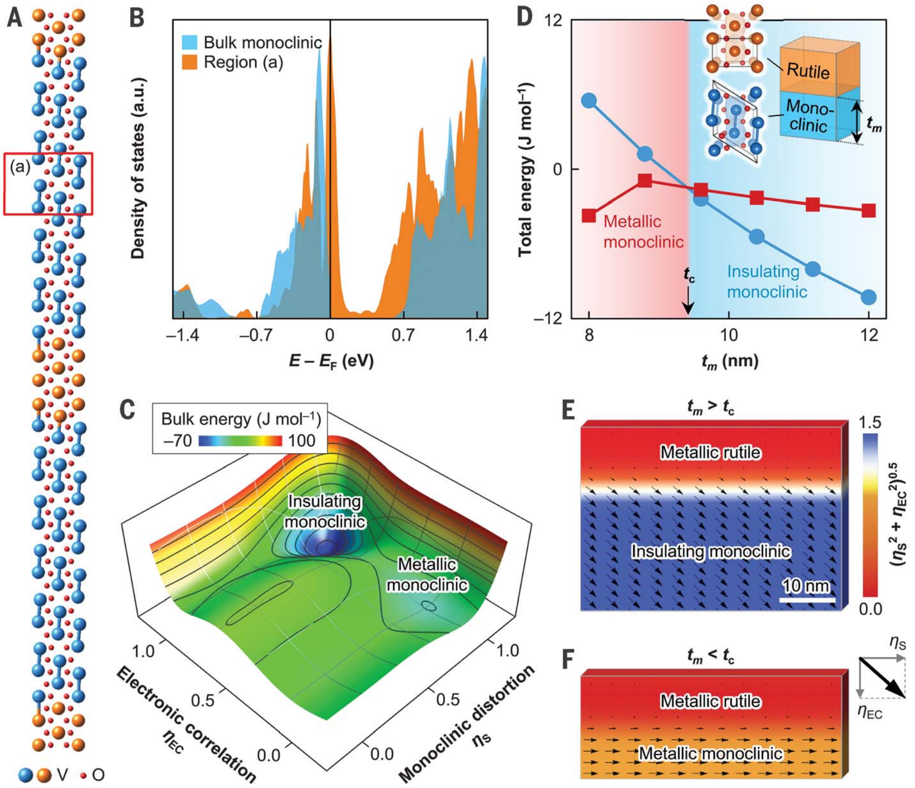

Fig. 4. Theoretical modeling of the metallic monoclinic VO$_2$ phase. (**A**) The rutile/monoclinic heterostructure used in the DFT calculation (*30*). V atoms are shown in two colors: orange for rutile VO$_2$ and blue for monoclinic VO$_2$. (**B**) The calculated density of states of the local monoclinic region [denoted by (a) in (A)] in the rutile/monoclinic heterostructure shows a metallic nature, distinct from the insulating nature of the bulk monoclinic VO$_2$ (blue). (**C**) Free energy landscape of bulk VO$_2$ at 287 K, just below the transition temperature. (**D**) Total energies as a function of t_m in the rutile/monoclinic heterostructure. t_c is estimated to be ~9.4 nm. (**E** and **F**) Stable states of the rutile/monoclinic heterostructure for $t_m > t_c$ (E) and $t_m < t_c$ (F). The arrows represent the two-component order parameter (η_S, η_{EC}); the color represents the norm $(\eta_S^2 + \eta_{EC}^2)^{0.5}$.

in phase-field modeling (*30*). The Landau potential incorporates two different order parameters: η_S, describing the structural transition [i.e., from rutile ($\eta_S = 0$) to monoclinic ($\eta_S = 1$) phase], and η_{EC}, describing the electronic correlations, which control the metal-insulator transition [i.e., from metal ($\eta_{EC} = 0$) to insulator ($\eta_{EC} = 1$)]. We found only two bulk equilibrium phases: the metallic rutile phase with little electronic correlation ($\eta_S = \eta_{EC} = 0$) at high temperatures, and the correlated insulating monoclinic phase ($\eta_S = \eta_{EC} = 1$) at low temperatures (fig. S13). However, in addition to these bulk equilibrium phases, we predict the presence of a nonequilibrium metallic monoclinic phase with suppressed correlation ($\eta_S = 1$ and $\eta_{EC} = 0$), as represented by the local minimum in the energy landscape just below the transition temperature (Fig. 4C).

We then used phase-field modeling to investigate phase stabilities in the experimentally studied rutile/monoclinic heterostructure. Figure 4D shows the total energy of the rutile/monoclinic heterostructure as a function of the thickness t_m of the monoclinic layer. The interfacial energy between metallic rutile and metallic monoclinic phases is naturally smaller than that between metallic rutile and insulating monoclinic phases in the phase-field model, owing to the homogeneous η_{EC} in the former case (*30*). When t_m is below critical thickness t_c, the interfacial energy contribution dominates over the bulk energy contribution, and as a result, the metallic monoclinic phase with suppressed correlation (i.e., $\eta_{EC} = 0$) becomes energetically preferred and stabilized (fig. S14). It is noteworthy that our experimental and theoretical results have consistently demonstrated the isostructural metal-insulator transition in device-relevant thin-film geometries of genuine VO$_2$, without the necessity of specific conditions, such as ultrafast photoexcitation (*21*, *22*), high pressure (*23*), or suppression of structural distortion at the surface (*5*, *25*). Stabilizing the monoclinic structure through our bilayer approach separates the electronic and structural phase transitions, in contrast to previous reports (*35*, *36*).

There has been a growing interest in nonequilibrium states in correlated materials (*21*, *22*, *37*), because of the opportunity to discover exotic physics not exhibited in equilibrium. Ultrafast spectroscopies have been mainly used for exploring nonequilibrium states; our study paves a way to stabilize and explore the nonequilibrium phase (e.g., metallic monoclinic state in VO$_2$) in a controlled way. Because VO$_2$ is a simple spin-½ system with one *d* electron (*38*), it will be intriguing to study the spin and orbital physics in the stabilized metallic monoclinic phase. We anticipate that our approach for artificial stabilization of nonequilibrium states will be generally applicable to correlated materials, so that a variety of unconventional phenomena can be designed through heterostructure engineering.

REFERENCES AND NOTES

1. M. Imada, A. Fujimori, Y. Tokura, *Rev. Mod. Phys.* **70**, 1039 (1998).
2. M. Uehara, S. Mori, C. H. Chen, S.-W. Cheong, *Nature* **399**, 560–563 (1999).
3. L. Zhang, C. Israel, A. Biswas, R. L. Greene, A. de Lozanne, *Science* **298**, 805–807 (2002).

4. E. Dagotto, *Science* **309**, 257–262 (2005).
5. R. G. Moore *et al*., *Science* **318**, 615–619 (2007).
6. Z. Yang, C. Ko, S. Ramanathan, *Annu. Rev. Mater. Res.* **41**, 337–367 (2011).
7. D. M. Newns *et al*., *Appl. Phys. Lett.* **73**, 780–782 (1998).
8. A. Cavalleri, Th. Dekorsy, H. H. W. Chong, J. C. Kieffer, R. W. Schoenlein, *Phys. Rev. B* **70**, 161102(R) (2004).
9. P. Baum, D.-S. Yang, A. H. Zewail, *Science* **318**, 788–792 (2007).
10. D. Maurer, A. Leue, *Mater. Sci. Eng. A* **370**, 440–443 (2004).
11. Y. Zhou, S. Ramanathan, *Proc. IEEE* **103**, 1289–1310 (2015).
12. F. J. Morin, *Phys. Rev. Lett.* **3**, 34–36 (1959).
13. R. M. Wentzcovitch, W. W. Schulz, P. B. Allen, *Phys. Rev. Lett.* **72**, 3389–3392 (1994).
14. T. M. Rice, H. Launois, J. P. Pouget, *Phys. Rev. Lett.* **73**, 3042 (1994).
15. S. Biermann, A. Poteryaev, A. I. Lichtenstein, A. Georges, *Phys. Rev. Lett.* **94**, 026404 (2005).
16. M. W. Haverkort *et al*., *Phys. Rev. Lett.* **95**, 196404 (2005).
17. M. M. Qazilbash *et al*., *Science* **318**, 1750–1753 (2007).
18. M. Liu *et al*., *Nature* **487**, 345–348 (2012).
19. M. Nakano *et al*., *Nature* **487**, 459–462 (2012).
20. J. Jeong *et al*., *Science* **339**, 1402–1405 (2013).
21. V. R. Morrison *et al*., *Science* **346**, 445–448 (2014).
22. D. Wegkamp *et al*., *Phys. Rev. Lett.* **113**, 216401 (2014).
23. E. Arcangeletti *et al*., *Phys. Rev. Lett.* **98**, 196406 (2007).
24. Z. Tao *et al*., *Phys. Rev. Lett.* **109**, 166406 (2012).
25. J. Laverock *et al*., *Phys. Rev. Lett.* **113**, 216402 (2014).
26. J. D. Budai *et al*., *Nature* **515**, 535–539 (2014).
27. V. Eyert, *Ann. Phys.* **11**, 650–704 (2002).
28. D. A. Muller, N. Nakagawa, A. Ohtomo, J. L. Grazul, H. Y. Hwang, *Nature* **430**, 657–661 (2004).
29. C. H. Griffiths, H. K. Eastwood, *J. Appl. Phys.* **45**, 2201–2206 (1974).
30. See supplementary materials.
31. R. Srivastava, L. L. Chase, *Phys. Rev. Lett.* **27**, 727–730 (1971).
32. L. Bai *et al*., *Phys. Rev. B* **91**, 104110 (2015).
33. X. Yuan, Y. Zhang, T. A. Abtew, P. Zhang, W. Zhang, *Phys. Rev. B* **86**, 235103 (2012).
34. C. Ko, Z. Yang, S. Ramanathan, *ACS Appl. Mater. Interfaces* **3**, 3396–3401 (2011).
35. M. Yang *et al*., *Sci. Rep.* **6**, 23119 (2016).
36. The supplementary x-ray data in (*35*) indicate that a structural transition remains.
37. J. Kim *et al*., *Science* **346**, 1205–1208 (2014).
38. H. He *et al*., *Phys. Rev. B* **94**, 161119(R) (2016).

ACKNOWLEDGMENTS

Funding: Supported by the NSF under DMREF grant DMR-1629270, AFOSR grant FA9550-15-1-0334, and Office of Naval Research N00014-13-1-0183. Transport measurement at the University of Wisconsin–Madison was supported by the U.S. Department of Energy (DOE), Office of Science, Office of Basic Energy Sciences (BES), under award DE-FG02-06ER46327. The work at Sungkyunkwan University was supported by National Research Foundation of Korea through the Basic Research Program (2009-0092809) and KISTI supercomputing center (KSC-2015-C3-067). The work at Penn State is also partially supported by the NSF MRSEC under grant DMR-1420620 (Y.S.). S.Y.C. and G.Y.K. acknowledge the support the Global Frontier Hybrid Interface Materials of the NRF funded by Korea Government (2013M3A6B1078872). K.S. acknowledges the Fundamental Research Program of the Korean Institute of Materials Science (PNK5570). The research at the University of Nebraska–Lincoln is supported by NSF through the Nebraska Materials Science and Engineering Center (MRSEC grant DMR-1420645). Use of the Advanced Photon Source, an Office of Science User Facility operated for the U.S. DOE Office of Science by Argonne National Laboratory, was supported by the DOE under contract DE-AC02-06CH11357. **Author contributions:** D.L. and C.B.E. conceived the project; C.B.E., M.S.R., and D.A.T. supervised the experiments; J.L., L.Q.C., and E.Y.T. supervised the theoretical calculations; D.L., J.P.P., and C.B.E. fabricated thin films and performed structural characterization; B.C., T.R.P., E.Y.T., and J.L. performed density functional theory calculations; Y.S., F.X., and L.Q.C. performed phase-field simulations; G.-Y.K., K.S., and S.-Y.C. performed scanning transmission electron microscopy experiments; N.C., T.H.K., J.-H.K., and M.S.R. performed transport measurements; P.J.R. and J.-W.K. performed temperature-dependent x-ray diffraction experiments; J.W.S. and D.A.T. performed Raman spectroscopy experiments; D.L., J.L., L.Q.C., M.S.R., E.Y.T., and C.B.E. prepared the manuscript; and C.B.E. directed the overall research. **Competing interests:** D.L. and C.B.E. are co-inventors on a U.S. patent application based on the results of this work filed by the University of Wisconsin–Madison. **Data and materials availability:** For our DFT calculations, we used VASP, a commercial software package (www.vasp.at/). All data are available in the manuscript or the supplementary materials.

SUPPLEMENTARY MATERIALS

www.sciencemag.org/content/362/6418/1037/suppl/DC1
Materials and Methods
Figs. S1 to S14
Table S1
Data S1
References (*39*–*59*)

17 February 2017; resubmitted 28 September 2017
Accepted 12 October 2018
10.1126/science.aam9189

SUPERCONDUCTIVITY

Uniaxial pressure control of competing orders in a high-temperature superconductor

H.-H. Kim[1]*, S. M. Souliou[2]*†, M. E. Barber[3], E. Lefrançois[1,2], M. Minola[1], M. Tortora[1]‡, R. Heid[4], N. Nandi[3], R. A. Borzi[5], G. Garbarino[2], A. Bosak[2], J. Porras[1], T. Loew[1], M. König[3], P. M. Moll[3], A. P. Mackenzie[3,6], B. Keimer[1], C. W. Hicks[3], M. Le Tacon[4]§

Cuprates exhibit antiferromagnetic, charge density wave (CDW), and high-temperature superconducting ground states that can be tuned by means of doping and external magnetic fields. However, disorder generated by these tuning methods complicates the interpretation of such experiments. Here, we report a high-resolution inelastic x-ray scattering study of the high-temperature superconductor $YBa_2Cu_3O_{6.67}$ under uniaxial stress, and we show that a three-dimensional long-range-ordered CDW state can be induced through pressure along the *a* axis, in the absence of magnetic fields. A pronounced softening of an optical phonon mode is associated with the CDW transition. The amplitude of the CDW is suppressed below the superconducting transition temperature, indicating competition with superconductivity. The results provide insights into the normal-state properties of cuprates and illustrate the potential of uniaxial-pressure control of competing orders in quantum materials.

Moderately doped high-temperature superconductors show an ubiquitous tendency toward charge order (*1*). Manifestations of charge ordering include striped order—an incommensurate modulation of both charge and spin that suppresses superconductivity in lanthanum-based cuprates (*2*, *3*)—and a biaxial charge density wave (CDW) with quasi–two-dimensional (2D) short-range order in the CuO_2 planes of all other cuprate families (*4*–*12*). The origin of CDW order and its relationship with superconductivity are widely debated issues. It is well-established that static CDW order and superconductivity compete; however, it is not clear whether the two orders are best described as mutually incompatible (*7*, *8*), as different manifestations of the same pairing interaction (*13*), or as different aspects of a composite order parameter (*14*, *15*). These issues have direct and important implications for the mechanism of high-temperature superconductivity (HTSC).

The $YBa_2Cu_3O_{6+x}$ ($YBCO_{6+x}$) family has been particularly well studied because doping-induced structural disorder is less severe than in other families. In this compound, the competition between superconductivity and CDW order is evidenced by the depression of the CDW amplitude upon cooling below the superconducting transition temperature (T_c) (*7*, *8*) and by its enhancement in magnetic fields that weaken superconductivity (*8*, *9*). Nuclear magnetic resonance (NMR) and x-ray studies further showed that in fields larger than ~15 T, a 3D long-range ordered uniaxial CDW (*16*–*19*) is induced. This 3D order is distinct from the 2D one, although they coexist and are related to each other; for example, they have the same in-plane incommensurability. The 3D order has an identifiable thermodynamic transition (*20*–*22*), whereas the 2D CDW onsets gradually (*23*, *24*), and it is not clear whether it constitutes an alternative ground state or is, for example, a vestige of the 3D order that is weakened by the interaction with superconductivity.

We used inelastic x-ray scattering (IXS) on a sample of $YBCO_{6.67}$ (T_c = 65K, doping p = 0.12) to show that uniaxial pressure along the crystallographic *a* axis can induce long-range 3D CDW order, in the absence of a magnetic field.

We first specify why we chose to work with uniaxial pressures. In the doping range of interest ($0.08 < p < 0.15$), hydrostatic pressure yields, through self-doping and other effects, an increase of T_c (*25*). A recent study of the biaxial charge modulation further revealed its rapid suppression under hydrostatic pressure (*26*). However, it has long been established that, at least in the limit of low pressures, the effect of hydrostatic pressure on T_c reflects a net sum of larger effects of uniaxial pressures that almost cancel each other out (*27*, *28*). In particular, close to $p \sim 0.12$, where the charge modulation is maximized, uniaxial pressure applied along the *a* axis suppresses T_c (*29*, *30*).

In this study, we pressurized the sample using a piezoelectric-based apparatus similar to that used in recent studies of ruthenium oxides (*31*–*33*) but modified to allow x-ray transmission through the apparatus and the sample. For maximum scattering intensity, the thickness of the sample should match the absorption length at the working wavelength (λ = 0.6968 Å for this experiment), which is ~40 μm. However, to withstand strong compression without buckling, the length-to-thickness ratio of the sample cannot be too large (*31*), and a 40-μm thickness implies a length that is inconveniently short for reliable mounting. Therefore, we prepared a thicker needle from a $YBCO_{6.67}$ single crystal then used a plasma focused ion beam (PFIB) to thin down to 40-μm thickness the central portion over a length of ~200 μm (Fig. 1). The x-ray beam, with a spot size of 50 × 40 μm^2, was considerably smaller than the thinned central portion of the sample, so highly uniform strain is expected in the probed volume. All the strain values in this paper were calculated by using capacitive displacement sensor built into the pressure cell, the changes in the *c* axis lattice parameter measured from the (0 0 6) Bragg peak and the changes in T_c (30). The highest compression we reached was $\varepsilon_{xx} \sim -1.0\%$, where *ac* susceptibility measurements showed that T_c decreases (at a rate increasing with strain) to 48 ± 5 K (30).

The data on the 2D biaxial CDW are shown in Fig. 2. The scattering intensity of the biaxial CDW peaks at the reduced momentum transfer $\boldsymbol{q}_{2D} = (h, k, l) = (0, 0.31, 0.5)$, in reciprocal lattice units (r.l.u.) of the orthorhombic crystal structure (*7*, *8*). By contrast, the 3D CDW peaks at $\boldsymbol{q}_{3D} = (0, 0.31, 1)$ (*16*–*19*). Here, we will mostly refer to the total momentum transfers $\boldsymbol{Q}_{2D}$ = (H, K, L) = (0, 0.31, 6.5) and $\boldsymbol{Q}_{3D}$ = (0, 0.31, 7), around which measurements were carried out and where the structure factor of the CDWs is maximum (*34*, *35*). The color maps in Fig. 2, A and B, show the raw IXS intensity at ε_{xx} = 0% (Fig. 2A) and at –1.0% (Fig. 2B). Both data sets were measured below T_c (30). Two characteristic features of the CDW are clearly visible: the quasi-elastic "central" peak at $\boldsymbol{Q}_{2D}$ and the superconductivity-induced Kohn anomaly in the phonon spectra. In unstrained conditions, the latter consists of a ~15% softening of the low-lying acoustical phonon (at ~8 meV) at $\boldsymbol{Q}_{2D}$ (*35*). Comparing Fig. 2, A and B, it can be seen that the quasi-elastic peak is enhanced by the

---

[1]Max Planck Institute for Solid State Research, Heisenbergstraße 1, D-70569 Stuttgart, Germany. [2]European Synchrotron Radiation Facility (ESRF), BP 220, F-38043 Grenoble Cedex, France. [3]Max Planck Institute for Chemical Physics of Solids, Nöthnitzer Straße 40, 01187 Dresden, Germany. [4]Institute for Solid State Physics, Karlsruhe Institute of Technology, Hermann-v.-Helmholtz-Platz 176344 Karlsruhe, Germany. [5]Instituto de Física de Líquidos y Sistemas Biológicos (IFLYSIB), UNLP–Consejo Nacional de Investigaciones Científicas y Técnicas (CONICET), La Plata, Argentina and Departamento de Física, Facultad de Ciencias Exactas, Universidad Nacional de La Plata (UNLP), c.c. 16, suc. 4, 1900 La Plata, Argentina. [6]Scottish Universities Physics Alliance, School of Physics and Astronomy, University of St Andrews, St Andrews KY16 9SS, UK
*These authors contributed equally to this work.
†Present address: Institute for Solid State Physics, Karlsruhe Institute of Technology, Hermann-v.-Helmholtz-Platz 176344 Karlsruhe, Germany.
‡Present address: ams AG, Tobelbader Straße 30, 8141 Premstätten, Austria.
§Corresponding author. Email: matthieu.letacon@kit.edu

applied pressure. In Fig. 2C, it is seen that this enhancement occurs smoothly. At the highest strain, the integrated intensity of the peak is close to two times larger than that of the unstrained sample (Fig. 2D). Its half-width-at-half-maximum (HWHM) σ, which is inversely proportional to the modulation correlation length $\xi = \frac{1}{2\pi\sigma}$, decreases modestly under pressure (Fig. 2D). We did not resolve any shift of $\boldsymbol{Q}_{2D}$ with ε_{xx}. Last, a comparison of Fig. 2, A and B, reveals an increase of the low-energy spectral weight under pressure. Its phenomenology and relation to the Kohn anomaly will be discussed below.

We observed a much more notable response to uniaxial pressure in the scattering pattern at $\boldsymbol{Q}_{3D}$. We first looked at the strain dependence of the elastic peak intensity along the $\boldsymbol{Q} = (0, 0.315, L)$ line at $T = 50$ K (Fig. 3A). At $\varepsilon_{xx} \sim -0.8\%$, a small, narrow peak appears at $\boldsymbol{Q}_{3D}$. When the compression is further increased, to $\varepsilon_{xx} \sim -1.0\%$, this peak becomes much more intense. It appears on top of the broad profile centered around $l = 0.5$ ($L = 6.5$) that arises from the 2D CDW. The profile of the 3D peak along K is shown on Fig. 3B. A weak 3D peak is visible at compressions as low as $\varepsilon_{xx} \sim -0.5\%$; however, the increase in intensity from 0.8 to 1.0% compression dwarfs the evolution at lower compressions.

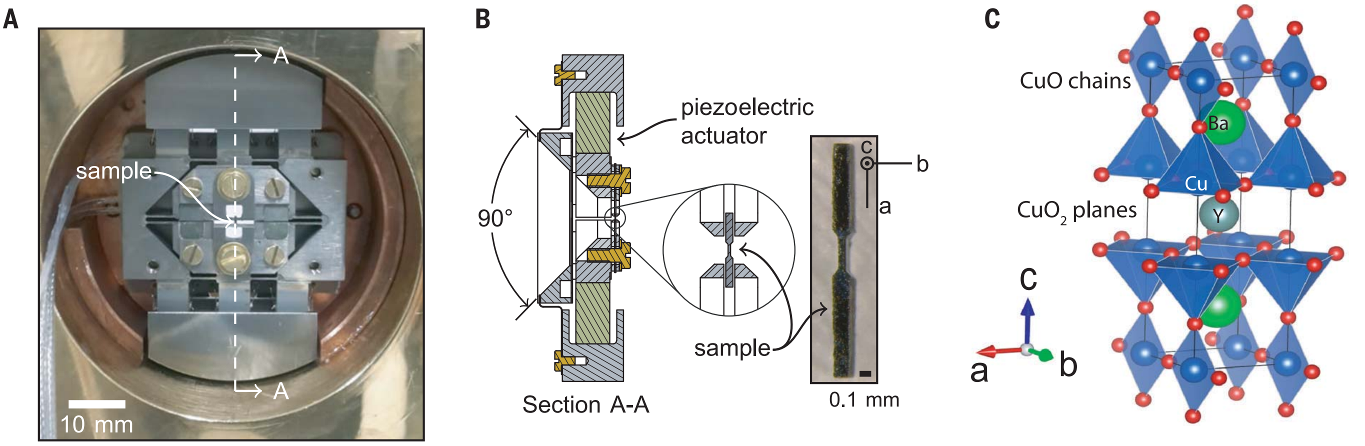

Fig. 1. Strain device. (**A**) Photograph of the piezoelectric device. (**B**) Sectional cut of the device and picture of the PFIB-thinned sample used for this experiment. (**C**) Unit cell of $YBa_2Cu_3O_{6+x}$ (here with $x = 1$). Strain is applied perpendicular to the CuO chains.

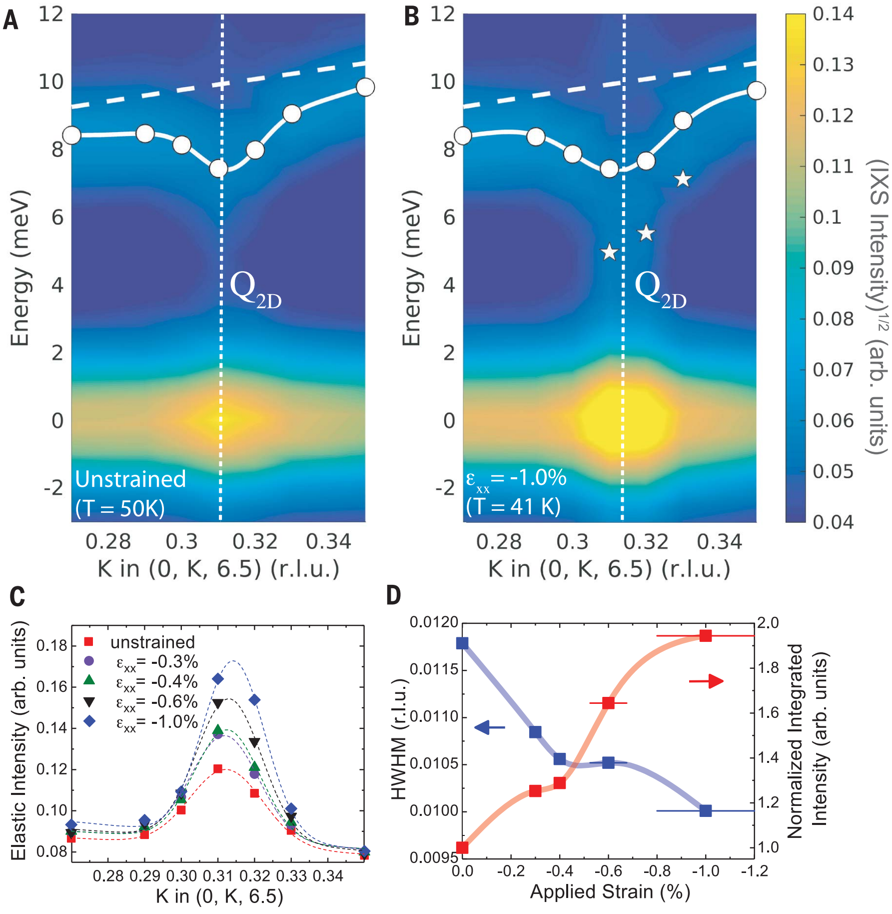

Fig. 2. Strain dependence of the IXS spectra around $\boldsymbol{Q}_{2D}$. (**A**) IXS intensity versus total momentum transfer for the unstrained sample at $T < T_c$. The square root of the intensity has been plotted to enhance the contrast between the phonon and the elastic line. The calculated dispersion of the low-lying acoustical mode is plotted as a dashed line. The solid line is a guide to the eye to the observed dispersion of this mode (fitted values are represented by the dots). (**B**) Same as in (A), but for $\varepsilon_{xx} \sim -1.0\%$. The stars indicate the energy of a soft optical phonon. (**C**) Strain-dependence of the quasi-elastic line intensity across $\boldsymbol{Q}_{2D}$ along the (0, K, 6.5) direction. (**D**) Strain dependence of the HWHM and of the integrated intensity (normalized to the unstrained value) of the quasi-elastic line at $\boldsymbol{Q}_{2D}$, integrated along K and normalized to the unstrained value.

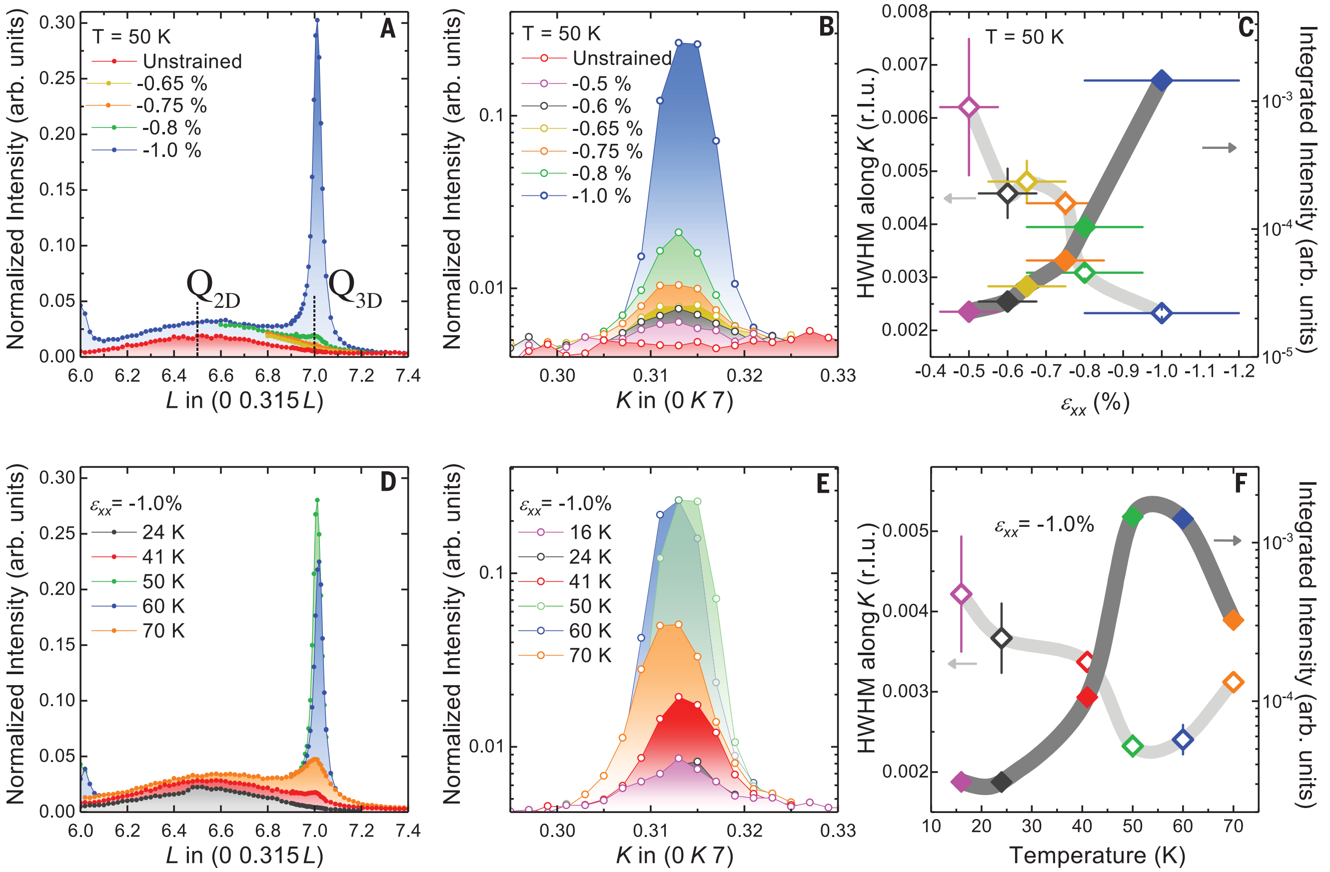

Fig. 3. Strain dependence of the quasi-elastic line at $\boldsymbol{Q}_{3D}$. (**A**) Quasi-elastic intensity at T = 50 K along the (0, 0.315, L) direction as function of a axis compression ε_{xx}. (**B**) Quasi-elastic intensity at T = 50 K along the (0, K, 7) direction as function of a axis compression ε_{xx}. (**C**) Strain dependence of the HWHM and the integrated intensity along the (0, K, 7) direction at T = 50 K. (**D**) Temperature dependence of the quasi-elastic intensity along the (0, 0.315, L) direction for ε_{xx} ~ –1.0%. (**E**) Temperature dependence of the quasi-elastic intensity along the (0, K, 7) direction for ε_{xx} ~ –1.0%. (**F**) HWHM and integrated intensities versus temperature at $\boldsymbol{Q}_{3D}$ for ε_{xx} ~ –1.0%.

The evolution of the integrated intensity, and the HWHM along K, are shown in Fig. 3C. At ε_{xx} ~ –1.0%, the HWHM is σ_b ~ 0.002 r.l.u. It is resolution-limited along L (σ_c ~ 0.02 r.l.u.). These correspond to respective (lower bounds for the) correlation lengths of $\xi_b = \frac{1}{2\pi\sigma_b}$ ~ $80b$ ~ 310 Å and $\xi_c = \frac{1}{2\pi\sigma_c}$ ~ $8c$ ~ 94 Å (the limitations of the scattering geometry did not permit investigation of ξ_a). These correlation lengths are larger than the values reported under a field of 26 T. The correlation lengths of the 2D CDW at 1.0% compression are ξ_b^{2D} ~ $16b$ ~ 65 Å and ξ_c^{2D} ~ c~ 12 Å. To estimate the correlation volume $\Xi = \xi_a \times \xi_b \times \xi_c$, we estimate ξ_a ~ ξ_b for both the 2D and 3D CDWs. For the 3D order, we find Ξ ~ 51,000 unit cells under uniaxial pressure for T ~ T_c, exceeding by more than two orders of magnitude that of the 2D CDW at ambient conditions (Ξ ~ 250 unit cells).

The temperature evolution of the 3D CDW at ε_{xx} ~ –1.0% is shown in Fig. 3, D to F. The peak is very strong at 60 K and weaker but still visible at 70 K. That is higher than the onset temperature of the 3D order observed under high field and higher than T_c of unstressed sample. On the low-temperature side, strong competition with superconductivity is apparent. At T = 41 K (below T_c), the peak at $\boldsymbol{Q}_{3D}$ has already lost ~90% of the integrated intensity recorded at 50 K and can hardly be distinguished from the background of the 2D order at lower temperatures. This is a much more rapid suppression than that seen for the 2D CDW (*7*).

To gain further insight on the relationship between the 2D and 3D orders, we investigated the pressure and temperature dependence of the phonon modes in the inelastic part of the spectra. In Fig. 4A, we show the phonon spectra in the absence of applied pressure at T = 50 K, along the (0, K, 7) direction. Well away from $\boldsymbol{Q}_{3D}$, three peaks are visible. These are well reproduced in ab initio lattice dynamics calculations (*30*) and correspond respectively to an acoustic phonon mode of the Δ'_4 irreducible representation (*36*) at ~8 meV, two optical modes (Δ'_1 and Δ'_4) at ~11 meV (which are not distinguishable in the measurement), and another Δ'_1 optical mode at ~15 meV. It can be seen that in the absence of strain, the acoustic-mode softening associated with the 2D CDW (*34*), and shown at $\boldsymbol{Q}_{2D}$ in Fig. 2A, extends along L and is visible at $\boldsymbol{Q}_{3D}$.

In Fig. 4B, we show the same spectra but with ε_{xx} ~ –1.0% and T = 41 K (to stay below T_c). Away from $\boldsymbol{Q}_{3D}$, the spectra are essentially unchanged. Near $\boldsymbol{Q}_{3D}$, on the other hand, a very strong phonon softening is observed, albeit not of the acoustic mode, which now disperses exactly as predicted by the ab initio calculations as K is swept through $\boldsymbol{Q}_{3D}$. In other words, the Kohn anomaly seen in Fig. 4A, at T = 50 K and ε_{xx} ~ 0%, is no longer present under ε_{xx} ~ –1.0%. This suppression of the acoustical Kohn anomaly can also be seen in Fig. 4C, where we show the L-dependence of the phonon spectra from $\boldsymbol{Q}_{2D}$ to $\boldsymbol{Q}_{3D}$ for both ε_{xx} ~ 0% and ε_{xx} ~ –1.0%. Without pressure, the acoustical phonon is soft along the entire L-line, which is in agreement with the data in Fig. 4A. At ε_{xx} ~ –1.0%, we can follow the hardening of the acoustical mode—the disappearance of the Kohn anomaly—as we traverse from $\boldsymbol{Q}_{2D}$ to $\boldsymbol{Q}_{3D}$. The mode that softens approaching $\boldsymbol{Q}_{3D}$ is a distinct feature, which we therefore identify as one of the optical modes. The temperature dependence of the phonon modes at $\boldsymbol{Q}_{3D}$ is shown in Fig. 4, D and E. At 70 K, the optical phonon is already very soft, which indicates that, unlike the acoustical Kohn anomaly, the optical mode softening

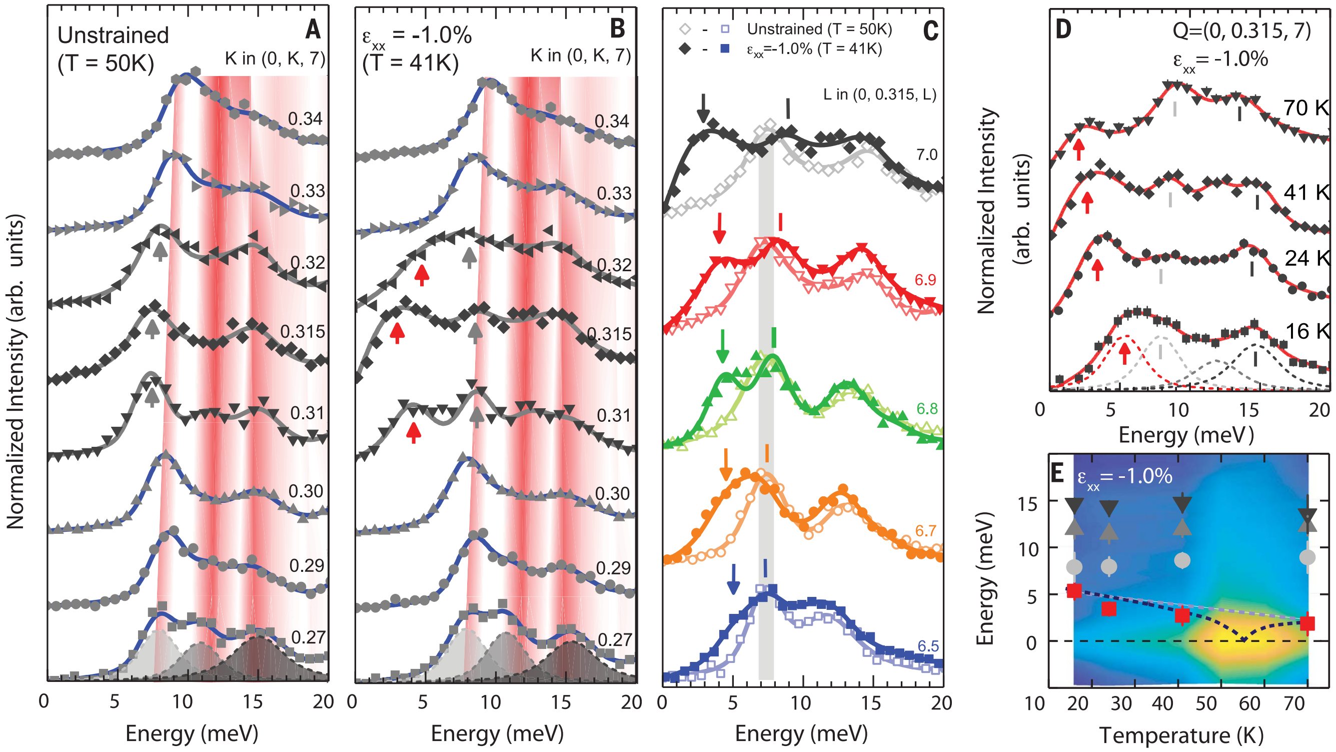

Fig. 4. Strain dependence of the phonon spectra around $\mathbf{Q}_{3D}$. (**A**) IXS intensity in the absence of strain recorded below T_c (at T = 50 K) along the (0, K, 7) direction. The elastic line has been subtracted (*30*). (**B**) Same, for ε_{xx} ~ –1.0%, and, to remain below T_c, at T = 41 K. In (A) and (B), the red lines represent the calculated structure factor of the phonons (*30*), the gray arrows indicate the acoustical phonon, and the red arrows indicate the soft optical mode. (**C**) L-dependence of the inelastic spectra. Open symbols indicate T = 50 K, ε_{xx} ~ 0; closed symbols indicate T = 41 K, ε_{xx} -1.0%. For the strained data, the ticks indicate the energy of the acoustical mode, and the arrows indicate the energy of the soft optical phonon. (**D**) Temperature dependence of the phonon spectra at $\mathbf{Q}_{3D}$ for ε_{xx} ~ –1.0%. Solid lines in (A) to (D) correspond to the least square fitting of the data (*30*). (**E**) Phonon energy versus temperature superimposed to the IXS intensity color map (log scale) at $\mathbf{Q}_{3D}$ for ε_{xx} ~ –1.0%. Dotted lines are guide to the eyes for possible scenarios for the temperature dependence of the soft-phonon energy.

is not induced by superconductivity. At 50 and 60 K, the soft phonon mode cannot be resolved from the strong elastic peak (*30*). The mode hardens below 50 K, as the long-range CDW order disappears in the superconducting state. Although a continuous hardening of the soft-phonon upon cooling through T_c cannot be completely ruled out with the data at hand (Fig. 4E), this behavior suggests a complete softening of this mode at Q3D, in analogy with soft-node–driven CDW orders [such as in 2H.-NbSe2 (*37*)].

The unambiguous identification of the soft phonon among the 36 allowed optical modes (*38*) is not a trivial task. Both Δ'_1 and Δ'_4 representations include an oxygen bond-stretching phonon around 60 meV (*39*) that exhibits pronounced dispersion anomalies close to $\mathbf{Q}_{3D}$ (*40*). The buckling mode (Δ'_1) also softens anisotropically along the 010 direction upon entering the superconducting state (*41*). Various scenarios have been discussed, attributing these anomalies to, for example, coupling of the phonons to dispersive collective charge excitations (*42*, *43*) or to hybridization with lower energy branches of the same symmetry (*44*).

Further work is required to determine which of these optical modes is driven soft under uniaxial pressure, to determine whether the softening is complete and to understand the mechanism yielding the disappearance of the acoustical phonon Kohn anomaly at $\mathbf{Q}_{3D}$. The absence of phonon softening in single-electron calculations indicates that electronic correlations need to be included in any theoretical treatment of the phonon softening and CDW formation (*45*).

From a theoretical point of view, unidirectional CDW are unstable against disorder, and a vestigial nematic state is expected instead. It has previously been discussed how short-range biaxial modulation of the charge density might emerge from an intrinsic unidirectional CDWs instability in the presence of quenched disorder (*23*, *46*, *47*), which locally reorients small uniaxial domains. Inhomogeneous distribution of the disorder strength has been invoked (*18*) to explain why the 2D order appears to strengthen under large magnetic fields even as unidirectional 3D order appears. Although one might expect the 3D order to grow at the expense of the 2D one, in this model this process occurs on top of a general strengthening of CDW order as superconductivity is suppressed by the magnetic field, and inhomogeneity in the strength of disorder allows spatially separated, coexisting domains of 2D and 3D order.

Similarly, our data indicate that strain-tuning efficiently strengthens the CDW and supports the formation of the 3D order, likely primarily in those regions where the pinning strength is the weakest. It will be interesting to see in the future whether the strength of the 2D order does eventually decrease as strain is further increased. More generally, further theoretical work is required to understand the strain-induced strengthening of the CDW, which cannot be solely attributed to the competition with superconductivity because the 3D CDW peak can already be induced above the nominal T_c of the sample.

Uniaxial stress will allow the relationship between the superconductivity and CDW to be investigated with high precision in future experiments. A magnetic field suppresses type II superconductivity inhomogeneously because of the presence of vortices, resulting in broad transitions. By contrast, the homogeneous tuning provided by stress could, for example, allow use of thermodynamic probes to determine whether CDW and superconductivity can coexist microscopically. Our piezoelectric-based apparatus constitutes a versatile tool that can be implemented in a large variety of experimental setups—in particular, at synchrotron facilities—thus opening perspectives for the study of correlated-electron materials.

REFERENCES AND NOTES

1. B. Keimer, S. A. Kivelson, M. R. Norman, S. Uchida, J. Zaanen, *Nature* **518**, 179–186 (2015).
2. J. M. Tranquada, B. J. Sternlieb, J. D. Axe, Y. Nakamura, S. Uchida, *Nature* **375**, 561–563 (1995).
3. M. Vojta, *Adv. Phys.* **58**, 699–820 (2009).
4. J. E. Hoffman *et al.*, *Science* **295**, 466–469 (2002).
5. C. Howald, H. Eisaki, N. Kaneko, M. Greven, A. Kapitulnik, *Phys. Rev. B* **67**, 014533 (2003).
6. W. D. Wise *et al.*, *Nat. Phys.* **4**, 696–699 (2008).
7. G. Ghiringhelli *et al.*, *Science* **337**, 821–825 (2012).
8. J. Chang *et al.*, *Nat. Phys.* **8**, 871–876 (2012).
9. S. Blanco-Canosa *et al.*, *Phys. Rev. Lett.* **110**, 187001 (2013).
10. T. P. Croft, C. Lester, M. S. Senn, A. Bombardi, S. M. Hayden, *Phys. Rev. B* **89**, 224513 (2014).
11. E. H. da Silva Neto *et al.*, *Sci. Adv.* **2**, e1600782 (2016).
12. W. Tabis *et al.*, *Phys. Rev. B* **96**, 134510 (2017).
13. A. Perali, C. Castellani, C. Di Castro, M. Grilli, *Phys. Rev. B Condens. Matter* **54**, 16216–16225 (1996).
14. S. A. Kivelson, E. Fradkin, V. J. Emery, *Nature* **393**, 550–553 (1998).
15. L. E. Hayward, D. G. Hawthorn, R. G. Melko, S. Sachdev, *Science* **343**, 1336–1339 (2014).
16. T. Wu *et al.*, *Nat. Commun.* **6**, 6438 (2015).
17. S. Gerber *et al.*, *Science* **350**, 949–952 (2015).
18. H. Jang *et al.*, *Proc. Natl. Acad. Sci. U.S.A.* **113**, 14645–14650 (2016).
19. J. Chang *et al.*, *Nat. Commun.* **7**, 11494 (2016).
20. F. Yu *et al.*, *Proc. Natl. Acad. Sci. U.S.A.* **113**, 12667–12672 (2016).
21. D. LeBoeuf *et al.*, *Nat. Phys.* **9**, 79–83 (2013).
22. T. Wu *et al.*, *Nature* **477**, 191–194 (2011).
23. L. Nie, L. E. H. Sierens, R. G. Melko, S. Sachdev, S. A. Kivelson, *Phys. Rev. B* **92**, 174505 (2015).
24. Y. Caplan, G. Wachtel, D. Orgad, *Phys. Rev. B* **92**, 224504 (2015).
25. S. Sadewasser, J. S. Schilling, A. P. Paulikas, B. W. Veal, *Phys. Rev. B* **61**, 741–749 (2000).
26. S. M. Souliou *et al.*, *Phys. Rev. B* **97**, 020503 (2018).
27. C. Meingast *et al.*, *Phys. Rev. Lett.* **67**, 1634–1637 (1991).
28. U. Welp *et al.*, *Phys. Rev. Lett.* **69**, 2130–2133 (1992).
29. O. Kraut *et al.*, *Physica C* **205**, 139–146 (1993).
30. Materials and methods are available as supplementary materials.
31. C. W. Hicks *et al.*, *Science* **344**, 283–285 (2014).
32. C. W. Hicks, M. E. Barber, S. D. Edkins, D. O. Brodsky, A. P. Mackenzie, *Rev. Sci. Instrum.* **85**, 065003 (2014).
33. A. Steppke *et al.*, Strong peak in T_c of Sr_2RuO_4 under uniaxial pressure. *Science* **355**, eaaf9398 (2017).
34. M. Le Tacon *et al.*, *Nat. Phys.* **10**, 52–58 (2014).
35. E. M. Forgan *et al.*, *Nat. Commun.* **6**, 10064 (2015).
36. K.-P. Bohnen, R. Heid, M. Krauss, *Europhys. Lett.* **64**, 104–110 (2003).
37. F. Weber *et al.*, *Phys. Rev. Lett.* **107**, 107403 (2011).
38. In presence of the oxygen-superstructure at this doping level (Ortho-VIII), even more phonons can be expected (36 is the number of optical modes expected for the ortho-I structure of $YBa_2Cu_3O_7$).
39. D. Reznik *et al.*, *Nature* **440**, 1170–1173 (2006).
40. D. Reznik, *Physica C* **481**, 75–92 (2012).
41. M. Raichle *et al.*, *Phys. Rev. Lett.* **107**, 177004 (2011).
42. L. Chaix *et al.*, *Nat. Phys.* **13**, 952–956 (2017).
43. E. Kaneshita, M. Ichioka, K. Machida, *Phys. Rev. Lett.* **88**, 115501 (2002).
44. L. Pintschovius *et al.*, *Phys. Rev. B* **69**, 214506 (2004).
45. Z. P. Yin, A. Kutepov, G. Kotliar, *Phys. Rev. X* **3**, 021011 (2013).
46. J. A. Robertson, S. A. Kivelson, E. Fradkin, A. C. Fang, A. Kapitulnik, *Phys. Rev. B* **74**, 134507 (2006).
47. A. Del Maestro, B. Rosenow, S. Sachdev, *Phys. Rev. B* **74**, 024520 (2006).
48. M. Le Tacon, Uniaxial pressure control of competing orders in a high temperature superconductor. Repository KITopen (2018); doi:10.5445/IR/1000086708

ACKNOWLEDGMENTS

We thank T. P. Devereaux, M.-H. Julien, S. A. Kivelson, D. Leboeuf, C. Meingast, J. Schmalian, and L. Taillefer for fruitful discussions, and FEI for assistance with the PFIB sample preparation. **Funding:** We acknowledge the support of the Helmholtz association through the program Science and Technology of Nanosystems and of the Max Planck Society. R.A.B. acknowledges partial financial support from Agencia Nacional de Promoción Científica y Tecnológica (PICT 2014 no. 2618) and CONICET (PIP 0446). **Author contributions:** IXS experiments were carried out by S.M.S., H.-H.K., E.L., M.M., M.T., A.B., and M.L.T. IXS data were analyzed by S.M.S. and M.L.T. X-ray diffraction experiments were carried out by H.-H.K., S.M.S., E.L., M.E.B., M.T., M.M., G.G., C.W.H., and M.L.T. R.H. carried out the ab initio calculations. M.E.B., N.N., R.A.B., and C.W.H. performed the susceptibility measurements. Single crystals studied in this work were prepared by J.P., T.L., and S.M.S. PFIB preparation was carried out by P.M.M. and M.K. The strain devices used in this study were built by C.W.H., with assistance from M.L.T., H.-H.K., and E.L. S.M.S. and M.L.T. conceived the project. A.P.M., B.K., C.W.H., and M.L.T. supervised the project. M.L.T. and C.W.H. wrote the manuscript with input from all the coauthors. **Competing interests:** C.W.H. has 31% ownership of Razorbill Instruments, which has commercialized apparatus on which that used in this work are based. **Data and materials availability:** Raw data and simulation codes used for all figures in this paper and the supplementary materials are available at (*48*).

SUPPLEMENTARY MATERIALS

www.sciencemag.org/content/362/6418/1040/suppl/DC1
Materials and Methods
Supplementary Text
Figs. S1 to S9
References (*49*–*55*)

2 March 2018; accepted 25 October 2018
10.1126/science.aat4708

NEUROSCIENCE

Fast track to the neocortex: A memory engram in the posterior parietal cortex

S. Brodt[1,2]*, S. Gais[1], J. Beck[1], M. Erb[2,3], K. Scheffler[2,3], M. Schönauer[1,2,4]

Models of systems memory consolidation postulate a fast-learning hippocampal store and a slowly developing, stable neocortical store. Accordingly, early neocortical contributions to memory are deemed to reflect a hippocampus-driven online reinstatement of encoding activity. In contrast, we found that learning rapidly engenders an enduring memory engram in the human posterior parietal cortex. We assessed microstructural plasticity via diffusion-weighted magnetic resonance imaging as well as functional brain activity in an object–location learning task. We detected neocortical plasticity as early as 1 hour after learning and found that it was learning specific, enabled correct recall, and overlapped with memory-related functional activity. These microstructural changes persisted over 12 hours. Our results suggest that new traces can be rapidly encoded into the parietal cortex, challenging views of a slow-learning neocortex.

Systems memory consolidation is considered a slow process of neuronal reorganization. Fresh memories rely on the hippocampus, which reinstates the cortical ensembles that were active during encoding, whereas neocortical memory develops more slowly, through frequent reactivation (*1*, *2*). Recent findings suggest that the posterior parietal cortex (PPC) can acquire a memory representation rapidly during learning (*3*, *4*). It is unclear whether these early contributions go beyond an online reinstatement of previous activity or whether they originate from a true neocortical engram. Methodological advances have made it possible to track engrams in rodents, yet they have remained elusive in humans (*5*–*7*). In humans, multivariate analysis of functional magnetic resonance imaging (fMRI) can assess active memory representations during encoding and retrieval (*8*, *9*), but this method is unable to distinguish between activity originating within a region and activity reinstated through input from another region. It thus cannot unequivocally reveal the permanent location of the dormant trace.

A memory engram has four defining features: (i) it must relate to a specific experience; (ii) it must engender an enduring change in the neural substrate; (iii) it can lie dormant for extended periods; and (iv) it must enable memory recall, thus having an impact on behavior (*10*, *11*). To elucidate where memory formation leads to lasting physical changes, the microstructural modifications, e.g., of synapse number and morphology, which can occur within minutes after learning must be assessed (*12*). Diffusion-weighted MRI (DW-MRI) is sensitive to the microstructure of brain tissue (*13*) and can image experience-driven structural plasticity in the human brain noninvasively and in vivo (*14*–*16*).

We used fMRI and DW-MRI to demonstrate the dynamic contributions of neocortical areas

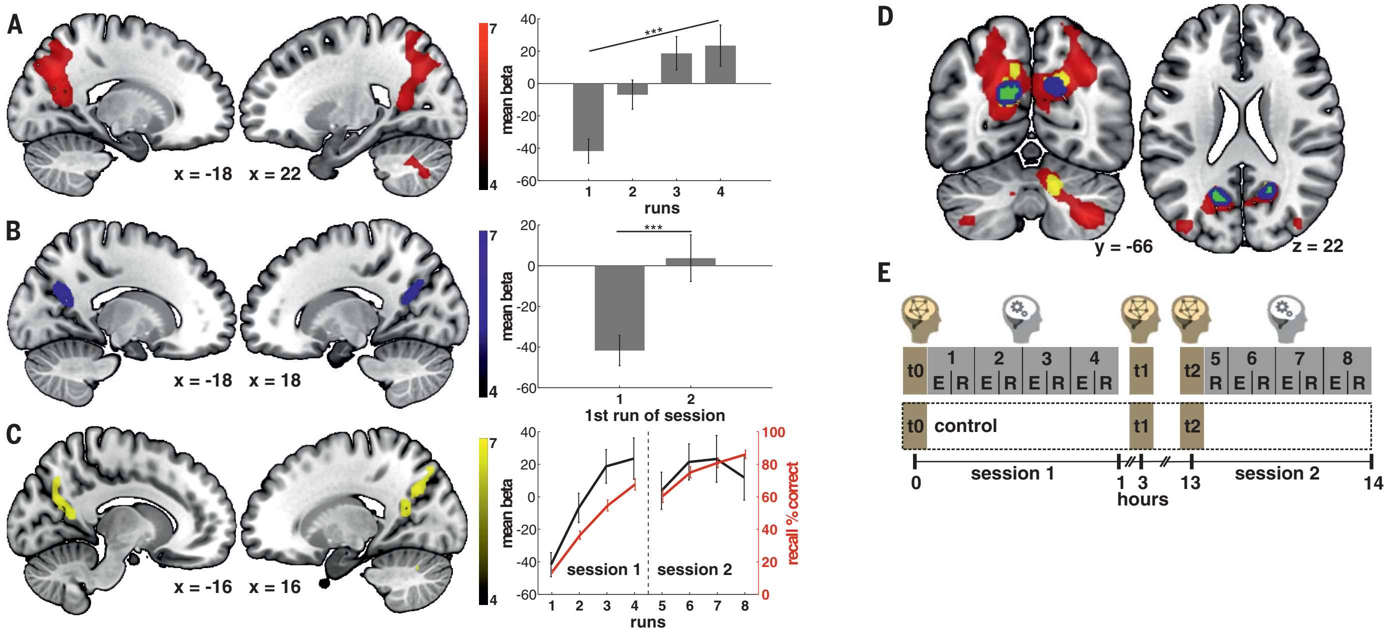

Fig. 1. Experience dependence, persistence, and correlation with performance of PPC activity during memory recall. (**A**) Experience-dependent increase with repetition. Mean beta values in the anatomically defined precuneus ROI for the first task session; linear contrast, $***P < 0.001$, $n = 39$. (**B**) Persistently elevated precuneus responses after 12 hours. Mean beta values; two-sided *t* test, $***P < 0.001$, $n = 39$. (**C**) Correlation of precuneus activation with memory performance. Mean beta values, black; mean percentage of correctly recalled item locations, red; one sample *t* test of *z*-transformed single-subject correlations, $P < 0.001$, $n = 39$. (**D**) Conjunction of the minimum statistic of all three analyses, green. Clusters exhibited significant peak-level effects at full-volume–corrected $P_{FWE} < 0.05$ and exceeded 10 voxels. No masking. Beta values were corrected for baseline activation. Data are means ± SEM. Corresponding data from encoding are shown in fig. S1 and table S2. (**E**) Experimental design. An object–location learning task was trained for eight encoding (E)–recall (R) runs with fMRI. DW-MRI was measured at t0 to t2. For the control condition, the learning task was omitted.

---

[1]Institute of Medical Psychology and Behavioral Neurobiology, University of Tübingen, Tübingen, Germany. [2]Max-Planck-Institute for Biological Cybernetics, Tübingen, Germany. [3]Biomedical Magnetic Resonance, Universitätsklinikum Tübingen, Tübingen, Germany. [4]Princeton Neuroscience Institute, Princeton University, Princeton, NJ, USA.
*Corresponding author. Email: svenja.brodt@uni-tuebingen.de

to memory during two sessions of four encoding-recall repetitions of an object–location association task (Fig. 1E, movie S1, and materials and methods) and to identify the location of the engram engendered by the memory. First, we examined in whole-brain analyses which regions displayed changes in functional activity that indicated memory representations. We identified an experience-dependent, increasing response over repeated retrieval in the bilateral precuneus and areas along the dorsal visual stream, the cerebellum, thalamus, and motor areas (linear increase in the anatomically defined precuneus over first session: $F_{1,38} = 26.76$, $P < 0.001$, $\eta^2 = 0.404$) (Fig. 1A and table S1A). This increased response to successfully encoded stimuli persisted over a 12-hour offline interval in the precuneus ($t_{38} = 4.50$, $P < 0.001$) (Fig. 1B and table S1B). The posterior parietal areas were also the only regions for which there was a significant correlation between memory performance and functional brain activity over retrieval repetitions (average correlation on the single-subject level: $r = 0.378$, $t_{38} = 6.15$, $P < 0.001$) (Fig. 1C and table S1C). The above contrasts did not yield significant clusters in an anatomical region of interest (ROI) analysis of the hippocampus; however, we

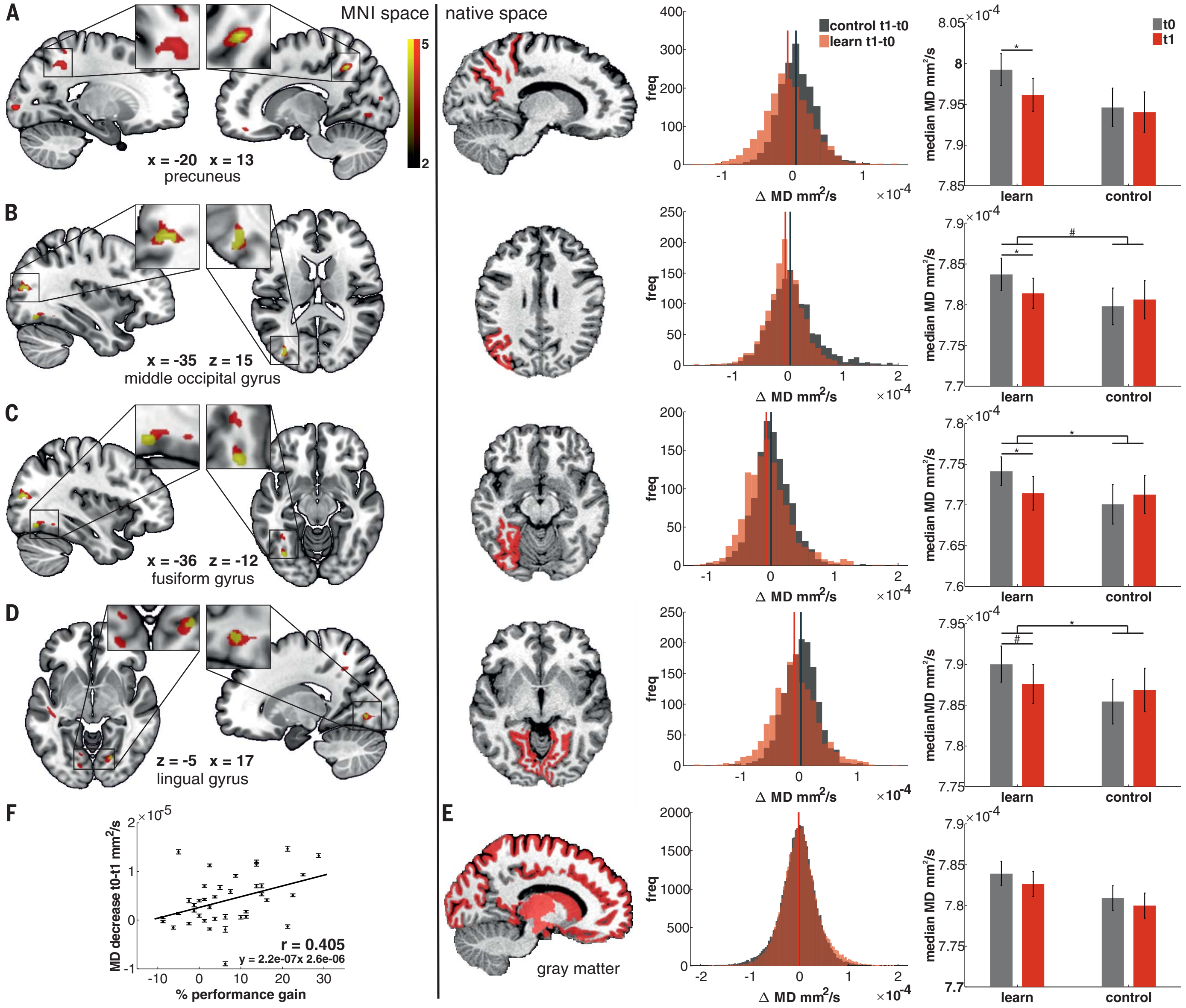

Fig. 2. Learning induces rapid microstructural changes in the neocortex. Statistical maps on the left display whole-brain Montreal Neurological Institute (MNI) space group-level analyses. Significant decrease from t0 to t1 for the learning condition, red, $n = 39$; significant interaction with the control condition, yellow, $n = 33$. Two-sided t tests. Clusters exhibited significant peak-level effects at $P_{\text{uncorr}} < 0.001$ and exceeded 10 voxels. No masking. ROI analysis on the anatomically defined precuneus confirmed peak-level effects at $P_{\text{FDR}} < 0.05$. The middle column shows sample gray matter masks of the native space analyses on the raw, unsmoothed MD of the anatomically defined gray matter ROIs. Distribution plots on the right show sample subject distributions of MD differences between t0 and t1 for all ROI voxels. Learning condition, red; control condition, gray; vertical lines represent medians. All ROIs in (**A**) to (**D**), but not the remaining gray matter (**E**), showed a left shift of the learning distribution, indicating an MD decrease and thus learning-induced structural plasticity. Bar graphs on the far right show group-level analyses, which confirmed region-specific learning-induced MD decreases. Repeated-measures ANOVAs, $n = 33$. #$P < 0.07$, *$P < 0.05$. Data are means ± SEM. (**F**) The mean raw MD decreases from t0 to t1 of all four ROIs were highly correlated to the overall performance improvement from session 1 to session 2. Pearson correlation, $n = 39$. Dots are single-subject values, and error bars are SEM.

observed a subsequent memory effect during encoding runs in the first task session, consistent with a role of the hippocampus in early encoding (fig. S4, table S9, and supplementary text). In contrast, a strict conjunction analysis confirmed that only the precuneus simultaneously fulfilled all of the above criteria (Fig. 1D and table S1D). Finally, to assess whether the activity patterns in the precuneus were content specific, we performed a multivariate pattern analysis. This analysis showed that it is possible to decode category information of the stimuli from this area during memory encoding ($P < 0.001$) (fig. S2 and table S3). Our findings showed that the precuneus can hold a representation of retrieved information (*8*, *17–20*). Still, the question remains, what type of information is processed in this area. We used associative, explicitly learned material, which is, because of the low number of learning repetitions, at the border between episodic and semantic memory. The precuneus is tightly integrated into a network of memory-related brain regions (*21*) and is located at the crossroads of multiple sensory pathways, which makes it ideal for the processing of abstract information or higher-order multimodal associations and a likely convergence zone for distributed memory functions. In fact, the parietal cortex plays a critical role in integrating new information into existing schemas and has been identified as a major node in the semantic system (*22*, *23*).

To qualify as an engram, a memory representation must induce persistent structural plasticity. DW-MRI, and in particular mean diffusivity (MD), allows measurement of changes in brain microstructure. Though it is only an indirect measure, there is strong evidence that decreased MD can reflect mechanisms of learning-dependent plasticity, e.g., astrocyte, myelin, or synaptic remodeling. Synapse density, brain-derived neurotrophic factor expression, and astrocyte activation increase after learning at the sites where MD decreases, suggesting a tight link to experience-induced structural plasticity (*14*, *16*, *24*). Traditional views suggest that learning-related changes in the neocortex need frequent hippocampal reactivation over extended periods to develop (*2*). Unexpectedly, we found robust microstructural changes, reflected by decreases in MD, already at 90 min after learning in several bilateral areas along the dorsal and ventral visual streams (Fig. 2, left, and table S4A), particularly in the precuneus [false discovery rate–corrected P value (P_{FDR}) < 0.05], but not in the hippocampus (see the supplementary text). To test whether these changes were learning specific, we compared them with changes observed in a control condition without learning between scans. We found significant learning-induced changes in the left precuneus (Fig. 2A and table S4B), the left middle occipital gyrus (Fig. 2B), the left fusiform gyrus (Fig. 2C), and the bilateral lingual gyri (Fig. 2D). For these four regions, analyses of variance (ANOVAs) on the mean raw MD values confirmed that the significant interaction effect was based on MD decreases in the learning condition and not in the control condition (table S5A). Analyses of the raw, unsmoothed, subject-native space MD data further corroborated these findings (Fig. 2, right, and table S5B). These morphological changes also correlated with memory performance. Subjects with higher structural plasticity had better memory retention from session 1 to session 2 (r_{39} = 0.405, P = 0.010) (Fig. 2F).

The final criterion of a memory engram is that it persists over time. We measured long-term MD changes 12 hours after learning. All regions that showed rapid learning-induced structural plasticity maintained these changes for more than 12 hours. A significant long-lasting reduction in MD was found again bilaterally in the precuneus, along the dorsal and ventral visual processing streams, and in frontal regions [uncorrected P value (P_{uncorr}) < 0.001] (Fig. 3 and table S6A). These changes did not occur in the control condition (interaction with control: P_{uncorr} < 0.005) (Fig. 3 and table S6B). Analyses of the mean raw MD values again confirmed this finding (Fig. 3, right, and table S5C). Using a whole-brain joint inference approach, we further identified the precuneus, the middle occipital gyrus, and the lingual gyrus as regions in which rapid and persistent learning-dependent structural plasticity can be found (Fig. 3E and table S7). Previous studies have mostly measured rapid structural plasticity in the human brain at delays similar to our short interval. Our data show that the microstructural changes in the regions that display learning-induced rapid structural plasticity remain stable for at least 12 hours.

We identified posterior parietal areas that fulfilled all defining conditions of a memory engram, i.e., they showed functional responses that were specifically related to the memory, were persistent over longer offline periods, and were relevant for later memory recall. These

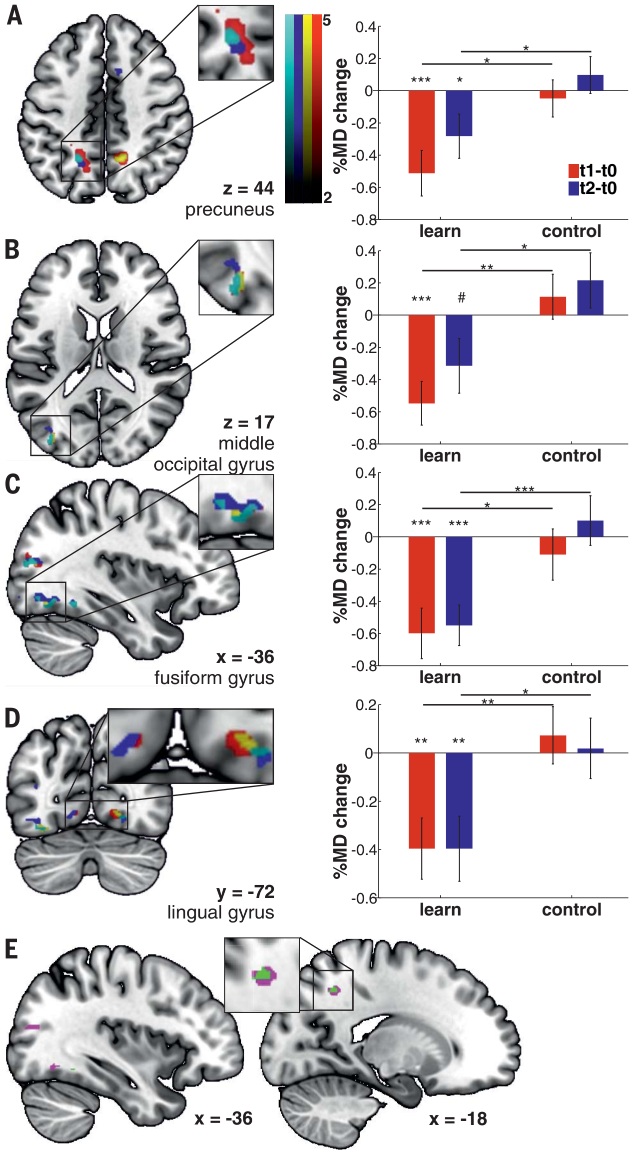

Fig. 3. Learning-induced persistent microstructural changes in the neocortex. (**A** to **D**) Long-term MD decreases. (Left) Whole-brain MNI space group-level analyses. Decreases from t0 to t2 for the learning condition, blue, n = 39; interaction with the control condition, cyan, n = 33. Short-term changes from Fig. 2 are shown in red and yellow. Two-sided t tests. All clusters exhibited significant peak-level effects at P_{uncorr} < 0.001 (learning condition) and P_{uncorr} < 0.005 (interaction) and exceeded 10 voxels. No masking. (Right) Mean raw MD changes for short-term (red) and long-term (blue) intervals. Repeated-measures ANOVAs confirmed that the interaction effects stem from a selective decrease in the learning condition. #P ≤ 0.07, *P < 0.05, **P < 0.01, ***P ≤ 0.001, n = 33. Data are means ± SEM. (**E**) Joint inference analyses on short-term and long-term MD decreases. Nonparametric combination test, purple, n = 33; conjunction analysis of the minimum statistic, green, P_{uncorr} < 0.001, n = 39. Clusters exceeded 10 voxels. No masking.

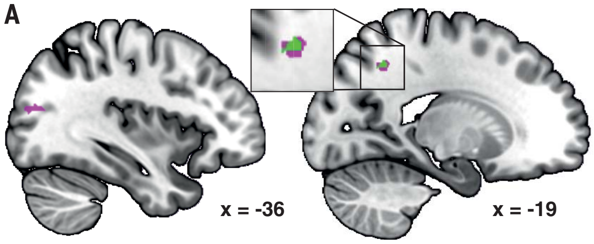

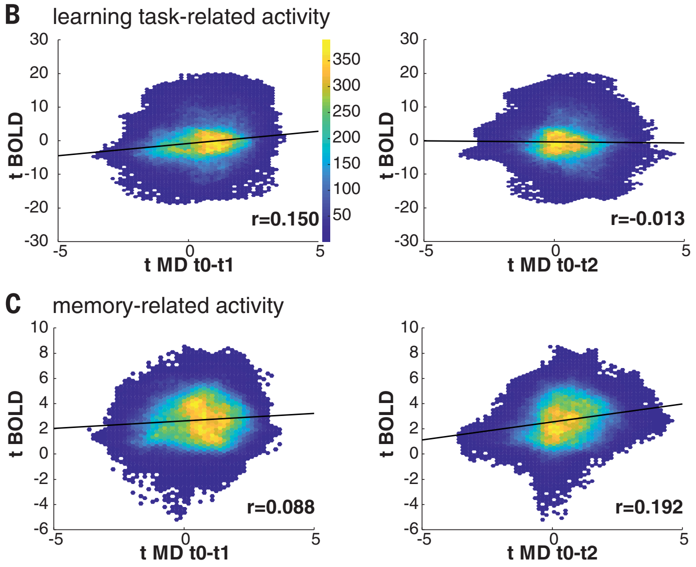

Fig. 4. Relationship between functional activity and microstructural plasticity. (**A**) Joint inference analyses of simultaneous learning-induced functional (recall) and microstructural changes. Nonparametric combination test, purple, full-volume–corrected $P_{FWE} < 0.05$, $n = 33$; conjunction analysis of the minimum statistic, green, $P_{uncorr} < 0.001$, $n = 39$. Clusters exceeded 10 voxels. No masking. Corresponding data with functional activity from encoding are shown in fig. S3. (**B** and **C**) Pearson correlations between t values from group analyses of functional activity and MD decrease; Steiger's z-test, $P < 0.001$, $n = 114{,}698$. Data points are bins of multiple voxels, and colors represent voxel frequencies per bin. (B) The correlation between general learning task-related activity and MD decreases from the short to the long interval. (C) The correlation with explicitly memory-related activity increases over time.

regions also showed structural–plastic changes that conformed to the same criteria. Thus, a true neocortical engram developed rapidly, after only four rounds of rehearsal. Similarly, studies in rodents have revealed that neocortical engram cells are already tagged during encoding and have detected experience-dependent microstructural changes as early as 1 hour after learning (*5*, *6*, *25*, *26*). We suggest that such rapid learning-induced neocortical plasticity arises from multiple encoding–recall repetitions (*4*, *27*). The PPC's ability to accumulate new information over several minutes (*28*) and learn associations between well-known object schemata (*29*) might allow particularly fast neocortical memory formation.

We next used joint inference to identify regions that meet mnemonic criteria in both imaging modalities. A nonparametric combination approach yielded significant clusters in the middle occipital gyrus [family-wise error corrected P value (P_{FWE}) < 0.05] (Fig. 4A and table S8A) and the precuneus. The latter also survived a strict conjunction analysis ($P_{uncorr} < 0.001$) (Fig. 4A and table S8B). Thus, diffusivity decreased in regions that were functionally involved in memory. Observed online memory representations are thus likely to rely on a true neocortical engram. Looking more broadly at the brain-wide relation between functional activity and structural plasticity, we found that learning task-related functional activity was associated with short-term decreases in MD (correlations of group-level t values, $n = 114{,}698$ voxels; short term: $r = 0.150$, long term: $r = -0.013$; difference: $z = 67.09$, $P < 0.001$) (Fig. 4B), whereas the memory-related linear increase in functional activity correlated more strongly with the long-term MD decrease (short term: $r = 0.088$; long term: $r = 0.192$; difference: $z = -42.98$, $P < 0.001$) (Fig. 4C). These findings suggest that different processes might underlie the microstructural changes at different time points after learning.

Although there is still debate about the functions of the different subregions of the PPC and their roles in working memory, memory-related attention, or reinstatement of previous experience (*3*, *8*), our study highlights the role of the medial PPC. Observing microstructural changes in the precuneus takes us from memory processing and reinstatement to the memory engram itself (*17*). The fast temporal dynamics that we observed challenge traditional models of slow systems consolidation (*2*) and suggest that new traces are encoded rapidly in the neocortex from the onset of learning. In addition, we detected learning-specific, persistent microstructural changes upstream along the dorsal and ventral visual pathways, which is in line with the notion of distributed neocortical memory traces (*8*, *11*). Apart from their role in perception, visual areas process memory content, suggesting memory storage also at this level (*30*, *31*). Indeed, many accounts regard perception and memory not as faculties of different systems but as being localized within the same distributed neural circuits (*28*). Combining functional imaging with diffusion imaging might help transform our view of how the brain translates perception into memory.

REFERENCES AND NOTES

1. J. L. McGaugh, *Science* **287**, 248–251 (2000).
2. P. W. Frankland, B. Bontempi, *Nat. Rev. Neurosci.* **6**, 119–130 (2005).
3. C. Sestieri, G. L. Shulman, M. Corbetta, *Nat. Rev. Neurosci.* **18**, 183–192 (2017).
4. S. Brodt *et al.*, *Proc. Natl. Acad. Sci. U.S.A.* **113**, 13251–13256 (2016).
5. T. Kitamura *et al.*, *Science* **356**, 73–78 (2017).
6. E. Lesburguères *et al.*, *Science* **331**, 924–928 (2011).
7. S. Tonegawa, X. Liu, S. Ramirez, R. Redondo, *Neuron* **87**, 918–931 (2015).
8. B. A. Kuhl, J. Rissman, M. M. Chun, A. D. Wagner, *Proc. Natl. Acad. Sci. U.S.A.* **108**, 5903–5908 (2011).
9. T. I. Brown *et al.*, *Science* **352**, 1323–1326 (2016).
10. R. Semon, *Mnemic Psychology* (G. Allen & Unwin Limited, 1923).
11. S. A. Josselyn, S. Köhler, P. W. Frankland, *Nat. Rev. Neurosci.* **16**, 521–534 (2015).
12. E. R. Kandel, *Science* **294**, 1030–1038 (2001).
13. S. Mori, J. Zhang, *Neuron* **51**, 527–539 (2006).
14. Y. Sagi *et al.*, *Neuron* **73**, 1195–1203 (2012).
15. S. Hofstetter, N. Friedmann, Y. Assaf, *Brain Struct. Funct.* **222**, 1231–1241 (2017).
16. T. Blumenfeld-Katzir, O. Pasternak, M. Dagan, Y. Assaf, *PLOS ONE* **6**, e20678 (2011).
17. J. Chen *et al.*, *Nat. Neurosci.* **20**, 115–125 (2017).
18. A. Gonzalez *et al.*, *Proc. Natl. Acad. Sci. U.S.A.* **112**, 11066–11071 (2015).
19. U. Rutishauser, T. Aflalo, E. R. Rosario, N. Pouratian, R. A. Andersen, *Neuron* **97**, 209–220.e3 (2018).
20. A. Akrami, C. D. Kopec, M. E. Diamond, C. D. Brody, *Nature* **554**, 368–372 (2018).
21. R. L. Buckner, J. R. Andrews-Hanna, D. L. Schacter, *Ann. N. Y. Acad. Sci.* **1124**, 1–38 (2008).
22. A. Gilboa, H. Marlatte, *Trends Cogn. Sci.* **21**, 618–631 (2017).
23. J. R. Binder, R. H. Desai, *Trends Cogn. Sci.* **15**, 527–536 (2011).
24. R. J. Zatorre, R. D. Fields, H. Johansen-Berg, *Nat. Neurosci.* **15**, 528–536 (2012).
25. T. Xu *et al.*, *Nature* **462**, 915–919 (2009).
26. K. K. Cowansage *et al.*, *Neuron* **84**, 432–441 (2014).
27. J. W. Antony, C. S. Ferreira, K. A. Norman, M. Wimber, *Trends Cogn. Sci.* **21**, 573–576 (2017).
28. U. Hasson, J. Chen, C. J. Honey, *Trends Cogn. Sci.* **19**, 304–313 (2015).
29. D. Tse *et al.*, *Science* **316**, 76–82 (2007).
30. S. A. Harrison, F. Tong, *Nature* **458**, 632–635 (2009).
31. J. P. Gavornik, M. F. Bear, *Nat. Neurosci.* **17**, 732–737 (2014).

ACKNOWLEDGMENTS

Funding: This project was supported by the European Social Fund and by the Ministry of Science, Research and the Arts Baden-Württemberg. **Author contributions:** S.B., S.G., M.E., K.S., and M.S. designed the research; S.B., J.B., M.E., and M.S. performed the experiments; S.B. and J.B. analyzed the functional and behavioral data; S.B. analyzed the diffusion data; S.B., S.G., and M.S. wrote the manuscript. **Competing interests:** The authors declare no competing interests. **Data and materials availability:** The raw data and computer code necessary to understand and assess the conclusions of the study can be downloaded from the Open Science Framework platform: osf.io/pnxje.

SUPPLEMENTARY MATERIALS

www.sciencemag.org/content/362/6418/1045/suppl/DC1
Materials and Methods
Supplementary Text
Figs. S1 to S4
Tables S1 to S9
References (*32*–*51*)
Movie S1

22 May 2018; accepted 10 October 2018
10.1126/science.aau2528

ARCHAEOLOGY

The earliest human occupation of the high-altitude Tibetan Plateau 40 thousand to 30 thousand years ago

X. L. Zhang[1,2], B. B. Ha[3], S. J. Wang[1,2], Z. J. Chen[3], J. Y. Ge[1,2,4]*, H. Long[5], W. He[3], W. Da[6], X. M. Nian[7], M. J. Yi[8], X. Y. Zhou[1,2,4], P. Q. Zhang[1,2,4], Y. S. Jin[1,2,4], O. Bar-Yosef[9], J. W. Olsen[10,11], X. Gao[1,2,4]*

The Tibetan Plateau is the highest and one of the most demanding environments ever inhabited by humans. We investigated the timing and mechanisms of its initial colonization at the Nwya Devu site, located nearly 4600 meters above sea level. This site, dating from 40,000 to 30,000 years ago, is the highest Paleolithic archaeological site yet identified globally. Nwya Devu has yielded an abundant blade tool assemblage, indicating hitherto-unknown capacities for the survival of modern humans who camped in this environment. This site deepens the history of the peopling of the "roof of the world" and the antiquity of human high-altitude occupations more generally.

The Tibetan Plateau (TP) is the highest and one of the most challenging environments inhabited by humans because of its perennial cold temperatures, low biomass productivity, and the dangers of hypoxia. As one of the last terrestrial environments occupied by humans (*1*), the timing and mechanisms of its colonization are of great interest. To date, there has been no concrete evidence of humans inhabiting the interior of the plateau before the Holocene, and only a few Paleolithic sites have been discovered around its margins (*2*–*8*) (fig. S1 and table S1).

Here, we report on our investigation of the Nwya Devu (ND) site located 4600 m above sea level (masl) in central Tibet and dated to at least 30 thousand years (ka) ago, making it the highest Pleistocene-age site yet identified (*9*). This discovery deepens considerably the history of human occupation of the TP and the antiquity of human high-altitude (>4000 masl) adaptations and encourages further investigation of the possibility that Denisovan-related DNA may have played a role in enabling Tibetans to live on the high plateau (*10*).

The ND site was discovered in 2013 during archaeological investigation of the eastern Changtang region in northern Tibet, which averages 5000 masl. The site is situated south of Siling Co and Co Ngoin lakes, ~300 km northwest of the Tibet Autonomous Region capital, Lhasa (Fig. 1), encompassing an area of ~1 km east-west by 2 km north-south. Thousands of stone artifacts made of black slate lie on the surface. In 2013 and 2016 to 2018, we carried out archaeological excavations and geological sampling to explore the site's taphonomy and the distribution of subsurface artifacts (materials and methods 2).

The ~170-cm-thick ND sedimentary sequence is situated on a terrace of Co Ngoin Lake, which has a surface elevation of ~4600 masl. This sequence can be divided into three layers from top to bottom (Fig. 2A). The 10- to 30-cm uppermost layer is composed of pebbly silt and fine sand. Many stone artifacts and some brecciated sediments were discovered on its surface. A 50- to 80-cm-thick stratum of well-sorted fine sands containing some angular gravel lies unconformably beneath Layer 1. In this horizon, a few channels filled with clast-supported boulders with a sandy matrix were observed, indicating temporary and swiftly flowing water. Additional features include periglacial involution, wind-eroded potholes, and pebbles densely distributed on the unconformity between Layers 1 and 2, suggesting long-term erosion under cold climatic conditions. Layer 3 comprises a sequence of alluvial deposits that consist mainly of sandy gravels enclosing shells of freshwater mollusks. Here, interlaced scouring channels developed extensively and were filled with highly weathered, silty, fine sands containing breccia, indicating strong erosion caused by high-energy water flow due to markedly warmer and more-humid conditions. A weathered and undulating unconformity capping Level 3 also indicates robust erosion associated with a wetter climate.

Anthropogenic stone artifacts have been recovered from the upper 138 cm of the sequence, including 3124 artifacts in Layer 1, 223 in Layer 2, and 336 from Layer 3. The Layer 2 artifacts were found mainly in channels but were almost absent in the fine sands that constitute the main body of this layer. No obvious typological, technological, or morphological differences can be detected among artifacts from these three discrete layers (tables S2 and S3), though more small pieces were discovered in Layer 1. We conclude that all artifacts discovered in the excavation

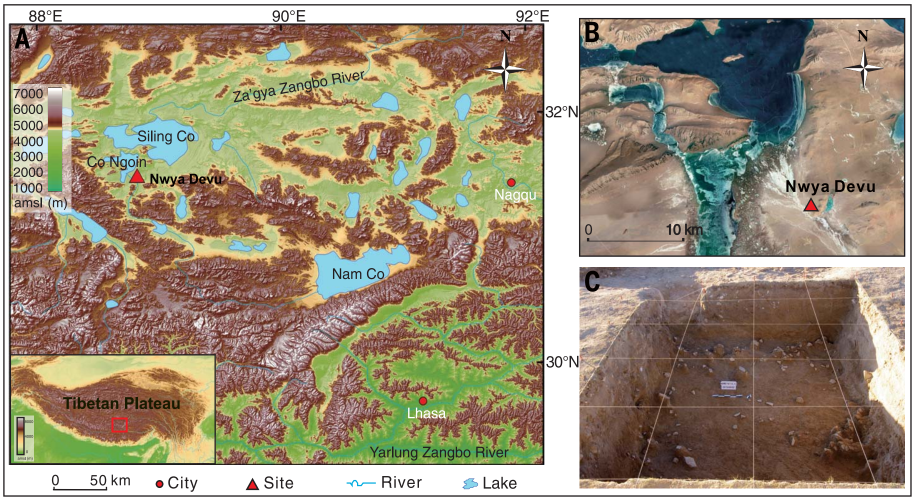

Fig. 1. The location of the ND site and excavation unit. (**A**) Regional map showing the location of the site. (**B**) Location of the site in relation to Co Ngoin and other large lakes. (**C**) Artifact distribution in Layer 3. Digital elevation model data for (A) from http://vterrain.org/Elevation/global.html. Satellite imagery for (B) courtesy of Google Earth.

---

[1] Key Laboratory of Vertebrate Evolution and Human Origins, Institute of Vertebrate Paleontology and Paleoanthropology, Chinese Academy of Sciences, Beijing 100044, China. [2] CAS Center for Excellence in Life and Paleoenvironment, Beijing 100044, China. [3] Tibetan Cultural Relics Conservation Institute, Lhasa 850000, Tibet Autonomous Region, China. [4] University of the Chinese Academy of Sciences, Beijing 100049, China. [5] State Key Laboratory of Lake Science and Environment, Nanjing Institute of Geography and Limnology, Chinese Academy of Sciences, Nanjing 210008, China. [6] Nagqu Prefecture Cultural Relics Bureau, Nagqu 852000, Tibet Autonomous Region, China. [7] State Key Laboratory of Estuarine and Coastal Research, East China Normal University, Shanghai 200062, China. [8] School of History, Renmin University of China, Beijing 100872, China. [9] Department of Anthropology, Harvard University, Cambridge, MA 02138, USA. [10] School of Anthropology, University of Arizona, Tucson, AZ 85721, USA. [11] Institute of Archaeology and Ethnography, Siberian Branch, Russian Academy of Sciences, Novosibirsk 630090, Russian Federation.
***Corresponding author. Email: gaoxing@ivpp.ac.cn (X.G.); gejunyi@ivpp.ac.cn (J.Y.G.)**

constitute a single assemblage, and Layer 3 is the primary cultural horizon. Artifacts found in the upper two layers are likely the result of reworking during the postoccupational formation of the site.

Because of the paucity of organic remains suitable for radiocarbon dating, the site's chronology was constructed mainly using optically stimulated luminescence (OSL) techniques (*11*). A total of 24 OSL dates for samples from three sections in the excavation unit (Fig. 2A) provide bracketing ages for the artifacts (table S4 and materials and methods 4.2).

In each section, OSL ages are generally consistent with stratigraphic order when taking standard deviations of age into account, and their chronostratigraphy is similar (Fig. 2B). The results show that the ages of Layer 1 range from ~13 ka to ~4 ka, suggesting a Holocene horizon. The accelerator mass spectrometry (AMS) ^{14}C dating of freshwater mollusk (*Gyraulus* sp.) shells from the bottom of Layer 1 (Fig. 2A) yielded an age of ~12.4 to 12.7 ka before the present, close to OSL dates generated from the same level (table S5), confirming the reliability of OSL dating. Chronometric ages for Layer 2 fall within a narrow range of ~25 to 18 ka, indicating deposition or reworking during the Last Glacial Maximum, which is consistent with our field observations and subsequent assessment of the prevailing climatic conditions at that time. Layer 3 yields ages of ~45 to 30 ka, in accordance with the AMS ^{14}C dating of mollusk shells (Fig. 2A, table S5, and materials and methods 4.1). On the basis of the OSL chronologies of the three sequences and two additional radiocarbon dates, the initial date of occurrence of stone artifacts at ND is estimated to be ~40 to 30 ka ago.

A total of 3683 stone artifacts were recovered from excavated layers over an area of 20 squares that measured 1 m by 1 m. The lithic assemblage includes blade cores, flake cores, blades, flakes, chunks, and tools (Fig. 3, figs. S2 to S6, table S2, and materials and methods 5). A distinctive feature of the assemblage is the production of blades and blade tools. Such blades were made from prismatic cores rather than Levallois cores, and most of the blades were detached from the cores' long, narrow faces (figs. S2 to S5 and table S6). Unidirectional flaking dominates the assemblage (72 of 91 pieces). Blade size varies considerably (table S7). Retouched tools include scrapers, awls, choppers, notches, and burins. Finely retouched formal pieces are rare, and most modification is expedient. All artifacts were produced from black slate derived from an outcrop on Nwya Devu Hill (figs. S7 and S8), ~800 m east of the excavation area. Considering the high ratio of debitage, the low number of curated tools, the size of the site, and its near proximity to the raw material source, we suggest that this site was a workshop where early Tibetans procured and knapped lithic material. No faunal remains, hearths, or structures have yet been uncovered.

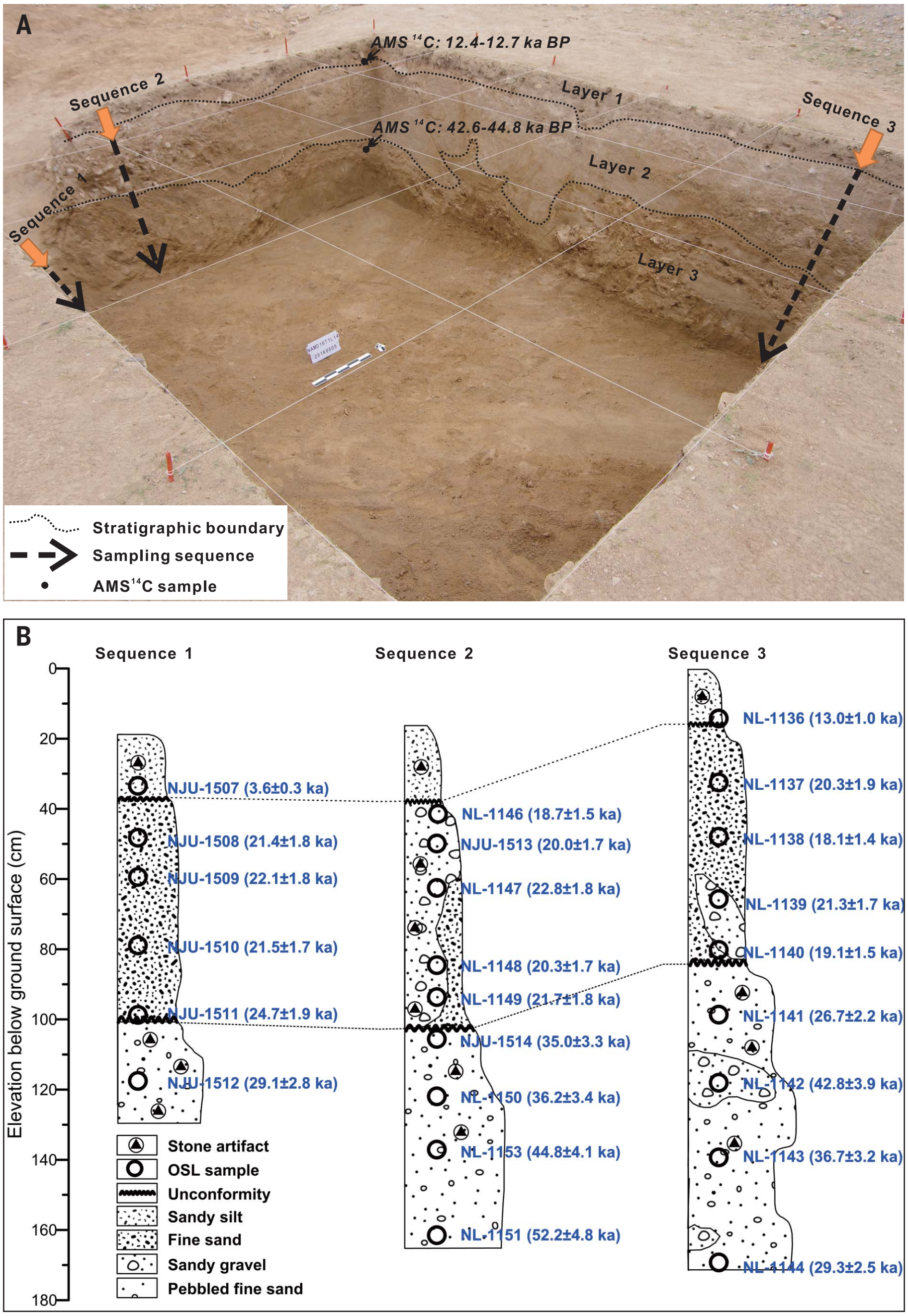

Fig. 2. Stratigraphic correlation of three sedimentary sequences and the position of OSL and AMS samples. (**A**) Diagram of sedimentary sequence and stratigraphic divisions at the site. Radiocarbon ages were determined after reservoir effect correction. (**B**) Stratigraphic correlation and OSL ages of three sequences.

ND is the first excavated stratified Paleolithic site in high-elevation Tibet. The extreme environment characterized by a pervasively cold, dry climate and atmospheric hypoxia presumably greatly constrained early human settlement in the region. The previous absence of reliably dated Paleolithic sites from the central TP (fig. S1 and table S1) led some archaeologists to propose that humans first colonized altitudes above 4000 masl only during the Holocene (*12*) or slightly before the Pleistocene-Holocene transition (*13*). Genetic studies imply different periods of human migration to the plateau, including the Neolithic and the late Paleolithic (*14*–*17*), and some genetic continuity between Tibet's initial Ice Age inhabitants and its modern indigenous population has been suggested (*15*). The age and typological characteristics of the lithic assemblage at ND indicate that modern humans bearing an advanced blade technology occupied this high-altitude area at least ~40 to 30 ka ago. This evidence establishes a record for the prehistoric conquest of this high-altitude environment, much earlier than current

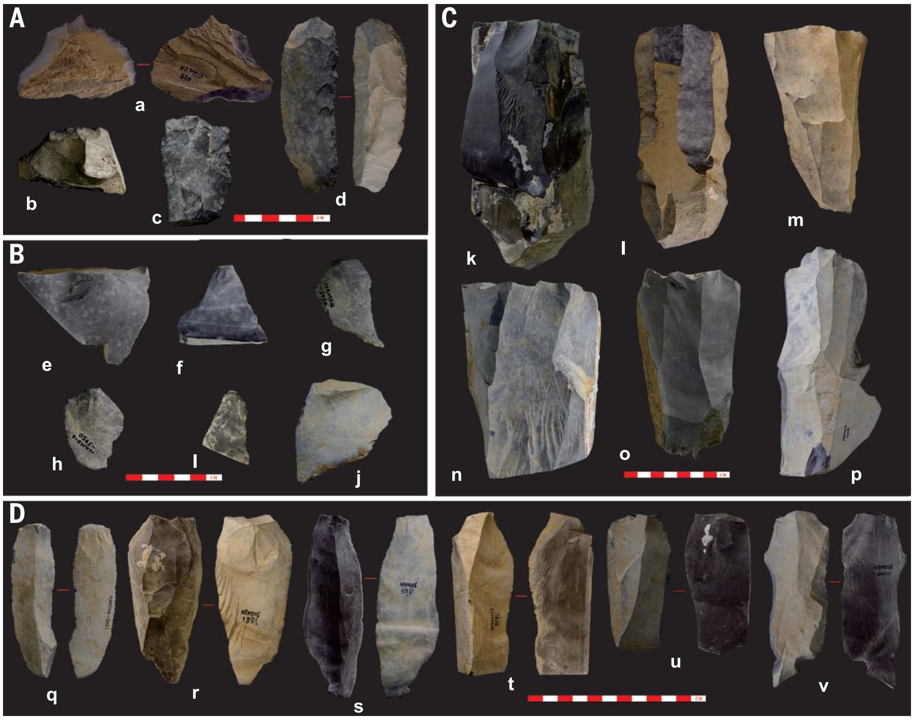

Fig. 3. Lithic artifacts unearthed at ND. (**A**) Tools. (a and b) Awl and side scraper, Layer 1; (c and d) side scrapers, Layer 3. (**B**) Flakes. (e and f) Layer 1; (g and h) Layer 2; (i and j) Layer 3. (**C**) Blade cores. (k and l) Layer 1; (m) Layer 2; (n to p) Layer 3. (**D**) Blades. (q) Layer 1; (r and s) Layer 2; (t to v) Layer 3.

evidence from the Andes for high-altitude colonization there suggests (*9*).

How did early humans respond to the combined stressors of hypoxia and scarcity of resources on the "roof of the world?" This occupation event in Tibet occurred during late marine isotope stage 3 (*18*), when ecological conditions on the high plateau were similar to or better than those today, thus allowing foragers to make repeated seasonal usage of the area for acquisition of lithic material and other resources. Meanwhile, the *EPAS1* gene region is thought to help reduce hypoxia in Tibetan populations, and the presence of this gene may be due to an infusion of DNA from Denisovan-related individuals (*10*). Hence, the environmental, genetic, and archaeological data complement one another, yielding a model for early Tibetan adaptation to the high plateau that combines biology and technology.

The abundance of prismatic blade cores at ND is nearly unique in China. Similar technocomplexes have been found at only a few sites in North China (*19*, *20*). Technologically, this lithic assemblage most closely resembles those classified as Early Upper Paleolithic in Siberia and Mongolia (*21*). On the basis of the typological similarities of the stone assemblages and hypotheses concerning the introgression of hominin ancestors, it is possible that early humans from Tibet and Siberia interacted at least 40 to 30 ka ago. Because Denisovans contributed 4 to 6% of their genetic material to the genomes of present-day Melanesians and may have been widespread in Asia during the late Pleistocene (*22*), the TP may be one region through which humans with Denisovan DNA diffused to the south, contributing an enhanced ability to adapt to the rigors of the hypoxic high-altitude environment.

The timing and dynamics of the permanent human settlement of the TP have generated much debate (*1*–*3*, *8*, *13*, *15*–*17*). Whereas some have argued that permanent occupation of the Earth's third pole was a relatively recent occurrence in which agriculture played a key role (*3*), others have suggested that biological adaptation to the plateau and its harsh environment required a much longer history and substantial period of residence (*1*, *23*), and a series of tentative trial steps must have been taken before successful adaptation was achieved (*12*). The discovery of the ND site, dated to at least 30 ka ago, has helped lift the curtain on this episode in the lengthy history of human exploration and colonization of the TP.

REFERENCES AND NOTES

1. P. J. Brantingham, X. Gao, *World Archaeol.* **38**, 387–414 (2006).
2. M. C. Meyer *et al.*, *Science* **355**, 64–67 (2017).
3. F. H. Chen *et al.*, *Science* **347**, 248–250 (2015).
4. Z. M. An, Z. S. Yin, B. Y. Li, *Curr. Anthropol.* **23**, 493–499 (1982).
5. B. Y. Yuan, W. W. Huang, D. Zhang, *Chin. Sci. Bull.* **52**, 2675–2679 (2007).
6. P. J. Brantingham, J. W. Olsen, G. B. Schaller, *Antiquity* **75**, 319–327 (2001).
7. D. B. Madsen *et al.*, *Archaeol. Res. Asia* **11**, 15–26 (2017).
8. M. Aldenderfer, *High Alt. Med. Biol.* **12**, 141–147 (2011).
9. K. Rademaker *et al.*, *Science* **346**, 466–469 (2014).
10. E. Huerta-Sánchez *et al.*, *Nature* **512**, 194–197 (2014).
11. R. G. Roberts, O. B. Lian, *Nature* **520**, 438–439 (2015).
12. P. J. Brantingham *et al.*, *Chin. Sci. Bull.* **48**, 1510–1516 (2003).
13. P. J. Brantingham, D. Rhode, D. B. Madsen, *Science* **329**, 1467 (2010).
14. L. L. Cavalli-Sforza, P. Menozzi, A. Piazza, *The History and Geography of Human Genes* (Princeton Univ. Press, 1994).
15. M. Zhao *et al.*, *Proc. Natl. Acad. Sci. U.S.A.* **106**, 21230–21235 (2009).
16. Z. Qin *et al.*, *Am. J. Phys. Anthropol.* **143**, 555–569 (2010).
17. C. M. Beall, *Annu. Rev. Anthropol.* **43**, 251–272 (2014).
18. Y. F. Shi, G. Yu, X. D. Liu, B. Y. Li, T. D. Yao, *Palaeogeogr. Palaeoclimatol. Palaeoecol.* **169**, 69–83 (2001).
19. F. Peng, H. Wang, X. Gao, *Quat. Int.* **347**, 12–20 (2014).
20. A. P. Derevianko, X. Gao, J. W. Olsen, E. P. Rybin, *Archaeol. Ethnol. Anthropol. Eurasia* **40**, 2–18 (2012).
21. F. Li, S. L. Kuhn, J. W. Olsen, F. Chen, X. Gao, *J. Anthropol. Res.* **70**, 35–67 (2014).
22. S. Sawyer *et al.*, *Proc. Natl. Acad. Sci. U.S.A.* **112**, 15696–15700 (2015).
23. C. M. Beall, *Annu. Rev. Anthropol.* **30**, 423–456 (2001).

ACKNOWLEDGMENTS

We thank J. L. Zhang, L. H. Li, W. D. Xiage, F. Y. Chen, Y. C. Zhao, C. Huang, T. Deng, S. Q. Wang, F. X. Wu, D. C. Liu, and J. S. Li for their assistance in the field. We are also indebted to H. Xie and R. P. Tang for their help in the laboratory. Our thanks go to L. P. Zhou, R. W. Dennell, A. S. Murray, F. J. Li, F. Li, M. Petraglia, A. M. Khatsenovich, S. H. Li, W. Q. Ji, B. Xu, and X. Y. Wang for their helpful discussions about lithic technology, fossil identification, and geomorphology. **Funding:** This research is supported by the Strategic Priority Research Program of Chinese Academy of Sciences, Pan-Third Pole Environment Study for a Green Silk Road (Pan-TPE) (grant no.: XDA2004010102), National Natural Science Foundation of China (grant nos.: 41572022, 41672024, 41672352, 41372362, and 41472026), the Strategic Priority Research Program of Chinese Academy of Sciences (grant no.: XDB26000000), the Excavation Funding and Emphatic Deployed Project of IVPP, CAS to X.L.Z., a research fellowship from the Youth Innovation Promotion Association CAS granted to H.L. (grant no.: 2015251), and a Chinese Academy of Sciences President's International Fellowship Initiative award (grant no.: 2018VCA0016) to J.W.O. **Author contributions:** X.L.Z., B.B.H., and X.G. obtained funding and initiated the project; X.L.Z., S.J.W., Z.J.C., W.D, J.Y.G., and M.J.Y. conducted field investigations and discovered the site; X.L.Z., S.J.W., X.G., W.H., W.D., P.Q.Z., and Y.S.J. excavated the site; J.Y.G. and X.Y.Z. conducted stratigraphic and taphonomic studies; H.L., J.Y.G., and X.M.N. performed the OSL dating; X.L.Z., P.Q.Z., Y.S.J., and M.J.Y. analyzed the stone artifacts; and X.L.Z., X.G., J.Y.G., H.L., J.W.O., S.J.W., and O.B.-Y. wrote the main text and supplementary materials with specialist contributions from the other authors. **Competing interests:** The authors declare no competing interests. **Data and materials availability:** All relevant data are available in the main text or the accompanying supplementary materials. All artifacts referred to in this study are curated in the Institute of Vertebrate Paleontology and Paleoanthropology, Chinese Academy of Sciences, Beijing, and are available for further research.

SUPPLEMENTARY MATERIALS

www.sciencemag.org/content/362/6418/1049/suppl/DC1
Materials and Methods
Figs. S1 to S18
Tables S1 to S10
References (*24*–*72*)

14 April 2018; accepted 10 October 2018
10.1126/science.aat8824

MATERNAL CARE

Prolonged milk provisioning in a jumping spider

Zhanqi Chen[1], Richard T. Corlett[1], Xiaoguo Jiao[2], Sheng-Jie Liu[3], Tristan Charles-Dominique[1], Shichang Zhang[2], Huan Li[1], Ren Lai[4], Chengbo Long[4], Rui-Chang Quan[1]*

Lactation is a mammalian attribute, and the few known nonmammal examples have distinctly different modalities. We document here milk provisioning in a jumping spider, which compares functionally and behaviorally to lactation in mammals. The spiderlings ingest nutritious milk droplets secreted from the mother's epigastric furrow until the subadult stage. Milk is indispensable for offspring survival in the early stages and complements their foraging in later stages. Maternal care, as for some long-lived vertebrates, continues after the offspring reach maturity. Furthermore, a female-biased adult sex ratio is acquired only when the mother is present. These findings demonstrate that mammal-like milk provisioning and parental care for sexually mature offspring have also evolved in invertebrates, encouraging a reevaluation of their occurrence across the animal kingdom, especially in invertebrates.

Parental food provisioning is often indispensable to an offspring's growth, development, and survival (*1*, *2*) and subsequently affects litter size, sex ratio, and offspring body size (*3*, *4*). Foods provided by parents can be classified into three forms: direct food sources, regurgitation feedings, and specialized food sources (*4*). Specialized foods include mammalian milk, as well as trophic eggs in amphibians and invertebrates (*4*–*6*), epidermal mucus in fish (*7*), and milk in cockroaches (*8*) and pigeons (*9*). However, these other foods are very different from mammalian milk in both duration of provisioning and degree of parent-offspring interaction. Parental food provisioning often stops when offspring acquire foraging ability (*4*), and provisioning for nutritionally independent offspring has mainly been reported from longer-lived vertebrates (*4*, *10*). Extended food provisioning frequently co-occurs with prolonged parental care, enhancing offspring fitness by providing assistance in foraging (*11*), teaching skills of foraging and competition (*12*), or influencing the morphology and behaviors of offspring (*13*). In extreme cases, parental care is extended to sexually mature offspring (*4*, *10*), but this has only been recorded in long-lived social vertebrates (*4*). Prolonged care increases offspring fitness by enabling them to allocate more time for learning foraging and social skills (*14*), antipredator behaviors, and defense against nest parasites and for selecting mates (*14*, *15*).

Toxeus magnus (Araneae: Salticidae) (*16*) is a jumping spider that mimics ants. The breeding nest is composed of either several large individuals (fig. S1), with two or more adults, or one adult female and several juveniles. This is a puzzling observation for a species assumed to be noncolonial and suggests that *T. magnus* might provide either prolonged maternal care or delayed dispersal. We thus questioned (i) whether *T. magnus* evolved long-lasting maternal care; (ii) if it has, whether the mother provides food for the offspring; (iii) what benefits could be gained from maternal care; and (iv) how long the mother provides an effective maternal care.

We first assessed how offspring developed and behaved under maternal care in laboratory conditions. No spiderlings were observed leaving the nest for foraging until they were 20.9 ± 1.2 days ($N = 207$, $N_{\mathrm{nest}} = 19$; SEM) old, and the mother was never seen to bring food back to the nest during this period, but offspring body lengths increased continuously (from 0.9 mm at hatching to 3.5 mm at 20 days, $N = 187$). Closer observations revealed that the mother provided a seemingly nutritive fluid, hereafter called milk,

---

[1] Center for Integrative Conservation, Xishuangbanna Tropical Botanical Garden, Chinese Academy of Sciences, Yunnan, 666303, China. [2] Center for Behavioral Ecology and Evolution, College of Life Sciences, Hubei University, Wuhan 430062, China. [3] Key Laboratory of Tropical Forest Ecology, Xishuangbanna Tropical Botanical Garden, Chinese Academy of Sciences, Yunnan, 666303, China. [4] Kunming Institute of Zoology, Chinese Academy of Sciences, Kunming 650223, Yunnan, China.
***Corresponding author. Email: quanrc@xtbg.ac.cn**

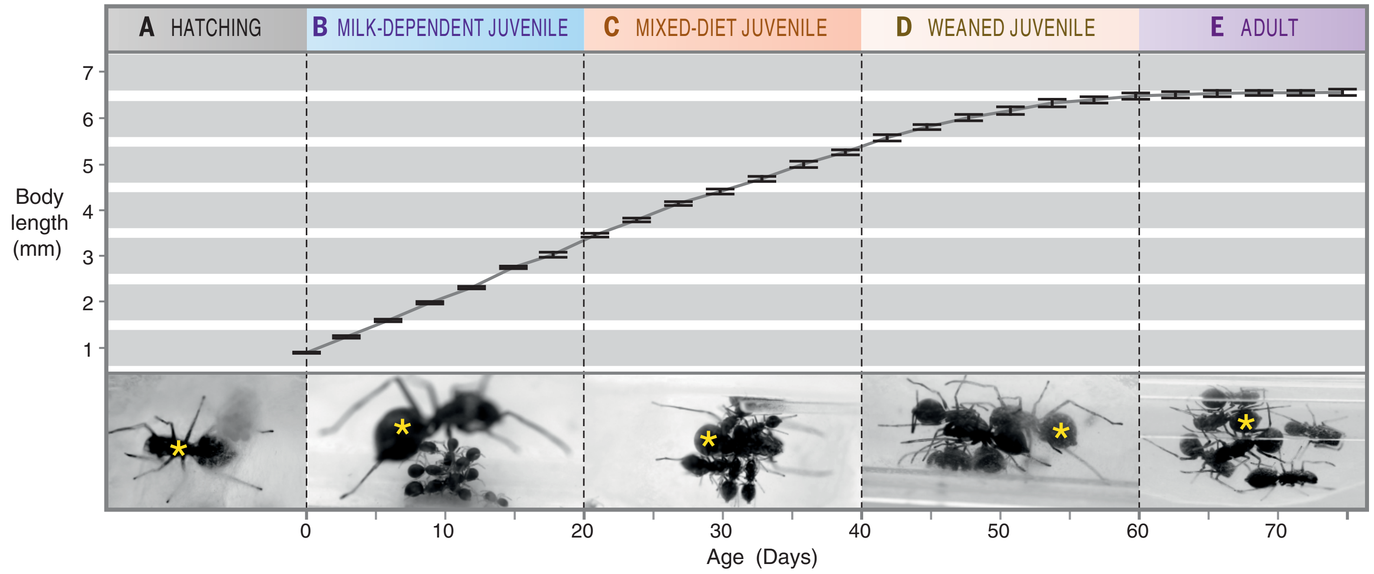

Fig. 1. *T. magnus* offspring body length growth and food resources during development. (**A**) Egg hatching. (**B**) Absolute milk dependence: Spiderlings do not leave the nest, and the mother releases milk droplets to the nest internal surface. (**C**) Spiderlings forage during the day and suck milk at night. (**D**) Subadults nutritionally independent but still return to nest. (**E**) Spiderlings reach sexual maturity, but some stay with the mother. *****The mother. $N = 207$ offspring, $N_{\mathrm{nest}} = 19$ surveyed nests, error bars (SEM).

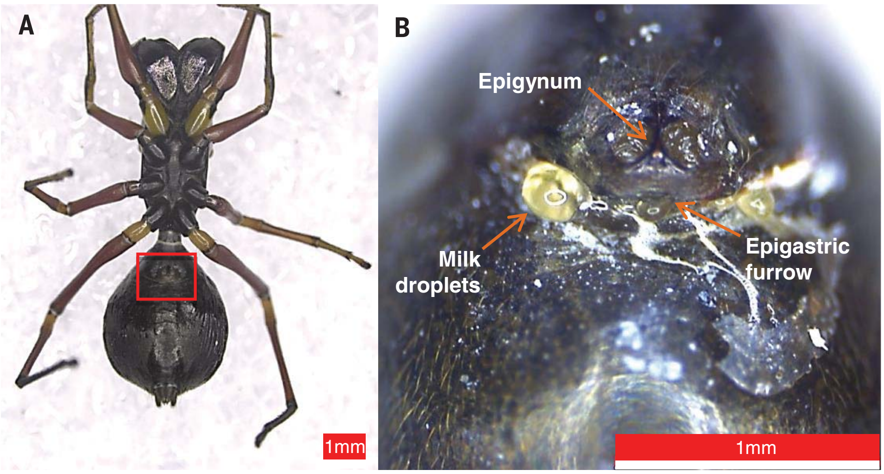

Fig. 2. Spider milk and its secretion site in *T. magnus*. (**A**) Ventral view of mother. (**B**) Milk droplets secreted after slight finger pressure on abdomen.

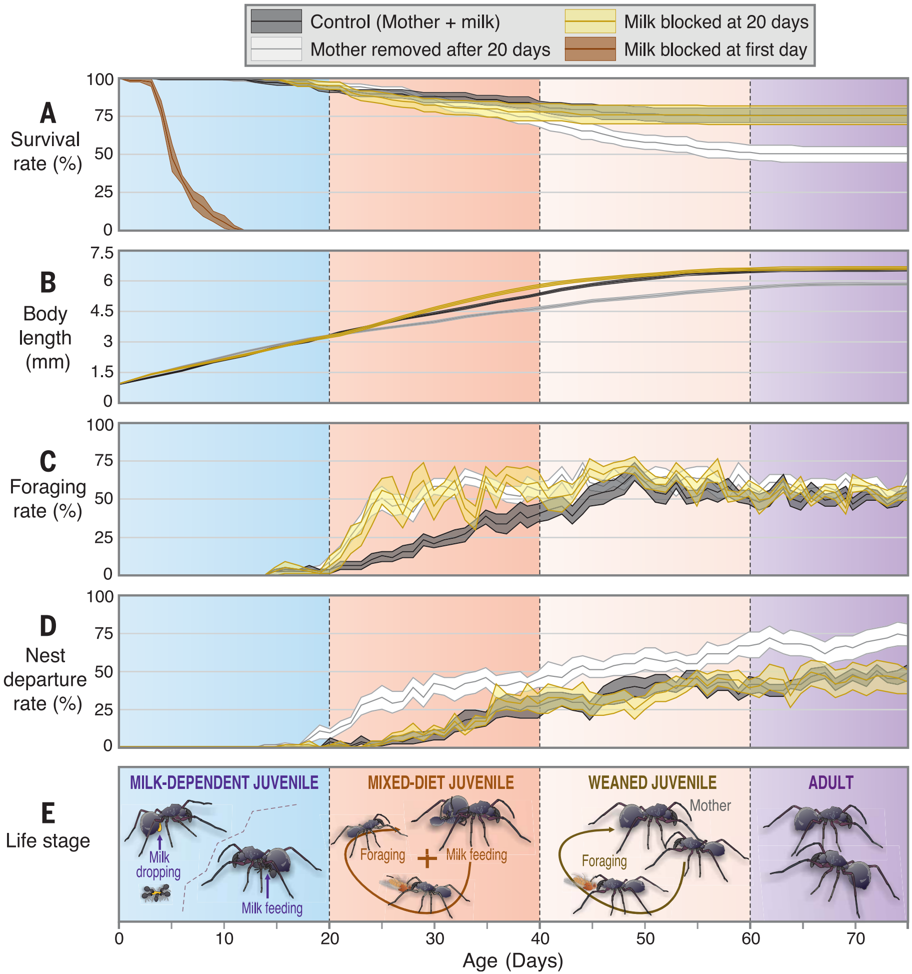

Fig. 3. Offspring development from hatching to independence under different treatments. MC (N = 187 offspring, N_{nest} = 19 surveyed nests), MR20 (N = 255 offspring, N_{nest} = 18 surveyed nests), MB20 (N = 101 offspring, N_{nest} = 8 surveyed nests), and milk blocked on the first day (MB1) (N = 62 offspring, N_{nest} = 5 surveyed nests). (**A**) Survival rate (surviving/hatched spiderlings). (**B**) Body length growth. (**C**) Foraging rate (foraged/surviving spiderlings). (**D**) Breeding nest departure rate (spiderlings that did not return to the breeding nest at night/surviving spiderlings). Error bars (SEM). (**E**) Life stages and food resource of spiderlings.

to the offspring. During the first week, she deposited milk droplets, excreted from her epigastric furrow, on the nest's internal surface. In response, spiderlings came and sucked the droplets (Fig. 1B). After the first week, milk deposition stopped and the offspring sucked directly from the mother's epigastric furrow (Fig. 1C and movies S1 and S2). Although spiderlings sometimes left the nest to forage from about 20 days, milk sucking continued until they reached the subadult stage at 37.5 ± 1.3 days (N = 167) (Figs. 1C), with body length of 5.26 ± 0.06 mm (around 80% of adult body length). From 40 days, milk feeding stopped, but spiderlings still used the nest at night after reaching sexual maturity within the next 20 days. Adulthood was reached at 52.2 ± 0.6 days with a body length of 6.57 ± 0.06 mm (N = 145) (Fig. 1D and fig. S2). Milk provisioning in *T. magnus* involves a specialized organ over an extended period, differing markedly from cockroaches, which deposit nourishing substances to the brood sac of developing embryos (*8*). In these aspects, *T. magnus* milk provisioning is more similar to mammalian lactation.

Observations under the microscope showed droplets leaking from the mother's epigastric furrow where the spiderlings sucked milk (Fig. 2, A and B). Spider milk total sugar content was 2.0 mg/ml, total fat 5.3 mg/ml, and total protein 123.9 mg/ml, with the protein content around four times that of cow's milk (*17*). We suggest this milk might have evolved from trophic eggs, unviable eggs functioning as a food for newly emerged offspring (*18*). The epigastric furrow is the egg-laying opening of spiders (*6*), and trophic eggs have evolved in diverse invertebrate taxa, including spiders (*6*). Trophic eggs are usually a one-time investment (*4*, *6*), but mothers may also supply progressive trophic eggs, as in the burrower bug *Adomerus triguttulus* (*18*). However, progressive provisioning usually stops after hatching (*19*), whereas spider milk is supplied continuously from hatching to subadult.

The mother continued nest maintenance throughout, carrying out spiderlings' exuviae and repairing nest damage. When receiving both maternal care and milk, 76% of the hatched offspring survived to adulthood. We also recorded a highly female-biased adult sex ratio: 84.14% (122/145). Although the mother apparently treated all juveniles the same, only daughters were allowed to return to the breeding nest after sexual maturity. Adult sons were attacked if they tried to return. This may reduce inbreeding depression, which is considered to be a major selective agent for the evolution of mating systems (*20*–*22*).

When we blocked the mother's epigastric furrow immediately with correction fluid after hatchling emergence, the hatchlings stopped development and died 10.4 ± 0.5 days later (Fig. 3A and fig. S3), showing their complete dependence on the milk supply. A separate experiment showed that correction fluid did not affect spiderlings' survivorship (fig. S6). We then tested why parental care and milk provisioning were continued after 20 days when the spiderlings were able to

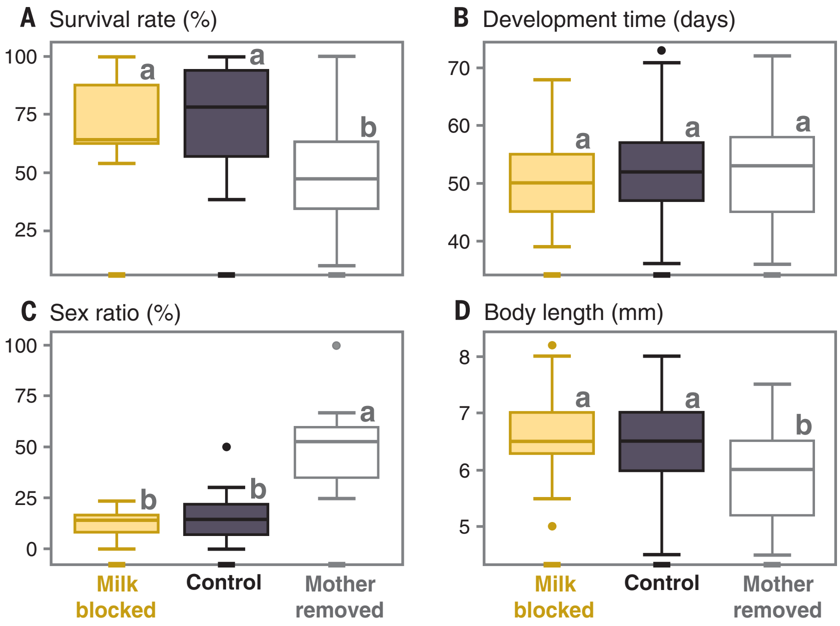

Fig. 4. Adult condition after three different treatments (MC, MB20, and MR20) of juveniles. (**A**) Survival of offspring to adult stage. (**B**) Development duration (days from hatching to maturity). (**C**) Adult sex ratio (mature males/total number of matured juveniles). (**D**) Adult body length. N_{MC} = 145 offspring, N_{MR20} = 121 offspring, N_{MB20} = 71 offspring, error bars (SEM). The letters "a" and "b" summarize the statistical grouping.

forage for themselves. We assessed the effects on survival, growth, foraging, and nest departure of (i) blocking the milk at this stage but leaving the mother in the nest to assess the effect of maternal care without milk provisioning and (ii) removing the mother from the nest to assess the combined effects of maternal care and milk provisioning. Removing the mother after 20 days significantly reduced survivorship (Fig. 3A) and body size (Fig. 3B) and increased foraging (Fig. 3C) and activities outside the nest (Fig. 3D). Blocking milk significantly reduced survivorship (Fig. 3A), but did not affect body size (Fig. 3B), and increased foraging (Fig. 3C) and activities outside the nest (Fig. 3D) compared with those receiving full maternal care and milk. Among spiderlings not receiving milk, those receiving maternal care survived significantly better (Fig. 3A), grew faster (Fig. 3B), and left the nest more rarely (Fig. 3D) than those without the mother, but both showed similar foraging frequency (Fig. 3C) (table S1 to S4). The milk-blocked spiderlings still attempted to suck milk from the mother (movie S3). These results show that from days 20 to 40, milk provisioning is not essential for spiderlings' survival, as they can compensate by foraging more, but has a positive effect on survivorship and development in lab conditions. In the field, milk provisioning, by reducing time spent outside the nest, might also reduce predation risk, as smaller offspring are more prone to predation (*23*). When spiderlings did not have milk, the higher survivorship with their mother present might be mediated by parasites. Although not quantified, parasites were observed on juveniles commonly without maternal care but rarely when the mother was present. Nest cleaning and repairing by the mother may partly explain this reduction in parasite loads. Nest parasites are common in invertebrates (*24*, *25*), and parental care usually plays a crucial role in reducing juvenile parasite infections (*4*, *10*, *25*).

Removing the mother at day 20 reduced the percentage of spiderlings reaching maturity [normal maternal care (MC) = 75.7 ± 4.6%; mother removed at 20 days (MR20) = 50.4 ± 5.3%] and reduced their adult body size (by 12%), whereas blocking milk did not change their adult survivorship [milk blocked at 20 days (MB20) = 73.8 ± 6.4%] or body size (MB20: 6.64 ± 0.07 mm) compared with the control (Fig. 4, A and D). Most notably, removing the mother greatly affected the adult sex ratio (female/total: MC = 0.84, MR20 = 0.50), whereas blocking milk did not (MB20 = 0.87) (Fig. 4C). Further analysis showed that the reduction of offspring body size after mother removal is not caused by a sex ratio change coupled with intersexual differences (table S6). No treatment impacted the timing of developmental stages (MR20: 52.5 ± 0.78 days, MB20: 50.5 ± 0.82 days, MC: 52.3 ± 0.60 days) (Fig. 4B and table S5). Thus, milk provisioning after 20 days does not affect adult survivorship, body size, sex ratio, and development time, but the mother's presence plays a key role in assuring high adult survival and normal body size. This may reflect the parasite defense discussed above. The mother's presence is also required for achieving the female-biased sex ratio of adult offspring. Sex role divergence theory suggests that the reproductive value of a population is heavily determined by the sex that invests more in parental care (*26*–*28*). In *T. magnus*, the mother invests much more than the male invests, predicting a female-biased sex ratio to be optimal for reproductive success with a polygamous mating system. Unequal adult sex ratios could be passively induced, as with the selective mortality with respect to sex in the bark beetle *Dendroctonus ponderosae* (*29*), or maternally induced, as in the spider *Oedothorax gibbosus* (*30*), but the mechanisms remain largely unclear.

In mammals, lactation is likely an adaptation mitigating an uncertain access to food resource as a juvenile and compensating for low probabilities for future reproduction (*31*). More generally, food provisioning helps promote offspring fitness by reducing risks linked to self-feeding (*32*). In nonmammals, we suggest that the most important ecological conditions favoring the evolution of lactation might be predation risk and uncertain food access. As a response, the mother's physiology, behavior, and cognition might have changed to adapt to providing milk and prolonged maternal care as in mammals (*33*). Extended parental care could have evolved in invertebrates as a response to complex and harsh living environments that require offspring skills (e.g., hunting, predator defense) to be fully developed before complete independence. Another aspect to investigate is whether lactation and extended parental care are accompanied by a reduction in offspring number because of milk production and parental care costs. Lastly, we anticipate that the discoveries presented in this study will encourage a reevaluation of the evolution of lactation and its occurrence across the animal kingdom.

REFERENCES AND NOTES

1. T. E. Martin, *Annu. Rev. Ecol. Syst.* **18**, 453–487 (1987).
2. J. K. Christians, *Biol. Rev. Camb. Philos. Soc.* **77**, 1–26 (2002).
3. J. S. Millar, *Ecology* **59**, 1055–1061 (1978).
4. N. J. Royle, P. T. Smiseth, M. Kölliker, *The Evolution of Parental Care* (Oxford Univ. Press, 2012).
5. J. C. Perry, B. D. Roitberg, *Oikos* **112**, 706–714 (2006).
6. R. Foelix, *Biology of Spiders* (Oxford Univ. Press, 2011).
7. J. Buckley *et al.*, *J. Exp. Biol.* **213**, 3787–3795 (2010).
8. B. Stay, A. C. Coop, *Tissue Cell* **6**, 669–693 (1974).
9. H. Beams, R. Meyer, *Physiol. Zool.* **4**, 486–500 (1931).
10. T. H. Clutton-Brock, *The Evolution of Parental Care* (Princeton Univ. Press, 1991).
11. D. K. Scott, *Anim. Behav.* **28**, 938–952 (1980).
12. A. L. Engh, K. Esch, L. Smale, K. E. Holekamp, *Anim. Behav.* **60**, 323–332 (2000).
13. A. Attisano, R. M. Kilner, *Anim. Behav.* **108**, 91–100 (2015).
14. N. B. Davies, J. A. Welbergen, *Science* **324**, 1318–1320 (2009).
15. C. Brown, K. Laland, *J. Fish Biol.* **59**, 471–493 (2001).
16. S. Saito, *Trans., Hist. Soc.* **13**, 32–61 (1933).
17. United States Department of Agriculture, (USDA), "Food Composition Database UPC: 763528306046," https://ndb.nal.usda.gov/ndb/search/list, [last accessed on 26/09/2018].
18. S. Kudo, T. Nakahira, *Oikos* **107**, 28–35 (2004).
19. T. Nakahira, *Naturwissenschaften* **81**, 413–414 (1994).
20. M. Szulkin, K. V. Stopher, J. M. Pemberton, J. M. Reid, *Trends Ecol. Evol.* **28**, 205–211 (2013).
21. D. Charlesworth, M. T. Morgan, B. Charlesworth, *Evolution* **44**, 1469–1489 (1990).
22. K. J. F. Verhoeven, M. Macel, L. M. Wolfe, A. Biere, *Proc. Biol. Sci.* **278**, 2–8 (2010).
23. J. N. Huang, R. C. Cheng, D. Li, I. M. Tso, *Proc. Biol. Sci.* **278**, 1356–1364 (2010).
24. T. Parmentier, W. Dekoninck, T. Wenseleers, *Anim. Behav.* **103**, 161–167 (2015).

25. A. M. Boulton, G. A. Polis, *Ecology* **83**, 282–287 (2002).
26. H. Kokko, M. D. Jennions, *J. Evol. Biol.* **21**, 919–948 (2008).
27. M. D. Jennions, L. Fromhage, *Philos. Trans. R. Soc. Lond. B Biol. Sci.* **372**, 20160312 (2017).
28. D. M. Ramsey, *J. Theor. Biol.* **266**, 675–690 (2010).
29. L. E. N. Lachowsky, M. L. Reid, *Ecol. Entomol.* **39**, 300–308 (2014).
30. B. Vanthournout *et al*., *Biol. Lett.* **10**, 20140159 (2014).
31. S. R. X. Dall, I. L. Boyd, *Proc. Biol. Sci.* **271**, 2049–2057 (2004).
32. A. Gardner, P. T. Smiseth, *Proc. Biol. Sci.* **278**, 196–203 (2010).
33. C. M. Lefèvre, J. A. Sharp, K. R. Nicholas, *Annu. Rev. Genomics Hum. Genet.* **11**, 219–238 (2010).

ACKNOWLEDGMENTS

We thank an anonymous referee and A. Jordan, L. Li, G. Liu, X. Yao, U. Gelin, X. Wang, and J. Chen for suggestions, X. Yang for equipment assistance, the Central Laboratory and Horticulture Department at XTBG for spider collection and maintenance, and Z. Wang and P. Wen for spider milk analysis. **Funding:** Work was supported by NSFC (no. 31370452) and CAS 135 and CAS-SEABRI (no. 2017 XTBG-F03). **Author contributions:** Z.C., R.C.Q., and X.J. designed experiments. Z.C. collected data and wrote the original manuscript. R.T.C., T.C.D., and R.C.Q. revised manuscripts and figures. S.J.L. analyzed data. S.Z. and H.L. assisted experiments. R.L. and C.L. analyzed milk composition. **Competing interests:** We declare no competing interests. **Data and materials availability:** All data are available in the main text or the supplementary materials.

SUPPLEMENTARY MATERIALS

www.sciencemag.org/content/362/6418/1052/suppl/DC1
Materials and Methods
Supplementary Text
Figs. S1 to S6
Tables S1 to S7
Captions for Movies S1 to S3
References (*34*)

16 March 2018; accepted 29 October 2018
10.1126/science.aat3692

CANCER

Human tumor genomics and zebrafish modeling identify *SPRED1* loss as a driver of mucosal melanoma

Julien Ablain[1]*, Mengshu Xu[2,3]*, Harriet Rothschild[1], Richard C. Jordan[2,4,5], Jeffrey K. Mito[1,6], Brianne H. Daniels[2,4], Caitlin F. Bell[7], Nancy M. Joseph[4], Hong Wu[8], Boris C. Bastian[2,3]†, Leonard I. Zon[1,9,10]†‡, Iwei Yeh[2,3]†‡

Melanomas originating from mucosal surfaces have low mutation burden, genomic instability, and poor prognosis. To identify potential driver genes, we sequenced hundreds of cancer-related genes in 43 human mucosal melanomas, cataloging point mutations, amplifications, and deletions. The *SPRED1* gene, which encodes a negative regulator of mitogen-activated protein kinase (MAPK) signaling, was inactivated in 37% of the tumors. Four distinct genotypes were associated with *SPRED1* loss. Using a rapid, tissue-specific CRISPR technique to model these genotypes in zebrafish, we found that *SPRED1* functions as a tumor suppressor, particularly in the context of *KIT* mutations. *SPRED1* knockdown caused MAPK activation, increased cell proliferation, and conferred resistance to drugs inhibiting KIT tyrosine kinase activity. These findings provide a rationale for MAPK inhibition in SPRED1-deficient melanomas and introduce a zebrafish modeling approach that can be used more generally to dissect genetic interactions in cancer.

Identification of driver genes in cancer is necessary for the development of precision therapies. Whereas sequencing of human tumors can point to potential oncogenes or tumor suppressors, robust animal models aid in implicating candidate drivers in malignant transformation. Discovery of new cancer genes and treatments is often hindered by the speed at which a model can be generated. In melanoma, certain genetic subtypes, including "triple wild-type" tumors (i.e., wild-type for *BRAF*, *NRAS*, and *NF1*) lack reliable models altogether. Developing new animal models through regular transgenesis and breeding is time consuming and labor intensive. There is a need for new and efficient modeling approaches to study cancer genes in vivo.

One tumor type in which genetics has not been fully explored is mucosal melanoma, which originates from melanocytes within mucosal epithelia (*1*–*3*). Mucosal melanomas harbor few point mutations, in keeping with their primary location on sun-protected sites (*4*, *5*). Instead, mucosal melanomas display genomic instability characterized by amplifications and deletions (*6*, *7*). Although dwarfed by the incidence of ultraviolet-induced melanomas in white populations, mucosal melanoma exhibits uniform incidence across ethnic groups and accounts for 9 to 22% of melanomas in Asian and black populations (*8*–*10*). Mucosal melanoma has a poor prognosis, with a 5-year survival rate of around 33% (*11*). In contrast to cutaneous melanomas, most mucosal melanomas do not harbor a known mitogen-activated protein kinase (MAPK) activating alteration. Mucosal melanomas harbor activating *KIT* mutations in 15% of cases, inactivation of *NF1* in 13% of cases, and *BRAF* [V600E (Val^{600}→Glu)] or *NRAS* [G12 (Gly^{12}), G13 (Gly^{13}), or Q61 (Gln^{61})] mutations in 6 and 8% of cases, respectively (*7*, *12*) (see table S1 for a summary of mucosal melanoma molecular studies). Treatment of *KIT*-mutant melanomas with inhibitors of KIT tyrosine kinase activity produces short-lived clinical responses (*13*–*15*). Thus, few patients with mucosal melanoma currently benefit from targeted therapies.

To better understand mucosal melanomas and to identify additional oncogenic alterations and therapeutic strategies, we extracted DNA from formalin-fixed paraffin-embedded primary or metastatic mucosal melanomas from 43 patients and performed targeted sequencing to high coverage (median of 300-fold mean coverage; see table S2 for clinical features and table S3 for sequencing metrics) (*16*). The average somatic mutation burden (calculated from 10 cases for which normal, nonlesional tissue was also sequenced) was low compared to other cancers (1.5 mutations/Mb), consistent with prior studies. Genomic instability in mucosal melanomas, as measured by two established metrics, was one of the highest among cancers (fig. S1). For each case, we identified point mutations, amplifications, and deletions known to be pathogenic in cancer (Fig. 1A). Alterations in *BRAF* (16%), *RAS* isoforms (16%), or *NF1* (14%), which account for MAPK-activating mutations in 86% of cutaneous melanomas (*17*), were collectively found in only 46% of mucosal melanomas. *BRAF* mutations consisted mainly of noncanonical mutations [L505H, G469A, L597R, and T599I (L, Leu; H, His; A, Ala; R, Arg; T, Thr; I, Ile)] (*18*–*20*) known to lead to weaker MAPK pathway activation than *BRAF* V600E. Activating *KIT* mutations occurred in 12% of cases. The distribution of mutations activating the MAPK pathway thus differs dramatically from that seen in cutaneous melanoma (Fig. 1B).

We identified genomic regions that are recurrently amplified and deleted across samples by GISTIC2 analysis, revealing a frequently deleted region at chromosome band 15q14, occurring in 21% of cases (Fig. 1C). All deletions of 15q14 included the *SPRED1* locus, and in three cases, *SPRED1* was the only gene within the deleted region. SPRED1 (sprouty-related, EVH1 domain-containing protein 1) is a negative regulator of the RAS-MAPK pathway (*21*, *22*). We estimated copy number at the *SPRED1* locus and classified *SPRED1* deletion as deep (nine cases) or shallow (four cases) (Fig. 2A and fig. S2). In two cases with shallow deletions of *SPRED1*, the remaining *SPRED1* alleles harbored truncating mutations, implicating *SPRED1* as the tumor suppressor gene at 15q14. *SPRED1* biallelic inactivation by deep deletion or by truncating mutation combined with loss of the wild-type allele affected 26% of cases (11/43), a frequency that is significantly greater than that in cutaneous melanoma (2.4%, Fisher's exact test, $P = 8.7 \times 10^{-7}$).

To confirm loss of SPRED1 protein expression in tumors with *SPRED1* biallelic inactivation, we performed immunohistochemistry for SPRED1 on 26 cases (8 with biallelic loss, 2 with monoallelic loss, and 16 without evidence of genetic inactivation of *SPRED1*) for which leftover tissue was available. In a melanocytic nevus that we used as the positive control, SPRED1 immunoreactivity was mainly in the cytoplasm, with accentuation near the membrane, in keeping with previous reports of SPRED1's subcellular localization (*21*). In all eight cases with inactivation of both *SPRED1* alleles, the majority of tumor cells did not show any immunoreactivity. Of the 16 mucosal melanomas in which we did not detect alterations of the *SPRED1* gene, eight displayed SPRED1 immunoreactivity similar to the positive control, whereas four had cytoplasmic staining and four had no SPRED1 immunoreactivity (Fig. 2B, fig. S3, and table S4). The absence of SPRED1 immunoreactivity in cases without *SPRED1* biallelic inactivation suggests that *SPRED1* was inactivated in these tumors by mechanisms not detected by our sequencing platform, such as by structural rearrangements within noncoding regions of *SPRED1* or by epigenetic silencing. Overall, 37% of the 43 mucosal melanomas we

---

[1] Stem Cell Program and Division of Hematology/Oncology, Boston Children's Hospital and Dana-Farber Cancer Institute, Boston, MA 02115, USA. [2] Helen Diller Family Comprehensive Cancer Center, University of California, San Francisco, San Francisco, CA 94158, USA. [3] Department of Dermatology, University of California, San Francisco, San Francisco, CA 94143, USA. [4] Department of Pathology, University of California, San Francisco, San Francisco, CA 94143, USA. [5] Department of Orofacial Sciences, University of California, San Francisco, San Francisco, CA 94143, USA. [6] Department of Pathology, Brigham and Women's Hospital, Boston, MA 02115, USA. [7] Department of Medicine, Stanford University Medical Center, Stanford, CA 94305, USA. [8] Fox Chase Cancer Center, Philadelphia, PA 19111, USA. [9] Harvard Stem Cell Institute, Harvard University, Cambridge, MA 02138, USA. [10] Howard Hughes Medical Institute, Boston Children's Hospital and Harvard University, Boston, MA 02115, USA.

*These authors contributed equally to this work.

†These authors contributed equally to this work.

‡Corresponding author. Email: iwei.yeh@ucsf.edu (I.Y.); leonard.zon@enders.tch.harvard.edu (L.I.Z.)

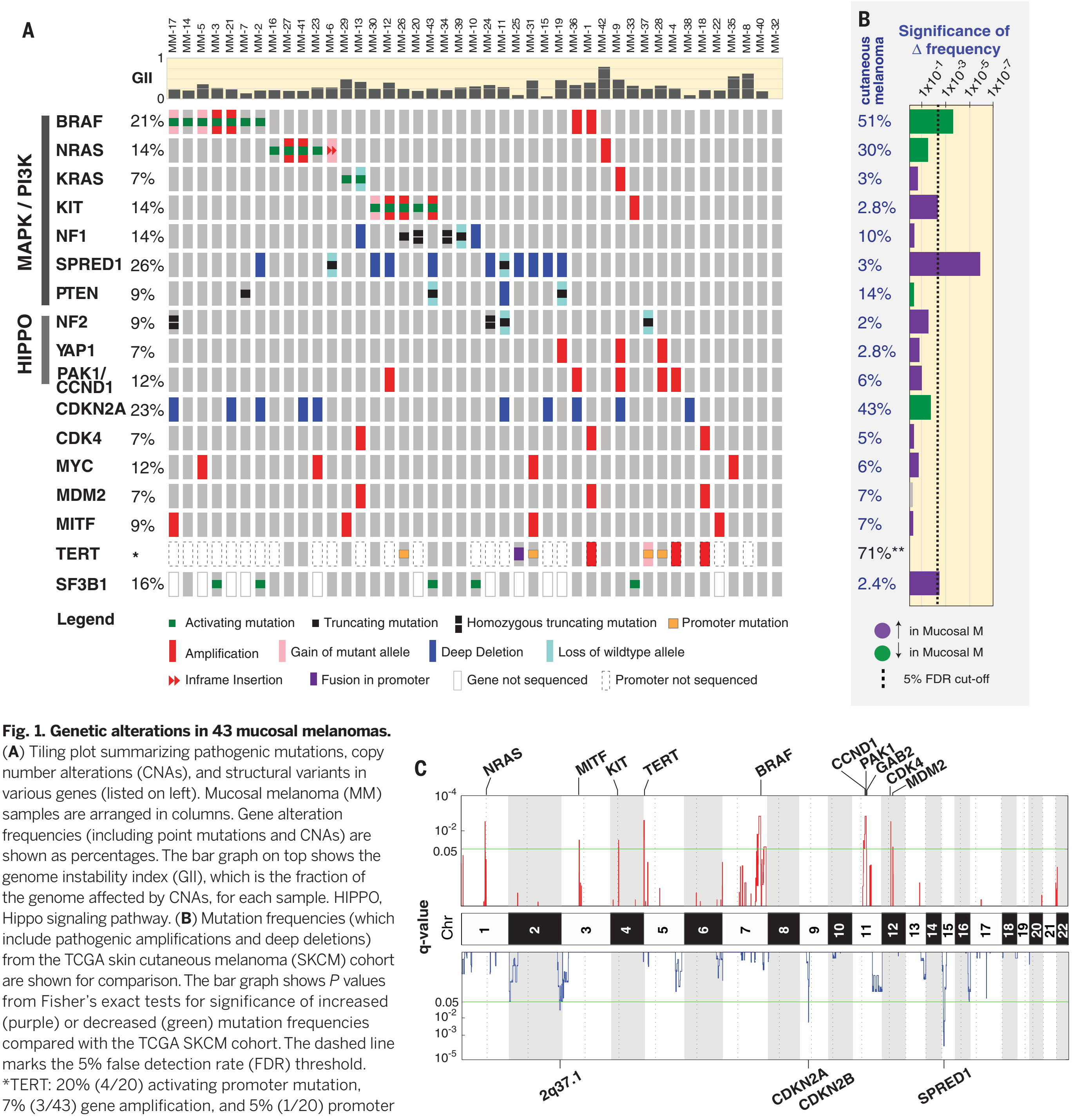

Fig. 1. Genetic alterations in 43 mucosal melanomas. (**A**) Tiling plot summarizing pathogenic mutations, copy number alterations (CNAs), and structural variants in various genes (listed on left). Mucosal melanoma (MM) samples are arranged in columns. Gene alteration frequencies (including point mutations and CNAs) are shown as percentages. The bar graph on top shows the genome instability index (GII), which is the fraction of the genome affected by CNAs, for each sample. HIPPO, Hippo signaling pathway. (**B**) Mutation frequencies (which include pathogenic amplifications and deep deletions) from the TCGA skin cutaneous melanoma (SKCM) cohort are shown for comparison. The bar graph shows *P* values from Fisher's exact tests for significance of increased (purple) or decreased (green) mutation frequencies compared with the TCGA SKCM cohort. The dashed line marks the 5% false detection rate (FDR) threshold. *TERT: 20% (4/20) activating promoter mutation, 7% (3/43) gene amplification, and 5% (1/20) promoter structural rearrangement. **TERT promoter mutation frequency in cutaneous melanomas (*29*). Mucosal M, mucosal melanoma. (**C**) GISTIC2 analysis identifies significant recurrent amplifications (red, top) and deletions (blue, bottom). Green lines indicate the *q* value thresholds for significance. Chr, chromosome.

examined showed evidence of *SPRED1* loss of function (biallelic inactivation and/or absence of SPRED1 protein by immunohistochemistry).

SPRED1 recruits NF1 to the plasma membrane, where NF1 catalyzes the conversion of active RAS-GTP (guanosine triphosphate) to the inactive RAS-GDP (guanosine diphosphate) state (*23*–*25*). Our analysis shows that *NF1* biallelic loss-of-function mutations (12%) occurred in a mutually exclusive pattern with *SPRED1* loss. Although this pattern of mutual exclusivity did not reach statistical significance, the functional relationship between SPRED1 and NF1 suggests that *SPRED1* inactivation and *NF1* inactivation play similar roles as driver mutations in mucosal melanoma. Altogether, complete inactivation of either *NF1* or *SPRED1* occurred in at least 49% of our cohort of tumors.

We next analyzed the genetic context of SPRED1 inactivation in melanoma. Most of the cases with SPRED1 loss (either by biallelic activation or loss of protein expression) were triple wild type (i.e., without activating mutations in *BRAF*, *RAS* isoforms, or biallelic loss

Fig. 2. Focused deletions at chromosome band 15q14 nominate *SPRED1* as a frequently lost tumor suppressor gene. (**A**) Heat maps show *SPRED1* deep deletion in nine tumors. Log_2-transformed copy number ratios are represented on a color scale. (**B**) SPRED1 immunohistochemistry (IHC) results for 26 tumors with available material. All samples with biallelic inactivation of *SPRED1* loss were negative for SPRED1. *In one sample, weak SPRED1 staining was present in 25% of tumor cells, suggesting the presence of a subclonal tumor population that retains SPRED1. (**C**) Shown are mucosal melanoma and TCGA skin cutaneous melanoma cases that harbor *SPRED1* biallelic loss-of-function mutations and/or exhibit loss of SPRED1 protein by IHC (for mucosal melanomas only), along with other MAPK pathway–activating mutations. In all cases where point mutations occur with gain or amplifications, the amplification occurs on the mutated allele. An asterisk indicates nonsense mutation. fs, frameshift; WT, wild type. Single-letter abbreviations for the amino acid residues are as follows: A, Ala; C, Cys; D, Asp; E, Glu; G, Gly; I, Ile; K, Lys; L, Leu; N, Asn; P, Pro; Q, Gln; R, Arg; S, Ser; T, Thr; V, Val; and W, Trp.

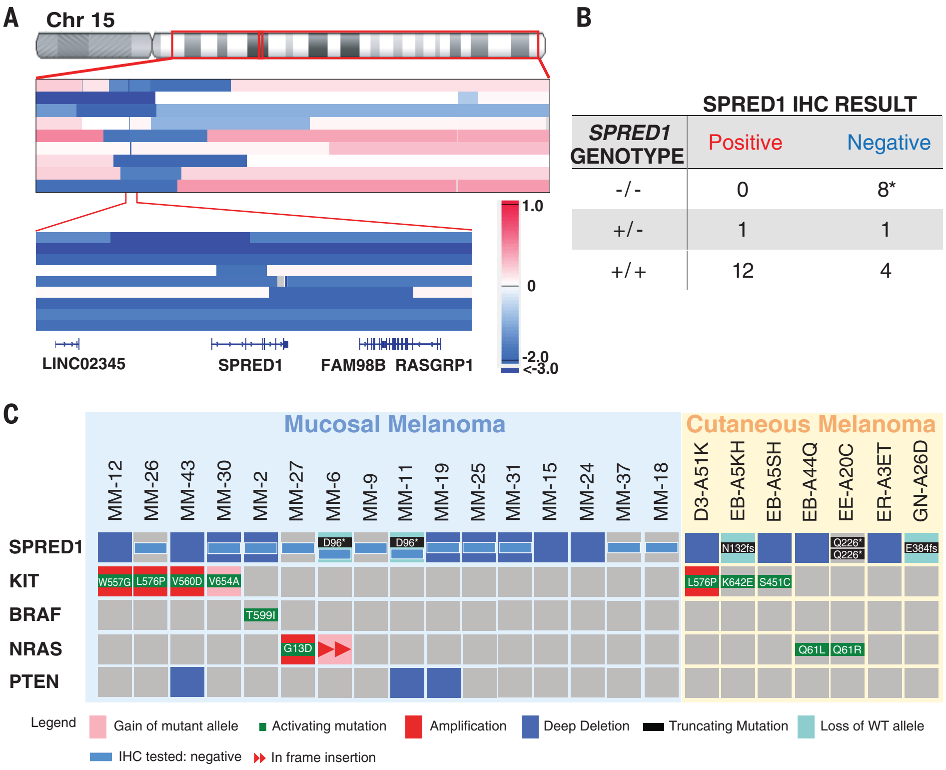

	SPRED1 IHC RESULT	
***SPRED1* GENOTYPE**	Positive	Negative
-/-	0	8*
+/-	1	1
+/+	12	4

Fig. 3. Melanoma modeling in zebrafish establishes genetic cooperation between *SPRED1* loss and *KIT* mutations. (**A**) Schematic representation of the MiniCoopR vector (left) and the CRISPR MiniCoopR vector (right), enabling melanocyte-specific gene expression or inactivation, respectively. *Pmitfa*, *mitfa* promoter; pA, polyadenylation signal; *ts*, tumor suppressor. Injection of MiniCoopR or CRISPR MiniCoopR vectors into *casper* (*mitfa*$^{-/-}$;*roy*$^{-/-}$) embryos rescues melanocyte formation in a mosaic fashion in adult zebrafish. Combinations of vectors expressing the oncogenes *KIT*^{K642E}, *BRAF*^{V600E}, or *NRAS*^{Q61R} and targeting *tp53* initiate melanoma. (**B** to **E**) Melanoma-free survival curves of *casper* zebrafish injected with the indicated combinations of vectors expressing *KIT*^{K642E}, *BRAF*^{V600E}, or *NRAS*^{Q61R} and targeting *tp53*, *pten*, and/or *spred1*. *P* values were calculated by log-rank test. ns, not significant.

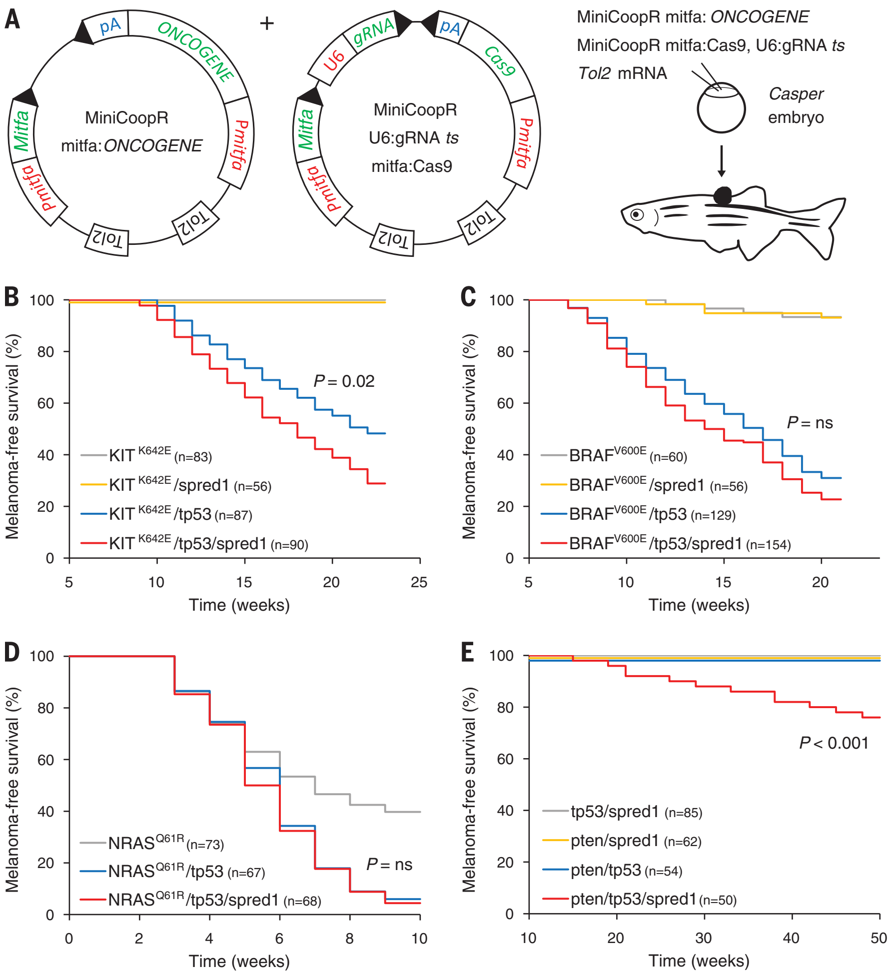

of *NF1*), both in our cohort of mucosal melanomas and in The Cancer Genome Atlas (TCGA) cohort of cutaneous melanomas. Notably, 30% of cases with SPRED1 loss (7/23) also harbored *KIT* alterations (Fisher's exact test, $P = 7.8 \times 10^{-6}$) (Fig. 2C). Another five cases with SPRED1 loss harbored alterations in *BRAF* or *NRAS*, and three cases had *PTEN* deep deletions. This pattern suggests that *SPRED1* inactivation may cooperate with other oncogenic events that activate the MAPK or phosphoinositide 3-kinase (PI3K) pathway.

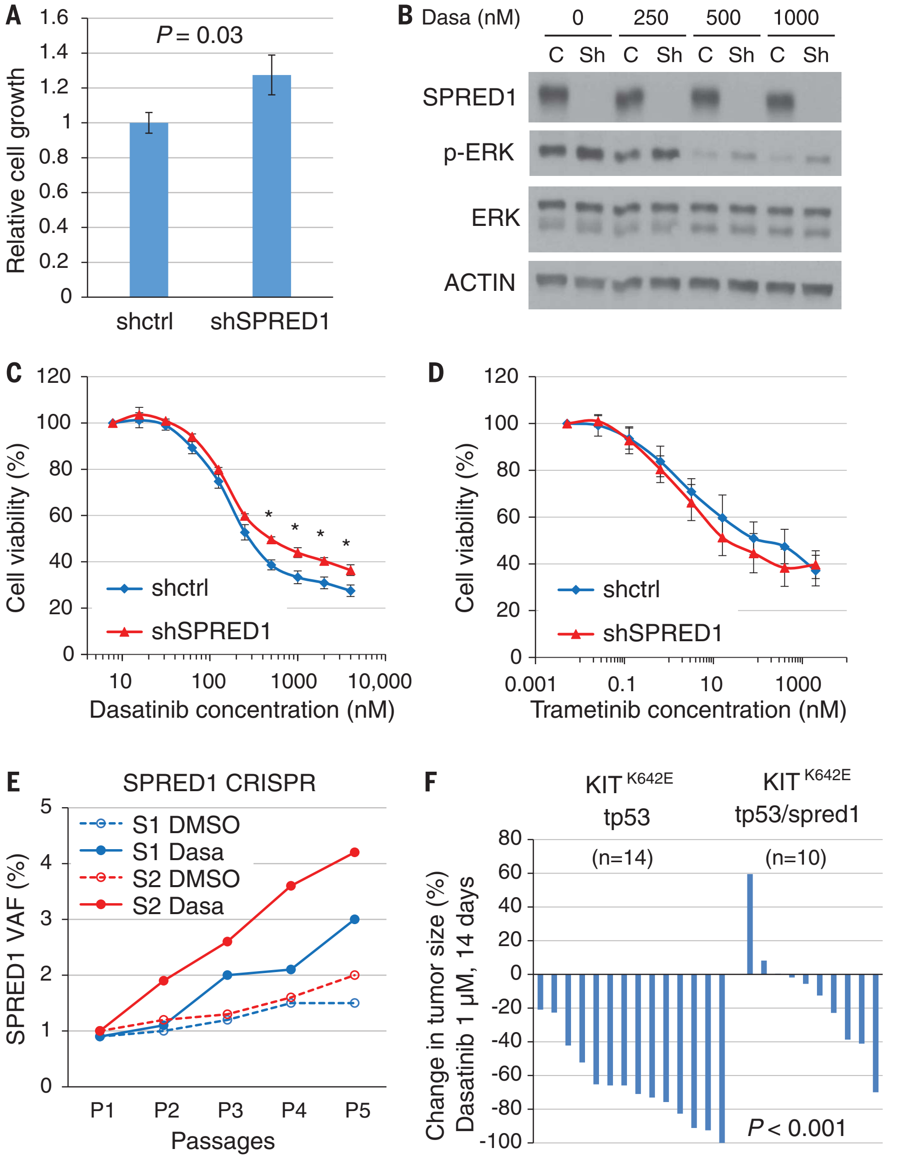

Fig. 4. Loss of *SPRED1* confers resistance to KIT inhibition in *KIT*-mutant melanoma by sustaining MAPK signaling and cell proliferation. (**A**) Proliferation of the KIT^{L576P}-driven human melanoma cell line WM3211 stably expressing a control shRNA (shctrl) or a shRNA directed against *SPRED1* (shSPRED1) measured after 4 days in culture and normalized to the control shRNA. Data are means ± SD of three independent experiments, and $P = 0.03$ by paired Student's *t* test. (**B**) Western blot analysis of MAPK pathway activity in the cells described in (A) treated with the indicated concentrations of dasatinib (Dasa) for 6 hours. C, shctrl; Sh, shSPRED1; p-ERK, phosphorylated ERK. Actin was used as a loading control. (**C** and **D**) Viability of the cells described in (A) treated with increasing concentrations of the KIT inhibitor dasatinib (C) or the MEK inhibitor trametinib (D) for 4 days. Data are means ± SD of three independent experiments, and $^*P < 0.05$ by paired Student's *t* test. (**E**) Evolution of frameshift variant allele fraction (VAF) in cultured WM3211 human melanoma cells transiently transfected with two independent vectors (S1 and S2) targeting *SPRED1* by CRISPR and treated with either dimethyl sulfoxide (DMSO) or 500 nM dasatinib over five passages. Data are from one representative experiment. (**F**) Quantification of tumor size in zebrafish injected with combinations of vectors expressing KIT^{K642E} and targeting either *tp53* or both *tp53* and *spred1*, after 14 days of 1 μM dasatinib treatment, relative to tumor size before treatment. $P < 0.001$ by two-tailed Student's *t* test.

To assess the function of *SPRED1* in melanoma in vivo, we created MAZERATI (Modeling Approach in Zebrafish for Rapid Tumor Initiation), a platform to rapidly model potential cancer drivers in vivo. Leveraging the power of transgenesis in zebrafish, we developed a robust method to express oncogenes and inactivate candidate tumor suppressor genes specifically in the melanocytes of the zebrafish using the MiniCoopR vector (*26*). We adapted our tissue-specific CRISPR system (*27*) to create the CRISPR MiniCoopR vector; this vector expresses Cas9 under the control of the melanocyte-specific *mitfa* promoter and contains a *mitfa* minigene that rescues melanocyte formation in a mosaic fashion upon injection into $mitfa^{-/-}$ embryos (Fig. 3A). We generated MiniCoopR vectors expressing the oncogenes *KIT* K642E (K, Lys), *BRAF* V600E, or *NRAS* Q61R, and CRISPR MiniCoopR vectors targeting the tumor suppressors *tp53*, *pten*, or *cdkn2a*. Except for the vector expressing *NRAS* Q61R, none of these vectors alone initiated cancer in adult *casper* zebrafish (*28*), pointing to the need for both oncogene expression and tumor suppressor loss to trigger melanoma formation (Fig. 3, B to E). Accordingly, combining a MiniCoopR vector expressing *KIT* K642E, *BRAF* V600E, or *NRAS* Q61R and a CRISPR MiniCoopR vector targeting *tp53* rapidly yielded melanomas (Fig. 3, B to E, and fig. S4). Of note, the anatomic location of *KIT*-mutant melanomas differed significantly from that of *BRAF* and *NRAS* mutant melanomas, as *KIT*-mutant melanomas occurred on the fins and internally more often than *BRAF* and *NRAS* mutant melanomas (fig. S4H). Inactivation of *cdkn2a* also cooperated with each of the three oncogenes to generate melanomas in vivo, whereas *pten* loss initiated melanoma formation in combination with *BRAF* V600E but not *KIT* mutants (figs. S5 and S6), pointing to differential impacts of PI3K pathway activation depending on the driving oncogene. These results indicate that our dual-vector MAZERATI system enables efficient and rapid generation of genetically defined primary tumors in F_0 adult animals within 3 months and can be used to test the effects of multiple combinations of oncogenes and tumor suppressor genes on tumorigenesis. In particular, we were able to model multiple genetic contexts in which *SPRED1* was lost in melanoma.

To determine the effects of *SPRED1* loss in these different contexts, we inactivated *spred1* using the CRISPR MiniCoopR vector in various zebrafish melanoma models. Targeting of *spred1* in combination with *tp53* did not result in melanoma formation within a year postinjection (Fig. 3E), suggesting that *SPRED1* loss is a weaker driver than *KIT*, *BRAF*, or *NRAS* mutation. Targeting *spred1* in combination with either *KIT* K642E or *BRAF* V600E also failed to initiate melanoma, indicating that *SPRED1* loss cannot substitute for the inactivation of tumor suppressor genes like *TP53* or *CDKN2A* (Fig. 3, B and C). Targeting *spred1* in the *KIT* L576P/*tp53* (P, Pro) or *KIT* K642E/*tp53* contexts significantly accelerated the onset of melanoma in our zebrafish model (Fig. 3B and fig. S7). Eleven of 14 (79%) *KIT* K642E/*tp53*/*spred1* tumors tested displayed clonal biallelic inactivation of *spred1* as assessed by sequencing of the CRISPR target sites. By contrast, *spred1* inactivation in the *BRAF* V600E/*tp53* or *NRAS* Q61R/*tp53* contexts did not significantly affect melanoma onset (Fig. 3, C and D). *Spred1* inactivation in zebrafish melanocytes also accelerated tumor onset in the *KIT* K642E/*cdkn2a* context (fig. S7). Conversely, *SPRED1* overexpression using the MiniCoopR vector significantly delayed melanoma development in vivo in the context of mutant *KIT* but not in the context of mutant *BRAF* (fig. S8). Targeting *spred1* in addition to *pten* and *tp53* resulted in late-onset melanomas, which were not observed when targeting *pten* and *tp53* alone (Fig. 3E). Thus, *spred1* inactivation accelerated melanoma onset in zebrafish in combination with mutant KIT expression or *pten* inactivation, but not mutant BRAF or NRAS expression, in the setting of *tp53* inactivation. These results establish *SPRED1* as a bona fide tumor suppressor gene in melanoma and demonstrate in vivo cooperation between *SPRED1* deletions and activating *KIT* mutations.

The human melanoma cell line WM3211 harbors a *KIT* L576P mutation and has intact SPRED1. We found that short hairpin RNA (shRNA)–mediated knockdown of SPRED1 in WM3211 cells increased their proliferation and MAPK activity (Fig. 4, A and B). These effects were not observed upon SPRED1 knockdown in BRAF-driven melanoma cells (fig. S9). Conversely, overexpression of SPRED1 in WM3211 cells decreased their proliferation and MAPK activity (fig. S10). These data indicate that SPRED1 modulates MAPK activation and cell proliferation in *KIT*-mutant melanoma. SPRED1 down-regulation by shRNA was associated with the persistence of a low, but detectable, level of extracellular signal–regulated kinase (ERK) phosphorylation in WM3211 cells treated with the KIT inhibitor dasatinib (Fig. 4B). SPRED1 knockdown also dampened the antiproliferative effect of dasatinib (Fig. 4C). We confirmed that this resistance to KIT inhibition was due, at least in part, to enhanced MAPK activity because it could be abolished by trametinib-mediated MAPK kinase (MEK) inhibition (Fig. 4D). We validated these results using a CRISPR approach. We found that in cultures of WM3211 cells suboptimally transfected with CRISPR vectors targeting *SPRED1*, the proportion of *SPRED1* frameshift mutant alleles sharply increased over time in dasatinib-treated cultures (Fig. 4E), whereas it modestly increased in vehicle-treated cultures. This result indicates that *SPRED1* knockout cells were under strong positive selection in the presence of KIT inhibitor. Finally, to test the effect of *SPRED1* loss on treatment of *KIT*-mutant tumors in vivo, we devised a protocol to treat adult zebrafish daily for 14 days. Dasatinib treatment of zebrafish with *KIT*-driven melanomas resulted in significant reductions in tumor size (fig. S11). However, the response to KIT inhibition was reduced with *spred1* knockout (Fig. 4F and fig. S12). These data suggest that *SPRED1* loss confers resistance to KIT inhibition in *KIT*-mutant melanoma by sustaining MAPK signaling and cell proliferation.

The increased incidence of *SPRED1* loss and *KIT* mutation in mucosal as compared to cutaneous melanoma (*7*) suggests that mucosal melanocytes are more susceptible to transformation by these alterations. The different anatomic distribution of melanomas initiated with *BRAF*, *NRAS*, or *KIT* mutations in our zebrafish model supports the concept of differential responses of melanocytes from different anatomic locations to oncogenic alterations. Our findings indicate that triple wild-type melanomas, in many cases, rely on MAPK hyperactivation mediated by *SPRED1* loss, often in the context of mutant *KIT*.

Our study establishes *SPRED1* as a major tumor suppressor gene in mucosal melanoma. Our findings have important consequences for the management of *KIT*-driven melanoma because they suggest that the loss of negative regulators of the MAPK pathway like *SPRED1* reduces the sensitivity of these tumors to KIT inhibition. Loss of *SPRED1* in *KIT*-mutant melanomas may, in part, explain the limited therapeutic efficacy of KIT inhibitors in melanoma as compared to their success in other *KIT*-mutant cancers, such as gastrointestinal stromal tumor. We show that melanomas that harbor *KIT* mutations and *SPRED1* loss depend on sustained MAPK signaling, indicating that combining KIT and MEK inhibitors may provide clinical benefit for patients with *KIT*-mutant melanomas. Screening for *SPRED1* status in melanoma, particularly those with *KIT* mutations, may prove useful to inform clinical and therapeutic decisions. Finally, our study illustrates the power of combining genomic analyses of human tumors with in vivo modeling to identify actionable driver alterations in cancer.

REFERENCES AND NOTES

1. F. G. Zak, W. Lawson, *Ann. Otol. Rhinol. Laryngol.* **83**, 515–519 (1974).
2. O. J. Clemmensen, C. Fenger, *Histopathology* **18**, 237–241 (1991).
3. A. W. Barrett, A. M. H. Raja, *Arch. Oral Biol.* **42**, 77–81 (1997).
4. S. J. Furney *et al.*, *J. Pathol.* **230**, 261–269 (2013).
5. M. Krauthammer *et al.*, *Nat. Genet.* **44**, 1006–1014 (2012).
6. J. A. Curtin *et al.*, *N. Engl. J. Med.* **353**, 2135–2147 (2005).
7. J. A. Curtin, K. Busam, D. Pinkel, B. C. Bastian, *J. Clin. Oncol.* **24**, 4340–4346 (2006).
8. K. Byrd-Miles, E. L. Toombs, G. L. Peck, *J. Drugs Dermatol.* **6**, 10–16 (2007).
9. Z. Chi *et al.*, *BMC Cancer* **11**, 85 (2011).
10. L. Altieri, M. K. Wong, D. H. Peng, M. Cockburn, *J. Am. Acad. Dermatol.* **76**, 250–257 (2017).
11. D. D. Kirchoff *et al.*, *Am. Surg.* **82**, 1–5 (2016).
12. E. Hodis *et al.*, *Cell* **150**, 251–263 (2012).
13. J. Guo *et al.*, *J. Clin. Oncol.* **29**, 2904–2909 (2011).
14. R. D. Carvajal *et al.*, *JAMA* **305**, 2327–2334 (2011).
15. F. S. Hodi *et al.*, *J. Clin. Oncol.* **31**, 3182–3190 (2013).
16. Materials and methods are available as supplementary materials.
17. Cancer Genome Atlas Network, *Cell* **161**, 1681–1696 (2015).
18. P. T. C. Wan *et al.*, *Cell* **116**, 855–867 (2004).
19. K. B. Dahlman *et al.*, *Cancer Discov.* **2**, 791–797 (2012).
20. H. Davies *et al.*, *Nature* **417**, 949–954 (2002).
21. T. Wakioka *et al.*, *Nature* **412**, 647–651 (2001).
22. A. Nonami *et al.*, *J. Biol. Chem.* **279**, 52543–52551 (2004).
23. I. B. Stowe *et al.*, *Genes Dev.* **26**, 1421–1426 (2012).
24. T. Dunzendorfer-Matt, E. L. Mercado, K. Maly, F. McCormick, K. Scheffzek, *Proc. Natl. Acad. Sci. U.S.A.* **113**, 7497–7502 (2016).
25. Y. Hirata *et al.*, *J. Biol. Chem.* **291**, 3124–3134 (2016).
26. C. J. Ceol *et al.*, *Nature* **471**, 513–517 (2011).
27. J. Ablain, E. M. Durand, S. Yang, Y. Zhou, L. I. Zon, *Dev. Cell* **32**, 756–764 (2015).
28. R. M. White *et al.*, *Cell Stem Cell* **2**, 183–189 (2008).
29. F. W. Huang *et al.*, *Science* **339**, 957–959 (2013).

ACKNOWLEDGMENTS

We thank C. Onodera and E. Talevich for helpful advice during data analysis. Many thanks to S. Liu and E. Martin for excellent technical assistance. We also thank S. Avagyan and M. Fazio for critical reading of the manuscript and helpful discussions. **Funding:** Funding for this study was provided by the Melanoma Research Foundation, the Dermatology Foundation, the Melanoma Research Alliance, the Ellison Foundation, the Starr Foundation, the V Foundation, the Terry Patters Melanoma Foundation, and the National Cancer Institute (1R35CA220481 to B.C.B., R01CA103846 to L.I.Z., K99CA201465 to J.A., U24CA196067 to R.C.J., and T32HL007627 to J.K.M.). L.I.Z. is a Howard Hughes Medical Institute Investigator. **Author contributions:** I.Y., J.A., M.X., B.C.B., and L.I.Z. designed the study. I.Y., B.C.B., H.W., N.M.J., B.H.D., and R.C.J. performed sample selection and collection. M.X. and I.Y. performed genetic analyses. M.X. and I.Y. performed immunohistochemistry, and I.Y. analyzed the results. J.A., H.R., and C.F.B. performed zebrafish experiments, and J.A. and J.K.M. analyzed the results. J.A. performed human melanoma cell line experiments and analyzed the results. I.Y., J.A., M.X., B.C.B., and L.I.Z. wrote the manuscript, and all authors provided constructive feedback. **Competing interests:** I.Y. received grants from Ignyta, Novartis, and Bayer, outside the submitted work. B.C.B. is a consultant for Lilly, Inc., outside the submitted work. L.I.Z. is a founder and stockholder of Fate Therapeutics, CAMP4 Therapeutics, and Scholar Rock, outside the submitted work. All other authors declare no conflicts of interest. **Data and materials availability:** Mucosal melanoma targeted DNA sequencing data have been deposited in dbGAP (project phs001594.v1). All plasmids described in this study have been deposited at Addgene.

SUPPLEMENTARY MATERIALS

www.sciencemag.org/content/362/6418/1055/suppl/DC1
Materials and Methods
Figs. S1 to S12
Tables S1 to S4
References (*30*–*70*)

12 July 2018; accepted 11 October 2018
Published online 1 November 2018
10.1126/science.aau6509

CANCER GENOMICS

Single-cell multiomics sequencing and analyses of human colorectal cancer

Shuhui Bian[1,2,3]*, Yu Hou[1,2]*, Xin Zhou[4]*, Xianlong Li[1,2]*, Jun Yong[1,5]*, Yicheng Wang[1,2]*, Wendong Wang[4], Jia Yan[1,2], Boqiang Hu[1,2], Hongshan Guo[1,2], Jilian Wang[4], Shuai Gao[1,2], Yunuo Mao[1,2], Ji Dong[1,2], Ping Zhu[1,2,3], Dianrong Xiu[4], Liying Yan[1,5], Lu Wen[1,2], Jie Qiao[1,3,5,6]†, Fuchou Tang[1,2,3]†, Wei Fu[4]†

Although genomic instability, epigenetic abnormality, and gene expression dysregulation are hallmarks of colorectal cancer, these features have not been simultaneously analyzed at single-cell resolution. Using optimized single-cell multiomics sequencing together with multiregional sampling of the primary tumor and lymphatic and distant metastases, we developed insights beyond intratumoral heterogeneity. Genome-wide DNA methylation levels were relatively consistent within a single genetic sublineage. The genome-wide DNA demethylation patterns of cancer cells were consistent in all 10 patients whose DNA we sequenced. The cancer cells' DNA demethylation degrees clearly correlated with the densities of the heterochromatin-associated histone modification H3K9me3 of normal tissue and those of repetitive element long interspersed nuclear element 1. Our work demonstrates the feasibility of reconstructing genetic lineages and tracing their epigenomic and transcriptomic dynamics with single-cell multiomics sequencing.

Colorectal cancer (CRC), a major cause of mortality, is characterized by heterogeneous features of genomic, epigenomic, and transcriptomic alterations (*1*–*4*), which are not separate events, as multiple cellular processes may interact to promote tumorigenesis (*5*, *6*). Intratumoral heterogeneity (ITH) across multiple layers of molecular features is a barrier for effective diagnosis and treatment (*7*). However, studies have been limited to analysis of bulk cells which consist of non–tumor cells and complex subclones and only reflect the average profiles of tumor samples. Single-cell genome and transcriptome sequencing have revealed ITH in several cancer types (*8*–*12*). However, single-cell sequencing has been limited in the ability to characterize multiple layers of molecular features of each genetic lineage.

Our scTrio-seq (single-cell triple omics sequencing) technique (*13*) can assess somatic copy number alterations (SCNAs), DNA methylation, and transcriptome information simultaneously from an individual cell. Here, we introduce scTrio-seq2, which integrates single-cell whole-genome bisulfite sequencing (scBS-seq) (*14*) and improves detection efficiencies (fig. S1 and table S1). In this study, we performed multiregional sampling and generated scTrio-seq2 profiles for 12 CRC patients (stage III or IV) (Fig. 1, fig. S2, and table S1). In total, ~1900 single cells passed quality control. Paired primary tumors and lymphatic or distant metastases were obtained from 10 patients (table S1). For patient CRC01, we obtained 534 single cells (after quality control) from adjacent normal colon (NC) tissue and 16 tumor regions, including the primary tumor (PT), the lymph node metastasis (LN), the liver metastasis (ML), and a posttreatment liver metastasis (MP) after chemotherapy (fig. S2).

Most cancer cells from six of our study patients (CRC01, CRC03, CRC04, CRC06, CRC09,

Fig. 1. Reconstruction of genetic lineages with scTrio-seq2. Global SCNA patterns (250-kb resolution) of CRC01. Each row represents an individual cell. The subclonal SCNAs used for identifying genetic sublineages were marked and indexed; for details, see fig. S6B. On the top of the heatmap, the amplification or deletion frequency of each genomic bin (250 kb) of the non-hypermutated CRC samples from the TCGA Project and patient CRC01's cancer cells are shown.

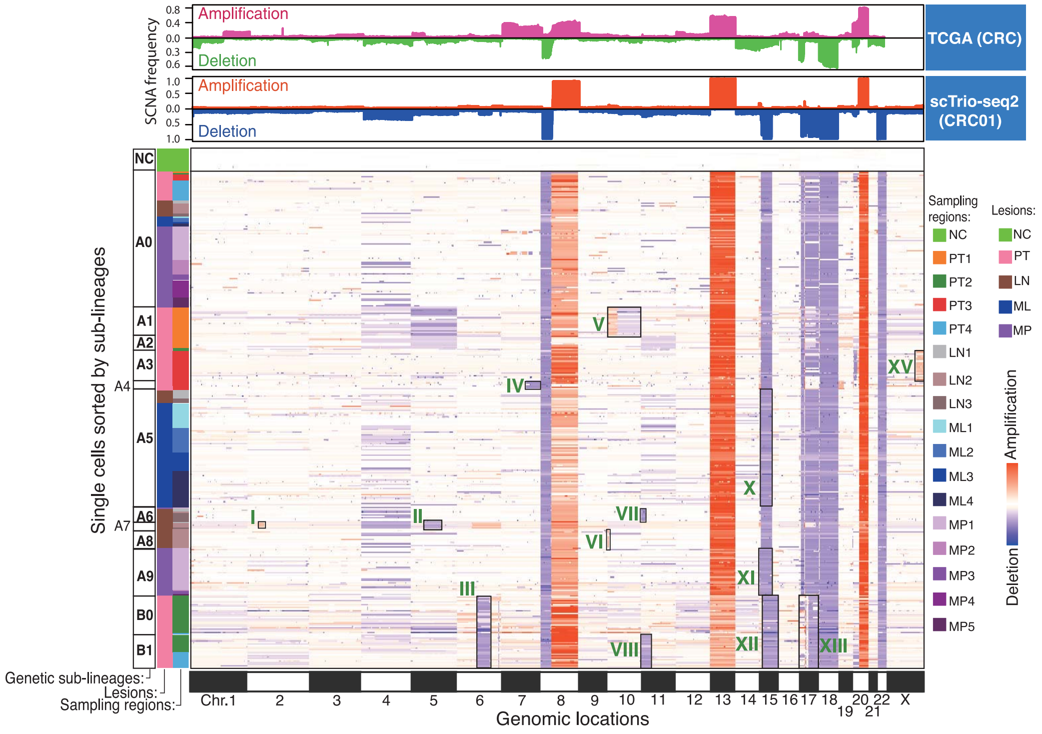

---

[1]Beijing Advanced Innovation Center for Genomics, College of Life Sciences, Department of Obstetrics and Gynecology, Third Hospital, Peking University, Beijing 100871, China. [2]Biomedical Pioneering Innovation Center and Center for Reproductive Medicine, Ministry of Education Key Laboratory of Cell Proliferation and Differentiation, Beijing 100871, China. [3]Peking-Tsinghua Center for Life Sciences, Academy for Advanced Interdisciplinary Studies, Peking University, Beijing 100871, China. [4]Department of General Surgery, Peking University Third Hospital, Beijing 100191, China. [5]Key Laboratory of Assisted Reproduction, Ministry of Education, Beijing 100191, China. [6]Beijing Key Laboratory of Reproductive Endocrinology and Assisted Reproductive Technology, Beijing 100191, China.
*These authors contributed equally to this work.
†Corresponding author. Email: jie.qiao@263.net (J.Q.); tangfuchou@pku.edu.cn (F.T.); fuwei@bjmu.edu.cn (W.F.)

and CRC11) were assigned to the CMS2 group (fig. S3, A to C), a canonical CRC group with abnormal activation of the WNT/β-catenin and MYC signaling pathways, frequent SCNAs, and non-hypermutation (*2*). Whole-genome sequencing (WGS) verified a low frequency of somatic single-nucleotide variations (SNVs) in tumors from CRC01 (fig. S3D) (*1*) and identified an oncogenic mutation of *NRAS* and inactivating mutations of *APC* and *SMAD4*, consistent with the features of non-hypermutated CRC (*1*).

For the 10 patients for whom we had DNA methylation data, we performed SCNA profiling of individual cells at 250-kilobase (kb) resolution (Fig. 1 and figs. S4A and S5). Significant focal SCNAs and probable gene targets were identified (fig. S4B and table S2) (*15*). Additionally, the SCNA profiles estimated from the transcriptome data were consistent with those estimated from DNA methylation data (fig. S4C). The scTrio-seq2 data confirmed the presence of one cancer cell with homozygous deletions of several whole chromosomes (fig. S4C).

Genomic alterations in tumors provide markers for lineage tracing (*16*, *17*). Clonal variants occur in early tumorigenesis, whereas subclonal SCNAs indicate the emergence of sublineages (Fig. 1 and figs. S6 and S7). As whole-chromosome or arm-level events are more likely to be acquired independently in different lineages (*18*, *19*), we mainly used subclonal breakpoints within chromosome arms to identify genetic lineages (fig. S6). For five patients for whom we had methylation data (for >90 cells), cancer cells were classified into several genetic sublineages (Fig. 1 and figs. S5 to S7). For CRC01, we identified 12 sublineages originating from two distinct lineages (A and B) on the basis of 21 subclonal breakpoints; each sublineage was supported by 4 to 8 subclonal breakpoints (Fig. 1 and figs. S6 and S7). The sublineage A5 of CRC01 was detected in both LN (17%) and ML (87%), indicating that these metastases had a common origin (*20*). In all five patients, the primary tumors showed more complex subclonal structures than the metastases, indicating that metastases tend to be clonal (fig. S7, B and C).

Genome-wide DNA hypomethylation was detected in individual cancer cells compared with paired NC cells (Fig. 2A and figs. S8 and S9A), consistent with findings in published studies (*3*, *4*). Genome-wide DNA methylation levels were relatively homogenous within a genetic lineage (or sublineage) but showed discrepancies among different lineages (or sublineages) (Fig. 2A and figs. S8C and S9). Tumor lineages' hypomethylated regions were significantly enriched in long terminal repeats (LTRs), long interspersed nuclear element 1 (LINE-1, L1), and heterochromatin regions (H3K9me3) ($P < 0.05$, Fisher's exact test); in contrast, tumor lineages' hypermethylated regions were enriched in CpG islands (CGIs), H3K4me3, and open chromatin ($P < 0.05$, Fisher's exact test) (fig. S10, A and B). A representative long differentially methylated region (DMR) (~34 kb) located in the heterochromatin region of chromosome 16 differed between lineages A and B of CRC01 (Fig. 2B). This region was hypermethylated in NC but heterogeneous in cancer cells (fig. S10C).

We further traced the dynamics of DNA methylation and gene expression during metastasis within one single lineage each for CRC01 and CRC10. Global DNA methylation levels were relatively stable during metastasis and accompanied by changes in focal regions, such as promoters (fig. S11, A to C). We did not observe obvious changes pre- or postmetastasis in the expression

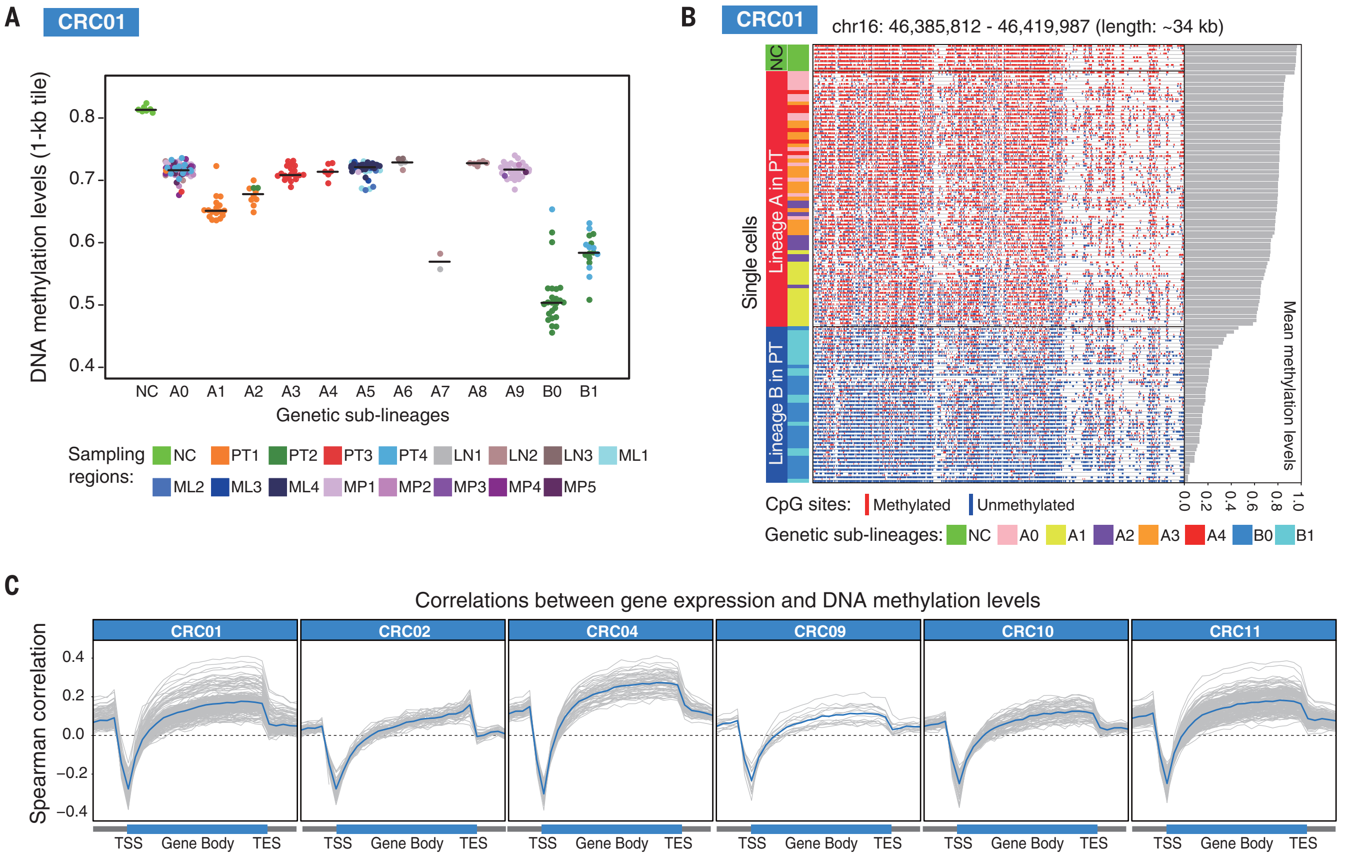

Fig. 2. Associations between DNA methylation and gene expression levels. (**A**) Single-cell global DNA methylation levels (1-kb tile) of each sublineage for patient CRC01. Colors represent sampling regions. Lines represent median values. (**B**) One representative DMR on chromosome 16 between genetic lineages A and B in the PT sample of CRC01. Each row shows one individual cell sorted by the mean methylation levels in the region. Each column shows one single CpG site. The bar plot on the right shows each cell's mean methylation levels in the region. (**C**) The correlations between gene expression levels and DNA methylation levels across gene bodies and their 15-kb flanking regions (Spearman correlations). The gray lines represents individual cells. The blue line represents the mean value for each patient. TSS, transcription start site; TES, transcription end site.

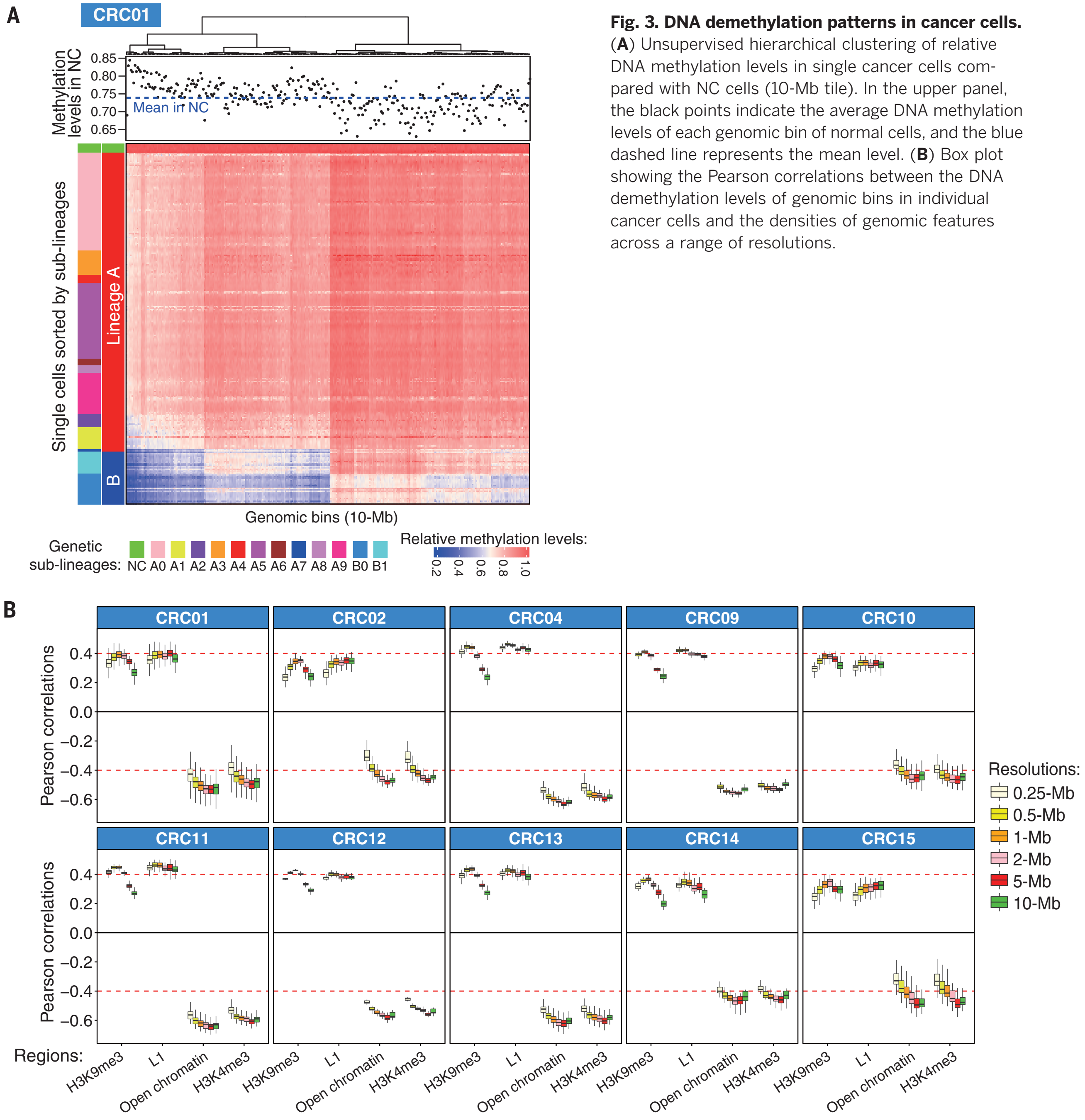

Fig. 3. DNA demethylation patterns in cancer cells. (**A**) Unsupervised hierarchical clustering of relative DNA methylation levels in single cancer cells compared with NC cells (10-Mb tile). In the upper panel, the black points indicate the average DNA methylation levels of each genomic bin of normal cells, and the blue dashed line represents the mean level. (**B**) Box plot showing the Pearson correlations between the DNA demethylation levels of genomic bins in individual cancer cells and the densities of genomic features across a range of resolutions.

levels or DNA methylation levels of epithelial–mesenchymal transition–related genes (fig. S11, D to G). Furthermore, we did observe molecular associations between the methylome and transcriptome of individual cells. Globally, the correlations between DNA methylation levels and gene expression levels were negative in promoter regions but positive in gene body regions in individual cells (Fig. 2C). The transcriptome groups were consistent with genetic lineages and DNA methylation groups for CRC04 but not for CRC01, CRC10, and CRC11 (fig. S12, A and B). Additionally, some promoters of genes associated with tumor proliferation and migration contained DMRs (*21*) (fig. S12, C and D).

Cancer cells experienced variable demethylation degrees across the whole genome, which were concordant within each genetic sublineage but varied in degree among different sublineages (Fig. 3A and fig. S13A). The relative demethylation degrees of cancer cells were correlated with the absolute DNA methylation levels of NC cells across the genome (fig. S13B), and this comparison suggested that the regions with higher DNA methylation levels in NC cells tended to undergo stronger demethylation in cancer cells.

DNA demethylation showed positive correlations with the densities of L1 and H3K9me3 modifications (of NC cells) but negative correlations with the densities of the H3K4me3 modifications and open chromatin (of NC cells) (Fig. 3B). Similar correlations were also observed between SNVs and chromatin state in the two patients for whom there were WGS data (fig. S13C), consistent with chromatin organization influencing regional SNV frequencies (*22*). Interestingly, L1, which is evolutionarily younger and more active than LINE-2 (L2) (*23*), experienced significantly stronger DNA demethylation than L2 in cancer

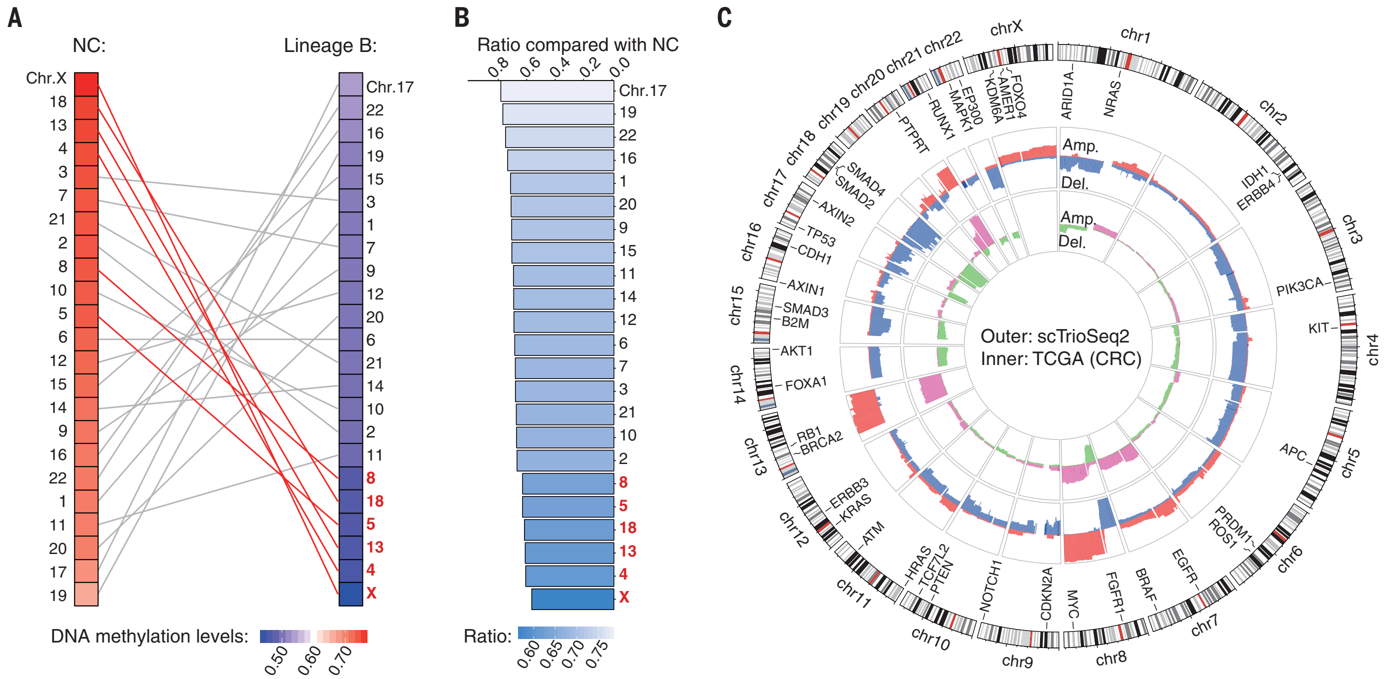

Fig. 4. Chromosomal patterns of DNA demethylation and SCNAs of CRC. (**A**) The chromosomal DNA methylation levels of NC cells and lineage B of CRC01. Chromosomes are ranked by their mean methylation levels within each lineage. The lines link the same chromosomes. The six chromosomes with the lowest DNA methylation levels in lineage B are highlighted in red. (**B**) The residual ratios of chromosomal methylation levels of lineage B compared with those in NC cells of CRC01. (**C**) Circos plot showing the amplification or deletion frequency of each genomic bin (250-kb resolution) of the nine CRC patients in our study. The minimum scale of coordinates is 18 Mb. Some oncogenes and tumor suppressor genes are labeled.

cells for all patients ($P < 2.7 \times 10^{-4}$, Wilcoxon rank-sum test) (fig. S13, D and E). This is in contrast to DNA demethylation during embryonic development, where L1 tends to retain higher DNA methylation levels than L2 (*24*, *25*). These results suggest that during tumorigenesis and progression, L1 and heterochromatin regions experience aberrant DNA demethylation, breaking the rules for normal development.

We further explored the chromosomal patterns of aberrant DNA methylation and genome instability of CRC. Chromosomal demethylation degrees were variable, with six chromosomes (4, 5, 8, 13, 18, and X) exhibiting stronger DNA demethylation than others (Figs. 4, A and B, and fig. S14A). These six chromosomes were also significantly enriched for stronger DNA demethylation in most patients ($P < 0.05$, hypergeometric test) (fig. S14B). Additionally, population analyses of the non-hypermutated CRC samples from the TCGA Project and our study showed that three of the hypomethylated chromosomes recurrently generated SCNAs (chromosomes 8, 13, and 18) (Fig. 4C and fig. S14C). Using WGS data, we found that five of the hypomethylated chromosomes were also significantly enriched for SNVs (chromosomes 4, 5, 8, 13, and X) ($P < 0.05$, hypergeometric test) (fig. S14D).

Unambiguously assigned cancer cell lineages enable characterization of their DNA methylation and gene expression features. We found that DNA methylation profiles are relatively stable within a single genetic lineage or sublineage. The differences in DNA methylation levels between the primary tumors and metastases could be mainly caused by the differences in the compositions of sublineages, but not de novo methylation or demethylation during metastasis. The DNA demethylation patterns of individual cancer cells were consistent among the 10 CRC patients whose DNA we sequenced. Thus, single-cell multiomics sequencing provides insights and resources for understanding the molecular alterations that occur during CRC progression and metastasis.

REFERENCES AND NOTES

1. Cancer Genome Atlas Network, *Nature* **487**, 330–337 (2012).
2. J. Guinney *et al.*, *Nat. Med.* **21**, 1350–1356 (2015).
3. T. Hinoue *et al.*, *Genome Res.* **22**, 271–282 (2012).
4. B. P. Berman *et al.*, *Nat. Genet.* **44**, 40–46 (2012).
5. P. A. Jones, S. B. Baylin, *Cell* **128**, 683–692 (2007).
6. J. S. You, P. A. Jones, *Cancer Cell* **22**, 9–20 (2012).
7. N. McGranahan, C. Swanton, *Cancer Cell* **27**, 15–26 (2015).
8. N. E. Navin, *Genome Res.* **25**, 1499–1507 (2015).
9. I. Tirosh *et al.*, *Science* **352**, 189–196 (2016).
10. I. Tirosh *et al.*, *Nature* **539**, 309–313 (2016).
11. A. S. Venteicher *et al.*, *Science* **355**, eaai8478 (2017).
12. H. Li *et al.*, *Nat. Genet.* **49**, 708–718 (2017).
13. Y. Hou *et al.*, *Cell Res.* **26**, 304–319 (2016).
14. S. A. Smallwood *et al.*, *Nat. Methods* **11**, 817–820 (2014).
15. C. H. Mermel *et al.*, *Genome Biol.* **12**, R41 (2011).
16. R. Gao *et al.*, *Nat. Genet.* **48**, 1119–1130 (2016).
17. N. Navin *et al.*, *Nature* **472**, 90–94 (2011).
18. R. Beroukhim *et al.*, *Nature* **463**, 899–905 (2010).
19. T. I. Zack *et al.*, *Nat. Genet.* **45**, 1134–1140 (2013).
20. K. Naxerova *et al.*, *Science* **357**, 55–60 (2017).
21. Y. Han *et al.*, *Pathology (Phila.)* **46**, 396–401 (2014).
22. B. Schuster-Böckler, B. Lehner, *Nature* **488**, 504–507 (2012).
23. R. Cordaux, M. A. Batzer, *Nat. Rev. Genet.* **10**, 691–703 (2009).
24. F. Guo *et al.*, *Cell* **161**, 1437–1452 (2015).
25. H. Guo *et al.*, *Nature* **511**, 606–610 (2014).

ACKNOWLEDGMENTS

We thank I. Bruce for polishing our manuscript. **Funding:** F.T. was supported by grants from the National Natural Science Foundation of China (81561138005, 31625018, and 81521002). This work was supported by the Beijing Advanced Innovation Center for Genomics at Peking University. **Author contributions:** F.T., J.Q., and W.F. conceived the project. S.B., Y.H., and F.T. wrote the manuscript with help from all authors. Y.H., X.Z., X.L., Jun.Y., Y.W., W.W., Jia.Y., H.G., S.G., and Y.M. performed the experiments. S.B., X.L., B.H., J.D., and P.Z. conducted the bioinformatics analyses. **Competing interests:** The authors declare they have no competing interests. **Data and materials availability:** The scTrio-seq2 data have been submitted to the NCBI Gene Expression Omnibus (GEO) under accession number GSE97693. WGS data have been deposited in the European Genome-phenome Archive (EGA) under the accession number EGAS00001003242. Analysis code is available at https://github.com/bianshuhui/CRC_code.

SUPPLEMENTARY MATERIALS

www.sciencemag.org/content/362/6418/1060/suppl/DC1
Materials and Methods
Figs. S1 to S14
Tables S1 and S2
References (*26*–*29*)

13 July 2017; resubmitted 24 August 2018
Accepted 25 October 2018
10.1126/science.aao3791

IMMUNOLOGY

Pathogen blockade of TAK1 triggers caspase-8–dependent cleavage of gasdermin D and cell death

Pontus Orning[1,2], Dan Weng[1,3]*, Kristian Starheim[1,2]*, Dmitry Ratner[1]*, Zachary Best[1], Bettina Lee[4], Alexandria Brooks[1], Shiyu Xia[5], Hao Wu[5], Michelle A. Kelliher[6], Scott B. Berger[7], Peter J. Gough[7], John Bertin[7], Megan M. Proulx[8], Jon D. Goguen[8], Nobuhiko Kayagaki[4], Katherine A. Fitzgerald[1,2], Egil Lien[1,2]†

Limited proteolysis of gasdermin D (GSDMD) generates an N-terminal pore-forming fragment that controls pyroptosis in macrophages. GSDMD is processed via inflammasome-activated caspase-1 or -11. It is currently unknown whether macrophage GSDMD can be processed by other mechanisms. Here, we describe an additional pathway controlling GSDMD processing. The inhibition of TAK1 or IκB kinase (IKK) by the *Yersinia* effector protein YopJ elicits RIPK1- and caspase-8–dependent cleavage of GSDMD, which subsequently results in cell death. GSDMD processing also contributes to the NLRP3 inflammasome–dependent release of interleukin-1β (IL-1β). Thus, caspase-8 acts as a regulator of GSDMD-driven cell death. Furthermore, this study establishes the importance of TAK1 and IKK activity in the control of GSDMD cleavage and cytotoxicity.

The robust and rapid induction of innate immune signaling is a hallmark of the host response to microbial infection. Successful pathogens subvert, thwart, or dismantle these defensive measures. Growing evidence suggests that the host recognizes these disruptive efforts, eliciting effective backup measures. Cell death processes, including apoptosis and pyroptosis, are integral components of the host response to infection. Multiprotein inflammasome complexes sense the presence of pathogens and activate inflammatory caspases, typically caspase-1 or caspase-11, leading to pyroptotic cell death and maturation of the inflammatory cytokines interleukin-1β (IL-1β) and IL-18. Pyroptosis is an inflammasome-driven cytotoxic process that occurs in macrophages after limited proteolysis of gasdermin D (GSDMD). The generation of an N-terminally cleaved fragment then creates large oligomeric membrane pores and causes lytic cell death (*1*–*7*). At present, caspase-1 and caspase-11 are the only known regulators of GSDMD in macrophages (*5*, *7*), although neutrophil elastase controls GSDMD cleavage in neutrophils (*8*).

Caspase-8 is an upstream activator of caspase-3 and controls apoptotic cell death. In addition, caspase-8 prevents RIPK3–MLKL (mixed lineage kinase domain–like protein)–dependent necroptosis. Increasing evidence indicates important roles for caspase-8 in inflammatory responses in macrophages infected with diverse pathogens. Caspase-8 activation can trigger NLRP3 inflammasomes (*9*) and may also serve as a backup measure when the caspase-1 pathway is blocked or deleted (*10*, *11*). Pathogenic bacteria of the genus *Yersinia* include *Y. pseudotuberculosis* and *Y. enterocolitica*, which cause gastrointestinal disease, and *Y. pestis*, the etiologic agent of plague. *Yersinia* bacteria, through the action of their type III secretion systems, release effectors that manipulate host cells. One of these, YopJ, is a strong activator of caspase-8 via RIPK1 (*12*, *13*). YopJ is an acetyl transferase that blocks the phosphorylation and activation of kinases TAK1, IκB kinase β (IKKβ), and mitogen-activated protein kinase (MAPK) kinases (*14*–*17*). The inhibition of TAK1 is associated with cell death and inflammation (*18*–*20*) and is not limited to *Yersinia*. Several additional pathogens, including *Pseudomonas*, *Vibrio*, and enteroviruses, also target TAK1 (*21*–*23*).

Yersinia bacteria induce cell death, caspase-1 cleavage, and IL-1β release, whereas mutants lacking YopJ do not (*12*, *13*) (fig. S1A). By comparing these responses in wild-type macrophages to responses in macrophages lacking RIPK3 or RIPK3–caspase-8, we previously found that caspase-8 is important for all of these effects (*12*). To investigate the pathways involved, we examined the acute inhibition of TAK1 kinase activity with TAK1 inhibitor (TAK1-i) 5z-7-oxozeaneol (5z7), a specific small-molecule inhibitor, as genetic deletion of TAK1 in macrophages leads to spontaneous death (*20*). TAK1-i induced cell death and IL-1β release in lipopolysaccharide (LPS)–stimulated macrophages (Fig. 1, A to C, and fig. S1, B to D). Similar findings were obtained with NG25, a second inhibitor of TAK1 (fig. S1C). TAK1-i also restored caspase-8–dependent death and IL-1β release in cells infected with YopJ mutant *Yersinia* (Fig. 1, A and B). We found that tumor necrosis factor (TNF) together with TAK1-i could induce similar responses (Fig. 1, D and E). RIPK1 can control caspase-8 activation and is necessary for cell death induced by *Yersinia* and TAK1 inhibition (*12*) (fig. S1, E to I). One function of TAK1 is to activate IKK, which also controls RIPK1 activity. Thus, IKK blockade may effectively trigger a pathway similar to that triggered by TAK1 inhibition (Fig. 1F and fig. S1I). Furthermore, TAK1's effects on IKK are likely key early events in this pathway, rather than effects on MAPK kinase and MAPKs such as p38 (fig. S1J). These responses may serve as a host mechanism to detect the pathological disturbance of TAK1 kinase activity.

TAK1 inhibition by *Yersinia* or by TAK1-i was associated with oligomerization of ASC (apoptosis-associated specklike protein containing a caspase activation and recruitment domain) (Fig. 1, G and H). This oligomerization was dependent on RIPK1, caspase-8, and NLRP3 but not caspase-1 or -11 (Fig. 1, H to J, and fig. S1K). Notably, pan-caspase inhibition blocked ASC oligomerization and IL-1β release but not cytotoxicity. This was likely because of RIPK3-dependent necroptosis triggered by caspase-8 inhibition (Fig. 1J and fig. S1, L to N). Macrophage death was independent of the NLRP3 inflammasome, and IL-1β release was partially dependent on NLRP3 (*24*) (fig. S2). The loss of Toll-like receptor 4 (TLR4), TRIF, or TNF receptor 1 (TNFR1) caused a significant reduction in cell death after bacterial infection or treatment with LPS and TAK1-i (fig. S3, A to C). This suggests activation of the RIPK1–caspase-8 death pathway downstream of TLR4-TRIF activation, perhaps with other contributing bacterial ligands, with concurrent TNF production and TNFR1 autocrine signaling (*25*). TAK1-i combined with additional stimulations, such as TLR2 and TLR7/TLR8 ligands, could also trigger TNFR1-, MyD88-, and caspase-8–dependent cell death and IL-1β release at later time points (fig. S3, D to H). Cell death induced by *Yersinia* has been proposed to be caspase-8–dependent apoptosis (*12*). Although caspase-3 and caspase-7 are activated by *Yersinia* (*12*, *13*) (fig. S4A), deficiency of these caspases did not affect cell death (*13*) (fig. S4B and table S1), and the combined action of multiple components may be necessary. Many *Yersinia*-infected cells display features of apoptosis, including membrane blebs, nuclear condensation, and DNA laddering (*12*). However, we observed significant cleavage of GSDMD after infection, indicating the simultaneous presence of pyroptotic processes (Fig. 1K). The detection antibody we used recognizes the N-terminal 30-kDa pore-forming pyroptotic fragment of GSDMD. *Yersinia* also induced a smaller, 20-kDa fragment and a

---

[1] Program in Innate Immunity, Department of Medicine, Division of Infectious Diseases and Immunology, University of Massachusetts Medical School, Worcester, MA 01605, USA. [2] Centre of Molecular Inflammation Research, Department of Clinical and Molecular Medicine, Norwegian University of Science and Technology, 7491 Trondheim, Norway. [3] Center for Molecular Metabolism, Nanjing University of Science and Technology, Nanjing 210094, China. [4] Department of Physiological Chemistry, Genentech, South San Francisco, CA 94080, USA. [5] Department of Biological Chemistry and Molecular Pharmacology, Harvard Medical School, and Program in Cellular and Molecular Medicine, Boston Children's Hospital, Boston, MA 02115, USA. [6] Department of Cancer Biology, University of Massachusetts Medical School, Worcester, MA 01605, USA. [7] Pattern Recognition Receptor Discovery Performance Unit, Immuno-inflammation Therapeutic Area, GlaxoSmithKline, Collegeville, PA 19426, USA. [8] Department of Microbiology and Physiology, University of Massachusetts Medical School, Worcester, MA 01655, USA.
*These authors contributed equally to this work.
†Corresponding author. Email: egil.lien@umassmed.edu

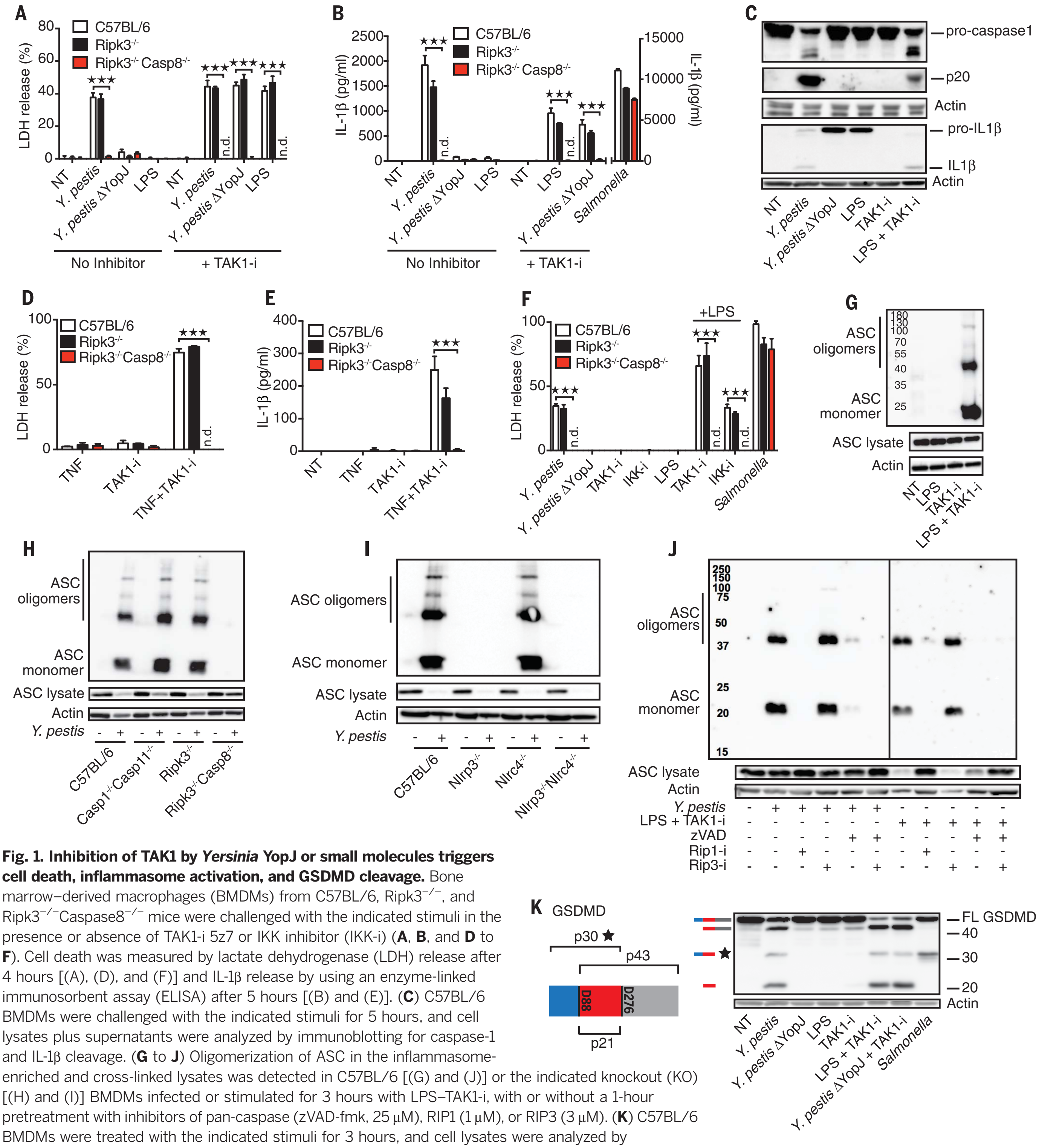

Fig. 1. Inhibition of TAK1 by *Yersinia* YopJ or small molecules triggers cell death, inflammasome activation, and GSDMD cleavage. Bone marrow–derived macrophages (BMDMs) from C57BL/6, Ripk3$^{-/-}$, and Ripk3$^{-/-}$Caspase8$^{-/-}$ mice were challenged with the indicated stimuli in the presence or absence of TAK1-i 5z7 or IKK inhibitor (IKK-i) (**A**, **B**, and **D** to **F**). Cell death was measured by lactate dehydrogenase (LDH) release after 4 hours [(A), (D), and (F)] and IL-1β release by using an enzyme-linked immunosorbent assay (ELISA) after 5 hours [(B) and (E)]. (**C**) C57BL/6 BMDMs were challenged with the indicated stimuli for 5 hours, and cell lysates plus supernatants were analyzed by immunoblotting for caspase-1 and IL-1β cleavage. (**G** to **J**) Oligomerization of ASC in the inflammasome-enriched and cross-linked lysates was detected in C57BL/6 [(G) and (J)] or the indicated knockout (KO) [(H) and (I)] BMDMs infected or stimulated for 3 hours with LPS–TAK1-i, with or without a 1-hour pretreatment with inhibitors of pan-caspase (zVAD-fmk, 25 μM), RIP1 (1 μM), or RIP3 (3 μM). (**K**) C57BL/6 BMDMs were treated with the indicated stimuli for 3 hours, and cell lysates were analyzed by immunoblotting for GSDMD cleavage. In the illustration of GSDMD, predicted cleavage sites and fragment sizes are indicated. Data are presented as the mean ± SD for triplicate wells from three or more independent experiments. For comparisons, Student's *t* test was used. ***$P < 0.001$. NT, nontreated; n.d., not detectable; Rip1-i, RIP1 inhibitor; FL, full-length.

larger p45 fragment, suggesting further cleavage of full-length protein (*26*) or p30 by caspase-3 at GSDMD Asp^{88} (fig. S4C). We found that GSDMD was a central mediator of both cell death and the release of IL-1β and IL-18, which are induced by *Yersinia* infection and treatment with LPS or TNF combined with TAK1-i or IKK inhibition and are controlled by RIPK1–caspase-8 (Fig. 2, A to G, and figs. S1, E to I, and S4, D and E). GSDMD also influenced YopJ- or TAK1-i–induced caspase-1 p20 cleavage and ASC oligomerization (Fig. 2, D, H, and I, and table S2). Excess extracellular potassium completely blocked ASC oligomerization and partially inhibited IL-1β release but did not affect cell death (Fig. 2, J to L, and

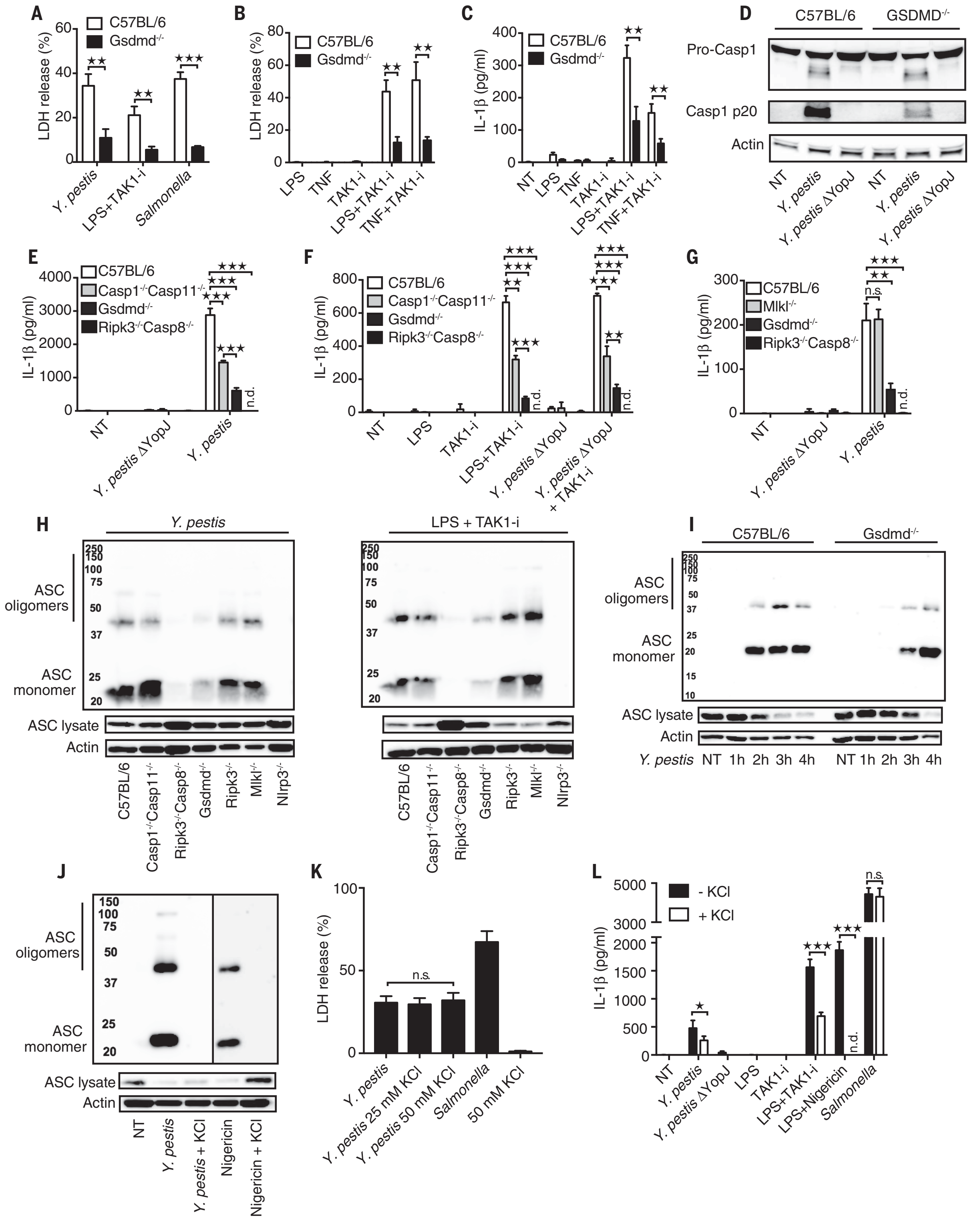

Fig. 2. GSDMD regulates cell death and inflammasome activation in response to TAK1 inhibition. (**A** to **G**) The indicated BMDMs were challenged with *Y. pestis*, a *Y. pestis* mutant lacking YopJ, or *Salmonella enterica* serovar Typhimurium or stimulated with the indicated ligands, TAK1-i, or ligands and TAK1-i. Cell death was measured by LDH release after 3 hours [(A) and (B)] and IL-1β release after 5 hours [(C) and (E) to (G)] or caspase-1 cleavage after 5 hours (D). (**H** to **J**) The oligomerization of ASC in the inflammasome-enriched and cross-linked lysates was detected in BMDMs after *Y. pestis* or LPS–TAK1-i challenge at the indicated time points (I) or after 3 hours. (**J** to **L**) BMDMs were treated with *Y. pestis*, *S.* Typhimurium, or nigericin and LPS in the presence or absence of 50 mM [(J) and (L)] or 25 mM (K) KCl, and the oligomerization of ASC was detected by immunoblotting. Cell death was measured by LDH release or IL-1β release by using ELISA. Data are presented as the mean ± SD for triplicate wells from three or more independent experiments. For comparisons between two groups, Student's *t* test was used; for more than two groups, analysis of variance (ANOVA) was used. n.s., not significant; *$P < 0.05$; **$P < 0.01$; ***$P < 0.001$.

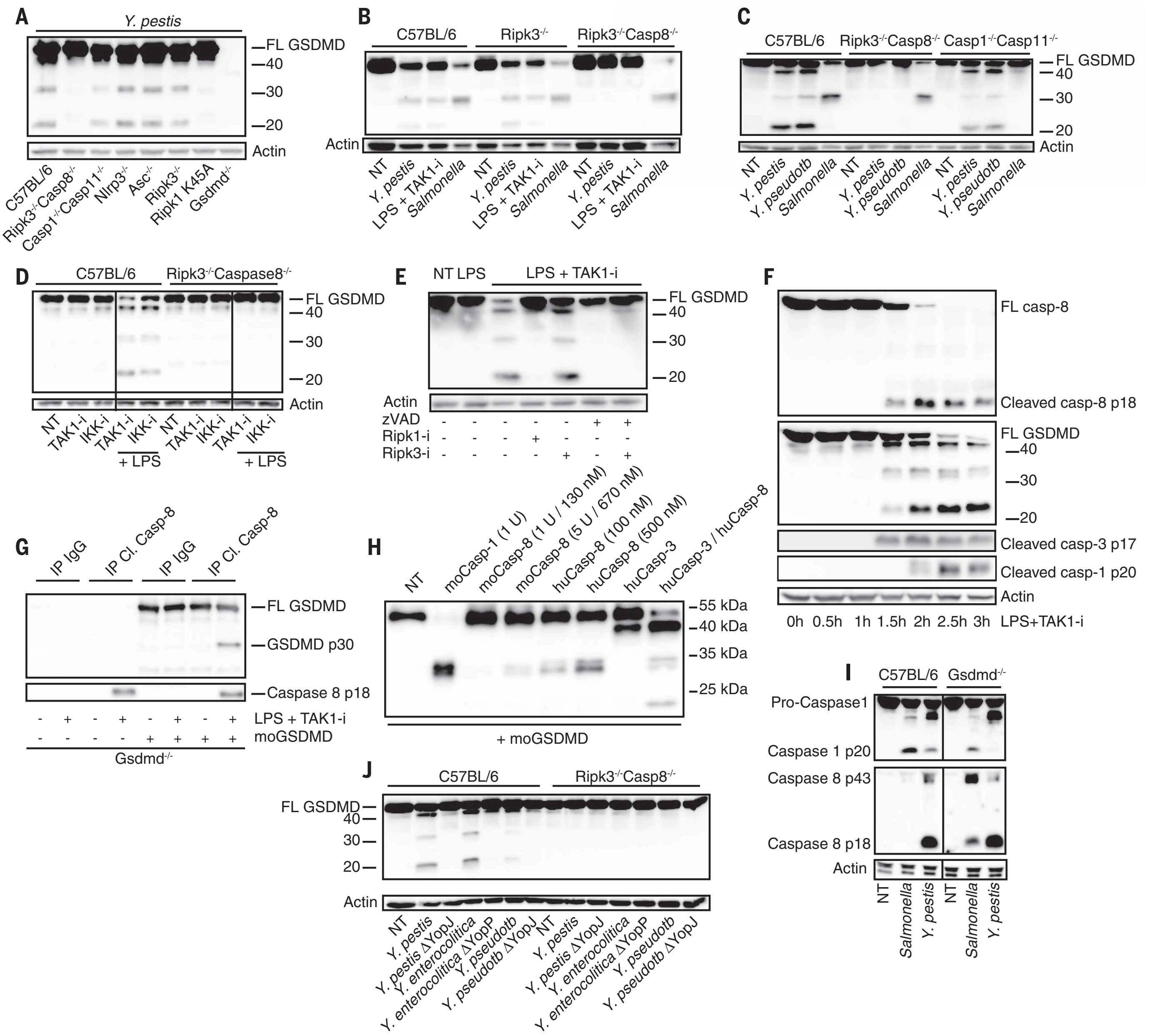

Fig. 3. Caspase-8–dependent GSDMD processing with little contribution by caspase-1 and -11. (**A** to **F**, **I**, and **J**) BMDMs from the indicated mouse strains were challenged with *Y. pestis*, *Y. pseudotuberculosis*, *Y. enterocolitica*, their YopJ (YopP in *Y. enterocolitica*) mutants, or *S.* Typhimurium or treated with LPS–TAK1-i. Cell lysates were harvested after 3 to 4 hours unless otherwise stated and analyzed by immunoblotting for GSDMD cleavage [(A) to (F) and (J)] and/or caspase-1, caspase-3, and caspase-8 cleavage [(F) and (I)]. K45A, Lys^{45}→Ala. (D) BMDMs from C57BL/6 or Ripk3$^{-/-}$Casp8$^{-/-}$ mice were treated with IKK-i and TAK1-i in the absence or presence of LPS. (E) BMDMs were pretreated with pan-caspase inhibitor zVAD-fmk, RIPK1 inhibitor (RIPK1-i), or RIPK3-i for 1 hour before being treated with LPS–TAK1-i. (**G**) Gsdmd$^{-/-}$ BMDMs were treated with LPS–TAK1-i for 3 hours and then immunoprecipitated with cleaved (Cl.) caspase-8 antibody. Immunoprecipitates (IPs) (G) or recombinant caspases (**H**) were incubated with recombinant mouse GSDMD at 37°C for 1 hour in a protein cleavage buffer before being analyzed by immunoblotting. Panels are representative of three or more independent experiments. IgG, immunoglobulin G; mo, mouse; hu, human.

table S2). Thus, RIPK1–caspase-8 appears to exert full control of the membrane damage that triggers potassium efflux. GSDMD displays partial control—possibly via GSDMD pore formation—over potassium efflux, and these signals direct NLRP3 activation, ASC oligomerization, and ultimately, IL-1β release. However, NLRP3 and caspase-1 and -11 do not appreciably contribute to cell death in this case (fig. S2, A and B).

GSDMD cleavage has previously been associated with caspase-1 and caspase-11 activity (*2*, *4*, *5*, *7*). By contrast, *Yersinia*- and TAK1-i–induced GSDMD p30 was entirely dependent upon RIPK1–caspase-8, with minor contributions from caspase-1 and -11 and RIPK3 (Fig. 3, A to E, and fig. S5, A to D). Caspase-8 and GSDMD were cleaved before the appearance of any detectable cleaved caspase-1 (Fig. 3F and fig. S5E). Thus, we have identified an additional pathway leading to processing of GSDMD. In addition, cleaved caspase-8 immunoprecipitated (by using a p18 antibody) from TAK1-i–LPS–treated GSDMD-deficient cells was capable of cleaving purified mouse GSDMD (Fig. 3G and fig. S5, F to H) and generating the p30 pore-forming fragment. Although recombinant caspase-8 may not process GSDMD as strongly as caspase-1 (*5*, *26*), increased

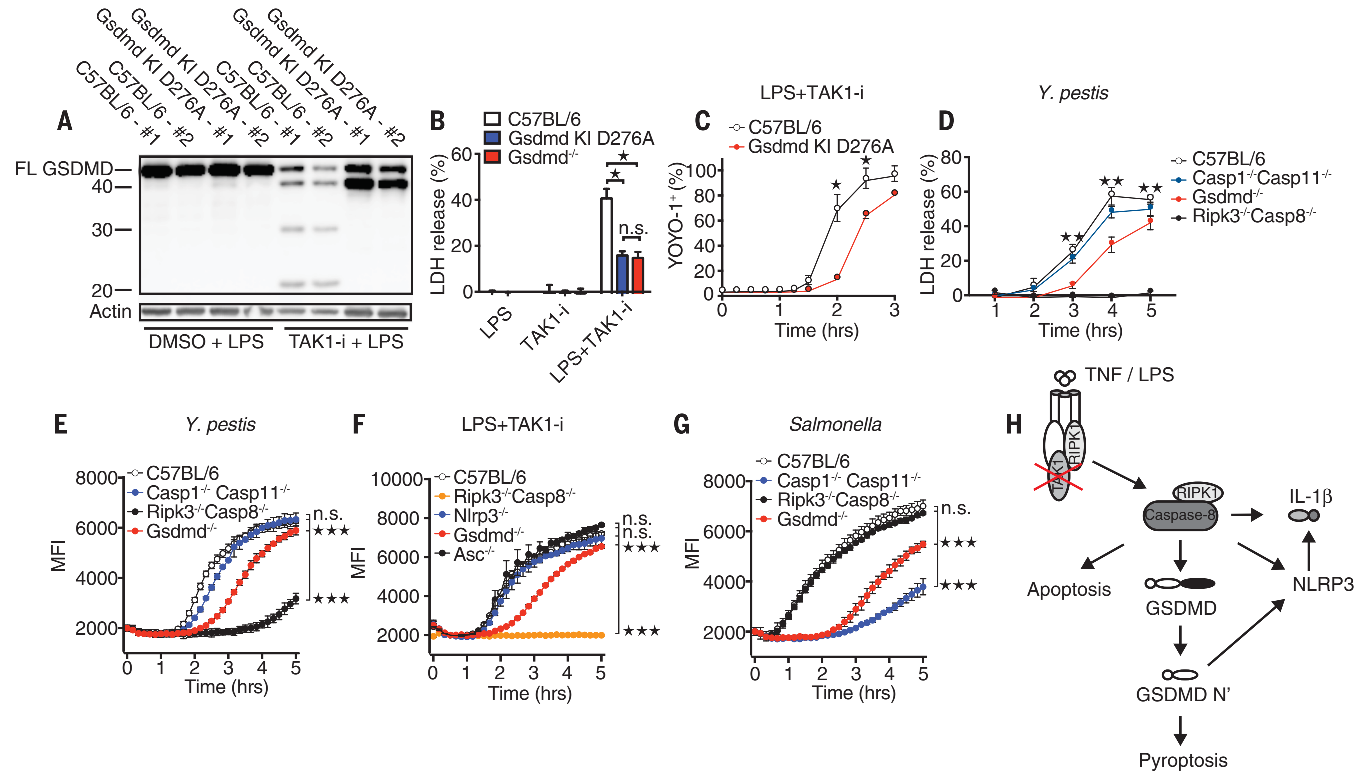

Fig. 4. The GSDMD Asp^{276} residue is critical for GSDMD processing and for regulation of cell death downstream of TAK1 inhibition. (**A**) Immunoblot of GSDMD cleavage in C57BL/6 or GSDMD D276A mutant BMDMs after treatment with LPS and LPS–TAK1-i. Cell death was measured by LDH release (**B** and **D**) or by the percentage of YOYO-1$^+$ cells (**C**) after challenge of the indicated genotypes with LPS–TAK1-i or *Y. pestis*. DMSO, dimethyl sulfoxide. (**E** to **G**) Cell death as measured by entry of EthD-1 into the cell. Samples were read every 10 min at 530-nm excitation and 645-nm emission wavelengths. BMDMs from the indicated genotypes were treated with *Y. pestis* (E), LPS–TAK1-i (F), or *S.* Typhimurium (G). Infections represented in (E) and (G) were without gentamicin. For (E) to (G), statistical analyses were performed on the area under the curve for the whole time course. MFI, mean fluorescense intensity. (**H**) Proposed model of TAK1 inhibition–induced caspase-8 activation and cell death. Data are presented as the mean ± SD for triplicate wells from two [(A) to (C)] or three or more [(D) to (G)] independent experiments. n.d., not detected. For comparisons between two groups, Student's *t* test was used; for more than two groups, ANOVA was used. *P < 0.05; **P < 0.01; ***P < 0.001.

concentrations of mouse and human caspase-8 cleaved GSDMD (Fig. 3H and fig. S5I). In addition, a mixture of both caspase-3 and caspase-8 reproduced the cleavage pattern induced by *Yersinia* or TAK1-IKK inhibition (Fig. 3H). The loss of GSDMD had no effect on caspase-8 activation, consistent with the hypothesis that GSDMD acts downstream of caspase-8 (Fig. 3I and fig. S5J). We observed YopJ-dependent caspase-8 cleavage, GSDMD processing, and cell death with *Y. pseudotuberculosis*, *Y. enterocolitica*, and *Y. pestis*, suggesting that the triggering of this pathway is conserved among these *Yersinia* species (Fig. 3J and figs. S1A and S5J). *Salmonella*, normally a strong activator of caspase-1 and GSDMD, induces the processing of caspase-8 when GSDMD is absent (Fig. 3I), as others have suggested (*10*, *11*). We note that *Yersinia* has several effectors inhibiting caspase-1 cleavage (*27*, *28*). This may contribute to the activation of caspase-8 upon infection by this pathogen. Treatment of macrophages from a GSDMD Asp^{276}→Ala (D276A) knock-in (KI) mouse (*29*) containing a mutation in the caspase-1–caspase-11 cleavage motif of GSDMD (^{273}Leu-Leu-Ser-Asp^{276}) with an LPS–TAK1-i combination revealed that the caspase-8–directed cleavage of GSDMD depended on the GSDMD D276 cleavage site (Fig. 4, A to C). These observations expand upon the requirement of caspase-1 or caspase-11 to proteolytically process GSDMD at D276 for cytotoxicity (*5*, *7*). Cell death time-course experiments showed that the absence of GSDMD, but not that of caspase-8, could be overcome by prolonged incubations with bacteria or TAK1-i–LPS (Fig. 4, C to G, and fig. S6). Thus, GSDMD is not the only mediator of cell death downstream of caspase-8 in the TAK1-IKK–regulated pathway. Rather, additional, still undefined components also participate in this process.

The ability of cells to mobilize countermeasures to detect pathogenic inhibition of key signaling pathways is becoming increasingly apparent. One recent example is the pyrin inflammasome pathway, where disturbances in RhoA guanosine triphosphatase by bacterial toxins trigger pyrin-driven caspase-1 activation (*27*, *28*, *30*). On the basis of our current findings, we propose that pathogen blockade of TAK1-IKK triggers a caspase-8–mediated cell death and inflammatory pathway involving GSDMD. GSDMD-mediated cell death has been considered a defining feature of pyroptosis (*4*, *5*, *31*). Our observations suggest that the blockade of the TAK1-IKK pathways leads to cytotoxicity, with features of both apoptosis and pyroptosis (Fig. 4H and fig. S7). Thus, conditions that affect many cellular processes, such as concurrent effects from bacteria and their secretion system components on different signaling proteins (*27*, *28*), can lead to cell death involving multiple pathways. Inhibition of TAK1 represents a strategy that several pathogens may use to their advantage. However, in the arms race between pathogens and their hosts, the host can sense these disturbances as pathogenic and counter these efforts with cytotoxicity and inflammation. This study broadens our understanding of the pathways leading to GSDMD activation and underscores the importance of GSDMD as a key driver of cell death and inflammation induced by a vast array of pathogens.

REFERENCES AND NOTES

1. L. Sborgi *et al.*, *EMBO J.* **35**, 1766–1778 (2016).
2. X. Liu *et al.*, *Nature* **535**, 153–158 (2016).
3. S. B. Kovacs, E. A. Miao, *Trends Cell Biol.* **27**, 673–684 (2017).
4. J. Shi, W. Gao, F. Shao, *Trends Biochem. Sci.* **42**, 245–254 (2017).
5. J. Shi *et al.*, *Nature* **526**, 660–665 (2015).

6. R. A. Aglietti *et al.*, *Proc. Natl. Acad. Sci. U.S.A.* **113**, 7858–7863 (2016).
7. N. Kayagaki *et al.*, *Nature* **526**, 666–671 (2015).
8. H. Kambara *et al.*, *Cell Rep.* **22**, 2924–2936 (2018).
9. J. E. Vince, J. Silke, *Cell. Mol. Life Sci.* **73**, 2349–2367 (2016).
10. I. Rauch *et al.*, *Immunity* **46**, 649–659 (2017).
11. D. P. A. Mascarenhas *et al.*, *PLOS Pathog.* **13**, e1006502 (2017).
12. D. Weng *et al.*, *Proc. Natl. Acad. Sci. U.S.A.* **111**, 7391–7396 (2014).
13. N. H. Philip *et al.*, *Proc. Natl. Acad. Sci. U.S.A.* **111**, 7385–7390 (2014).
14. U. Meinzer *et al.*, *Cell Host Microbe* **11**, 337–351 (2012).
15. R. Mittal, S.-Y. Peak-Chew, H. T. McMahon, *Proc. Natl. Acad. Sci. U.S.A.* **103**, 18574–18579 (2006).
16. S. Mukherjee *et al.*, *Science* **312**, 1211–1214 (2006).
17. N. Paquette *et al.*, *Proc. Natl. Acad. Sci. U.S.A.* **109**, 12710–12715 (2012).
18. N. Vanlangenakker *et al.*, *Cell Death Differ.* **18**, 656–665 (2011).
19. M. B. Menon *et al.*, *Nat. Cell Biol.* **19**, 1248–1259 (2017).
20. R. K. S. Malireddi *et al.*, *J. Exp. Med.* **215**, 1023–1034 (2018).
21. X. Lei *et al.*, *J. Virol.* **88**, 9830–9841 (2014).
22. X. Zhou *et al.*, *Cell Rep.* **3**, 1690–1702 (2013).
23. C. He *et al.*, *Infect. Immun.* **85**, e00239-17 (2017).
24. Y. Zheng *et al.*, *PLOS Pathog.* **7**, e1002026 (2011).
25. L. W. Peterson *et al.*, *J. Immunol.* **197**, 4110–4117 (2016).
26. C. Y. Taabazuing, M. C. Okondo, D. A. Bachovchin, *Cell Chem. Biol.* **24**, 507–514.e4 (2017).
27. D. Ratner, M. P. A. Orning, E. Lien, *J. Leukocyte Biol.* **101**, 165–181 (2017).
28. D. Ratner *et al.*, *PLOS Pathog.* **12**, e1006035 (2016).
29. B. L. Lee *et al.*, *J. Exp. Med.* **215**, 2279–2288 (2018).
30. H. Xu *et al.*, *Nature* **513**, 237–241 (2014).
31. L. Galluzzi *et al.*, *Cell Death Differ.* **25**, 486–541 (2018).

ACKNOWLEDGMENTS

We thank G. Germain for help with mice; V. Dixit, N. Kayagaki, and K. Newton (Genentech) for providing GSDMD and RIP3 KO mice; W. Kaiser, E. Mocarski, D. R. Green, and C. Dillon for sending caspase-8 RIP3 double-KO mice; M. O'Riordan for providing *S.* Typhimurium; I. Brodsky and J. Bliska for providing *Y. pseudotuberculosis*; R. Adkins and G. Cornelis for providing *Y. enterocolitica*; G. Salvesen and S. Snipas for providing recombinant caspase-8 and caspase-3; and GlaxoSmithKline and J. Bertin for providing RIPK1 and RIPK3 inhibitors, as well as RIPK1 Lys^{45}→Ala mutant mice. We also thank the A. Poltorak lab for discussions and for sharing data from their unpublished studies and N. Silverman and T. Espevik for critically reading the manuscript. **Funding:** The work was supported by National Institutes of Health grants AI07538 and AI129527 (to E.L.), AI067497 and AI083713 (to K.A.F.), AI095213 (to D.R.), AI139914 (to H.W.), AI075118 (to M.A.K.), and HL092610 (to A.B.); the Norwegian Cancer Society grants 7699133 (to K.S.) and B05035/001 (to E.L.); the UMass Medical School Summer Undergraduate Research Experience Program funding to Z.B.; and the Research Council of Norway Center of Excellence Funding Scheme project 223255/F50 (to P.O., E.L., K.A.F., and K.S.). **Author contributions:** P.O. performed the research with contributions from D.W., K.S., D.R., Z.B., B.L., and A.B. S.X., H.W., M.A.K., S.B.B., P.J.G., J.B., M.M.P., J.D.G., and N.K. provided reagents, mice, and advice. The project was developed by E.L. and supervised by E.L. with input from K.A.F., P.O., K.A.F., and E.L. wrote the paper with help from the other authors. **Competing interests:** B.L. and N.K. are employees of Genentech. S.B.B., P.J.G., and J.B. are employees and shareholders of GlaxoSmithKline. H.W. is a co-founder and consultant for SMOC Therapeutics. K.A.F. is a consultant for Quench Bio. **Data and materials availability:** All data needed to evaluate the conclusions in this paper are present either in the main text or in the supplementary materials. MLKL KO mice were obtained via a material transfer agreement (MTA) with the Walter and Eliza Hall Institute of Medical Research. Caspase 8–deficient mice were obtained via an MTA with the University Health Network, Toronto. RIPK3 KO mice, GSDMD KO mice, GSDMD cleavage-dead KI mice, and mouse GSDMD antibody were obtained via an MTA with Genentech. RIPK1 kinase-dead KI mice and RIPK3 and RIPK1 inhibitors were obtained via an MTA with GlaxoSmithKline.

SUPPLEMENTARY MATERIALS

www.sciencemag.org/content/362/6418/1064/suppl/DC1
Materials and Methods
Figs. S1 to S7
Tables S1 and S2
References (*32–57*)

6 June 2018; accepted 17 October 2018
Published online 25 October 2018
10.1126/science.aau2818

MICROBES WITHIN THE HOST
IN HEALTH AND DISEASE

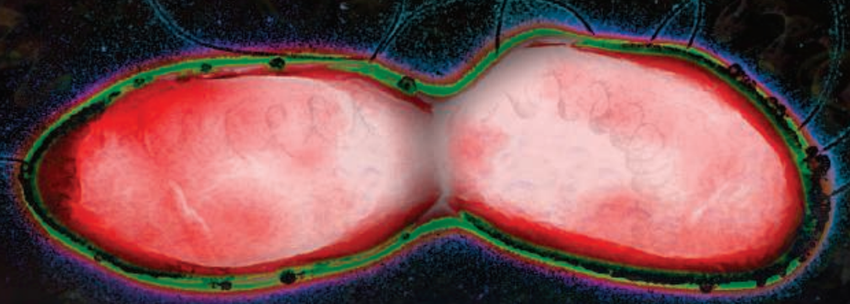

13th Annual Salk/Fondation Ipsen/Science Symposium on Biological Complexity

January 22 - 24, 2019 • Salk Institute for Biological Studies, La Jolla, CA

THE SYDNEY BRENNER NOBEL LECTURE JEFFREY GORDON *WASHINGTON UNIVERSITY IN ST. LOUIS*

KEYNOTE LECTURE
MARGARET MCFALL-NGAI *UNIVERSITY OF HAWAII AT MANOA*

SESSION 1: GUT-BRAIN AXIS
JANELLE AYRES (Chair) *SALK INSTITUTE FOR BIOLOGICAL STUDIES*
SARKIS MAZMANIAN *CALIFORNIA INSTITUTE OF TECHNOLOGY*
ROSA KRAJMALNIK-BROWN *ARIZONA STATE UNIVERSITY*
JOHN CRYAN *UNIVERITY COLLEGE CORK, IE*

SESSION 2: IMMUNOMETABOLISM
SUSAN PRESCOTT (Chair) *UNIVERSITY OF WESTERN AUSTRALIA, AS*
RUSLAN MEDZHITOV *YALE UNIVERSITY*
LUKE O'NEILL *TRINITY COLLEGE DUBLIN, IE*
RUTH LEY *MAX PLANCK INSTITUTE, GE*

SESSION 3: CANCER AND CANCER THERAPIES
LAURENCE ZITVOGEL (Chair) *GUSTAVE ROUSSY, FR*
CINDY SEARS *JOHNS HOPKINS MEDICAL INSTITUTE*
OMER YILMAZ *MASSACHUSETTS INSTITUTE OF TECHNOLOGY*
THOMAS GAJEWSKI *UNIVERSITY OF CHICAGO*

SESSION 4: HOST-PATHOGEN INTERACTIONS
DENISE MONAK (Chair) *STANFORD UNIVERSITY*
ANDREAS BÄUMIER *UNIVERSITY OF CALIFORNIA, DAVIS*
THAD STAPPENBECK *WASHINGTON UNIVERSITY IN ST. LOUIS*
HERBERT "SKIP" VIRGIN *WASHINGTON UNIVERSITY IN ST. LOUIS*

SESSION 5: IMMUNE-MICROBE INTERACTIONS
LORA HOOPER (Chair) *UNIVERSITY OF TEXAS SOUTHWESTERN MEDICAL CENTER*
GREGORY BARTON *UNIVERSITY OF CALIFORNIA, BERKELEY*
ANDREW MACPHERSON *UNIVERISTY OF BERN, SW*
YASMIN BELKAID *NATIONAL INSTITUTE OF HEALTH, NIAID*

SESSION 6: MICROBIAL COMMUNITIES IN HEALTH AND DISEASE
MARTY BLASER (Chair) *NEW YORK UNIVERSITY*
SUSAN LYNCH *UNIVERSITY OF CALIFORNIA, SAN FRANCISCO*
DAN LITTMAN *NEW YORK UNIVERSITY*
MICHAEL FISCHBACH *STANFORD UNIVERSITY*

ORGANIZING COMMITTEE: JANELLE AYRES · JAMES LEVINE · VALDA VINSON

SCIENTIFIC PROGRAM COMMITTEE: JANELLE AYRES (CHAIR) · RON EVANS · MICHAEL KARIN
ROB KNIGHT · MANUELA RAFFATELLU · INDER VERMA (PAST CHAIR) · VALDA VINSON · CAROLINE ASH

ONLINE REGISTRATION and INFORMATION: www.salk.edu/SFIS2019
CONTACT: events@salk.edu
#SFIS2019

ABSTRACT SUBMISSION DEADLINE: December 19, 2018 **REGISTRATION DEADLINE:** January 4, 2019

Poster design by Jamie Simon, Salk Institute

FONDATION IPSEN

salk®
Where cures begin.

Science
AAAS


AAASTravels

Alaska Aurora Borealis

March 28 - April 3, 2019!

Come discover the great beauty of Alaska in winter, and see the greatest light show on earth! Also see Alaskan wildlife in winter near Seward, and then take the train from Talkeetna to Fairbanks, passing lofty 20,310 foot Denali (Mt. McKinley) en route. See the Ice Festival in Fairbanks and learn about the Aurora from Geophysical Institute scientists. Watch a local sled dog team, and see the Aurora Borealis dance across the night sky. $2,995 pp + air

For a detailed brochure, call (800) 252-4910
All prices are per person twin share + air

BETCHART EXPEDITIONS Inc.
17050 Montebello Rd, Cupertino, CA 95014
Email: AAASInfo@betchartexpeditions.com
www.betchartexpeditions.com

DOES YOUR LAB COMBINE COMPUTATIONAL AND EXPERIMENTAL STRATEGIES TO INVESTIGATE SIGNALING NETWORKS?


Michal Hershfinkel, Elias Aizenman, Glen Andrews, and Israel Sekler *Sci. Signal.* 3, mr2 (6 July 2010) Image: Omer Barad, Department of Molecular Genetics, Weizmann Institute of Science, Rehovot, Israel.

Science Signaling | AAAS
CELL SIGNALING IN PHYSIOLOGY AND DISEASE

Find out more about the scope of the journal and submit your research today. **ScienceSignaling.org**

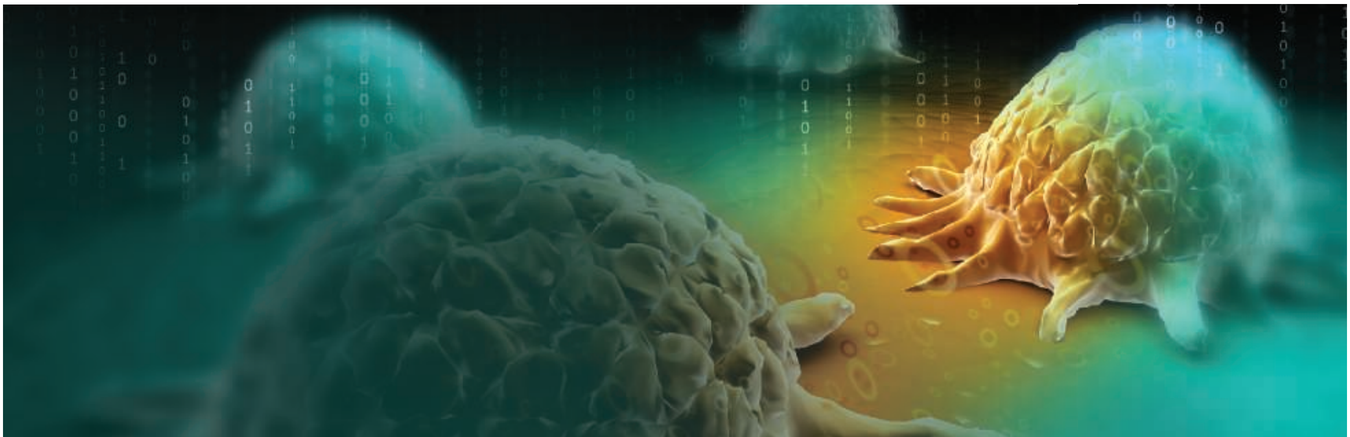
2019
AAAS MARTIN AND ROSE WACHTEL CANCER RESEARCH
AWARD

Recognize the work of an early career scientist who has performed outstanding work in the field of cancer research. Award nominees must have received their Ph.D. or M.D. within the last 10 years. The winner will deliver a public lecture on his or her research, receive a cash award of **$25,000**, and publish a Focus article in *Science Translational Medicine*.

For more information visit
www.aaas.org/aboutaaas/awards/wachtel
or e-mail wachtelprize@aaas.org.
Deadline for submission: **February 1, 2019**.

Science Translational Medicine | AAAS

Superresolution, Single-Molecule Fluorescence Microscope

The Nanoimager from Oxford NanoImaging (ONI) is a desktop-compatible, superresolution, single-molecule fluorescence microscope with localization precision reaching 20 nm. It supports various modes of operation: single-molecule, localization-based superresolution for quantitative cellular imaging; single-particle tracking in live cells; digital confocal microscopy; and structured illuminated microscopy (SIM) as well as single-molecule fluorescence resonance energy transfer (FRET) for measuring molecular interactions in the 2 nm–10 nm range. The Nanoimager is a cost-effective solution that operates on a standard laboratory bench, features whole-body heating for live experiments, and does not require an optical table or darkroom. It is a Class 1 laser product with unrivaled stability. Unlimited licenses to ONI's NimOS software allow seamless operation and rapid quantitative data analysis with intuitive presentation of results.

Oxford NanoImaging (ONI)
For info: +44-(0)-1865951820
www.oxfordni.com

High-Throughput, Label-Free Cell Interaction Platform

LUMICKS has released z-Movi, a platform that enables scientists to effectively screen and sort thousands of immune cells in parallel based on their strength of interaction to specific targets, such as tumor cells. Biological and pathological phenomena are heavily dependent on cells interacting with specific targets, including ligands, proteins, or other cells. The z-Movi technology is based on a simple principle: By using noninvasive forces, it is possible to precisely separate immune cells bound to other cells. Depending on how much force is needed to separate the interacting components, cell–cell interaction strength can be measured directly and quantitatively in thousands of cells simultaneously. Cells can be sorted afterward based on interaction strength and isolated for further processing. In this way, researchers can develop personalized therapies that are faster, cheaper, and have fewer side effects than current treatments.

LUMICKS
For info: +31-(0)-20-598-79-84
www.lumicks.com/cell

Hepatic Nonparenchymal Cells

Lonza has added hepatic stellate cells, Kupffer cells, and liver-derived endothelial cells to its liver-cells portfolio. These hepatic nonparenchymal cells give scientists the building blocks to create more physiologically relevant in vitro models, including cocultures and 3D cell cultures, for enhanced liver disease research. Hepatic nonparenchymal cells are involved in normal liver function, including transport, metabolism, and growth—however, they also play important roles in the immune response. These cells can also be involved in the formation of common liver diseases [hepatitis, nonalcoholic steatohepatitis (NASH), and cirrhosis]. By offering all four major liver-cell types (hepatocytes, stellate cells, Kupffer cells, and liver-derived endothelial cells), Lonza offers a one-stop shop for scientists looking to source human liver cells for their drug discovery research.

Lonza
For info: 800-638-8174
www.lonza.com

Refractive Index Detector

The Differential Refractive Index (DRI) Detector from Testa Analytical Solutions is a next-generation instrument for challenging gel permeation chromatography/size-exclusion chromatography (GPC/SEC) applications. Its high sensitivity makes it the perfect companion for characterization of natural and synthetic polymers as well as protein investigations. The instrument works at the same wavelength as multi-angle light scattering (MALS) and static light scattering (SLS) detectors, enabling determination of both absolute concentration and total mass balance. It operates from room temperature up to 80°C. Designed to operate in both horizontal and vertical orientations, the compact detector has the versatility to fit your available benchspace. While developed for use with GPC/SEC multidetector systems, the DRI Detector also provides unbeatable performance in more classical HPLC applications, such as detection of sugars, and is available optimized for low flow rates down to 300 µL/min.

Testa Analytical Solutions
For info: +49-30-864-24076
www.testa-analytical.com

Column Series for Biotherapeutics

bioZen from Phenomenex is a series of liquid chromatography (LC) solutions for bioseparations in pharmaceutical, biopharmaceutical, and academic research. The series encompasses both proven and entirely new media spanning two particle platforms—core-shell and thermally modified fully porous. The initial bioZen product line features seven chemistries for UHPLC and HPLC characterization of biotherapeutics, such as monoclonal antibodies, antibody–drug conjugates, and biosimilars. The offering includes specific LC chemistries for analysis of aggregates and total monoclonal antibodies, intact mass and fragments, peptide mapping and quantitation, and glycan mapping. All bioZen media, particle sizes, and phases are available in Phenomenex's new, biocompatible titanium hardware, which minimizes secondary reactions, carryover, and other recovery issues to provide better overall reproducibility than stainless-steel hardware. It also reduces the time typically spent on column priming and does not interfere with protein or peptide integrity.

Phenomenex
For info: 310-212-0555
www.phenomenex.com

Evaporator for Kilo-Scale Preparative Chromatography

Configured with a 5-L 316 stainless-steel evaporation vessel, the Rocket 4D Synergy from Genevac offers productive automated removal of solvent for labs running kilo-scale preparative chromatography equipment. Such labs have traditionally relied upon several rotary evaporators to remove the large volumes of solvent resulting from sample fractions. This time-consuming manual process requires a dedicated operator to top-up dry ice in cold traps, feed the systems with more product, and watch them continually. With the Rocket 4D Synergy, you simply load your sample, select a method, press start, and walk away—the system will do the rest. Compact in size, the instrument allows you to dry or concentrate your samples with complete confidence, as it uses proprietary vacuum technology to suppress solvent bumping and foaming—problems associated with sample loss when using large-scale rotary evaporators.

Genevac
For info: 845-255-5000
www.spscientific.com/rocket4dsynergy

Electronically submit your new product description or product literature information! Go to www.sciencemag.org/about/new-products-section for more information.

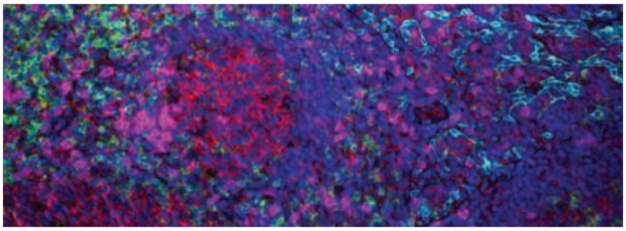

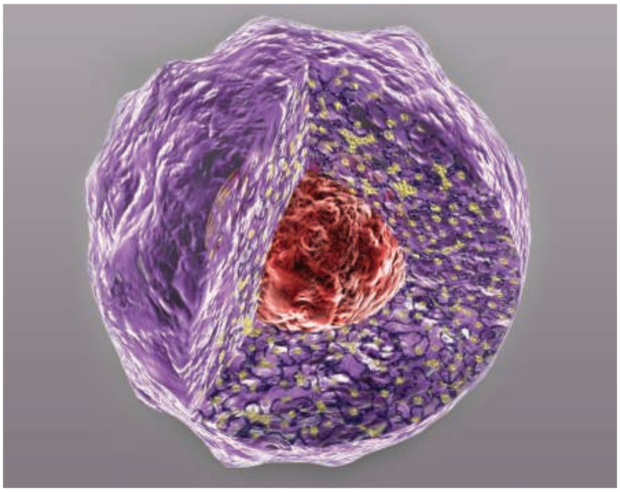


NEW ENGLAND BioLabs® Inc.
be INSPIRED
drive DISCOVERY
stay GENUINE

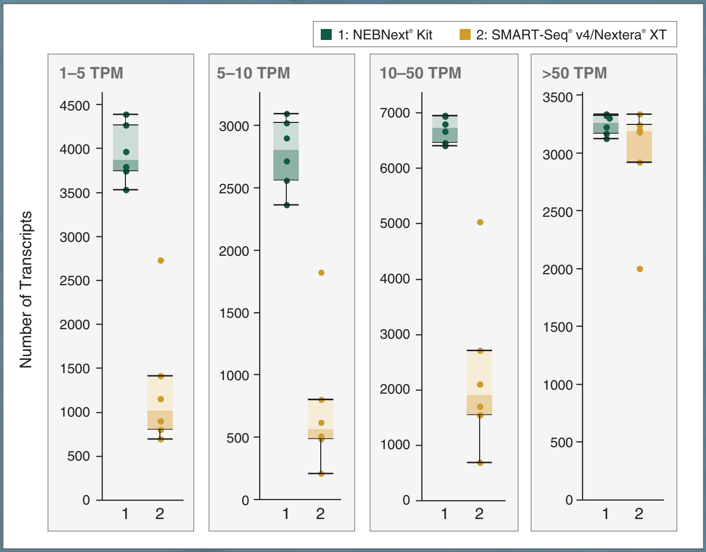
1: NEBNext® Kit
2: SMART-Seq® v4/Nextera® XT
Number of Transcripts
1–5 TPM
0
500
1000
1500
2000
2500
3000
3500
4000
4500
1
2
5–10 TPM
0
500
1000
1500
2000
2500
3000
1
2
10–50 TPM
0
1000
2000
3000
4000
5000
6000
7000
1
2
>50 TPM
0
500
1000
1500
2000
2500
3000
3500
1
2

Science Careers

SCIENCE CAREERS ADVERTISING

For full advertising details, go to ScienceCareers.org and click For Employers, or call one of our representatives.

AMERICAS

+1 202 326-6577
+1 202 326-6578
advertise@sciencecareers.org

EUROPE, INDIA, AUSTRALIA, NEW ZEALAND, REST OF WORLD

+44 (0) 1223 326527
advertise@sciencecareers.org

CHINA, KOREA, SINGAPORE, TAIWAN, THAILAND

+86 131 4114 0012
advertise@sciencecareers.org

JAPAN

+81 3-6459-4174
advertise@sciencecareers.org

CUSTOMER SERVICE

AMERICAS

+1 202 326-6577

REST OF WORLD

+44 (0) 1223 326528

advertise@sciencecareers.org

ScienceCareers
FROM THE JOURNAL SCIENCE AAAS

ScienceCareers.org

ASSISTANT PROFESSOR POSITIONS

Ecohydrology and Marine Biology

The Department of Biological Sciences at the University of Alabama invites applications for two full-time (9-month) tenure-track faculty positions at the rank of **Assistant Professor in Ecohydrology** and **Marine Biology** to begin August 2019.

For the **Ecohydrology** position, the successful applicant will establish an extramurally funded and internationally recognized research program centered on interactions and feedbacks between ecological and hydrological processes at any point in the water cycle. Applicants should employ integrative, multi-scale approaches that combine field-based data and modeling to characterize relationships between the water cycle, regional climate, and the dynamics of terrestrial and/or aquatic ecosystems, while remaining committed to excellence in teaching and mentoring undergraduate and graduate students. We are particularly interested in applications from individuals with a strong foundation in biological and ecological sciences and a demonstrated record of research in improving our understanding of hydrologically coupled processes at scales ranging from individual plants to entire regions, especially in the context of global environmental change. The successful candidate will be encouraged to leverage Alabama's unique and diverse habitats and water resources to support an innovative research program, and to forge collaborations with the NOAA National Water Center, which opened on the UA campus in 2014, and the diverse faculty at UA and Dauphin Island Sea Lab with interests in water-related research. Teaching responsibilities will include basic undergraduate courses in general biology or ecology, as well as specialized undergraduate and graduate courses in the successful candidate's area of expertise.

The **Marine Biology** position will be based at the Dauphin Island Sea Lab (DISL; **www.disl.org**) on the Alabama Coast near Mobile. DISL offers excellent research facilities and support. We seek a highly innovative and collaborative scientist with a strong academic background in Marine Biology. The successful candidate is expected to establish an active, independent research program and attract extramural funding while also mentoring and teaching undergraduate and graduate students. Candidates whose research addresses problems facing marine systems such as coral bleaching and disease, ocean acidification, eutrophication, and other anthropogenic impacts are especially encouraged to apply. Applicants should have demonstrated experience using modern analytical techniques to address fundamental questions in their area of research. The successful candidate will be a highly motivated individual with the ability to interact with other faculty members in the Department of Biological Sciences and at the DISL and who demonstrates a strong record of publishing in peer-reviewed journals. Teaching responsibilities will include an undergraduate course in Marine Biology, as well as specialized undergraduate and graduate courses in the successful candidate's area of expertise.

Candidates for both positions must have a Ph.D. in the Biological Sciences or a related field and postdoctoral (or equivalent job) experience. Evidence of significant intellectual contributions to their respective fields and a demonstrated commitment to teaching at both the undergraduate and graduate levels are also required. The successful applicants will be expected to establish extramurally funded and relevant research programs. A complete application includes (1) an application letter; (2) CV; (3) statement of research interests and goals; (4) statement of teaching interests and philosophy; and (5) a list of at least four references (including contact information). Letters of reference will be requested by the search committee as appropriate. To apply, complete the online application at **https://facultyjobs.ua.edu/postings/44041** for the Ecohydrology position; or **https://facultyjobs.ua.edu/postings/44171** for the Marine Biology position, and upload all requested documents. Questions about the Ecohydrology position may be addressed to Dr. Jon Benstead (**jbenstead@ua.edu**; 205-348-9034) and for the Marine Biology position to Dr. Julie Olson (**jolson@ua.edu**; 205-348-2633). Consideration of applications will begin December 15, 2018 and will continue until the positions are filled. Prior to hiring, the final candidates will be required to pass a pre-employment background investigation. The anticipated start date is August 16, 2019. Additional information about the Department of Biological Sciences and these positions can be found on our website at **http://bsc.ua.edu**. Applications from women and members of under-represented groups in Biology are especially encouraged. The University of Alabama is an Equal Opportunity/Equal Access Employer and actively seeks diversity among its employees.

THE UNIVERSITY OF ALABAMA®

Not just for bots:

The changing career landscape in AI

Artificial intelligence (AI) is impacting science in new and exciting ways as researchers are using it to better understand society and find solutions to problems across diverse disciplines. And as the application of AI expands, so too do the career opportunities.

By Alaina G. Levine

Artificial intelligence (AI) is an exploding discipline, and the race is on to deploy it to make products and services smarter, faster, and able to accomplish tasks that humans simply cannot do. With this ultramarathon of investments in AI across many sectors around the globe, including academia, comes new career opportunities.

There is a growing realization that as AI expands, certain jobs will die out. But on the other side of this (bit) coin, there is an increasingly urgent need for experts to help build AI models, and for domain experts who are strategic and creative enough to envision ways to use AI in their specialty. In fact, the World Economic Forum reports that the fastest growing skill on LinkedIn is AI.

So what exactly is AI? **Zhi-Hua Zhou,** professor and head of the Department of Computer Science and Technology at Nanjing University in Nanjing, China, and dean of the university's School of AI, puts it simply:

"AI researchers are trying to invent/develop techniques and tools that are able to help people to do work that requires some intelligence. With the help of these techniques and tools, people will find life easier and more enjoyable because more time and energy can be used to do interesting rather than boring things. AI can be analogous to steam power: Steam power helped humans to do manual labor, while AI will help humans to do intellectual labor."

Maggie Johnson

Wanted: Domain experts

In the dynamic world of AI, where data science, deep learning, and machine learning are being used to improve products and outputs in fields as far apart as astronomy, health care, transportation, security, and banking, scientists and engineers are finding that their skills are highly prized in multiple career tracks and sectors, says **Maggie Johnson,** vice president of Education and University Programs for Google, where she manages technical education for all Google staff. In a firm like Google, she notes, there are those with Ph.D.'s in highly technical AI-adjacent areas, such as computer science, statistics, mathematics, and data science. "They are defining the actual algorithms and what the models look like," she says.

As the models have become more sophisticated, these technical AI experts have found professional paths in R&D divisions, where they conduct ongoing research as "consultants"—helping different arms of their company with AI needs, and most interestingly, working in product teams across entire organizations.

This fanning-out of AI expertise among various enterprises has naturally led to another path for Ph.D.'s: as domain experts who comprehend AI well enough to successfully apply its models to improving systems in their discipline, notes Johnson. They need to have programming skills and knowledge of computer languages, such as Python, for instance—but it's more critical for them to be able to see the potential for advancing products that incorporate AI. Take for example, a project at Google, where employees are aiming to use AI in the health care space to diagnose disease through retinal scans.

IMAGES: (FROM TOP) © DANI3315/SHUTTERSTOCK.COM; GOOGLE

Upcoming features

Postdocs: Careers in Diversity–February 1 ■ Cancer Research: Precision Medicine–March 15 ■ Postdocs: DIY and Science Hacking–August 30

"We actually hire doctors," says Johnson. "We bring in physicians and scientists because we can't understand the datasets, but they do."

And Google is not the only firm that sees the value of hiring scientists and engineers for AI-innovation roles. If you have a doctorate in niche areas such as epidemiology, materials science, physics, plant sciences and agriculture, or industrial engineering—among others—chances are there is a company that can utilize your knowledge as they build AI-centric products. At Hitachi Limited, the Tokyo-headquartered multinational conglomerate with interests in construction machinery, railway systems, elevators, health care, banking, and government systems and infrastructure, Fellow **Kazuo Yano** (whose doctorate is in physics) leads AI investigations.

Yano sees his role as both strategic and tactical. "I am writing code for AI as well as talking to customers," he says. "The customers don't know what AI is or what it can provide for them. I understand the very real requirements of the customers and the market."

But for the product teams, it is imperative to have highly educated domain experts, adds Yano. "We have a lot of researchers and engineers who are domain specialists, such as railway experts and finance experts who joined the AI team to make those systems smarter," he says.

In fact, **Avik Sarkar,** officer on special duty and head of the data analytics cell for the National Institution for Transforming India (NITI Aayog), a government-focused think tank based in New Delhi, believes that domain specialists are the future of AI. "Become a domain expert," he says. "The wonders and magic of AI only work when you know your domain very well."

At 3M, the powerhouse materials science company based in Minneapolis-St. Paul, Minnesota, **Jennifer Schumacher,** whose varied background includes a Ph.D. in neuroscience, cofounded and leads research in the AI Cluster in the Corporate Research Systems Laboratory (CRSL).

Schumacher and her team can contribute to any of 3M's diverse products and businesses; most recently, the team has incorporated AI and data science solutions into digital displays, traffic signs, HVAC filters, digital oral care, and even Post-it notes. **Yixiong Chen,** senior product engineer in 3M's CRSL in Shanghai, aims to do the same for 3M's clients and interests in Asia. He graduated with a Ph.D. in control theory and control engineering only four years ago from the Chinese Academy of Sciences. "We are trying to find opportunities in our organization to deploy this technology and introduce AI-related knowledge to 3M China," he says. "This is a growing team."

Deep learning in academia *and* industry

Scientists who like the culture of academia and the impact of industry may be interested to know that it is possible to craft a career in AI that spans both, as **Joelle Pineau** has done. She is a professor of computer science at McGill University and the leader of the Facebook AI Research team in Montreal. "When it comes to working in AI, there is a huge spectrum of positions," says Pineau, adding that more universities are open to this type of job model.

PHOTO: FACEBOOK

Joshua Bloom is another example—he holds a professorship in the astronomy department of the University of California, Berkeley, while working at GE Digital as vice president for data analytics (which includes AI-related projects). "I am more aware of joint appointments in faculty and industry than I was five years ago," he shares.

"When it comes to working in AI, there is a huge spectrum of positions."
—Joelle Pineau

He came to his dual career when, as a university researcher, he saw a huge uptick in the volume of astrophysical data and no way to parse and understand it in a reasonable amount of time. He not only devised solutions for astronomy, but ended up using his machine-learning knowledge to cofound a company, which was then acquired by GE Digital. His new "mothership" was quite happy for him to continue his scholarship in academia while contributing to their data science and AI interests within the context of the company.

Because the potential for AI applications is seemingly limitless, the career opportunities are growing like gangbusters. "There are no defined [career] ladders, but one can surely move step-by-step in order to adopt an influential career in AI," says **Komal Sharma Talwar,** cofounder of an intellectual property and technology analytics tool, XLPAT, and founder of TT Consultants (headquartered in Chandigarh, India, with offices in Taiwan and the United States). "Once you know about data science, machine learning algorithms, and models, your next career choice is deciding what job you really want," she notes. "However, the path does not end there. To be successful in the AI domain, one should continue to learn higher-level algorithms and how to apply them for different functions."

The code to career opportunities

Recruiting for AI roles in industry, in both the R&D and domain divisions, can be "unconventional," says Yano. For AI researchers who want to build the "engines" of AI, a strong theoretical physics or mathematics background is useful, he says, pointing to one of his colleagues who joined Hitachi recently with a background in theoretical particle physics after having spent a decade in academia. Pineau looks for people with very strong mathematical and programming skills, but also those

cont.>

Joshua Bloom

Featured participants

3M
www.3m.com

Computer Science and Artificial Intelligence Laboratory (CSAIL), Massachusetts Institute of Technology
www.csail.mit.edu

Facebook AI Research
research.fb.com/category/facebook-ai-research

GE Digital
www.ge.com/digital

Google AI
ai.google.com

Hitachi Limited
www.hitachi.com

McGill University
www.mcgill.ca

Nanjing University
www.nju.edu.cn/en

National Institution for Transforming India–NITI Aayog
niti.gov.in

University of California, Berkeley
www.berkeley.edu

University of Oviedo
www.aic.uniovi.es

XLPAT
www.xlpat.com

who "have a spark and are hungry to learn, who have initiative and curiosity, who want to jump in and learn and exercise autonomy." **Pete Warden,** technical lead of Google's Research Machine Intelligence Division in Palo Alto, California, adds that "the single biggest skill we look for is the ability to experiment and be able to work through problems in a disciplined way."

To recruit AI professionals who can "apply state-of-the-art technology to the real world," says Yano, you have to think outside the box. "The field is changing so much that [candidates] have to be flexible . . . and need experience with real-world data." This is key, adds Bloom. "Get real-world experience," he echoes. "That means owning something and building something that someone uses and contributes to."

For recruitment purposes, Warden relies on competitions that allow individuals to show off their programming skills. Google runs its own set of open-source data science competitions, called Kaggle competitions, which serve as a metric and a credential for would-be engineers interested in gaining an advantage in the AI marketplace. Hackathons, where computer programmers get together [either virtually or in real life (IRL)] and collaborate to develop a usable product, can also serve this purpose.

However, there is disagreement as to the virtues of these online competitive programming events. Bloom says that you need to have experience scaling-up your work. "There is a wide gulf between people who win Kaggle competitions and those who can build code that can be robust and trustworthy in production . . . it's as big a gulf as you can imagine. Given the brittleness of AI, the attention to that kind of detail, and [the fact] that what you build is only going to be a larger part of a machine, you can't teach that," he says. "We look not only for experience in programming and AI, but also for people who have lived the pain of seeing it through to production."

This "pain" can be experienced through an internship, something that Talwar highly encourages. "For those about to graduate, they should try their hands at real data through internships in order to be well acquainted with AI algorithms and how to apply them," she stresses.

Daniela Rus, director of the Computer Science and Artificial Intelligence Laboratory (CSAIL) as well as the Andrew (1956) and Erna Viterbi Professor of Electrical Engineering and Computer Science at the Massachusetts Institute of Technology (MIT) suggests doing internships at startups—or it could also mean learning about many of these concepts on your own. "Academic institutions like MIT offer a lot of their courses online, including ones aimed at working professionals who want to build their knowledge in big data, cybersecurity, and the Internet of Things," she says.

In addition to online platforms like those at MIT, there are many others, such as Coursera, where one can take courses and learn these skills. There are also intensive fellowships where Ph.D. scientists and engineers get to address real-world problems presented by partner companies. The Insight Data Science Fellows Program is one example that continues to expand.

"Just do it. Jump in," says Schumacher. "If you are not formally trained, there are publicly available ways to prove you have these skills—so leverage all the resources [you can] online."

The future of AI careers

The future is bright for STEM-educated pros from all fields to work toward a career in AI. As **Beatriz Remeseiro,** assistant professor in the computer science department at the University of Oviedo, Spain, shares, "AI experts have become some of the most in-demand and best-paid talent in today's technological marketplace." Talwar agrees, adding, "The world is moving toward automation at a fast pace, and so is the demand for AI skills."

Zhou notes that now is an especially exhilarating time to be in AI, both from the perspective of enjoying its technical challenges and because of its job outlook. "AI is beginning to change our lives and the world, and it is exciting to get involved," he says. "It is a young but flourishing field, where there are many interesting and challenging problems waiting to be conquered. Furthermore, the world has a serious shortage of AI experts, and a big job market is waiting for people who pursue these careers."

Alaina G. Levine is a science writer, science careers consultant, professional speaker, and author of *Networking for Nerds* (Wiley, 2015).

PHOTO: PEG SKORPINSKI

PURDUE UNIVERSITY

Tenure-Track Professorships in Quantum Information Science
Departments of Chemistry and Physics & Astronomy
College of Science, Purdue University

The Departments of Chemistry and Physics & Astronomy in the College of Science at Purdue University invite applications for up to five positions in Quantum Information Science (QIS). These positions would be at the assistant/associate level with the potential for full professor appointments based on scholarly record. When appropriate, successful candidates may be considered for joint and interdisciplinary appointments across the College.

QIS is at the frontier of several traditional research disciplines including condensed matter physics, atomic, molecular, and optical physics, information theory, applied math and computer science, and chemistry. QIS strives to harness the unusual quantum mechanical properties of superposition and entanglement to provide breakthrough advances for computing, secure communications, and novel device functionalities. As such, QIS is part of a large-scale interdisciplinary hiring effort across key strategic areas in the College of Science—Purdue's second-largest college, comprising the physical, computing, and life sciences—these positions come at a time when the College is under new leadership and with multiple commitments of significant investment.

The College of Science is especially seeking to enhance our existing strengths in research at the interface of Chemistry and Physics and growth within Computer Science and Math through strategic hiring of creative scientists to be part of the cutting-edge interdisciplinary environment provided by Purdue University. Successful candidates will have research interests that can build a comprehensive suite of capabilities in experimental and/or theoretical quantum computing with superconducting qubits, spins in semiconductors and other condensed matter systems, cold atomic ions, Rydberg, photonic systems chemical physics, or quantum materials. Also of inherent interest for progress in this field are quantum algorithm research and information theoretic analysis.

Candidates must have a PhD in physics, chemistry, math, and computer science, or other fields related to QIS, with outstanding credentials in research, an excellent track record of publications and potential for developing a vibrant research program, as well as a strong commitment to excellence in teaching. Successful candidates are expected to develop a vibrant research program supported by extramural funding and teach courses at the undergraduate and/or graduate level. Applicants should submit a letter of application electronically, including their curriculum vitae, summary of planned research, and a statement on teaching philosophy, to: **https://hiring.science.purdue.edu/**. Applicants should also arrange for three letters of recommendation to be uploaded. Applications will be reviewed beginning **December 1, 2018**, and will remain in consideration until the position is filled.

All of Purdue University's Departments are committed to advancing diversity in all areas of faculty effort, including scholarship, instruction, and engagement. Candidates should address at least one of these areas in their cover letter, indicating their past experiences, current interests or activities, and/or future goals to promote a climate that values diversity and inclusion.

A background check will be required for employment in this position. Purdue University is an ADVANCE institution.

Purdue University is an EOE/AA Employer. All individuals, including minorities, women, individuals with disabilities, and veterans are encouraged to apply.

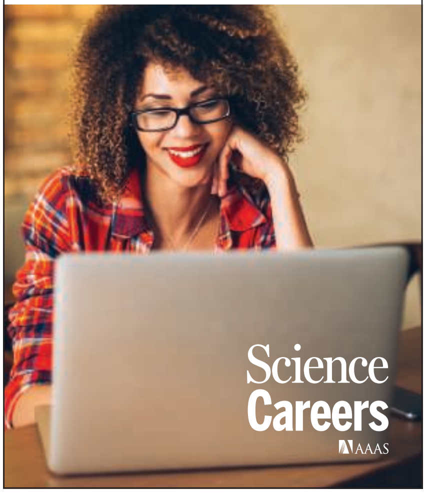

Stony Brook University

Assistant Professor
Molecular Genetics and Microbiology
Center for Infectious Diseases

The successful candidate will establish a vigorous extramural research program in the area of tick-borne diseases, participate in the Department's educational mission of graduate and medical school teaching, and perform university and departmental service.

The Department (**http://www.mgm.stonybrook.edu/index.shtml**) and the adjacent Center for Infectious Diseases (**http://www.stonybrook.edu/commcms/cid/**) provide a highly interactive scientific community. The Department and School of Medicine have been at the forefront of research on tick-borne diseases, including pivotal contributions toward discovery and characterization of the Lyme disease agent. The position offers competitive startup support and salary, quality research space, and a dynamic intellectual environment. Stony Brook University maintains state-of-the-art core facilities that deliver support in a number of areas including microscopy and animal imaging, flow cytometry and cell sorting, genomics, transcriptomics, proteomics, bioinformatics, animal maintenance, and BSL3 containment. The recently completed Laboratory for Comparative Medicine includes an insectarium and provides facilities for animal BSL3 studies.

Required Qualifications: Ph.D. or M.D. and at least three years of postdoctoral experience. Established research in the area of tick-borne diseases.

Preferred Qualifications: Candidates that demonstrate the ability to obtain extramural funding are preferred.

To ensure full consideration, applications should be received by January 31, 2019. Review of applications will continue until the position is filled. Those interested in this position should submit a State Employment Application, cover letter, CV, three-page research statement, and the names and addresses of three references as a compiled PDF to **mgm_facultyposition@stonybrook.edu** (on line submission required). Competitive applicants will be asked to have letters of recommendation sent to the search committee at a later date. Please also fill out an online Applicant Information Survey. Do not submit this survey to the department.

Faculty Search Committee - Tick Borne Diseases
Molecular Genetics and Microbiology
130 Life Sciences Building, Stony Brook, NY 11794-5222
Email: mgm_facultyposition@stonybrook.edu

For a full position description or application procedures, visit:
www.stonybrook.edu/jobs (Ref. # F-9962-18-11)

Stony Brook University is an affirmative action/equal opportunity employer and educator.

INSPIRING INNOVATION

Two $100K (CAD) prizes recognizing research excellence and community engagement that tackle the global challenge of sustainably, equitably and nutritiously feeding the world's growing population. Nominations for the 2019 awards close January 31st, 2019. Visit **arrellfoodinstitute.ca** to learn more.

Arrell Global Food Innovation Awards

Neuroscience Post-doctoral Programme

Linköping University is one of Sweden's six large universities, currently enrolling 27,000 students. The Centre for Systems Neurobiology involves some 50 independent research groups, from the Faculty of Medicine and the Faculty of Science and Engineering, as well as the University Hospital.

The Centre for Systems Neurobiology is now seeking Postdoctoral Fellows within several neuroscience research areas: Neurodegenerative disease, Neuroendocrinology/neuroimmunology, Neuroimaging/modelling, Neurophysiology, Psychiatric neuroscience and addiction, and Sensory systems. Applications will be reviewed continuously. For full consideration please apply as soon as possible.

LINKÖPING UNIVERSITY

For more details regarding the Centre, the different research labs involved in the programme, and to submit a letter-of- intent please visit: liu.se/en/research/center-for-systems-neurobiology. For information regarding the university and the region, please visit: liu.se, eastsweden.com.

WORKING LIFE

By **Francis Aguisanda**

At the end of the road, a new start

I never thought my mom's first tour of Stanford University would be of the psychiatric ward. When I arrived in sunny California 2 years earlier to start my Ph.D. studies, I was on top of the world. But that feeling of triumph vanished quickly. The uncertainty that had nagged at me for years grew overwhelming. I loved learning new things and talking about science, yet I couldn't envision working at the bench for the rest of my life. But after building my identity around being a scientist, how could I turn away? Stanford was, in many ways, my Hail Mary. If I was going to be happy, it had to be there—right?

I loved the students in my program. My classes were marvelously interesting and challenging. I found a mentor who cared about his students. I was pursuing fascinating research questions. I had a nice apartment, the most supportive and wonderful girlfriend imaginable, and loving parents. Despite all this, I was profoundly unhappy.

When you have so much to be thankful for, are you really going through a hard time? I was suffering under the simmering pressure of graduate school. But graduate students are expected to work hard. I didn't see my problems as legitimate, so I didn't seek help.

That was my biggest mistake. I had behaved similarly a few years earlier, when the end of a long-term relationship sent me spiraling into a deep depression. I didn't seek help then either, and I was proud of the fact that I didn't need any. I had more important things to do than focus on my own sadness.

ILLUSTRATION: ROBERT NEUBECKER

"I didn't see my problems as legitimate, so I didn't seek help."

In grad school, I kept giving myself milestones when I thought I would stumble upon happiness. Maybe after I passed my classes, I'd be happy. Maybe after I found the right lab and project, I'd be happy. I tried to kick the proverbial can so far down the road that it would disappear over the horizon. But there it was, staring me in the face: joy, just beyond my reach.

It's difficult to describe what it feels like to reach the end of the road. For me, it meant months of leaving the lab in the middle of the day because I couldn't breathe, anxiety wrapped around my throat and refusing to let go. I would sneak to a secluded corner under a staircase to cry or sit in the pews of the beautiful campus church, hoping that the heavy doors would keep terrible thoughts from breaking in. One day, I stayed home from lab. I made my coffee, answered emails—and prepared to end my life.

But as I talked to my girlfriend that afternoon, I found myself telling her that I was having bad thoughts. She dropped everything, ran home to see me, and called a hotline. The therapist recommended that I go to the emergency room.

The doctors diagnosed me with major depressive disorder, with episodes of anxiety. After 6 days in the psychiatric ward, I spent 3 months going to therapy for 20 hours a week and started to take antidepressants. My graduate school life came to a screeching halt. I felt guilty for leaving the lab so abruptly, but my graduate program director sent a simple, welcome message: Take all the time you need, and we'll be ready to talk when you are.

Hitting a brick wall as fast as I did was a pretty clear sign that I needed to make some changes. A few months after leaving the hospital, I set up a meeting with the program director, bracing myself for what I thought was the inevitable end of my graduate school career. My director, however, proposed a solution I hadn't thought possible: What if I stayed in the program but left the bench and studied what I really love?

Now, that's exactly what I'm doing, exploring the world of science communication research. And before you ask, no, I have no idea where it will lead. But thinking about my future now fills me with a grand sense of adventure—not the dread I used to feel when I considered working another day in the lab. My director has made it clear that my mental health is his priority, and that it should be mine as well. That expectation has made a world of difference. ■

Francis Aguisanda is a Ph.D. student at Stanford University in Palo Alto, California, and a crisis counselor for the U.S. National Suicide Prevention Lifeline (1-800-273-8255).

Send your career story to SciCareerEditor@aaas.org.

Published by AAAS